Proceedings of the Twentieth Annual Precise Time and Time Interval (PTTI) Applications and Planning Meeting

A meeting held at the
Sheraton Premiere Hotel
Tysons Corner/Vienna, Virginia
November 29- December 1, 1988

Proceedings of the Twentieth Annual Precise Time and Time Interval (PTTI) Applications and Planning Meeting

A meeting held at the
Sheraton Premiere Hotel
Tysons Corner/Vienna, Virginia
November 29 - December 1, 1988

Sponsored by

U.S. Naval Observatory
NASA Goddard Space Flight Center
Space and Naval Warfare Systems Command
Naval Research Laboratory
National Institute of Standards and Technology
Army Electronics Technology
and Devices Laboratory
Rome Air Development Center
USAF Space Command

PRECISE TIME AND TIME INTERVAL (PTTI) APPLICATIONS AND PLANNING MEETING

ORDER FORM FOR PROCEEDINGS

	Year	Cost	Available	Unavailable
1	1969			X
2	1970	$25.00	X	
3	1971	$25.00	X	
4	1972			X
5	1973			X
6	1974	$25.00	X	
7	1975	$25.00	X	
8	1976			X
9	1977			X
10	1978	$25.00	X	
11	1979	$25.00	X	
12	1980			X
13	1981		X	
14	1982	$25.00	X	
15	1983			X
16	1984	$25.00	X	
17	1985	$25.00	X	
18	1986	$20.00	X	
19	1987	$25.00	X	
20	1988	$35.00	X	

Please circle copy(ies) requested and make out the check to "Treasurer, PTTI". **Please do not add personal names or addresses to the pay line on the check.** We cannot accept invoices. Please return the check and the Order Form to:

Mrs. Sheila Faulkner
Chairman, PTTI Executive Committee
U.S. Naval Observatory
Time Service Department
34th and Massachusetts Avenue, N.W.
Washington, D.C. 20392-5100

(202/653-1460)

It is with great regret that we must announce we can no longer absorb the cost of air mailing the "Proceedings" to international addresses; therefore, the "Proceedings" will be sent by Surface Mail. However, if you wish to pay the air mail postage, we will notify you of the cost before mailing. For example, Air Mail to Europe is currently estimated at $26.00 for the first 4 pounds. Each additional half pound is over $3.00.

When you register for the PTTI Meeting or order the "Proceedings", your name is added to the Mailing List to automatically receive future meeting information and a copy of the Proceedings.

EXECUTIVE COMMITTEE

Sheila C. Faulkner, Chairman
U.S. Naval Observatory

David W. Allan
National Institute of Standards and Technology

James A. Buisson
U.S. Naval Research Laboratory

Jimmie B. Collie
Space and Naval Warfare Systems Command

Hugh S. Fosque
NASA Headquarters

Raymond Granata
NASA Goddard Space Flight Center

Denise A. Kaya
USAF Space Command

Dr. William J. Klepczynski
U.S. Naval Observatory

Dr. Arthur O. McCoubrey
National Institute of Standards and Technology

Dr. John R. Vig
Army Electronics Technology and Devices Laboratory

D . H. Beat Wackernagel
AF Space Command

Dr. Joseph D. White
U.S. Naval Research Laboratory

Dr. Gernot M.R. Winkler
U.S. Naval Observatory

Dr. Nicholas F. Yannoni
Rome Air Development Center

OFFICERS

GENERAL CHAIRMAN
PROFESSOR BRADFORD PARKINSON
Stanford University

TECHNICAL PROGRAM COMMITTEE
CHAIRMAN
DR. HENRY FLIEGEL
The Aerospace Corporation

ASSISTANT TECHNICAL PROGRAM
COMMITTEE CHAIRMAN
S. CLARK WARDRIP
Bendix Field Engineering Corporation

EDITORIAL COMMITTEE CHAIRMAN
DR. RICHARD L. SYDNOR
Jet Propulsion Laboratory

PUBLICITY COMMITTEE CHAIRMAN
JIMMIE B. COLLIE
Space and Naval Warfare Systems Command

TECHNICAL ASSISTANCE
PAUL KUSHMEIDER
Bendix Field Engineering Corporation

SESSION CHAIRMEN

SESSION I

Michael Ellett

Hughes Aircraft Company

SESSION II

William J. Klepczynski

U.S. Naval Observatory

SESSION III

Edward C. Jones

Naval Research Laboratory

SESSION IV

Ronald Beard

Naval Research Laboratory

SESSION V

James Wright

Computer Sciences Corporation and Raytheon Company

ARRANGEMENTS

Sheila C. Faulkner
Paul J. Kushmeider

FINANCE COMMITTEE

Dr. William J. Klepczynski
Sheila C. Faulkner

RECEPTIONISTS

Nicolette Jardine, U.S. Naval Observatory
Bettejean McNight, Naval Research Laboratory
Betty Wardrip, Bendix Field Engineering Corporation
Frances Wright, Naval Research Laboratory

PTTI ADVISORY BOARD COMMITTEES

1989

OFFICE	NAME	ORGANIZATION
Chairman	Mr. S. Clark Wardrip	BFEC
Vice Chairman	Mr. Martin B. Bloch	FEI
Finance Committee	Mr. Martin B. Bloch, Chairman	FEI
	Mr. S. Clark Wardrip	BFEC
	Mr. James L. Wright	CSC/RC
Exhibits Committee	Dr. Martin Levine, Chairman	FTS
	Dr. James A. Barnes	Austron
	Mr. Jack McNabb	TRAK
	Mr. William J. Riley	EG&G
	Mr. Don Mitchell	Austron
	Dr. Robert F. C. Vessot	SAO
	Mr. Roger J. Hesse	DATUM
Guest Speaker Committee	Mr. Robert H. Kern, Chairman	KERNCO
	Professor Carroll O. Alley	University of Maryland
	Dr. Leonard S. Cutler	HP
	Professor Bradford Parkinson	Stanford University
	Dr. Victor S. Reinhardt	Hughes
	Dr. Samual R. Stein	Ball/Efratom
	Dr. Richard L. Sydnor	JPL
Reports Committee	Mr. Terry N. Osterdock, Chairman	STI
	Mr. Alvin G. Bates	APL
	Mr. Paul F. Kuhnle	JPL
	Mr. Paul J. Kushmeider	BFEC
	Professor Harry Robinson	Duke University
	Mr. Philip E. Talley	Aerospace

NOTE: NON-GOVERNMENT OFFICERS OF THE PTTI ARE AUTOMATICALLY MEMBERS OF THE PTTI ADVISORY BOARD FOR THE YEAR(S) THAT THEY ARE IN OFFICE.

1989 PTTI ADVISORY BOARD MEMBERSHIP

Prof. Carroll O. Alley
University of Maryland
Department of Physics and Astronomy
College Park, Maryland 20742
301/454-3405

Dr. James A. Barnes
Austron, Inc.
3300 Mitchell Lane
Boulder, Colorado 80301
303/440-7282

Mr. Alvin G. Bates
Johns Hopkins University
Applied Physics Laboratory
Johns Hopkins Road
Laurel, Maryland 20707
301/953-5419

Mr. Martin B. Bloch
Frequency Electronics, Inc.
55 Charles Lindbergh Boulevard
Uniondale, New York 11553
516/794-4500

Dr. Leonard S. Cutler
Hewlett-Packard Company
1651 Page Mill Road
Palo Alto, California 94304
415/857-5259

Dr. Henry F. Fliegel
The Aerospace Corporation
Building 120, M5/685
2350E El Segundo Boulevard
El Segundo, California 90245
213/336-7452

Mr. Roger J. Hesse
DATUM
1363 S. State College Boulevard
Anaheim, California 92806
714/533-6333

Dr. Martin Levine
Frequency and Time Systems, Inc.
34 Tozer Road
Beverly, Massachusetts 01915
617/927-8220

Mr. Robert H. Kern
Kernco, Inc.
28 Harbor Street
Danvers, Massachusetts 01923-0678
617/777-1956

Mr. Paul F. Kuhnle
Jet Propulsion Laboratory
4800 Oak Grove Drive
M/S 298
Pasadena, California 90803
818/354-2715

Mr. Paul J. Kushmeider
Bendix Field Engineering Corporation
One Bendix Road
Columbia, Maryland 21045
301/964-7672

Mr. Jack McNabb
TRAK Microwave Corporation
4726 Eisenhower Boulevard
Tampa, Florida 33614-6391
813/884-1411

Mr. Donald Mitchell
Austron, Inc.
P.O. Box 14766
Austin, Texas 78761-4766
512/251-2313

Mr. Terry N. Osterdock
Stanford Telecommunications, Inc.
2421 Mission College Boulevard
Santa Clara, California 95054
408/982-5903

Professor Bradford W. Parkinson
Stanford University
Hamsen Labs, Via Palou
Stanford, California 94305-4085
415/726-1454

Dr. Victor S. Reinhardt
Hughes Aircraft
Space and Communications
S12/W322, P.O. Box 92919
Los Angeles, California 90009
213/416-0160

1989 PTTI ADVISORY BOARD MEMBERSHIP (Cont.)

Mr. William J. Riley
EG&G, Inc.
35 Congress Street
Salem, Massachusetts 01775
617/745-3200

Professor Harry Robinson
Duke University
Department of Physics
Durham, North Carolina 27706
919/684-8226

Dr. Samuel R. Stein
Ball Efratom Division
P.O. Box 589
Broomfield, Colorado 80020
303/460-2017

Dr. Richard L. Sydnor
Jet Propulsion Laboratory
4800 Oak Grove Drive
M/S 298
Pasadena, California 91109
818/354-2763

Mr. Philip E. Talley
The Aerospace Corporation
550 Margo Avenue
Long Beach, California 90803
213/336-7597

Dr. Robert F. C. Vessot
Smithsonian Astrophysical Observatory
60 Garden Street
Cambridge, Massachusetts 01945
617/495-7272

Mr. S. Clark Wardrip
Bendix Field Engineering Corporation
P.O. Box 6147
Vandenberg Air Force Base,
California 93437
805/865-3214

Mr. James L. Wright
CSC and Raytheon Company
Eastern Test Range
Building 989, MU 840
Patrick Air Force Base, Florida 32925
305/494-2014

FOREWORD

These Proceedings contain the papers presented at the Twentieth Annual Precise Time and Time Interval Applications and Planning Meeting. The meeting was held at the Sheraton Premiere Hotel in Tysons Corner, Virginia. A good attendance at the meetings and the banquet was an indication of the continuing interest in the field. We had a number of invited papers, some of which are included in these Proceedings. Some papers are missing because they were not received in time for publication. The question and answer periods following each talk are included, but they are marred this year by the lack of cooperation among the questioners in not speaking with the microphones.

There were 205 registered attendees (down from 225 last year). Of the attendees, 119 were from East of the Mississippi (67 last year), 62 were from West of the Mississippi (137 last year) as well as 24 from 11 foreign countries (17 from 9 last year).

The objective of these meetings is to provide an opportunity for program planners to meet those who are engaged in research and development and to keep abreast of the state-of-the-art and latest technological developments. At the same time, they provide an opportunity for engineers to meet program planners.

The success of these meetings depends on the efforts of the Program Chairman and the Individual Session Chairmen and the organization of the entire meeting by the Chairman of the Executive Committee. Without their unstinting labor, such meetings could not be held.

The purpose of the PTTI Applications and Planning Meeting is to give Managers, Systems Engineers, Program Planners, and Industry:

- A forum for presentation and discussion of current and future programs and requirements
- A general and in-depth review of plans and trends in PTTI applications
- An opportunity to discuss results, accomplishments, and problem areas in the application of PTTI technology
- A review of new developments which influence PTTI applications

CONTENTS

SESSION III
Alternative Time Transfer Techniques

Chairman: Edward C. Jones
Naval Research Laboratory

SESSION IV
Solving Timing System Problems

Chairman: Ronald Beard
Naval Research Laboratory

SESSION V
New Developments in Timing Applications

Chairman: James Wright
Computer Sciences Corporation and Raytheon Company

Aspects of Coordination (Management) of Precise Time and Time Interval (PTTI) Systems.

Gernot M. R. Winkler
U.S. Naval Observatory
Washington, DC. 20392–5100

Those who do not remember the past
are condemned to relive it.
Santayana

INTRODUCTION

Systems that use precise timing and/or precise frequency are generally electronic systems that operate over extended geographical areas and involve many different types of equipment. The concept development, implementation management, and operation of such systems present, of course, all the problems that arise if we deal with large, diversified systems. The only thing one can say in general terms is that in almost all such cases, with very few exceptions (the Polaris submarine system, or the U–2 projects were such exceptions), totally unforeseen problems arose that forced a scaling down, increasing costs, and delaying substantially, or even preventing, the completion of the system. In retrospect this is easy to see. What is very difficult is foresight, i.e., to find out at the very beginning of the project how improvements could be accomplished and costly pitfalls avoided. This is even more important in the case of systems that involve PTTI. The problems that are peculiar to PTTI are amenable or altogether avoidable with a relatively small effort if, from the very beginning, one is aware of past similar problems in other systems [1]. This contribution discusses broadly the specific PTTI problem areas as they arise in the R&D phase; it will also address questions of operations; finally it will touch upon questions that usually arise whenever we have to "coordinate" anything. (The quotation marks are to indicate that this is a popular euphemism for situations where you will be blamed without having had real authority.)

THE DENIAL PHASE

In almost all cases of PTTI systems R&D that I have observed over the last thirty years, the system managers denied that they were to be concerned with timing. "No, we only use precise frequency control, only relative synchronization is needed, we must remain completely independent". These are some of the comments one hears when the question of timing is raised by the consultant or observer who learns about the new system. It is, of course, an entirely natural attitude because why would any manager want to become involved with questions that do not seem germane to the task? It should be easy to inform people that experience shows that one will get involved with typical timing problems even if one can't see it yet. But unfortunately, the denial attitude is supported, strengthened, and advanced beyond a reasonable degree by the present management culture that insists on overly precise cost estimates and cost accounting from the beginning. It is always hard to explain in detail the

reasons why one proposes to include in the estimated budget items that have no obvious connection with the task at hand. But this forces from the very beginning of the project an attitude of mind that is hostile to mental efforts over and beyond the absolutely necessary. I can only compare this with the constrictive effects of a cup of lemon juice taken as aperitif at the beginning of a dinner. The mind suffers constriction, too, in such a climate! In fact, we need the exact opposite effect. We need to enlarge our vision and expend a large part of the mental energy at the beginning of the project and not when we find that we are getting into trouble. This means that all possible scenarios must be envisioned and analyzed regarding their impact on the system under design. It is extremely difficult to convey to those who have not personally paid the price of past mistakes, the consequences of stopping too soon. I beseech you to envision, if you can, the full magnitude of our intellectual limitations. Following the eminent example set by Socrates 2400 years ago, it has always been seen as the highest achievement for the human mind to understand his own ignorance and to grasp the enormous difficulty in overcoming it, if only so slightly. There is no hope of gaining some insight unless this understanding is achieved first. I find no better way to illustrate this all important point then to give you in the appendix, with the author's permission for which I am most grateful, some personal reminiscences by "Jack" Pierce. His is the voice of many decades of experience, because he is the inventor of the Omega system and a truly eminent contributor to LORAN and other radio navigation and communications system technology.

It is true that the recommended extensive preparation may be costly. Possibly we have to call for help and advice ($500 to $1000 per day for an experienced consultant). But without doing this at the beginning, the chances are great that much more expensive problem- fixing will have to be done later or even towards the end of the development when these unforeseen problems will surface.

The best way to start is always with a pilot project that will allow the people who have to make decisions some familiarization with potential problems. The crucial questions that must be answered and clarified in the case of a PTTI system are the following: Why are precise clocks (or frequency standards) necessary, how often should they be re-calibrated to maintain system coherence, and in what environment must the equipment operate?

THE SPECIFIC TECHNICAL PTTI ASPECTS.

Suppose we find ourselves involved with such a project. Then we will examine the following details:

- 1. What clock (or frequency standard) performance is really needed? It is very important that we are realistic at this point. We must not specify much more than what is needed, including a margin of safety (as a rule of thumb, a factor of ten). I am a great believer in conservative designs, and the inclination to get the best available performers is natural and laudable, but we must remember that engineering is the art of finding a sound compromise between conflicting requirements. Price is the least important consideration compared with the other "payments" for excessively sophisticated choices. Super high performance clocks entail substantial problems such as shorter life, greater sensitivity to the environment, and expensive support.

- 2. What are the environmental conditions? This is also a very important subject. Lest we forget, high-precision timing and frequency control are applications of highly advanced technology. The environmental sensitivity of the devices used is a rather steep function of the performance expected. It may be more cost effective to increase environmental protection (such as shock and vibration absorbers, acoustic shielding, external temperature and humidity control) as compared with the use of specially hardened frequency standards. An obvious exception to this would be

radiation hardening where the use of lead very quickly leads to unacceptable weights. In such cases, different system approaches may be required.

- 3. How often can we re–calibrate the frequency standards and clocks? This brings us back to item 1. Why do we use high–performance clocks in the first place? What we gain is independence, in most general terms. The more independence we need, the greater the requirements for clock performance at the points where independence is needed. This seems like a silly triviality, yet I have witnessed lengthy committee meetings where one agonized over possible savings by putting greater stability into the operational center of a PTTI system at the expense of a substantial relaxation (use of cheaper clocks) at the outlying parts of the system. The original idea, why clocks were needed in the first place, was lost after several years of development and frequent changes. Again, why are clocks to be used at all?

- 4. What do we mean when we talk of synchronization? We must specify an acceptable time error within the system. Of course, it is always perfectly possible to avoid the use of high–precision clocks or frequency standards by re–calibrating at very short intervals. A good example is color television. The receivers use extremely cheap quartz crystal oscillators for the generation of the color reference phase (the 3.5 MHz subcarrier). The necessary precision is secured by phase locking the crystal oscillator to the transmitted color burst reference every 16 milliseconds (ms). As one can see, it is necessary to refine our concepts of synchronization. We must specify not only the acceptable tolerance but also the time interval over which this tolerance is to be maintained. In addition, we must also specify the measurement or calibration accuracy that is necessary to achieve and maintain the tolerance over the specified time. This last point is usually forgotten, but a rule of thumb is that we want to measure with the highest precision that can be achieved economically (at reasonable expense). Today that means the use of 1 ns resolution for time interval meters. As an example, assume that a tolerance of 1 microsecond (us) is required with re–synchronization in intervals of 10 days. That implies a frequency (rate) calibration to better than 100 ns/day (about 1 part in ten to the 12th). In order to do this within one hour, we need a counter resolution of 1 ns and also signals that can give us a precision of a few nanoseconds. Therefore, the stated tolerance of 1 us over 10 days entails a requirement for a 1 ns calibration capability. One can say that the operational requirement over a certain time and the need to calibrate (check) the clock in a reasonably short time entails a magnification factor for the timing precision, 240 in our example. Please note that the setting of requirements is not as simple as it often seems to be taken. All this, of course, assumes that the clocks can maintain the required frequency stability over the time specified.

- 5. How will the logistics and support for the PTTI equipment be arranged and managed? Clocks from reputable sources have MTBF's in excess of 30,000 hours. Such a performance is not easy to achieve and, indeed, after model changes the number drops immediately and will remain lower than before the change, until a continuing feedback loop from customer back to the development team and production can flush out the new weaknesses. Of course, there is going to be a problem if the development team has been disbanded in the meantime. While repair is best arranged through replacement and vendor repair, each larger PTTI system should have a central office or person to supervise the performance of the system (especially the clocks) and for record keeping. The office that started with the pilot projects, worked out the specifications, and did the design, should also arrange training and operational supervision. Even though our systems today are being designed with as much automation as possible built into everything, one must not believe that this will reduce the need for supervision completely. Another possible pitfall is in the acceptance of "turnkey" systems. The special requirements for training, performance

supervision, and logistics, after acceptance from the contractor, may not be fully recognized by the user who, up to this point, had no opportunity to develop sensitivities to problems peculiar to PTTI.

- 6. Primary and backup power for the PTTI instruments, particularly clocks, distribution amplifiers and time code generators, is also an important subject for study and concern. In the long run, this may well be the most important point to consider. In many locations it will be necessary to provide some form of backup generator to protect against longer outages. But public power may not only be unreliable, it is probably "dirty" as well. Therefore, it is highly recommended to operate all sensitive equipment from conditioned (no–break) power because experience has shown that equipment operating directly from public power has a significantly higher breakdown rate than equipment running from conditioned (e.g., no–break) power. This power source must never run motors, air conditioners, or anything that produces surges and voltage spikes; only the really critical equipment must be on this power source. In addition to AC backup, all critical equipment must have a DC backup. The use of small separate supplies is uneconomical and has a poor reliability record. There are large 24V (and 48V) supplies available that use large (automotive type size but high quality standby) batteries. These have a much longer life, do not need to be exercised, and cost relatively less than small batteries. It is imperative that a second, spare, or standby PTTI system, if available, must be operated from a second, independent power system to assure real standby capability. In other words, a "vertical" separation of the systems is required. It would even be desirable to schedule access and maintenance for this second system at times different from the main system because people are the source of the high correlation of "accidental" events (we tend to make a mistake thoroughly).

- 7. Operations. It is possible and inexpensive to automate, and control remotely, most of the regular operations such as measurements and adjustments. However, it would be a grave error to assume that this removes the need for careful selection and training of those who are in PTTI operations. Furthermore, all activities have a natural tendency to degenerate without continuous vigilance. Therefore, inspections or some form of quality control is mandatory. Unfortunately, when resources are cut, this is the first area that suffers because there are no immediate obvious effects. It is partially for this reason that performance specifications (such as measurement precision, clock tolerances, etc.) must be set to the highest level the system is capable of, whatever the system tolerance is. It is a most dangerous idea, but widely held, that a marginal performance is still acceptable, if it just meets the stated system tolerance. This almost amounts to permitting a time bomb in the system. It is the equivalent of a time bomb because by allowing slack in the system performance, one abandons the best and only way to discover immediately if something ill is developing, before the system operations are affected in dangerous ways. This is, after all, why mature designers will always use margins of safety to protect the system from the unforeseen small problems. In other words, we are recommending to operate in a way that maintains an operational margin of safety. One cannot press this point hard enough because a general spirit of permissiveness, once allowed entrance, will propagate rapidly and endanger the system before we know it. On the contrary, we must insist on a spirit of excellence and it would be beneficial if worker incentives could be provided for any consistent performance that is better than specified. Here, again, a superficial idea of cost savings may be a contributing factor. It is a mistaken idea because the costs of poor system performance or breakdowns are vastly in excess of the proposed incentives to excellence that would go a long way in prevention, or timely discovery, of serious problems.

- 8. The Benefits of Operating in Time Coordination with UTC Against Complete Independence. It is less expensive to use UTC as an external benchmark for a timed system as compared to a completely arbitrary rate and epoch, and it provides great operational benefits. The reason is simply that at negligible cost, the world's most advanced timing becomes available for calibration, stabilization, performance evaluation, and recovery after breakdowns [2]. A necessary condition for this is, of course, that interfaces with other PTTI systems have been designed into the system at key points. There is also no penalty in regards to an imagined dependency because, as we have seen above, one can make the "lifeline" arbitrarily long by simply setting tolerance and re–synchronization properly. There is also no penalty for classified systems to use UTC as benchmark because the progress of time, as such, is the most predictable thing we know and we can't and should not attempt to keep the time of day secret. It is the "when" that can be easily protected, if necessary. This understanding has been reached eventually by every timed system that I have observed, Omega, LORAN, Transit, DSCS, etc.; each one had to install more sophisticated PTTI capability as the operational experience dictated. The GPS is somewhat of an exception (but only in this respect) because it has been designed from the start with precision timing as the well understood central principle of operations [3]. A related question should also be mentioned. That concerns specifications of the interfaces for time codes and standard frequency. In this area, a new standard is being drafted by a working group involving NRL and others.

COORDINATION AND MANAGEMENT

It is not my intent to compete in these few comments with the flood of good advice that is available in print and in countless "How to Improve Your Managerial Performance" seminars. Of course, if you are a professional manager then you should stop right here, because you already know everything. Others, less professional, may want to avail themselves of some of the management bestsellers. Here, I wish only to make some remarks that reflect my own observations from having seen the fate of quite a few systems, from design to shutdown; and having worked in quite a few different environments.

There is no question that planning and control are essential for success. What I have observed, however, is that systems that were somehow protected from excessive management attention achieve a consistently superior performance compared to those that enjoy the full benefits of professional management. Here, I am offering my own explanation. Engineers and scientists have an instinctive respect for truth: they must find and understand the facts, unless they are phonies. (In this case they repeat the buzz words they hear from others). Engineers are also conservative and like to be careful. This is rather unique because everywhere else, the primary objective is not care and truth but expediency. This is particularly so in politics, in sales, and often in management. The higher up we go, the more urgent the call for expediency becomes. But one cannot serve two masters. Things look different if one's primary objective is expediency and not truth. It is much more difficult and requires much more doubt to see the facts as they are than most people realize.

I am not talking so much about the deliberate lie and distortion of truth. But, if you evaluate stated performance, an allowance for "optimism" must be made, particularly if the speaker is in the "sales" mode and not in the "objective" mode. Unfortunately, this bias is very different from case to case, making comparisons extremely difficult. In some cases I know, an extremely conservative attitude even goes the other way, claiming much less than is actually achieved routinely. The only way to resolve the problem is, again, to make inquiries and to rely on proven reputation. This is very difficult in the government procurement process which is still too occupied with the idea of least initial cost. I stress this point because our success will be exactly commensurate with the realism of

our assumptions and designs. This seems to be unknown in certain quarters because otherwise why would they thrive on euphemisms? The deliberate distortion seems to be an indispensable tool in much of modern life. In fact, we have become accustomed to this. The punishment, however, comes quickly when the perpetrators of the lie start believing it themselves. If this happens in management, the results will be serious. It makes them blind to reality and then they fall into the ditch. Even if there is no willful distortion, an excessive optimism, or lack of self critique is almost equally dangerous.

There are other observations that worry me. The fantastic success in many areas of science and technology, combined with certain deficiencies in our education and great luxury in lifestyles, has created a blasé attitude on the part of many, often coupled with outright intellectual arrogance (we know it all, we can do everything with money). How are we going to communicate in such a climate? Effective communication always requires a certain match of the intellectual level and a willingness, nay, eagerness on the part of the listener to understand the message. This is where the personal style and energy of the "coordinator" has to come in. In brief, what I recommend is a synthesis of a realistic optimism with a tremendous respect for the problems, of understanding the technical details and pitfalls, the selling of the project to those we need as partners, and the motivation of a high quality work force. It is particularly in this last area where the classical scientific management has failed because it was too simplistic. Yet much of our industry, and most of the actual operation of the government, is still dominated by obsolete ideas, many of them in new appearances. The worst of them is the idea that there is such a thing as management as such, without a specific technical background. In any high-tech area, and PTTI is definitely high-tech, you will fail unless you obtain, and can keep, a substantial commitment from your co-workers for high quality work. This can't be done with management buzz words or gimmicks. Loyalty, both ways, example, honesty, and technical competence are indispensable.

I have mentioned deficiencies in our education. The point that is important for us here, and that goes beyond the main concern of the current public debate and the recent report of a presidential commission[1], is the insufficient preparation for the complex situations with which we have to deal in the modern world, especially in complex modern systems and their management [4]. We see the conspicuous results of poor and immature management all around us. Most have their roots in a failure to grasp the difficulties in their full dimensions, and in a lack of vision (even interest!) for the magnitude of the likely consequences of hasty actions. It is so much easier to act than to think, and so many managers have the silly idea that acting, as such, with only quick and superficial intellectual preparation is all that is needed! (And if we know nothing we still can re-organize and change the name of the organization to something more impressive!)

I have discussed one remedy before, the General Systems Approach as an educational discipline [5]. Some familiarity, gained possibly in self study, with the abstract ideas of complex general systems (including catastrophe theory and concepts such as chaos) will, at least in some way, assist with an accelerated gaining of some degree of genuine wisdom, i.e., a feeling for the right measure. Without right measure we will vacillate between extremes. This feeling for the measure, therefore, is indispensable for deciding, not what can be done, but what should be done.

NOTES AND LITERATURE

[1] A technical overview of PTTI with some references has been given in my article "What Is PTTI?" in the 17th Proceedings of the PTTI, p.33-44.

[2] A very good example for the gradual learning of the benefits of operating on UTC is described

[1] American Education: Making it Work, William Bennet, April 29, 1988

in Mr. Vannicola's paper on the Omega system, in this volume.

[3] The parenthetical exception refers to the fact that even in this case other problems arose that forced substantial and costly changes late during development. At least a part of these complications would have been avoided if greater use could have been made of the substantial practical experience that had been gained with the operation of the pilot project, NRL's TIMATION. But this is not so easy in the face of all kinds of difficulties that arise, and compromises that must be made, in the process of getting large systems contracts under way.

[4] There is no question that our education has become too narrow. It had to be, because the universities and the students wanted to maximize the immediate utility of the young professional. In my opinion, we have gone much too far because the technology changes so rapidly that the first thing can only be to be firm in the fundamental principles; the specific details must be learned on the job at any rate. In addition, as we progress and take on greater responsibilities, we not only need additional professional skills, but also need to develop much broader views and sound judgment because no effort stands isolated on its own but is embedded in the system of our country and in our culture. The present educational background is of little help because of the narrowness and short range outlook of the curricula, except, of course, in the liberal arts. On the other hand, a liberal arts university education by itself can be useless, or even harmful, unless a practical trade or profession has been mastered in addition. Otherwise, the young noble person has been prepared for great things but will feel as an outcast because he can't do and can't understand practical, useful things. Hence the mandatory need for continuing self development of all. More details along these lines are given in my lecture notes on Self Development, available on request. In the meantime one must continue with his lifelong professional education but should also sometimes start with Plato if one is an engineer, and with a course in science, electronics, or computers, if one is a liberal arts major. C.P. Snow was the first one to observe the dangerous communications gap between the "Two Cultures" and those who followed his advice have been able to enrich their lives greatly and avoid the terrible shallowness so typical of much of modern management and science.

[5] As a very brief and superficial start that can only give an overall impression, see my paper "Introduction to Systems Approach" in the 10th Proceedings of the PTTI (p.1–15). I recommend some of the literature cited, particularly references 4, 12, 13, 25, 26, and 33. In addition to these it would be useful to gain an understanding of the basics of catastrophe theory because, by gaining insight into the causes of system collapse, one will hesitate stressing a system more than necessary. As long as one keeps intellectually curious and active one will avoid a dangerous narrowing of his views. For those who are engaged in creative work, or have responsibilities in any way connected with such work, one should recommend a repeated reading (once per week) of the following appendix. I believe it conveys the essence of excellence.

APPENDIX

"NEVER STOP THINKING"

J. A. Pierce

My text is intended to warn against the danger of believing that one has finished. The feeling of triumph that he enjoys when he has reached the end of a difficult course may itself be enough to blind him to any further advance that might be possible. In

a foot race, or when killing an enemy, a clear end can be distinguished. But in most activities in life, every achievement is usually only a step on a long path.

An early violation of the truth I am claiming came when I was helping a few others in the design of the first LORAN receiver. We measured the difference in the time of arrival of two trains of pulses by triggering an oscilloscope sweep at their repetition frequency and then delayed one pulse until it could be visually made to coincide with one in the other train. In the presence of noise, the persistence of vision caused the display of several pulses of continuously-varying shapes, and it was difficult to judge which way to turn the knob of the delay control. Only when it was *too* late to be incorporated in the design, did it occur to me that we should have made one of the pulses appear in dotted lines while the other was continuous. The sense of an error in the matching would than have been conspicuous. I still blush a little to realize that a few minutes of thought at the right moment could have made possible this improvement, and have made the operation of seventy-five thousand receivers a little easier. Another case of the violation of my theme is easier to explain. I heard of it in 1960, when I was serving as a member of the Polaris Command Communications Committee of the U.S. Navy. The giant, very-low-frequency radio transmitter at Cutler, Maine had begun to operate at 14,000 hertz. The committee was astounded to be told that on the first voyage of the SSBN George Washington, when no more than half way across the Atlantic Ocean, the signals received from Cutler were lost the moment the ship submerged.

The trouble was found to be just a bad case of local interference. The Polaris vessels used several kilowatts of 400-hertz power. The antenna leads had thoughtlessly been led through the same conduits as the 400-hertz line, and the thirty-fifth harmonic of the power frequency was far louder than the Cutler signal from the submerged antenna.

This error was corrected, at least for the moment, by changing the frequency of Cutler to 14,700 hertz. I have never heard how the antenna leads are now arranged.

Another omission for which I feel personally guilty is connected with the choice of 10.2 kilohertz for the primary carrier frequency for Omega Navigation System. An earlier experimental system measured the phase difference between trains of 200-hertz modulation on signals received from pairs of stations. The Navy Electronics Laboratory, the Naval Research Laboratory, and I all had equipment for measuring the 200-hertz modulation. It therefore saved each of us a little effort to transmit pre-Omega signals at 10,200 hertz and beat them against ten-kilohertz frequency standards. The final decision to use 10.2 kilohertz in an operating system was not made until several years after I had heard about the difficulty with the Polaris signals. This knowledge notwithstanding, it did not occur to me that the 170th harmonic of the 60-hertz power frequency would ever rest very long in the narrow receiver pass-band.

I suppose, also, that it never occurred to me that a sine wave that was relatively pure could possibly have a measurable harmonic of such a high order. The cases of such interference, which are now occasionally reported, may arise from the extensive use of silicon- controlled voltage regulators. These do terrible things to 50 or 60 hertz waveforms, but fortunately, they are used to control only a tiny fraction of our electric power. From the beginning, it should have been clear to me that offsetting the Omega frequencies from coherence with any frequencies measured in the decimal system would have been a worth-while safety feature. Had we, say, adopted for the primary frequency five megahertz divided by 491 (yielding about 10183.3 hertz), it would have made no difference in the operation of Omega and would have forever protected the system from foreign signals or interference at frequencies measured in integral numbers of hertz.

I have recently found myself wondering whether the unfortunate destruction of an Iranian passenger aircraft by the U.S.S. Vincennes may not have been caused in part by such a premature termination of thought. Listening carefully to radio and television

comments about the incident, I have at times heard "experts" remark that "the Aegis system is not designed to indicate the size of an attacking aircraft". Aegis is no more than a very sophisticated set of radars. Even a simple radar tells us the distance and direction of an object and whether the reflected signal is strong or weak. Because the distance is known, the strength of the reflected signal is an excellent measure of the size of the target.

It seems possible that the designers of Aegis may have become so hypnotized by their ability to track dozens or hundreds of objects and exhibit their positions and rates of closure, that they may have neglected to add to each indication a note that the target is large or small. If so, a valuable part of the original information is being thrown away. This may be an example of what worries me: the cessation of thought at a critical point in a design.

I should add to my argument the obvious fact that ideas come only to minds which are ready to receive them. This preparation may be the result of study, worry, prayer, dreams, or experience. It is, of course, the primary reason for education. Probably all of us have had an idea come "like a bolt from the blue". In thinking over a few of my own experiences of this kind, I have realized that the most dramatic and important instances had come at the end of the longest periods of contemplation and worry. This is exactly the converse of the threat that I am preaching against: the belief that the end has been reached. It is precisely at this point, after long study and much thought, that one's mind is best prepared to continue, offering the chance of attaining something better than what originally had been sought.

THE PROJECT BEGINS WITH:

- o INVENTORY OF SCENARIOS
- o SPECIFICATIONS FOR PILOT PROJECT
- o PILOT PROJECT
- o CRITIQUE OF PILOT PROJECT

  (Consultants)
- o SYSTEMS SPECIFICATIONS

WHAT CLOCK PERFORMANCE IS REQUIRED?

- o SET ACCEPTABLE TIME/FREQUENCY TOLERANCE
- o APPLY A SAFETY MARGIN (less or equal to 10X)
- o SELECT CLOCK TYPES
- o CHECK ENVIRONMENTAL CONDITIONS

  Temperature, Magnetic Fields, Vibration,
  Pressure, Humidity, Accelerations

HOW OFTEN CAN WE RE-CALIBRATE THE CLOCKS?

- o MORE INDEPENDENCE REQUIRES BETTER CLOCKS
- o FROM COMPLETE INDEPENDENCE TO TIGHT PHASE LOCK LOOP
- o WHY ARE GOOD CLOCKS IN THE SYSTEM?

  Ask this question at every design change.

TO MEET AN ACCEPTABLE TOLERANCE

WE MUST MEASURE AS ACCURATELY AS POSSIBLE.

EXAMPLE: TOLERANCE = 1 MICROSECOND OVER 10 DAYS

Measurement and setting of rate to within 100 ns/day

We need a capability to do this over 1 hour

Requires a resolution of $<$ 4 ns

Magnification Factor 240

EVERY PTTI SYSTEM NEEDS A PTTI OFFICE

for

- SUPERVISION OF PERFORMANCE
- LOGISTICS
- TRAINING
- RECORDS KEEPING

POWER SUPPORT

- PRIMARY POWER -- PUBLIC UTILITIES
- BACK-UP -- AC
- NO-BREAK -- AC
- BATTERIES -- DC

Maintain "vertical" separation of systems!

OPERATIONS

- INSIST ON EXCELLENCE
- GIVE INCENTIVES TO PROMOTE BETTER THAN MINIMAL PERFORMANCE
- MAINTAIN INDEPENDENT EVALUATION OF PERFORMANCE

DANGERS OF MANAGEMENT

- DEFICIENT MANAGEMENT
- OVER-MANAGEMENT
- COMMUNICATIONS GAPS
- WRONG PERSONNEL POLICIES
- EUPHEMISM - EXPEDIENCY
- INCOMPLETE ACCOUNTING
- LACK OF TECHNICAL COMPETENCE AND JUDGMENT

COORDINATORS SUCCEED BY:

- MANAGERIAL COMPETENCE
- PLEASING PERSONALITY - SKILLFUL COMMUNICATION
- TECHNICAL COMPETENCE
- WISDOM

WHAT IS THE ORDER OF IMPORTANCE?

STATE–OF–THE–ART FIBER OPTICS FOR REFERENCE FREQUENCY DISTRIBUTION OVER SHORT DISTANCES*

George Lutes and Lori Primas
Jet Propulsion Laboratory
California Institute of Technology

Abstract

We have characterized a number of recently developed fiber optic components that hold the promise of unprecedented stability for passively stabilized frequency distribution links. These components include a fiber optic transmitter, an optical isolator and a new type of fiber optic cable. A novel laser transmitter exhibits extremely low sensitivity to intensity and polarization changes of reflected light due to cable flexure. This virtually eliminates one of the shortcomings in previous laser transmitters. A high isolation, low loss optical isolator has been developed which also virtually eliminates laser sensitivity to changes in intensity and polarization of reflected light. A newly developed fiber has been tested. This fiber has a thermal coefficient of less than 0.5 ppm/$^{\circ}C$, nearly 20 times lower than the best coaxial hardline cable and 10 times lower than any previous fiber optic cable. The use of this fiber in frequency distribution systems will greatly enhance the stability. These and other components are highly suitable for distribution systems with short extent, such as within a building. A test was performed to demonstrate the insensitivity to cable flexure when these new components are used in a fiber optic link. The standard loose tube fiber optic cable was installed between the control room and the cone of an antenna in a NASA/JPL Deep Space Station. The round trip cable length was 850 meters. Delay variations in the fiber optic cable were measured and compared to delay variations in an adjacent coaxial cable. Phase delay was monitored while antenna movement flexed the cables. The measured stability of the fiber optic cable was found to be substantially superior to that of the coaxial cable. In this paper, we will present results of our tests and provide the design for a stable distribution link, together with the projection of the stabilities achievable with the present state–of–the–art.

Distribution systems degrade the phase and frequency stability of transmitted frequency reference signals[1]. A reduction in Signal–to–Noise Ratio (SNR) of a transmitted signal and delay changes in the transmission path are the primary causes of degradation. These effects are caused by distribution system noise which reduces the SNR, and variations in the environmental temperature, which cause delay changes. The degree of delay change is dependent on the Thermal Coefficient of Delay (TCD) of the distribution system components.

Fiber optic systems have several major advantages over conventional distribution systems, which usually employ coaxial cables. Having all dielectric cable, fiber optic systems are not subject to ground loops and are generally immune to pick–up of Electromagnetic Interference (EMI) and Radio

*This work represents the results of one phase of research carried out at the Jet Propulsion Laboratory, California Institute of Technology, under contract with the National Aeronautics and Space Administration.

Frequency Interference (RFI). The very low loss at high frequencies in a fiber optic system helps preserve the SNR of a transmitted signal. Also, new fiber optic cables with very low TCD, recently developed and available commercially, can greatly reduce temperature induced delay changes.

A major disadvantage of fiber optic systems in frequency distribution applications has been their sensitivity to changing reflections back into the laser diode[2]. Changes in reflection are caused by cable flexure and vibration and result in delay changes across the laser diode. Recent developments, which will be described in this paper, have virtually eliminated this problem.

Because of the potential improvements in performance, the Jet Propulsion Laboratory (JPL) is developing stable short distance fiber optic links to distribute local frequency references within the Deep Space Networks (DSN's) Deep Space Stations (DSS's). These links will distribute the frequency reference signals from the frequency and timing interface in each station to the users within the station.

The requirements for the short links are quite different from the requirements for the long links used for frequency reference distribution between stations at the Goldstone, California Deep Space Communications Complex (DSCC). Because of cost–performance tradeoffs between short fiber optic links and coaxial cable links, the short fiber optic links must be relatively inexpensive, simple and reliable.

The long distance fiber optic links are more expensive and more complex with optical and electronic feedback to stabilize the delay of a transmitted signal. The long links enable the use of a centralized frequency and timing facility thus reducing the number of expensive frequency standards needed in a DSCC. Therefore, a higher cost for these links can be justified.

The performance of short fiber optic links is expected to be considerably better than the performance of an equivalent coaxial cable link. The fiber optic link will eliminate ground loops and provide considerable improvement in the thermal stability of the cable. The optical fiber's superior thermal stability will reduce the need to add mass and insulation to the cable to increase its time constant. It will also reduce the temperature stability requirement for the air conditioning systems in certain areas of the stations.

The cables used in short fiber optic links within a station may be exposed to temperature variations that can exceed 6 $^{\circ}C$ in 20 minutes and 30 $^{\circ}C$ in 12 hours over some portion of their length. They obviously cannot be buried like long links at Goldstone to benefit from temperature isolation provided by burial. These links may also be subjected to vibration from equipment such as air conditioners. For some applications the cables will be routed through the antenna wrap–up where they will be flexed when the antenna is moved. This relatively dynamic environment requires that the links be insensitive to cable vibration and flexure and that cables with low TCD be utilized.

In the remainder of this paper new technology that can be used to meet the special requirements of the short distance fiber optic frequency reference distribution links will be discussed. Test results on an experiment that demonstrates an optically isolated laser's insensitivity to cable flexure and vibration will also be presented. Finally, a state–of–the–art fiber optic frequency distribution link for short distance applications will be described.

Reducing Instabilities Caused by Reflections

Cable flexure can cause group delay changes as large as 200 ps across a fiber optic link if no means is used to desensitize the laser diode to reflections. Optical isolation of the semiconductor laser diode can reduce such changes to less than 0.03 ps. The optical isolation can be obtained by the use of bulk optical isolators using the Faraday principle.

Optical isolators of this type consist of a polarizer to fix the polarization of the laser light, followed by a Faraday rotator which rotates the polarization vector by 45°. The light at the output of the

rotator enters an output polarizer with its axis 45° rotated with respect to the polarization axis of the first polarizer. Therefore, the light passes through the output polarizer unimpeded. Because the Faraday principle is nonreciprocal in the forward and reverse directions, reflected light back into the isolator assembly experiences a rotation angle which is crossed with the axis of the input polarizer. The reflected light is therefore blocked providing the reverse isolation.

The degree of isolation achieved by this type of isolator strongly depends on the amount of light scattering within the isolator. Once polarized reflected light scatters within the isolator, the polarization is lost, and components that do not have their axis crossed with the exit polarizer pass through and degrade the isolation.

Optical isolators of this type are manufactured by several companies. The isolation afforded is typically 35 to 40 dB and the forward loss is typically less than 2 dB. Although this level of isolation is very good it is not adequate for precise fiber optic frequency distribution. In order to improve laser isolation, one company in Japan has developed a laser diode with an integral dual (two isolators in series) optical isolator[3]. This approach provides high isolation at the expense of an additional isolator and additional forward loss.

An optical isolator system developed at JPL to be used in frequency distribution links has up to 70 dB isolation and 1.3 dB forward loss[4]. The JPL isolator system was assembled from a commercial bulk isolator, as described above, and expanded beam single–mode fiber connectors (Fig. 1). The first expanded beam connector expands and collimates the optical beam emitted by the fiber. The highly collimated beam passes through the isolator elements and is collected by the second connector. The total loss is only 1.3 dB in the forward direction.

The improvement in isolation for the JPL system is due to the narrow acceptance angle of the expanded beam connectors. The collimated reflected light with the appropriate polarization is rejected by the exit polarizer. While the narrow acceptance angle of the input connector rejects the scattered reflected light exiting the isolator because it is not parallel to the axis of the isolator.

Low Thermal Coefficient of Delay Optical Fiber

Sumitomo Electric Industries, Ltd. of Japan has developed a low Thermal Coefficient of Delay (TCD) single–mode optical fiber[5]. This is an elegant means for reducing frequency instabilities in a reference frequency distribution system. It affords considerable improvement in transmission stability without adding to the complexity or reducing the reliability of the transmission system.

The TCD of this fiber has been measured at JPL and found to be less than 0.5 parts per million per $°C$ (ppm/$°C$) from 0 $°C$ to 30 $°C$. At around 0 $°C$ the TCD is zero. It rises slowly as the temperature rises and is 0.5 ppm at about 30 $°C$. The curve in Fig. 2 shows the TCD for this fiber in ppm/$°C$ versus temperature. Figure 3 compares the TCD of this fiber with the TCD of standard single–mode fiber and 7/8 inch diameter coaxial hardline # 64–875 RG254/U. This coaxial hardline has the lowest average TCD for any coaxial cable measured by the Time and Frequency Systems Group at JPL. It can be seen that the TCD of the fiber at 25 $°C$ is 20 times lower than that of the coaxial cable. Use of the low TCD optical fiber would result in an Allan deviation 20 times lower than a system using the RG254/U coaxial cable.

The TCD of a standard optical fiber results from two effects, the temperature dependence of the index of refraction of the fiber material, and the thermal coefficient of expansion of the fiber. An increase in temperature causes the index of refraction to decrease which in turn decreases the group delay through the fiber. An increase in temperature also causes expansion of the fiber which results in an increase in the group delay through the fiber. These two effects partially cancel resulting in a TCD for standard single-mode fiber of about +7ppm/$°C$[6].

Sumitomo achieves a low TCD fiber by coating a standard fiber with an inner layer of elastic material and an outer layer of liquid crystal material having a negative thermal coefficient of expansion. This liquid crystal material compresses the fiber longitudinally with rising temperature. The compression of the fiber increases the index of refraction of the fiber material which increases the group delay through the fiber. Compression of the fiber also decreases the change in length of the fiber which decreases the group delay through the fiber. The result of these two effects is to impart a negative TCD to the fiber.

The thermal coefficient of expansion of the liquid crystal material is too high and would result in a net negative TCD for the fiber if it were applied directly to it. The layer of elastic material between the fiber and the liquid crystal coating couples the right amount of force from the liquid crystal material to the fiber to result in a near zero TCD for the fiber.

TEST RESULTS

A single–mode fiber system using an isolated laser was tested *in situ* to demonstrate the capability to transmit precise reference frequencies through an antenna wrap–up. For this test a single–mode six fiber cable was installed, as shown in Fig. 4, from the control room through the wrap–up of an antenna at the Goldstone DSCC. The cable, which is 850 meters long, is flexed when the antenna is moved.

A 100 MHz reference signal was transmitted through one fiber in the cable to the antenna and returned through another fiber back to the control room. At the control room the phase of the return signal was compared to the phase of the transmitted signal. Without the optical isolator between the cable and the laser transmitter phase jumps were observed in the return signal when the antenna was moved. Figure 5(a) shows these phase jumps. However, when the optical isolator was used no phase jumps were observed as shown in Fig. 5(b).

The resultant Alan deviation for these measurements is shown in Fig. 6. The phase jumps observed when the optical isolator is not used cause the Alan deviation to be higher. The optical isolator eliminates the phase jumps and therefore reduces the Alan deviation.

A STABLE DISTRIBUTION LINK

Figure 7 is a block diagram of a stable fiber optic distribution link which uses the developments described in this paper. The reference signal to be transmitted is applied to the modulation input of the laser transmitter. The laser transmitter is either desensitized to reflections or is followed by an optical isolator. A low TCD optical fiber carries the transmitted signal from the laser transmitter to the optical detector. The optical detector is followed by a high gain wideband amplifier with low TCD. A phase locked filter at the output of the link reduces the noise bandwidth of the receiver which reduces the short term noise of the signal. The bandwidth of this PLL is adjusted for best overall frequency stability which depends on the quality of the oscillator in the PLL and the quality of the signal being transmitted.

CONCLUSION

Stable short distance fiber optic links for frequency reference distribution have been demonstrated. They have been found to be as good as coaxial systems for short term noise and much better than coaxial systems for long term stability. This improved long term stability results in a lower Alan deviation than can be achieved with coaxial cable under identical environmental conditions. In some

critical applications active electronic feedback is used to reduce thermally generated delay change. The use of low TCD optical fiber may in some cases eliminate the need for active electronic reduction of delay variations. This could result in less complex distribution systems for some applications.

ACKNOWLEDGMENTS

The authors thank P. Tu, N. Mroczka, and W. Diener, for making measurements presented in this paper. The authors also thank S. Kato, S. Tanaka, T. Kakuta and M. Shindo of Sumitomo Electric USA, Inc. and Sumitomo Electric Industries, Ltd. for providing low TCD fiber for testing and for the information and data they provided. Finally the authors thank L. Maleki, J. Dick, R. Sydnor and R. Logan for their help and support throughout the course of this work.

REFERENCES

1. G. Lutes, "Reference Frequency Distribution Over Optical Fibers: A Progress Report", Proceedings of the 41st Annual Symposium on Frequency Control, pp. 161–166, IEEE Catalog No. 87CH2427–3, Philadelphia, PA, May 1987.

2. K. Y. Lau, "Microwave phase stability of directly modulated semiconductor injection lasers", Applied Physics Letters, Vol.52, No. 17, 25 April 1988.

3. Matsushita Electric Corporation of America, Secaucus, N.J., Model IMS09111–33.

4. G. Lutes, "Optical isolator system for fiber–optic uses", Applied Optics, Vol. 27, No. 7, 1 April 1988.

5. T. Kakuta, S. Tanaka, "LCP coated optical fiber with zero thermal coefficient of transmission delay time", Sumitomo Electric Industries, Ltd., 1, Taya–cho, Sakae–ku, Yokohama, 244, Japan.

6. A. Bergman, S. T. Eng, A. R. Johnston, and G. F. Lutes, "Temperature dependence of phase for a single–mode fiber cable", Proc. Third International Conference on Integrated Optics and Optical Fiber Communications, p. 60, OSA–IEEE, April 27–29, 1981, San Francisco, CA.

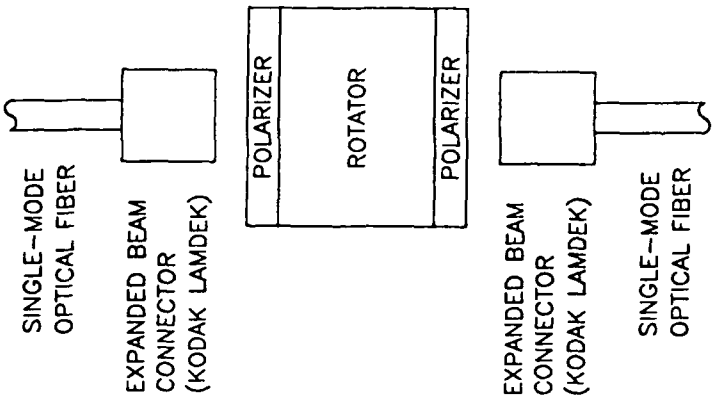

Fig. 1 A block diagram of the low loss, high isolation optical isolator for fiber optic applications.

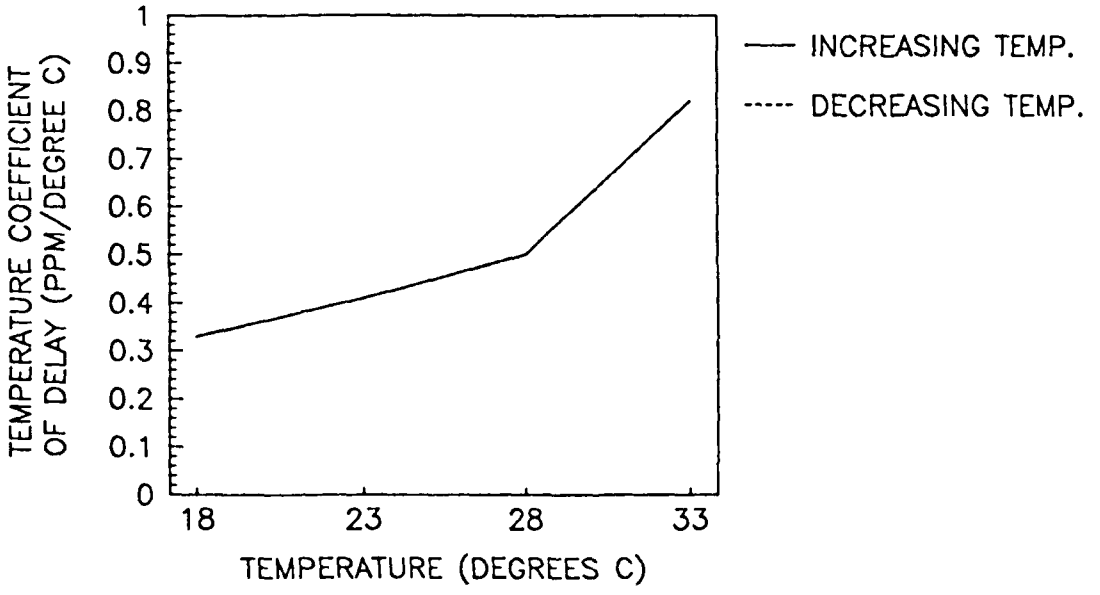

Fig. 2 The rate of change of group delay with respect to temperature for the Sumitomo low TCD fiber.

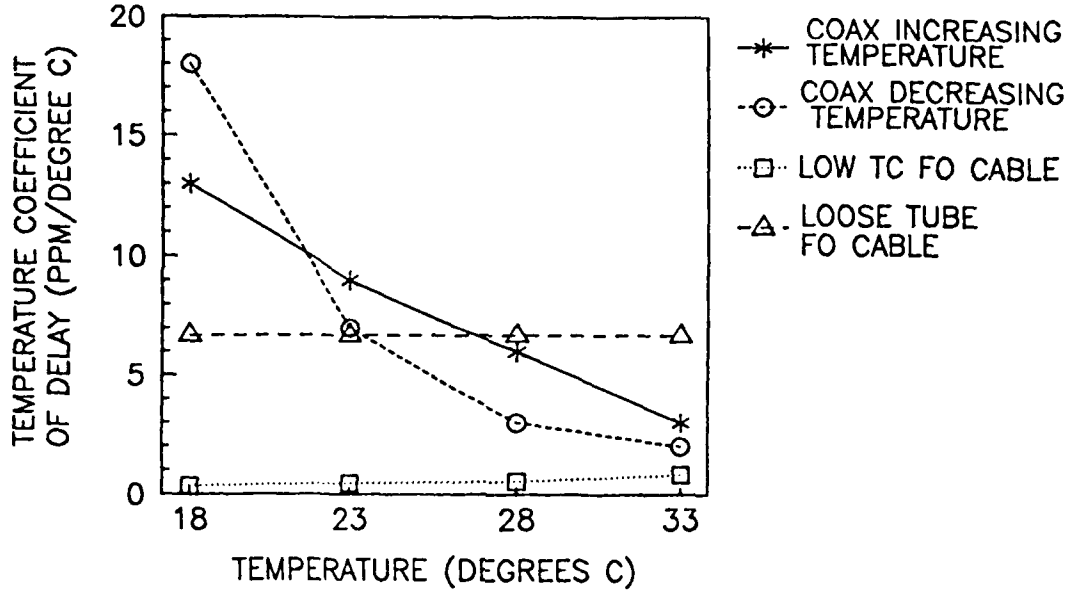

Fig. 3 A comparison of TCD's for the Sumitomo fiber, standard single-mode fiber and 64-875 RG254/U, 7/8 inch diameter Coaxial cable.

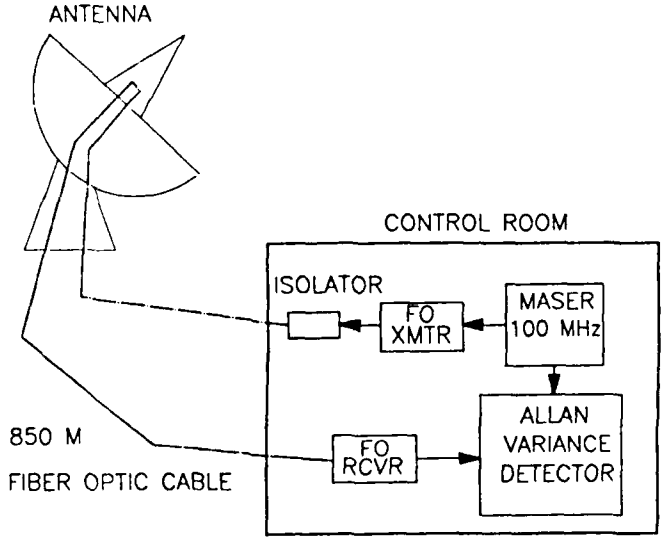

Fig. 4 A block diagram of the in situ phase stability test.

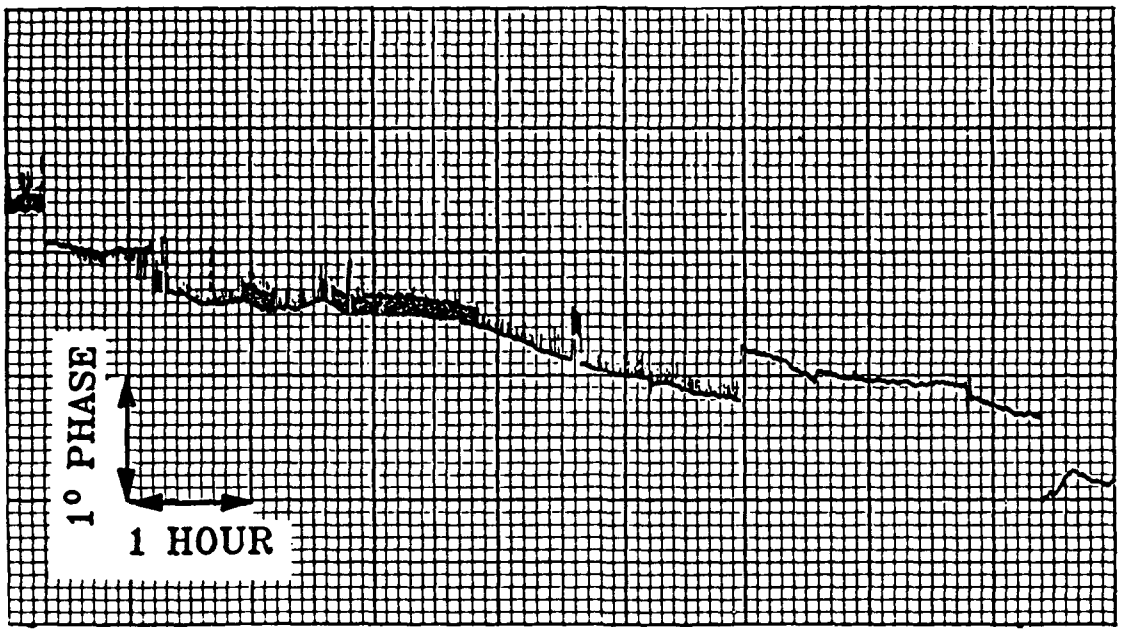

(a)

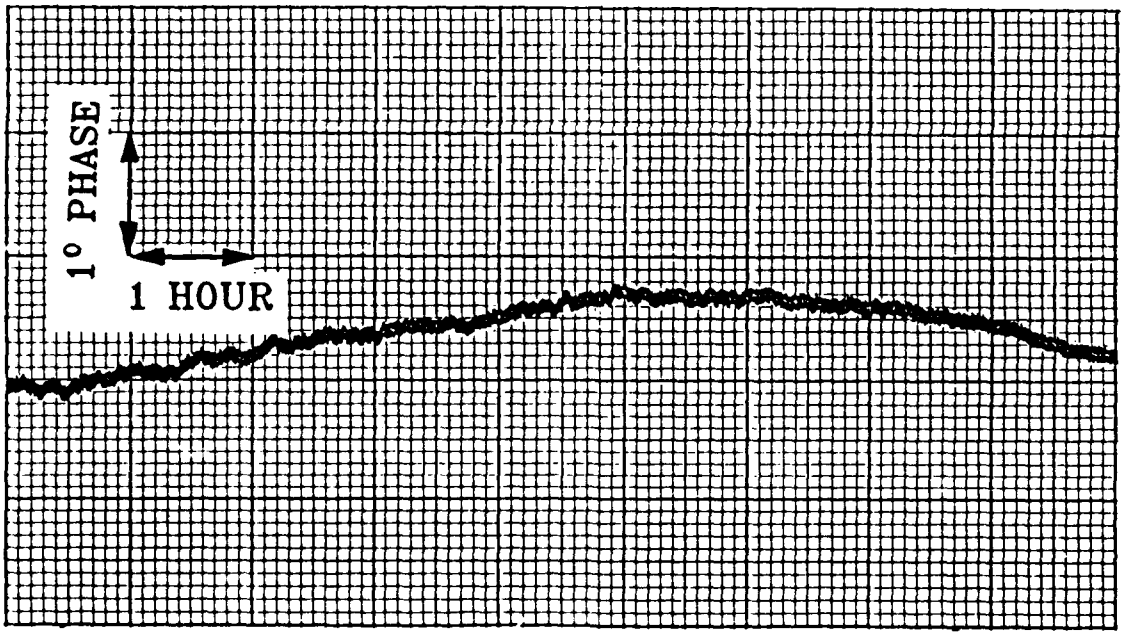

(b)

Fig. 5 Phase measured across a fiber optic link which was installed through an antenna wrap-up such that the cable was flexed when the antenna moved: (a) without an optical isolator after the laser transmitter, (b) with an optical isolator after the laser transmitter.

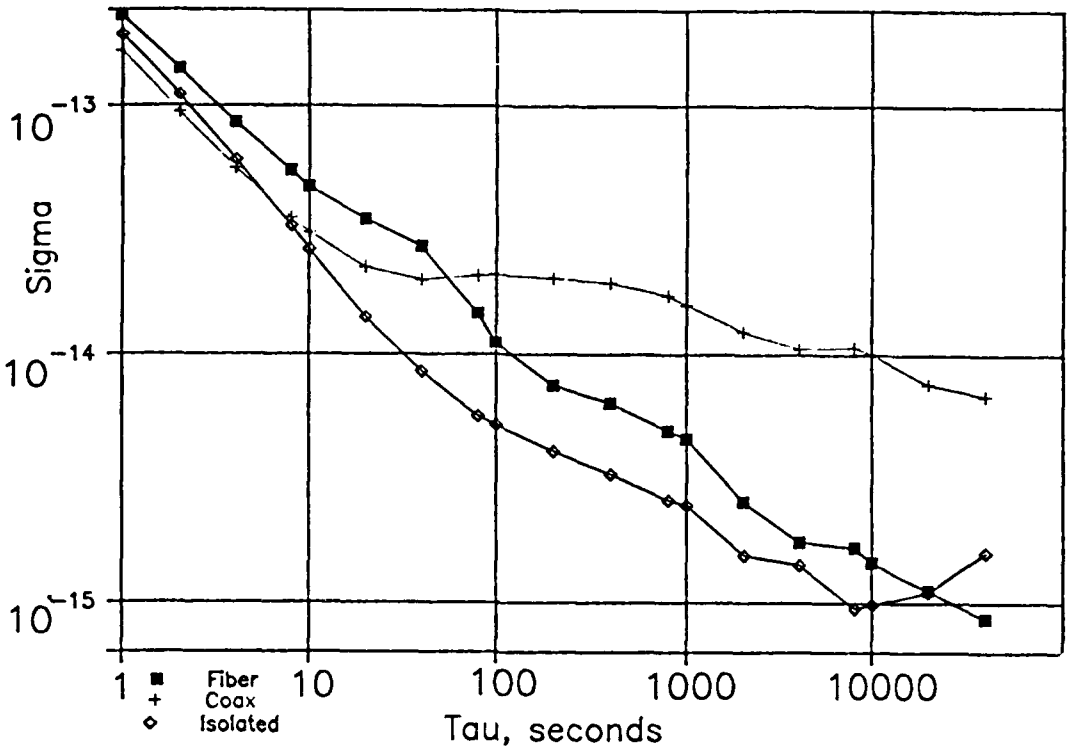

Fig. 6 The Allan variance of the phase noise shown in Fig. 3 (with and without an optical isolator) and for a coax cable installed in a similar route.

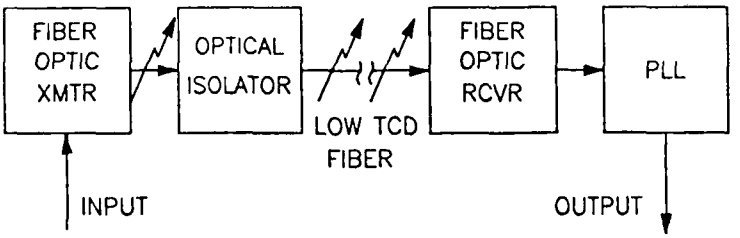

Fig. 7 A block diagram of a stable fiber optic frequency reference distribution link.

QUESTIONS AND ANSWERS

QUESTION Unidentified, not into mike...

MR. LUTES The fiber is commercially available at this time. It is relatively expensive, so we wouldn't want to use it for long runs, it is around $5 per meter, but for a few hundred meters it is probably a reasonable price. I sure that if you contact Sumitomo that you will be able to buy it. As far as the other characteristics of the fiber go, it is virtually impossible to tell it from a standard single mode fiber.

SAMUEL WARD, JPL: Not into mike...

MR. LUTES: The long term drift in the fiber is just the thermal drift of the fiber. The particular fiber that we used in that test was not the low thermal coefficient fiber, it was a standard fiber with 7 ppm per degree C coefficient of delay. It was going up an antenna where it was exposed to the outside temperature, so the temperature varied over a wide range.

STEVE KNOWLES, NAVAL SPACE SURVEILLANCE CENTER: I know that it is difficult to come up with an exact costing in these systems, but could you make a comparison of the cost of the fiber optic system compared with a coaxial cable system?

MR. LUTES: We have not done a lot of work to reduce the cost to very low levels. The parts that we are using are still quite expensive, but there are things that we could do to reduce the cost. We could use an inexpensive short wavelength laser. Over these short distances the laser doesn't have to put out much power so we could use a $1000 unit. This is really a reasonable cost compared to the kinds of coaxial cables we use to go up an antenna which cost $10,000 or more per cable. The receivers are less than $1000, and $5 per meter for the low temperature coefficient fiber. Then you have the cost of the phase locked filter. That can vary a lot, depending on how good you need the signal to be.

STABILIZED FIBER OPTIC FREQUENCY DISTRIBUTION SYSTEM*

Lori E. Primas
George F. Lutes
Richard L. Sydnor
Jet Propulsion Laboratory
Pasadena, California 91109

Abstract

A technique for stabilizing reference frequencies transmitted over fiber optic cable in a frequency distribution system is discussed. The distribution system utilizes fiber optic cable as the transmission medium to distribute precise reference signals from a frequency standard to remote users. The stability goal of the distribution system is to transmit a 100 MHz signal over a 22 km fiber optic cable and maintain a stability of 1 part in 10^{17} for 1000 seconds averaging times. Active stabilization of the link is required to reduce phase variations produced by environmental effects, and is achieved by transmitting the reference signal from the frequency standard to the remote unit and then reflecting back to the reference unit over the same optical fiber. By comparing the phase of the transmitted and reflected signals at the reference unit, phase variations on the remote signal can be measured. An error voltage derived from the phase difference between the two signals is used to add correction phase. An improved version of a previous electronic stabilizer has been built and results of its performance are reported.

Introduction

With the current advances in the development of precise frequency standards, greater emphasis is being placed on frequency distribution systems that can distribute the reference signal derived from a standard without appreciably degrading it. The high cost of developing and maintaining a state-of-the-art frequency standard makes it beneficial to have one precise standard at a complex and to distribute the reference signal from this standard to various users within the complex. Often the reference signal must be distributed tens of kilometers. Furthermore, future scientific experiments may also gain from having coherent signals at several remote locations.

The Deep Space Network, supported by JPL/NASA, is a prime contender for such a distribution system. The DSN consists of three complexes located at Goldstone, California, Madrid, Spain and Canberra, Australia. At each complex there are at least four stations, each supported by a parabolic dish antenna with an ultra- sensitive receiving system requiring a precise frequency reference. Currently each complex is supported by a primary hydrogen maser and a backup hydrogen maser. Projects supported by the DSN that require this type of distribution system include unmanned space flight

*This work represents the results of one phase of research carried out at the Jet Propulsion Laboratory, California Institute of Technology, under contract sponsored by the National Aeronautics and Space Administration

projects, flight radio science, radio and radar astronomy, very long baseline interferometry, geodynamic measurements and search for gravitational waves.

The frequency distribution system at the DSN complex at Goldstone, California must distribute reference frequencies generated by a hydrogen maser over distances as great as 30 km. The 100 MHz signal generated by the maser typically has an Allan deviation of 1 part in 10~15 for 1000 seconds averaging times. To ensure minimal degradation of the reference signal, the distribution system should be at least ten times more stable than the frequency standard. With expected future improvements in frequency standards, even greater stability of the distribution system will be necessary.

There are two basic limitations in frequency distribution systems. The first is a distance limitation set by the signal-to-noise-ratio (SNR) of the received signal. The SNR is limited by the amount of available input power from the frequency source and the loss in the distribution system. The second limitation is the degradation of the frequency stability due to variations in the group delay of the signal as it is transmitted through the medium. The variations in group delay are caused by physical changes in the transmission medium. A constant rate of change in group delay does not effect the frequency stability, but a change in the rate of group delay does degrade the frequency stability. This is shown in the following equation:

$$\frac{d(\Delta f)}{dt} = f\frac{d^2D}{dt^2} \tag{1}$$

where D is the group delay, Δf is the frequency offset and f is the transmitted frequency. Variations in group delay are due primarily to temperature changes in the transmission medium. Thus they can be reduced by decreasing the temperature change, increasing the time constant of the medium, by choosing a medium with a small thermal coefficient of delay (TCD), or by the use of optical and electronic feedback.

Previous Vs. Current Frequency Distribution Systems

As previously stated, frequency distribution systems have been primarily limited by the distance allowable for distribution and the effects of changing group delay. Coaxial distribution systems are especially subject to these limitations. The loss in 7/8 inch diameter coaxial cable at 100 MHz is 0.5 dB/100 ft and the TCD is greater than 15 ppm/°C at 25°C. The transmission length required to transmit a certain input power through a transmission medium and maintain a certain SNR is given by,

$$L = \frac{Pin - SNR + 204}{32.81\alpha} \tag{2}$$

where,

L = Length in kilometers

Pin = Input power in dBW

SNR = signal-to-noise ratio in dB

α = cable attenuation in dB/100 ft.

Thus, with 1 kilowatt of input signal power, a 100 MHz reference signal can only be distributed 7 km and maintain a SNR of 120 dB, the level required by the fiber optic link. This assumes a thermal noise power in a matched load resistance at 300°K of -204 dBW/Hz.

Microwave distribution systems have also been used in the complex at Goldstone, California. Microwave distribution systems have shortcomings in that they are highly susceptible to interference and require large input powers and repeaters to go several kilometers. Because of the limited bandwidth of microwave systems, the 100 MHz signal cannot be transmitted over microwave links directly.

Fiber optic cable is the best distribution medium for transmitting precise reference frequencies. The loss in typical fiber optic cable is less than 0.5 dB/Km at the optical wavelength of 1300 nm. A typical laser transmitter puts out 0 dBm and is attenuated less than 11 dB over 22 Km. Standard single mode fiber optic cable has a TCD of 7 ppm/°C making it less susceptible to temperature changes than coaxial cable. The fiber optic cable used at the Goldstone complex is buried 1.5 m under the ground, making the fiber quite insensitive to diurnal temperature changes. Fiber optic cable has the additional advantages that the fiber is insensitive to electromagnetic interference (EMI) and radio frequency (RFI) and can be made less sensitive to microphonics using an optical isolator between the laser transmitter and the fiber optic cable. An additional advantage of fiber optic cable as the transmission medium is that the superior performance of the optical components make it quite practical to transmit the signal simultaneously in both directions in the same fiber. This proves to be a key factor in actively stabilizing the distribution system.

Active Stabilization Of A Fiber Optic Frequency Distribution System

Passive stabilization of fiber optic transmission links, such as burial of the cable, is not sufficient for maintaining stabilities in the range required for many applications. When stabilities higher than a part in 10^{15} are required the link must be actively stabilized.

The phase conjugator is the key element of the actively controlled fiber optic distribution system. The frequency distribution system consists of a reference unit, containing the frequency standard, and a remote unit, where the frequency standard is to be transmitted. The method for actively controlling the phase variations in the fiber is based on maintaining a constant phase relation between the input phase and the phase of the received signal.

A signal passing through the fiber optic cable in both directions experiences identical delay in the two directions. The midpoint of the signal is at the far end of the cable and experiences exactly half of the round trip delay. If the phases of the transmitted and received signals at the reference end of the cable are conjugate, the phase at the remote end is independent of phase delays in the medium (see Figure 1). An electronic device that detects the phases of the transmitted and received signals at the input to the fiber and adds enough phase to maintain conjugation is called a phase conjugator (see Figure 2).

The reference unit consists of the frequency standard, the phase conjugator, a fiber optic transmitter, a fiber optic receiver, an optical coupler and a phase-lock loop (PLL) (see Figure 3). The remote unit consists of a 50/50 mirror, a fiber optic receiver and a PLL.

The phase conjugator compares the phase of the transmitted and received signals in the reference unit and an error voltage derived from the phased difference is used to control a voltage-controlled oscillator (VCO) (see Figure 4). The particular design of this phase conjugator requires a 100 MHz reference signal and a 20 MHz auxiliary signal. A previous design used a single 100 MHz reference signal, but required two precisely matched phase detectors and tightly controlled signal levels. By using the 20 MHz auxiliary signal, a single phase detector can be used to measure phase error.

The 100 MHz signal and the 20 MHz signals are multiplied together in mixer M1 to produce 80 MHz and 120 MHz signals. A power splitter (S1) separates the signal out of the mixer (M1) into two signal paths. Band pass filters in each signal path separate the 80 MHz and 120 MHz signals. The 80

MHz signal and the 100 MHz signal from the VCO are multiplied in mixer (M2) to produce a 20 MHz intermediate (IF) signal. The 20 MHz IF signal contains the instantaneous phase difference between the VCO signal and the 80 MHz signal.

The 120 MHz signal and the 100 MHz signal reflected from the remote unit are multiplied together in mixer (M3) to produce another IF signal. This 20 MHz IF signal contains the instantaneous phase difference between the reflected signal (100 MHz) and the 120 MHz signal.

The phase detector (PD) receives the two 20 MHz IF signals and produces an error voltage that is proportional to the phase difference between them. The error voltage is applied to the VCO control input through the inner loop filter (ILF). Delay changes in the fiber optic cable result in changes in the control voltage. This voltage controls the phase of the VCO relative to the reference 100 MHz signal.

The output of the VCO is divided into two signals in the RF power splitter (S2). One of the signals is received by mixer M2 and the other modulates the optical carrier emitted from the laser transmitter.

The modulated optical signal is transmitted to the remote unit through the optical coupler. The 50/50 mirror at the remote unit reflects half of the optical signal back toward the reference unit while the other half passes through the mirror to the optical receiver. The receiver demodulates the optical signal and amplifies the resulting 100 MHz RF signal. A PLL filters the signal to be used at the remote unit. The reflected optical signal returns to the reference unit where it passes through the optical coupler and is detected by another optical receiver. This signal is also filtered by another PLL and provides a constant amplitude signal into mixer M3. With the signal back at the reference unit, the system loop is closed.

Stabilizer Test Setup

The latest version of the stabilizer consists of each element packaged in an aluminum shield box with 60 dB of power supply filtering. A new laser that is less sensitive to refections back into the laser was also used. The 80 MHz and 120 MHz band pass filters were also improved.

The stabilizer does require initialization using a manual phase shifter (see Figure 4). The phase shifter is used to compensate for the delays in the fiber optic transmitter and fiber optic receiver, to ensure that the phases of the transmitted and received signals are conjugate at the input to the fiber.

The stabilizer was tested with a 4 km link of fiber which was placed on a fiber optic test rack (see Figure 5). The test rack allows better air circulation and thus a shorter time constant for our tests. The entire rack was placed in a test chamber where the humidity, temperature, and pressure could be varied. The temperature in the chamber was varied in temperature steps of various sizes and over various time intervals. The phase at the receiver and the transmitter in the reference unit and the phase at the remote unit receiver were compared to the 100 MHz reference signal (see Figure 6).

Results

Several tests were performed with the stabilizer. By measuring the response of the stabilizer to a step change in temperature and to a linear variation in temperature, the correction factor of the stabilizer was determined. For a step change in temperature from 15°C to 35°C, the phase at the transmitter and receiver in the reference unit changed by 90 degrees and the phase at the remote unit changed by about 2 degrees, thus the stabilizer provided a 45 times improvement (see Figure 7). The glitch in the curve is probably due to optical leakage of the 100 MHz through the coupler directly into the reference unit receiver, causing a cross modulation of the leakage signal and the reflected signal. If the results

of this experiment are considered over the first hour, the reference phases changed by 25 degrees while the remote phase changed by 0.5 degrees, for a 50 times improvement (see Figure 8). Results from the test with a linear change in temperature show 20 degrees of phase change at the reference unit and 0.1 degrees of phase change at the remote unit, resulting in a 200 times improvement (see Figure 9). The ripple effect in the remote unit phase is probably due to reflections from the end of the fiber into the fiber optic transmitter. With more optical isolation this effect should be reduced.

Future Improvements

The results of initial tests on the stabilizer are encouraging. The factor of 10 times reduction in phase variations with the stabilizer seems to be readily attainable, with potential for even greater improvements. New tests with a sinusoidal variation in temperature over diurnal time periods need to be performed to simulate more realistic time and temperature variations. Current tests have put the stabilizer through conditions too severe to realistically simulate field conditions.

The first step in improving the stabilizer is to reduce the losses in the system. Once losses are reduced, the return signal will be much larger than the leakage signal through the coupler. Specifically if the return signal is 40 dB greater than the leakage signal, the resulting phase variation will be 0.57 degrees. By reducing the losses and making the return signal 60 dB greater than the leakage signal, the resulting phase variation will be 0.057 degrees.

After the losses have been reduced any further problems with leakage may be eliminated by using techniques such as transmitter/receiver switching. By not allowing the transmitter and receiver to be on at the same time eliminates the interference problem of the leakage signal.

Conclusion

A method of active stabilization of frequencies distributed over fiber optic cable has been demonstrated and proves to be more than adequate for current frequency standards and distribution lengths. Current frequency standards require a ten times reduction in phase variations, and the described stabilizer provides at least 40 times reduction over a 4 Km link. Theoretical calculations predict phase reduction factors of 500 will be attainable by reducing optical losses and leakage.

Acknowledgments

The authors wish to thank Phuong Tu, Bill Diener and Al Kirk for their helping in making the measurements and preparing this paper.

References

1. JPL publications 400-333 1/88, "The Deep Space Network."

2. G. Lutes, "Reference Frequency Distribution Over Optical Fibers: A Progress Report", Proceedings of the 41st Annual Frequency Control Symposium, pp. 161-166, May 27-29, 1987.

3. G. Lutes, "Experimental Optical Fiber Communications Link," The Telecommunications and Data Acquisition Progress Report 42-59, pp. 77-85, Jet Propulsion Laboratory, July-August 1980.

4. G. Lutes, "Optical Fibers For The Distribution Of Frequency And Timing References," Proceedings of the 12th Annual Precise Time and Time Interval (PTTI) Applications and Planning Meeting, pp. 663-680, NASA Conference Publications 2175, Goddard Space Flight Center, Dec. 1980.

5. A.P. Sage, Liner Systems Control, Matrix Publishers, Inc.,1987.

6. F. M. Gardner, Phaselock Techniques, John Wiley and Sons, Inc.,1966.

7. L. Primas, G. Lutes and R. Sydnor, "Fiber Optic Frequency Transfer Link", Proceedings of the 42nd Annual Symposium On Frequency Control, pp. 478-484, June 1-3,1988.

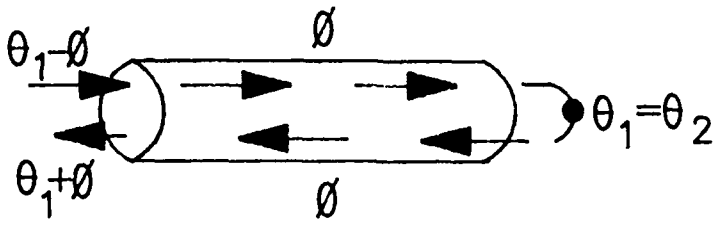

$$\theta_2 = (\theta_1 - \phi) + \frac{(\theta_1 + \phi) - (\theta_1 - \phi)}{2} = \theta_1$$

FIGURE 1. PHASE CONJUGATION AT INPUT TO OPTICAL FIBER

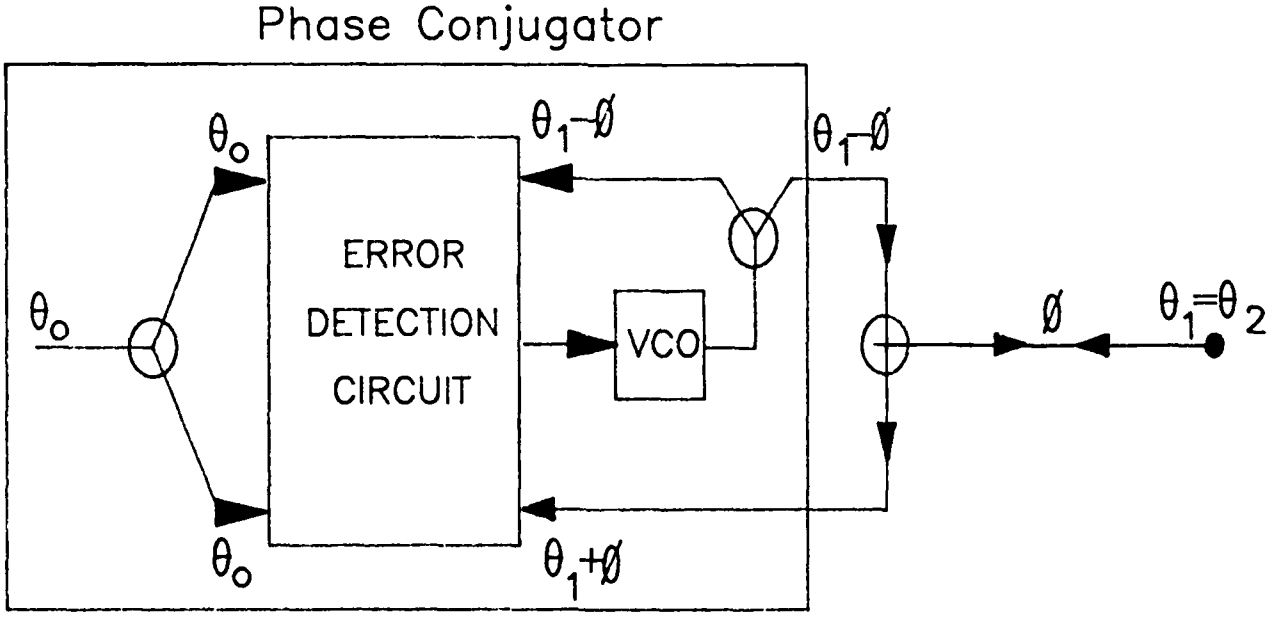

FIGURE 2. PHASE CONJUGATOR

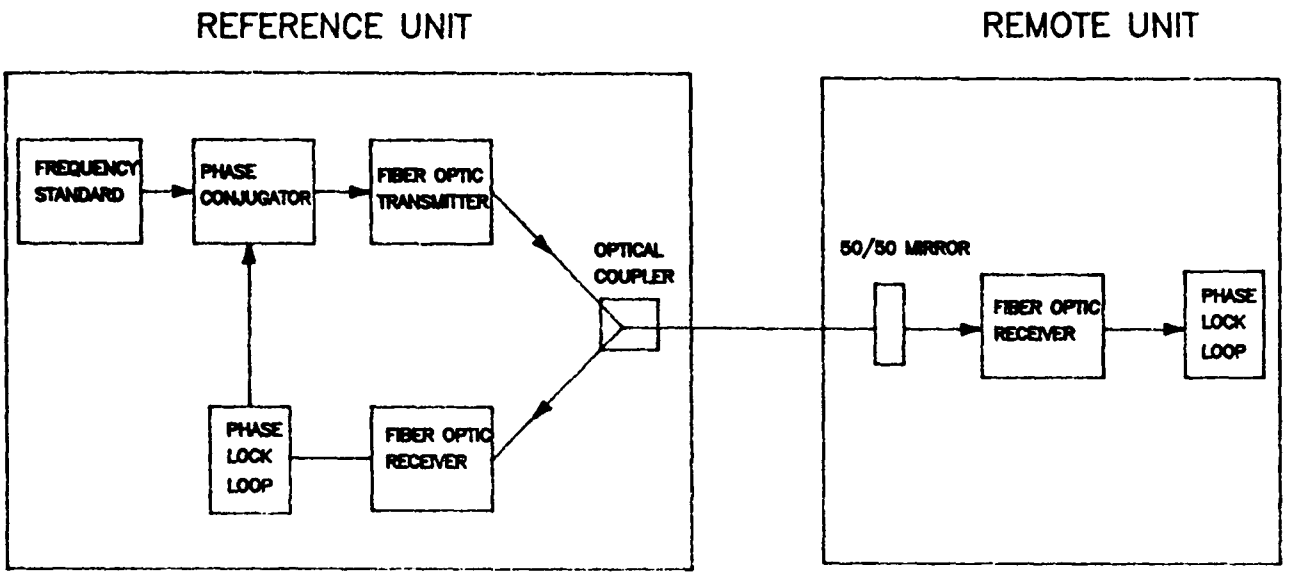

FIGURE 3. FIBER OPTIC FREQUENCY DISTRIBUTION SYSTEM

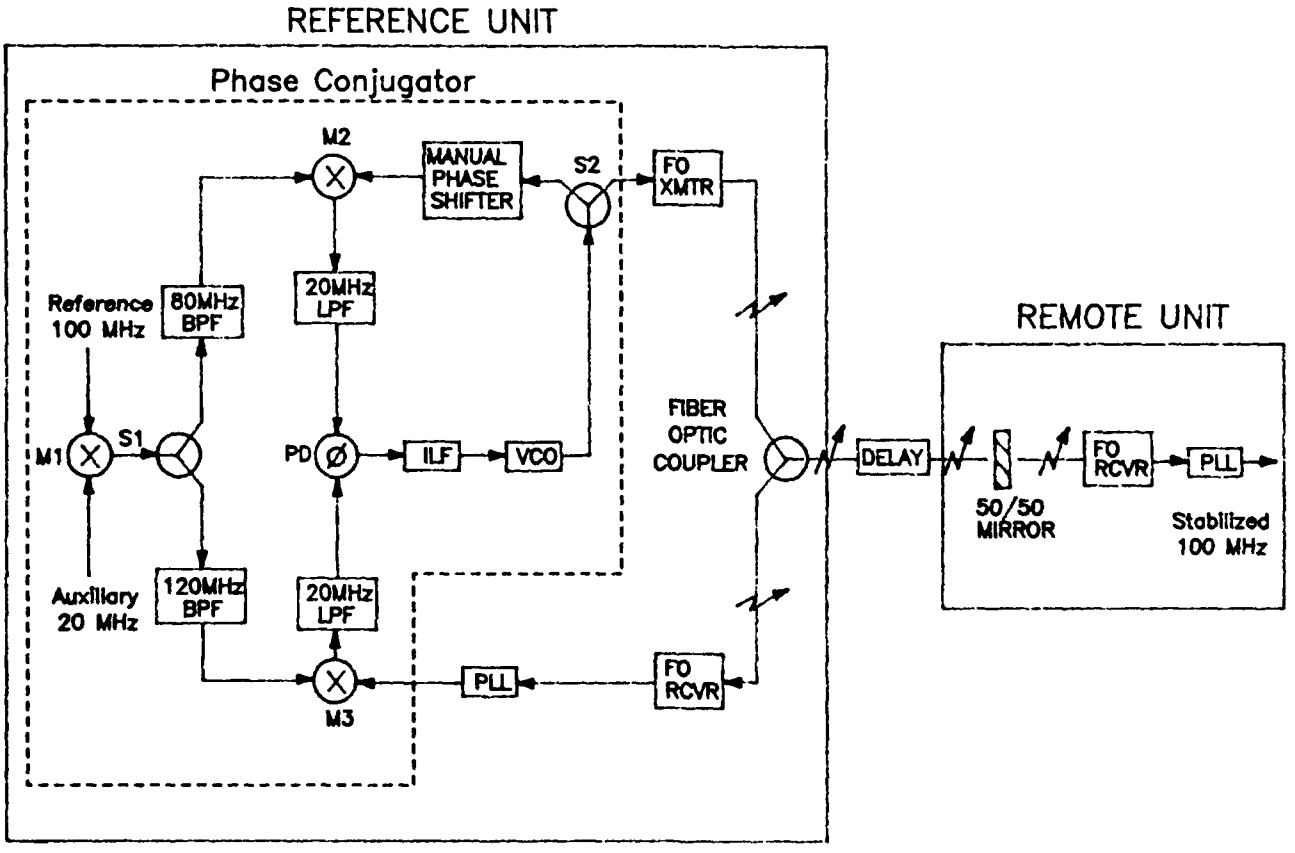

FIGURE 4. BLOCK DIAGRAM OF FIBER OPTIC STABILIZER

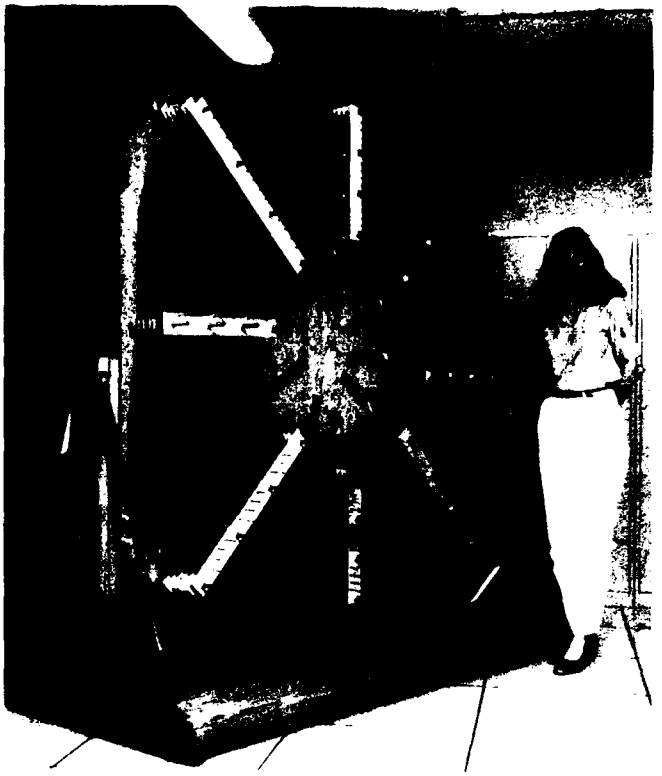

FIGURE 5. TEST RACK FOR FIBER OPTIC CABLE

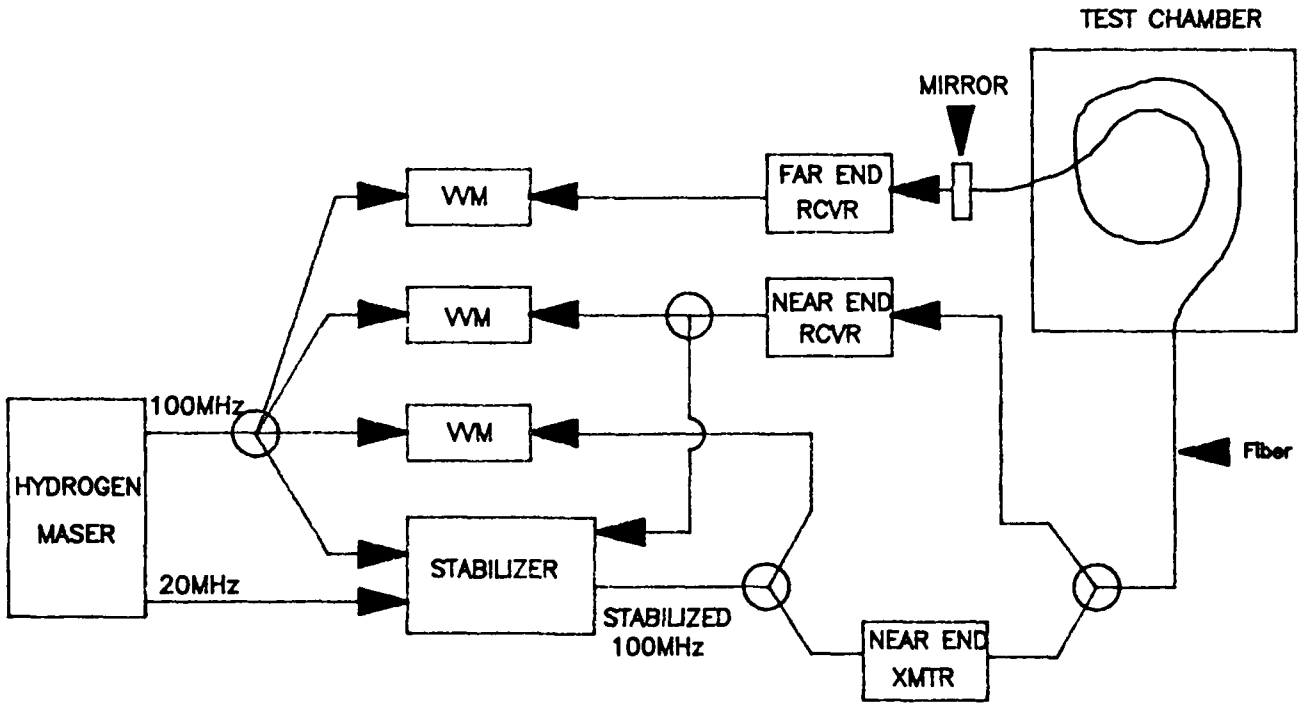

FIGURE 6. FIBER OPTIC STABILIZER MEASUREMENT SETUP

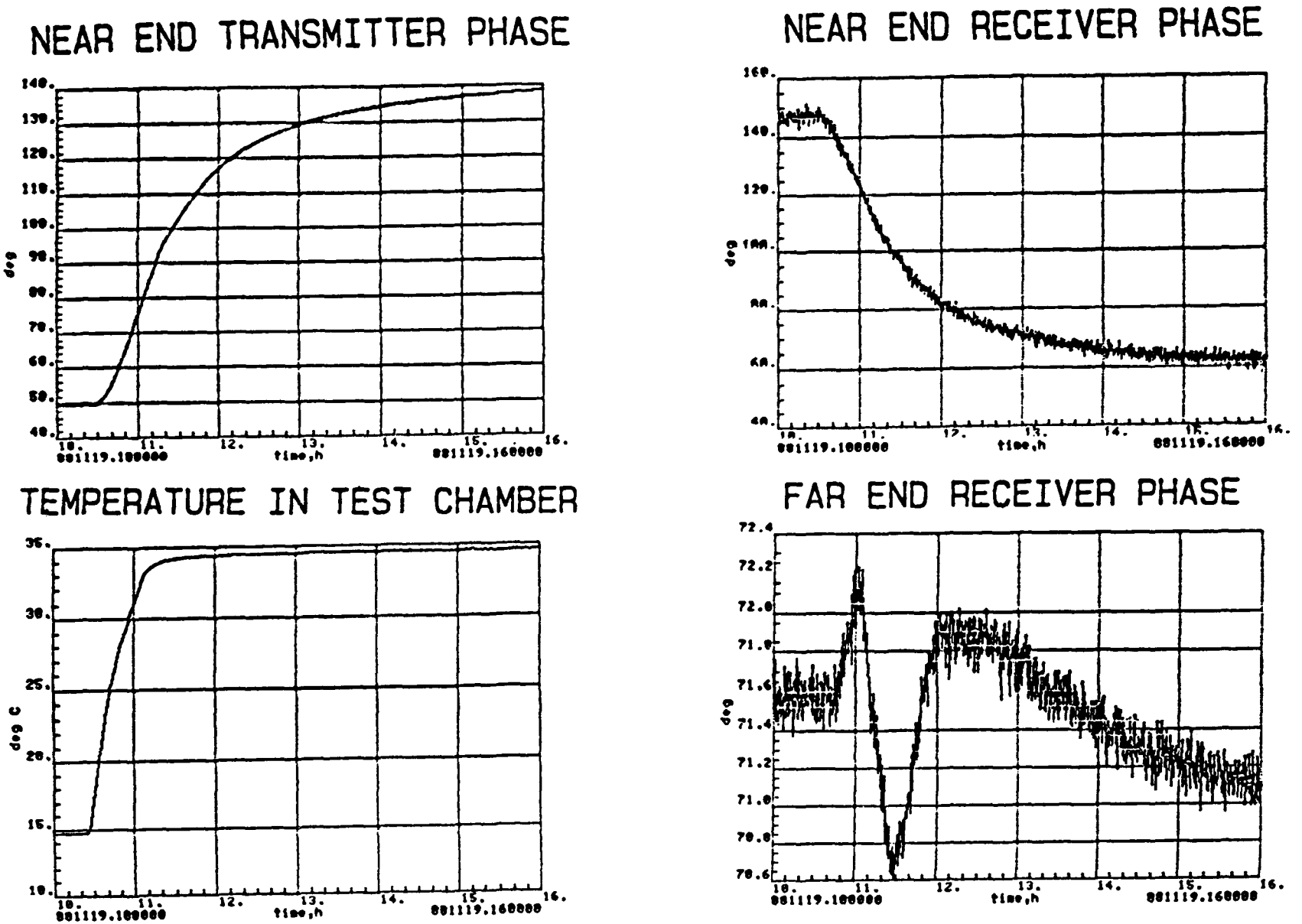

FIGURE 7. FIBER OPTIC TEST RESULTS STEP CHANGE IN TEMPERATURE 15°C TO 35°c

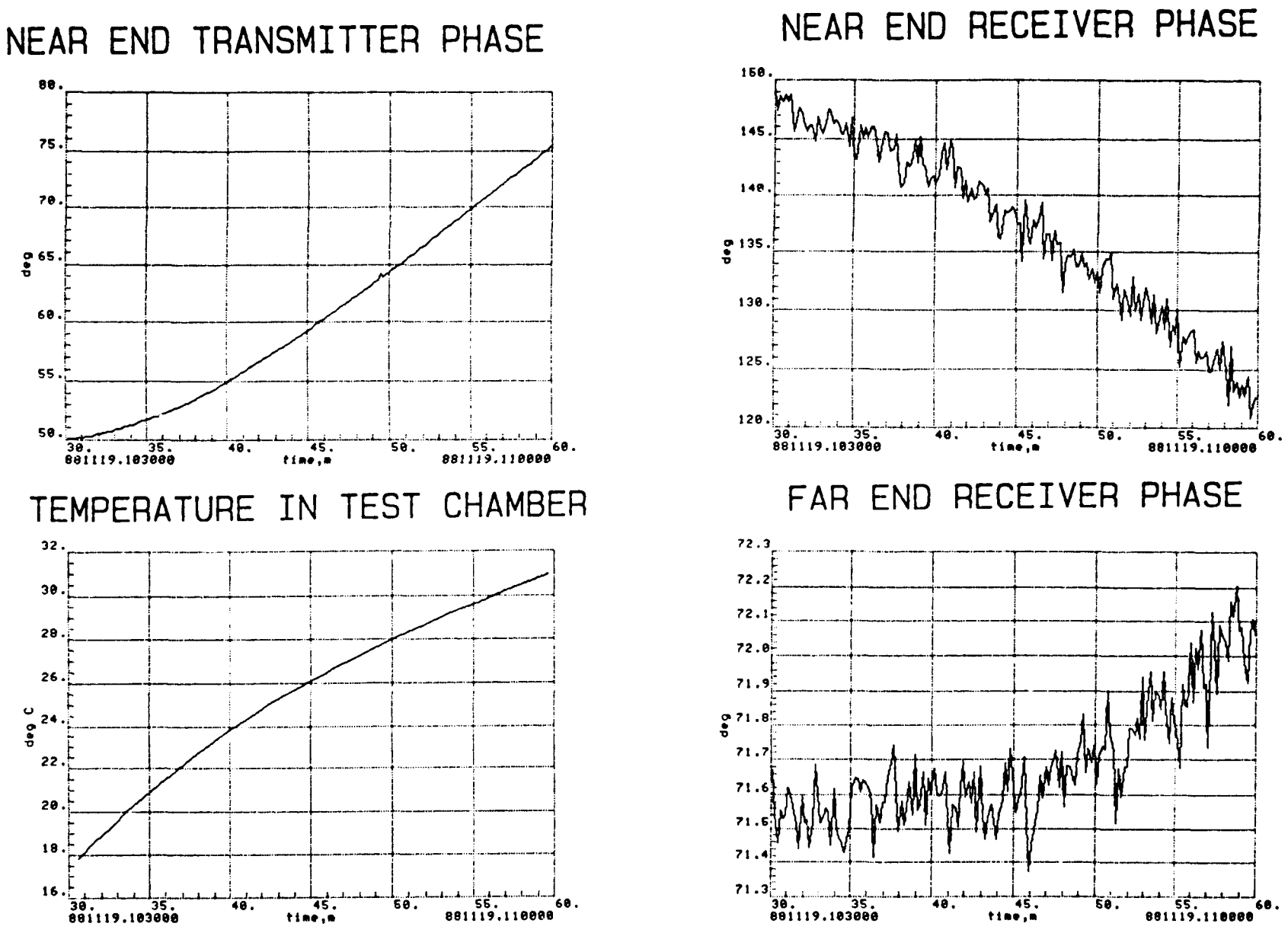

FIGURE 8. FIBER OPTIC TEST RESULTS STEP CHANGE IN TEMPERATURE 15°C TO 35°C

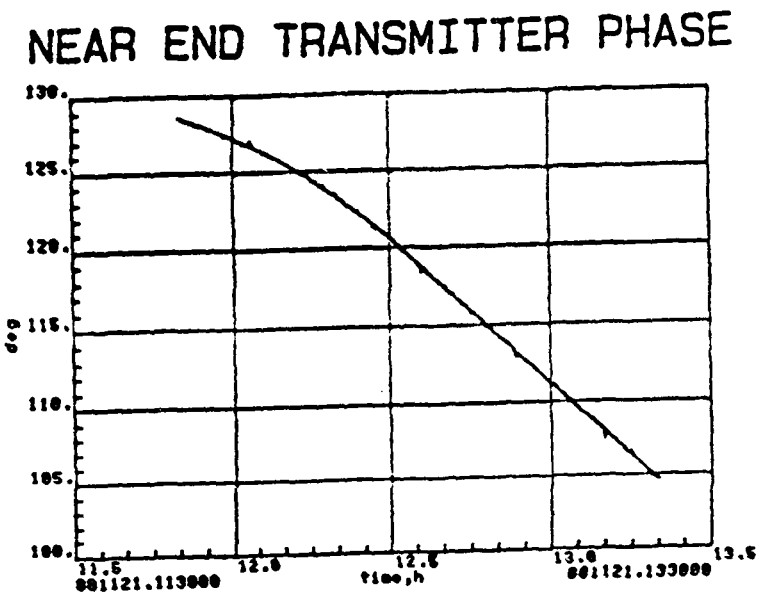

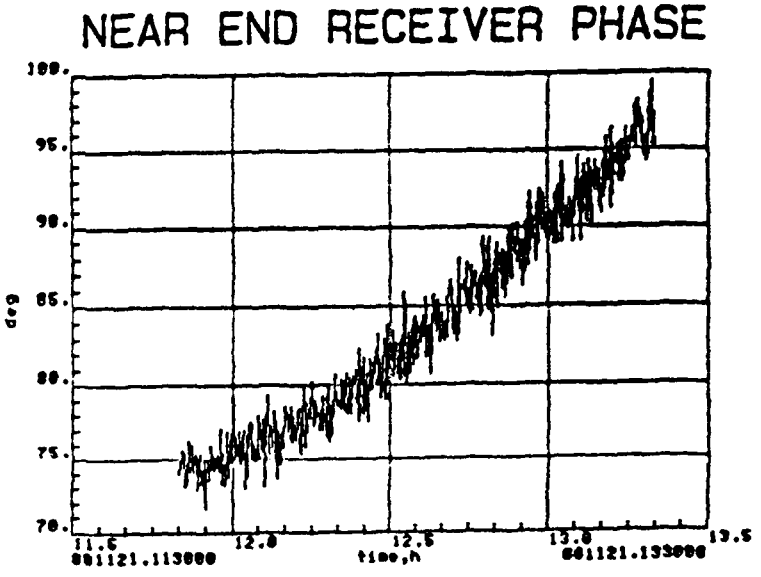

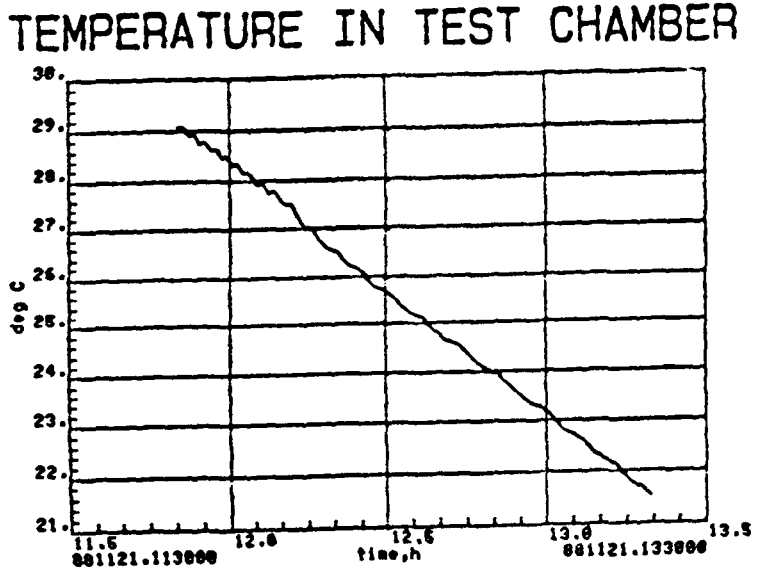

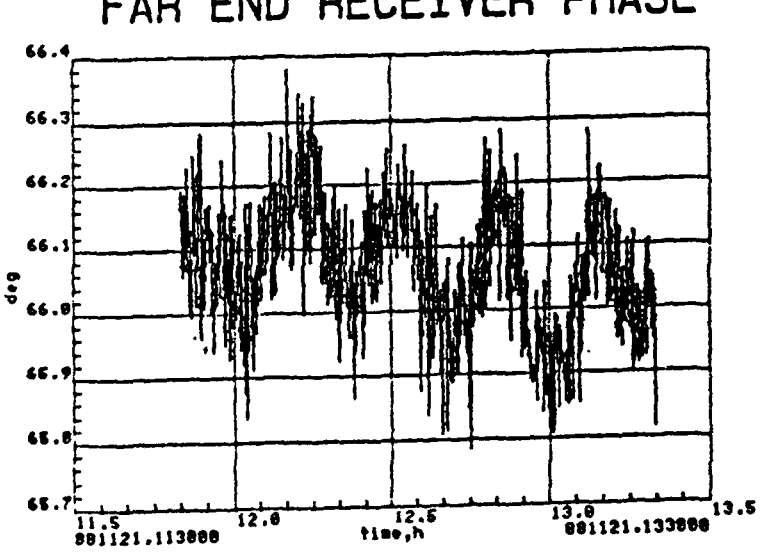

FIGURE 9. FIBER OPTIC TEST RESULTS LINEAR CHANGE IN TEMPERATURE 29°C TO 22°C

THE SYSTEM DESIGN OF 100MHz NEW FREQUENCY STANDARD WITH AN EXCELLENT BEHAVIOR

Mao Ruida and Wang Xiaohua
Beijing Institute of Radio Metology and Measurement

ABSTRACT

The purpose of this paper is to analyze a system which uses a passive quartz resonator as its frequency reference , an assemble system design approach has been proposed which uses both phase–lock and frequency–lock techniques to obtain an optimum transfering of frequency stability of the reference signal by selecting the optimal bandwidth. The phase noise of 100MHz assemble system output can be below −120dB / Hz near carrier 10Hz, the corre sponding frequency stability for sample time over one second can be finally improved to $\sigma_y(\tau) = 2 \sim 3 \times 10^{-13} (\tau \geqq 1s)$. Theoretical analysis and system design on 5MHz frequency–lock loop and 100MHz phase–lock loop have been proposed in this paper, some experimental results have also been given.

INTRODUCTION

The inherent noise of the best quartz resonator is indeed much lower than that of the crystal oscillator using this resonator. This paper is intended to have an analysis on 100MHz PLL and 5MHz FLLusing quartz resonator as frequency reference. In terms of the given phase noise spectrum of quartz resonator $S_{\varphi r}(f)$, 5MHz VCXO $S_{\varphi q1}(f)$ and 100MHz VCXO $S_{\varphi q2}(f)$, the optimal noise bandwidth for these two loops can be determined,and the output signal can be obtained which has superior frequency stability over a wide range of sample time.

It is estimated that the ultimate performance of the above system can be comparable to that of the Rb^{87}maser when sample time is over one second, and the system can also get excellent performance in millisecond–level by a built–in high power low noise crystal oscillator which has an Allan Variance of $\sigma_y(\tau) = 5 \times 10^{-12} / 1ms$. By using phase–lock technigue, the phase noise of 100MHz system output can be below−120dB / Hz near carrier 10Hz.

A simple and effective method of determing the optimal loop bandwidth is to use the given $S_\varphi(f)$ curves in the engineering. The expecting result can be achieved by simulating calculation and experiments.

5MHz FREQUENCY LOCK SYSTEM

The system block diagram is shown in Figure 1. Similar to the system scheme of superconducting –cavity stabilized oscillator. The 5MHz crystal oscillator output is phase modulated at 1KHz prior to reflection from the resonator. When the frequency of the incident carrier is close to the resonant frequency

of the passive quartz resonator, the carrier and phase modulated sidebands are reflected from the resonator. This result to the conversion of some of the incident signal into an amplitude modulated reflected signal which is detected with a low noise square law detector. After AC amplified, the AC–error signal is applied to the synchronous detector, the output of the synchronous detector is a voltage proportional to the difference between the crystal oscillator frequency and the passive resonant frequency. After DC amplifier, filtering, the voltage is fed back to the varactor input of the 5MHz crystal oscillator.

The bandwidth of the quartz resonator at half power is $f_B = f_0 / 2\theta_L$ where Q_L and f_0 are quality factor and the center frequency of the quartz resonator respectively.

It can be proved that the above system is an equivalent frequency discrimination serve system which has the following advantages:

1. For the carrier and phase modulated sides travel along the same transmission line, the variation of transmission length has the same effect on carrier and phase modulated sides, after the square law detector, the effection can be compensated.
2. The input signal to square law detector is obtained by the reflection from the quartz resonator instead of the transmission, the modulation frequency can be selected much more than the half bandwidth of the quartz resonator. Thus the feedback gain may be made very large, limited only by noise in electronic components in the loop and drift in DC amplifier.
3. To obtain the best long–term frequency stability, the quartz resonator can work at the optimal power assumption.

We have derived that when carrier frequency ω_c satisfies $\omega_c - \omega_0 \ll \omega_B$, the AC–error signal is proportional to $(\omega_c - \omega_0)$, the sensitivity of the equivalent frequency discriminator is:

$$S_d = -4aRP_c \frac{V_2}{V_1} \frac{\theta_0}{\theta_0 + \theta_E} \frac{K_{ac}\eta}{f_B} \tag{1}$$

Where:

- a is the current sensitivity of the detected diode.
- P_c is the incident carrier power.
- V_1 is the incident carrier amplitude.
- V_2 is the amplitude of the first pair of the phase–modulated sidebands.
- θ_0 is the unloaded quality factor.
- θ_E is the external quality factor.
- K_{ac} is the gain of the AC amplifier.
- η is the efficiency of the synchronous detector.

If the frequency fluctuation of 5MHz crystal oscillator is taken into account , we can derive that the equivalent frequency discriminator represent a frequency response function of a single–pole low–pass filter to the noise of different frequency. Then the open loop transfer function can be written as:

$$H_0(s) = G_0 D(s) F(s) \tag{2}$$

Where:

$$D(s) = \frac{1}{1 + \frac{s}{\omega_B}} \tag{3}$$

D(s) is called the normalized transfer function for the equivalent frequency discriminator.

F(s) is the transfer function of all other components.

G_O is the overall gain.

In our system, the other electronic components in the serve loop have been designed so the F(s) is mainly determined by the active filter in DC amplifier. The isolation amplifier, preamplifier, and synchronous detector all contribute negligibly to F(s).

The close loop transfer function is :

$$H(s) = \frac{H_0(s)}{1 + H_0(s)} = \frac{G_0 D(s)F(s)}{1 + G_0 D(s)F(s)} \tag{4}$$

Actually, the noise in every components in the loop will have an effect on the output frequency stability. If these effections are considered.We get the equivalent noise model for the serve system which is shown in Figure 2.

In which: $\Delta\omega_{on}$ and $\Delta\omega_{cn}$ represent the frequency fluctuation of the quartz resonator and the crystal oscillator respectively.Vn_1 respesent the output noise voltage of the frequency discriminator.Vn_2 represent the input noise voltage of the loop filter. $\Delta\omega_{pn}$ and $\Delta\omega_{in}$ represent the frequency fluctuation of the phase modulator and the isolation amplifier respectively.

Since these noise are random and independent from each other. The relative frequency fluctuation of the output signal is determined by the addition of the individual frequency fluctuation.

$$S_{Y_L}(f) = S_{Y_0}(f)|H_L(s)|^2 + [S_{Y_P}(f) + S_{Y_I}(f)]|H_L(s)|^2 + [S_{Vn_1}(f) + S_{Vn_2}(f)]\cdot \left|\frac{K_{dc}K_v F(s)}{1 + s_d K_{dc} K_v D(s)F(s)}\right|^2 + S_{Y_C}(f)|H_H(s)|^2 \tag{5}$$

where:

$$H_L(s) = \frac{S_d K_{dc} K_v D(s)F(s)}{1 + S_d K_{dc} K_v D(s)F(s)} \tag{6}$$

$$H_H(s) = \frac{1}{1 + S_d K_{dc} K_v D(s)F(s)} \tag{7}$$

From (5) we concluded that the close-loop system has a low-pass filter characteristics to the noise of passive quartz resonator and other loop elements, and a high-pass filter characteristics to the noise of VCXO. So the superior frequency stability of the close-loop system output can be obtained by selecting the optimal loop bandwidth.

100MHZ PHASE LOCK SYSTEM

The system block diagram is shown in Figure 3. The VHF voltage controlled oscillator is

phase-locked by an error signal, and the 5MHz FLL output is frequency multiplied by a low noise multiplier and phase detected with a VCXO in quadrature. Such a PLL is designed mainly for improving both the long-term and short-term frequency stability of the VHF VCXO. When the loop is locked. The output signal of VCXO will contain various random phase noise. Of these noises some are from the 5MHz reference sourse $S_{\varphi r}(f)$. Other are caused by the inherent noise of $S_{\varphi q}(f)$, the operational amplifier noise $S_{\varphi ka}(f)$, phase discriminator noise and so on. For simplicy these different noises are added in their corresponding loops respectively. The equivalent noise model of the PLL is shown in Figure 4.

From this noise model, the output signal noise power spectrum can be expressed as:

$$S^{l}_{\varphi q}(f) = [n^2 S_{\varphi r}(f) + S_{\varphi n}(f) + S_{\varphi k_a}(f) + \frac{S_{\varphi ka}(f)}{K_{\varphi}^{\ 2}}]\left|H_L(S)\right|^2 + S^{f}_{\varphi q}(f)\left|H_H(S)\right|^2 \tag{8}$$

where $H_L(s)$ is the loop transfer function:

$$H_L(s) = \frac{K_d K_{\varphi} K_{vco} F(s)}{S + K_d K_{\varphi} K_{vco} F(s)} \tag{9}$$

$$H_H(s) = 1 - H_L(s) \tag{10}$$

If each element of this loop is carefully designed, its introduced noise can be ignored. The output of the locked crystal oscillator is expressed as:

$$S^{L}_{\varphi q}(f) = n^2 S_{\varphi r}(f)\left|H_L(S)\right|^2 + S^{f}_{\varphi q}(f)\left|H_H(S)\right|^2 \tag{11}$$

Supose the noise power spectrum $S_{\Phi r}(f)$ and $S_{\Phi q}(f)$ for the reference sourse and VCXO are given respectively, the optimal loop bandwidth B_L of the PLL can be obtained by graphic method. Generally, we consider the crosspoint of the two curves $S_{\varphi r}(f)$ and $S_{\varphi q}(f)$ as the optimal value of ω_n. In our system, two-order active filter is adopted and the loop parameters R_1, R_2, R_F, C and $K_F(o)$ can be easily calculated.

At present, the noise power spectrum of 5MHz quartz resonator $S_{\varphi r}(f)$, 5MHz VCXO $S_{\varphi q1}(f)$, and 100MHz VCXO $S_{\varphi q2}(f)$ can be made:

$$S_{\varphi r(f)} = 2 \times 10^{-13} f^{-3} + 10^{-19.0} f^{-2}$$

$$S_{\varphi q1}(f) = 10^{-10.3} f^{-3} + 10^{-17.4}$$

$$S_{\varphi q2}(f) = 10^{-6.8} f^{-3} + 10^{-12.0} f^{-1} + 10^{-16.0}$$

Using the above FLL and PLL serve system, and the loop elements being low noise designed, the phase noise of 100MHz system output near carrier 10Hz can be expected below -120dB / Hz, and -137dB / Hz near carrier 100Hz, the background noise remains -160dB / Hz.

Now, both 5MHz FLL and 100MHz PLL system have been developed in our institute, and all the loop elements in these two serve system are made by ourself. Experiments showed that the above system approach is visible, and the long term frequency stability of the 100MHz output signal can be finally improved by a factor of 100. The short-term frequency stability can be made to $\sigma_y(\tau)$: $2 \sim 3 \times 10^{-13} (\tau \geqq 1s)$, $3 \times 10^{-11} (\tau = 1ms)$. Further research work is going to be done.

CONCLUSION

An assemble system design approach has been proposed which uses both phase lock and frequency lock technigues to obtain an optimal transfering of frequency reference.So that the output frequency of this system would have an excellent behavior within a large extent.

The ultimate performance of such a system is to have a good frequency stability for sample time from 1ms to 100s. A simple and effective method of determing the optimal loop bandwidth is to use the given $S_{\varphi}(f)$ curves in the engineering.The expecting result can be achieved by simulating calculation.

REFERENCES

1. F. L. Walls and S.R.Stein, "A frequency lock system for improved quartz crystal oscillator performance", IEEE Trans. on instrumentation and measurement, vol IM–27, PP.249–252, Sept. 1987.
2. S. R. Stein, "The superconducting–cavity stabilized oscillator and an experiment to detect time variation of the fundamental constants"Ph. D. dissertation stanford Univ, 1974.
3. S. R. Stein, "A systen approach to high performance oscillator", proc. 32th Ann. Freq. control symposium, PP. 335–337, May 1981.
4. S. R. Stein and F. L. Walls, "Composite oscillator systems for meeting user needs for time and frequency" Proc 10th PTTI , PP17–33, Nov 1987.

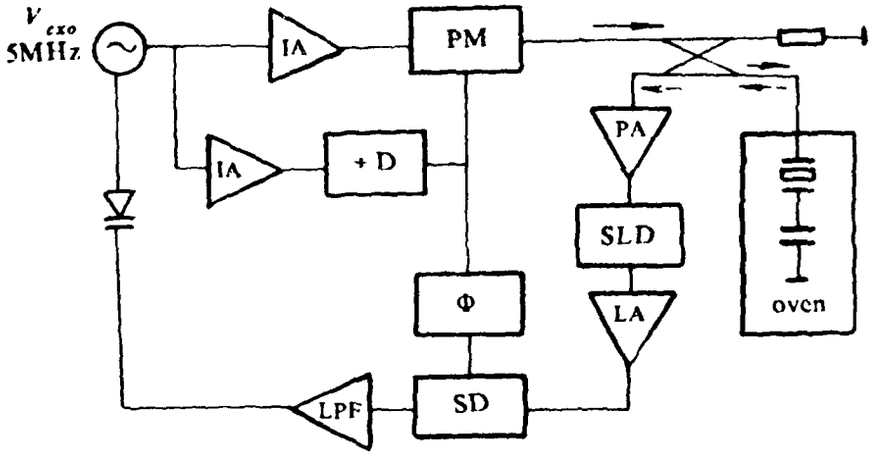

Figure 1. Block diagram of 5 MHz frequency lock system

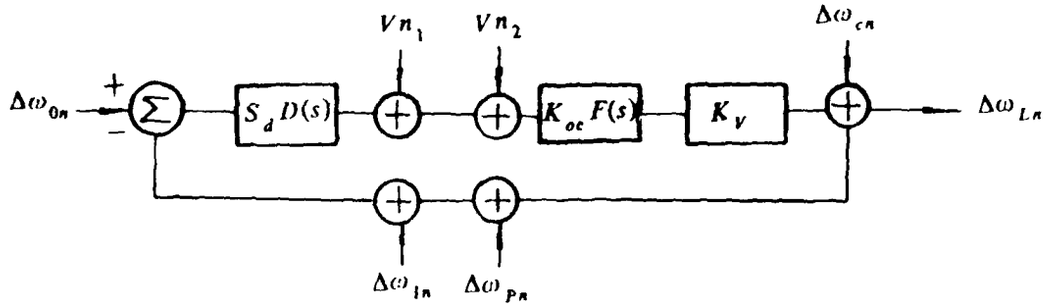

Figure 2. Equivalent noise model of 5MHz FLL system

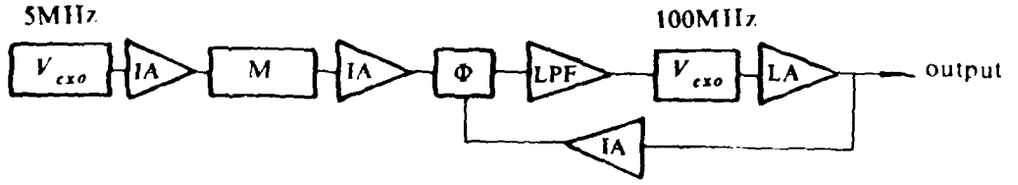

Figure 3. Block diagram of 100MHz phase-lock system

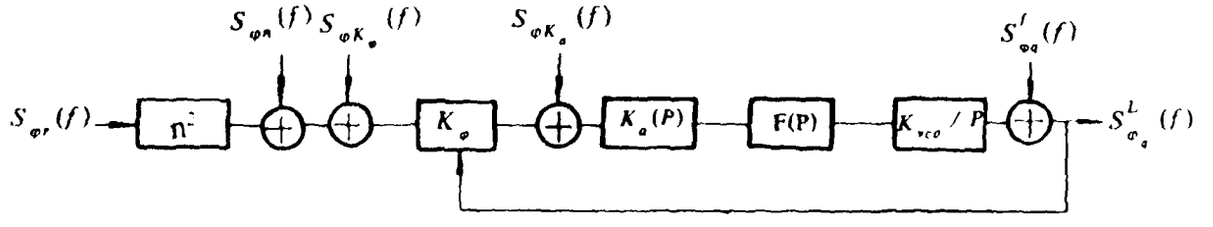

Figure 4 Equivalent noise model of 100MHz PLL system

A FIRST ACCOUNT OF LONG TERM STABILITY RESULTS OBTAINED ON VARIOUS CESIUM STANDARDS BY THE POWER SENSITIVITY MINIMIZATION TECHNIQUE.*

Andrea De Marchi
University of Ancona
Ancona, Italy.

Abstract

In an effort to improve the long term stability of Cesium beam standards available on the market a full accuracy analysis of such devices was carried out in recent years. The outcome has been published in various papers.

According to this analysis, and to measurements which have been taken to confirm it, microwave power sensitivity seems to be the most relevant parameter as far as long term stability is concerned. Power insensitive settings have been shown to exist, and a number of standards have been singularly analyzed and aligned in such a way as to minimize their power sensitivity.

In this paper the principles of this technique are reviewed and long term stability results are summarized for several standards kept in different environments. A discussion is also given of the validity of this technique for the improvement of long term stability in Cesium beam standards.

Introduction

It is known that commercially available Cesium beam standards show often frequency variations, for long averaging times, greater than expected from the shot noise of the beam. The latter appears in $\sigma_y(\tau)$ plots as the expected and well understood white frequency noise section, with $\tau^{-1/2}$ slope at short term, which at long term is usually overcome by less well understood random walk and/or flicker processes, as mentioned above. The occurrence of such long term frequency variations can be directly related to the inaccuracy of the standard. In fact it is only through long term changes of existing biases that processes other than the shot noise of the beam can affect the frequency. These changes can be induced by variations of beam, electronics or environmental conditions.

In order to understand and possibly correct this problem it is therefore necessary to study the accuracy of the whole system and describe its various biases, so that they can be reduced or at least made insensitive to whatever parameters affect them most. This has been done, and the most relevant biases in well built commercial standards, besides the C-field bias, which is clearly the biggest, but is very stable in normal operating conditions) turned out to be Rabi pulling and cavity pulling [1,2]. Both these effects are equivalent in one way or another to a power dependent background slope, near

*This work was supported by the National Bureau of Standards, by the US Naval Observatory and by the US Air Force.

center frequency, in the beam CW signal vs. excitation frequency plot. This gives a power dependent error signal at center frequency when modulation is on, which in turn produces a power dependent offset in the output frequency when the servo loop is closed. As a result the most relevant factor in determining variations of these biases is the instability of the microwave power used to excite the atomic transition [2].

All other bias effects known to exist, including cavity phase shift and 2nd order Doppler shift, do not contribute to power shifts in a relevant way [1,2].

Theoretical and experimental studies have been carried out on both cavity pulling and Rabi pulling for existing standards. These studies have shown that:

1) Rabi Pulling is an oscillating function of the C-field, and a number of field values exist for which this effect vanishes [3]. Power sensitivity is also an oscillating function of C-field, and shows vanishing points if the cavity is not badly mistuned [4-6], although the period of the oscillations can not always be explained with the simple theory of [3].

2) When the cavity is carefully tuned the zero crossing points of Rabi pulling coincide with the zero power sensitivity points; if it is slightly mistuned the field values at which power sensitivity vanishes are accordingly displaced in a predictable way [6].

3) Temperature and humidity coefficients and long term stability depend on power sensitivity, and are greatly improved by operation at a power insensitive point [4-7].

These studies confirm the relevance of power sensitivity and that accuracy (i.e. the reduction of biases, at least the power sensitive ones) is the key to long term stability. It appears therefore possible to obtain better long term performances from Cs standards by either stabilizing the power or operating at a zero power sensitivity point. This work analyzes the second solution.

The fact that the existing theory not always predicts accurately the shape of the power sensitivity curve, in particular the oscillation period (it seems that it is the role played by e transitions which is in some cases yet to be understood), does not prevent experimental determination of the field values for which the power sensitivity vanishes. It is therefore always possible to pursue its optimization with a tune-up routine involving solely power shift measurements and tweaking of C-field and microwave cavity.

This paper is a review of the results obtained so far with this approach. Two variations have been tried in following it. One was to tune the cavity close enough to perfect tuning to make sure that zero crossings exist, and tweak the C-field onto one of them. The advantage of this is that it is easy to reduce power sensitivity well below 10^{-13}/dB. The other was to try and balance power shifts near an extreme of the Rabi pulling curve. The advantage of this was thought to be that variations of the Rabi pulling curve would in this case reintroduce power sensitivity only in the second order. Results obtained with either technique are reported here and seem promising, particularly when the first approach was used.

Review of results

Six clocks were realigned between the spring of 1986 and the fall of 1988 following the philosophy outlined above. Five of them were HP standards option 004, employing a double beam tube (the so called supertube), and one was an FTS standard. All were measured for long term stability in the initial state, for later reference, then analyzed more or less in depth prior to realignment. The purpose of this analysis was either to simply identify a zero crossing or also to improve the understanding of the different bias effects, their reciprocal importance and their power dependence. Useful information

was acquired along the way toward the task of describing a suitable alignment procedure which would make use of the newly gained knowledge. A number of long runs were taken at what were considered interesting set points in order to get information on the long term stability obtained with the alignment considered. Most runs were taken with good temperature control. Some of the $\sigma_y(\tau)$ plots are reported here.

In some cases work had to be performed on the tuning of the microwave source (the SRD stage which constitutes the final step of the frequency multiplier), in order to improve stability with temperature and time of its output power, so that the requirements on power sensitivity of the standard would be relaxed.

For two HP standards a balance was sought of the power shifts due to Rabi pulling and to cavity pulling. As shown below, results obtained in this way were good, but not exceptional. All the other standards were set at a zero crossing of power sensitivity. The best long term stabilities were obtained in this way.

No fundamental difference was found between standards from the two different manufacturers in C–field periodicity and relevance of power sensitivity for long term stability. This is interesting because the electronics are based on very different design approaches in the two cases, and the servo loop modulation in particular does influence value and power sensitivity of bias effects [3,9].

In the following, numbers 1 through 6 will be used to identify the standards which have been worked on. Their manufacturer's serial numbers are given in [10] together with property indications.

Clock #1 was received from USNO in March 1986 and shipped back in September 1987 upon tube failure. After the reference long term stability run a first quick overview of the power shift curve vs C–field was done with an external microwave source which made use of a Gunn oscillator for power availability. The Gunn was phase locked on Cs frequency to the output of an external synthesis chain similar to the internal one. The following long term run at a C–field where a zero power sensitivity was found with this set–up showed that cavity pulling was important and that power sensitivity should therefore be measured with the same microwave structure used in operation. The following months were dedicated to understanding in detail the role of cavity pulling, acquiring an accurate power sensitivity curve with the cavity well tuned, and taking measurements of long term stability and temperature coefficient at different power sensitivity points. The standard was then aligned at best at a zero crossing of power sensitivity at 39 kHz, and a long term stability measurement was taken. Subsequently the C–field was moved to 38.8 kHz in order to gain information on how critical the setting really is. Results relative to this standard are reported in fig. 1 through 4. In fig.1 the power sensitivity curve is shown as measured with the cavity well tuned. In fig.2 are reported the $\sigma_y(\tau)$ plots vs AT1 of the standard before any work was done on it (fig.2a), at the 39 kHz zero crossing (fig.2b), and 200 Hz away from the zero crossing (fig.2c). It appears that great improvements in long term stability can be obtained by reducing the power sensitivity of a standard, and that for the best results knowledge of the actual zero crossing C–field and realization of the same are quite critical. In fig.3 a plot is shown of the measured long term stability vs power sensitivity, and in fig.4 is a similar plot for temperature sensitivity. The reason why the latter seems to have a limitation for low values is not clear. Most of these results were already reported in [4–6]. Measurements of 2g flip frequency variations were also taken close to zero crossing, they did suggest the existence of an effect, but the results were not conclusive enough to justify reporting at the time.

Clock #2 was received from USNO in May 1986 and shipped back in January 1988 upon tube failure. It was then received again with a new tube in July 1988 for further research. A similar routine was initially followed as for #1, except that the power sensitivity curve was not studied as exhaustively. Instead, efforts were concentrated in optimizing the power stability and determining carefully the position of the zero crossings. Temperature sensitivity at different points was also measured for this standard, as well as frequency variations for 2g flips. The power sensitivity curve was found not to

be too different from that of #1, and results for TempCo and 2g flips were also similar. In fig.5 $\sigma_y(\tau)$ plots are shown for the reference run (fig.5a) taken before work was started, and for the run taken at the zero crossing at 38.9 kHz after realignment (fig.5b). The latter stability curve is relative to the initial 60 days period of the run, when the clock was not weighed in the time scale. During this time no deviation from a white frequency noise process was observed down to the middle 10^{-15}. Because the standard was performing so well the run was continued to gain information on the long term changes that the set point may undergo. After roughly six months of exceptionally stable behaviour a frequency step of 6×10^{-14} was observed. Shortly thereafter a loop adjustment was made (the frequency change was 1.5×10^{-14}) and the power sensitivity was remeasured (it turned out to be about 1.5×10^{-14}, with an uncertainty of 1×10^{-14}). The stability in the following two months was not as good as in the previous period, as it seemed to start flickering in the high 15s. Tube failure followed soon, and when the clock was received with a new tube an extensive analysis was initiated aimed at understanding what the accuracy of a standard of this type could be. A zero crossing very close to the 39 kHz one of the previous tube was then identified, and another long term run will be taken before this clock is shipped back.

Clock #3 was received from USNO in October 1986 and is still being observed at NBS as of this late 1988. The microwave source was not properly working when the standard was received and it had to be retuned. After the reference long term stability run was taken for later reference, power sensitivity was measured to be about 1×10^{-13} per dB at the initial operating point. The standard in fact was performing very well, as is shown in fig.6a. It seemed to be a good idea to try on it a compensation between the power shifts caused by Rabi pulling and cavity pulling. A long run was also taken, at a tuning for which power sensitivity was a few parts in 10^{13}/dB, with the microwave source not tuned up for best stability. The $\sigma_y(\tau)$ plot relative to this run is shown in fig.6b. The relevance of power stability and power sensitivity is dramatically underlined by it. With the power source finally stable, and the sensitivity compensated at best, the clock was then kept in observation for a long period to gain insight on the validity of the technique. The stability plot relative to the first 60 days of this run is shown in fig.6c. A slight improvement can be noticed from the initial setting, perhaps a factor of two in long term stability. This corresponds to the measured power sensitivity improvement. It must be pointed out that applying this technique is made awkward by the trial and error process involved. It appears that smaller power sensitivities can be more easily obtained by looking for a zero crossing. The humidity coefficient after tune-up was also measured for this clock as part of a survey that was carried out at NBS early this year on several standards and reported in [8]. Its coefficient turned out to be $-1.6 \times 10^{-15}/\%$, a factor of three smaller than the average of the other clocks. It seems safe to assume that the effect of humidity on the output frequency would come from power variations. These could be caused for example by variations in temperature of the microwave source due to redistributions of the thermal paths.

Clock #4 was available only for a ten days in August 1987, from Falcon Air Force Basis, in Colorado Springs, and was realigned at a zero crossing of power sensitivity at 43.06 kHz. The residual power shift at that point was less than 3×10^{-14}/dB. It must be noticed that the Rabi pulling curve was very different in this tube from the one of #1 and #2. No long term run was taken at NBS before or after tweaking. The data taken prior to realignment show a flicker floor in long term stability worse than 10^{-13} relative to the USNO reference. After realignment of the C-field the long term stability was consistently about 2×10^{-14} relative to the same reference (see for example fig.7), even after several on-off cycles of the supply power. It is to be underlined that the environment around this unit was not stabilized in any way during the observation period, which put the peak to peak temperature variations in the range of several degrees centigrade and the humidity range from 30 to 50%, as shown in fig.8a and 8b. Still the standard performed at the 2×10^{-14} level.

Clock #5 was carried to NBS by USNO personnel in September 1987, and was worked on for

5 days before being carried back to USNO. No long term data are available for the clock before realignment, as the tube had just been changed. The technique used in this case was the one seeking balance between power shifts, but the time available was not enough to complete a satisfactory job. As a result the residual sensitivity was about 1×10^{-13}/dB, which would yield a long term stability in the middle 14s with a stable microwave power source.

Clock #6 is an FTS clock, and was analyzed at the Aerospace Corp. with an automatic measurement system. The power sensitivity curve obtained is shown in fig.9. The curve does not substantially differ from that of HP tubes, although it seems to die out faster at high C–fields. The uncertainty in these measurements is too big to determine the zero crossing points with the precision necessary to guarantee high long term stability. However no further testing was done. Two runs at the Zeeman frequencies indicated in fig.9 are being taken at NBS starting last October 10. The stability corresponding to the point at 37 kHz as obtained from the initial 20 days of the present run is shown in fig.10. The 20 days run taken at 44 kHz appeared to yield a stability floor around 10^{-13}.

Conclusions

A review of the work performed in the last three years on the improvement of long term stability in Cesium beam standards by the power minimization technique, and a first account of the results obtained shows that indeed power sensitivity is the single most important parameter in determining the level of the observed flicker and random walk processes. Since other parameters are much less important it turns out to be possible to improve long term stability either by stabilizing the power or by reducing the sensitivity. Environmental sensitivity is also reduced in this way. Setting the C–field very close to a zero crossing of power sensitivity appears to be an easier and more effective technique than trying to compensate the shifts due to different effects. Finding a zero crossing with sufficient precision and realigning a standard requires approximately two weeks in the present state of development with the equipment used in this work.

Potential shortcomings of using this technique as a solution to the long term stability problem are the following:

1) The position of power insensitive points is velocity distribution dependent. Because of this it may vary with small changes in the beam optics (related to mechanical stress or deflecting magnets relaxation), with the direction of the gravitational field, and obviously from tube to tube. Therefore a standard should sit in the position in which it was tweaked, with respect to the gravitational field, and that it must be realigned whenever the Cesium tube is substituted due to end of its life.

2) Operation at a particular Zeeman frequency is required. If the synthesizer is not readjusted this may impose an offset in the output frequency which may not be acceptable to some users. Even when the offset is acceptable, or the synthesizer is readjusted to match the new C–field, this fact inhibits the freedom of tuning the output of the standard by acting on the C–field.

3) Once the standard is carefully aligned, power sensitivity can be reintroduced during the life of the tube by variations in time, due to the environment or to ageing, in anything that contributes to the alignment of the C–field with the power insensitive points. Examples of such variables are C–field current, cavity tuning and any velocity distribution determining element mentioned above.

References

[1] J.H.Holloway, R.F.Lacey: "Factors which limit the Accuracy of Cesium atomic beam frequency standards", Proc. 7th CIC (1964).

[2] A,De Marchi: "The Accuracy of Commercial Cesium Standards", Proc. Fourth Symposium on Frequency Standards and Metrology, Ancona (1988). Springer.

[3] A.De Marchi, G.D.Rovera, A.Premoli: "Pulling by neighboring transitions and its effects on the performance of Cesium beam frequency standards", Metrologia 20, p.37 (1984).

[4] A.De Marchi: "Understanding environmental sensitivity and ageing of Cesium beam frequency standards", Proc. 1st European Freq. and Time Forum (1987).

[5] A.De Marchi: "New insights into causes and cures of frequency instabilities (drift and long term noise) in Cesium beam frequency standards", Proc. 41st Freq. Contr. Symp. (1987).

[6] A.De Marchi: "Rabi Pulling and long term stability in Cesium beam frequency standards", IEEE Trans. UFFC, Nov.1987.

[7] E.Bava, F.Cordara, V.Pettiti, P.Tavella: "Analysis of the seasonal effects on a Cesium clock to improve the long term stability of a time scale", 19th Annual PTTI (1987).

[8] J.E.Gray, H.E.Machlan, D.W.Allan: "The effect of humidity on commercial Cs beam atomic clocks", Proc.42nd Freq. Contr. Symp. (1988).

[9] A.De Marchi, A.Premoli, G.D.Rovera: "Effects of servo–loop modulation in atomic beam frequency standards employing a Ramsey cavity", IEEE Trans. UFFC–34,6 (1987).

[10] #1: HP1653 of USNO

#2: HP1343 of USNO

#3: HP2315 of USNO

#4: HP 660 of USNO

#5: HP 583 of USNO

#6: FTS168 of Aerospace

Fig.1

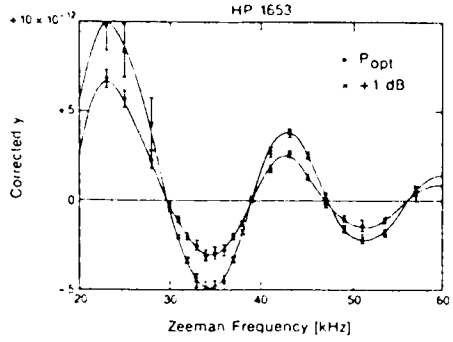

Fig 1 Experimental results for Rabi pulling of one standard analyzed. Reported relative frequency data y are measured residual differences from AT1 (NBS) once C-field and synthesizer offsets are removed

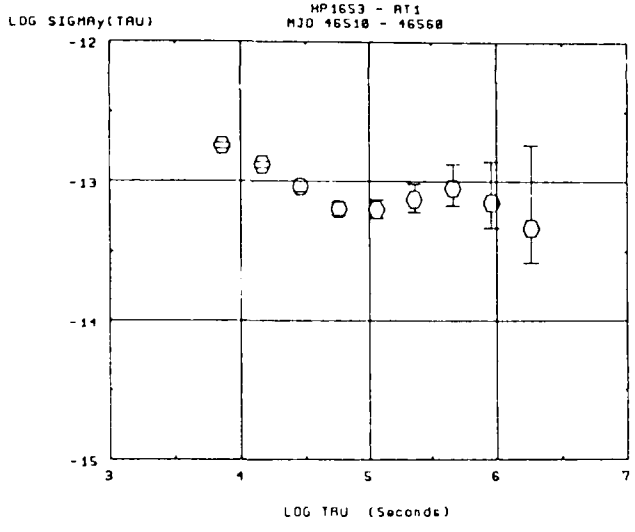

Fig.2a - f_Z = 53 kHz, initial setting.

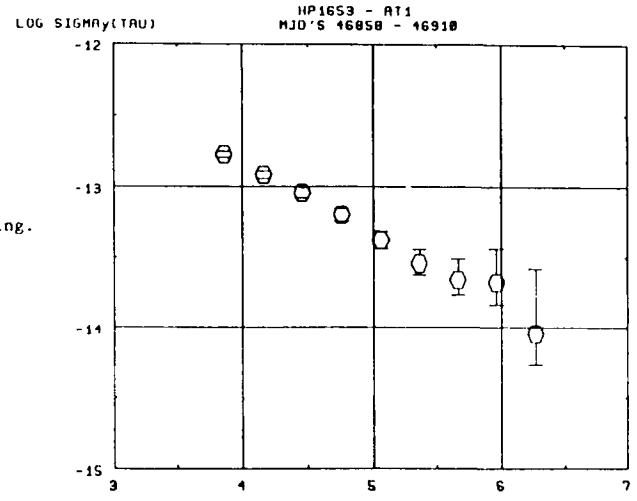

Fig.2b
f_Z = 39 kHz
zero crossing.

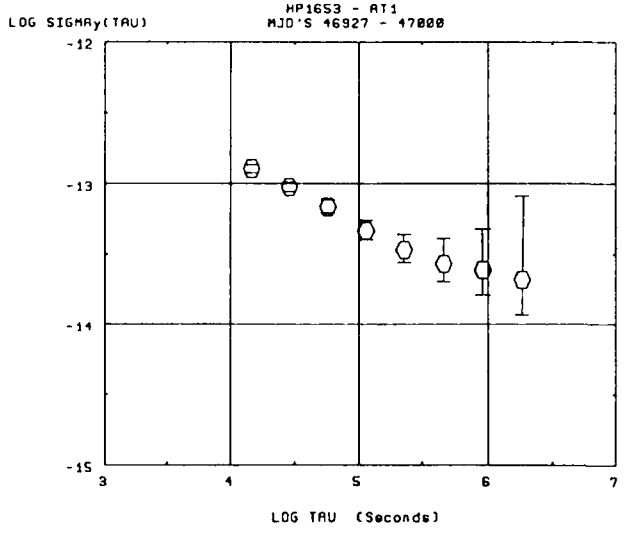

Fig. 2c
f_Z = 38.8 kHz
200 Hz from
zero crossing.

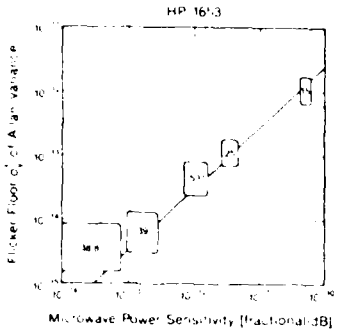

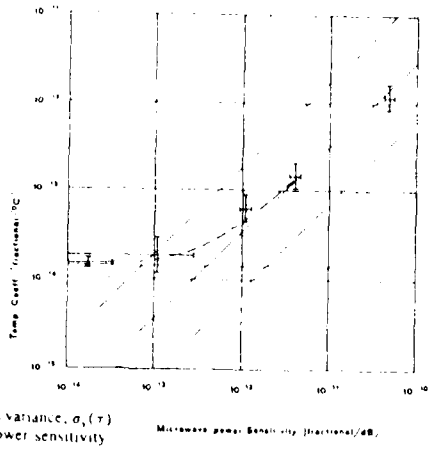

Fig.3 Measured flicker floor levels of square root of Allan variance, $\sigma_y(\tau)$ of one standard analyzed, as function of microwave power sensitivity. Corresponding Zeeman frequency is indicated in kHz in box at each point. Box brackets uncertainty for each point. Dotted lines above and below solid line are examples of where flicker floor values may be for microwave power generators more and less stable than one in standard under test.

Fig.4

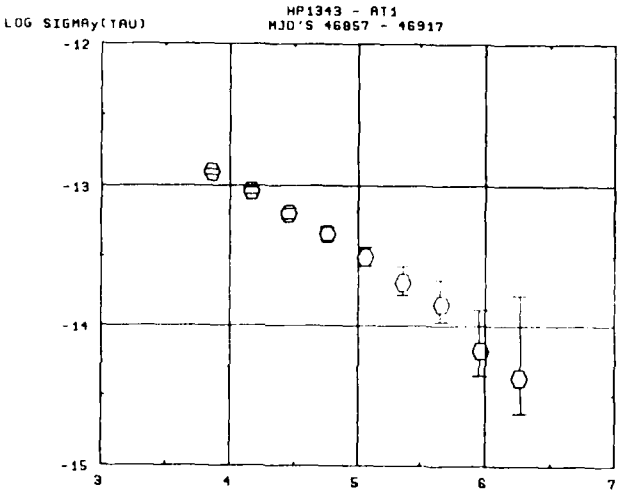

Fig. 5b
f_z 38.9 kHz
zero crossing.

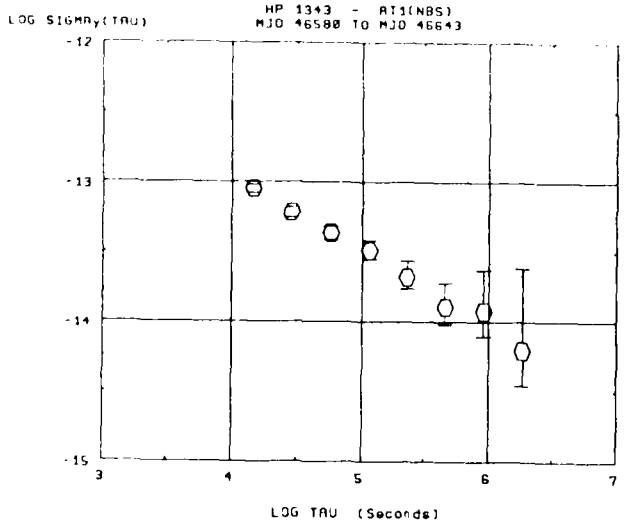

Fig. 5a
f_z= 53 kHz
initial setting.

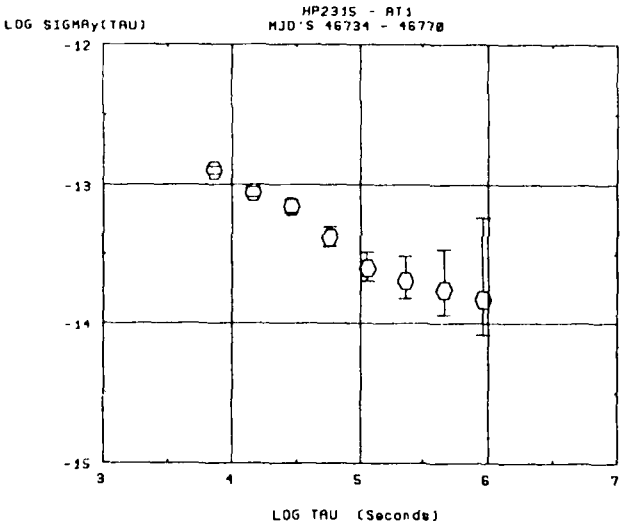

Fig. 6a
f_z= 53 kHz
inizial setting.

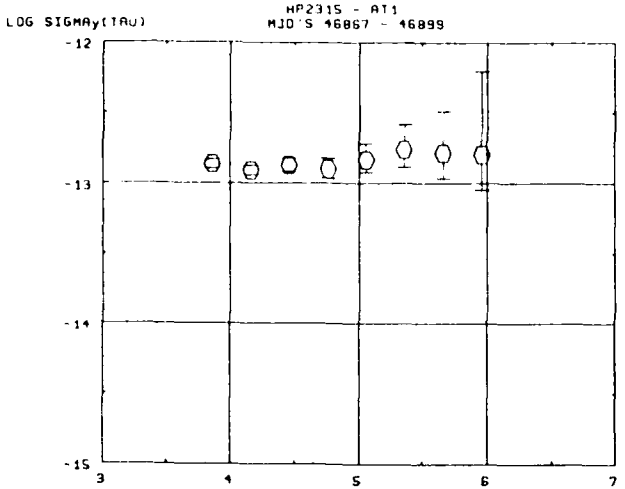

Fig. 6b
f_z= 53 kHz
5x10^{-13}/dB Power coefficient,
Unstable Power.

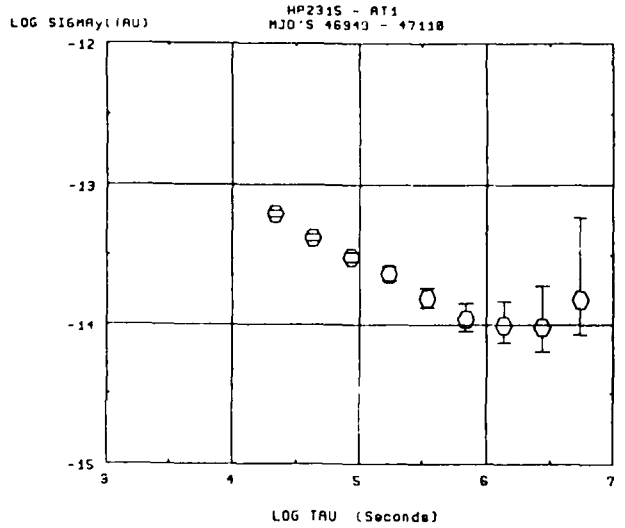

Fig. 6c
f_z= 53 kHz
Compensation by cavity tuning.

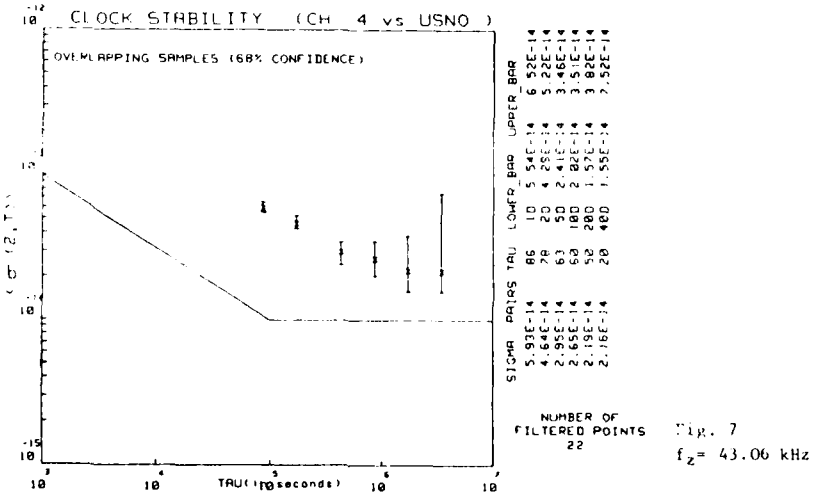

Fig. 7
f_z= 43.06 kHz

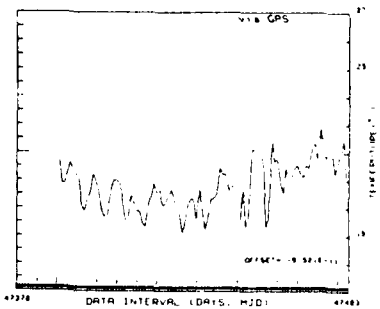

Fig. 8 a

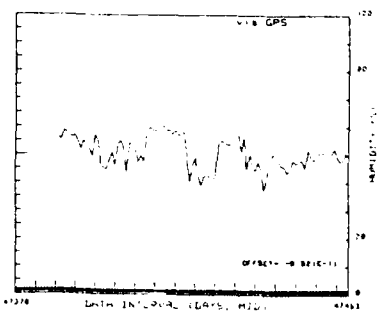

Fig. 8b

Fig. 9

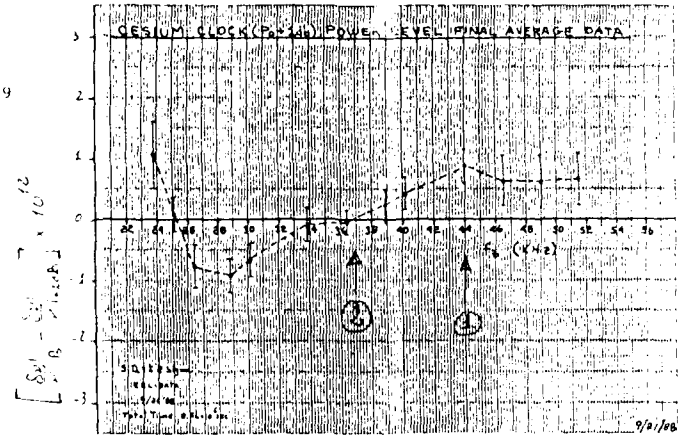

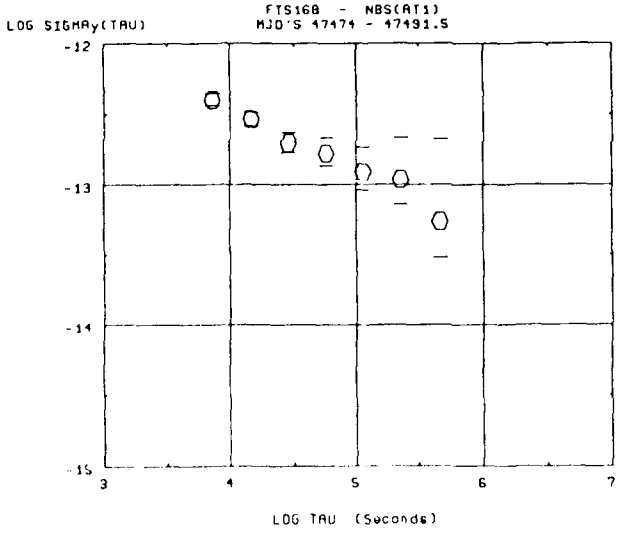

Fig. 10
f_z = 32 kHz

THE CIVIL GPS SERVICE

W. J. Klepczynski & L. G. Charron
U. S. Naval Observatory
Washington, DC 20392

Abstract

This paper will summarize the efforts which have been made to facilitate the establishment of a Civil GPS Service. Because there is very little definitive information currently available, the paper will highlight some of the activities which have taken place. Those items of interest to the PTTI community will be stressed.

INTRODUCTION TO THE CIVIL GPS SERVICE (CGS)

The Air Force has stated that it will have no resources available for the distribution of data in support of civil users when the GPS system becomes operational. Recognizing that there is a group of civilian users who now get the information they need for planning and for reducing special series of observations from contacts at the GPS Master Control Station (MCS), the Air Force has made a special effort to assist the civilian community in organizing for the time when the present channels of data distribution will be transferred to a single channel within the ORMS (Operational Status and Capability [OPSCAP] Reporting and Management System). The ORMS will be the primary means of distributing GPS data to the military community. It will also be the means by which selected GPS data will be distributed to the the civil community.

In 1986, the Air Force issued a contract to the Applied Research Laboratories of the University of Texas (ARL-UT) to help study the problem. What is presented here is a synopsis of what happened under that study and what has occurred since the study was published [1]. As an outgrowth of that study, the Civil GPS Service (CGS) was established. It has the overall administrative responsibility for providing information and data to the civil community. The Civil GPS Information Center (CGIC) will acquire and disseminate the information.

There is not much which can be said definitively at this time on either the CGS or the CGIC. Plans for both are still in a state of flux. While the Department of Transportation (DoT) has agreed to be the lead Department in establishing the CGS, no Agency within the DoT has yet been tasked with its operation. What will be required of the CGIC is still being discussed.

CGS STEERING COMMITTEE

In December, 1986, after consulting with many members of the GPS user community, one of the first things which ARL-UT did was to recommend the establishment of a Steering Committee for the Civil GPS Service. The charter (Figure 1) for the Steering Committee consisted of 2 main responsibilities. The first was to consider and review the system design of the Civil GPS Information Center, the primary vehicle for the acquisition and distribution of GPS data to the civilian community. The next was to review the administrative structure of the CGS itself. It was thought best that the Steering Committee meet quarterly and that it initially be chaired by someone from the Department

of Defense (DoD). The composition of the initial 18 member Steering Committee was 10 members from either the military or civilians associated with military organizations and 8 representatives from other civilian government agencies, universities and private organizations. Figure 2 outlines the organizations represented by these people.

As the members became more familiar with the concepts involved during the following year, it was thought best to have a chairperson from the civil, rather than from the military community. The committee determined that the Department of Transportation (DoT), as part of its civil radio navigation responsibilities, was best suited to undertake the CGS function. The DoT concurred. During the transition period, the CGS Steering Committee was co–chaired by a representative of DoD and DoT. Early in 1988, the transition was complete and David Scull, Research and Special Projects Administration (RSPA), DoT, was named sole Chairperson of the Steering Committee.

The items discussed under the charter for the Steering Committee were varied (Figure 3). Some of the issues which dealt with the Administrative Structure of the CGS were the concern of the CGS: to interact smoothly with civil GPS users and the Air Force GPS administration; to be an advocate for civil use of GPS; and to deal with liability concerns. In fact, this last issue may turn out to be one of the greatest impediments to be overcome by the CGS.

With regard to the CGIC, the possibility of using an existing GPS data base as an interim, demonstration system was also considered. There were also lively discussions on the impact of GPS Security Policy on the data provided to the CGIC by ORMS. This led to a proposal that Selective Availability not be done to at least one satellite in response to the wishes of the PTTI community. More will be said on this proposal later.

Figure 4, taken from Reference 1, gives a possible depiction of the envisioned CGS. The CGS oversees the CGIC and interacts with GPS Management and the Civilian User Community. The CGIC receives GPS data from the ORMS and distributes it to the Civilian User Community. It will also receive GPS data from any other additional sources that provide it. Because it may not be able to verify or guarantee the accuracy and precision of all this data, the question of liability arose.

An additional consideration is the provision of information to the civil user who has been granted access to the non–degraded signal. This may possibly require another layer in the structure of the CGIC.

CGS USER SURVEY

Concurrent with the formation of the Steering Committee, ARL–UT proceeded to prepare a user survey which was issued during the summer of 1987. The survey was an attempt to assess user requirements and determine the methods the civilian community preferred for acquiring and disseminating data. In the Fall, a User Workshop was held in conjunction with the First Technical Symposium of the Satellite Division of the Institute of Navigation at Colorado Springs, CO, to discuss the results.

There were 178 responses to this CGS User Survey. Of them, 55% were from domestic users and 45% from foreign users. Most of those who responded had requirements for some form of GPS data either daily or weekly. Obviously, all those who responded were experienced GPS users. It was impossible to identify and send the survey to probable GPS users even though some groups were identified as potential users.

There seemed to be an equal division among users who required pre–event data, real–time data and those who needed after–the–fact data within a week or two. In response to the question on how the user would prefer to receive needed GPS data, computer modems and publications were the choice of about 50% of the respondents. Machine readable disks and tapes were also desired. There was also a strong interest in voice recordings.

The GPS configuration status, timetables of scheduled events and orbital information were the types of information most frequently requested or needed. There was also a large response for timing information. This was to be expected since the survey was distributed over the U.S. Naval Observatory (USNO) Automatic Data Service (ADS).

CIVIL GPS INFORMATION CENTER (CGIC)

The Civil GPS Information Center will be the primary distribution point for GPS data to the civilian users. Figure 5 highlights some of the points concerning the CGIC which have been discussed by the CGS Steering Committee. The main concerns of the CGS Steering Committee in regard to the CGIC have been whether the CGIC can be self-supporting and the amount of processing or re-formatting of the GPS data that it should do. Unfortunately, nothing definitive can be stated about this very crucial and important aspect of the CGIC. It is a desirous goal of the CGS Steering Committee that the CGIC be able to generate sufficient revenues to be self-supporting. However, in order to be self-supporting, it seems that the CGIC will have to be very responsive to the requirements and needs of the civilian community. Whether this can be done efficiently and in a cost-effective manner is very difficult to estimate at this time. It is almost impossible to factor the question of liability into the estimates.

THE INTERFACE CONTROL DOCUMENT

As stated earlier, the GPS Master Control Station has provided data to the civil community for use in planning and reducing observations. However, once the GPS is operational the Air Force will no longer have the resources necessary to continue this support on a personal basis. Part of the ARL-UT effort was intended to determine what was required to transfer necessary GPS data from the ORMS to a single civil GPS Information Center for further distribution to the civil community. The result of this effort was Vol. III of Ref. 1, entitled The Interface Control Document for the Civil GPS Service Interface to the OPSCAP Reporting and Management System. Figure 6 shows some of the GPS data which was noted as being required by the PTTI community.

The Interface Control Document has been found to be a useful starting point in the determination of requirements. After review of this draft ICD, it is apparent that some revision must still be made. Of immediate concern is that some information stated as a requirement could jeopardize security. Obviously that information could not be provided. The various sub-committee working groups discussed below will attempt to further define actual requirements.

PTTI PROPOSAL

While not yet operational, GPS has become the primary world-wide time distribution system. More and more systems are investing in less expensive GPS timing receivers rather than in expensive clocks. With the implementation of Selective Availability (S/A) which would degrade the GPS navigation transmissions, this cost saving could be negated. This is a cause for concern within both the civil and the military timing communities. Both ephemeris and clock information would be affected.

To minimize the impact, Paul Wheeler of the U.S. Naval Observatory (USNO), at a meeting of the CGS Steering Committee, proposed that no degradation be applied to at least one satellite. By this means then, full timing accuracy would be available at least once per day for global time transfer while not affecting the navigation degradation required by DoD. Later, for redundancy and reliability, it was suggested that a second satellite be left undegraded. This second satellite would be located directly opposite from the first. D. Allan of the National Institute for Standards and Technology

(NIST, formerly NBS) has suggested that one additional satellite with partial degradation be added to this proposal. The partially degraded satellite would prove useful for increasing Common View Time Transfer coverage.

This proposal, with an endorsement by the Oceanographer of the Navy, has been submitted to the Assistant Secretary of Defense (Command, Control, Communications and Intelligence) by USNO in its 1988 Annual Summary of PTTI Requirements and Operations. Since the issue of S/A is one of security, any negative impact on national security must be evaluated. This is currently being done.

CURRENT DEVELOPMENTS

Since GPS is a truly global system, the CGS Steering Committee at its November 1988 meeting, invited representatives of several international civil groups to participate in its deliberations. Under consideration for the CGIC is the establishment of international nodal points for the dissemination of GPS data. With this in mind a sub–committee, under the chairmanship of G. Preiss of Norwegian Mapping has been formed to investigate the interest and the requirements of such a node.

At the same time, a timing sub–committee under the chairmanship of W. Klepczynski, USNO, was formed to further investigate the timing requirements of the civil user. Using the Interface Control Document for the Civil GPS Service described above as a starting point, a refinement of the data items required, the format of the data, the preferred means of dissemination and the frequency/timeliness of distribution will be attempted. Input from the user community is needed. The draft Interface Control Document is available from the Defense Technical Information Center, FDRA, Cameron Station, Alexandria, VA 22304–6145 and from the National Technical Information Service, 5285 Port Royal Road, Springfield, VA 22161.

In addition, a surveying sub–committee was established under the chairmanship of W. Strange of the National Geodetic Service, NOAA. This group will be concerned with the GPS data requirements of the surveying community.

The effort of defining the Civil GPS Service and the CGIC will continue during the next year. There are several issues that must still be resolved and much work remains to be done.

REFERENCES

1) Tucker, Arnold J., A GPS Information and Data System for the Civil Community, ARL–TR–88–11, Four Volume Set, Vol. I– Requirements of the Civil GPS User, Vol. II–Appendices to Volume I, Vol. III–Interface Control Document, Vol. IV– Synopsis of CGS User Workshop, published by Applied Research Laboratories, University of Texas at Austin, P.O. Box 8029, Austin, TX 78713–8029.

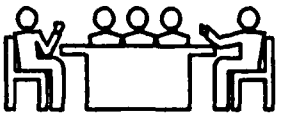

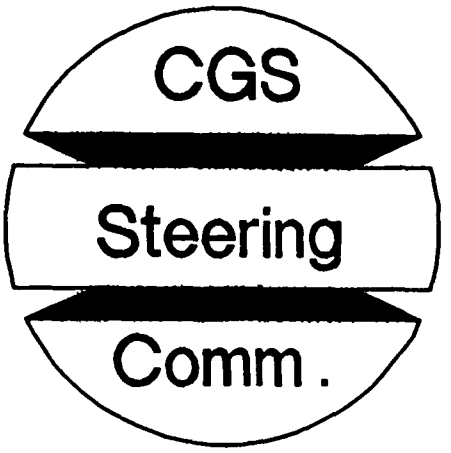

CHARTER

- Review System Design of CGIC
- Review Administrative Structure
- Meet Quarterly
- Now Chaired by DoT
- Consider the ability of the CGS to:
  a) be self-supporting;
  b) interact smoothly with DoD; and
  c) be an advocate for civil use of GPS

Figure 1 – Highlights of Items Considered within the Charter of the CGS Steering Committee

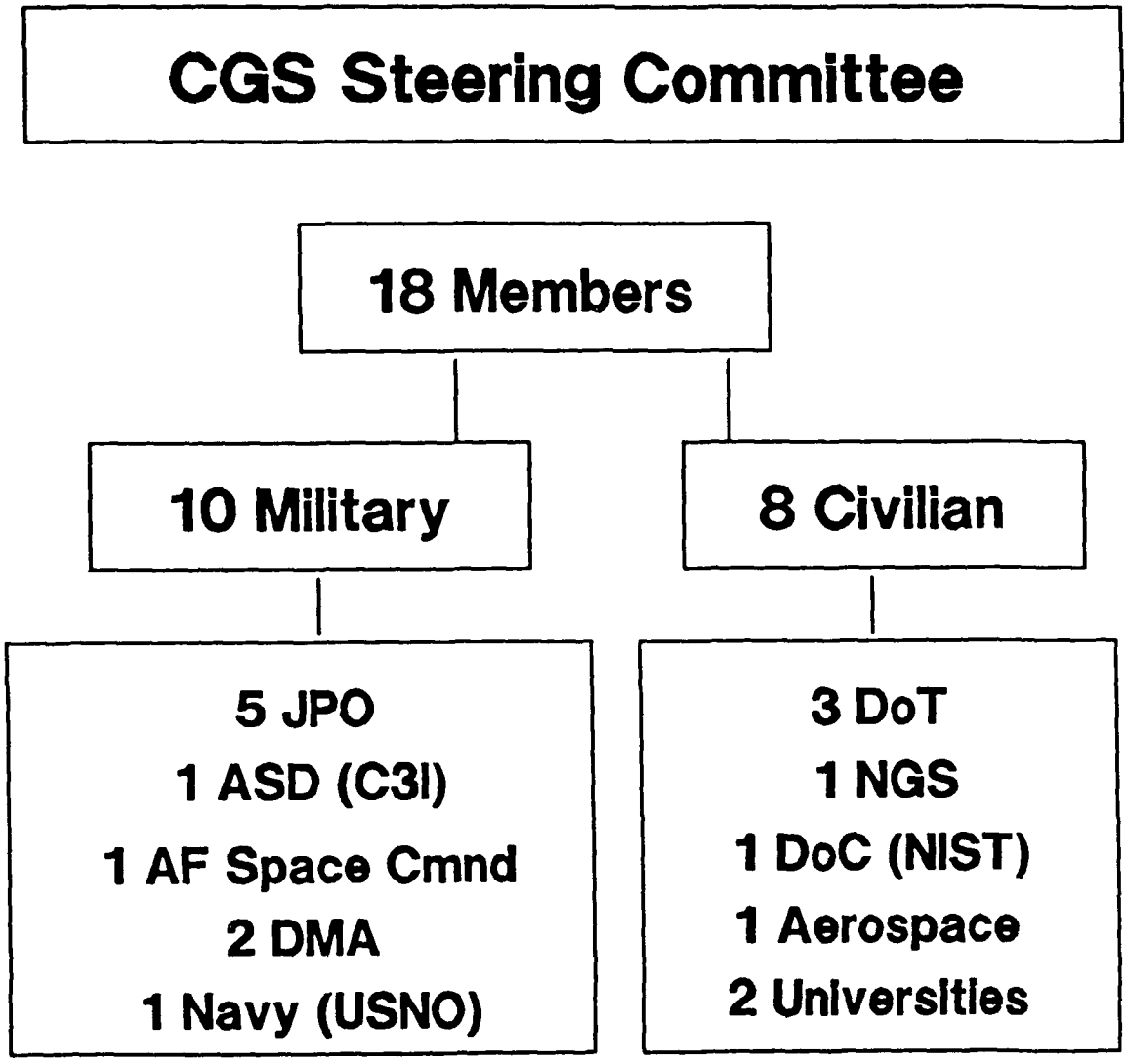

Figure 2 – Initial Composition of the CGS Steering Committee

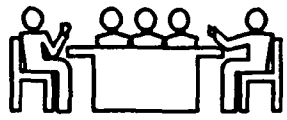

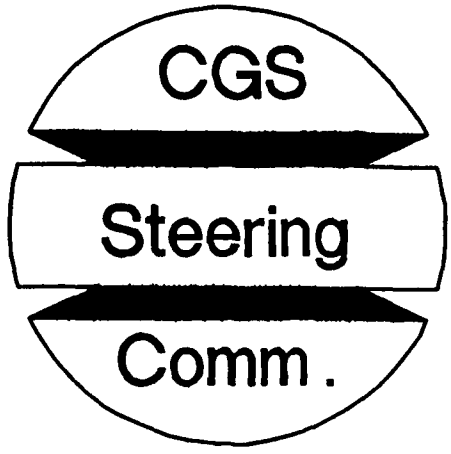

TOPICS

- Administrative Structure of CGS
- Interim System
- Liability Considerations
- Impact of GPS Security Policy on GPS
- PTTI Proposal for Undegraded Time

Figure 3 – Some of the Topics Discussed by the CGS Steering Committee

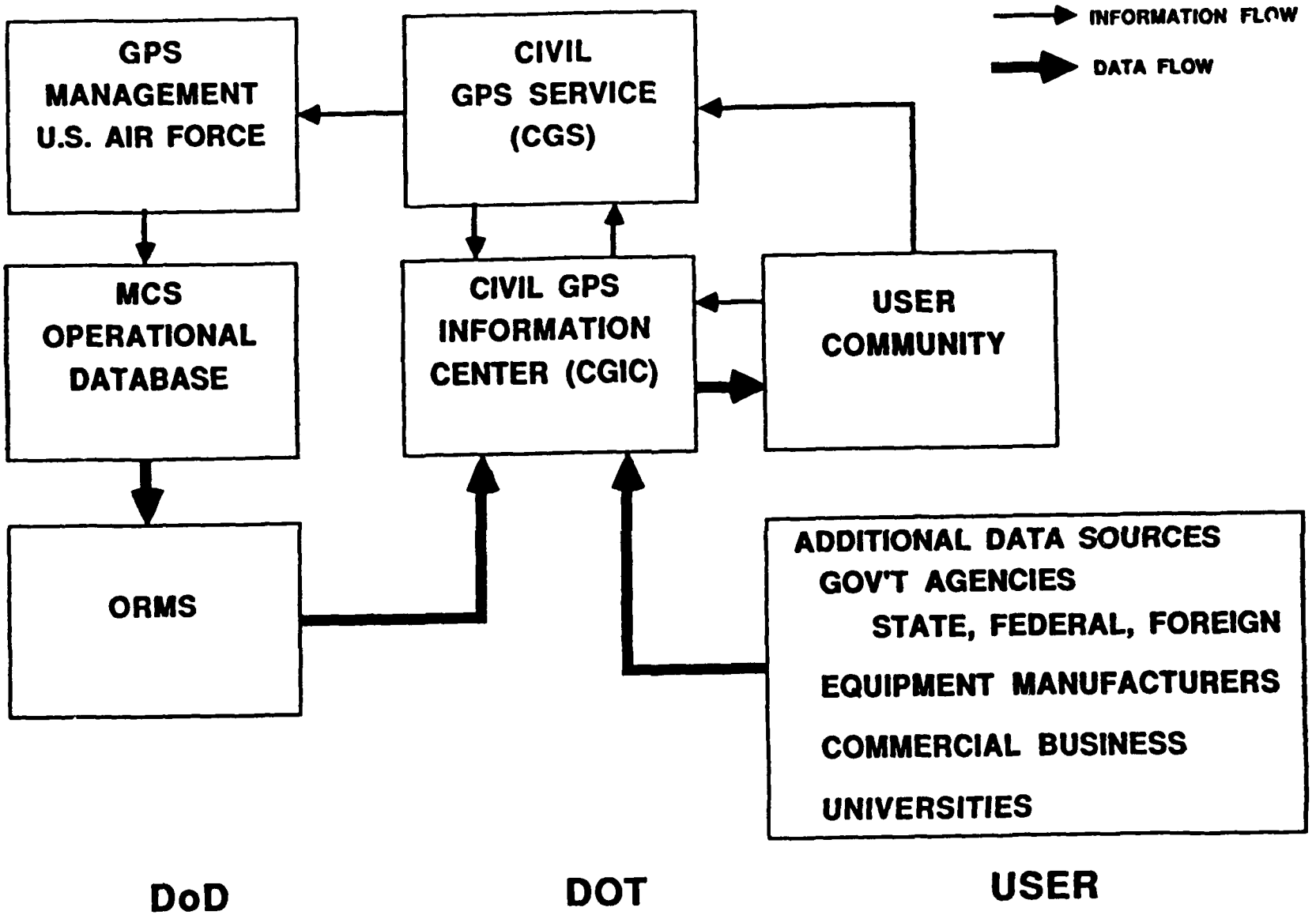

Figure 4 – One Possible Way to Depict the Interaction of the CGS with the Civilian User Community and the Air Force

CIVIL GPS INFORMATION CENTER

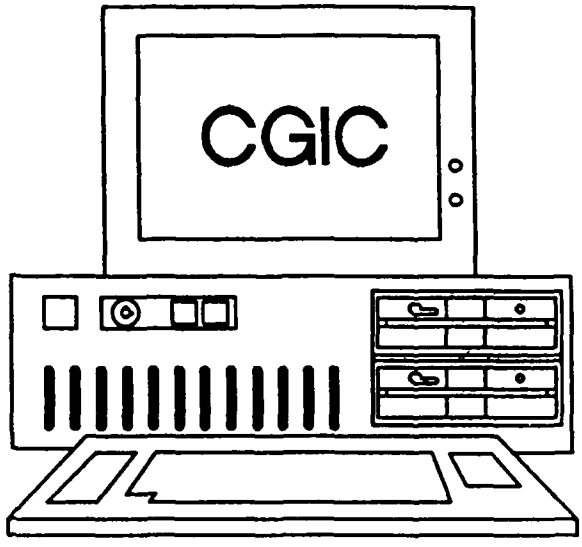

* Controlled by CGS
* Stores and Formats Data
* Data Distribution Point to the Users
* Receives GPS Nav Status Info from Operational Status and Capability (OPSCAP) Reporting and Management System (ORMS)

Figure 5 – Areas of Concern for the Civil GPS Information Center

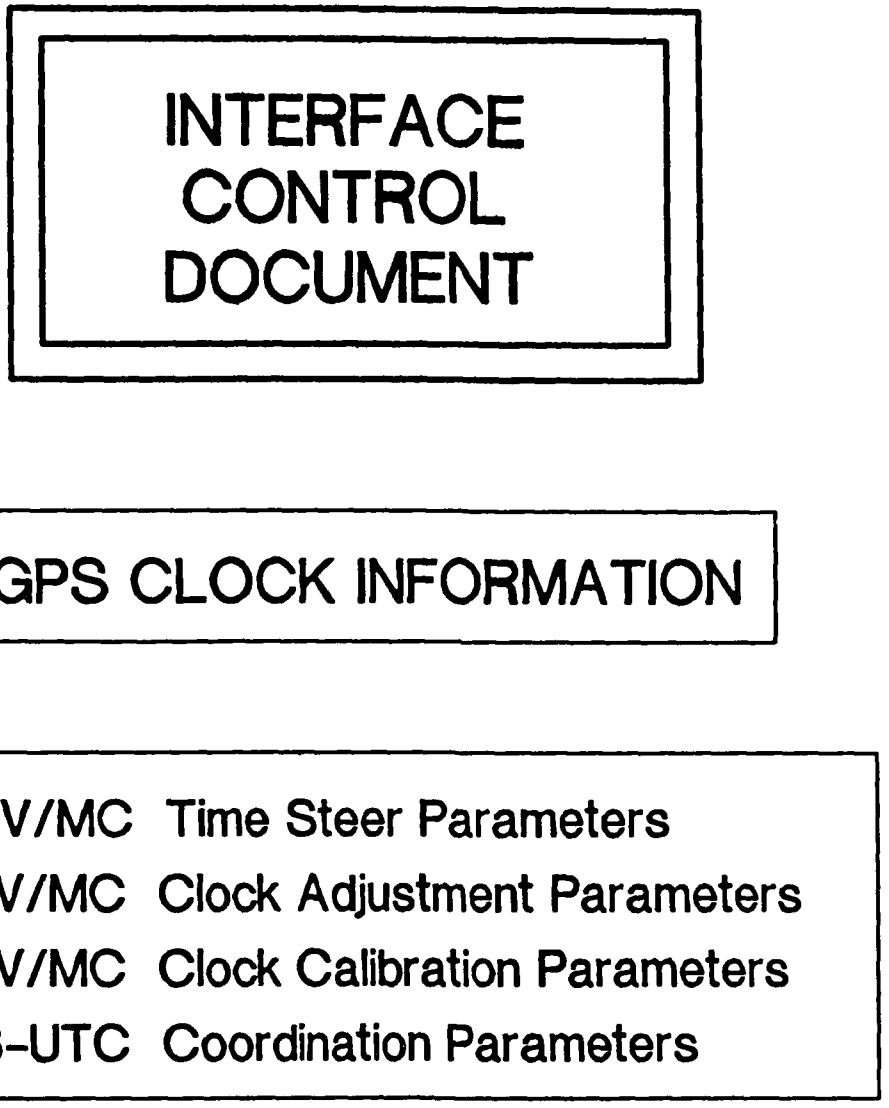

Figure 6 – GPS Clock Information in the Draft Interface control Document Which is of Use to the PTTI Community

QUESTIONS AND ANSWERS

UNIDENTIFIED QUESTIONER, Not into the microphone...

DR. KLEPCZYNSKI: I am sorry that John Scull is not here. No, there is no official list of users. There is a list of the people that respond to the survey, and that forms the user list as such.

UNIDENTIFIED QUESTIONER, Not into the microphone...

DR. KLEPCZYNSKI: We plan to become active as soon as possible, probably in the next two or three months. The plans are that the selective availability will be enabled as soon as the Block II satellites are launched. The satellites that are currently flying will not be affected by selective availability. They should still be around for another two or three years. We have to get our foot in the door and make our wishes know before the policy becomes firm and cannot be changed. We feel that, if it can be done in the next two or three months, it will still be possible to influence the policy-making decision.

JIM SEMLER, INTERSTATE ELECTRONICS: One of the things that has been mentioned is changing the GPS orbital parameters—increasing the orbital altitude. This has a certain effect in that you no longer get a repeating ground track, which is useful in doing common-view tracks from day-to-day. I wonder if there has been any consideration of those effects.

DR. KLEPCZYNSKI: That is correct. In fact, that is the proposal from the Joint Program Office. GPS has three sets of four satellites, and if the satellites are increased in altitude by another 50 kilometers, the current periodicity will change. Consequently, the geometry with respect to the earth will be changing from day-to-day. That is why three sets of four satellites were chosen. As the geometry over the earth changed, they would switch to another set. The decision to lift the satellites another 50 kilometers in orbit, to my understanding, is still not definite yet. There are still some things to be ironed out because there are certain technical questions within the satellites themselves as to how they will be affected by this rise of another 50 kilometers. So that is not 100% firm yet.

DR. KLEPCZYNSKI: Please let it be known what the problems might be. This is a very important question.

DR. GERARD LACHAPELLE, UNIVERSITY OF CALGARY, CANADA: I am quite concerned with the ionospheric effect because if there is only one or two satellites which are not implemented with selective availability, it means, that for time transfer, we will not have the same capability to decrease the effect of the ionosphere by observing any satellite in view. That will put, in my opinion, a severe restriction on the capability to perform time transfer. Do you have any comments on that?

DR. KLEPCZYNSKI: Yes, as a mater of fact, since there are no more questions and we have ten more minutes scheduled, I might ask Myron Moranian to show a few slides on the effect of the modeled ionosphere corrections vs. the measured ionosphere corrections. At the observatory we have two dual-frequency timing receivers which are used both in Washington and in Florida. We have been tracking and doing observations with these two. We have some preliminary data which, if Myron would come up and show and discuss, will show you the effect of the ionosphere. If I may steal Myron's message, the improperly modeled ionosphere can give errors on the order of at least ten nanoseconds or so. While this is not a large amount, it can still be significant. For a lot of users, that may not be too bad.

Myron Moranian showed the slides in question at this point.

JOHN KLOBUCHAR, AIR FORCE GEOPHYSICS LABORATORY: I would like to first ask a question and then make a couple of comments. What are you using for an ionospheric

model?

DR. KLEPCZYNSKI: The model transmitted by the satellites.

MR. KLOBUCHAR: I know a little bit about that and I must caution you that that model is advertised as a 50% RMS model. Anyone who tries to use it for more than that does so at his own peril. Secondly, any attempt to use daily values, or even more often values of solar flux does that at his own peril also. Numerous studies have been made of the ionosphere in which it is shown that the short term correlation of the total electron content, or time delay if you will, does not correlate very well with the day–to–day values of solar flux. The original decision to use the five–day running mean of solar flux in that model and the Master Control Facility had some unfortunate start–up problems and some recurring problems, but that is probably the "best" way to do it anybody that wants to get better than about 50 or 60% RMS should come and listen to my talk tomorrow after lunch.

DR. KLEPCZYNSKI: We have a comment here from Dr. Winkler.

DR. WINKLER: Dr. Klobuchar, what is your estimation of the correlation for the same moment for geographically distant locations? That is the problem that you have in common view.

DR. KLOBUCHAR: Yes. For the correlation to do you any good, it has to be very high. If the correlation is 0.7, that only explains 28% of the residuals. A correlation distance of deviations from monthly average at two stations, for instance, I know the time delay at Washington due to the ionosphere and I call up a colleague in Boulder and I say to David Allan "Hey, it is ten percent higher than normal today", it isn't going to ten percent higher in Boulder. The correlation distance is of the order of 1500 kilometers or so for that 0.7, and it is less, of course, for correlation that is higher.

DR. KLEPCZYNSKI: It seems extremely fortuitous that the measured ionospheric corrections are agreeing with the model at this point in time because of the low solar activity at this point.

DR. LACHAPELLE, UNIVERSITY OF CALGARY, CANADA: In northern Canada, with selective availability and one frequency we could have errors as high as 100 nanoseconds in time transfer. If we didn't have selective availability we could watch many satellites continuously, some towards the south and somewhat decrease that. With selective availability would give us a problem. Another problem is that under strong auroral conditions we would have loss of phase lock on the carrier. This has already been seen at some times in the north. It has a very strong correlation with magnetic storms. This will have a severe effect on GPS navigation and time transfer as well.

DR. Klepczynski: That is an interesting observation. I guess that another observation is that the difference between the measured time delays and the model will be a function of time that varies throughout the year, and also a function of solar activity.

DAVID ALLAN, NIST: It is probably worth mentioning that there are code–free ionospheric calibrator receivers being made. One exists at the Paris Observatory and the accuracy of that one seems to be extremely good, on the order of a nanosecond or so. In the future we can anticipate, for the civil user, a code–less type of receiver for calibrating the ionosphere.

DR. KLEPCZYNSKI: We will hear about that receiver two papers from now.

DR. WINKLER, ASSN.: It is clear that, in the best of all worlds, we would have all satellites unchanged. For the moment it is clear also that the best way to kill any proposal is to make it unreasonable. That is a technique that is used over and over again in political circles. If you don't like a proposal, improve it so that it becomes unacceptable. I think that we have the same situation in our proposal to make two satellites undegraded. Of

course, it would be better to have three, or four, or five undegraded, but that is the best way to make it unacceptable and we would have no relief whatsoever. I think that a little bit is better than nothing at the moment. In the present situation it is my firm belief that the only chance that you have is, at most, two undegraded satellites. The question then is "How is this going to affect your operations?" I can only repeat Dr. Klepczynski's request to let us know your opinions about that.

USE OF GPS TO SYNCHRONIZE THE AT&T NATIONAL TELECOMMUNICATIONS NETWORK

E. W. Butterline,
AT&T End User Organization,
Network Operations Group

J. E. Abate, G. P. Zampetti,
AT&T Bell Laboratories

Abstract

Presently, AT&T synchronizes its national networks using analog signals derived from a cesium clock ensemble having a precision of a few parts in 10^{-12}. These analog signals have well served the need for precise frequency in what was predominantly an analog network. However, the AT&T network is rapidly being transitioned to a digital network which needs precise time rather than frequency. As a result, several alternatives were considered and the one chosen was a new system based on Global Positioning System (GPS).

The GPS based system, termed a Primary Reference Clock or PRC, employs a GPS receiver providing long term timing accuracy along with duplicated disciplined rubidium oscillators providing short term (ie. one day) stability. Under computer control, these three elements are verified against each other and against identical PRC systems in other parts of the network. The PRC system produces a digital signal used to synchronize a master clock in the node which in turn produces a signal that is (1) used to synchronize all other clocks in the node, and (2) distributed on a digital basis to all neighboring nodes. By use of monitoring equipment at each PRC, the performance of the master clock at every AT&T network node will be verified against the GPS signal at each PRC. For the first time, a national telecommunications network will be monitored and verified to be performing to a precision approaching Universal Coordinated Time (UTC).

INTRODUCTION

Synchronization of telecommunication networks is becoming increasingly important as the evolution of digital switching and transmission facilities becomes the norm in today's national networks. The lack of adequate synchronization for these networks would impair many of the information signals important to the functioning of industry and government. To meet the need for high quality synchronization, AT&T has developed a new verifiable synchronization network.

This paper describes this new synchronization network focusing on the new AT&T Primary Reference Clock (hereafter referred to as the PRC), its verification methodology and capabilities, and the inter–node and intra–node methodology for distributing its timing reference to nodes and systems throughout AT&T's digital and remaining analog networks. The PRC employs a GPS receiver providing long term timing accuracy along with duplicated disciplined rubidium oscillators providing short term (ie. one day) stability. Under computer control, these three elements are verified against each other and against identical PRC systems in other parts of the network. The PRC system produces a digital signal used to synchronize a co–located master clock in the node, which in turn produces a

signal that is: (1) used to synchronize all other clocks in the node, and (2) distributed on a digital basis to all neighboring nodes. By use of monitoring equipment at each PRC location, the performance of the master clocks at neighboring AT&T network nodes are verified against the PRC signal. For the first time, a national telecommunications network is monitored and verified to be performing to a precision approaching Universal Coordinated Time (UTC).

BACKGROUND

Presently, AT&T synchronizes its own national telecommunications network, as well as providing synchronization signals to most of the Regional Bell Operating Companies and many independent telephone companies, using analog signals derived from a cesium clock ensemble [1]. This ensemble, known as the Basic Synchronization Reference Frequency (BSRF) is located in Hillsboro, MO., and has a long term accuracy of a few parts in 10^{-12}. The 2048 KHz reference frequency from the BSRF is distributed on analog radio and coax systems as illustrated in Figure 1.

When BSRF was installed, AT&T used frequency division multiplexing in which even the most critical equipment could tolerate a 10^{-9} frequency offset. This frequency accuracy can be easily obtained from the BSRF distribution system even with transmission impairments such as dropouts, protections switching, and phase hits. The analog signals used to carry the BSRF reference frequency have well served the need for precise frequency in what was predominantly a long haul analog telecommunications network.

Today, however, AT&T is rapidly being transitioned to an all digital network in which time division transmission and switching functions are critical [2]. In general, synchronization of networks using time division systems encompasses bit, frame and network timing issues [3].

The bit timing level of synchronization deals with physical layer timing issues such as: clock insertion and recovery, transmission line jitter, sampling windows in eye patterns, and ones density. These issues are addressed in the fundamental design of the transport system and by adhering to engineering rules such as repeater spacing and maximum number of repeater spans.

The frame timing level of synchronization deals with identifying groupings of bits (time slots) which can be associated with a particular user. A framing signal encoded in the digital transmission system typically accomplishes this function. When time slots within a digital stream need to be processed separately, a frame alignment process is performed on an incoming stream. Once framing is determined, each time slot can be identified and stored for processing. The main synchronization issues at the frame level of synchronization are reframe time and framing loss detection.

The network timing level deals with processing of time slots. Under ideal conditions, time slots are sent from the source node at a perfectly uniform rate, delivered over the transmission system with a fixed delay, and clocked into the receiving node buffer. The receive node will then read the time slot currently in the store after a fixed delay. Assuming no random or systematic offset of the receive node clock relative to the sending clock, this processing will continue with no variation in the buffer and complete time slot integrity.

The objective of network timing, is to approach this idealized scenario. Time slot buffers (more commonly termed frame alignment buffers) can accommodate 125μs of systematic time error and 18μs of random time error without slipping time slots. The maximum long term systematic frequency departure allowed at the output of a network clock is 1×10^{-11}. This requirement has been established for a number of years both domestically [4,5] and internationally [6,7], and is based on achieving satisfactory slip rates on an end to end basis for the most critical services (voiceband data, facsimile, video, secure voice and secure data). Provisional short term requirements allow from 1 to 10 microseconds of time error in a day at the output of a network clock. The short term requirements are being put in

place to ensure that random or cyclical daily timing variations will not produce daily slips.

The performance objective of 1×10^{-11} for digital network timing is two orders of magnitude greater than the frequency accuracy required for analog transmission. The current synchronization plan to time the digital offices of AT&T was based on using the existing analog distribution system and implementing clocks to receive this signal and achieve the 1×10^{-11} recommendation.

This plan was first implemented in the early 1980's. Analysis of this architecture has been performed. The overall results of this evaluation produced two key findings. First, with evaluation and some minor redesign of the BSRF timing signal receiver algorithms, the 1×10^{-11} performance objective is achievable. Second, the 1×10^{-11} or better objective is subject to certain transmission and operational impairments levels which are not guaranteed to be obtained on all systems at all times based on normal network operations. Thus, although typical performance is several parts in 10^{-12}, it is possible, under certain condition, for a node to degrade to parts in 10^{-10} for a short period.

As a result, AT&T is deploying a network of distributed primary reference clocks to synchronize its digital network. These clocks will use the Global Positioning System (GPS) to provide long term timing accuracy to network nodes or buildings at fourteen locations within the continental United States.

This new synchronization network will have rich interconnectivity and the unique capability of verification at several levels. Verification is the capability to directly monitor the timing performance of each office or node. This capability enables AT&T to detect and resolve timing degradation before it becomes service impacting. Verification ensures uniform compliance of domestic and international timing standards at all nodes, and provides a cost effective tool to sectionalize and resolve timing problems.

AT&T's NEW PRIMARY REFERENCE CLOCK STRATEGY

Figure 2 illustrates the architecture of the new verifiable timing distribution plan. In addition to the fourteen PRC's located in the contiguous United States, PRC's will be located in Hawaii and Puerto Rico. This new synchronization network will have verification capability which permits the detection of timing degradation. The PRC reference is transmitted to other nodes, called secondary nodes, which do not contain a PRC. The PRC simultaneously monitors the reference it receives from at least two other PRC nodes as well as secondary nodes. The monitoring of neighboring PRC locations provides long term stability data. By employing a n-corner hat decomposition [8] of the PRC level stability data, the long term timing stability of each PRC location will be tracked and verified to parts in 10^{-13}. The architecture is designed so that secondary nodes are monitored by two independent PRCs. This provides a means to sectionalize nodal timing instability from transmission path timing instability. By deploying PRC's close to secondary locations, uniformly stable transmission path performance is attained both for transmitting and monitoring performance. Daily transmission path stability should exceed several parts in 10^{-12}.

In searching for a source of precise timing for a PRC, three alternatives were studied. The first was to continue to use a single cesium ensemble at one location along with a digitally based distribution system. The second and third would use regionally distributed PRC's using either LORAN-C or GPS and disciplined timing elements. Using a single cesium ensemble offers some economies, but does not permit nationwide verification, nor does it offer performance improvement over today's network. Using a nodal based system offers a broad based verification capability. LORAN-C was judged inferior to GPS in terms of time transfer accuracy, inherent operations, and future capabilities, so GPS was chosen to provide AT&T with a long term time reference.

Rubidium oscillators were selected over quartz and cesium as the disciplined timing elements. Our

strategy in using the GPS system was based on using a twenty–four hour observation period to obtain a a time and frequency error estimate. There are many reasons for this choice. First, a daily ensemble average effectively removes the daily systematic bias errors which arise in the time transfer process of GPS from user position errors and other sources. Second, ensemble averaging of the satellite tracks reduces random error sources as well as intentional degradation added to reduce the accuracy of the standard service. Third, evaluation of ensemble tracks permits the removal of outlying data which can contaminate the steering process.

For periods less than one day, a set of duplicated rubidium oscillators provide timing stability. The stability of the disciplined rubidium over the 24 hour interval between steering updates is equivalent to the stability of the steering update data from the GPS satellite tracks. For a 24 hour steering interval, rubidium oscillators proved to provide the best cost/performance tradeoff. Quartz oscillators cannot obtain the daily stability performance achievable from GPS, and cesium oscillators provide no real stability advantage and are more costly.

An AT&T 3B-2 computer is used to steer the rubidium oscillators and to verify their performance relative to one another and to the GPS receiver. The block diagram given in Figure 3 illustrates the interconnectivity of the PRC's computer, and indicates the DS1 [1] inputs from the other nodes and clocks used for timing monitoring. In the figure, the rubidium oscillators (Rb) are shown communicating with the disciplined controllers which in turn communicate with the 3B–2 monitor computer. The computer performs control, performance verification, and error recovery functions.

The timing outputs of the PRC are a pair of DS1 primary rate digital signals. The PRC outputs are used to provide timing reference to a master clock in a node containing typically many clocks. The master clock, known as the Building Integrated Timing Supply, or BITS, provides timing reference to all other clocks in that node as illustrated in Figure 4. The BITS provides input to a device known as a Clock Distribution Unit whose function is to provide multiple DS1 outputs to all clocks in the node requiring digital reference (eg. No. 4 ESS switch, DACS transmission system) and frequency locked clocks for analog frequency division multiplex (FDM) equipment.

INTER–NODE AND INTRA–NODE REFERENCE DISTRIBUTION

Buildings containing a PRC are known as Primary Nodes. Buildings which do not contain a PRC are known as Secondary Nodes and obtain their timing reference from a Primary Node in most cases, or from other Secondary Nodes in rare cases. Timing to Secondary Nodes is distributed on a digital basis using two DS1 signals which are routed over diverse facilities from different PRC's. These DS1 signals carry both traffic and synchronization reference between nodes as illustrated in Figure 5. The reference information is bridged from a cross–connect device known as a DSX–1 and transmitted to the clock of the system selected as the BITS. Thereafter, the reference distribution is the same as in the Primary Node. The timing is embedded in the DS1 traffic carrying signal as that signal is referenced to the BITS clock within the Primary Node which is the source for the reference.

VERIFICATION METHODOLOGY

As illustrated in Figure 6, there are four levels of verification that are used. The first is an ongoing verification of GPS performance by various laboratories such as the National Bureau of Standards,

[1] A DS1 is the primary rate synchronous digital signal used in the network. It is a 1544 Kbps signal consisting of 24 64 kbps time slots. Each time slot typically carries a single direction voice circuit.

the Naval Observatory, and the Network Synchronization Laboratory at AT&T Bell Laboratories at Holmdel, NJ. This high level verification results in long term changes in the synchronization network operations such as upgrading of steering algorithms.

The second level of verification is within the PRC itself. The PRC determines the relative timing instability or uncertainty associated with the three clocking elements in the system (the two disciplined rubidium oscillators and the GPS receiver). A three corner hat technique is used to decompose the pair-wise instability measurements between the three components, and determine the timing stability produce by each element. This technique can effectively detect marginal performance in any of the three clocking elements. This technique is limited to detection of short term daily timing instability, since in the long term, rubidium timing is not independent of the GPS receiver.

The third level of verification, called the Primary Tier (or long term) verification uses an N corner hat technique to determine the long term time uncertainty or noise of each of the Primary Nodes (eg. A, B, and C in Figure 6).

Finally, the fourth level, or Secondary Tier Verification, extends verification down to the Secondary Nodes, where the signals returning from the Secondary Node BITS clocks are monitored by at least two PRC's to determine their performance.

PERFORMANCE

Figure 7 illustrates the performance of the AT&T Primary Reference clock as compared to the current AT&T cesium ensemble and telecommunication synchronization standards. In Figure 7, the time keeping error relative to UTC is shown in seconds on the ordinate along with the observation time on the abscissa shown in seconds.

In case (1), the slope of the ANSI and CCITT specification is the allowed long term frequency accuracy of a PRC of 1×10^{-11}. The ANSI and CCITT specifications allow for a maximum daily time instability of 3000 ns which is reflected by the horizontal asymptote.

Case (2) shows typical performance of the AT&T cesium ensemble. It is monitored relative to LORAN-C and found to perform with a long term accuracy within a few parts in 10^{-12}. The daily timing stability is limited by diurnal transmission delay variation of typically 100 ns.

Case (3) shows the time keeping performance of the rubidium disciplined oscillator assuming a failure condition in which no daily steering is applied. It is based on a simplified assumption of optimal calibration of initial time, frequency and drift, and a benign environment. The control system applies feed forward correction for drift and temperature, and the thermal design maintains small ambient temperature variation 5 $^{\circ}C$ daily objective. Monte Carlo simulation of the holdover performance including temperature variation and residual calibration errors have recently been done which indicated that the PRC can maintain 1×10^{-11} for a period of 2 weeks without steering.

Cases (4) and (5) show the PRC performance under normal conditions. Case (4) shows the PRC three sigma time error specification of 200 ns. The PRC three sigma performance bound is based on measurements and analysis of the PRC components and simulation of the Kalman based steering algorithm. Case (5) shows typical performance based on a limited data recently obtained on a prototyped unit. The unit is achieving a daily rms stability of 25 ns (3×10^{-13}).

It is important to note that even though current standards allowed for plesiochronous operation of primary reference clocks, all the PRCs in AT&T will be maintained to within 280 ns (three sigma) of each other with an absolute accuracy approaching UTC (1×10^{-13} weekly rms stability).

CONCLUSIONS

AT&T is deploying a GPS based system, termed a Primary Reference Clock or PRC, which employs a GPS receiver providing long term timing accuracy along with duplicated disciplined rubidium oscillators providing short term (ie. one day) stability. Under computer control, these three elements are verified against each other and against identical PRC systems in other parts of the network. For the first time, a national telecommunications network will be monitored and verified to be performing to a precision approaching UTC.

REFERENCES

[1] J. F. Oberst,"Keeping Bell System Frequencies on the Beam," Bell System Record, March, 1984

[2] J. E. Abate, L. H. Brandenburg, J. C. Lawson, W. L. Ross, "No.4 ESS: The Switched Digital Network Plan," Bell System Technical Journal, Vol. 56, No. 7, pp. 1297-1320, Sept. 1977.

[3] J. E. Abate, J. R. Rosenberger, and M. Yin, "Keeping the Integrated Digital Network in Sync," Bell Laboratories Record, Sept. 1981

[4] AT&T Technical Reference PUB 60110, "Digital Synchronization Network Plan," December, 1983.

[5] American National Standard for Telecommunications,"Synchronization Interface Standards for Digital Networks," ANSI T1.101-1987

[6] CCITT Recommendation G.811, "Timing Requirements at the Output of Primary Reference Clocks Suitable for Plesiochronous Operation of International Digital Links."

[7] CCITT Recommendation G.824, "The Control of Jitter and Wander Within Digital Networks which are Based on the 1544 kbit/s Hierarchies."

[8] C. A. Greenhall, "A Likelihood Approach to the M-Cornered Hat-Preliminary Report," Proceedings of PTTI, 1987.

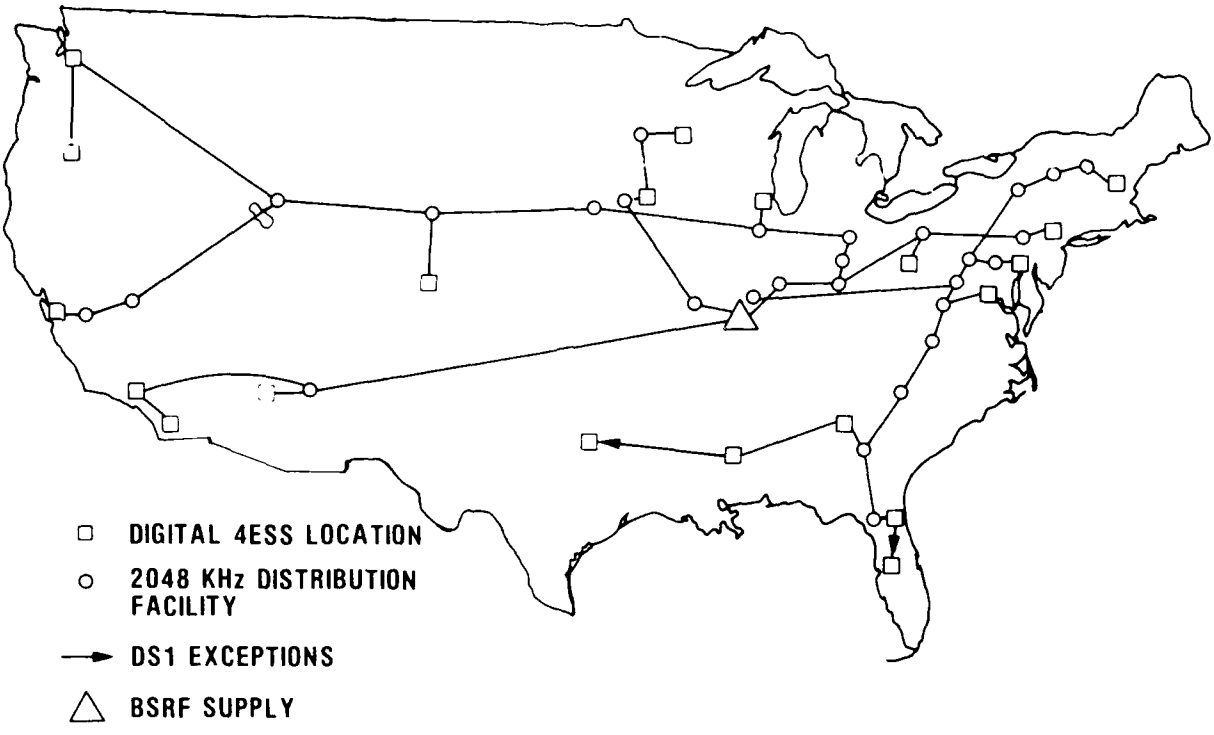

FIG. 1 CURRENT AT&T PRIMARY TIER ANALOG REFERENCE DISTRIBUTION SYSTEM (REPRESENTATIVE)

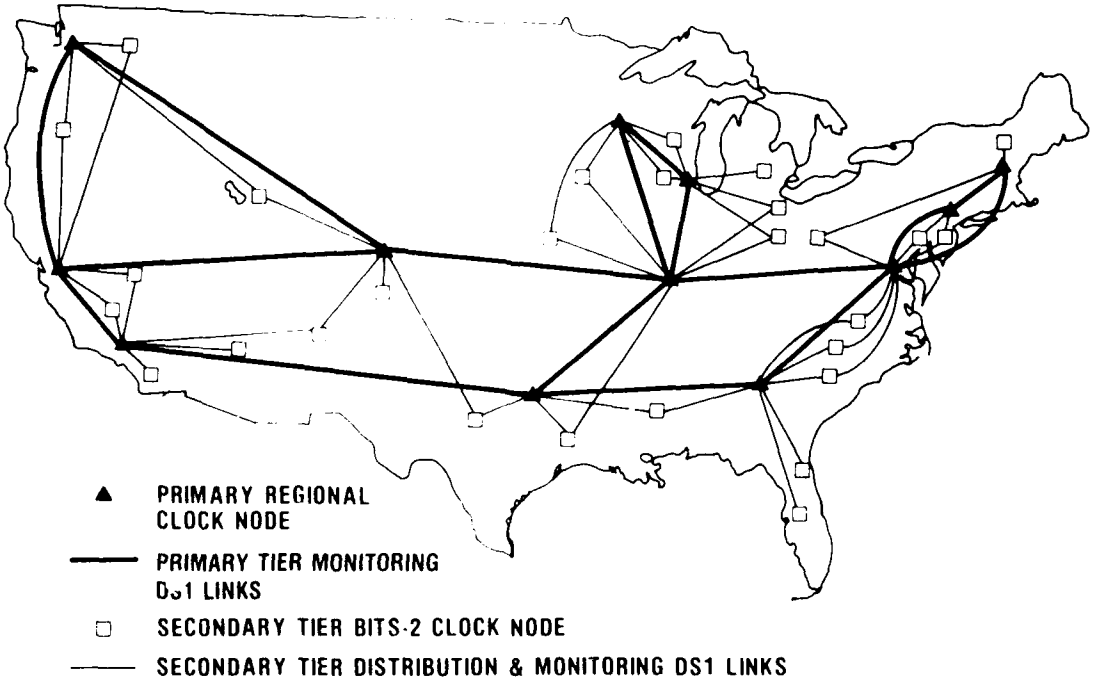

FIG. 2 NEW VERIFIABLE DIGITAL SYNC PLAN (REPRESENTATIVE)

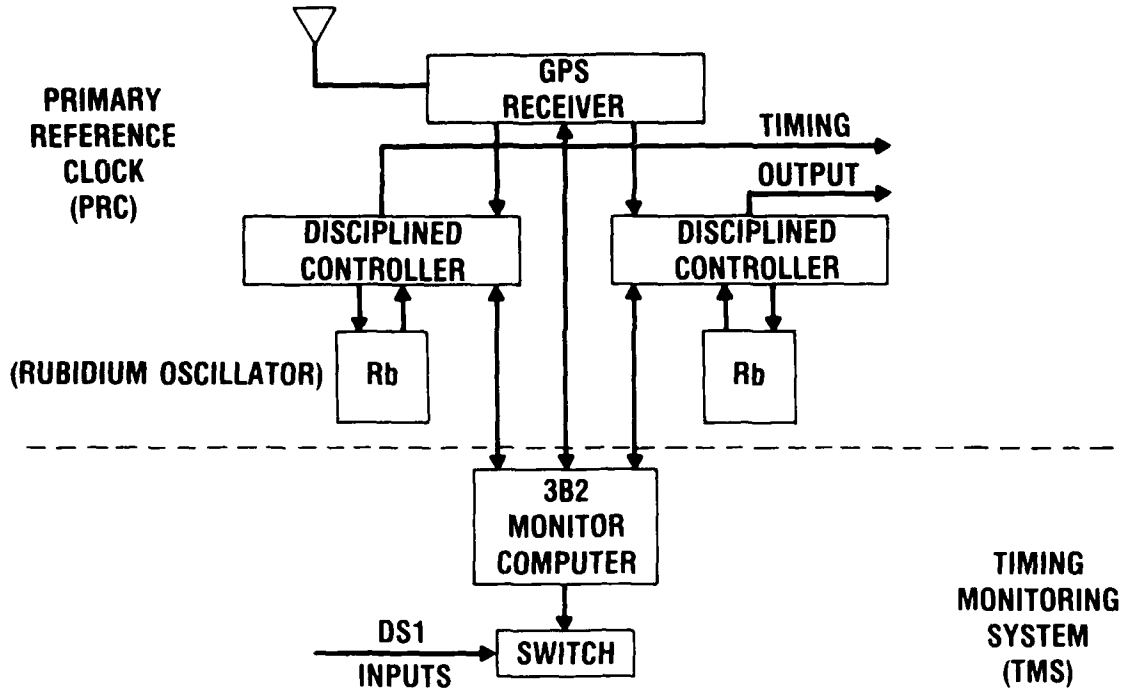

FIG. 3 PRIMARY REFERENCE CLOCK AND TIMING MONITORING SYSTEM

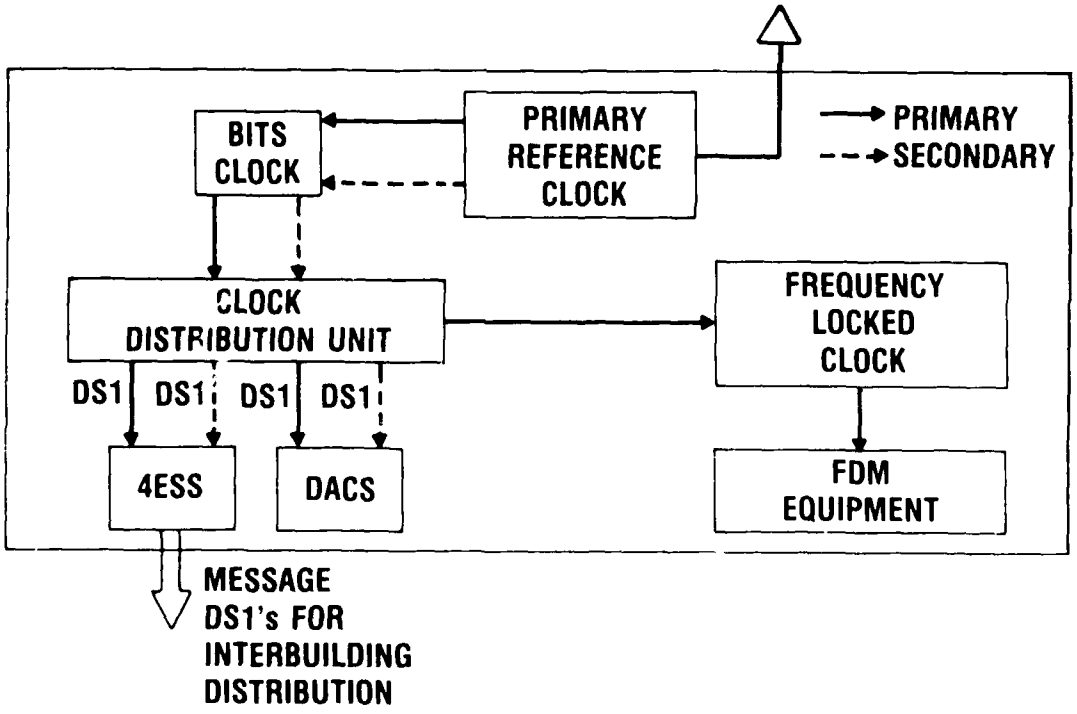

FIG. 4 PRIMARY NODE TIMING DISTRIBUTION

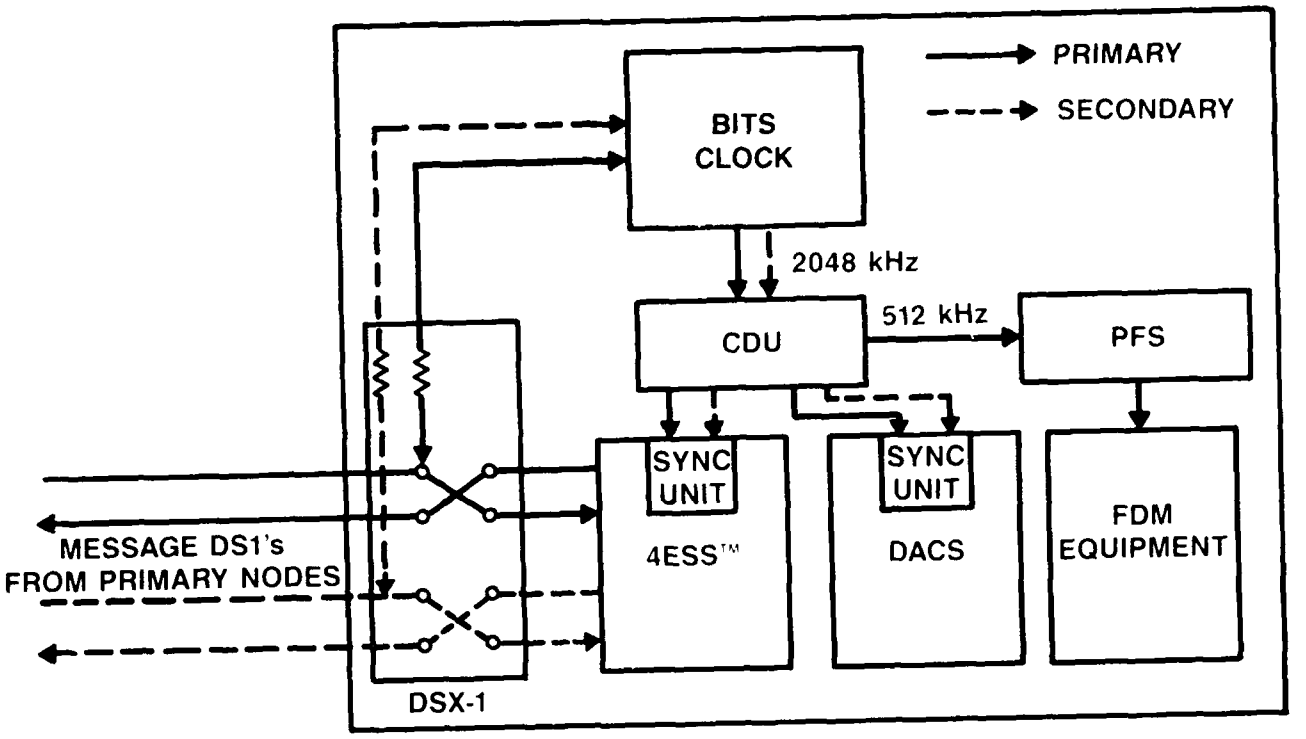

FIG. 5 SECONDARY NODE TIMING DISTRIBUTION

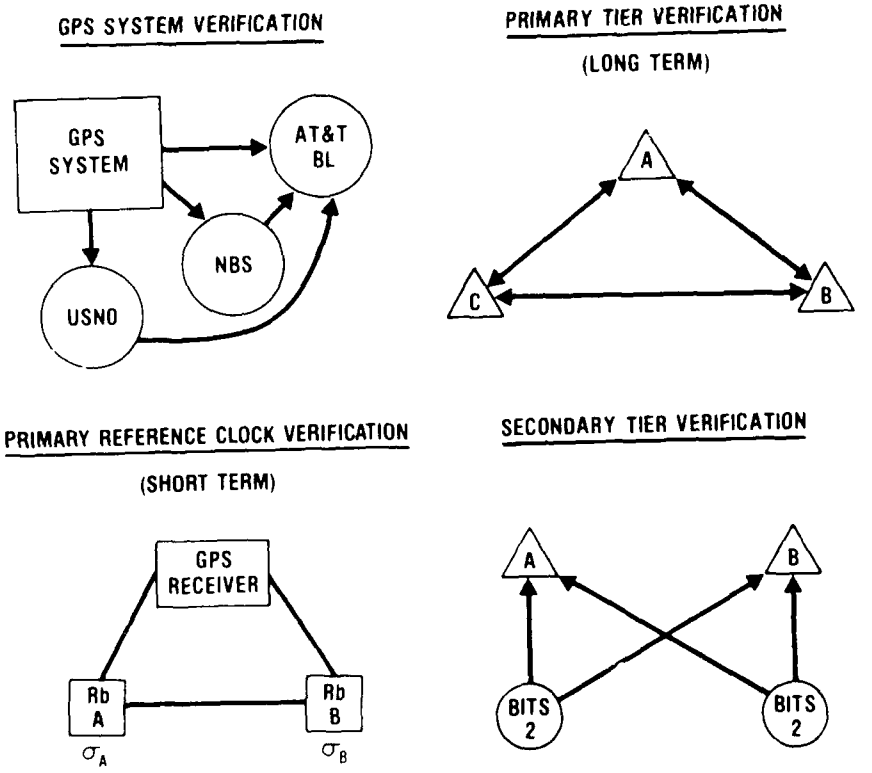

FIG. 6 LEVELS OF VERIFICATION

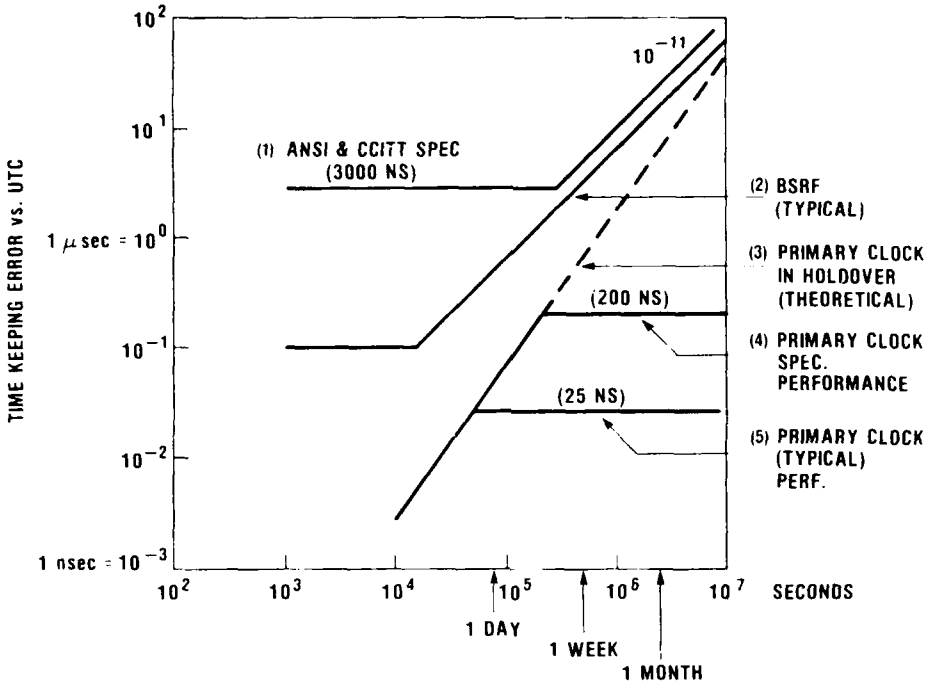

FIG. 7 PERFORMANCE COMPARISONS

QUESTIONS AND ANSWERS

DAVID ALLAN, NIST: Two questions—first, the slope on the red line is not due to a frequency offset since it is steeper than the frequency offset. Is there any explanation as to why it is that steep?

MR. ZAMPETTI: That slope is not due to a frequency offset. It does converge to the frequency offset, and I believe that it is an optimal calibration estimate, assuming random walk FM as a residual. I believe that that slope is plotted correctly as random walk FM. That is a theoretical curve that we just put on for comparison. It shows that the Rubidium is excellent. We have done some simulations incorporating thermal instabilities, calibration errors and other things and have found that for a period of two weeks the system is rock solid and would not require any action. It would still maintain the 10^{-11} stability specification.

MR. ALLAN: The second question is: When you steer the Rubidium, do you use C-field tuning?

MR. ZAMPETTI: Currently, that is what you are using.

MR. ALLAN: If that is not done perfectly, which it never can, of course, then it adds noise to the system. It is an unnecessary noise if one dealt with the measurements instead of trying to tune the C-field.

MR. ZAMPETTI: We are very enthusiastic supporters of synthesis steering. As the system progresses there is the possibility of doing that. It was not available to us as a matter of practical course, but it is something that we are seriously considering.

A DUAL FREQUENCY GPS RECEIVER MEASURING IONOSPHERIC EFFECTS WITHOUT CODE DEMODULATION AND ITS APPLICATION TO TIME COMPARISONS

M. Imae*, W. Lewandowski and C. Thomas
Bureau International des Poids et Mesures (BIPM)
Pavillon de Breteuil
F-92312 Sèvres Cedex, France

C. Miki
Communications Research Laboratory
Nukui Kita-machi, Koganei-shi
184 Tokyo, Japan

*Permanent address: Communications Research Laboratory as for C. Miki above.

ABSTRACT

The GPS (Global Positioning System) satellites have become widely used for daily time comparisons between the major time and frequency laboratories. The precision of time comparison by GPS satellites is now between one and a few tens of nanoseconds depending upon the distance between the laboratories. In the case of long-distance time comparisons, the ionospheric effect is one of the largest sources of uncertainty. To compensate for the ionospheric effect, we have developed a novel GPS receiver which measures the total electron content (TEC) along the signal path to the GPS satellite. It uses the property of cross-correlation between the P-code (Precise-code) signals which are transmitted from GPS satellites by L_1 (1575.42 MHz) and L_2 (1227.6 MHz), without demodulating P-code signal. Preliminary results using the prototype receiver give, for about 3 minutes observation time, an uncertainty in the measurement of TEC of $2 \times 10^{16}/m^2$, equivalent to an uncertainty in the delay of L_1 signal of 1 ns. We have begun to apply the results of this receiver to the time comparisons between USA and Europe.

INTRODUCTION

The major errors of time comparisons by simultaneous trackings of GPS satellites (common view [1]) come from satellite position, receiving antenna position, estimation of ionospheric and tropospheric delays, calibration of receiver differential delays and radio-signal multi-paths.

GPS receiver transportation [2] and adapted means of reception largely reduce some of them. Short-distance comparisons (up to 1000 km) are weakly affected by satellite position error and by ionosphere effects [3], furthermore receiving antenna coordinates can be redetermined [4], allowing time transfer with uncertainties of a few nanoseconds.

This research was carried out at BIPM. M. Imae was partly supported by the French Government through the Groupe de Recherches de Géodésie Spatiale.

But long distance time links, like USA-Europe, are performed with a rather bad precision, of the order of a few tens of nanoseconds. This is mainly due to satellite position errors and rather bad estimations of ionospheric delays, deduced from a ionospheric compensation model accessible to users of one frequency GPS receivers and providing a relative precision of 50 % [5].

We have developed a new codeless dual frequency GPS receiver, named GTR2, for measuring the total electron content (TEC) of ionosphere along the line of sight and then the GPS signal ionospheric delay.

In the following a brief description of GTR2 is given. The obtained results are shown and analyzed by comparison with values coming from the ionospheric compensation model and also with values deduced from vertical sounding measurements. At last GTR2 results are applied to time transfer between Paris Observatory (OP, Paris, France) and the United States Naval Observatory (USNO, Washington D.C., USA).

1. GTR2 DESCRIPTION

A radio signal of carrier frequency L which crosses ionosphere is delayed by a quantity expressed, at the first order approximation, as follows:

$$T_{ion}(L) = \alpha \cdot \frac{TEC}{L^2} \qquad (1)$$

T_{ion} is expressed in ns, L in Hz, α is a coefficient equal to 134,36 and TEC is the total electron content (in m^{-2}) of ionosphere along the signal path.

TEC, which is directly linked to the electron density and thickness of ionosphere, largely varies with solar activity, local time, longitude and latitude of the reception station. Examples are given in Table 1 with the corresponding ionospheric delays for both carriers L_1 (1575,42 MHz) and L_2 (1227,6 MHz) of GPS radio signals.

Table 1: Examples of vertical propagation delays of GPS L_1 and L_2 signals

TEC	$T_{ion}(L_1)$	$T_{ion}(L_2)$	$T_{ion}(L_2) - T_{ion}(L_1)$
2×10^{16} *1	1.08 ns	1.78 ns	0.7 ns
1×10^{17}	5.4 ns	8.9 ns	3.5 ns
1×10^{18} *2	54.0 ns	89.0 ns	35.0 ns

*1: typical value for night time of solar minimum
*2: typical value for day time of solar maximum

The propagation delay depends on the frequency and TEC can be estimated using a dual frequency method:

$$TEC = \frac{T_{ion}(L_2) - T_{ion}(L_1)}{\alpha} \left(\frac{1}{L_2^2} - \frac{1}{L_1^2} \right)^{-1} \qquad (2)$$

Recently, for purpose of precise geodesy, several different types of interferometric equipments using GPS dual frequency have been realized [6-9]. These are codeless devices with separate reconstructions of L_1 and L_2 signals.

In the same way, GTR2 does not need to demodulate P-code but its original principle relies upon the cross-correlation between P-codes carried by L_1 and L_2: because L_1 P-code and L_2 P-code are exactly identical and emitted in phase, the cross-correlation of the received P-codes gives access to the quantity $T_{ion}(L_2) - T_{ion}(L_1)$, as shown in figure 1.

TEC is then measured along the line of sight of the GPS satellites which allows ionospheric compensation on the real signal path.

2. GTR2 RESULTS

GTR2 is located at BIPM, Sèvres, France (longitude: 2,2 E and latitude: 48,8 N).

GTR2 program includes all observable satellites from BIPM but priority is given to the scheduled common views between Paris and Washington.

GTR2 works with 4 minute sequences: about 1 minute to point its directive antenna (gain 10 dBi for L_1 and L_2 frequencies) and about 3 minutes to perform the observation. The averaged value of TEC is provided with an uncertainty of 2×10^{16} m^{-2} which corresponds to an uncertainty of 1 ns for L_1 ionospheric delay.

Figure 2a shows L_1 ionospheric delays obtained on 1988 september 7. The diurnal effect is evident. The measured values are here converted to vertical estimations using a simple geometric expression based on the assumption that ionosphere is a sperical shell, lying from 200 to 450 km altitude and with uniform electron density. Figure 2b presents in details some values obtained for satellites 6 and 12 in early morning. The observed slight discrepancies correspond to an elevation effect. In fact, GTR2 measurement noise increases for high TEC values occuring for small satellite elevations ($\leq 25°$) and the vertical conversion model is badly adapted in this case.

GTR2 measurements can be compared to values issued from ionosphere compensation model. These values are accessible from a one frequency GPS receiver located in Paris Observatory and correspond of course to the same scheduled trackings. Figure 3 comes from a five days analysis (1988 October 5 to 9) where about 130 trackings were available. Measured values are very often larger than model ones, the disagreemant can even reach 20 ns. The discrepancy exceeds 10 ns for 28 % of the values and 5 ns for 62 % of the values.

At last GTR2 results are confirmed by measurement methods of vertical soundings: ionospheric delays, deduced from the values of the critical frequency of ionosphere F2 layer (foF2) measured by Centre National d'Etude des Télécommunications (CNET) in Lannion (France, longitude: 3,3 W and latitude: 48,4 N) are reported on figure 4 and agree fairly well with our measures.

3. APPLICATION TO TIME COMPARISONS

GTR2 measured ionospheric delays can be used to improve the daily time comparisons between OP (Paris, France) and USNO (Washington DC, USA).

Figure 5a shows a one week OP-USNO time comparisons obtained with raw GPS receiver output data. When measured ionospheric delays correct OP data, the biaises are largely reduced as shown on figure 5b and OP-USNO time transfer is performed with a much higher precision.

Of course, it would be necessary to operate such a correction for both involved laboratories and satellite ephemeris errors remain. Nevertheless this first study appear to be full of promise.

CONCLUSION

A prototype of a codeless dual frequency GPS receiver operates on a regular basis at BIPM since September 1988. This equipment is able to provide measured ionospheric delays along GPS satellite lines of sight with an uncertainty of 1 ns. For our immediate purpose of improvement of long distance time transfer, this device brings a very interesting gain in precision. Furthemore its structure is very simple with no need of precise measurements of time interval or high accuracy frequency sources as atomic frequency standards, so it appears as an efficient complement of traditional one frequency GPS receivers. At last, though it exists other methods to measure ionospheric effects as utilisation of Faraday rotation or dual frequency transmitted by Navy Navigation Satellite System (NNSS), they will soon become unavailable and GPS appears to be one of the most important ionospheric monitoring system. Then our codeless receiver belongs to a very promising generation of equipments which would widely overstep geodesy and time transfer purposes.

Acknowledgements

The authors wish to thank the Groupe de Recherches de Géodésie Spatiale who partly supported M. Imae's work at BIPM. The authors are also grateful to Dr. Hanbaba of CNET for his rapid report of foF2 data.

REFERENCES

[1] Allan D.W. and Weiss M.A., "Accurate time and frequency transfer during common view of a GPS satellite", Proc. 34th Annual Symp. on Frequency Control, 1980.

[2] Lewandowski W., Weiss M.A. and Davis D., 1986, "A calibration of GPS equipment at time and frequency standard laboratories in the USA and Europe", Proc. of the 18th PTTI meeting p. 265-279, [also published in Metrologia, 24, p. 181-186 (1987)].

[3] Guinot B. and Lewandowski, W., "Use of the GPS time transfer at the Bureau International des Poids et Mesures", Proc. 19th Annual Precise Time and Time Interval Applications and Planning Meeting, 1987.

[4] Guinot, B., Lewandowski W., 1988, "Nanosecond time comparisons in Europe using the GPS", Actes, 2nd European Frequency and Time Forum, p. 187-193.

[5] Kloubuchar J.A., "Ionospheric Correction for the Single Frequency User of the Global Positioning System", IEEE Trans. on NTS, 1982.

[6] Stansell T.A. Jr., Chamberlain S.M. and Brunner, F.K., "The First Wild-Magnavox GPS Satellite Surveying Equipment: WM-101", Proc. of the 1st International Symposium on Precise Positioning with the Global Positioning System, 1985.

[7] Ladd J.W., Counselman C.C. and Gourevitch S.A., "The Macrometer Dual-Band Interferometric Surveyor", Proc. of the 1st International Symposium on Precise Positioning with the Global Positioning System, 1985.
[8] MacDoran P.F., Miller R.B., Buennagel L.A. and Whitcomb J.H., "Codeless Systems for Positioning with "NAVSTAR-GPS", Proc. of 1st International Symposium on Precise Position with the Global Positioning System, 1985.
[9] Sugimoto Y., Kurihara N., Kiuchi H., Kaneko A., Kawase S., Sawada T., Shirado T. and Saburi Y., "Development of GPS Positioning System PRESTAR", Proc. 1988 Conference on Precision Electromagnetic Measurements, p. 101-102.

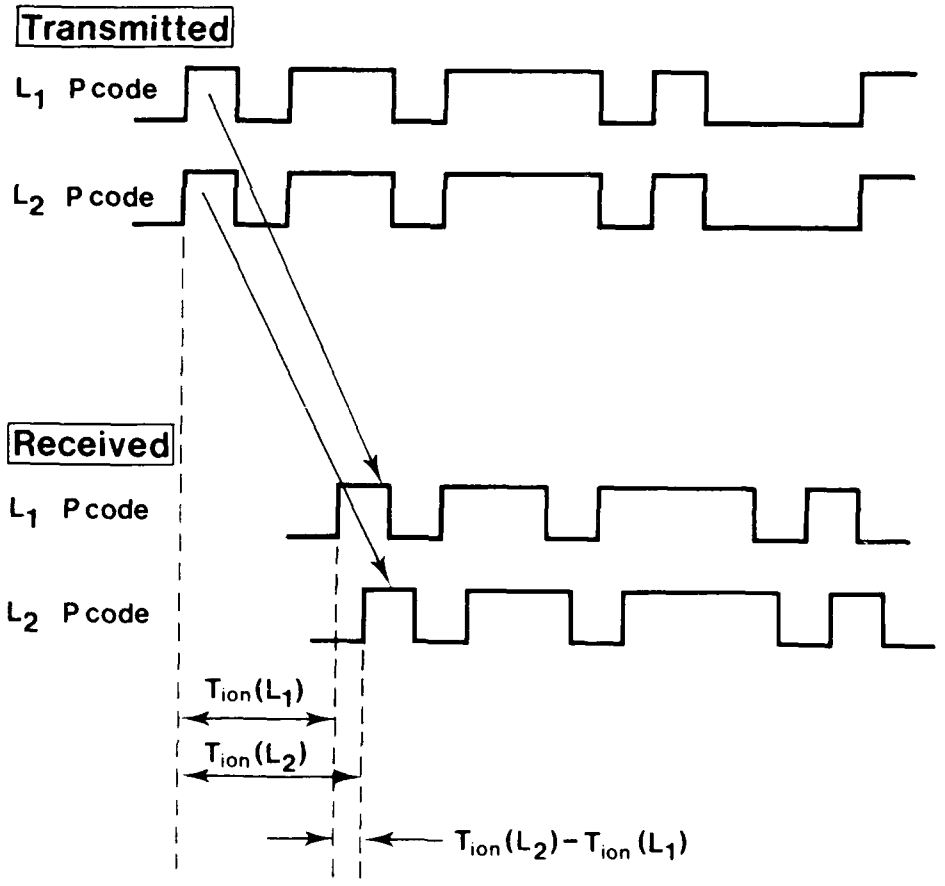

figure 1. Transmitted and received L_1 and L_2 P-codes.

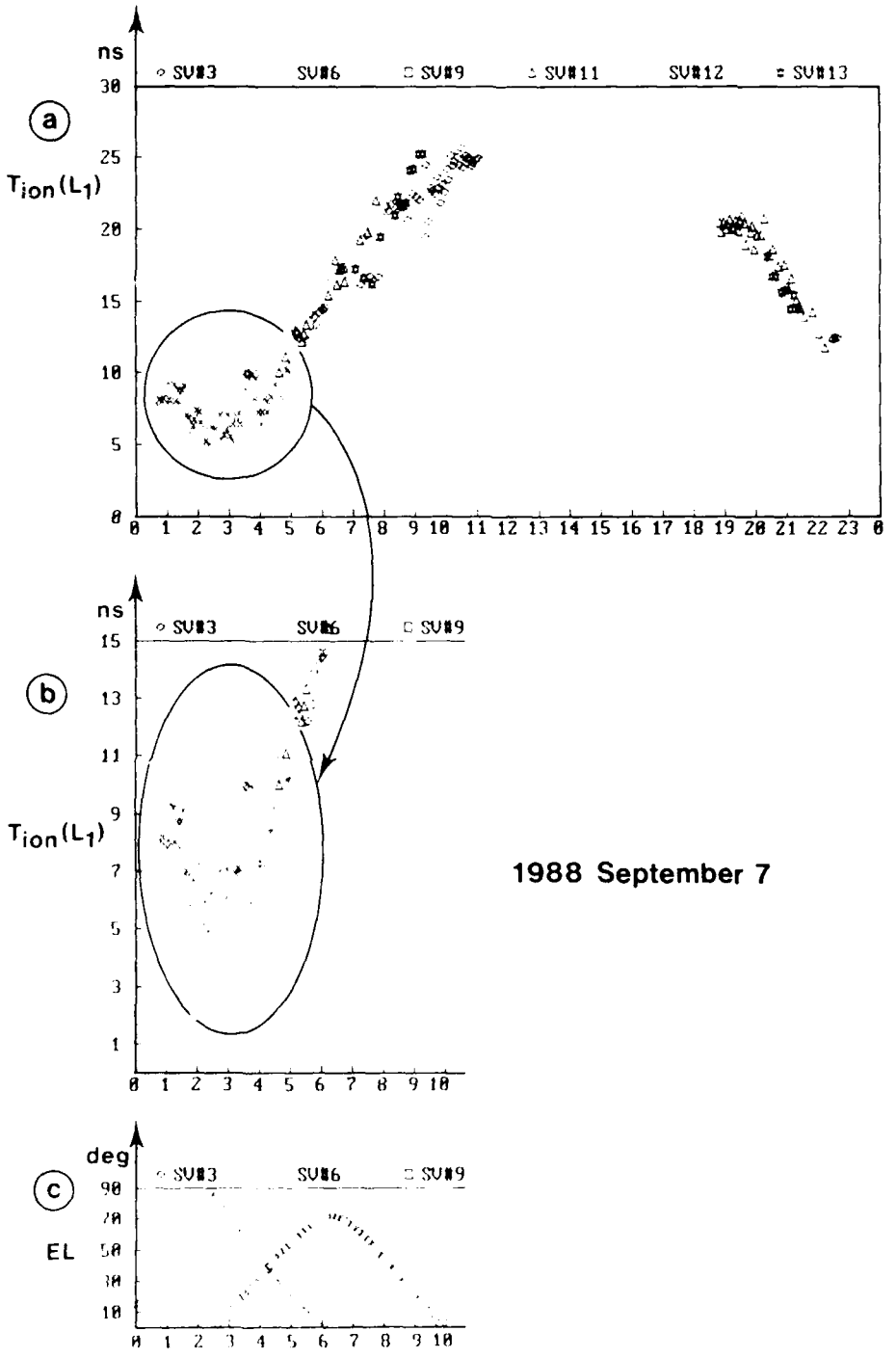

figure 2. Vertical L_1 ionospheric delays calculated from GTR2 results obtained on 1988 September 7

a - diurnal results

b - detailed SV 6 and 12 values for early morning

c - corresponding SV 6 and 12 elevations

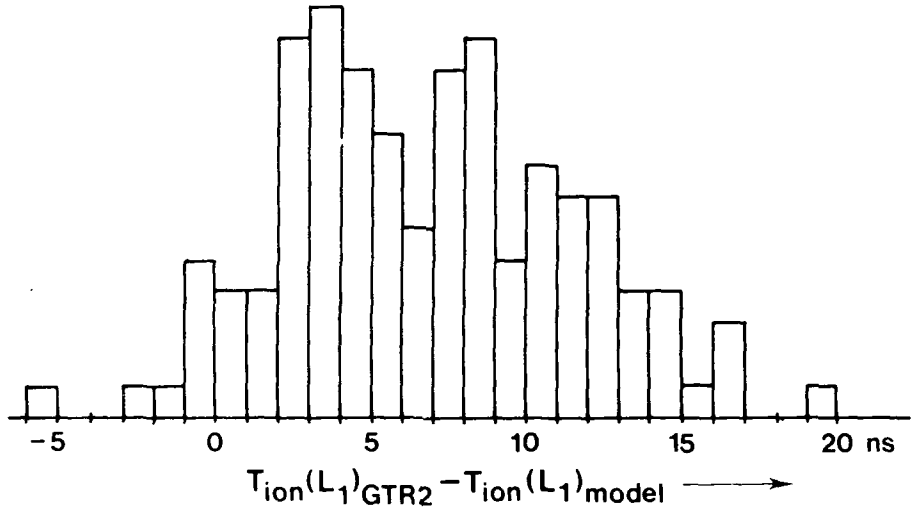

figure 3. Histogram of the values $T_{ion}(L_1)_{GTR2} - T_{ion}(L_1)_{model}$, obtained from 130 trackings for a five days period (no vertical convertion is applied)

- $T_{ion}(L_1)_{GTR2}$ are GTR2 measurement
- $T_{ion}(L_1)_{model}$ are the ionospheric compensation model estimations.

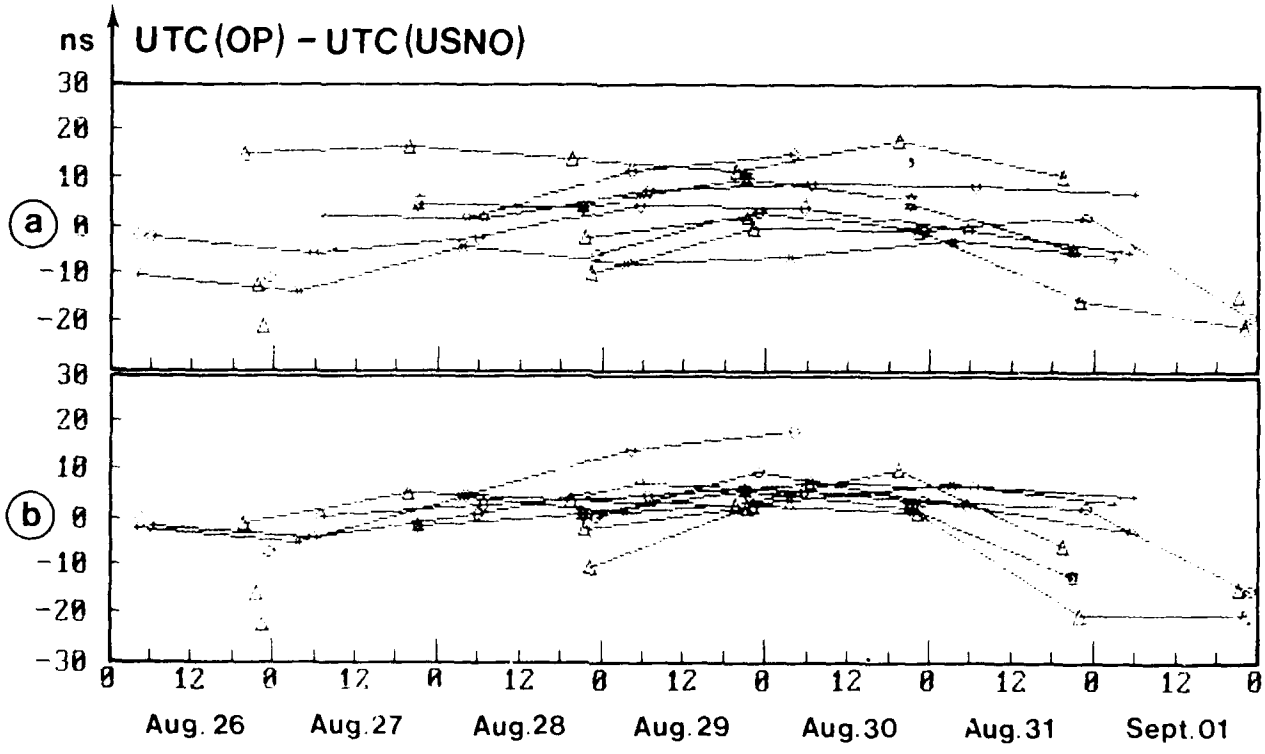

figure 5. Example of time comparison between OP and USNO
a - before correction
b - after correction of OP receiver output data.

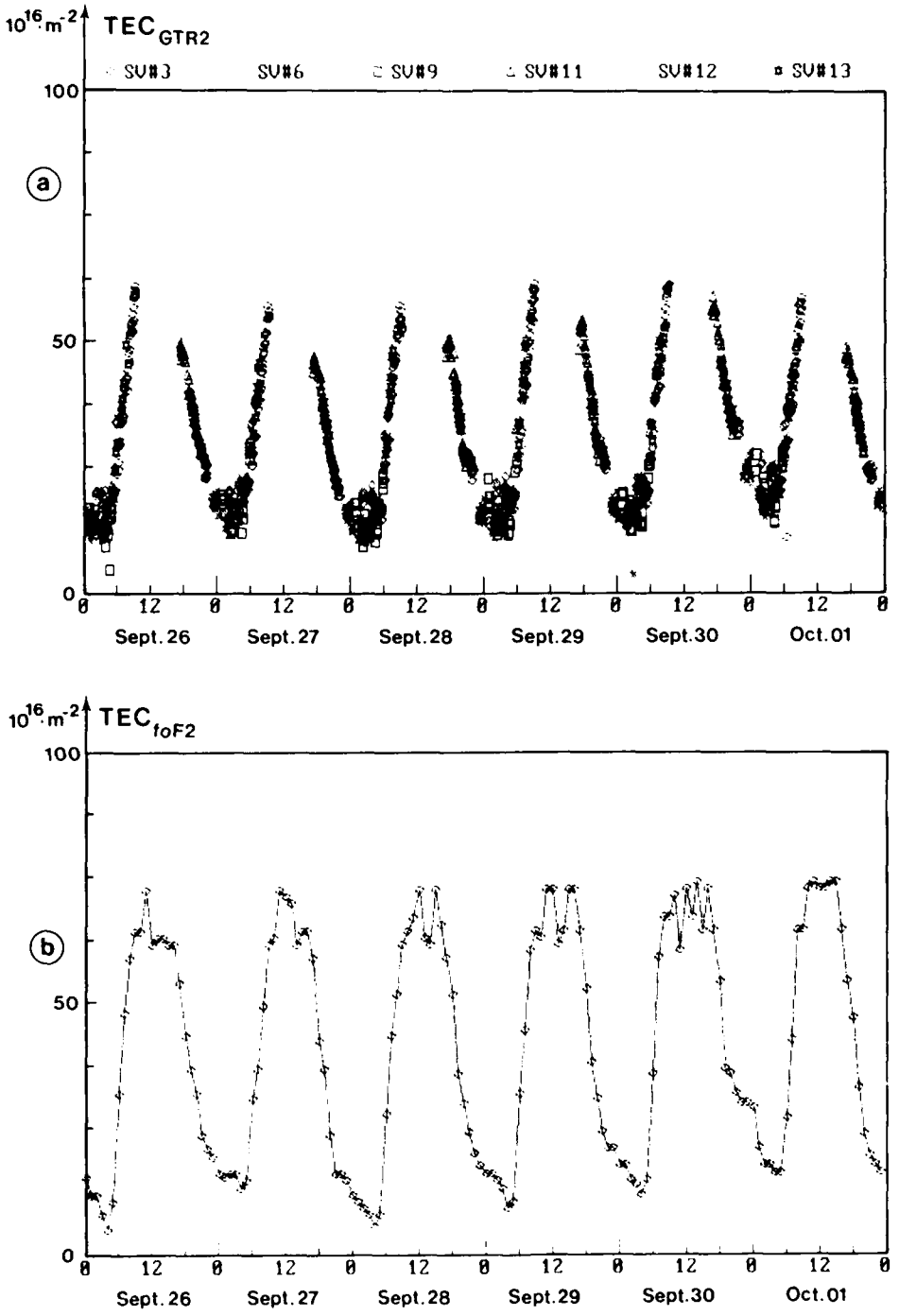

figure 4. Comparison between GTR2 measurement and results obtained by CNET Lannion.
a - vertical TEC deduced from GTR2 measurement.
b - vertical TEC deduced from CNET foF2 measurement.

QUESTIONS AND ANSWERS

JIM SEMLER, INTERSTATE ELECTRONICS: You mentioned the directional antenna. Do you think that you would have a problem operating with an omnidirectional one?

DR. THOMAS: It could not work with an omnidirectional antenna. It is a question of gain.

MR. SEMLER: The second question that I had was: You mentioned one nanosecond scatter on your ionospheric measurements. Was that averaged over the tracking interval?

DR. THOMAS: Yes. We have a three minute observation. Each measurement takes three seconds and we use a fast Fourier Transform to reduce the noise. The one nanosecond is the standard deviation of these observations over the (approximately) three minutes.

DR. GERARD LAPACHELLE, UNIVERSITY OF CALGARY: Because your antenna is a directive antenna, I assume that you have not tried to use your equipment in a dynamic mode. Could you comment on that and the possibility of adapting your equipment to a dynamic user with a multichannel capability? If you could do that, you could turn your equipment into a magnificent multipurpose geodetic type of equipment.

DR. THOMAS: At the present time we have not looked into that.

MR. YANAMADRA SOMAYAJULA, S. M. SYSTEMS AND RESEARCH CORPORATION: You mentioned one nanosecond for your measurements. What kind of integration time did you use?

DR. THOMAS: The integration time was three minutes.

DR. GERNOT WINKLER, USNO: The reason that you need more gain is that you do not decode the P-Code?

DR. THOMAS: Yes.

DR. WINKLER: The second question is: Do I see that you seem to have a systematic difference between the model and your measurements? Something like ten nanoseconds.

DR. THOMAS: Yes, but this was only the analysis for a given period—a five day period at the beginning of October. Another period could be different, this is only a sample. You see that at the beginning of September the discrepancy could be larger. I can not give a general conclusion from this data.

ORBIT PERIOD FREQUENCY VARIATIONS IN THE GPS SATELLITE CLOCKS

Everett R. Swift
Bruce. R. Hermann
Space and Surface Systems Division (K10)
Naval Surface Warfare Center
Dahlgren, Virginia 22448, USA

Abstract

A history of the GPS satellite clock behavior has been accumulated as a result of the weekly precise ephemerides produced at the Naval Surface Warfare Center (NSWC) under sponsorship of the Defense Mapping Agency (DMA). These ephemerides are produced using smoothed pseudorange data collected at a global set of ten tracking stations. The GPS satellite and station clocks are estimated simultaneously with the orbits. Time and frequency offset estimates are generated at one-hour intervals using a stochastic clock model. Studies using interferometric techniques to separate orbits and clocks have indicated that significant orbit period variations are present in the GPS satellite clocks. For PRN6/NAV3, which is currently operating on a rubidium frequency standard, these variations have amplitudes as large as 50 ns during the middle of eclipse season. For the four satellites operating on cesium frequency standards, the amplitudes of these variations are less than 15 ns. It is assumed that thermal cycling is the cause of these variations. The stochastic clock model has been tuned to allow the frequency offset state to track these variations. Starting with the first GPS week in 1988, this tuning has been used in NSWC's production processing. A brief description of the tuning experiments is given along with Allan variances computed for two satellite clocks based on the hourly estimates accumulated over a period of thirty weeks.

INTRODUCTION

The GPS precise ephemerides and clocks have been computed at NSWC since the beginning of 1986 using the OMNIS Multisatellite Filter/Smoother (MSF/S) software system [1,2]. This system incorporates the square root information implementation of the Kalman filter and Rauch-Tung-Striebel fixed-interval smoother and processes data for all satellites and stations simultaneously. Current production processing consists of MSF/S fits using eight days of data for each week (the GPS week plus a half day on each end) so that adjacent fits overlap by one day. Smoothed ionospherically corrected pseudorange data collected at a global network of ten tracking stations are used in these fits. Five of the stations are the Air Force's Operational Control Segment monitoring stations in Colorado Springs, Ascension, Diego Garcia, Kwajalein, and Hawaii. Multiple STI receivers are deployed at each of these sites allowing all satellites in view to be tracked simultaneously. The other five stations are operated by DMA and are located in Australia, Argentina, England, Ecuador, and Bahrain. A TI4100 receiver

is deployed at each of these sites. Currently only one receiver is at each site so that only four satellites can be tracked simultaneously. Each station's receivers are driven by a Hewlett-Packard cesium frequency standard (HP 5061A-004).

Reference trajectories for all satellites are integrated using a truncated WGS 84 gravity field, point mass gravity fields for the Sun and Moon, solid earth tides, the ROCK4 radiation pressure model (with a y-axis acceleration), and a 5-minute integration step. The observations are processed in one-hour mini-batch intervals. This means that the Kalman filter process noise covariance matrix is only added in when propagating from one interval to the next and all observations within an interval are processed in one Kalman measurement update. An observation sigma of 75 cm is assigned to each smoothed pseudorange. The following parameters are estimated simultaneously for each weekly fit:

- For each satellite:
  - Orbital elements
  - Radiation pressure scale modeled stochastically
  - Y-axis acceleration modeled stochastically
  - Clock parameters (see next section)
- For each station except for the master station:
  - Clock parameters (see next section)
- Polar motion and rate of change of UT1-UTC modeled as random constants.

The WGS 84 station coordinates are held fixed in the estimation procedure. This procedure generates fitted trajectory files for each satellite and a clock file containing the time and frequency offsets between each satellite's clock and GPS time and frequency at one-hour intervals.

CLOCK MODEL

Nominal clock offsets for both the satellites and stations, which consist of second order polynomials in time with possibly step changes, are removed from the smoothed pseudorange data residuals before they are used in the orbit/clock estimation procedure. Corrections to this nominal for each satellite clock are modeled as the outputs of a third order linear system with white noise inputs. The three corrections are called frequency drift $\delta\ddot{\tau}$, frequency offset $\delta\dot{\tau}$, and time offset $\delta\tau$. The model in current state continuous variables is given by:

$$\begin{pmatrix} \dot{\delta\ddot{\tau}} \\ \delta\dot{\tau} \\ \delta\tau \end{pmatrix} = \begin{pmatrix} 0 & 0 & 0 \\ 1 & 0 & 0 \\ 0 & 1 & 0 \end{pmatrix} \begin{pmatrix} \delta\ddot{\tau} \\ \delta\dot{\tau} \\ \delta\tau \end{pmatrix} + \begin{pmatrix} w_1 \\ w_2 \\ w_3 \end{pmatrix} \tag{1}$$

The model is actually implemented in discrete form using pseudoepoch state variables as described in [2]. The frequency drift state is modeled as a random constant for the fit, i.e., no white noise drives this state so its spectral density, q_1, is set to zero. The white noise, with spectral density q_2, driving the frequency offset state defines the random walk frequency noise variations for the model. The white noise, with spectral density q_3 , driving the time offset state defines the white frequency noise variations. No explicit flicker noise parameter is present in this model. The Allan variance corresponding to this model is then given by

$$\sigma_y^2(\tau) = \frac{q_3}{\tau} + \frac{q_2\tau}{3} \tag{2}$$

where τ is the averaging time in seconds. Figure 1 shows this relationship in graphical form. The same model, but without the frequency drift state $\delta\ddot{r}$, is used for the station clock corrections. The clock for the master or reference station is constrained to be the assumed offset between this clock and GPS time. Therefore all clock solutions are estimated relative to GPS time. Using these models for the satellite and station clocks, the orbit, clock, and polar motion parameters are estimated simultaneously for all satellites using the MSF/S system.

CLOCK MODEL TUNING RESULTS

During each year there are two time spans when a given GPS satellite enters the Earth's shadow on every revolution. These eclipse seasons cause larger thermal variations within the spacecraft than for the rest of the year, and consequentially may cause larger clock frequency variations. Three weeks were selected for use in the tuning experiments based on which satellites were or were not experiencing eclipses. These were GPS weeks 403 (September 27-October 3, 1987), 413 (December 6-12, 1987), and 419 (January 17-23, 1988). PRN6/NAV3, PRN9/NAV6, and PRN12/NAV10 were in the middle of their eclipse season during week 403. The other four satellites were in the middle of their eclipse season during week 419. No satellites were being eclipsed during week 413. Weeks related to eclipse season were selected because previous work done by Aerospace Corporation, IBM, and NRL [3] has indicated that thermal cycling of the rubidium clocks on PRN6/NAV3 and PRN9/NAV6 was worst during eclipse season. All the other satellites except PRN8/NAV4 were operating on cesium frequency standards during these three weeks. PRN8/NAV4 was operating on a quartz crystal standard.

To tune the stochastic clock model a way of separating the clock and orbit estimates was needed. The interferometric processing approach was adopted to do this separation. By differencing two simultaneous pseudorange measurements for the same satellite from a pair of stations, the satellite clock effects are removed from the measurement. The globally distributed ten-station network provides almost continuous two- station tracking that allows this differencing for the entire orbit. Measurement differencing to remove satellite clock effects is equivalent to solving for independent time offsets for each satellite at each measurement time. To test this equivalency, single difference measurements using the smoothed pseudorange data for week 403 were derived and used for orbit determination. This differencing introduced measurement noise correlations and redundant measurements that were not properly handled in the orbit estimation procedure due to limitations of the software. For comparison, the MSF/S system was configured to solve for independent satellite time offsets for each measurement time along with the orbits. The orbits determined by these two approaches differed by less than 0.5 m root-mean-square (RMS) in each component. The second method is preferred because it fully accounts for the correlations and additionally provides satellite time offset estimates. These estimates do contain some very high frequency noise, which is not the actual clock behavior but due to aliasing of the measurement noise into the estimates.

Figure 2 contains a plot of the time offset corrections to the nominal for week 403 for PRN6/NAV3 derived using the second interferometric method. The aliased noise is present in the plot but is hard to see because of an orbit period, nearly sinusoidal variation of amplitude 50 ns. Figure 3 contains a plot of the time offset corrections for PRN3/NAV11 for week 413. The noise is now more obvious because the orbit period variation is less than 15 ns in amplitude. For the three weeks processed using this technique, the observed variations were worst during the mid-eclipse week for the two rubidium clocks (PRN6/NAV3 and PRN9/NAV6) with 35 ns amplitude worst case variations for PRN9/NAV6. The

cesium clock variations were always less than 15 ns in amplitude (worst case was for PRN3/NAV11 for week 413) and no correlation with eclipse season was observed.

Two strategies were tested for specifying the two white noise spectral densities available in the adopted model. These strategies were designed to allow the model to accomodate the orbit period clock variations with the one-hour mini-batch interval processing used in production. The interferometric results described above were considered "truth". A 12-hour period sinusoid of amplitude 10 ns results in a peak of at most 1.31×10^{-12} in the square root of the Allan variance at an averaging time of 6 hours. Both strategies were based on the assumption that the Allan variance of the model at 6 hours must be able to accomodate the variations observed using the interferometric technique. The first strategy involved increasing the white noise driving the time offset state (white frequency noise) much more than the white noise driving the frequency offset state (random walk frequency noise) so that the white frequency noise part of the Allan variance curve was above the required level at 6 hours. The second strategy involved increasing the white noise driving the frequency offset state and leaving the white noise driving the time offset state at a realistic level so that the random walk frequncy part of the Allan variance curve was above the required level at 6 hours. This second approach is consistent with the assumption that the clock frequency is actually changing due to thermal effects and the pseudorange measurements include the integrated effect of these changes.

The RMS differences over all satellites between the orbits derived interferometrically and those derived using spectral densities based on the first strategy were 0.6 m in the radial direction, 1.2 m in the along-track direction, and 0.6 m in the cross-track direction. Using spectral densities based on the second strategy these were 0.2 m, 0.5 m, and 0.3 m respectively. The RMS clock differences were 3.0 ns for the first strategy and 2.0 ns for the second. Figure 4 contains a plot of the time offset corrections for PRN6/NAV3 for week 403 using white noise spectral densities based on the second strategy. Comparing this plot with the plot in Figure 2 indicates that the time offset estimates agree with the interferometric results but do not contain the high frequency noise. Figure 5 gives the corresponding frequency offset corrections. A sinusoidal frequency variation of amplitude 1.46×10^{-12} gives, when integrated, a sinusoidal time offset variation of amplitude 10 ns. Therefore integrating the frequency offsets in Figure 5 should approximate the time offsets in Figure 4. For the first strategy the peak-to-peak frequency offset variation was approximately 3×10^{-12} less than in Figure 5. Therefore the frequency offset state did not track the total variation. Figures 6 and 7 give the time and frequency offset corrections for PRN3/NAV11 for week 413 corresponding to Figure 3. The second strategy resulted in better agreement with the interferometric results and allowed the frequency offset state to track the assumed thermal effects.

ALLAN VARIANCE COMPUTATIONS

The white noise spectral densities for equation (2), determined using the second strategy above, were adopted for the MSF/S production runs beginning with the first full week of 1988 (GPS week 417). In a plot similar to Figure 1, the resulting Allan variance models for the satellites are shown in Figure 8. The procedures required to compute Allan variances from the clock solutions derived using these statistics are described in this section.

The Allan variance processing begins with the MSF/S satellite clock offset file which is the result of an eight day fit centered on each GPS week. The data consists of the mini- batch time of week, the time offset, and the frequency offset for all satellites. In order to use these files to compute Allan variances, the weekly files must be joined together and corrected for any clock jumps that might have occurred. This requires performing the steps listed below for each satellite.

1. Remove duplicate estimates of offsets at each end of week.

2. Eliminate all clock jumps from the offsets.

3. Compute fractional frequencies from each offset.

4. Fit and remove a first degree polynomial from the resulting fractional frequencies.

5. Compute and plot the Allan variances.

The 24-hour overlap region at the beginning/end of each week was removed by using a weighted average to form a smooth transition. As time progresses in the overlapping region, the sinusoidal weighting function gradually shifts from full weight for the first week to full weight for the second week.

The time of all clock jumps are listed in the clock file. This information is relied on to identify and eliminate each occurrence of a jump from the time or frequency offsets. The removal is performed in several steps. The first step consists of a least squares fit of a four coefficient function to the last 24 offsets before the jump. This function consists of a straight line plus a sinusoid. A second function of the same type is then used to fit the first 24 offsets after the jump. The two fitted functions are then evaluated at the midpoint of the interval in which the jump occurs. The difference between the two results at the midpoint is the jump amplitude and is added to all succeeding time offsets. Subsequent jumps from the same satellite in later weeks are handled in the same manner. Removing jumps by this method destroys the true offset magnitude, but this is of no consequence to the Allan variance computation.

Fractional frequencies can be computed from both the time offsets and the frequency offsets. In fact, the frequency offsets are fractional frequencies directly. The time offsets can be converted to fractional frequencies by computing the difference between two consecutive time offsets and dividing by the one-hour time interval between them.

The Allan variance is computed from the corrected fractional frequencies. Before beginning this computation, an independent least squares straight line fit is made to fractional frequencies from both the time offsets and frequency offsets to remove the frequency drift from the data. The Allan variance can then be computed using the residual fractional frequencies from the time offsets and/or from the frequency offsets.

Representative Allan variance plots are presented for the GPS weeks 417-446 (January 3 through July 30, 1988). A plot for a satellite with a rubidium frequency standard (PRN6/NAV3) is shown in Figure 9. The pronounced fluctuations seen in this Allan variance are due to the periodic oscillations that are present in the time offsets (Figure 4) and frequency offsets (Figure 5). A portion of Figure 9 is enlarged in Figure 10 to show this effect in detail. The first null is close to the orbital period of 43082 seconds. The true performance of this rubidium without the periodic component can be estimated by connecting the nulls in Figures 9 and 10.

An Allan variance plot for a satellite (PRN3/NAV11) with a cesium frequency standard is presented in Figure 11. The effects on the Allan variance of the periodic signals in Figures 6 and 7 is evident.

Allan variances computed for any satellite based on clock files from the MSF/S system derived using the model statistics shown in Figure 8 will always be below the curves drawn in this figure. In order for the clock solutions to represent the true performance of the frequency standards, the time and frequency offsets must not be artificially constrained by the model. The plots show that the computed Allan variances are well below the curves of Figure 8 and consequently are representative of the satellite clock performance.

CONCLUSIONS

Significant orbit period frequency variations are present for the GPS Block I satellites, especially for those operating on rubidium frequency standards. The results of a tuning experiment for the stochastic clock model used in the MSF/S orbit/clock determination system indicate that these variations can be accurately estimated. The adopted model statistics allow realistic Allan variances for the satellite frequency standards to be computed from these satellite clock estimates.

Tracking the performance of the GPS frequency standards is of interest to many users in the time transfer community. The satellite clock estimates derived using the MSF/S system provide a continuous history of satellite time and frequency offsets as a by-product of the precise ephemeris computations.

References

1. Swift, E. R., "NSWC's GPS Orbit/Clock Determination System," Proceedings of the First Symposium on Precise Positioning with the Global Positioning System, April 15-19, 1985, Rockville, Maryland.

2. Swift, E. R., Mathematical Description of the GPS Multisatellite Filter/Smoother, NSWC TR87-187, Naval Surface Warfare Center, Dahlgren, Virginia, October, 1987.

3. Presentations at GPS Control Segment Performance Analysis Working Group Meetings, 1985-1987.

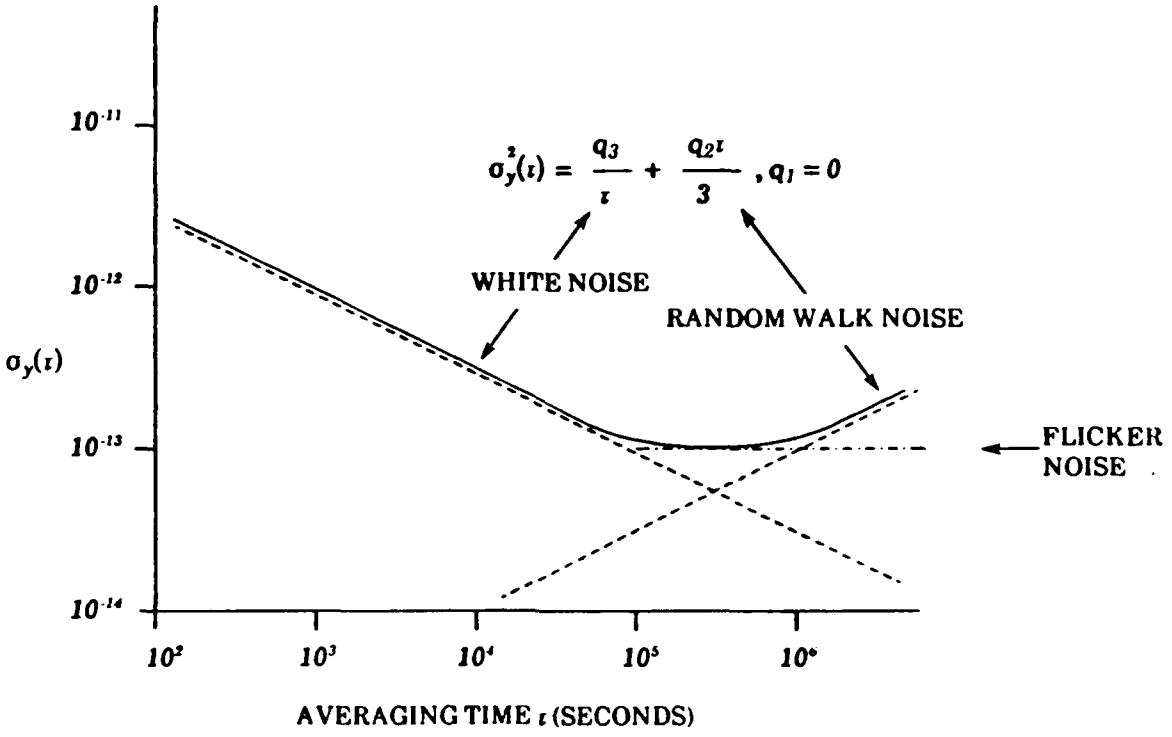

FIGURE 1. CORRESPONDENCE BETWEEN CLOCK MODEL SPECTRAL DENSITIES AND ALLAN VARIANCE

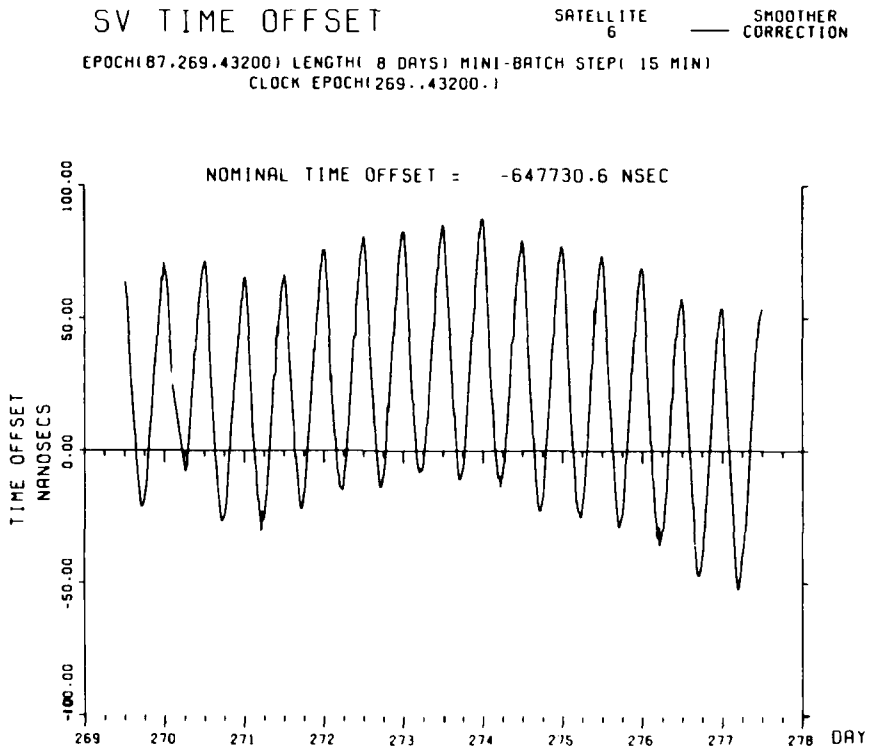

FIGURE 2. INTERFEROMETRIC TIME OFFSET CORRECTIONS FOR PRN6/NAV3 FOR WEEK 403

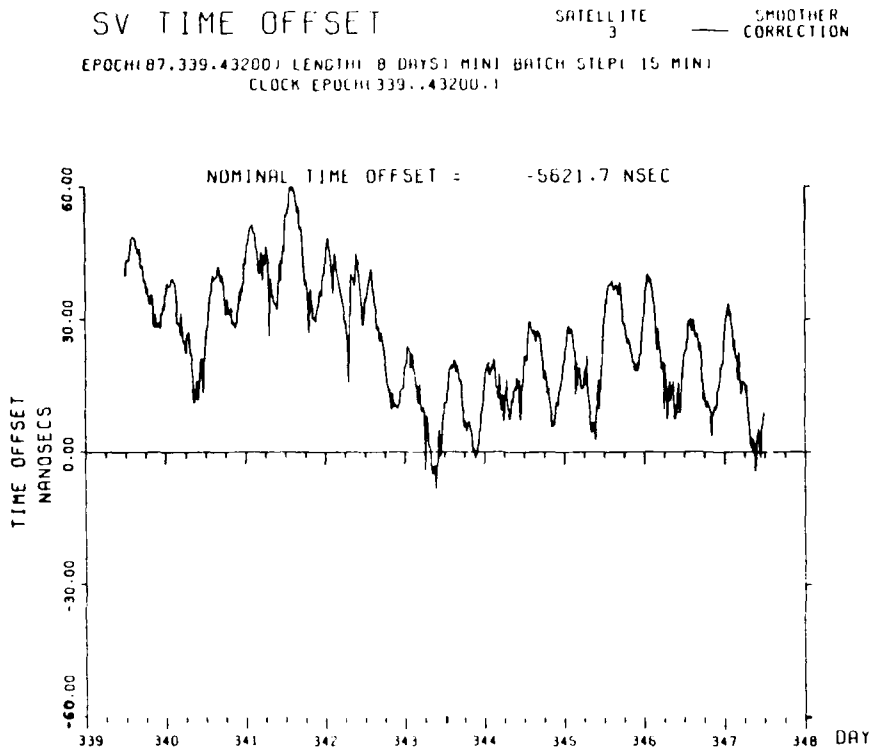

FIGURE 3. INTERFEROMETRIC TIME OFFSET CORRECTIONS FOR PRN3/NAV11 FOR WEEK 413

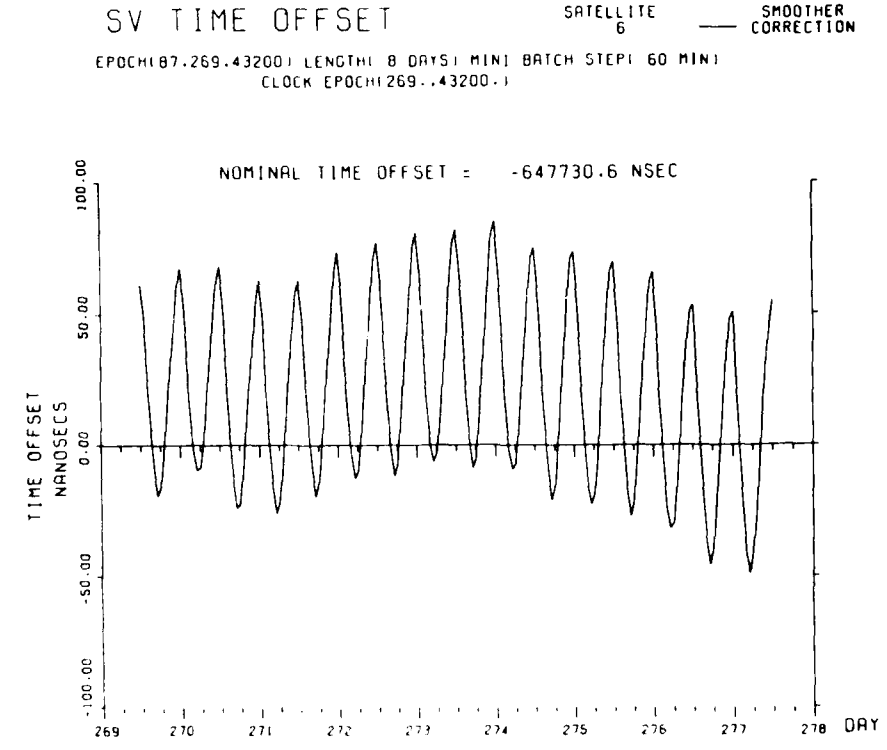

FIGURE 4. STRATEGY 2 TIME OFFSET CORRECTIONS FOR PRN6/NAV3 FOR WEEK 403

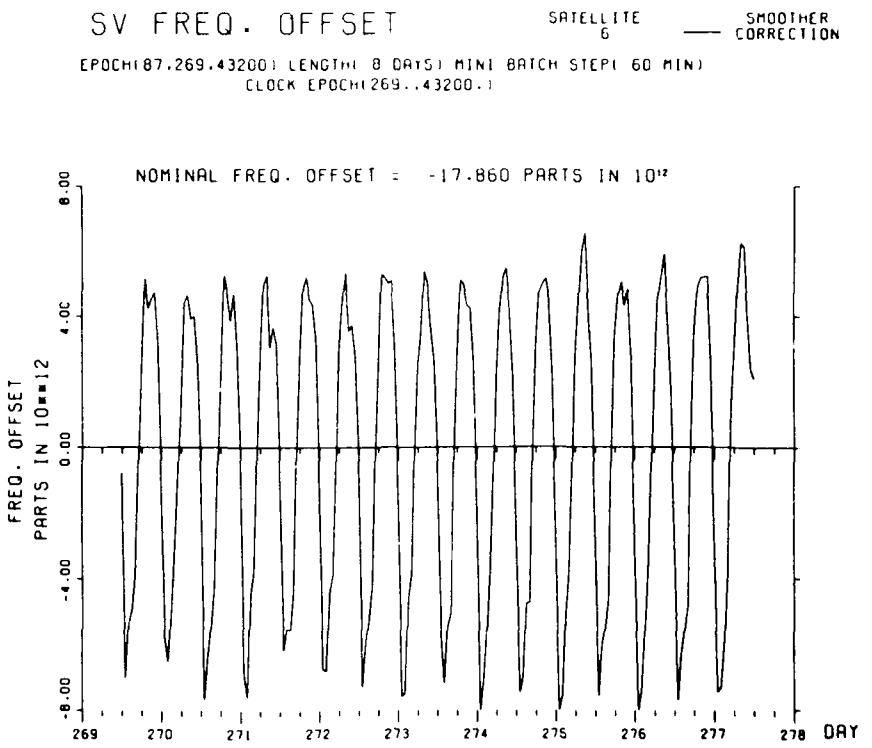

FIGURE 5. STRATEGY 2 FREQUENCY OFFSET CORRECTIONS FOR PRN6/NAV3 FOR WEEK 403

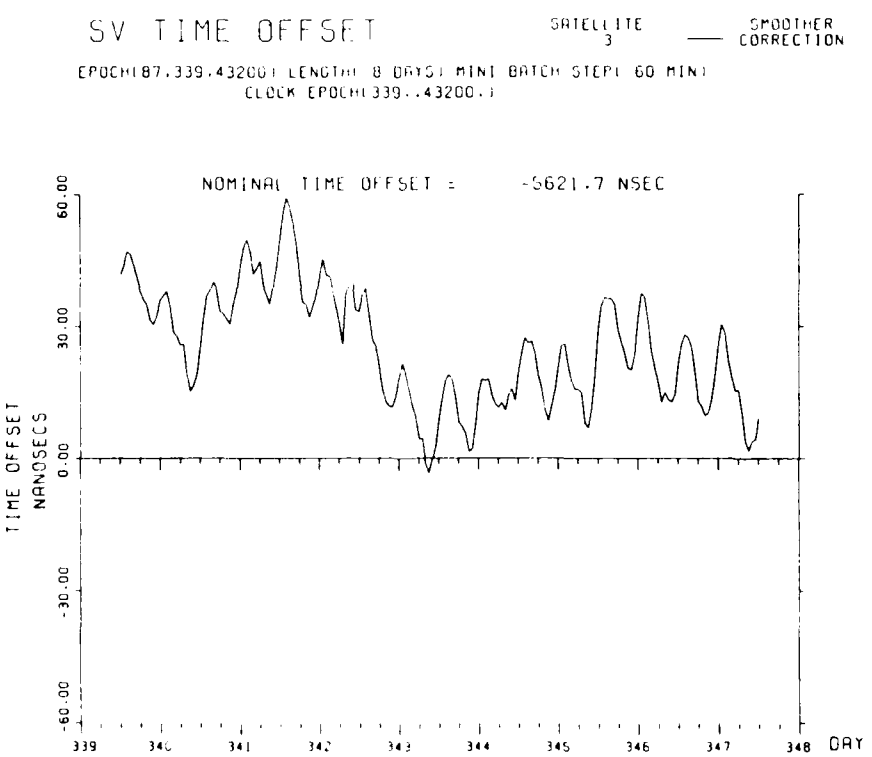

FIGURE 6. STRATEGY 2 TIME OFFSET CORRECTIONS FOR PRN3/NAV11 FOR WEEK 413

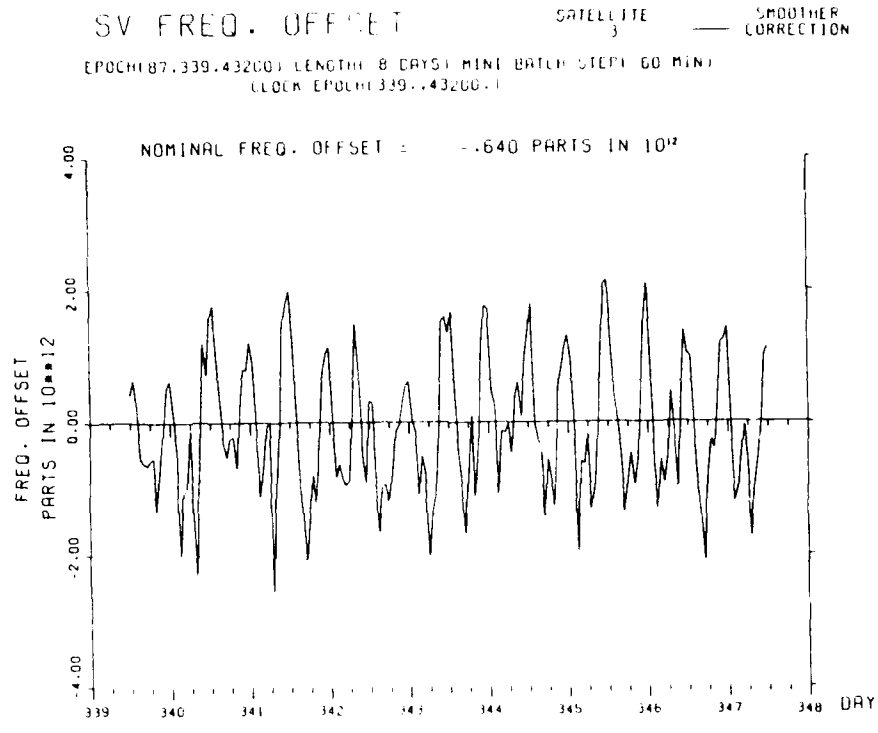

FIGURE 7. STRATEGY 2 FREQUENCY OFFSET CORRECTIONS FOR PRN3/NAV11 FOR WEEK 413

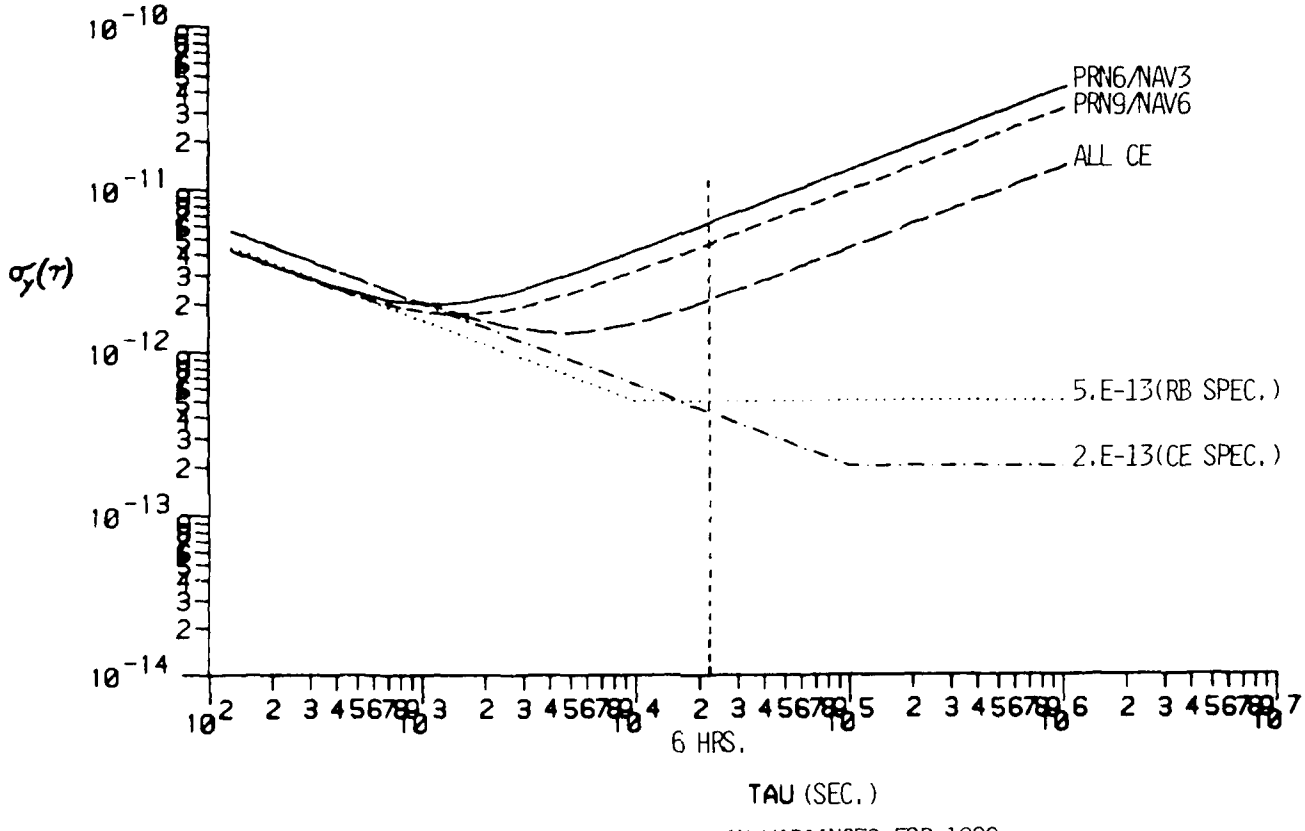

FIGURE 8. MODEL ALLAN VARIANCES FOR 1988

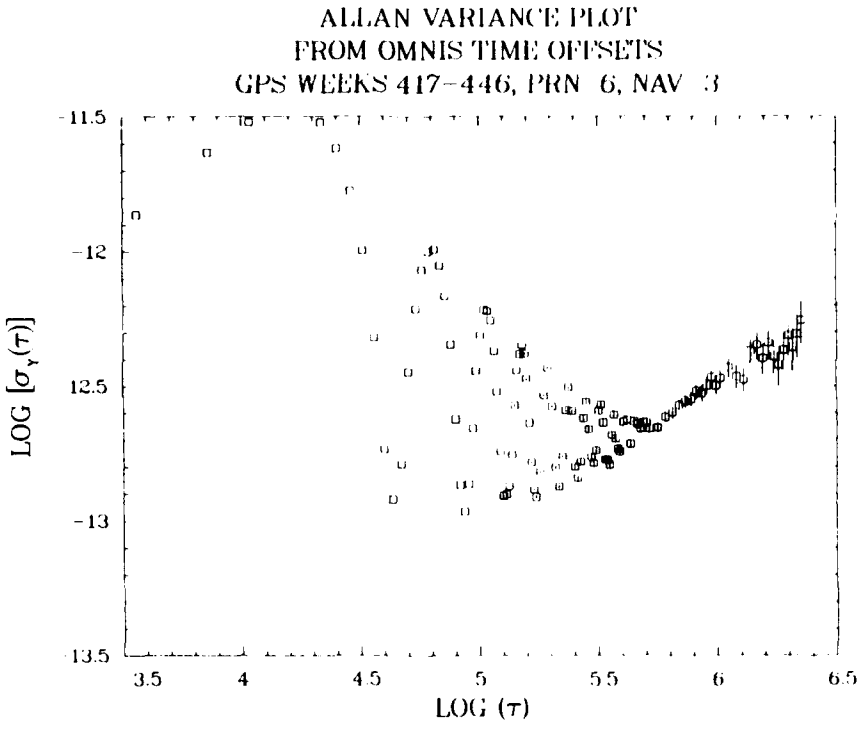

FIGURE 9. ALLAN VARIANCE FOR PRN6/NAV3 FOR WEEKS 417-446, 1988

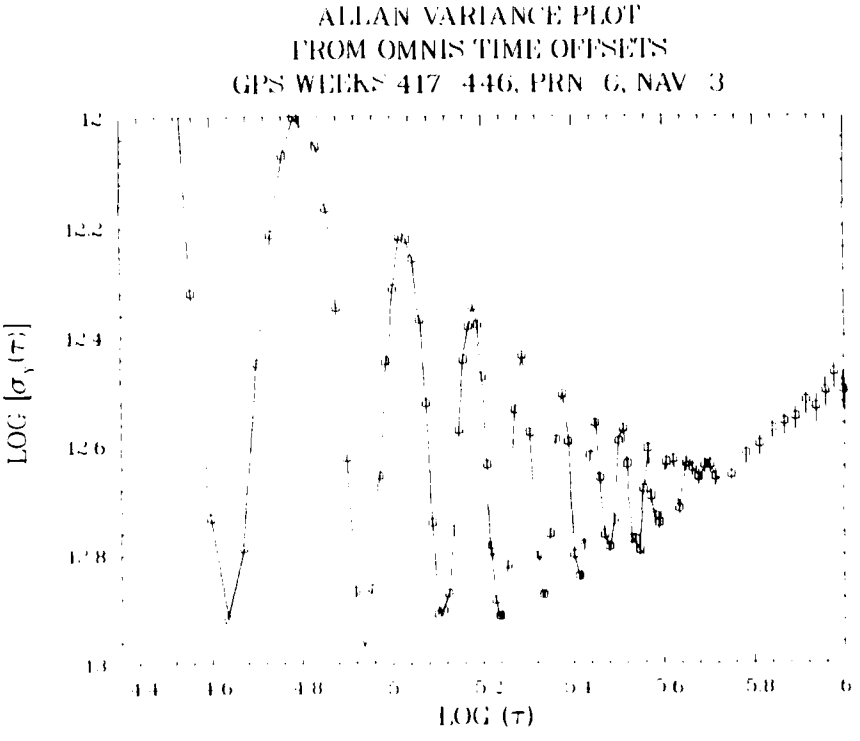

FIGURE 10. ENLARGEMENT OF A PORTION OF FIGURE 9

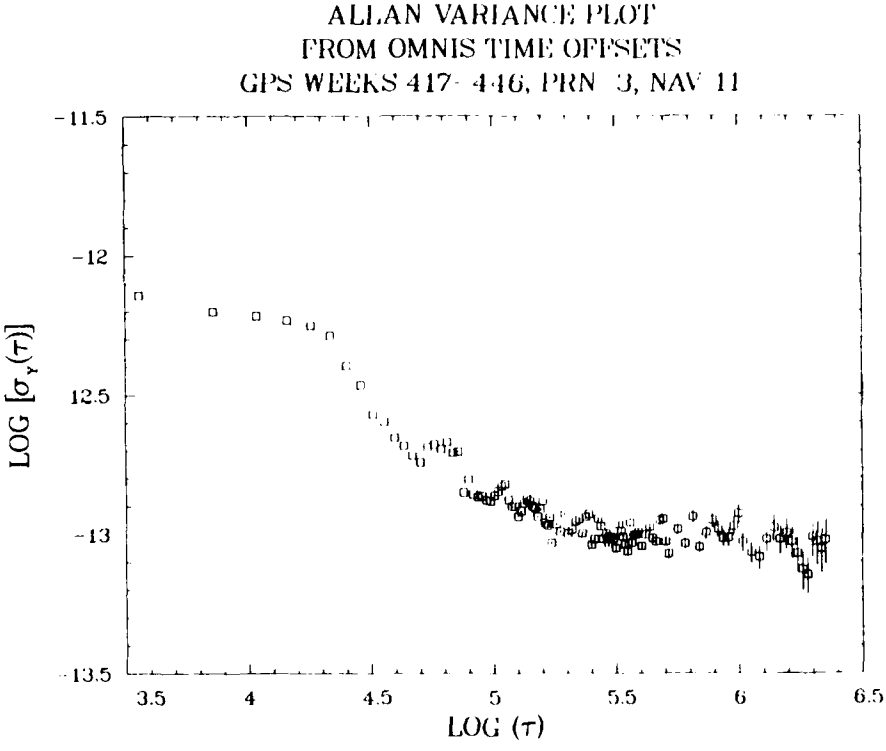

FIGURE 11. ALLAN VARIANCE FOR PRN3/NAV11
FOR WEEKS 417-446, 1988

QUESTIONS AND ANSWERS

MARK WEISS, NIST: What is the difference between the broadcast ephemeris and your precise ephemeris in, say, meters?

MR. SWIFT: That is a difficult question. We believe that our ephemeris is good to 3–5 meters.

MR. WEISS: How far off is the broadcast ephemeris?

MR. SWIFT: I think that it could be off fifteen meters. The rubidium ones are probably worse than the cesium ones.

MR. WEISS: Is all the variation in the clock put into the ephemeris, or is some put into the broadcast ionospheric model as well?

MR.SWIFT: I don't think that any of it gets into the ionospheric model. It all goes into the ephemeris.

DAVID ALLAN, NIST: Did you say that for PRN3 this was worst case and that it wasn't during an eclipse?

MR. SWIFT: That's right, this was worst case of all the cesiums for those three weeks.

MR. ALLAN: Why would it not be worse during an eclipse?

MR. ALLAN: I don't know.

DR. GERNOT WINKLER, USNO: A sinusoidal variation in time can be interpreted as an integrated variation of frequency or as a phase modulation. If you interpret that as a phase modulation, which can come from any temperature sensitive point in the circuitry, the statistics would look quite different. Have you considered that possibility?

MR. SWIFT: I have been assuming, based on all the information that I have obtained, that the general consensus is that it is a frequency variation due to the temperature sensitivity of the clock.

JIM SEMLER, INTERSTATE ELECTRONICS: I will vouch for Everett's numbers for the precision ephemeris. We have been using it at Interstate pretty successfully for about two years now. I have question for you concerning the interferometric processing of those differences. Did you use your Kalman filtering for that? How did you process the data?

MR. SWIFT: Yes, we used the Kalman filter. We essentially gave it infinite Q's and processed it with 15 minute mini-batches, which is our measuring interval. That is how we implemented the independent estimate.

A CALIBRATION OF GPS EQUIPMENT IN JAPAN*

M. Weiss and D. Davis
National Institute of Standards and Technology

Abstract

With the development of common view time comparisons using GPS satellites the Japanese time and frequency standards laboratories have been able to contribute with more weight to the international unification of time under the coordination of the Bureau International de Poids et Measures (BIPM). During the period from June 1 through June 11, 1988, the differential delays of time transfer receivers of the Global Positioning System (GPS) were calibrated at three different laboratories in Japan, linking them for absolute time transfer with previously calibrated labs of Europe and North America. The differential delay between two receivers was first calibrated at the National Institute of Standards and Technology (NIST, formerly the National Bureau of Standards) in Boulder, Colorado, USA. Then one of these receivers was carried to each of the three laboratories: the Tokyo Astronomical Observatory (TAO), the Communications Research Laboratory (CRL), both in Tokyo, and the National Research Laboratory of Metrology (NRLM) in Tsukuba City. At each lab data was taken comparing receivers. Finally the traveling receiver was taken back to NIST for closure of the calibration. On the way back the GPS receiver at the WWVH radio station of NIST in Hawaii was also calibrated. We report here the results of this calibration trip, along with some interesting problems that developed concerning this technique.

Introduction

The motivation for calibrating time transfer receivers of Global Positioning System (GPS) signals has been discussed before (1,2,3). We will summarize the concerns here. The method of clock comparisons using Global Positioning System (GPS) satellites in common view between each pair of stations has become the de facto standard for comparisons of clocks in the major time standards laboratories participating in the international unification of time under the coordination of the Bureau International des Poids et Mesures (BIPM). At least 60 percent of the clocks which enter into the establishment of the International Atomic Time (TAI), as well as all of the primary frequency standards contributing to the length of the second within TAI, are directly linked by GPS.

The BIPM establishes a tracking schedule at regular intervals which ensures that pairs of stations track satellites simultaneously, measuring their local clocks against time as transmitted by the satellites. These measurements are brought together and differenced between pairs of stations to obtain measurements between laboratories. This differencing of common view measurements cancels the GPS clocks and, to a large extent, many of the systematic measurement errors (2). A time transfer accuracy of 10 ns has been expected and apparently realized in many cases. It is difficult to verify this accuracy, since there are no operational time transfer system of equal or greater accuracy. Problems with realizing this accuracy can be divided into three categories:

(1) Inaccuracy of the GPS

(2) Local problems

(3) Data processing techniques

Errors in time transfer via a single GPS satellite are due to errors in: satellite ephemerides, ionospheric modeling, tropospheric modeling, local antenna coordinates, calibration of delays in local equipment, or due to multipath interference. Inaccuracy of the GPS refers to errors in the satellite ephemerides and ionospheric models as transmitted from the satellites. The tropospheric model is fixed in the receivers and is typically a simple cosecant function of elevation normalized by a function of local height. Errors here might be considered as either part of the GPS system or a problem with the local receiver and environment. Errors in local antenna coordinates or equipment calibration delays or multipath around the antenna are local problems.

A measure of inaccuracy of the GPS is a time transfer closure around the world. The resultant value should be zero. Figure 1 shows the residuals from three common view time transfers: (PTB–NIST), (TAO–PTB), and closing with (NIST– TAO), where PTB is the Physikalisch Technische Bundesanstalt, Braunschweig, Fed. Rep. of Germany. These are residuals over four years: 1985–1988. One can see the maturation of the system. The data over the months of August through November of 1988 are at the end of the plot with a mean of 8.3 ns, and a standard deviation of 7.7 ns. This is consistent with an accuracy estimate of 10 ns for each individual leg. The problem with different data processing techniques is related to the GPS inaccuracy in that there are systematic errors in GPS common view data. A time series of common view measurement differences at one sidereal day intervals with a given satellite can be biased from a similar time series made using a different satellite, or even using the same satellite at a different time (figures 2 and 3)(4,5). The satellites are in 12 hour sidereal orbits. Hence the geometric relationship between the satellite and the ground stations repeats once per sidereal day. For this reason, the tracking schedule prepared by the BIPM sets track times that repeat once per sidereal day. Biases between tracks taken at different times can cause different methods of processing common view data to yield significantly different results.

We discuss the local problems in a little more detail since they are particularly relevant for this paper. The quality of data is degraded by several local sources of errors:

1) Wrong calibration of GPS receivers (instrumental delay, antenna cable, connection to the local clock)

2) Poor shape of the pulse of the local time reference

3) Tropospheric correction error

4) Multipath due to signal reflection at the receiving site

5) Errors in antenna coordinates

Thus this calibration helps to eliminate an important contribution to GPS time transfer error in Japan. Since Japan is somewhat isolated from other major timing laboratories, GPS common view is an important link for including the Japanese labs in TAI.

We note here that we have tabulated information about the system of generating and comparing UTC using GPS in common view for each of the labs visited. Included is information about the ensemble of clocks and the environmental control for these clocks in table 2, and the local 1 pps in table 3. The coordinates of all three locations in Japan are based on geometric measurements from Tokyo Datum and conversions to WGS–72 and WGS–84. All receivers use the WGS–84 coordinate

system except the on-line receiver at TAO. Since this experiment, as of July 1, 1988 the TAO has been applying the WGS-84 coordinate system to the measured residuals in their own computer, before putting their measurements on the Mark III system. In an experiment at NIST we have seen that the use of the different coordinate systems, WGS-72 versus WGS-84, both to compute satellite position and to convert local antenna coordinates from geodetic to geocentric produced a bias in the calibration of 3.6 ns, and increased the standard deviation from 1.9 to 3.1 ns. This is consistent with our measured standard deviation of 3.3 ns on the on-line receiver at TAO.

Calibrations at NIST

For common view time transfer only the relative delays through receivers are important. To obtain a measure of ref A-ref B we subtract the two measurements against GPS: GPS-ref. Any common delay through the two GPS receivers will cancel. Since we have several GPS receivers at NIST which we monitor carefully, we are able to keep track of their relative delays even when one changes. We have maintained the receiver NBS10 as a standard for measuring relative delays through receivers. For this reason NBS10 has been used as an informal transfer standard for intercomparison of receiver delays between timing laboratories.

The technique for calibrating a remote receiver is to first calibrate a receiver at NIST against NBS10, then carry that calibrated receiver to the remote site and measure tracks in common with the receiver there, and finally bring the receiver back to NIST and close with another calibration against NBS10. The delay between two receivers can be calibrated for time transfer by setting them up to track in common view, at close distances with carefully measured relative coordinates. This allows cancellation of time transfer errors due to satellite ephemeris errors or mis- modeling of the ionosphere. Also, there should be no errors due to incorrect relative coordinates. Differences in measurements due to multi-path still remain. Any instabilities in the receivers become appropriately part of the calibration.

For this trip we first tracked satellites with the receiver NBS23 at NIST in common with tracks on three other receivers, one of which was NBS10. The antenna coordinates of all four receivers were known to within 1 m relative to each other. This was done for weeks. The standard deviations were usually below 2.5 ns. I shall call NBS23 the "traveling receiver" for this calibration trip, since it was the one which was carried. The traveling receiver was then carried to Japan, where it was used to calibrate timing delays of receivers there. Finally, it was returned to the U.S.A. where it was again calibrated against NBS10 for closure. The final calibration showed an offset of 4 ns with a standard deviation under 2.5 ns. To correct for this, all measurements made in Japan have been corrected by 2 ns to obtain an estimate of lab receiver vs. NBS10.

Calibrations at TAO

The traveling receiver was set up the night of June 1. Two receivers of different manufacture were calibrated at TAO. The older receiver is used for data put on the Mark III system for international time comparisons in cooperation with the BIPM. We will call this the "on-line receiver." The second receiver is a newer one which we will call the "back- up receiver." After one day of data we discovered that the 1 pps reference for the back-up receiver had a long rise time, about 50 ns at 90%, since it was coming from old equipment. The people at TAO therefore changed on June 2 to a different digital clock with a fast rise time of about 2 ns. The pulse for both the on-line receiver and the traveling NIST receiver were already coming from this digital clock. After this change both calibrations had standard deviations of 3.5 ns. The calibrated delays are listed in Table 1 below.

Calibrations at CRL

The NIST receiver was set up at CRL on Saturday, June 4, and taken down on June 6. The standard deviation of the data was 13.5 ns. This is large when one considers we are trying to calibrate these delays to within a few ns. CRL has a unique receiver of their own design. It appears to have a large overall delay as compared to other receivers, hence the possibility for more deviations in the measurements. They also use their own ionospheric model. The rise time of the 1 pps to both receivers was of the order of 20–30 ns at 90%. These factors contributed to the large deviation in the data. Coordinate errors were ruled out, both since the two antennae were within 1 m, and since there are deviations of the order of 30 ns on some of the same tracks from one day to the next. The calibration results are listed in Table 1 below.

Calibrations at NRLM

The NBS receiver was set up at NRLM on the afternoon of June 6. Tracks were continued until June 10. NRLM had two GPS receivers NRLMA and NRLMB. These were of a manufacture new to common view time transfer, with software which had not been used before in a timing receiver. In fact the software had been newly issued to NRLM within the previous week to facilitate the common view comparisons of this experiment. In reducing the data we also had a large standard deviation here: 15.5 ns for NLRMA, and 36.6 ns for NRLMB. In this case we found indication of coordinate errors since the day to day deviation of the calibration using a single track was typically under 4 ns, and we had 4 or 5 days of data on most tracks.

The measurement residuals and the elevations and azimuths as recorded from the end of the tracks, resolved to 1 degree, were used to estimate any coordinate change implied by the data. The process is illustrated in figures 4 and 5. Both figures are polar plots of the location of the tracks, indicated by X's, at NRLM in elevation and azimuth. Thus, each X denotes a track which was repeated each day. Next to each X in figure 4 is the residual for that track of the measurements NRLMB–NBS10 after averaging over all the days and then removing the mean of all the measurements. One can see here a large bias in the north south direction. The positioning solution in this case resulted in a 16 m change. Figure 5 shows the residuals after removing the effect of the coordinate change. One can see there is still a large deviation in the residuals.

The coordinate change for NRLMA was rather puzzling. The result was a 3.5 m change largely in the east direction. Yet the antennae themselves were only 2 m apart to begin with. It is possible there was some problem with the software in the receiver. This is reinforced further since the standard deviation of the measurements from NRLMA after correcting for the coordinate change was still 14.6 ns. The coordinate change for the NRLMB receiver was 16.0 m in the north direction, 2.6 m in the east direction, and 0.7 m vertically. A coordinate error here is more plausible in that the antenna for this receiver was somewhat removed to a quieter RF area, and had been surveyed. Though, the residuals after the change still had a standard deviation of 15.2 ns.

Table 1. Calibration Results Local Receiver–NBS10					
Lab & Rcvr	Date	No. pts	Mean (ns)	RMS (ns)	Coordinate version
TAO on–line	June 1–4	47	–11.7	3.3	WGS–72
TAO back–up	June 1–4	44	+15.0	3.5	WGS–84
CRL	June 4–6	34	–68.1	13.5	WGS–84
NRLM A	June 6–10	87	–61.5	15.5	WGS–84
		after the estimated coordinate change:			
			–62.3	14.6	WGS–84
NRLM B	June 6–10	87	–169.1	36.6	WGS–84
		after the estimated coordinate change:			
			–172.2	15.2	WGS–84

Table 2. Clock Ensemble and Local UTC						
Lab i	Clock ensemble	Source of UTC(i)	Point of UTC(i)	temp. control	humid. control	Faraday shield
TAO	8 Comm. Cs. w/ supertubes	1 Comm. Cs. w/ supertube	Start of time interval counter	yes	yes	yes
CRL	1 lab Cs. 11 Comm. Cs. 3 H–masers	Ensemble of 5–6 Comm. Cs.	Start of time interval counter	+/–0.5 deg C	+/–10%	–40dBm
NRLM	2 HP5061–004 1 HP5061	1 HP5061–004	Start of time interval counter	23.0 +/– 0.3 deg C	50% +/– 3%	E field: 120dB B field: linear 20 dB @ 1KHz 110 dB @ 1MHz

Note: "Comm." is used as an abbreviation of "Commercial"

Table 3. Shape of the local 1pps		
Lab	90% Rise Time (ns)	Voltage Level
TAO	4 ns	0–5
CRL	25 ns	0–5
NRLM	10 ns	0–5

References

1. W. Lewandowski, M. Weiss, D. Davis, "A Calibration of GPS Equipment at Time and Frequency Standards Laboratories in the USA and Europe," Metrologia 24, pp 181–186 (1987).

2. J. A. Buisson, O. J. Oaks, M. J. Lister, "Remote Calibration and Time Synchronization (R–CATS) Between Major European Time Observatories and the US Naval Observatory Using GPS," in Proc. 17th Precise Time and Time Interval Applications and Planning Meeting, Washington DC (1985), pp 201–222.

3. T. Morikawa, et. al., "Calibration of the Delay Time in GPS and GMS Time Comparison Receivers of Japan and Australia Using Portable Reference Receivers," submitted to IEEE I&M fall 1988.

4. M. A. Weiss, D. W. Allan, "An NBS Calibration Procedure for Providing Time and Frequency at a Remote Site by Weighting and Smoothing of GPS Common View Data," IEEE IM-36,572-578 (1987).

5. M. A. Weiss, "Apparent Diurnal Effects in the Global Positioning System." in Proc. 19th Precise Time and Time Interval Applications and Planning Meeting, Redondo Beach, CA (1987), pp 33-48.

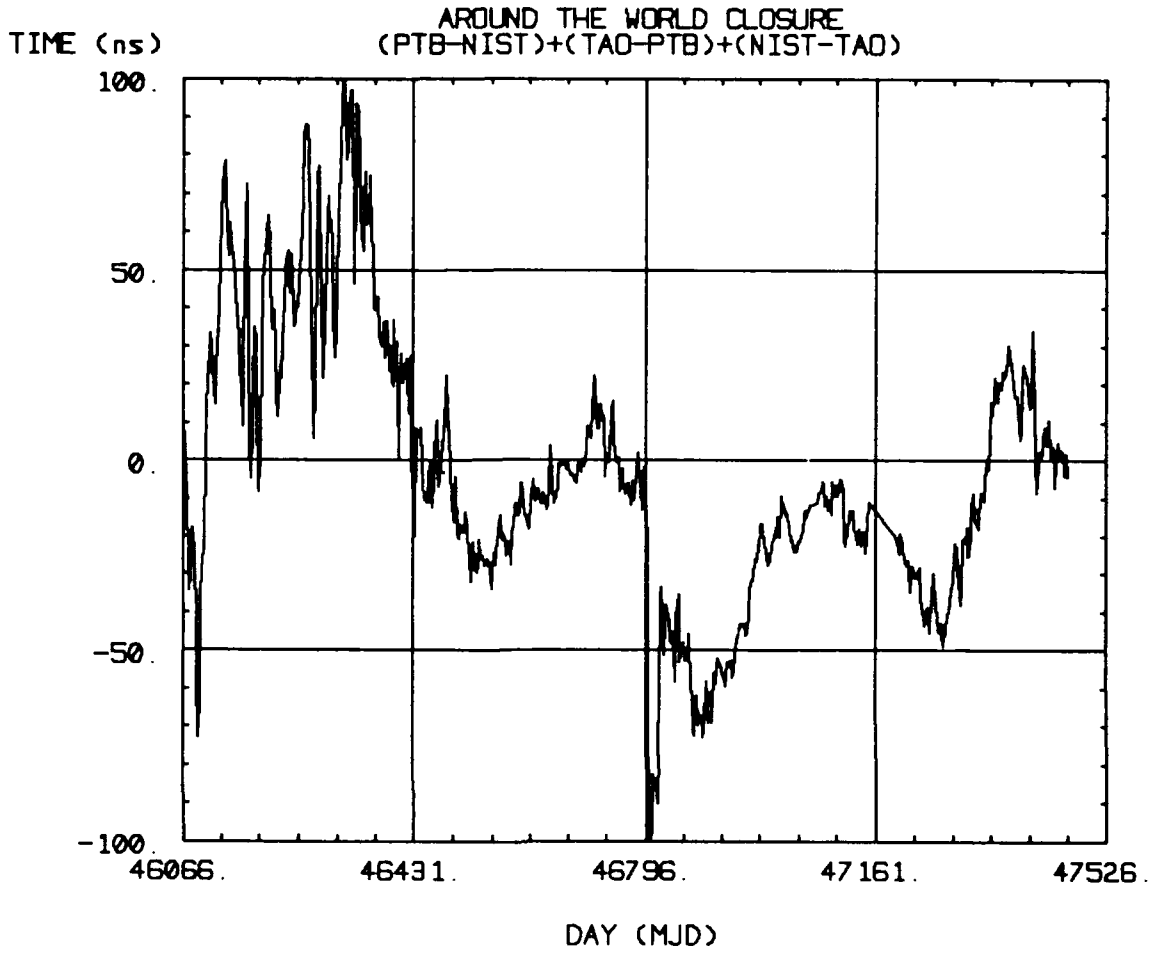

Figure 1: The residuals from three common view time transfers: (PTB-NIST), (TAO-PTB), and closing with (NIST-TAO), over four years: 1985, starting MJD 46067, 1986, starting MJD 46432, 1987, starting MJD 46796, and 1988, starting MJD 47161. One can see the maturation of the system, as the residuals generally decrease and become more well-behaved over the years. The sharp drop in early 1987 coincides with the coordinate change from WGS-72 to WGS-84. The data over the months of August through Novenber of 1988 are at the end of the plot with a mean of 8.3 ns, and a standard deviation of 7.7 ns. This is consistent with an accuracy estimate of 10 ns for each individual leg.

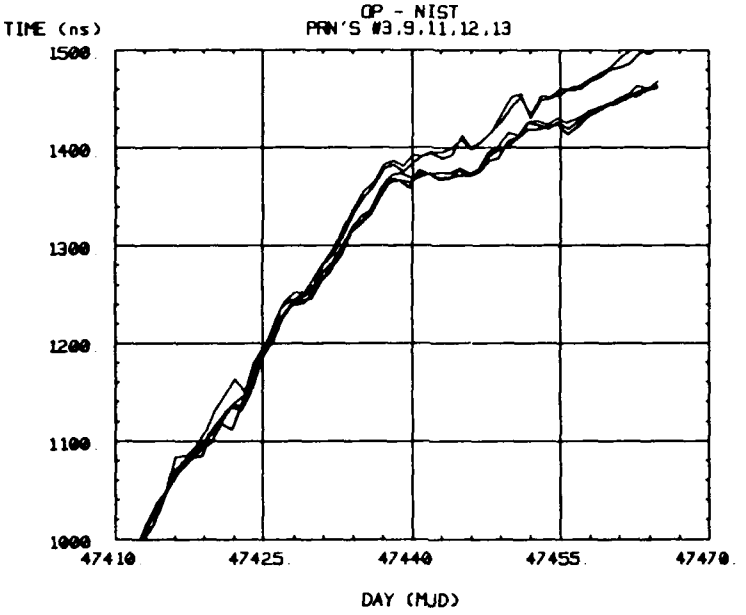

Figure 2: Measurements taken once per sidereal day on satellites in common view between Observatoire Paris, in Paris , France, and NIST, Boulder, Colorado show biases between measurements taken via different satellites. The biases change over time, and can be as large as 40 ns.

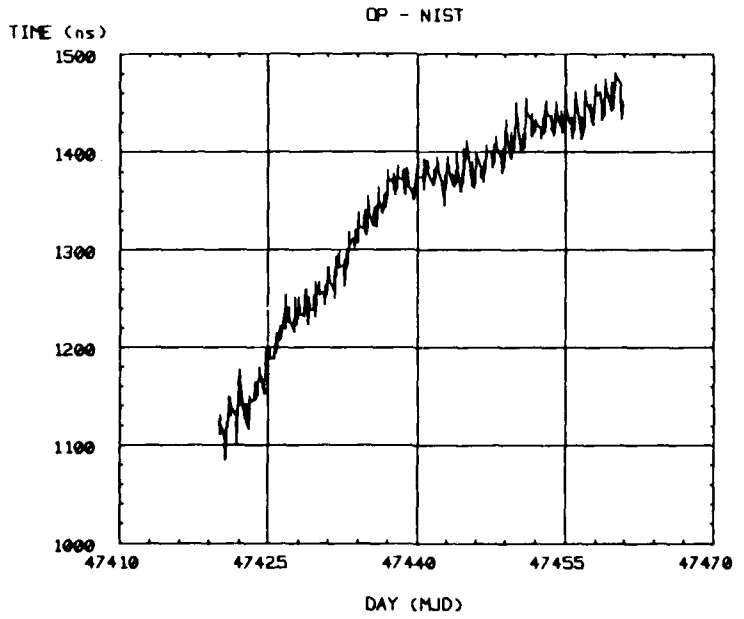

Figure 3: If one uses all common view data available in one chronological time series, the biases appear as noise with a large diurnal signature.

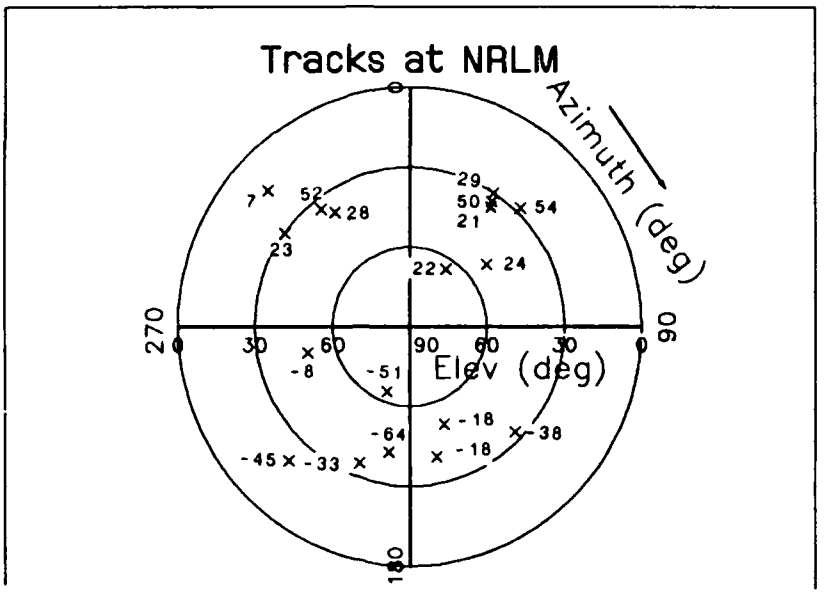

Figure 4: A polar plot of the location of the tracks, indicated by X's, at NRLM in elevation and azimuth. Thus, each X denotes a track which was repeated each day. Next to each X is the residual in ns for that track of the measurements NRLMB-NBS10 after averaging over all the days and then removing the mean of all the measurements. The residuals imply a positioning error of 16 m north, 2.6 m east, and 0.7 m vertical. The positioning error in the north direction can be seen heuristically by noting that the residuals are generally more negative to the south and positive to the north.

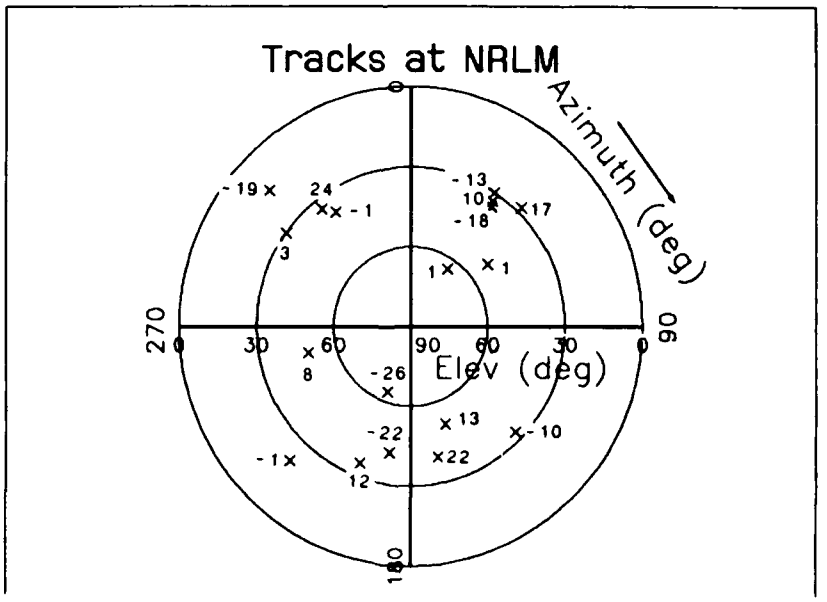

Figure 5: A polar plot of the tracks at NRLM as in figure 3, but now the numbers next to the X's have been adjusted from figure 3 to account for the positioning solution. The standard deviation has dropped from 36.6 ns to 15.2 ns, though this is still quite large.

QUESTIONS AND ANSWERS

JIM SEMLER, INTERSTATE ELECTRONICS: Can you briefly describe the architecture of the receivers that you were calibrating?

DR. WEISS: I am not too familiar with the architecture of all the different receivers, they are quite different designs. They were all operated in a mode that was single–channel, C/A code receivers. I really don't know the different architectures.

DR. GERARD LAPACHELLE, UNIVERSITY OF CALGARY: You mentioned that the multipath reached as much as three nanoseconds. You were lucky because with the chip rate of the code, you could get a delay error as much as 900 nanoseconds. In certain navigation situations, even with the P–code we have seen as much as 30 to 50 nanosecond delay because of multipath. It is possible to combine the code with the carrier to limit this.

DR. WEISS: Yes, if you have a carrier–locked receiver, as long as you do not slip a cycle, the most error that you can get is one cycle. That is the stability of the measurement, you still have the problem of identifying the cycle that you are locking on. The only way to determine the pseudo–range is with the code. You still have to start with a code measurement to identify a cycle. What you mentioned about the deviation due to multipath–a reflected wave can come in as much as 300 meters or 900 nanoseconds out and still in some way influence the integration. The farther out it is, the less that is going to pull the lock of the receiver. There really is a trade–off between how far out it is, in terms of how far it's going to pull the lock, and how much leverage it has in pulling it. Typically what we have seen is errors between 3 and as much as 10 nanoseconds. There have been other studies that indicate more than that, but I haven't seen anything on the order of 30 to 50.

DESIGN CONSIDERATIONS AND PERFORMANCE OF A SPACEBORNE HYDROGEN MASER FREQUENCY STANDARD[1]

E.S. Richter and B.A. Bettencourt
Space and Communications Group
Hughes Aircraft Co., Los Angeles, CA

H.T.M. Wang and R.R. Hayes
Hughes Research Laboratories
Malibu, CA

ABSTRACT

An engineering development model (EDM) of a compact hydrogen maser atomic clock for spaceborne applications has been built by Hughes Aircraft Company, Space and Communications Group (S&CG). The clock weighs 29.1 kg and has a power consumption of 64 Watts. The clock has demonstrated an excellent immunity to baseplate temperature variations during thermal vacuum tests, maintaining a fractional frequency stability of 2×10^{-15} for a 10^5 sec averaging time in the presence of a 10°C sinusoidal baseplate temperature modulation. The drift rate is also quite low, a few parts in 10^{-15}/day as measured against a VLG11 conventional maser. The design criteria, several technical solutions and the possibility of further reductions in size and weight are discussed.

INTRODUCTION

In May of 1983, Hughes S&CG was awarded a contract by the Naval Research Laboratory to build a hydrogen maser for use on GPS satellites. The design is based on an oscillating compact maser developed at Hughes Research Laboratories (HRL).[2] Although the basic design and overall functionality remain unchanged, the majority of the mechanical and electrical subsystems had to be substantially modified to satisfy stringent launch, size and weight requirements. Telemetry interfaces for monitoring and control also had to be added to allow remote operation. Some of the more salient features of the final design will be presented in this paper, together with preliminary stability data.

STRUCTURAL DESIGN OVERVIEW

An isometric drawing of the maser is shown in Figure 1. The physics unit is supported at two places by titanium stanchions: at the plenum assembly (which houses the getter and ion pumps) and at the junction of the physics unit with the microwave front-end electronics. These stanchions bolt to an aluminum baseplate, which provides support for mounting to the spacecraft.

To achieve its small size and light weight, the maser employs an electrode-loaded cylindrical cavity with one removable end cap. Four loading electrodes are plated on the outer surface of the teflon-coated maser storage bulb. It is much more difficult to achieve a high cavity Q using plated electrodes than it is with the old technique (used in the HRL design) of affixing copper foil electrodes using epoxy adhesives. However, plating provides mechanical rigidity which is critical to preserving the frequency of the cavity under the shake and vibration of launch. An added benefit of plating is a much smaller temperature coefficient of cavity resonant frequency. To achieve the benefits of plating, a new process of depositing high conductivity silver films on a quartz surface had to be developed, in part because the conventional technique, which employs chrome, cannot be used due to the residual magnetic fields that chrome generates.

The solid stem of the storage bulb is clamped at one end of the cavity by a funnel fitting, while the beam entrance stem is permitted axial movement at the other end. This allows for dimensional changes during warmup. The cavity is cantilevered from one end of the surrounding titanium vacuum chamber using four titanium leaf springs. The patented mounting technique isolates the cavity from force changes that would otherwise be transmitted due to mounting surface expansions or contractions. The leaf springs and the delrin washers provide effective thermal and electrical isolation of the cavity.

Five layers of 14 mil thick concentric hypernom magnetic shields with removable tapered end-caps surround the titanium vacuum chamber.[3] The neck transition of each shield is thickened to reduce vibration induced stresses, and the shields are held in place axially by a series of spacers.

The quartz dissociator is housed in a stainless steel enclosure and is designed to operate in vacuum. The dissociator housing mounts to the plenum assembly using a gold wire seal. The demountable plenum and maser vacuum chambers are joined through a compression seal inside the plenum chamber. A single nut on the threaded tubulation connecting the two chambers is used to compress the gold o-ring.

The microwave front end electronics employs MIC technology. The rest of the clock and the control electronics use standard spacecraft electronic construction. All electronic housings are fabricated from aluminum.

THERMAL SUBSYSTEM

The space maser is expected to maintain a specified frequency stability of $1 \times 10^{-11}/\sqrt{\tau}$ for an averaging time τ in the range of $1 < \tau < 10^6$ sec when the temperature at the spacecraft interface is within the acceptance range of 15 to 45°C, with a maximum excursion of 4°C per orbit. The maser is allowed to operate with degraded performance over the qualification range of 0 to 60°C. This is a very stringent thermal design requirement.

The design approach is to decouple the microwave cavity from the environment using low emittance surface finishes, multilayer insulation blankets and thermal isolators. This passive design is augmented by proportionally-controlled zonal heaters. The goal is to control the temperature of the microwave cavity to within 1 millidegree C. Changes in cavity frequency which result from this small temperature variation are then servoed out by means of a cavity-control system (to be discussed in a following section).

The temperature control servos employ thermistor sensors in a resistive bridge network. DC heaters are used on the outermost shield, the two necks of the vacuum chamber, and the front end electronics for coarse regulation. AC heaters are used inside the magnetic shields to minimize magnetic perturbations. These 20 kHz fine-zone heaters are located on the surface of the vacuum chamber.

HYDROGEN FLOW SYSTEM

The hydrogen flow system makes extensive use of metal hydrides for compactness, lightweight and reliability.[4] A regulated flow of molecular hydrogen from a metal hydride source is dissociated by a rf discharge to form an atomic beam. Atoms in the undesired atomic states are stripped from this beam by means of a quadrupole magnet, while those in the desired state (the upper level of the maser transition) are deflected into the teflon coated storage bulb inside the microwave cavity. The resonant microwave radiation emitted by the atoms in the cavity provides the stable clock reference signal.

The 0.6 moles of hydrogen stored in the lanthanum nickel aluminum hydride supply will last at least twice the 7 year design life of the maser. Normal maser operation requires a hydrogen flow rate of less than

$3x10^{-5}$ torr-liter/sec. The entrance and exit openings of the dissociator are chosen to provide a dissociator operating pressure of 50 millitorr, a value which was empirically found to provide good hydrogen dissociation efficiency, ease of ignition and reliable operation.

The thin walled palladium-silver alloy tube hydrogen flow regulator in our earlier design was found to lack a positive shut off for baseplate temperatures above 40°C. At temperatures higher than 60°C, the uncontrolled permeation rate was so high that flow regulation became very poor. The design was modified by substituting nickel for the palladium-silver alloy. By properly sizing and annealing the nickel tube, the increase in power consumption was made insignificant. The revised design enabled positive shut-off of hydrogen flow at temperatures beyond 80°C.

The dissociator operates with about 3 watts of rf drive power. To minimize possible radio frequency interference, the dissociator is completely enclosed by the metal vacuum envelope. The rf power is generated by a single transistor oscillator coupled to a starting and sustaining electrode structure. Optimizing the coupling network is a tedious procedure due to the capacitive coupling between the electrodes and the metal walls. Good discharge ignition and reliable dissociator operation has, nonetheless, been obtained.

The plenum assembly houses two getter slugs. Although one getter is more than enough for a 7 year life, a second is provided to reduce the powdering of the getter with hydrogen absorption. The powder is confined by encasing the getters in sintered 316L stainless steel filters which also serve as baffles to prevent excessive thermal radiation from reaching the state selector magnet and the cavity region during getter activation. Two 2 liter/sec ion pumps are attached to the plenum assembly. These pumps are throttled down and operated at a low voltage to reduce hydrogen pumping.[5] Their function is to pump the small amount of non-getterable residual gases. The pump current during normal maser operation is typically a few microamps.

CLOCK AND CONTROL ELECTRONICS

A block diagram of the maser receiver electronics is shown in Figure 2. It is basically a triple conversion coherent heterodyne receiver phase-locking a slave voltage-controlled crystal oscillator (VCXO) operating at the GPS standard frequency of 10.23 MHz. The buffered VCXO system output is adjustable in steps of $2x10^{-13}$ over a range greater than $7x10^{-10}$. Since the natural Q of the compact cavity used in this maser is too low to sustain maser oscillation, the design uses external gain and positive feedback to raise, or enhance, the cavity Q. A phase shifter and an attenuator, each independently programmable, are contained in the Q-enhancer circuit to enable setting the desired gain and phase shift.

A cavity stabilization servo system is an integral part of the receiver. The servo system operates by alternately injecting test signals at the half power points of the Q-enhanced cavity. The test signals are produced by upconverting the output of a switched synthesizer (alternating between 11.809 and 11.779 MHz at a 52 Hz rate) with the 1432.199 MHz local oscillator. The transmitted test signals are synchronously detected for any asymmetry in cavity transmission. Any imbalance forms the error signal for the servo system controlling the bias voltage of the varactor reactance tuner.

The microwave front end and the cavity stabilization servo, both of which critically affect maser performance, are located with the physics package in a controlled environment. The remainder of the maser electronics is contained in the side lobe package (Figure 3). The relationship between the contents of the side lobe electronics unit and other maser components is shown in Figure 4. To increase packing density, the majority of the boards are multilayer (4 to 8 layers). The boards are heat sunk and low signal level boards are isolated from higher signal level boards.

STABILITY DATA

Since the dominant perturbation on a satellite borne atomic clock is ambient temperature variation, the preliminary testing of the maser has concentrated on thermal vacuum effects. The stability of the maser has been measured in a vacuum chamber. The maser baseplate was bolted to an aluminum heat exchanger plate through which a temperature-controlled ethylene glycol solution was circulated. The temperature of this solution, which was controlled by a computer-driven heater-chiller, could be raised, lowered, or made to follow a predetermined temporal profile. Stability data were collected on a dual-mixer-time-difference system with a conventional hydrogen maser, the VLG11 P10, as reference.[6]

The data shown in Figure 5 were taken at a constant baseplate temperature of 30°C. As shown by the phase data, the phase variation is, after subtracting a fitted drift of -4.66×10^{-15} per day, less than 1 nanosecond over the 5.9 days interval. The drift rate is consistent with the normal observation for the VLG11 P10. The Allan variance plot shows that the stability is almost an order of magnitude better than the design requirement. As indicated by the insert in Figure 6, a stepwise baseplate temperature change from 30 to 37°C during the run caused no observable effect. In an earlier experiment, the baseplate temperature was sinusoidally modulated between 21.5 and 30°C with a 12 hour period; Figure 7 shows the synchronously collected phase and temperature data for the first 3 days of this run. Phase data and the computed Allan variance for the complete run are shown in Figure 8. These results demonstrate the effectiveness of the design and excellent stability performance of the maser.

SUMMARY REMARKS

A laboratory design for an oscillating compact hydrogen maser has been completely re-engineered for space application. Careful attention was paid to the structural design to meet vibration criteria, to the thermal subsystem to meet projected spacecraft temperature variations, to the hydrogen flow system to maintain proper operation in excess of the 7 year mission, and to the electronic subsystems by incorporating space qualifiable electronic components.

Stability tests were performed on an EDM which was fabricated from components which had survived vibration testing. The clock has shown excellent immunity to baseplate temperature variations and exceptional long term stability.

The EDM is significantly smaller and lighter than a conventional hydrogen maser, but does not represent a limit in maser size and weight reduction. Indeed, a subcompact maser, CHYMNS-IIIb, has been fabricated and tested at HRL. This maser, displayed and operated at the 1987 PTTI meeting in Redondo Beach, California, has a physics unit having only 1/3 the volume and about 2/3 the weight of the EDM. Although there is slight degradation in short term stability, the electronics limited long term stability is unchanged. It is therefore not unrealistic to expect that a hydrogen maser with far superior stability can be packaged as a drop-in substitute for a cesium clock on board GPS satellites.

REFERENCES

1. This work has been supported by US Naval Research Laboratory under contract number N00014-83-C-2120.

2. H.T.M. Wang, "Characteristics of Oscillating Compact Masers", Proc. 36th Ann. Symp. on Freq. Control (1982), pp. 249-254.

3. D.U. Gubser, S.A. Wolf and J.E. Cox, "Shielding of longitudinal magnetic fields with thin, closely spaced, concentric cylinders of high permeability material", Rev. Sci. Instrum., 50, 751 (1979)

4. H.T.M. Wang, "Application of Metal Hydrides For Gas Handling in Hydrogen Masers", Proc. 37th Ann. Freq. Contr. Symp. (1983), pp. 7-11.

5. D.U. Gubser, S.A. Wolf, A.B. Jacoby and L.D. Jones, "Magnetic Shielding and Vacuum Test for Passive Hydrogen Masers", Proc. 13th Ann. PTTI (1981), pp. 791-799

6. The measurement system was furnished by NRL and we are grateful to NRL for making it available. The system was developed by Mr. A. Gifford of NRL who also wrote the program for data acquisition and analysis.

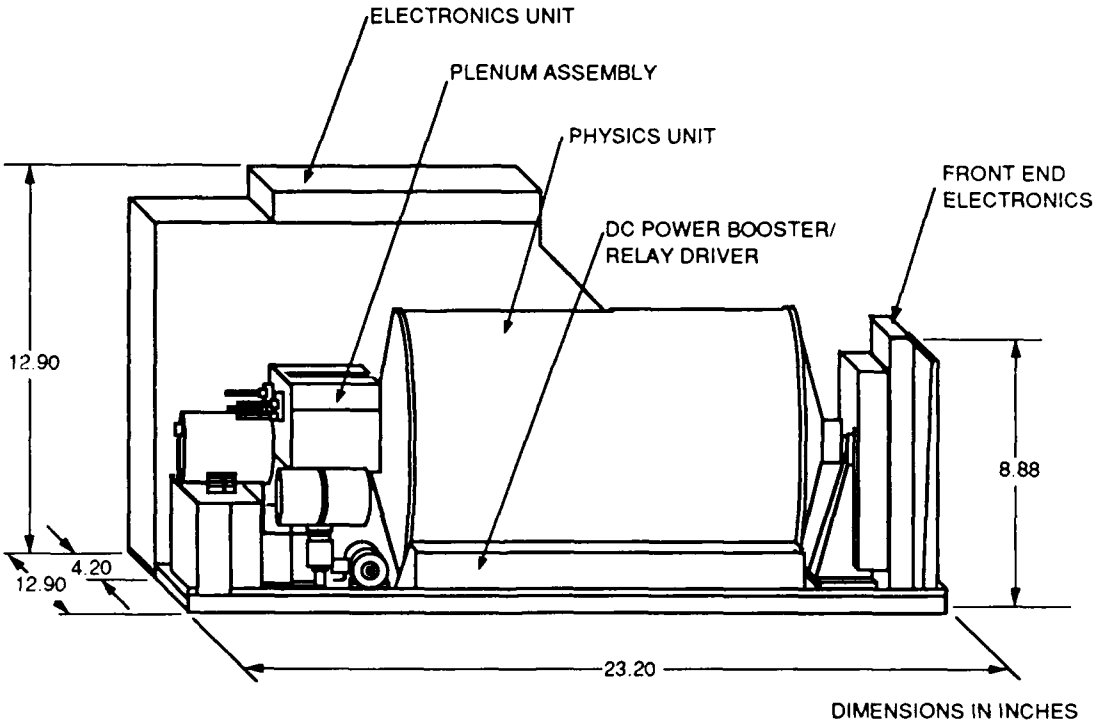

FIGURE 1. OUTLINE DRAWING

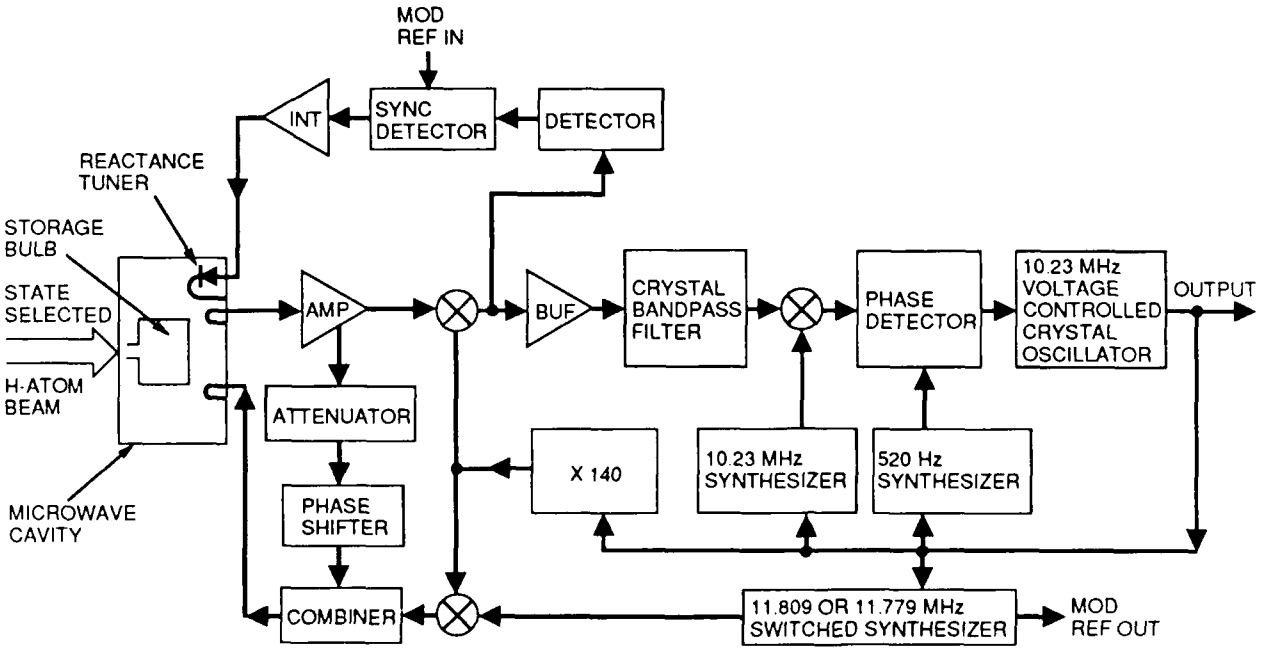

FIGURE 2. RECEIVER BLOCK DIAGRAM

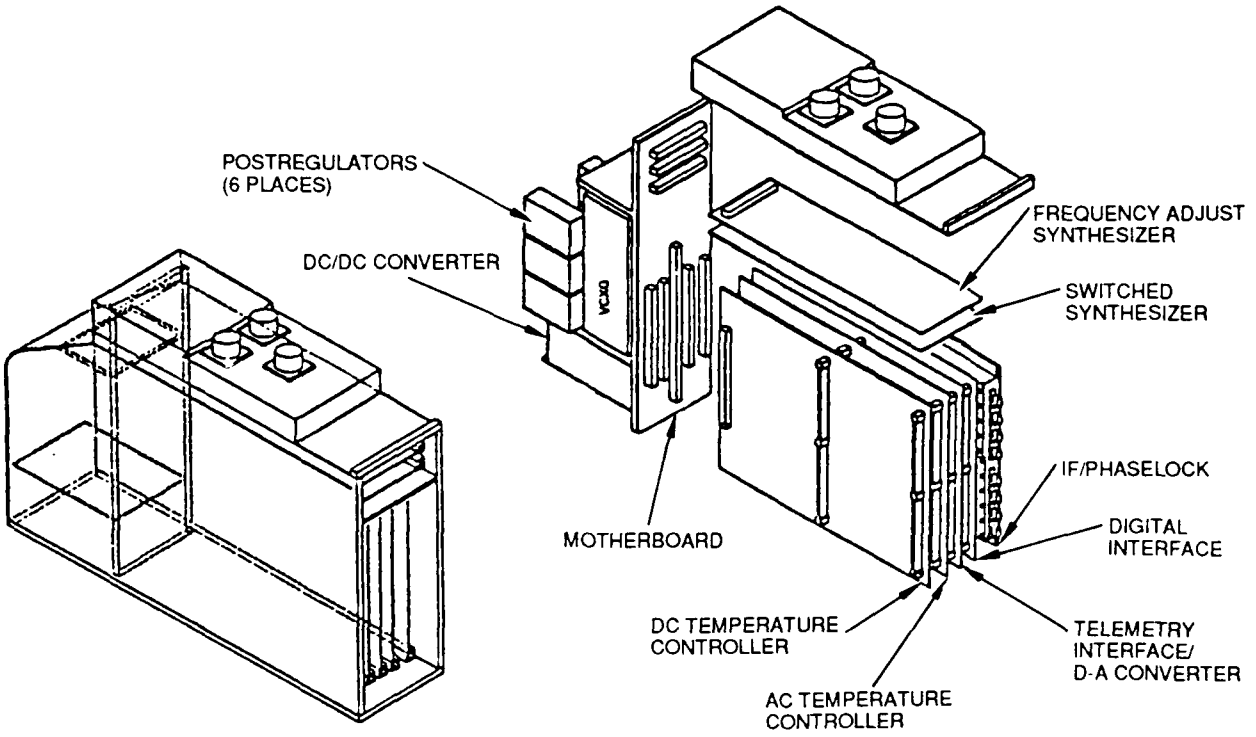

FIGURE 3. ELECTRONICS UNIT LAYOUT

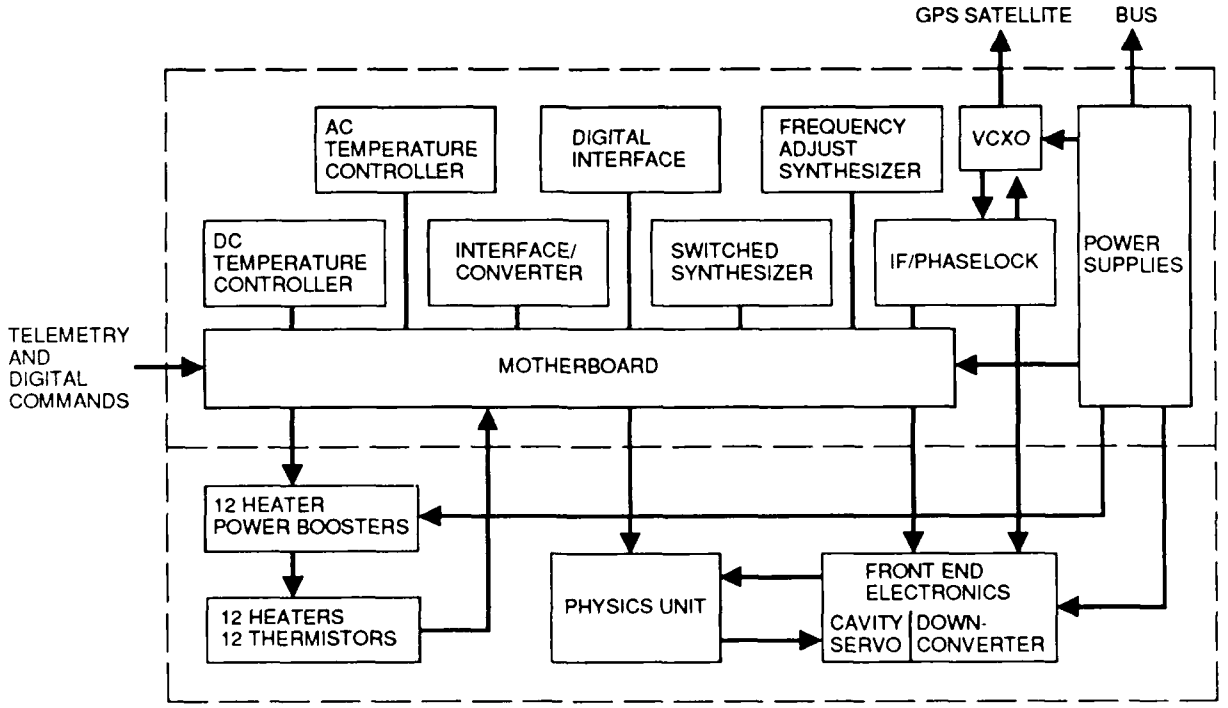

FIGURE 4. ELECTRONICS UNIT BLOCK DIAGRAM

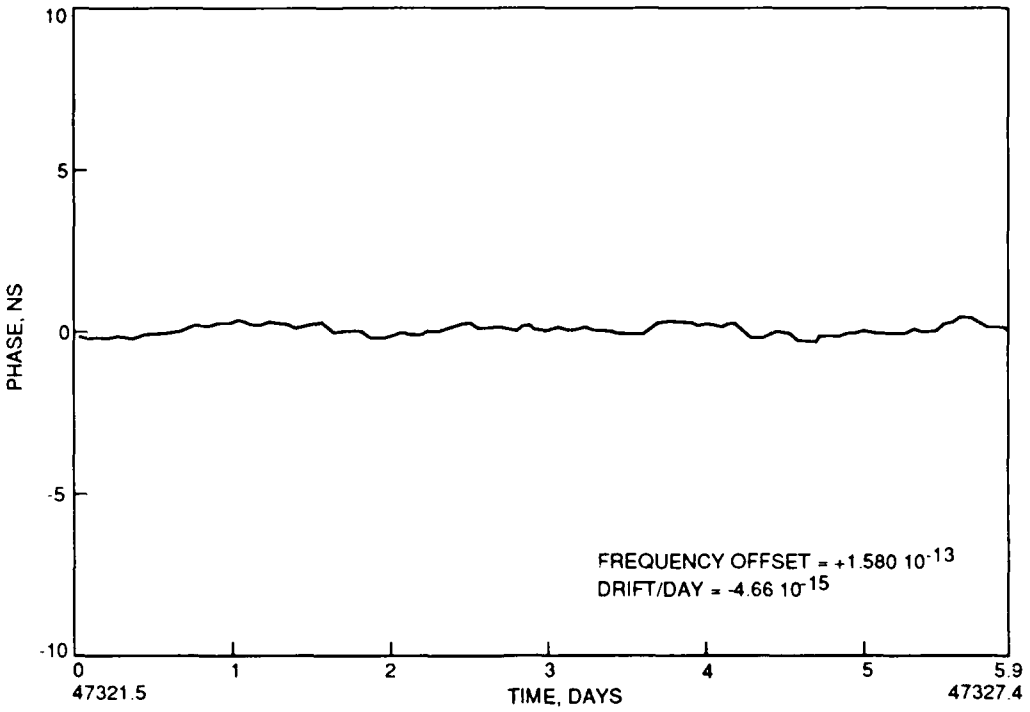

a) PHASE (DRIFT REMOVED) EDM-SM VERSUS VLG11 P10

SIGMA	PAIRS	TAU	LOWER BAR	UPPER BAR
$2.34\ 10^{-14}$	139	1H	$2.22\ 10^{-14}$	$2.52\ 10^{-14}$
$1.83\ 10^{-14}$	137	2H	$1.72\ 10^{-14}$	$2.00\ 10^{-14}$
$1.20\ 10^{-14}$	133	4H	$1.10\ 10^{-14}$	$1.38\ 10^{-14}$
$7.62\ 10^{-15}$	125	8H	$6.20\ 10^{-15}$	$8.92\ 10^{-15}$
$5.63\ 10^{-15}$	109	16H	$4.30\ 10^{-15}$	$7.46\ 10^{-15}$
$2.22\ 10^{-15}$	77	32H	$1.59\ 10^{-15}$	$3.87\ 10^{-15}$
$7.44\ 10^{-16}$	13	64H	$5.34\ 10^{-16}$	$2.58\ 10^{-15}$

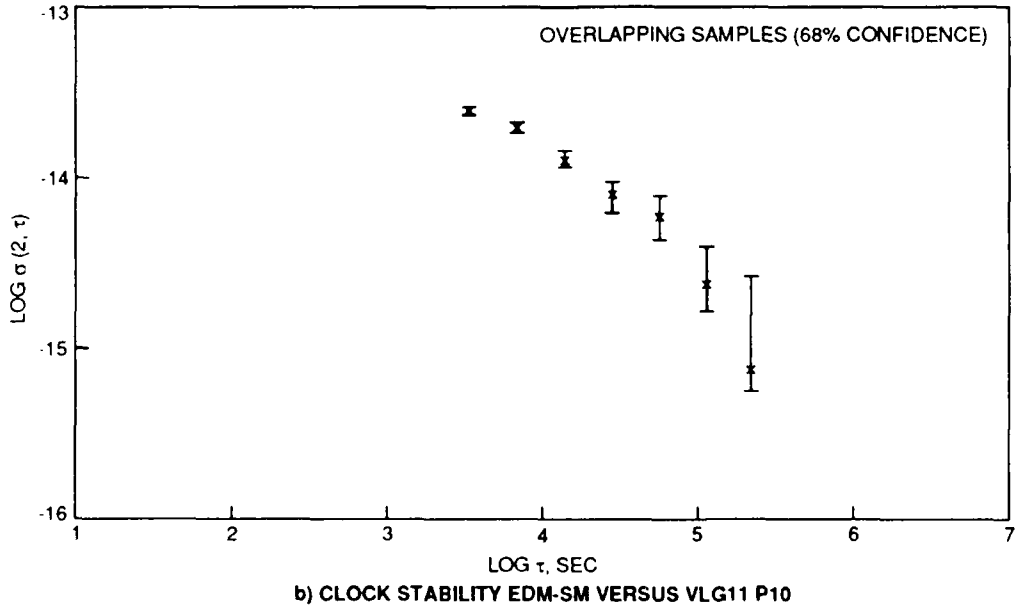

b) CLOCK STABILITY EDM-SM VERSUS VLG11 P10

FIGURE 5. ENGINEERING DEVELOPMENT MODEL IN VACUUM - BASEPLATE TEMPERATURE AT 30°C

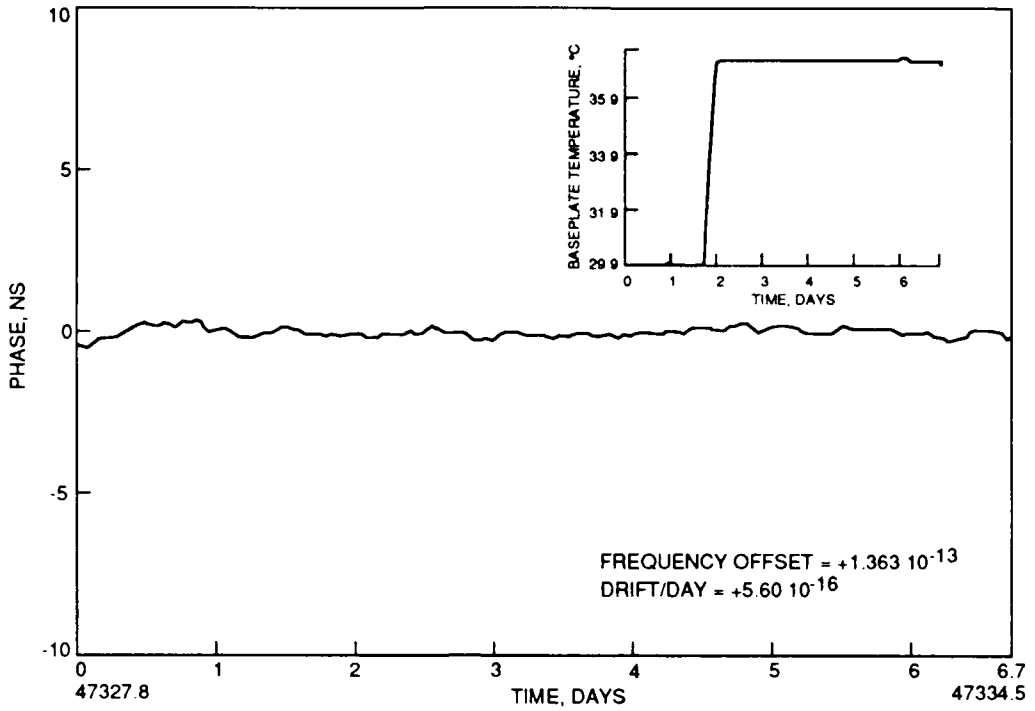

a) PHASE (DRIFT REMOVED) EDM-SM VERSUS VLG11 P10

SIGMA	PAIRS	TAU	LOWER BAR	UPPER BAR
$2.05\ 10^{-14}$	159	1H	$1.95\ 10^{-14}$	$2.20\ 10^{-14}$
$1.58\ 10^{-14}$	157	2H	$1.49\ 10^{-14}$	$1.72\ 10^{-14}$
$1.12\ 10^{-14}$	153	4H	$1.03\ 10^{-14}$	$1.27\ 10^{-14}$
$6.93\ 10^{-15}$	145	8H	$5.70\ 10^{-15}$	$8.02\ 10^{-15}$
$3.53\ 10^{-15}$	129	16H	$2.73\ 10^{-15}$	$4.54\ 10^{-15}$
$2.11\ 10^{-15}$	97	32H	$1.53\ 10^{-15}$	$3.42\ 10^{-15}$
$1.03\ 10^{-15}$	33	64H	$7.38\ 10^{-16}$	$2.91\ 10^{-15}$

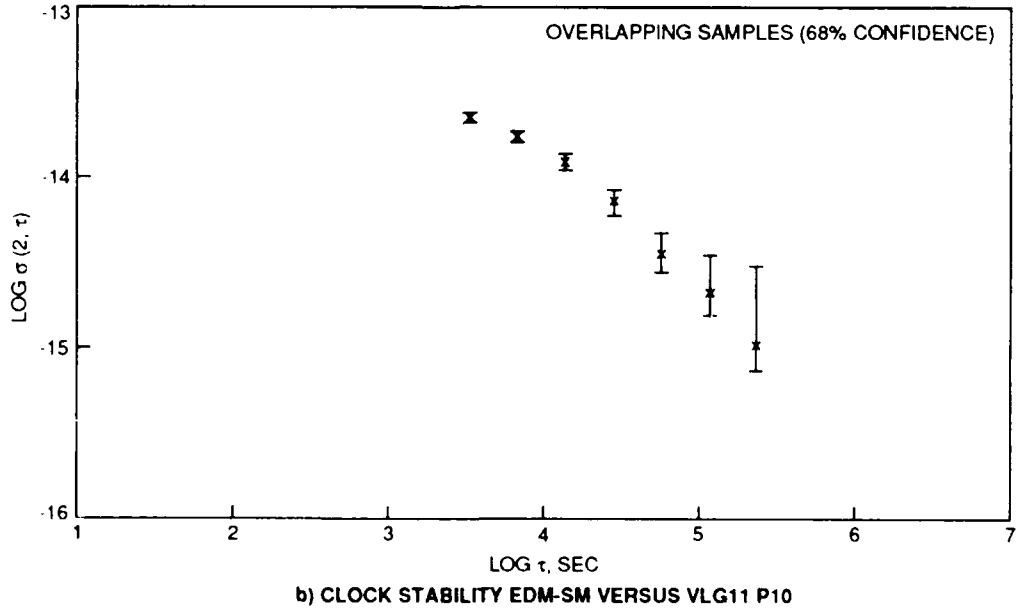

b) CLOCK STABILITY EDM-SM VERSUS VLG11 P10

FIGURE 6. ENGINEERING DEVELOPMENT MODEL IN VACUUM - BASEPLATE TEMPERATURE RAISED 7°C (2°C/HOUR)

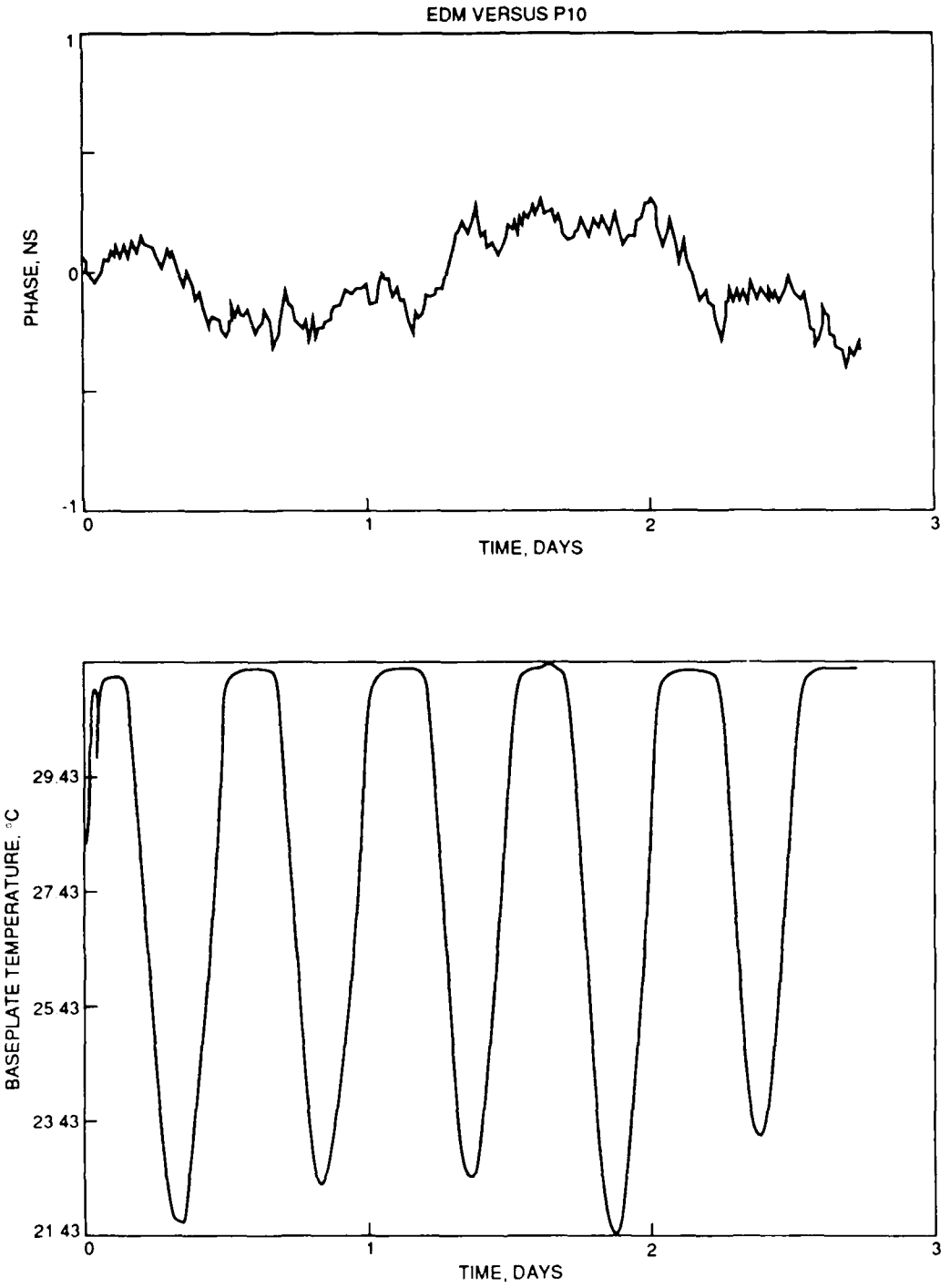

FIGURE 7. ENGINEERING DEVELOPMENT MODEL THERMAL TEST

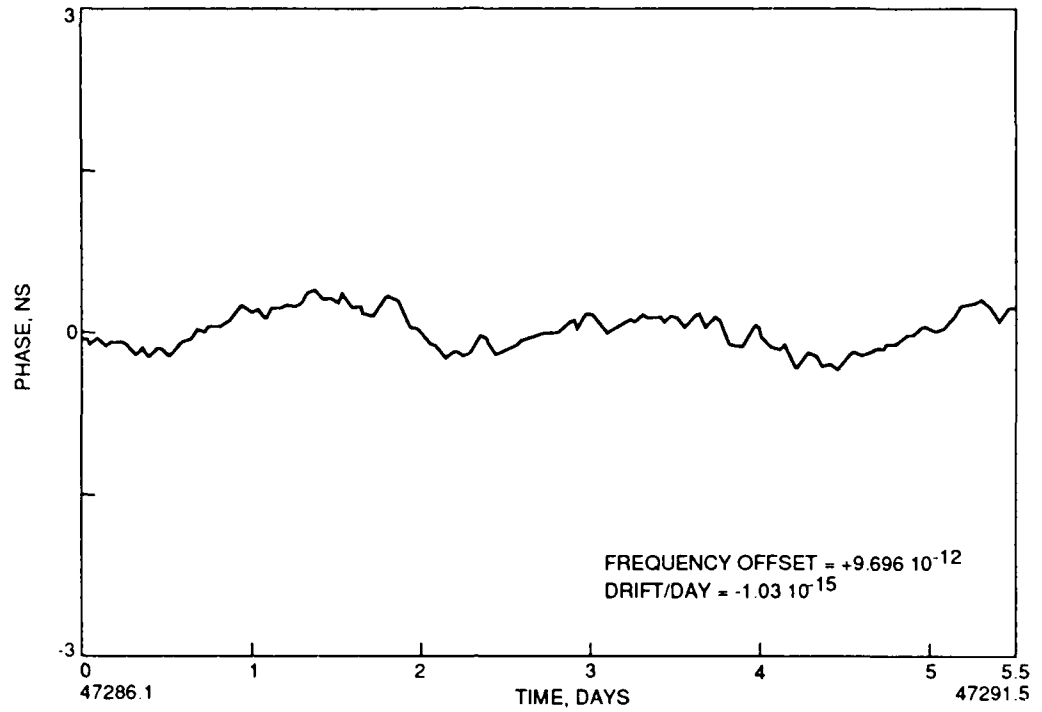

a) PHASE (DRIFT REMOVED) EDM VERSUS P10

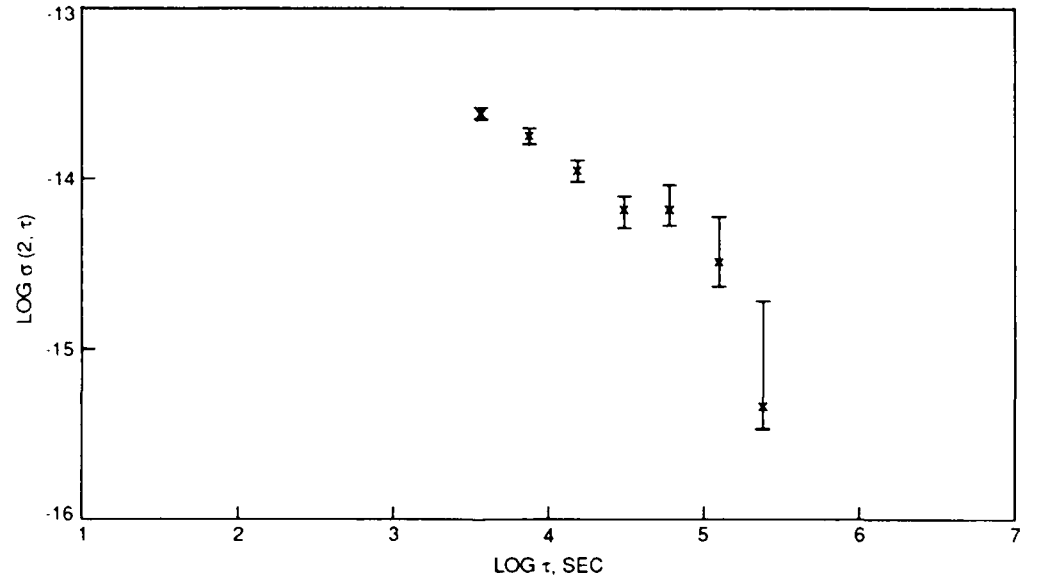

b) CLOCK STABILITY EDM VERSUS P10

FIGURE 8. ENGINEERING DEVELOPMENT MODEL STABILITY WITH 10°C BASEPLATE TEMPERATURE MODULATION

REDUCTION OF CAVITY PULLING IN A PASSIVE HYDROGEN MASER

W.M. Golding*, V.J. Folen, A.F. Frank, J.D. White, R.L. Beard
Naval Research Laboratory
Washington D.C. 20375

ABSTRACT

A new method for detection of the hydrogen resonance in a passive maser, has been tested and experimentally verified. This technique, which reduces the effect of cavity pulling on system performance, makes use of several amplitude and phase measurements of the combined transfer function associated with the cavity and hydrogen line. The atomic resonant frequency, determined in this way, has been shown to be essentially free from cavity pulling. For example, we have measured pulling factors 40 times lower than those measured using pure amplitude or phase techniques for the detection of the hydrogen resonance. The smaller cavity pulling factor is important in systems where cavity tuning errors are thought to yield an intrinsic limit on overall clock performance. The technique can be useful as a diagnostic tool, or as the hydrogen resonance detection method in an operational passive maser.

INTRODUCTION

This paper will show that sampling at discrete frequencies both the phase and amplitude of the forward transfer function of a passive hydrogen maser can yield a discriminator characteristic which is essentially free from cavity pulling. This approach reduces the severe requirements placed on the cavity servo in a passive system. The nominal pulling factor, when detecting by standard techniques, is proportional to the ratio of the cavity Q to the hydrogen line Q. In our system, which is a miniature passive hydrogen maser, this pulling produces 2×10^{-14} fractional frequency error per hertz of cavity tuning error. Therefore, to meet long term stability goals of 1×10^{-15}, we require that the cavity, the nominal resonant frequency of which is $1420.405 MHz$, be controlled to $\approx 0.050\ Hz$. Control of the cavity resonator to this degree requires extremely stable and accurate measurement of the resonance, along with the ability to tune the resonance in a way which does not degrade the measurement accuracy. This can be difficult to achieve and maintain. Utilizing sampling of the phase and amplitude of the forward transfer function, we have designed a system to lock to the hyperfine frequency rather than some specific characteristic of the overall transfer function, such as the maximum of the amplitude response. This design has yielded a reduction of cavity pulling by a factor of 40 in our present system. With further development, we hope to be able to reduce the pulling factor to the extent that the cavity servo will no longer be critical, thereby simplifying the implementation of a passive system.

THE MASER TRANSFER FUNCTION

In the paper by Viennet, Audoin and Desaintfuscien [1] and also in the paper by Lesage and Audoin [2], a useful model for the steady state response of a hydrogen maser is given. The model assumes that the atomic medium obeys the Bloch equations. The resonant microwave cavity of the model is driven by both the induced magnetization of the atomic hydrogen, and by an interrogating field.

The scattering parameters for the maser are derived largely from the the references [1] and [2]. The negative impedance concepts are well explained in [3]. The normalized forward transfer function for a two port maser, driven by a matched generator, and driving a matched load is derived in [1] and [2]. We have used this transfer function to fix the parameters of the equivalent circuit shown in figure 1. The relevant parameters of the equivalent circuit are the cavity impedance Z_c and the negative atomic impedance Z_a. For the angular frequency of the probing signal ω, near to both the cavity (ω_c) and hydrogen (ω_0) resonances, one obtains

* Sachs/Freeman Associates, Landover, MD

$$Z_c(\omega) \cong R_c(1 + jT_{cu}(\omega - \omega_c)) \tag{1}$$

$$Z_a(\omega) \cong \frac{-R_a}{1 + jT_2(\omega - \omega_0)}. \tag{2}$$

It is convenient to normalize both Z_c and Z_a to R_c. We define $\hat{Z}_c \equiv Z_c/R_c$ and $\hat{Z}_a \equiv Z_a/R_c$. The coupling parameters β_1 and β_2 are,

$$\beta_1 = \frac{n_1^2 Z_0}{R_c} \qquad and \qquad \beta_2 = \frac{n_2^2 Z_0}{R_c}, \tag{3}$$

where Z_0 is the characteristic impedance of the external transmission lines, and R_c is the resistive part of the cavity impedance. The ideal transformer ratios are n_1 and n_2. We define the normalized generator impedance as $\hat{Z}_g \equiv Z_g/Z_0$ and the normalized load impedance as $\hat{Z}_l \equiv Z_l/Z_0$.

From this equivalent circuit, the complete set of scattering parameters for the two port maser can be calculated. The scattering parameters are found to be,

$$S_{11} = \frac{\nu_{11} + jT_c(\omega - \omega_c) - \frac{\alpha}{1+S}/(1 + jT_2(\omega - \omega_0))}{1 + jT_c(\omega - \omega_c) - \frac{\alpha}{1+S}/(1 + jT_2(\omega - \omega_0))} \tag{4}$$

$$S_{21} = \frac{\nu_{21}}{1 + jT_c(\omega - \omega_c) - \frac{\alpha}{1+S}/(1 + jT_2(\omega - \omega_0))} \tag{5}$$

$$S_{22} = \frac{\nu_{22} + jT_c(\omega - \omega_c) - \frac{\alpha}{1+S}/(1 + jT_2(\omega - \omega_0))}{1 + jT_c(\omega - \omega_c) - \frac{\alpha}{1+S}/(1 + jT_2(\omega - \omega_0))} \tag{6}$$

$$S_{12} = \frac{\nu_{12}}{1 + jT_c(\omega - \omega_c) - \frac{\alpha}{1+S}/(1 + jT_2(\omega - \omega_0))}, \tag{7}$$

where the relation $\alpha/(1 + S) = R_a/(R_c(1 + \beta_1 + \beta_2))$ has been used. The ν_{ij} are simply functions of the coupling parameters. They are,

$$\nu_{11} = \frac{1 - \beta_1 + \beta_2}{1 + \beta_1 + \beta_2} \tag{8}$$

$$\nu_{22} = \frac{1 - \beta_2 + \beta_1}{1 + \beta_1 + \beta_2} \tag{9}$$

$$\nu_{21} = \nu_{12} = \frac{2\sqrt{\beta_1\beta_2}}{1 + \beta_1 + \beta_2}. \tag{10}$$

The two critical frequencies of the system are the $(F = 1\ ,\ m_F = 0\ ) \rightarrow (F = 0\ ,\ m_F = 0\ )$ hyperfine transition frequency, and the cavity resonant frequency,

ω_0 = the unpulled angular transition frequency of the atomic hydrogen

ω_c = the angular resonant frequency of the microwave cavity.

The relevant system time constants are,

T_1 = longitudinal time constant of the atomic hydrogen

T_2 = transverse time constant of the atomic hydrogen

T_c = the time constant of loaded cavity resonator i.e. $\hat{Z}_g, \hat{Z}_l = 1$

T_{cu} = the time constant of unloaded cavity resonator.

Other relevant system parameters are defined as follows:

$$\alpha = KQ_cT_1T_2I \qquad \text{oscillation threshold parameter}$$

$\alpha = 1$ at oscillation threshold, and $0 \leq \alpha < 1$ for passive operation

$$S = \frac{T_1T_2b^2}{1 + T_2^2(\omega - \omega_0)^2} \qquad \text{the saturation factor}$$

$$Q_c = \frac{\omega_c T_c}{2} \qquad \text{loaded Q of the resonant cavity}$$

$$Q_a = \frac{\omega_0 T_2}{2} \qquad \text{Q of the atomic line}$$

$$K = \frac{\mu_0 \eta \mu_B^2}{\hbar V_c} \qquad \text{coupling parameter} \tag{11}$$

$\mu_0 =$ permeability of free space

$\mu_B =$ Bohr magneton

$V_c =$ the cavity volume

$\eta =$ the cavity filling factor

$\hbar =$ Planck's constant over 2π

$I =$ net atomic hydrogen flux in atoms/second

$b =$ amplitude of the cavity magnetic field.

Further details regarding these quantities are given in [1], [2], [4] and [5].

The scattering parameters are useful for precise calculation of the effects of microwave measurement errors on system performance. The principal errors of concern are those due to source and load mismatch, the effects of lossy transmission lines, residual reflections in the measurement path, limited measurement isolation or directivity, the effects of dispersion in the cavity resonator, and the effects of nearby cavity modes. All of these imperfections can be analyzed by properly modifying the two port scattering parameter model of the maser given in equations (4) through (7). Their effect on long term stability of the system can then be derived through sensitivity analyses.

In a system in which the generator and load reflection coefficients are Γ_g and Γ_l, respectively, we find that the measured value of S_{21} is given by

$$S_{21,m} = \frac{S_{21}}{1 - S_{11}\Gamma_g - S_{22}\Gamma_l + \Gamma_g\Gamma_l(S_{11}S_{22} - S_{21}S_{12})}, \tag{12}$$

where we have,

$$\Gamma_g = \frac{\hat{Z}_g - 1}{\hat{Z}_g + 1} \qquad \textit{and} \qquad \Gamma_l = \frac{\hat{Z}_l - 1}{\hat{Z}_l + 1}. \tag{13}$$

Or, in terms of the normalized impedances, we obtain

$$S_{21,m} = \frac{\sqrt{\beta_1\beta_2}}{2}\left(\frac{(\hat{Z}_g+1)(\hat{Z}_l+1)}{\hat{Z}_c+\hat{Z}_a+\beta_1\hat{Z}_g+\beta_2\hat{Z}_l}\right). \tag{14}$$

If $\hat{Z}_g$ and $\hat{Z}_l$ can be considered to have constant magnitude and phase over the frequency range of interest, then $S_{21,m}$ is seen to be inversely proportional to the total loop impedance seen from inside the cavity. Under these conditions, we can make the following approximation:

$$S_{21,m} \cong \frac{k}{\hat{Z}_T}, \tag{15}$$

where the total loop impedance, $\hat{Z}_T$ is given by,

$$\hat{Z}_T = \hat{Z}_c + \hat{Z}_a + \beta_1\hat{Z}_g + \beta_2\hat{Z}_l, \tag{16}$$

and k is a complex constant.

COMMON DETECTION TECHNIQUES

Two means of detection of the hyperfine resonance ω_0 are commonly considered, namely, maximum amplitude detection and phase inflection detection. The case of maximum amplitude detection is fairly intuitive. The discriminator characteristic becomes the first derivative of the magnitude of $S_{21,m}$ and we can set our crystal servo to lock to the point where this derivative is zero. This is equivalent to locating the frequency (ω_A) where,

$$\left.\frac{\partial|\hat{Z}_T|}{\partial\omega}\right|_{\omega_A} = 0. \tag{17}$$

For the condition of negligible saturation, this criterion produces a pulling factor of,

$$P_A = \frac{Q_c}{Q_a(2-\alpha)}, \tag{18}$$

where the pulling factor P_A is defined as,

$$P_A \equiv \frac{\omega-\omega_0}{\omega_c-\omega_0}, \tag{19}$$

and ω_A is the detected frequency. The subscripts A and p differentiate between the different detection techniques.

If the detection criterion of phase inflection is used, we must force the servo to lock to the frequency (ω_p) at which,

$$\left.\frac{\partial^2\varphi}{\partial\omega^2}\right|_{\omega_p} = 0,$$

where

$$\hat{Z}_T(\omega) \equiv \left|\hat{Z}_T(\omega)\right| e^{j\varphi(\omega)}. \tag{20}$$

This can be shown to yield a pulling factor P_p that is equal to the Q ratio,

$$P_p = \frac{Q_c}{Q_a}. \tag{21}$$

As the oscillation parameter α approaches unity in (18), P_A approaches P_p. In contrast, P_p is independent of α. Since the spin exchange contributions to the overall relaxation are small at low hydrogen flux we

can assume that Q_a remains constant as α is varied by changing the atomic flux. Thus, when the cavity is mistuned in a passive maser, the dependence of P_A on α would yield in the amplitude detection technique a sensitivity to flux variations not present with the phase detection technique.

Both the amplitude and the phase detection techniques can be implemented by applying a sinusoidally frequency modulated carrier to the hydrogen resonance, and detecting the amplitude modulation produced on the output signal. Ideally,there will be no amplitude modulation detected if the carrier frequency is equal to ω_0. The amplitude detection technique is implemented by modulating at frequencies less than the bandwidth of the hydrogen response whereas the phase technique is implemented by modulating at frequencies much greater than this bandwidth [6].

SWITCHED FREQUENCY MODULATION TECHNIQUES

We are presently using switched frequency modulation techniques to simulate various detection criteria. The experimental system is diagrammed in figure 2. The network analyzer is referenced to the slaved oscillator and is used to produce signals at fixed frequencies relative to the oscillator. Switched frequency modulation refers to the process of stepping a CW signal through a fixed set of discrete frequencies. The signal remains at a single frequency for a fixed interval of time during which some measurement is made. Usually the amplitude and/or phase of the steady state response is measured and then the next frequency is selected and the measurement is repeated. Using this technique, we build up a set of measurements of the steady state transfer function. These measurements contain information about the absolute frequency of the slaved oscillator relative to the hydrogen resonance line. By using frequencies well separated from the hydrogen line, so that only the cavity response is sensed, we obtain information about the cavity resonance relative to the crystal oscillator. All this information is used to control both the crystal and the cavity, closing both servo loops.

Using switched frequency techniques, we have tried three different schemes for detection of the hydrogen resonance. They are amplitude, phase and impedance detection. The amplitude and phase detectors are discrete simulations of the two detection schemes described in the previous section. They are implemented by sampling the transfer function and estimating either the first derivative of the amplitude or the second derivative of the phase of $S_{21,m}$. In both cases, the estimate of the derivative is used as the error signal in the servo. It can be shown that the pulling factor for the two techniques is essentially the same as their continuous modulation counterparts.

IMPEDANCE DETECTION

The impedance detection technique is implemented using switched frequency techniques. As its name implies, it is based on measurements of the total loop impedance $\hat{Z}_T$. The loop impedance is defined by (15) and (16). One can obtain this impedance by inverting the measurement of $S_{21,m}$ and setting the constant $k = 1$. In the present model, we will now assume that the external terminations are well matched. That is, $\hat{Z}_g$ and $\hat{Z}_l$ are real, frequency independent and equal to one. These effects can be lumped into the resistive part of the cavity impedance and the external terminations assumed to produce cavity loading but no cavity tuning. In view of these assumptions, one obtains

$$\begin{aligned} \hat{Z}_T &= \hat{Z}_c + \hat{Z}_a + \beta_1 + \beta_2, \\ \hat{Z}_T &\propto 1 + jT_c(\omega - \omega_c) - \frac{\alpha/(1+S)}{1 + jT_2(\omega - \omega_0)}. \end{aligned} \tag{22}$$

Figure 3 shows a plot of $\hat{Z}_T$ in the impedance plane for $S = 0$, and for the cavity mistuned by approximately half its bandwidth. Angular frequency is the parameter running upwards along the curve. Note that the phase and magnitude of the impedance at any frequency are easily obtained by drawing the vector from the origin to the point on the curve corresponding to that frequency. The measured magnitude and phase will be the magnitude and phase of that vector.

The curve is made up of two simple curves, a straight line running from $X = -\infty$ to $X = +\infty$, and a circle tangent to that line at $\omega = \omega_0$. The straight line is due to the cavity impedance, and the circle is due to the atomic impedance. The relative pulling factors of the different servos are easily seen from this diagram. The frequency at which the amplitude servo will lock is that point on the circle (ω_A) which makes the magnitude of the measurement vector a minimum. The phase servo will lock at the point on the circle (ω_p) at which the measured phase is equal to the phase of the point where the hydrogen circle and cavity baseline touch. The pulling factors of the different techniques are gauged by noting the relative distance along the hydrogen circle between the point of lock (either ω_A or ω_p) and ω_0. For the parameters represented by this particular impedance plot, it is apparent that the amplitude servo pulling factor is roughly half that of the phase servo.

This graphical interpretation of the pulling factor has led us to look for ways in which we could force the crystal servo to lock directly to ω_0. This would result in a pulling factor of zero simply because there would always be zero distance on the circle between the lock point and ω_0 regardless of the cavity mistuning. A similar technique for locking to ω_0 is described in [7].

With reference to the impedance plot of figure 4, the impedance detection technique is based upon the observation that a vector **A** tangent to the hydrogen circle will point parallel to the straight line of the cavity response only if the point of tangency is at ω_0. We formulate the servo condition then, such that **A** must be parallel to **B** if $\omega_x = \omega_0$. **B** is a vector which points in the direction of the straight line representing the cavity impedance. The servo system must be able to measure the vectors **A** and **B** and to adjust the crystal frequency ω_x so that **A** is held parallel to **B**.

To estimate the vectors **A** and **B**, the impedance $\hat{Z}_T$ is calculated at the following four frequencies:

$$\begin{aligned} \omega_1 &= \omega_x - \delta \\ \omega_2 &= \omega_x - \epsilon \\ \omega_3 &= \omega_x + \epsilon \\ \omega_4 &= \omega_x + \delta. \end{aligned} \tag{23}$$

Here, ω_x is the crystal probe frequency and ϵ, δ are modulation frequencies producing test frequencies that are on and off the line, respectively. We now form **A** and **B** using $\hat{Z}_T(\omega)$ from (22). Let,

$$\begin{aligned} \mathbf{A} &= \hat{Z}_T(\omega_3) - \hat{Z}_T(\omega_2) \\ \mathbf{B} &= \hat{Z}_T(\omega_4) - \hat{Z}_T(\omega_1). \end{aligned} \tag{24}$$

The condition that **A** be parallel to **B** is the same as $Im(AB^*) = 0$, where A and B are taken to be the complex form of the vectors. We calculate that,

$$Im(AB^*) = -\frac{8\alpha T_c T_2^2 \delta\epsilon(\omega_x - \omega_0)}{(1 + T_2^2(\omega_x - \omega_0 + \epsilon)^2)(1 + T_2^2(\omega_x - \omega_0 - \epsilon)^2)} \tag{25}$$

$$\cong -\frac{8\alpha T_c T_2^2 \delta\epsilon}{(1 + (T_2\epsilon)^2)^2}(\omega_x - \omega_0), \tag{26}$$

with the approximate form valid for $\omega_x - \omega_0 \ll \epsilon$. The expression $Im(AB^*)$ is zero for $\omega_x = \omega_0$, independent of the value of the cavity frequency. Therefore, we see that the impedance detection scheme should produce no cavity pulling.

EXPERIMENTAL VERIFICATION

We have empirically shown that there is a large reduction in cavity pulling when using the impedance detection scheme in the experimental setup shown in figure 2. The measurement of pulling factor was done by varying the cavity frequency by $\pm 2kHz$ about the cavity lock point and measuring the resulting change in output frequency when using a given detection scheme. In order to change detection schemes we simply hit a softkey on the controlling computer (no hardware attached to the maser need be changed). This eliminates the possibility that the cavity Q or tuning coefficients might change between measurements. We were able to measure a pulling factor of 2×10^{-14} per hertz of cavity tuning using amplitude detection and 5×10^{-16} per hertz of cavity tuning using impedance detection. This represents a reduction in pulling of a factor of 40.

The residual pulling that we see now is not completely explained. It could be related to saturation of the hydrogen line, delay in the measurement circuit, or dispersion in the sapphire cavity. Anything that would make the true transfer function differ from the ideal of figure 3 could cause some residual pulling and is therefore suspect. Efforts are now under way to eliminate the major sources of the residual pulling and thus reduce the cavity pulling by another factor of ten.

ACKNOWLEDGEMENTS

We are grateful to Mr. Ken Uglow for the many illuminating discussions concerning these techniques. We would also like to thank Mr. Al Gifford and Mr. Ed Powers for their help in the use of the clock measurement system at NRL.

REFERENCES

[1] J.Viennet et al., "Cavity Pulling in Passive Frequency Standards," IEEE Trans. on Instrumentation and Measurement, Vol. IM-21, No. 3, Aug. 1972.

[2] P. Lesage and C. Audoin, "Amplitude Noise in Passively and Actively Operated Masers," Proc. of the 33rd Annual Symposium on Frequency Control, pp. 515-535, 1979.

[3] R. L. Kyhl et al., "Negative L and C in Solid State Masers." Proc. of the IRE, Vol. 50, No. 7, July 1962.

[4] D. Kleppner et al., "Theory of the Hydrogen Maser,"Phys. Rev., Vol. 126, No. 2, 603-615, April 15, 1962.

[5] D. Kleppner et al., "Hydrogen-Maser Principles and Techniques," Phys. Rev., Vol. 138, No. 4A, A972-A983, 17 May, 1965.

[6] G. Busca and H. Brandenberger, "Passive H Maser," Proc. of the 33rd Annual Symposium on Frequency Control, pp. 563-568, 1979.

[7] K. Uglow, "A Signal Processing Scheme for Reducing the Cavity Pulling Factor in Passive Hydrogen Masers," Proc. of the 18th Annual PTTI Applications and Planning Meeting, pp. 621-629, 1986.

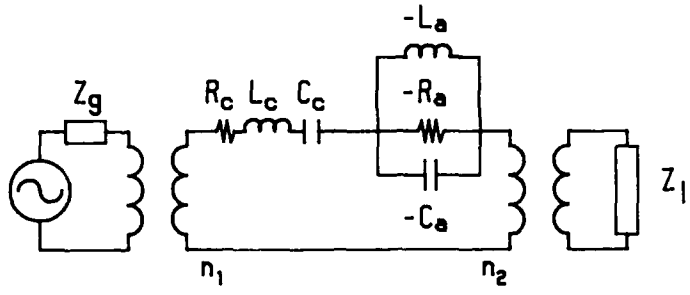

figure 1. Equivalent circuit of the passive maser

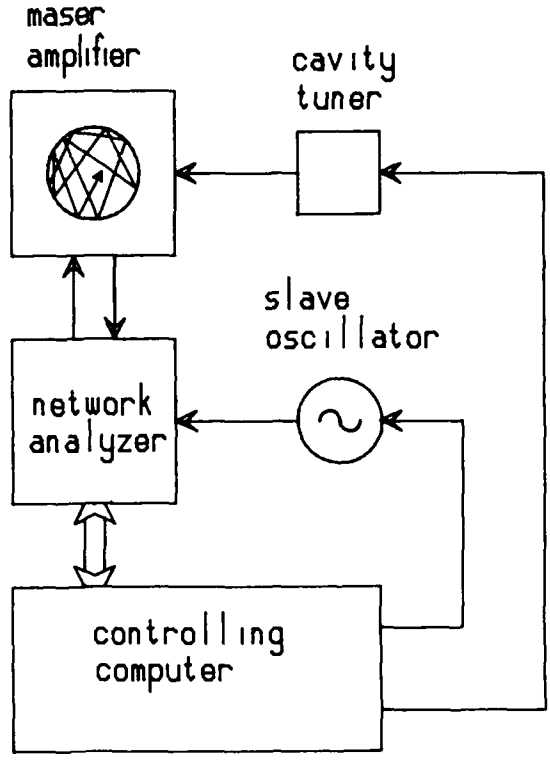

figure 2. Block diagram of the experimental system

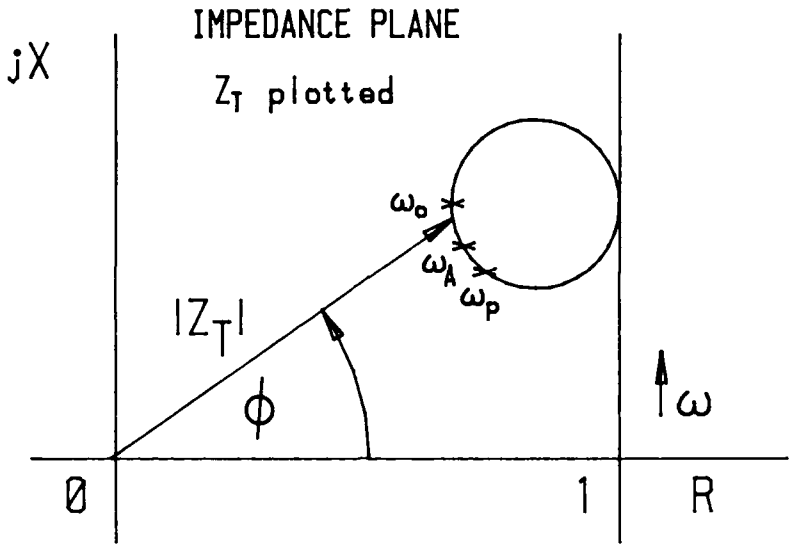

figure 3. Graph of Z_T in the impedance plane, showing the locations of ω_o, ω_A and ω_p.

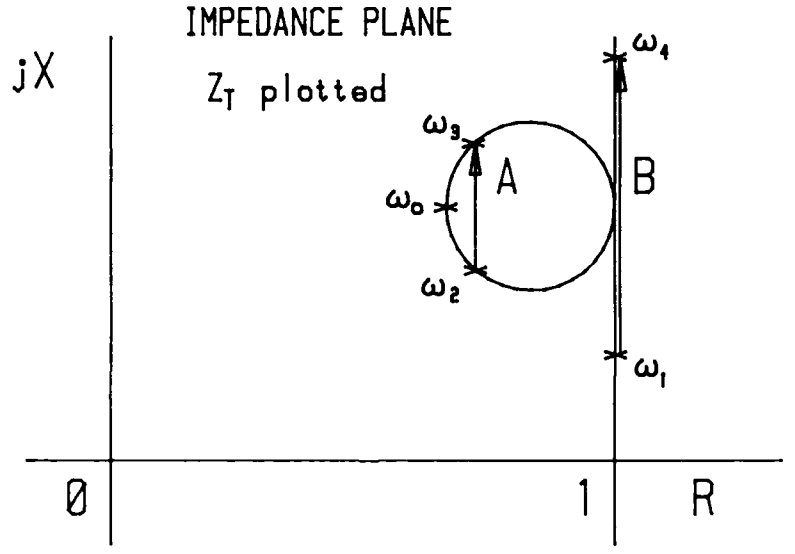

figure 4. Impedance plane diagram describing the impedance detection method.

THE EVOLUTION OF SYNCHRONIZATION IN THE WORLD-WIDE OMEGA NAVIGATION SYSTEM

V. Vannicola and H. McManus
Omega Navigation System Center
Alexandria Va. 22310-3998

Abstract

If the accuracy of the Omega Navigation System were to be limited at all times solely by unpredictable propagation disturbances, the relative timing with which the signals are transmitted must be controlled to an accuracy of less than 0.5 microseconds. Tests of VLF signal transmissions over long distances have established that the timing stability of such signals will exceed one microsecond for at least some period of time. Prior to 1972 the Naval Electronic Laboratory Center (NELC) now the Naval Ocean System Center (NOSC) was the synchronization control center for Omega and made the necessary calculations and adjustments using reciprocal path measurements. However, without external measurements the mean system "walked" from Coordinated Universal Time (UTC). After the U. S. Coast Guard and the Japanese Maritime Safety Agency (JMSA) became responsible for the synchronization of the Omega system a more sophisticated technique was developed. This method still relied on a reciprocal path technique, but also included a statistical filter which tracked each cesium frequency standard at the transmitting stations and computed optimal phase adjustments based on internal path measurements. In 1977 with seven of the eight network stations on-line, external measurement source such as LORAN-C and portable clock measurements tied the Omega system to UTC time. In November 1985 Global Positioning System (GPS) data from Omega station Liberia was used for the first time as an external input to the existing Synchronization software package. By early 1987 GPS monitor receivers were installed at all the Omega Transmitting Stations. In 1988 data from the transmitting stations in the southern hemisphere was used to remove a 2-3 microsecond bias which greatly improved the synchronization throughout the Worldwide Omega Navigation System.

INTRODUCTION

Omega is a very low frequency (VLF 10-14 kHz) radio navigation system with a total of eight worldwide stations (Figure 1) transmitting phase synchronized signals at five frequencies (10.2, 11.05, 11.333, 13.6 and a station specified unique frequency) in a time-multiplexed format (Figure 2). The Omega system is designed to provide a worldwide all-weather position fix capability with 2-4 nautical miles accuracy (2dRMS). For the phase contour pattern, whose position is defined to be stationary, the timing signal of the stations must be synchronized. Operationally, the signals of each station are independently timed with cesium frequency standards and synchronization instructions are generated and issued by the Japanese Maritime Safety Agency (JMSA) in Tokyo, with the U. S. Coast Guard Omega Navigational System Center (ONSCEN) acting as the back up.

In the early to mid 1960's Omega entered the development stage, with four transmitters located in Norway, Trinidad, Hawaii and New York. Of these four original stations, Norway and Hawaii remain

today as full power operational stations. Australia was brought on-line in 1982 to complete the eight station worldwide network. In an effort to minimize synchronization errors Loran-C timing data was introduced in the northern hemisphere stations in 1976. In 1988 GPS data from the transmitting stations in the southern hemisphere was used to remove a 2-3 microsecond bias which synchronized all Omega stations well within 0.5 microseconds relative to UTC traceable to the U. S. Naval Observatory (Figure 3). Synchronization is maintained by having each of the eight station report to JMSA and ONSCEN, the computing centers, signal phases of 10.2 and 13.6kHz of all other stations within range with respect to its own signal along with timing information from LORAN-C and GPS. The computing centers determine the deviation of each signal phase from the system mean and using this external timing information directs the stations to adjust their timing rates to minimize deviations as illustrated in Figure 4.

HISTORICAL DEVELOPMENT

Master-Slave Mode

At inception, and for many years thereafter, the developmental Omega system was operated in a master slave mode in which transmitters were designated as master or slave. The master transmitter was driven by a frequency standard of moderate stability (1 part in 1010). Master transmissions were monitored near the remote slave transmitter (10-30 km), which broadcasted on a subsequent transmission segment in phase coherence with the received master signal. Slave transmitters, therefore, approximated in-phase reflectors. This method of synchronization is traditional with many navigational systems, having originated with LORAN A and DECCA. Compared to "absolute" synchronization, slaving has the advantage of not requiring costly precision frequency standards and the disadvantage of requiring different specifications of the master-slave relationship in system design. Also, navigators may not alter the established master-slave relationship and must use the prescribed lines-of-positions (LOPs).

Absolute Mode

The idea that Omega transmitters be operated from precision frequency standards originated with a suggestion by J. A. Pierce of Cruft Laboratory, Harvard University in 1960. The possibility of Omega becoming a global system with redundant information available would allow the navigator to select transmitters in any convenient manner so as to obtain usable signals and geometry. Absolute synchronization provides this particular advantage, as well as the following:

a. Improved accuracy from reduction of the number of active propagation paths from three to two for a single LOP.

b. Improved reliability.

c. Simplified use of the system for time and frequency dissemination, as all transmitters are an equivalent source of precise time.

These considerations and the concurrent advancement of the state of the art of cesium frequency standards rendered absolute operation both desirable and practical. Initial exploratory attempts at absolute synchronization were not made until 1965. At that time, no cesium standards had been installed and quartz oscillators were still in use at the four R & D Omega stations. The original experiments involved Canal Zone and Hawaii using an intermittent transmission schedule of approximately 12 hours per day. This procedure required that data for Hawaii observed in the Canal Zone

and for Canal Zone data observed in Hawaii be transmitted to San Diego where timing/phase control information was derived. This interrupted schedule, together with a lack of redundancy in timing equipment rendered many phase/timing jumps which probably occurred during off air periods or as a result of timer power loss. Because of the poor stability of the existing standards, prompt transmission and utilization of data and control information were necessary. In practice, communications delays were substantial and technical operation was not completely successful, even though useful navigation signals were transmitted. This early operation illustrated the need for redundant precision frequency standards and emphasized the importance of communications in a reciprocal path control procedure. In early 1966 cesium standards were installed at Norway, Hawaii, New York and Trinidad (moved from Canal Zone) along with updated timing equipment. This began modern Omega in the absolute mode of operation.

Cesium Standards

The synchronization method chosen for this R & D system implementation was developed by J. A. Pierce in late 1965. This procedure was initiated in late February of 1966 with three stations and was extended to include Norway in April. Each station would measure the phase difference (10.2 and 13.6 kHz) with the other stations and then compute and make appropriate adjustments using Predicted Propagation Corrections (PPC's), weights and references. Each station would then adjust based on measurements of the other stations and all stations would therefore be adjusting on each other. During this period the original four R & D stations were transmitting and using this self-adjusting procedure in which each station made discrete daily phase changes to remove one third of the calculated errors observed on reciprocal data. By mid May a ten microseconds epoch error had developed (measured by portable cesium clock) at Norway and that station was removed from general adjustment procedure and placed under direct control of Omega New York which was able to track their signals. This modified procedure proved satisfactory for the summer of 1966. However, the mean system "walked" and administrative difficulty ensued. The administrative troubles together with degraded performance led to a change from the Pierce procedure to one involving an active control site which determined all synchronization adjustments. The new procedure necessitated a central control site which was located at the Navy Electronics Laboratory Center (NELC) now Naval Ocean System Center (NOSC) in San Diego. This method relied on the reciprocal path technique to detect synchronization disparities, but also included a statistical filter which tracked each cesium oscillator and computed optimum phase adjustments based on internal path measurements.

The four stations would send their observations on 10.2 and 13.6 kHz by message weekly to the control center where they would determine the daily phase adjustments to be applied to each station. In addition to the phase data, phase shifter positions were also sent, which enabled the control center to keep a history file of the back-up cesium frequency offsets. If the on-line cesium failed, the back-up system would be available with it's own historical offset, and continuity would be maintained.

EXTERNAL MEASUREMENTS

LORAN-C

External measurements are valuable in reducing synchronization errors resulting from biases in PPC's. Over the past 18 years Omega synchronization methods went through three major phases. In the 1970-1976 time frame "internal" synchronization via reciprocal Omega signal measurements was used. This method synchronized the stations to within 3-5 microseconds of each other. However, since this method did not tie the system to UTC or any other external timing source the system "walked." At

one point the system was out by 29 microseconds with respect to U. S. Naval Observatory (USNO) Master Clock. This was promptly removed in the fall of 1975 before the new stations in Argentina, La Reunion and Liberia became operational. In an effort to reduce the timing errors and tie the system to UTC, Loran–C timing equipment was installed at four stations (Norway, Hawaii, North Dakota and Japan) during the period of 1976–79. After proper calibration of the timing paths this data was introduced to the synchronization process. In October 1977 the Japan Maritime Safety Agency was given the primary responsibility for synchronization execution and the dissemination of synchronization and frequency corrections to the stations. The Omega Navigation System Center maintains a back–up synchronization capability. With the implementation of Loran–C as an external timing source in the northern hemisphere, the system was steered to UTC within 2–3 microseconds although the individual stations in the northern hemisphere were held within one microsecond of UTC. This method was a big improvement to synchronization and the system time became traceable to the U. S. Naval Observatory as illustrated in Figure 5.

Global Positioning System (GPS)

With the advent of GPS, a real–time, accurate, external timing system became available for all Omega stations in the southern hemisphere plus Liberia. Initially the test bed with the prototype GPS receiver was introduced at North Dakota and compared with existing Loran–C timing. Figure 6 is a comparison plot of the two systems for a typical month. The timing of Omega station Liberia was always suspicious as reported by various portable clock trips. A GPS timing receiver was introduced to the timing configuration of Liberia in early 1985 which confirmed earlier reports of a constant bias of about three microseconds. In November of that year, GPS data was used for the first time as an external timing source in the synchronization process which removed a long standing bias as shown in Figure 7. The GPS receivers were placed in an automatic mode of operation which selected the best geometrically suited satellite. One observation was made per day and every Monday the data was sent to the synchronization control center. By mid 1987 all Omega stations were configured with GPS timing receivers. As the confidence level grew with the GPS equipment and data the southern hemisphere stations were moved on–line one at a time.

Argentina was the first to be brought on–line in January 1988. The resulting effect it made on the synchronization process is shown in Figure 8. This was followed by Australia (Figure 9) in March and La Reunion (Figure 10) in May bringing all the southern hemisphere stations into the synchronization process with external sources. Figure 3 shows that having GPS timing available in the southern hemisphere has increased the Omega system synchronization accuracy well within 0.5 microseconds with minimum weekly corrections applied and tied to UTC which is traceable to the U. S. Naval Observatory.

The ability to synchronize the individual Omega stations to within 0.5 microseconds and ultimately the system has been achieved as envisioned by the originators. The present policy is that GPS timing data is not a substitute for the current synchronization program but rather serves as a highly weighted external input to the current program. A study is now being made to determine how we can more effectively use this highly accurate resource and at the same time continue to use current reciprocal Omega VLF measurements. Dependence on GPS solely can lead to the problem encountered in September 1988 when the Department of Defense (DOD) decided to change the satellite message format which disabled many GPS receivers.

According to the 1986 version of the U. S. Federal Radionavigation Plan (FRP) there are about 21000 known Omega users of which less than 10% are DOD users. The current thinking is that Omega will be available at least 15 years after GPS becomes fully operational. In this paper we have tried to make the Timing community aware of a very cost–effective system like Omega that can be used as

a worldwide timing system. By employing special techniques one should be able to recover epoch to better than one microsecond traceable to UTC (USNO) and frequency accuracy on the order of a few parts in 10^{12}. Omega transmissions offer the following:

- Advantages:
  1. Continuous operation 24 hours per day.
  2. High reliability of the stations and repeatability of propagation.
  3. Eight stations providing worldwide coverage.
  4. Extreme range providing redundancy, if one station is off air for maintenance.
  5. Transmissions controlled by atomic standards.
  6. Time is traceable to UTC (USNO).
  7. Reception is relatively simple and inexpensive.
- Disadvantages:
  1. Occasional propagation disturbances such as Sudden Ionospheric Disturbances (SID's).
  2. Propagation complexities which can result in modal or long-path interference.
  3. Repeated measurements at various frequencies or other time disseminated methods required to initially set or periodically verify coarse epoch.

REFERENCES

1) Swanson, E. R., Kugel, C. P., "VLF Timing: Conventional and Modern Technique including Omega," IEEE, Vol. 60, No. 5, pp. 540–551, May 1972.

2) Swanson, E. R., Kugel, C. P., "Naval Electronic Laboratory Center Omega Synchronization and Control." R & D, 19 March 1971.

OMEGA SYSTEM TRANSMITTING STATION LOCATIONS

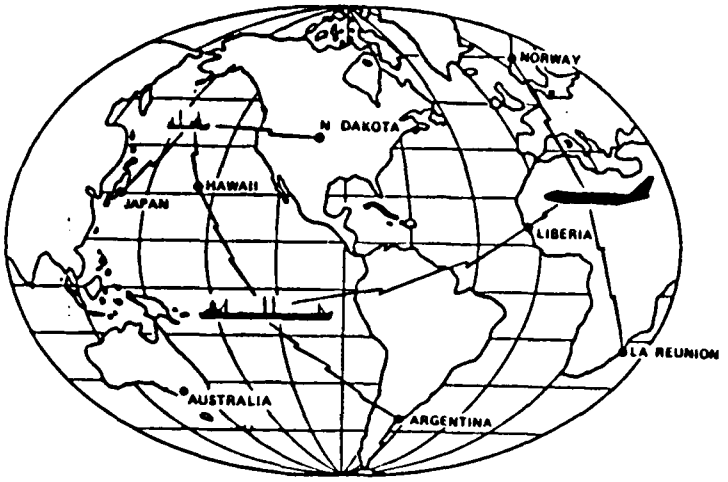

- EIGHT TRANSMITTING STATIONS (EACH AT 10 KW)
- SIGNALS RADIATED ON A TIME-SHARE BASIS WITH A REPETITION PERIOD OF 10 SECONDS
- FIVE SIGNAL FREQUENCIES – 10.2, 11.05, 11.33, 13.6, kHz PLUS A UNIQUE FREQUENCY FOR EACH STATION
- ALL WEATHER GLOBAL SIGNAL COVERAGE
- POSITION FIX ACCURACY 2 TO 4 nm (2drms)
- *TIMING 0.5–1.0 MICROSECONDS* TRACEABLE TO USNO (MC)

EIGHT WORLDWIDE STATIONS PROVIDING ALL WEATHER VLF RADIO NAVIGATION AND TIMING

FIGURE 1

OMEGA SIGNAL TRANSMISSION FORMAT

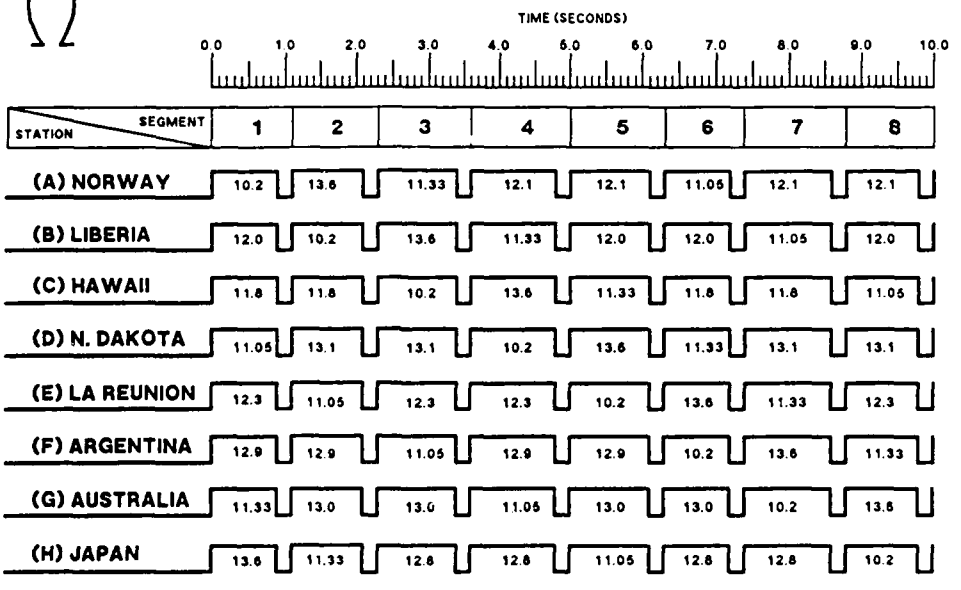

FIGURE 2

OMEGA NAV SYSTEM

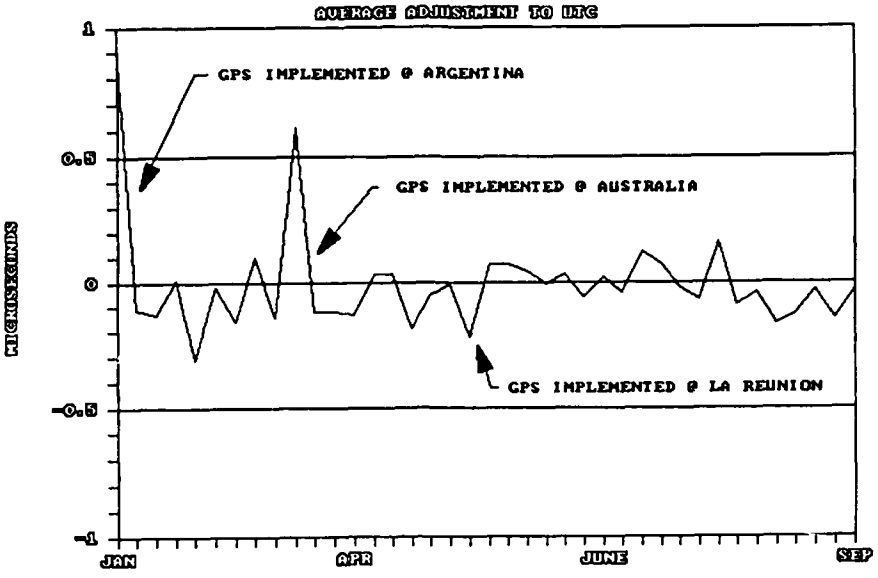

1988
SYSTEM ADJUSTMENT

FIGURE 3

OMEGA SYNCHRONIZATION PROCESS

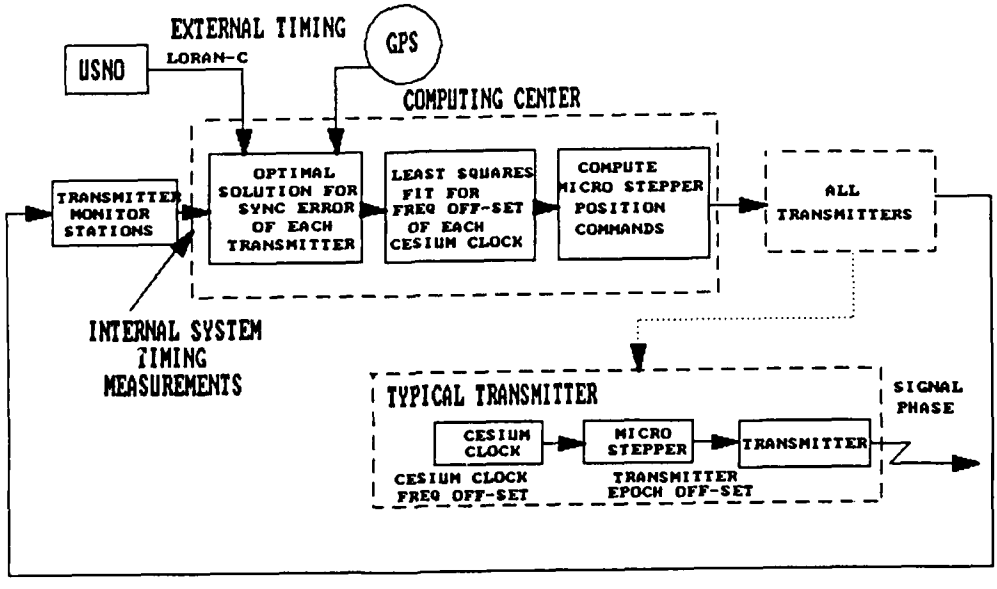

FIGURE 4

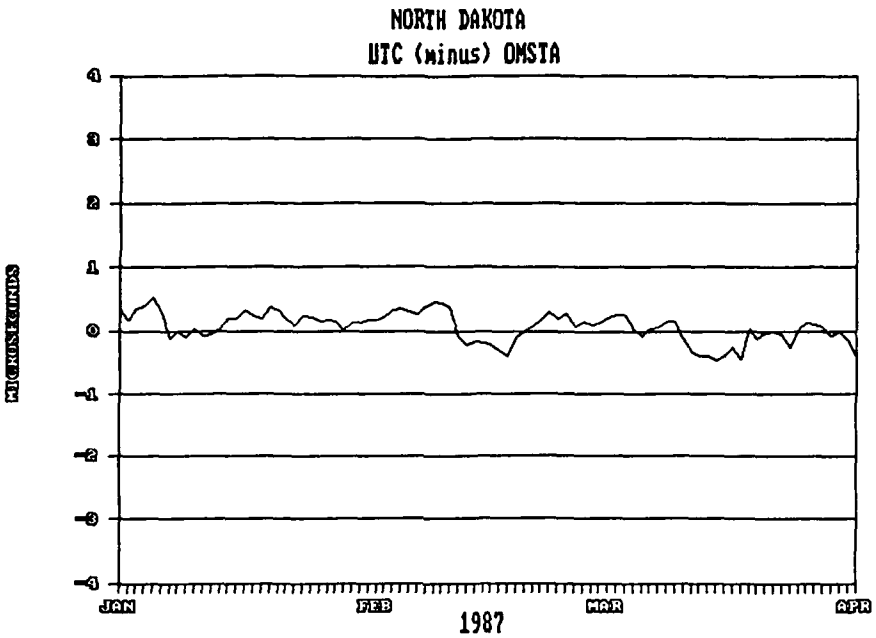

FIGURE 5

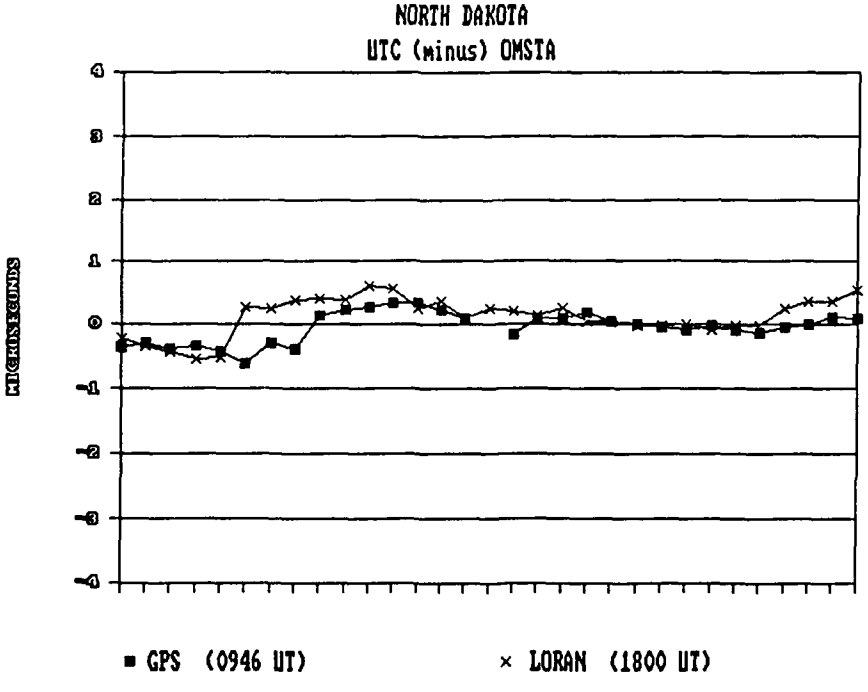

FIGURE 6

LIBERIA

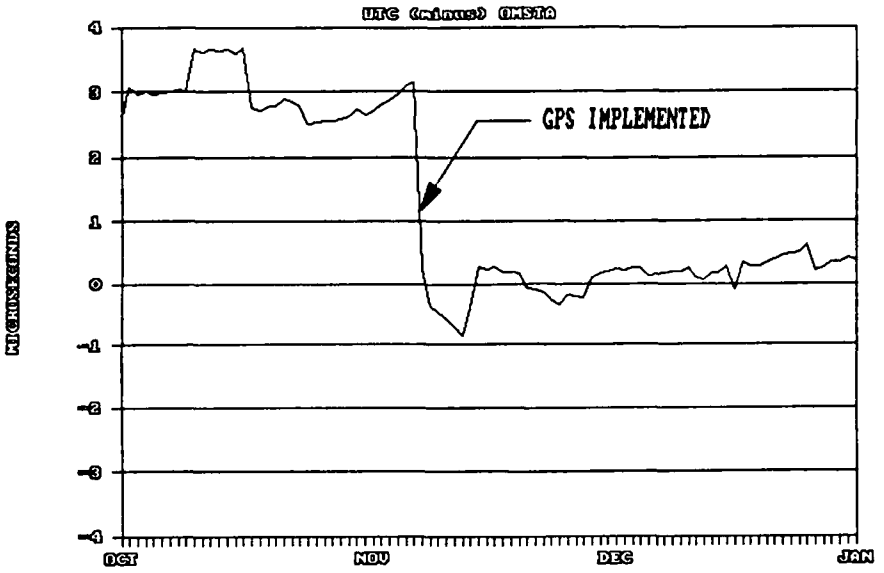

1985

GPS

FIGURE 7

ARGENTINA

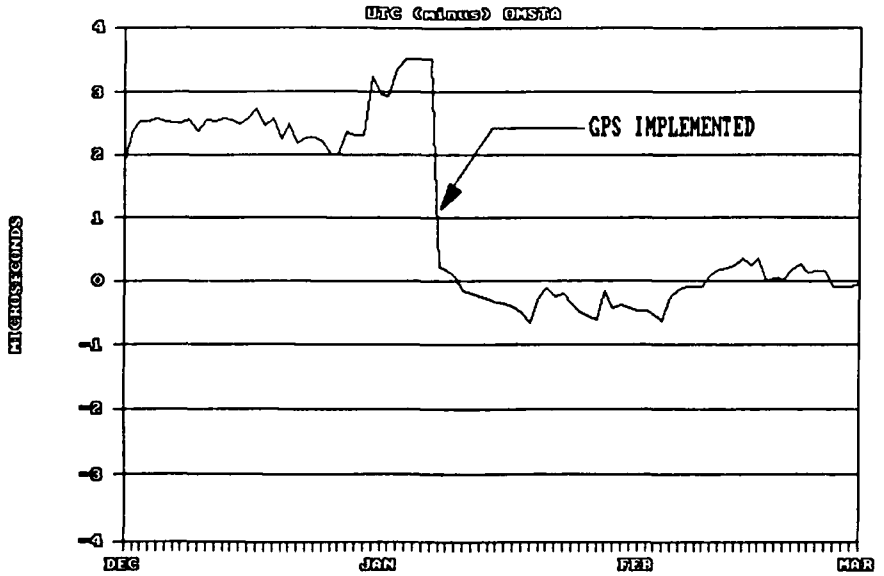

1987/88

GPS

FIGURE 8

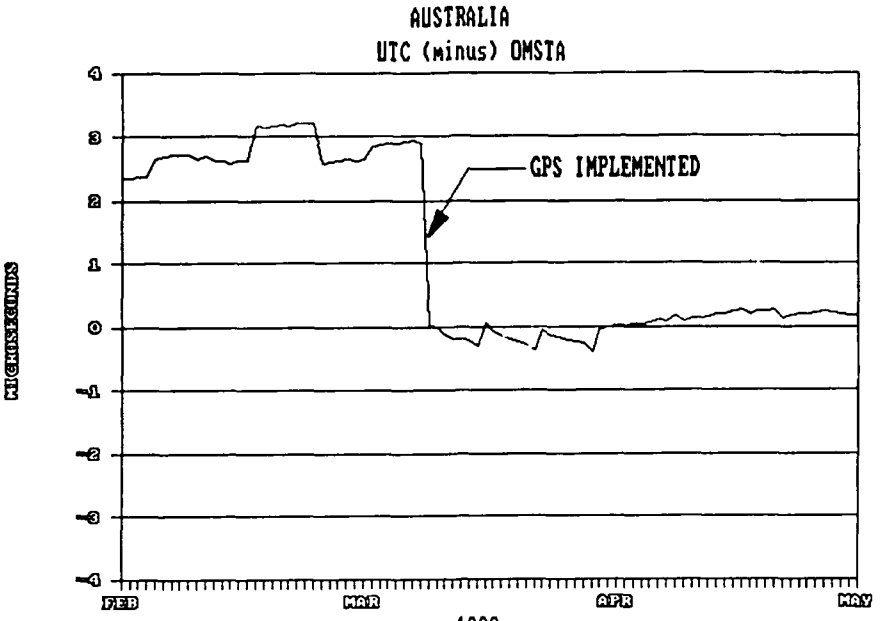

1988

GPS

FIGURE 9

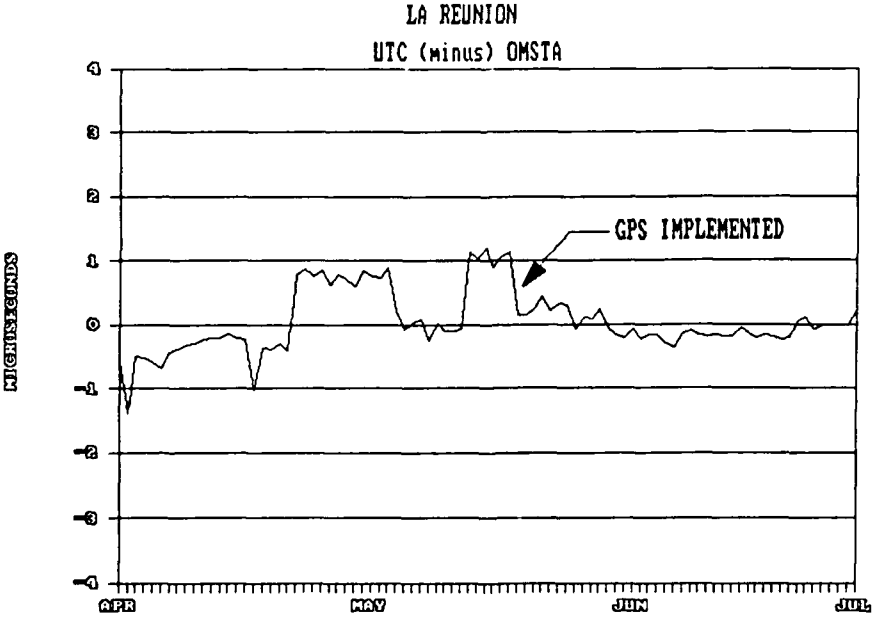

1988

GPS

FIGURE 10

QUESTIONS AND ANSWERS

DR. GERARD LAPACHELLE, UNIVERSITY OF CALGARY: Could you summarize for us the improvement in accuracy for Omega due to GPS timing. Both for the absolute mode and also confirm or not confirm as to whether a gain in accuracy is obtained when operating in a differential mode.

MR. VANNICOLA: The accuracy is proven by the plots. We can maintain the stations to well within a half microsecond of UTC. Right now we are going through a process of improving our PPC's (Propagation Prediction Correction) for the diurnal change which are hard to predict because about 50% of them are going through some sort of diurnal change all the time. We are going to try to make available to the public better PPC's.

DR. LAPACHELLE: Did the two-dimensional accuracy improve for the typical ship-borne or air-borne user due to the improvement in GPS timing?

MR. VANNICOLA: I don't think that you would have noticed that. The errors in navigation are mostly propagation. Timing has improved, but not navigation. I will say this-we are not going to GPS as an external timing system solely. This was proven in September, when GPS decided that they were going to change the format. Our receivers were not able to receive the timing signals. We plan to correct the PPC's on a baseline, then pull out the external input and see how close we maintain it.

MEASUREMENTS OF THE PROPAGATION TIME OF LORAN-C SIGNALS

Tadayoshi Hara, Koji Horiai, Katsuhisa Sato,
Mitsumi Fujishita, Satoshi Sakai, Kenzaburo Iwadate
and Kazuyoshi Asari
Division of Earth Rotation
Mizusawa Astrogeodynamics Observatory
National Astronomical Observatory
2-12 Hoshigaoka, Mizusawa, Iwate, 023 Japan

Abstract

LORAN-C signals of Iwo Jima (9970-M) and Hokkaido (9970-X) of the Northwest Pacific chain were received at 21 locations in northern Japan to estimate the accuracy of time comparison by the LORAN-C method. The distance between transmitting sites and receiving sites ranges from 24 km (9970-X to Onbetsu, Hokkaido) to 1777 km (9970-M to Ajigasawa, Aomori). The Navy Navigation Satellite System was used to determine the antenna location to an accuracy of ±10 m, which is necessary to estimate the propagation time. The secondary phase is calculated by the Millington-Pressey method using Brunavs's approximate formula for secondary phase computation and an effective conductivity map. The phase delay shows a general tendency of +0.65 microseconds per 100 km with resect to a wave moving at vacuum velocity. The range of deviation is ±0.5 microseconds. The observed phase shows the additional delay of about 0.35 microseconds per 100 km. With this correction applied, the observed phase deviates usually in the range of ±0.5 microseconds. However, sometimes the observed phase shows deviations as much as ±1.5 microseconds, which seem to be due to the terrain effect.

INTRODUCTION

The LORAN-C signals reveal a very high precision potential in time comparison as stable as ±0.1 microseconds or better in the region where the ground wave is utilized. The LORAN-C method, however, sometimes shows pretty large offsets in time epoch comparison compared with other, for example portable clock, methods. The main purpose of this paper is to estimate the accuracy of time comparison via the LORAN-C method. Discussions are confined to the ground wave. There are some problems which are concerned with time comparison, such as the identification of the reference tracking point, system delay calibration, and propagation delay estimation. the accuracy of the system delay calibration is around ±0.2 microseconds, which includes the effect of delay variations according to the setting of the center frequency of the notch filters for the Decca signals (Horiai, et al. 1983). The propagation delay over sea water can be estimated pretty accurately. The one over land is pretty erroneous and limits the time comparison accuracy. So, the discussion will be made mainly on the accuracy of estimation of the propagation time of the ground wave over land. We would like also to estimate the effect of terrain on ground wave propagation by experiments, because the effect seems to

be strongly associated with the accuracy of time comparison. The terrain effect is considered to be dependent on the topography of the site and experimental examination is indispensable.

OUTLINE OF THE HARDWARE

The received signals are Iwo Jima (9970–M) and Hokkaido (9970–X) of the Northwest Pacific chain. The receiving sites are 21 points in northwest Japan as shown in Fig. 1. Distances of the propagation paths over sea, land and mixed range from 24 to 1777 km. Two sets of LORAN receivers, Austron model 2000C and Aerospace Research Inc. model LFT–504 were used at the mobile sites and fixed site, Mizusawa, respectively, to compare the phase of the received signals. The time differences between 9970–M/X and UTC(ILOM) were monitored regularly at the fixed site. Loop antennas were used with both receivers and were set to point to the transmitting sites.

A Hewlett–Packard cesium beam clock model 5061A was used as a portable clock (PC) with the aid of a portable power supply.

The Navy Navigation Satellite System receiver, Magnavox model MX–1502, was used to determine the location of the mobile sites. The formal error of the estimated three dimensional coordinates are about ± 10 m after a data accumulation of twenty four hours. Measurements were conducted automatically with the aid of a laptop computer system, Epson model HC–88. Ambient temperature was also recorded, to monitor the rate change of the portable clock due to temperature change. The temperature coefficient of our portable clock was determined in our laboratory as $+1.0 \times 10^{-13}$ per degree before the experiments. We tried to maintain the ambient temperature as stable as ± 5 degrees so that the clock error remains within ± 0.1 microseconds during the experiments. The effects of magnetic field and humidity seemed to be less than ± 0.1 microseconds and they were not monitored throughout our experiments.

OUTLINE OF THE EXPERIMENTS

The experiments were conducted as follows:

Year	Received Signals	Visited Sites
1984	9970–M	Miyatojima, Hanaizumi, Wakuya
1985	9970–M	Katsuura, Tsukuba
	9970–X	Erimo, Kosode, Taro, Tsukuba
1986	9970–M	Kizukuri, Ajigasawa, Odate
		Takanosu, Maebashi, Noshiro, Inubo
	9970–X	Maebashi, Sano, Shibetsu, Hinata
		Onbetsu, Makubetsu, Inubo

Time synchronization between UTC(ILOM) and 9970–X was made using the received value at Onbetsu, Hokkaido where the distance from the transmitting station was 24 km and is considered to be the best to obtain time synchronization accurately, because the error of the time delay estimation seemed to be the smallest.

Time synchronization between 9970–M and 9970–X was confirmed by receiving both signals at Cape Inubo in the Chiba prefecture, where both propagation paths were over sea water.

Phase deviations were derived as follows; 9970–M/X - UTC(ILOM) are regularly monitored at Mizusawa and labeled A; time difference data 9970–M/X - UTC(ILOM) is labeled B; phase deviations

are obtained by subtracting A from B. The data were reduced to the same epoch by interpolation. corrections were made for propagation delay, system delay and emission delay (Horiai, et. al., 1983)

The secondary phase was calculated by the Millington–Plessey method using Brunavs's approximate formula for phase delay computation (Samaddar, 1979; Brunavs, 1977) with the aid of the effective conductivity map (CCIR, 1986), where the terrain effect is included. The formula C of Brunavs's paper which has eight variable coefficients was used. Permittivity was set at 81 and 15 for sea and land, respectively. The parameter (alpha) which is connected with the lapse rate of the Earth's atmosphere is taken as 0.75. The method explained here to calculate the secondary phase will be called "our method" hereafter.

RESULTS

Time synchronization was attained between LORAN-C(9970-M/X) and UTC(ILOM) to an accuracy of about ±0.2 microseconds.

Time synchronization was confirmed between 9970–M and X to an accuracy of about ±0.1 microseconds.

The estimated secondary phase delay by our method has a general tendency of +0.65 microseconds per 100 km in northern Japan with a range of deviation of ±0.5 microseconds as shown in Fig. 2. The observed phase deviation becomes larger by this amount if we use the above linear relation instead of the delay calculated by our method.

The observed phase variation shows that additional phase delay of +0.35 microseconds per 100 km is necessary in addition to the secondary phase delay calculated by our method.

The observed phase usually shows a discrepancy in the range of ±0.5 microseconds with exceptions of +1.5 microseconds observed at Erimo, Hokkaido and -1.5 microseconds observed at Noshiro, in the Akita prefecture if the correction of +0.35 microseconds per 100 km is made in addition to the secondary phase delay calculated by our method.

Phase deviations of ±0.2 microseconds and offset of -0.2 microseconds were observed for the propagation path in the distance range from 1200 to 1500 km over sea water. The negative offset Shows that the conductivity of the sea water is smaller than 5 S/m, if the ground conductivity of 0.01 S/m is correct for the propagation path from Hokkaido station to Onbetsu.

DISCUSSION

The additional phase delay of +0.3 microseconds per 100 km seems to be due to the terrain effect and partly due to the low conductivity layer which is just under the Earth's surface.

The large phase delay observed at Erimo is probably due to steep mountains which are just in front of the site.

The large phase advance observed at Noshiro is probably explained by a smaller effect of terrain than expected, because this site is 100 km away from the mountains.

The conductivity map which was used here is for the frequency of 100 MHz. The map for 100 kHz would improve the accuracy of the estimation of the propagation time of the ground wave. The effect of the terrain would, however, be larger than the one which would be improved by using the more precise value for the conductivity. The phase integration method would pursue the terrain effect more effectively.

ACKNOWLEDGEMENT

This research was supported in part by the Japan Society for Promotion of Science "Study of the Earth Rotation with Radio Interferometers". We are pleased to give our thanks to Mr. T. Inoue of the National Research Laboratory of Metrology in Tsukuba and Mr. H. Sugiuchi of the Inubo Branch of the Communication Research Laboratory for their cooperation to conduct this experiment. We are also obliged to Mr. T Drour and D. C. Slagle of the United States Coast Guard for their discussion on the propagation delay. We are indebted to Mr. T. C. Johnston at the Hokkaido station for his warm cooperation with our experiment.

REFERENCES

1) Brunavs, P., 1977, Phase lags of 100 kHz radio frequency ground wave and approximate formulas for computation

2) CCIR, 1986, World atlas of ground conductivities, Document 5/1015-E, XVIth Plenary Assembly, Dubrovnik, p.75

3) Horiai, K., M. Fujishita, T. Hara, M. Aihara, 1938 Clock comparison system at the International Latitude Observatory of Mizusawa, Proc. Int. Latit. Obs. Mizusawa, No. 22, pp 1–9

4) Samaddar, S. N., 1979, The theory of LORAN-C ground wave propagation—A review, Navigation, Vol. 26, No. 3, pp. 173–187

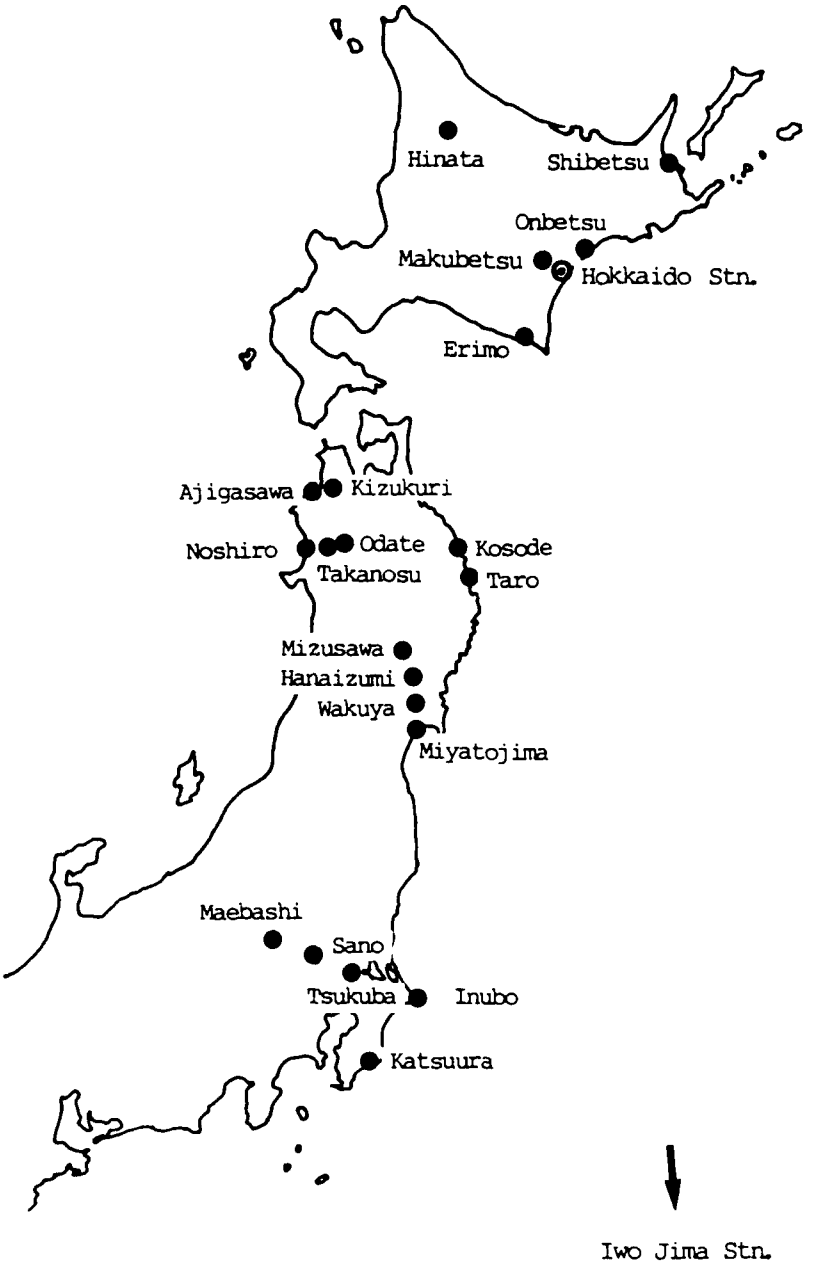

Figure 1. Sites of experiments of Loran-C receptions. The signal from Hokkaido is received through mountainous region at Hinata, Erimo, Mizusawa, Tsukuba, Sano, and Maebashi. Odate, Takanosu, Noshiro, Kizukuri, and Ajigasawa are in the similar situation as above for the signal from Iwo Jima.

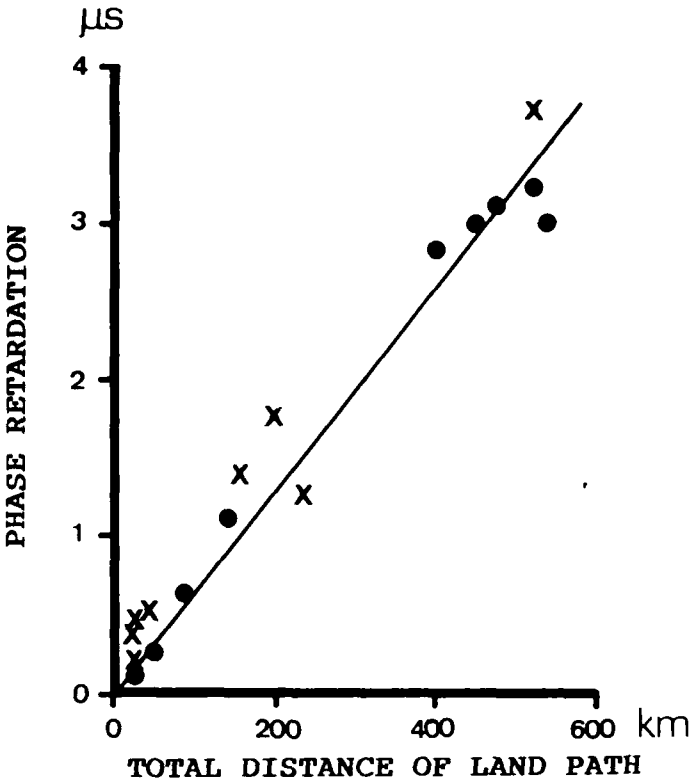

Figure 2. Calculated secondary phase delay shown in units of micro-seconds. The integrated distance of the land path of the propagation of the ground wave is taken for abcissa. The dots are for the received data from Iwo Jima and crosses are Hokkaido. The thin line shows the phase delay of +0.65 micro-seconds per 100km in respect to a wave moving at the vacuum velocity.

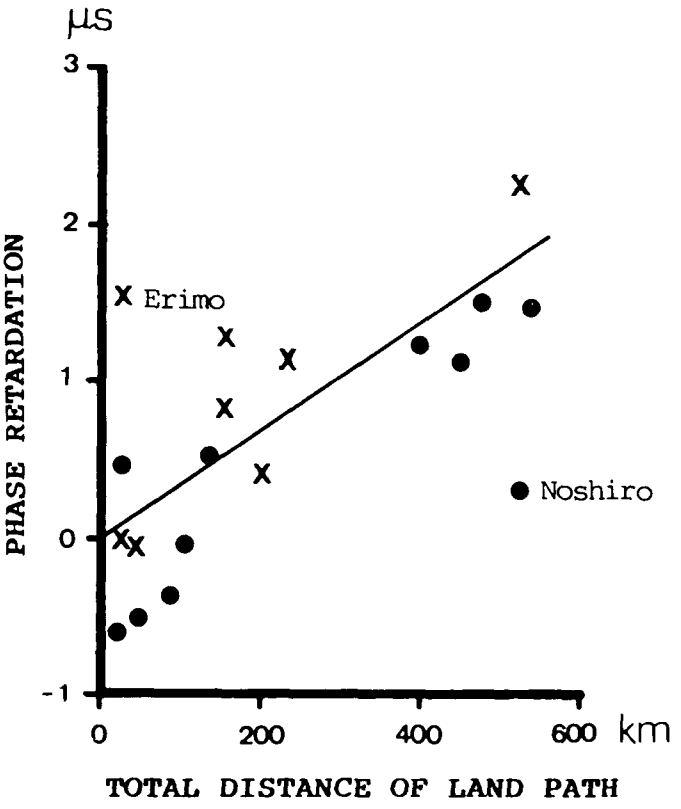

Figure 3. Phase deviations of received signals. The symbols and abscissa have the same meaning as Figure 2. The thin line shows the phase delay of +0.35 micro-seconds per 100km. The received sites are shown only for Erimo and Noshiro because these show very large deviations.

METEOROLOGICAL INFLUENCES ON LORAN-C PROPAGATION OVER SEA AND LAND IN MEDITERRANEAN SEA CHAIN

Zoran M. Marković

Federal Bureau of Measures and Precious Metals
Mike Alasa 14, 11000 Belgrade, Yugoslavia

ABSTRACT

Loran-C phase variations of signal from the Master of the Mediterranean Sea chain at Sellia Marina were measured simultaneously at three receiving sites, located on sea, coast and land. The effect of terrain over which the signal is propagated is considered together with the influence of weather parameters on the phase variations at the transmitter, along the signal paths and at the receiving sites. Based on an analysis of these data, correlations among these variations are examined, and correction is introduced to the measured results, in order to improve precision of mutual and international comparisons via Loran-C.

INTRODUCTION

Eleven collaborating laboratories which contribute data on atomic time - TAI use Mediterranean Sea Loran-C chain for their international comparisons, five of which receive the signals from Master station, 7990-M |1|.

International comparisons of the cesium clock in Federal Bureau of Measures and Precious Metals, UTC(YUZM), for twelve years now, have been carried out via Loran-C, Master at Sellia Marina, and by clock transportation |2|. Variations of phase of a received Loran-C signal in Belgrade have been observed as seasonal, as well as diurnal |3|. These variations have also been studied elsewhere in the world |4| - |7|,but our intention was to study them for our particular propagation path.

An experiment aimed at analysis of Loran-C time of arrival - TOA variations on sea and land was realized in July 1987.

Using three Loran-C receivers, times of arrivals of the signals from the Master of the Mediterranean Sea chain were measured simultaneously on sea, coast and land, in relation to the times of atomic clocks on the island, in Split and in Belgrade, respectively. Together with TOA measurements, temperature of air at receiving antenna sites was also measured. In order to analyze correlations between time of arrival variations and weather parameters, meteorological data were obtained from meteorological stations along the propagation paths.

ANALYSIS OF PHASE VARIATIONS AT DIFFERENT RECEIVING SITES

Geometry of receiving sites during the experiment on sea, coast and land in relation to Master at Sellia Marina is shown in Figure 1, together with geographical configuration of the paths over which Loran-C ground wave signal is propagated. The lay out of meteorological stations located close along the propagation paths, which supplied information on air temperature, humidity and pressure, are also shown in Figure 1.

Elevation profiles for two propagation paths are shown in Figure 2, since the path towards the island coincides for the most part with the path of receiving site located in Split. Elevations of meteorological stations are shown on these profiles, but it should be noted that air pressures measured in them were reduced to sea level for the purpose of calculations and analyses. In order to examine meteorological influences, the paths were divided into segments, presuming that characteristics of propagation medium within each segment were nearly the same from meteorological point of view.

The measurement system used in Belgrade is described in reference [3], and it was almost the same in other two sites. Characteristics of atomic clocks were determined in the beginning and at the end of the experiment by clock transportation, so that the rate of atomic clocks during the experiment was determined and removed from the data. Measurements were carried out every second with resolution of 20 ps. Results of measurement were filtered by means of a recursive discrete filter which approximates a special case of Wiener filter,

$$\hat{x}_i = \frac{1}{\tau + 1} (x_i + \tau \hat{x}_{i-1}) \qquad (1)$$

where τ amounts to 14 400. By filtering data, time of arrival variations were reduced by about 3.5 times.

Figure 3 presents time of arrival variations following filtering for receiving sites on sea, coast and land with phase

variations being larger in signals propagated over land and traversing a mountain range. A correlation between these variations is observed, resulting from phase changes in the transmitter and following propagation through the common part of the medium. Phase variations, which are neither recorded at the same time, nor are they of equal intensity at all the three sites, appear mainly due to changes in the medium in the vicinity of the receiving antenna.

METEOROLOGICAL INFLUENCES ON GROUND WAVE PROPAGATION

Total phase lag ϕ, of propagated ground wave of Loran-C signal can be expressed as [5]

$$\phi = \frac{\omega}{c} n_a \alpha + d_c \qquad (2)$$

where n_a is the surface refractive index, d is the distance between the transmitter and the receiver in meters, ω/c = 3.3355693 ns/m, and ϕ_c is the secondary phase correction, which can be determined approximately from [8]

$$\phi_c \simeq (n_a a\ \omega/c)^{1/3}\ \alpha^{2/3}\ \tau_0\ (d/a) \qquad (3)$$

where a is the radius of the Earth, τ_0 is derived from the boundary condition at the surface of the ground, and α is associated with the slope of the profile of refractive index with altitude. Over average land τ_0 is of the order of 0.89.

Phase of the primary wave depends directly on n. But the phase of the secondary factor depends on n, gradient of n through factor α, and the ground surface impedance which enters into τ_0. Parameter α is a function of surface refractive index and its gradient with respect to altitude Z, or lapse rate, and is given by

$$\alpha = 1 + \frac{a}{n} \frac{dn}{dZ} \qquad (4)$$

Weather parameters, such as temperature, pressure and humidity, influence the behavior of atmospheric refractive index [9] in a complex way, but the following simplified formula relating the refractive index with these various parameters has been found to be useful in practical work in radiometeorological studies,

$$(n - 1)\ 10^6 = N = \frac{77.6}{T} \left(P + \frac{4810e}{T}\right) \qquad (5)$$

where N is refractivity, T is temperature in K, P is atmospheric pressure in mb, and e is partial water vapour pressure in mb. The second term of eqn. (5) contains humidity term e, and it is therefore called the wet term. The first term is known as the dry term.

Comparative analysis of TOA variations and refractivity (N-total) changes for the three receiving sites did not offer a satisfactory correlation. This can be explained by the fact that lapse rate is practically constant in summer, as well as that wet term amounted to 20 % of the refractivity (N-total) all the time in the area observed by the experiment.

A significant (negative) correlation between TOA variations and the changes of dry term of refractivity is shown in references |5| and |6|. Variations of TOA at different receiving sites with integrated dry term, $\bar{N}$-dry, data for each particular path,are plotted in Figure 4. Integrated dry term,$\bar{N}$-dry,data were obtained as a weighted mean of N-dry from all segments of a particular path according to length of the segments, as they are shown in Figure 2. High degree of (negative) correlation is obvious for all the three receiving sites, i.e. on sea, coast and land.

However, it is not always possible to obtain meteorological data for calculation of integrated dry term from a large number of meteorological stations along propagation path, especially not with the frequency which would be necessary. In Europe, signal path frequently crosses over several states, making this problem even more serious. In a situation where only dry term is important, as shown in references |5| and |7|, secondary phase factor increases (decreases) with the increase (decrease) of the values of α. This implies that when temperature increases (decreases), both α and TOA (time of arrival) increase (decrease), which may be interpreted as high positive correlation between temperature and TOA variations.

Instead of further examination of the correlation between TOA variations and the changes of integrated air temperature which could be obtained as the weighted mean from temperatures associated with corresponding segments along the path, it was decided to examine the correlation between TOA variations and air temperature changes at the receiving site. Figure 5 presents TOA variations together with air temperature changes at the receiving site for the three receiving sites on sea, coast and land. The figure clearly shows high degree of correlation between the presented temperature changes and the time of arrival variations for different receiving sites.

A common presentation of air temperature and corresponding time of arrival for the receiving sites on sea, coast and land is given in Figure 6. Each datum is a couple of measured values at the moment results were recorded. The straight line which is the best approximation of the dependence between time of arrival variations and air temperature changes has been

determined by the method of linear least square fit, and it is presented in this Figure. Time of arrival variation of Loran-C signal, due to air temperature change (coefficient equal to the slope of the straight line), amounted to A_1 = 3.3 ns/°C for the receiving site on sea, A_2 = 3.1 ns/°C for the receiving site on coast, and A_3 = 3.1 ns/°C for the receiving site on land. In June 1986 the coefficient was A = 2.8 ns/°C for the same receiving site on land, in Belgrade. During the winter this coefficient can be as high as A = 78 ns/°C, as it was in November 1985 for the receiving site in Belgrade |10|.

Time of arrival values t (ns), presented in Figure 3, obtained after filetring, were corrected by application of linear dependence shown in Figure 6, by means of the following equation

$$t_k = t - AT \qquad (6)$$

where t_k is corrected time of arrival in ns, A is the coefficient (slope of straight lines from Fig. 6) in ns/°C, and T is air temperature in °C.

Figure 7 shows Loran-C time of arrival variations after correction for the value of corresponding air temperature has been introduced, for the receiving sites on sea, coast and land. After correction, the effective value of variations was reduced by about 2 times for all three receiving sites. Even after correction, phase variations are larger in signals propagated over land than in those propagated over sea. Time of arrival variation after correction was in Split 4.9 ns (1σ), and in Belgrade 6.0 ns (1σ), meaning that after correction uncertainty in comparison between Belgrade and Split was 7.7 ns (1σ). Minimum time of arrival variations were during the day, between 11 a.m. and 3 p.m., when total variations of the corrected phase was around 10 ns. The possibility of comparison of atomic clocks in Belgrade and Split by Loran-C is actually the difference of times of arrival of these two cities. Total variation of the difference of corrected times of arrival is below 50 ns.

CONCLUSION

Loran-C phase variations of signal from the Master of the Meditarranean Sea chain measured at receiving sites on sea, coast and land are significantly correlated with integrated dry term of refractivity as well as with air temperature at the receiving site. By presenting time of arrival as a linear function of air temperature, applying the linear least square fit method, it is possible to introduce a correction on measured results,

which enables reduction of time of arrival variations by factor 2 for all three receiving sites. It is shown that even a simple correction based on a single influence quantity, considerably improves precision of mutual and international comparisons via Loran-C.

ACKNOWLEDGEMENT

The author wishes to acknowledge Prof.Dr. Dragan Stanković and Mr. Vlado Mamula for their contributions in collecting and analysis of the data.

REFERENCES

1. BIPM, BIH Annual Report for 1987.

2. Z.M. Marković and S. Hajduković, "The time and frequency comparisons via Loran-C and National TV network in Yugoslavia", in Proc. 16th Annual PTTI Meeting, pp. 419-426, November 1984.

3. Z.M. Marković, "Long-term stability of Yugoslav primary time and frequency standard", Master´s thesis, University of Belgrade, 1986.

4. G.M.R. Winkler, "Path delay, its variations, and some implications for the field use of precise frequency standards", Proc. IEEE, Vol. 60, No. 5, pp. 522-529, May 1972.

5. R.H. Doherty and J.R. Johler, "Meteorological influences on Loran-C ground wave propagation", J. Atmospheric and Terrestrial Physics, Vol. 37, pp. 1117-1124, 1975.

6. W.N. Dean, "Diurnal variations in Loran-C groundwave propagation", in Proc. 9th Annual PTTI Meeting, pp. 297-316, March 1978.

7. S.N. Samaddar, "Weather effect on Loran-C propagation", Navigation: J. Inst. of Navigation, Vo. 27, No.1, pp. 39-53, 1980.

8. J.R. Johler, W.J. Kellar, and L.C. Walters, "Phase of the low radiofrequency ground wave", NBS Circular 573, June 1956.

9. B.R. Bean and E.S. Dutton, "Radio Meteorology", NBS Monograph 92, March 1966.

10. Z.M. Marković, "Air temperature Loran-C time of arrival correlationsrelationships", in press.


EUROPE
Scale 1:30 million
0
500 km
Arctic Circle
Norwegian Sea
North Sea
Faeroes
Shetland Islands
Orkney Islands
Hebrides
Ben Nevis
Great Britain
Ireland
Dublin
London
English Channel
Brittany
Bay of Biscay
Paris
Loire
Massif Central
Alps
Rhine
München
Amsterdam
Bruxelles
Jutland
København
Oslo
Stockholm
Kebnekaise
Lofoten Is.
Nordkapp
Murmansk
Kola Peninsula
White Sea
Baltic Sea
G. of Finland
Helsinki
Leningrad
Ladoga
Onega
Valdai Hills
Moskva
Volga
Central Russian Uplands
Don
Kharkov
Kiyev
Dnepr
Ukraine
Sea of Azov
Crimea
Black Sea
Bosporus
Istanbul
Berlin
Elbe
Oder
Praha
Warszawa
Vistula
Wien
Budapest
Danube
Carpathians
Beograd
Sofija
Balkan Mts
Athinai
Aegean Sea
Crete
Cyprus
Adriatic Sea
Roma
Vesuvius
2912
1277
Etna
3340
Sicily
Corsica
Sardinia
Balearic Is.
Algiers
Madrid
3478
3404
Str. of Gibraltar
Gibraltar
Mediterranean Sea
Caspian Sea
Caspian Depression
Astrakhan
Volga
Urals
Mesopotamia
Euphrates
Tigris
Baghdad
Kurdistan
A
B
C
D
E
F
G
H
I
1
2
3
4
L
M
X
10°
20°
30°
40°
50°
60°
70°

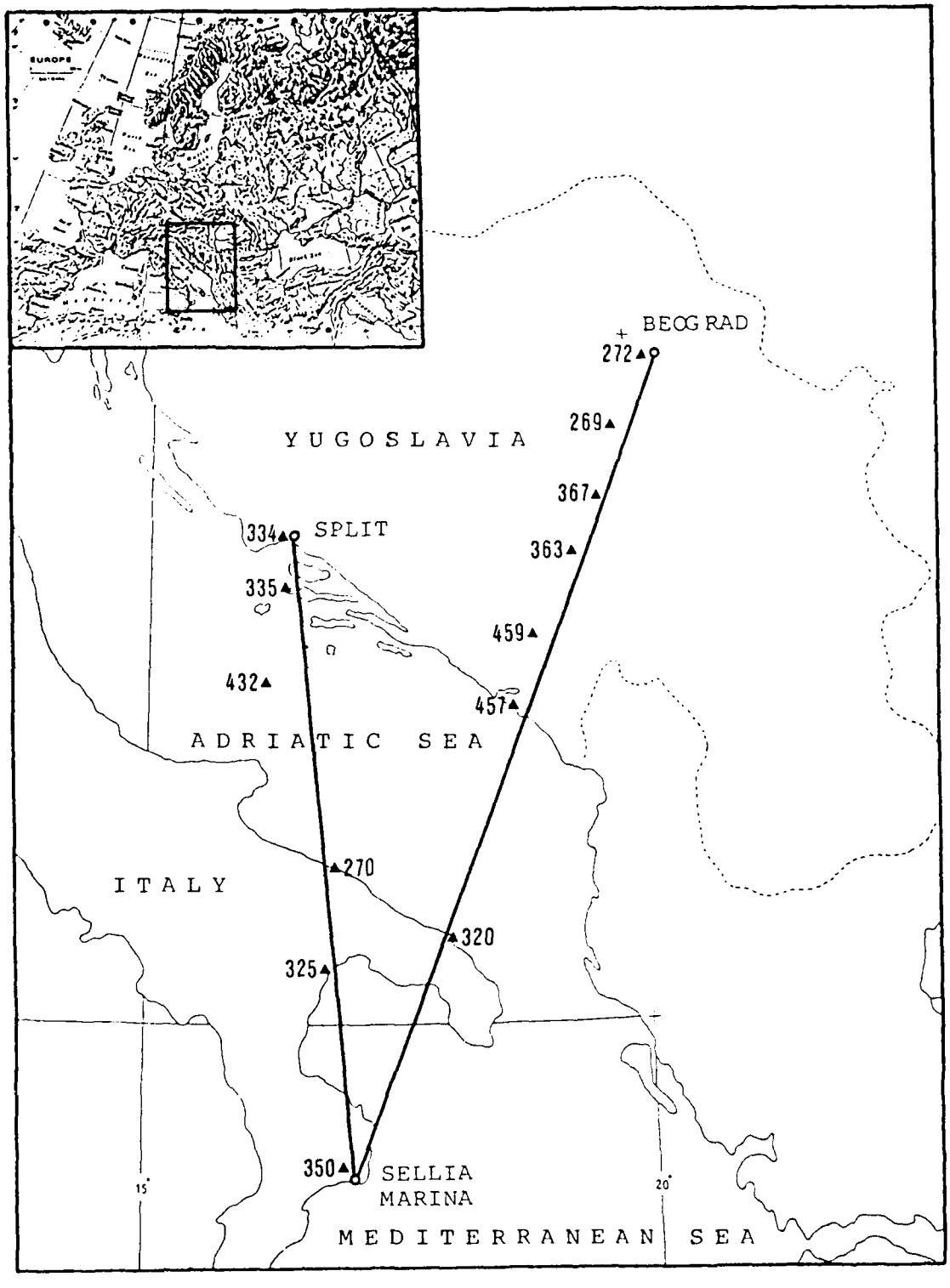

Figure 1. Geometry of receiving sites in relation to Master at Sellia Marina and meteorological stations designated by codes

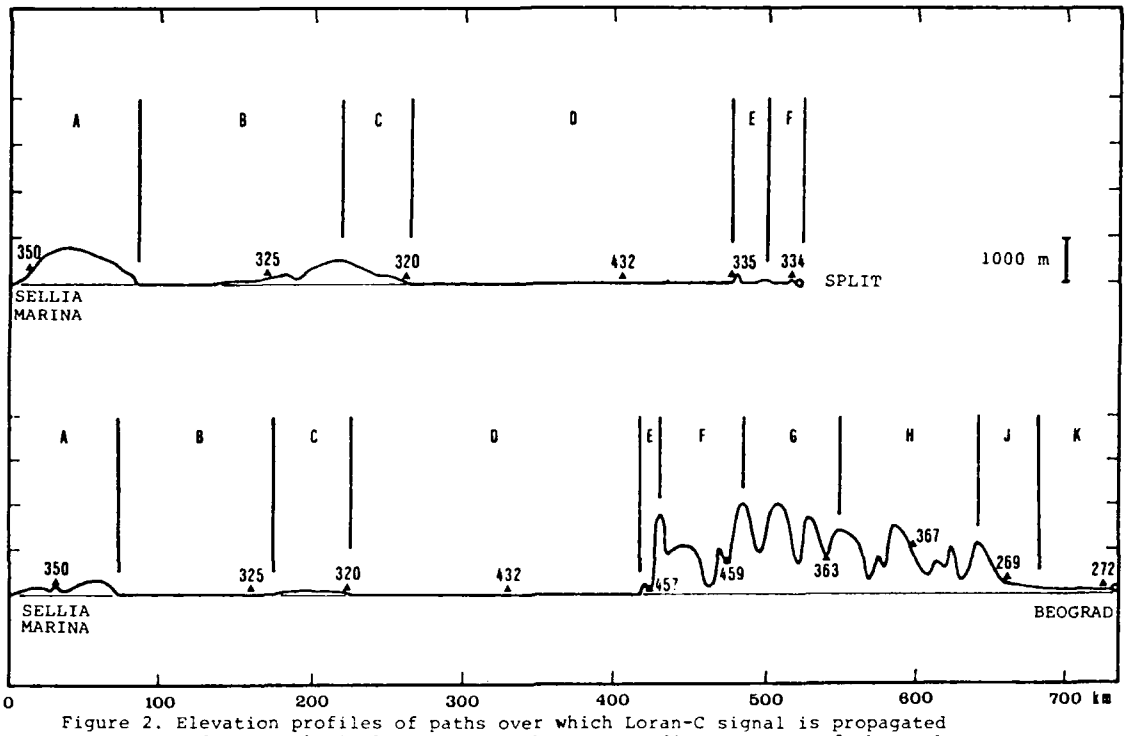

Figure 2. Elevation profiles of paths over which Loran-C signal is propagated and meteorological stations with corresponding segments of the paths

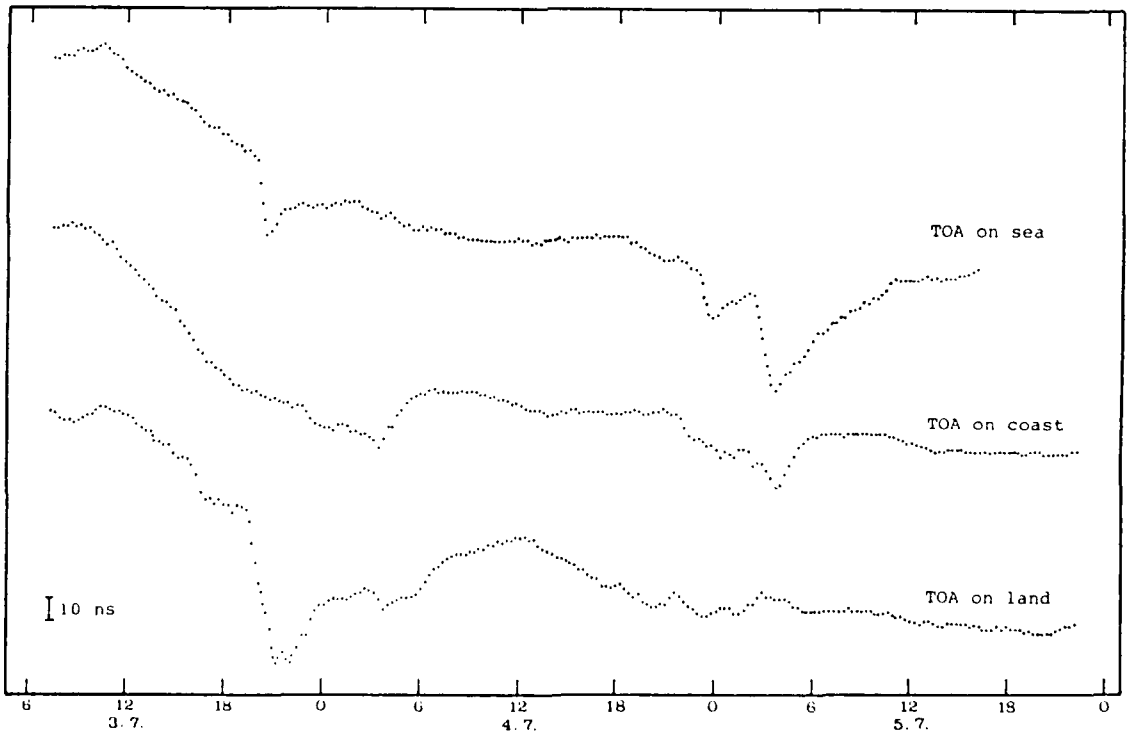

Figure 3. Loran-C time of arrival variations at different receiving sites

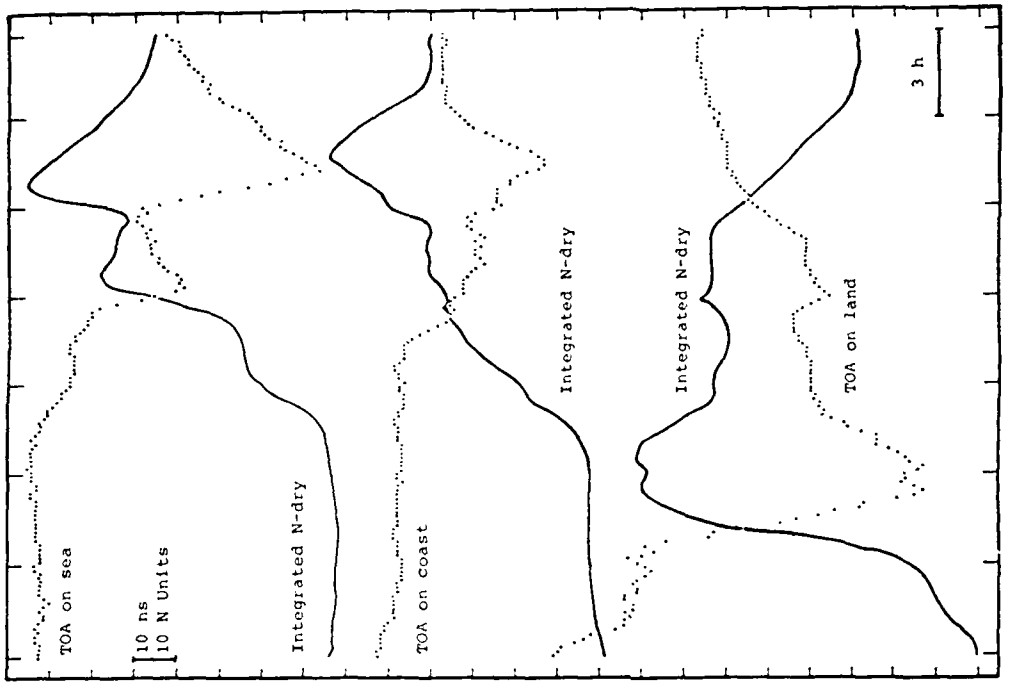

Figure 4. Loran-C time of arrival variations at different receiving sites with integrated N-dry changes along the corresponding paths

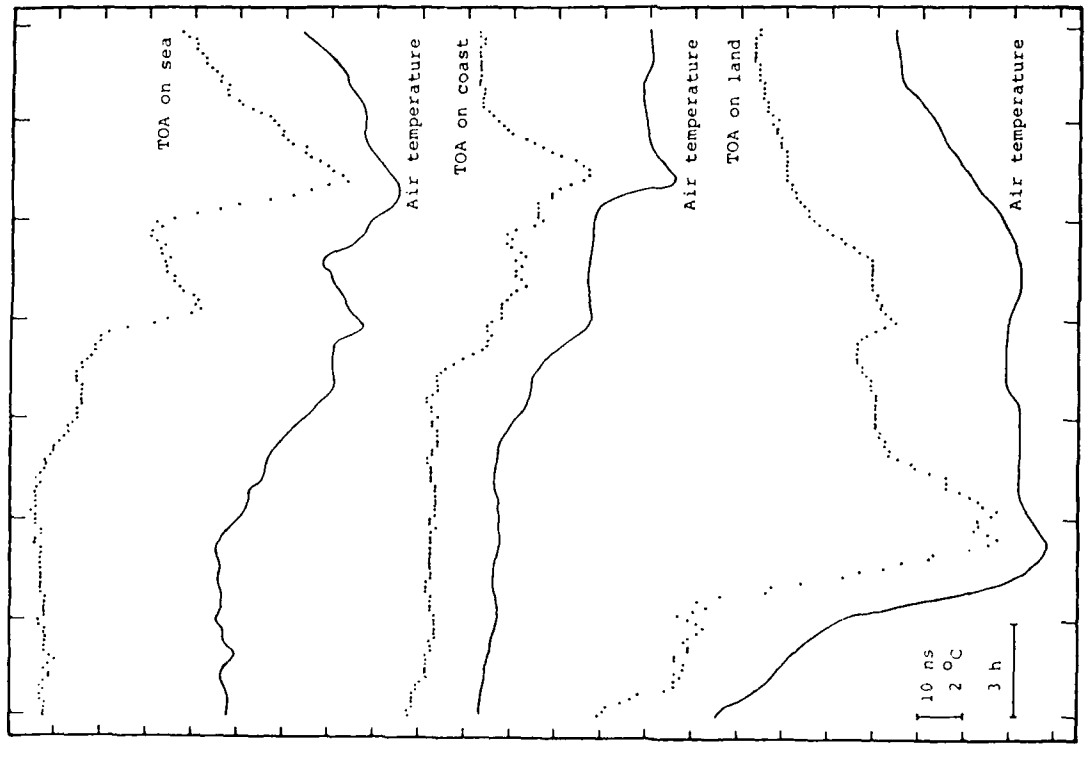

Figure 5. Loran-C time of arrival variations with air temperature changes at different receiving sites

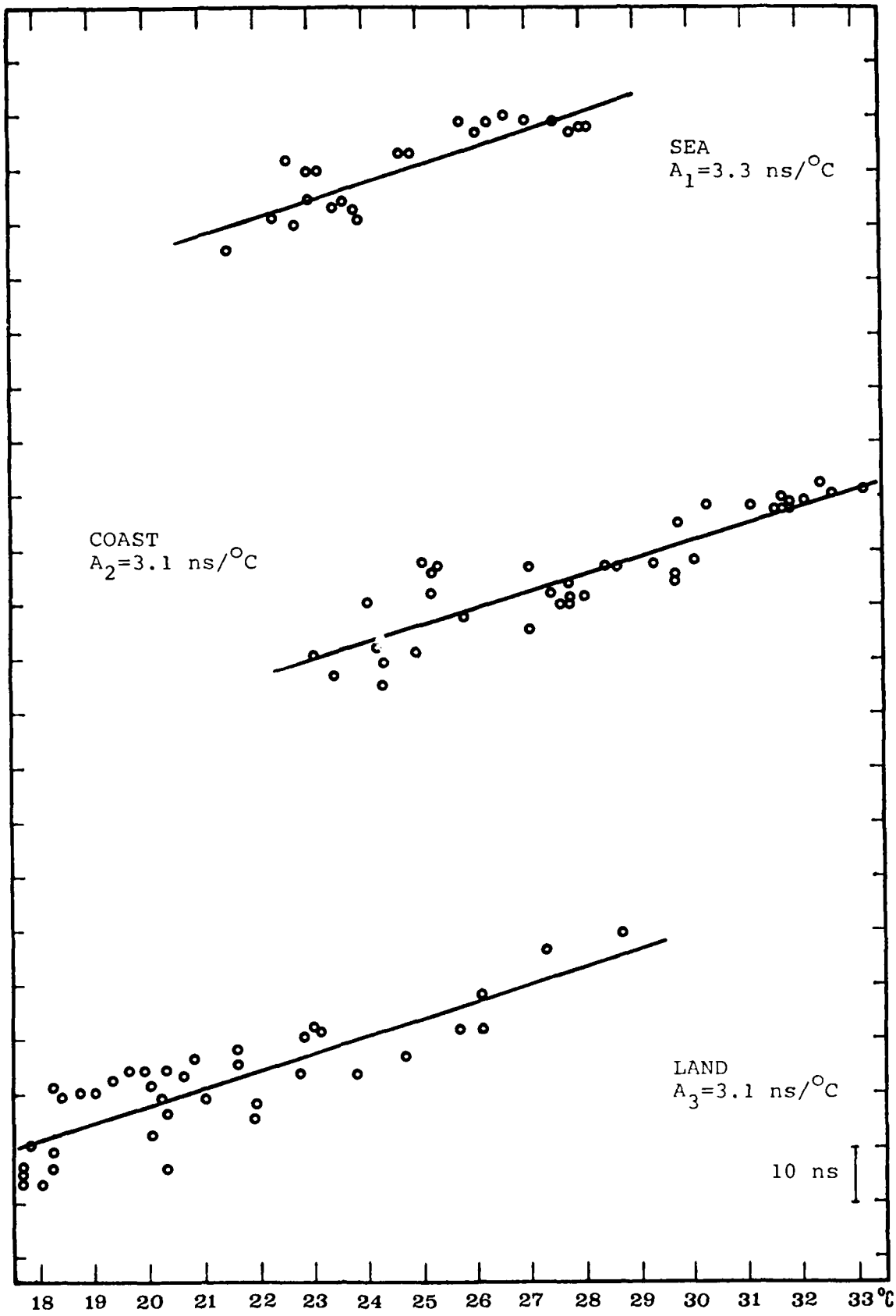

Figure 6. Common presentation of air temperature and time of arrival at different receiving sites

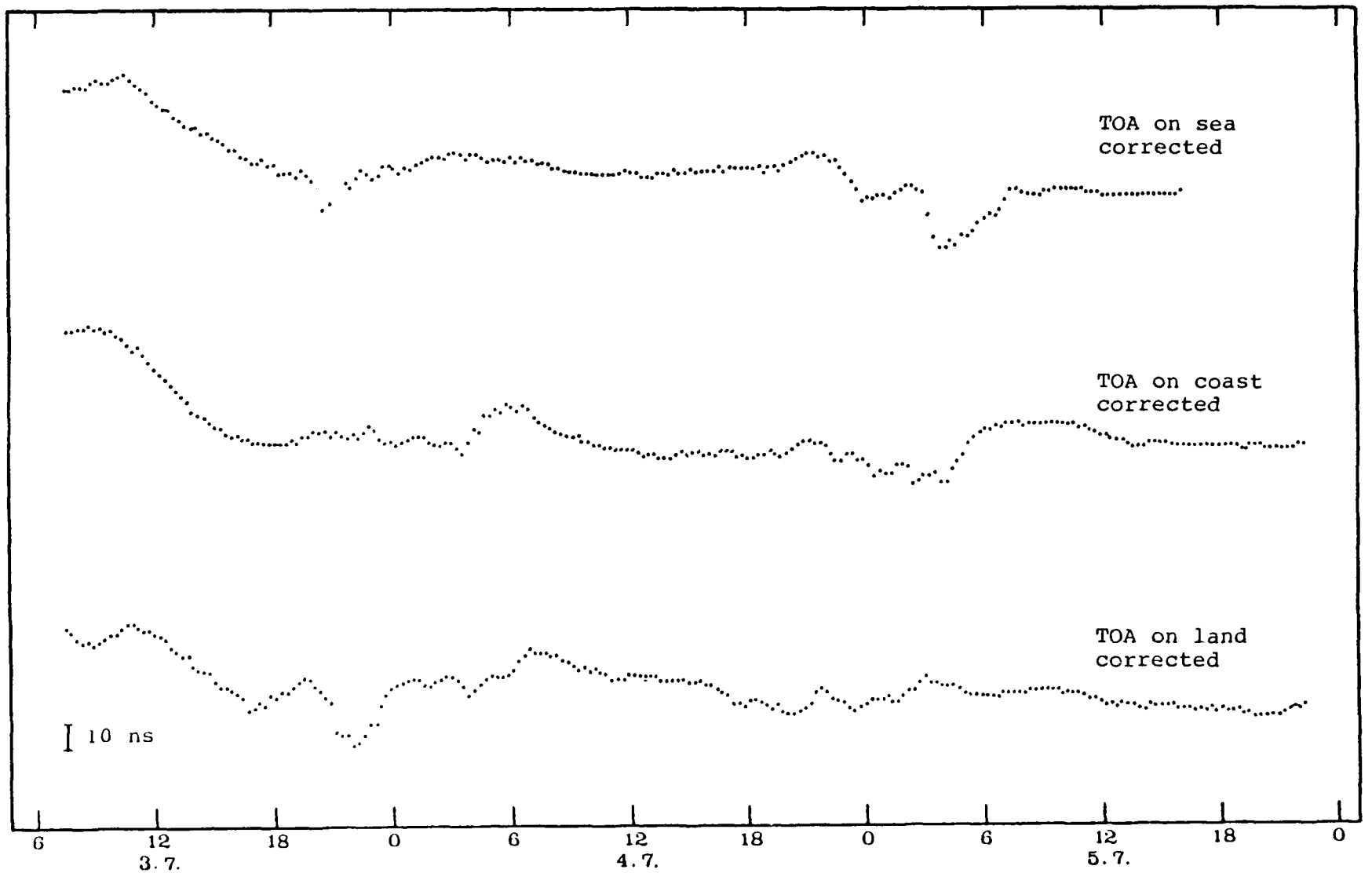

Figure 7. Loran-C time of arrival variations after correction for the value of corresponding air temperature

LORAN-C TIMING CALIBRATION OF CARIBOU, ME.

R.E. Keating, C.F. Lukac, G.H. Luther, and L.G. Charron
U.S. Naval Observatory
Washington, D.C. 20392-5100

Abstract

Results of timing calibrations made during the summer of 1986 on the Caribou, ME. LORAN-C transmitter with a mobile vehicle equipped with Global Positioning System (GPS and LORAN-C receivers are presented. At 0000 July 24, 1986, UTC(USNO MC) - LORAN(Caribou, 9960)= $-3.01\ \mu s \pm 0.10\ \mu s$**, and UTC(USNO MC) - LORAN(Caribou, 5930)=** $-5.07\ \mu s \pm 0.10\ \mu s$.

INTRODUCTION

The U.S. Naval Observatory (USNO) has been monitoring LORAN-C transmissions for 28 years. It publishes the results of its measurements weekly so that users of Precise Time and Time Interval (PTTI) may use LORAN-C transmissions to determine the time difference between a PTTI User clock and the Naval Observatory Master Clock (USNO MC).

The published measurements of the Observatory are corrected for various receiver delays, cable delays, etc. As time passes, however, the determinations of the values of the various delays become more and more uncertain because of changes in equipment, cabling, and changes in personnel. In addition, ambiguities sometimes arise concerning proper identification of the third cycle tracking point on the received LORAN-C signal.

In order to control the errors which may possibly result, the Observatory, from time to time, sponsors timing calibration trips to the vicinity of one or more LORAN-C transmitters in order to measure and determine the precise timing relationship between the USNO MC and a LORAN-C transmitter. This is a report of a timing calibration carried out in July 1986 by USNO on the 9960 East Coast and 5930 Canadian LORAN-C transmissions as emitted by the Caribou, ME. LORAN-C transmitter.

MEASUREMENT PROCEDURE

A detailed description of the measurement procedure has been previously given.[2] In general, the procedure consisted of identifying geodetic bench marks in the vicinity of the LORAN-C transmitter located at various multiples of one LORAN-C wavelength (3 Km) from the transmitter. Where geodetic bench marks could not be located at a suitable distance from the transmitter, another site was located on a map and a Mobile Electronic Laboratory (MEL) containing LORAN and GPS receivers driven to the site. The GPS receiver was then used to determine the latitude and longitude of the selected site. While the GPS measurement was being made, the time of reception of the LORAN-C signals from the transmitter was measured by a time interval counter. See Fig. 1.

After completion of measurements at a site, the MEL was driven to the next selected site and the measurements repeated. In this manner, time of reception (TOR) measurements were made on the CARIBOU, ME. LORAN-C transmissions on the 9960 and 5930 repetition rates at a sequence of sites as approach was made to the CARIBOU transmitter.

Finally, the MEL was driven to the CARIBOU transmitter and measurements were made directly on the emitted signal as picked up by a whip antenna mounted on the MEL.

All measurements were made against portable cesium clock, PC1710.

MEASUREMENT SITES

Only two geodetic benchmarks at suitable sites from the CARIBOU transmitter were located. Several days were spent searching for other benchmarks; but it was later determined that one of the most desirable benchmarks had probably been destroyed or buried when a large mansion had been constructed. At other sites, benchmarks were located but were inaccessible to the MEL. For example, a benchmark was located at the top of a ridge but the "road" leading to the ridge top went up at a 55-60 degree grade which the MEL was not capable of handling. For this, and other mundane reasons, use of the GPS receiver to determine the latitude and longitudes of the map selected sites at which the LORAN-C TOR measurements were made, was essential to the success of this timing calibration. The two geodetic benchmarks located at suitable sites which were used are identified as "EASTON 1916 1983" and "HELLSTROM 1941".

Finding a benchmark can turn into an elaborate detective investigation. As Fig. 1 shows, the EASTON benchmark is located somewhere within a wheat field. Were it not for the friendly help of Mr. John F. Hoyt, on whose property the benchmark was located and who kindly gave us permission to enter upon his property, we might never have located the EASTON benchmark. See Figs. 2, 3, and 4. Table 1 is a list of the sites and benchmarks at which measurements of LORAN TOR were made. It also gives the GPS position as determined by the GPS receiver. It should be noted that the GPS measurements had to be made when the GPS satellites were available during an approximate 6 hour window. The need to plan LORAN TOR measurements around the times during which the GPS satellites were available was the controlling factor in determining when measurements were made. The sites are listed in a sequence in which the geometric distance to the CARIBOU transmitter monotonically decreases.

TABLE 1

GPS DERIVED POSITIONS

	SITE	LATITUDE				LONGITUDE			
		°	'	"		°	'	"	
1.	DET-A NAVASTRO	44	24	15.192	N	068	00	45.324	W
2.	HELLSTROM BM	46	53	21.716	N	068	16	13.545	W
3.	7 LAMBDA	46	37	18.456	N	067	52	03.054	W
4.	6 LAMBDA	46	39	00.768	N	067	51	58.776	W
5.	KEDDY'S INN	46	40	03.851	N	068	00	39.417	W
6.	EASTON BM	46	40	26.778	N	067	51	05.298	W
7.	5 LAMBDA	46	40	51.588	N	067	52	22.974	W
8.	4 LAMBDA	46	42	29.958	N	067	52	10.074	W
9.	3 LAMBDA	46	44	07.638	N	067	52	14.712	W
10.	2 LAMBDA	46	45	30.648	N	067	53	57.840	W
11.	1.5 LAMBDA	46	46	05.904	N	067	56	26.262	W
12.	1 LAMBDA	46	46	48.228	N	067	56	00.594	W
13.	Caribou Xmitter	46	48	27.199	N	067	55	37.713	W

The position given in Table 1 for the Caribou transmitter is the WGS 72 position, not a GPS derived position.

TIME OF RECEPTION (TOR) MEASUREMENTS

Two LORAN-C receivers were used. Receiver 1 (designated R1) was used in its wide band (WB) mode and tracked the end of the third cycle of the CARIBOU 9960 signals. Receiver 2 (designated R2) also was used in wide band mode but was set to track the end of the third cycle of the CARIBOU 5930 signals. The two receivers operated continuously; and, in order to insure good tracking while the MEL was in motion, the tracking point of each receiver was shifted six cycles into the LORAN-C signal waveform and the bandwidth changed to narrowband. Only after arriving at a site and upon placing the LORAN-C whip antenna on the benchmark or next to the GPS antenna, were the receivers switched to wideband and the tracking point shifted out of the LORAN-C waveform by six cycles. After the wideband, third cycle TOR measurements were made against PC1710, the two receivers were switched back to narrowband and the tracking point shifted back into the LORAN-C signal waveform by six cycles. This procedure avoided errors and ambiguities in cycle identification and also insured that there were no changes in receiver delays caused by turning the receivers off. It also permitted identification of potential measurement sites which were, because of local interference or other reasons, unsuitable for TOR measurements.

Table 2 gives the raw time of reception (TOR) measurements which were made.

DATA REDUCTION

The TOR measurements in Table 2 have to be reduced by subtracting out the propagation time for the geometric distance, the propagation phase correction as computed according to NBS Circular 573, the 9960 Caribou Emission Delay of 13797.2 microseconds for the R1 measurements, and the measured cable, antenna multicoupler, and receiver delays. For receiver R1, the measured combined cable, multicoupler, and receiver wideband delay is 19.05 microseconds. For receiver R2, the combined wideband delay is 19.14 microseconds. Finally, the 30 microseconds for the end of the third cycle must be removed.

The geodesic geometric distance of each site from the transmitter was calculated using the Sodano algorithm and the GPS measured positions in Table 1. Then the propagation phase correction was taken from a table which is generated by a computer program that calculates the phase correction according to the theory specified in NBS Cir. 573(Ref. 1). The assumed ground conductivity was 0.005 mhos/meter; and the permittivity was 15. The air index of refraction was taken as 1.000338 and the velocity of light as 299792458 meters/sec.

The results of the distance and phase calculations are given in Table 3.

TABLE 2

TIME OF RECEPTION (TOR) MEASUREMENTS

	Site	1986		UT	PC1710 - R1 (30,WB,9960) microseconds	PC1710-R2 (30,WB,5930) microseconds
1.	DET-A NAVASTRO	28	Jul	1832	14745.00	
				1854		950.42
2.	HELLSTROM BM	26	Jul	2032	13944.04	
				2034		149.19
				2251		149.13
				2252	13944.04	
3.	7 LAMBDA	23	Jul	1950	13922.03	
				1951		126.81
4.	6 LAMBDA	23	Jul	2034		117.15
				2035	13912.32	
5.	KEDDY'S INN	20	Jul	2042	13908.20	112.68
		21	Jul	1445	13908.09	112.66
		22	Jul	1233	13907.76	112.45
				1938	13907.75	112.58
		27	Jul	1943		113.11
				1944	13907.78	
		28	Jul	1223		113.10
				1224	13907.73	
6.	EASTON BM	22	Jul	2121		109.36
				2200		109.34
				2122	13904.65	
				2154	13904.65	
		23	Jul	0015		109.32
				0818	13904.66	
7.	5 LAMBDA	23	Jul	2108	13900.46	
				2120		105.25
8.	4 LAMBDA	23	Jul	2141	13891.55	
				2142		96.35
9.	3 LAMBDA	23	Jul	2214	13881.98	86.76
10.	2 LAMBDA	23	Jul	2259	13871.30	
				2300		76.14
11.	1.5 LAMBDA	23	Jul	2338		71.98
				2340	13867.15	
12.	1 LAMBDA	24	Jul	0016		68.38
				0017	13863.63	
13.	XMITTER (Direct from Whip Ant.)	25	Jul	1822		42.47
				1916	13837.41	

TABLE 3

CALCULATED DISTANCES AND PHASE CORRECTIONS

	Site	Geometric Distance D Kilometers	D/(c/n) μs	Phase Corr. (NBS573) μs	Total Phase Corr. μs
1.	DET-A NAVASTRO	267.198	891.58	1.87	893.45
2.	HELLSTROM BM	27.717	92.49	0.54	93.03
3.	7 LAMBDA	21.148	70.56	0.48	71.04
4.	6 LAMBDA	18.098	60.39	0.45	60.84
5.	KEDDY'S INN	16.811	56.10	0.44	56.54
6.	EASTON BM	15.922	53.13	0.43	53.56
7.	5 LAMBDA	14.663	48.93	0.41	49.34
8.	4 LAMBDA	11.879	39.64	0.40	40.04
9.	3 LAMBDA	9.099	30.36	0.37	30.73
10.	2 LAMBDA	5.849	19.52	0.36	19.88
11.	1.5 LAMBDA	4.483	14.96	0.37	15.33
12.	1 LAMBDA	3.094	10.33	0.42	10.75

For the direct measurements with the whip antenna probe under the Caribou transmitter antenna, a total of 35 μs consisting of 5.0 μs near field phase correction and 30 μs for the end of the third cycle, must be subtracted from the measurements. In the case of Caribou 9960, it was also necessary to remove a synchronization error of 0.2 μs between the on time 9960 group repetition rate generator and PC1710 and the Caribou Emission Delay.

RESULTS

After subtracting the above corrections from the Table 2 measurements, one obtains the values in Table 4 for the time differences PC1710 - LORAN(Caribou,5930) and PC1710 - LORAN(Caribou, 9960).

DIRECT MEASUREMENTS ON EMITTED SIGNAL

At the Caribou Xmitter, the timing of the LORAN-C signals for both the Caribou 5930 Master and the Caribou 9960 Slave were measured against PC1710. This measurement was done by manually superimposing, using an oscilloscope, a group repetition rate generator pulse (GRP) on the end of the third cycle of the Xmitter signal taken directly from the whip probe antenna, followed by a time interval measurement of the difference between PC1710 and the superimposed GRP pulse.

For the Caribou 5930 Master, Figs. 5, 6, and 7, show, for increasing oscilloscope sweep rate and vertical amplification, the relationship between the superimposed GRP pulse and the Caribou Master signal. Figs. 8, 9, and 10 show the relationship achieved for the Caribou 9960 Slave signal. Note that in both cases, there is no ambiguity as to where the Loran signal starts and the placement of the rising GRP pulse to coincide with the end of the third cycle. The timing measurements made on the GRP pulse thus synchronized with the emitted LORAN-C signals are given in Item 13, Table 2.

TABLE 4

REDUCED MEASUREMENTS FOR PC1710 - CARIBOU

	SITE	DATE 1986		UT	PC1710-L5930 μs	PC1710-L9960 μs
1.	DET-A NAVASTRO	28	Jul	1832	+7.83	
				1854		5.30
2.	HELLSTROM BM	26	Jul	2032		4.76
				2034	7.02	
				2251	6.96	
				2252		4.76
3.	7 LAMBDA	23	Jul	1950		4.74
				1951	6.63	
4.	6 LAMBDA	23	Jul	2034	7.17	
				2035		5.23
5.	KEDDY'S INN	20	Jul	2042	7.40	5.41
		21	Jul	1445	6.98	5.30
		22	Jul	1233	6.77	4.97
				1938	6.90	4.96
		27	Jul	1943	7.43	
				1944		4.99
		28	Jul	1223	7.42	
				1224		4.94
6.	EASTON BM	22	Jul	2121	6.66	
				2200	6.64	
				2122		4.84
				2154		4.84
		23	Jul	0015		4.85
				0818	6.62	
7.	5 LAMBDA	23	Jul	2108		4.87
				2120	6.77	
8.	4 LAMBDA	23	Jul	2141		5.26
				2142	7.17	
9.	3 LAMBDA	23	Jul	2214	6.89	5.00
10.	2 LAMBDA	23	Jul	2259		5.17
				2300	7.12	
11.	1.5 LAMBDA	23	Jul	2338	7.51	
				2340		5.57
12.	1 LAMBDA	24	Jul	0016	8.49	
				0017		6.63
13.	XMITTER (Direct from Whip Ant.)	25	Jul	1822	7.42	
				1916		5.21

FINAL RESULTS

Because of the danger of near field phase deviations, the measurements made in and under the transmitter are used only as a check of the measurements made in the radiation zone. Using the PC1710 - LORAN-C(Caribou) values for the first ten radiation zone sites, one obtains:

$$\text{PC1710} - \text{L9960(Caribou)} = +7.02\mu s \pm 0.1\mu s \quad (1)$$

and

$$\text{PC1710} - \text{L5930(Caribou)} = +5.00\mu s \pm 0.01\mu s \quad (2)$$

at 0000 July 24, 1986.

The value for UTC(USNO MC) - PC1710 at 0000 July 24, 1986 as adjusted by portable clock closure value and the GPS timing measurements made on PC1710 while in the field was -10.03 μs. Using this value, the final timing calibration result is:

$$\text{UTC(USNOMC)} - \text{L9960(Caribou)} = -3.01\mu s \pm 0.10\mu s \quad (3)$$

and

$$\text{UTC(USNOMC)} - \text{L5930(Caribou)} = -5.07\mu s \pm 0.10\mu s \quad (4)$$

at 0000 July 24, 1986.

These values may be compared with an independent timing calibration of the Seneca, N.Y. 9960 Master transmitter, reported at the 1986 PTTI Applications and Planning Meeting:

$$\text{UTC(USNOMC)} - \text{L9960(Seneca)} = -3.43\mu s \pm 0.10\mu s \quad (5)$$

at 1611 Jul 14, 1986. Taking into account the fact that there are 14 days between the measurements made at the Seneca 9960 Master and the Caribou 9960 Slave, it is clear that the 9960 Northeast LORAN-C chain is correctly synchronized internally to better than 0.4 microsecond.

REFERENCES

1. Johler, J.R., Kellar, W.J., and Walters, L.C., "Phase of the Low Radiofrequency Ground Wave," NBS Circular No. 573, June 1956, National Bureau of Standards, Boulder, CO.
2. Keating, R.E., Lukac, C.F., Luther, G.H., and Charron, L.G., "Timing Calibration of the Northeast U.S.A. LORAN-C Chain(9960)," Proceedings of the Eighteenth Annual PTTI Applications and PLanning Meeting, December 2-4, 1986.

Fig. 1. Mobile Vehicle in wheat field in which EASTON benchmark is located.

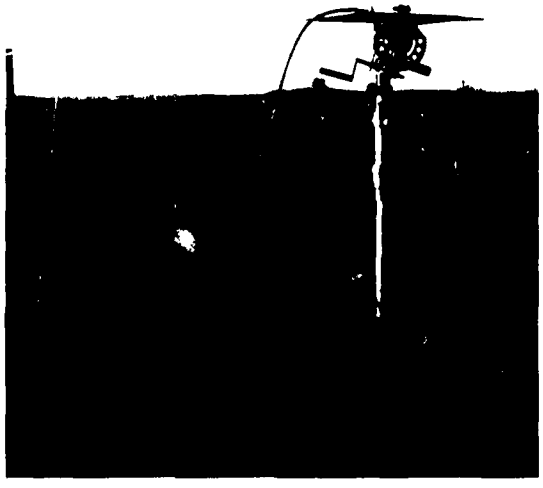

Fig. 2. GPS and LORAN Antennae Setup at EASTON BM.

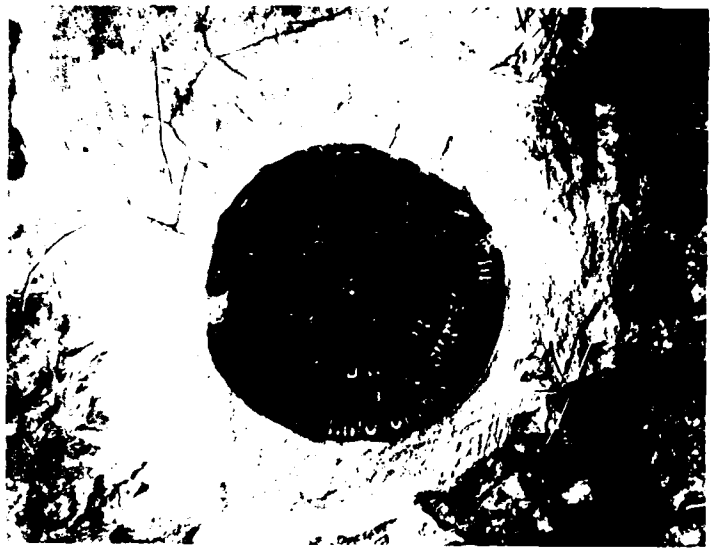

Fig. 3. EASTON Benchmark.

Fig. 4. GPS and LORAN Antennae Setup on top of MEL at Keddy's Inn.

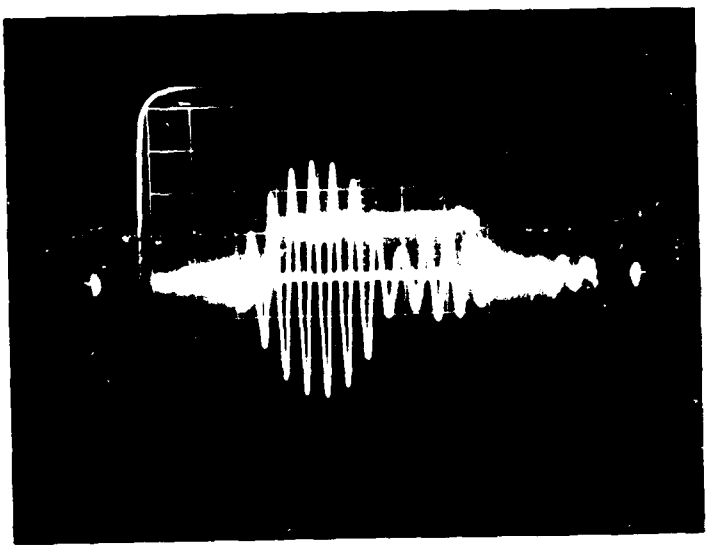

Fig. 5. Caribou 5930 Master with superimposed GRP pulse. Vertical oscilloscope setting for LORAN signal is 0.5 V/d; sweep is 20 microseconds/d.

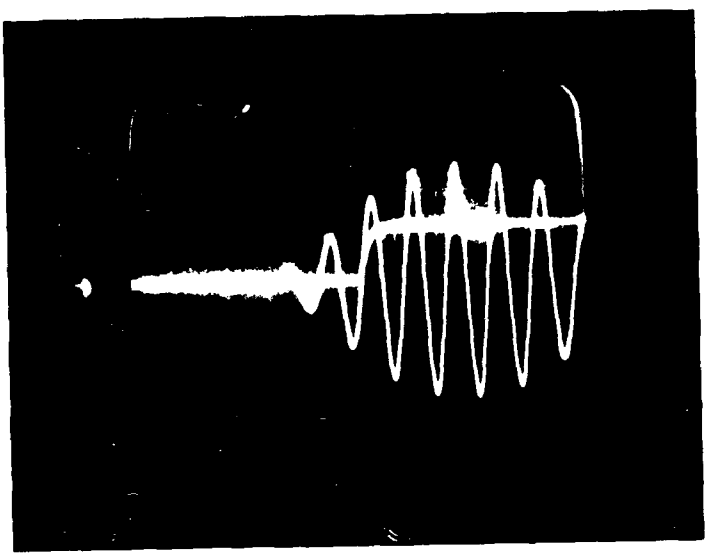

Fig. 6. Same as Fig. 5 but with sweep set at 10 microseconds/d.

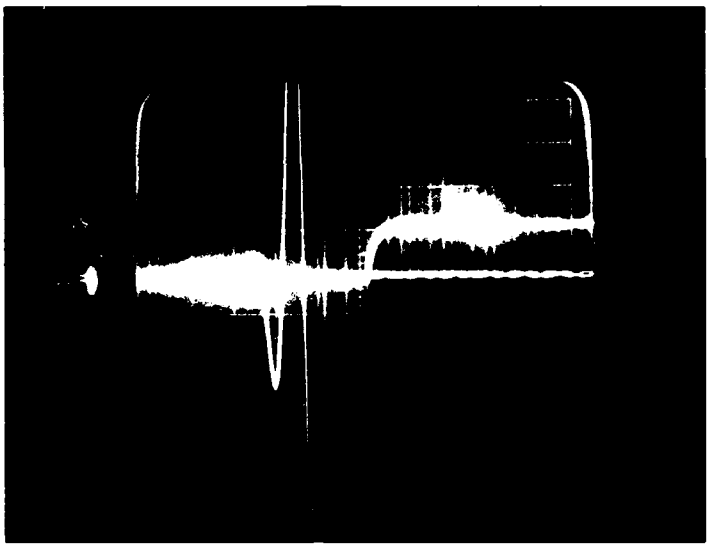

Fig. 7. Same as Fig. 6 but with oscilloscope vertical for LORAN signal set at 0.01 V/d. Note unambiguous start of Caribou 5930 Master waveform and the setting of the GRP pulse at the end of the third cycle.

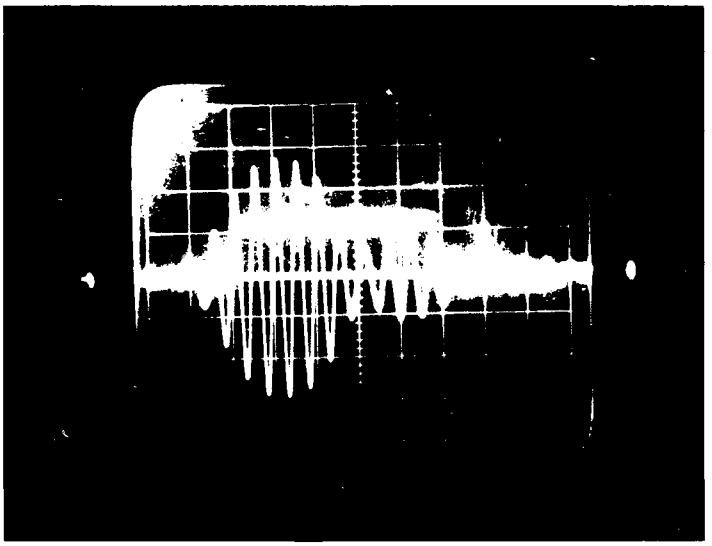

Fig. 8. Caribou 9960 Slave with superimposed GRP pulse. Vertical oscilloscope setting is 0.5 V/d; sweep is 20 microseconds/d.

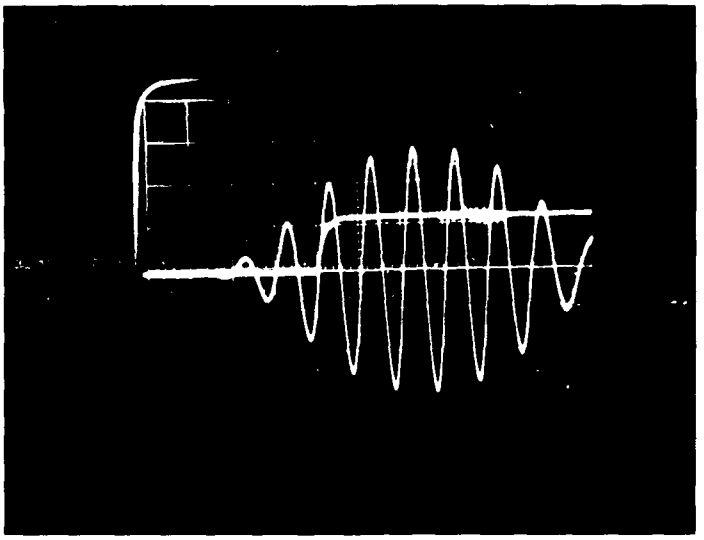

Fig. 9. Same as Fig. 8 but with sweep set at 10 microseconds/d.

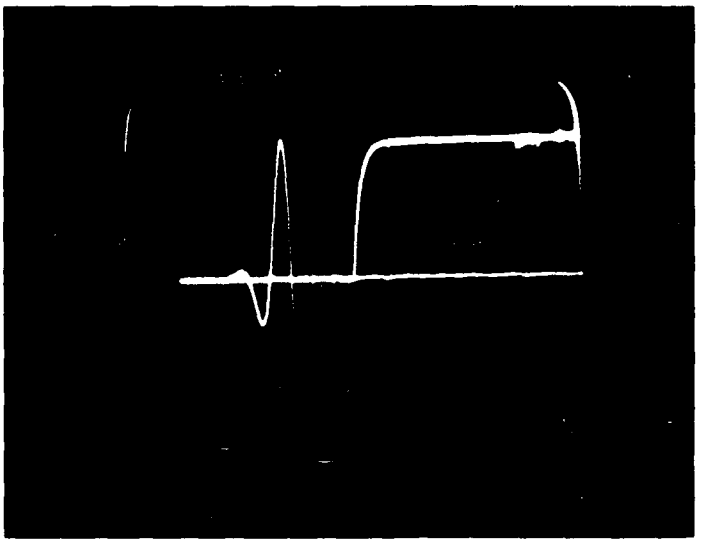

Fig. 10. Same as Fig. 9 but with vertical set at 0.01 V/d. Note unambiguous start of Caribou 9960 Slave waveform and the setting of the GRP pulse at end of the third cycle.

DISCIPLINED RANGE TIME CODE TRANSLATORS WITH SUB-MICROSECOND ACCURACY

Shelby Bass, Roger Olson and Jack McNabb
Trak Systems, Division of Trak Microwave Corp.
4726 Eisenhower Blvd. Tampa, FL 33634

Serial Time Code signals have long been used to transfer time over various communication channels and media over both short and long distances. Generally, the accuracy of this method of time transfer has been thought of in terms resolution of the code modulation — for instance, 1 second for IRIG-B, 0.1 seconds for IRIG-A, etc. However, in most Time Codes, the carrier frequency is coherent with the modulation and thus provides the means for much greater resolution and accuracy. In the case of the IRIG-B code, with its 1 kHz carrier, time resolution of better than one thousandth of a carrier cycle is now possible, leading the way to sub-microsecond time transfer accuracy. Newly developed precision Time Code Translators with this capability are now being used to improve the accuracy of time transfer throughout several large Missile Test Range timing networks.

A typical Range timing distribution network is shown in Fig. 1A. Precision time is kept at a central timing site on the Range; converted at that site to all the various time signals required by the Range users; then all of these signals are transferred to the various remote sites on the Range by use of a communication network. Because of the wide variety of bandwidths of the many different timing signals used on a large Range, the distribution and communication elements are complex, inaccurate, and difficult to maintain. As shown in Figure 1B, a Range timing network can be greatly simplified by using only IRIG-B (modulated 1 kHz) to transfer time from Timing Central to all remote sites. This signal was selected because of its ease of transmission over relatively narrow band communication networks. To obtain good time transfer accuracy the chief constraint on a communication channel is that it must have propagation delay that is very stable with regard to time and temperature. The noise properties of the communication channel are not very important since the noise that is picked up in transmission can be overcome by the use of long term filtering at the receiving end. The key to this timing system approach was the development of a precision, low cost time code translator to be put at each remote site to receive the IRIG-B signal and to regenerate the various timing signals needed by individual users. At the more important sites, an IRIG-B signal from the translator output can be returned to Timing Central to monitor the performance of the overall system.

Trak Systems in Tampa, FL has developed two time code instruments for these applications: The Model 8700 and the Model 8400B, as shown in figure 2. The units are essentially identical except for the greater number of different types of time signals available from the larger Model 8700. Both units use an internal ovenized quartz oscillator that is disciplined to the incoming IRIG-B code by use of a micro- processor based second order phase locked loop. During periods of poor signal reception the units free run with the quartz oscillator locked to its latest corrected frequency. Thus, when the IRIG-B signal is present, the quartz oscillator in the translator is kept continuously calibrated to the accuracy of the Timing Central IRIG-B, which is usually based on Cesium Standards. The disciplined quartz oscillators are of 10^{-9} per day stability, which allow a loop time constant in the

order of 1 hour for this application. This time constant provides excellent filtering of the noise picked up by the IRIG–B signal during transmission over the communication system.

The performance of these Translators is summarized in Figure 3. The primary problem in the development of these translators has been in achieving a phase locked loop algorithm that acquires rapidly; that is stable; and that provides good noise filtering. Our objective was to provide output timing signals with long and short term accuracy of better than 1 microsecond with an acquisition time of less than 2 hours from a cold oscillator start. In actual Range installations, the 8700's have typically yielded output timing noise levels of 500 nsec pp. The 8400B's have an improved phase detector design are typically yielding output timing noise levels of 300 nsec pp. Much of the evaluation has been done over a 12 mile telephone pair land line. When used on quiet short haul lines these translators exhibit output noise levels as low as 100 nsec pp. Much more testing is needed to fully determine the long term accuracy of the translators and the long term stability of the communication system propagation delays, however it appears that the overall system goal of 1 μsec is now being realized.

Figure 4A is an example of the time base noise on an IRIG–B signal at the input of the Translator after transmission over 12 miles of telephone cable and terminating amplifiers. This noise was observed to be typically 10 microseconds peak–to– peak with worse cases to 30 microseconds pp. The spectral properties of this noise has not been adequately measured. The larger noise spikes appear to be a few seconds in duration. Noise components of 1 μsec amplitude were observed to exist for up to 30 second durations. The resulting output from the Translator is shown in Figure 4B.

Figure 5 shows the major circuit elements used in these translators. The incoming IRIG–B code is detected and processed by somewhat conventional time code reader circuitry. When several frames of error free and sequential code have been detected, the incoming code is used to initially jam synchronize the translator. Very accurate detection of the carrier zero crossing near the middle of the once per second frame marker pulse is then used to measure both the frequency of the phase of the internal local oscillator as compared to the incoming signal. A micro– processor is used to process the error signals and to slowly correct the oscillator frequency and phase by analog frequency control of the oscillator thru a DAC. At initial turn–on, the DAC is first used to control the frequency of the oscillator. After about 15 to 20 minutes, when the oscillator drift has reached acceptable levels, the translator is again jam synchronized to the incoming code to a phase accuracy of about 10 μsec. The final phase control process then begins. The reduction of the initial phase error from the 10 μsec level down to less than 1 μsec typically takes about an hour. The micro-processor is also used to control the action of most of the other circuit elements. Once a code error or a code dropout is detected, the unit immediately inhibits external time updates; freezes the DAC at its average control point; and proceeds to free run on the internal oscillator. To avoid the use of bad code, strict code re–acquisition rules must then be met before returning to the use of the incoming code. The translator has internal dip switches for setting fixed propagation delay corrections to a resolution of 1 μsec. Conventional code generators are used to provide a multiplicity of output codes and rates.

Figure 6 shows the main elements of the final control algorithm. The phase error between the internal oscillator and the incoming code is measure once per second to an resolution of 100 nsec. The error signal is then filtered with an 8 second moving average. To obtain the lead time constant necessary to stabilize the second order loop, the error is in essence processed over two parallel paths: a proportional path and an integrating path. These paths are combined and applied to the DAC to control the frequency of the oscillator. The oscillator itself provides the second integration (from frequency to phase). The DAC provides a total frequency control range of about $\pm 10^{-6}$ with a resolution of 10^{-9}. The effective time constant of the closed loop is about 1 hour. In the current implementation, the proportional path is in fact very non-linear and is limited to just three values 0, +X, and -X. The value of X was chosen to give reasonably fast acquisition, but also to limit the frequency changes in the oscillator at any one time. This type of control, with a small value of X has

the advantage making the unit almost insensitive to input noise amplitude. The integrating path is accomplished digitally by the micro-processor, forming a perfect drift-free integrator.

Computer simulation studies were used to optimize the control algorithms. Initial studies were done on a PC, using Lotus 123 (c) and were very effective in solving early stability problems. Later and more comprehensive simulations at Trak used an AT computer and "C". The simulations were found to be very useful in speeding up the development, as the time required for testing of the actual hardware is quite long. One interesting finding in the simulations was that the control actually improves with some input noise. The noise acts like "dither" in a mechanical servo and allows control beyond the resolution of the phase measuring circuit and the DAC. It was also noted that the initial moving average processing is of no particular value and can in fact contribute to loop instability if the average is too long. A short moving average was thought to be necessary for protection against large noise spikes, but it is really not needed because of the hard limits put on the oscillator control. Figure 7 shows typical result of some of the early stability studies that were done with Lotus 123. The limit cycle oscillation around the 100 nsec resolution limit of the phase detector was seen in actual test data, but its amplitude is reduced by input noise.

In achieving 1 microsecond time transfer accuracy with IRIG- B, we are near the limit of accuracy of the phase detector. With the 1 khz carrier, this implies that the phase detector errors are less that 1/1000 of a carrier cycle. Thus, if higher levels of accuracy are needed, the use of higher frequency codes is recommended: IRIG-A for 100 nsec systems; and ultimately IRIG-G for 10 nsec systems. For the higher levels of accuracy, development is needed on a more precise time code Generator for use at the central site. In fact some of the data accumulated with the 1 microsecond systems indicate that the Generator may be a substantial source of error in these systems. By far the largest body of work yet to be done is in better understanding propagation delay changes in the communication links. For the first time, with these precision Translators, we have the tools to see and to measure the components of system error that were previously masked by the inaccuracy and noise in the Translator.

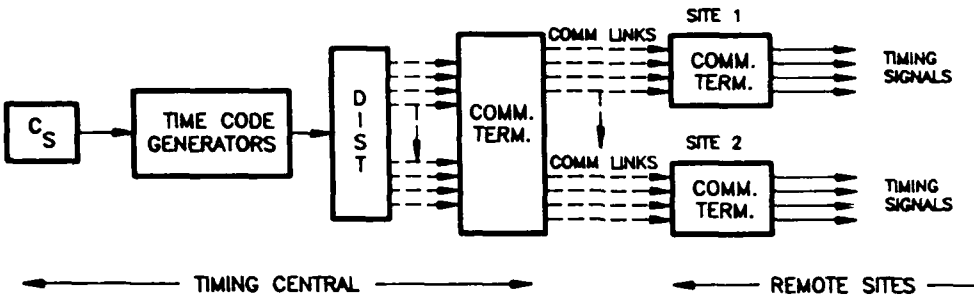

FIGURE 1A. OLD STYLE RANGE TIMING NETWORK

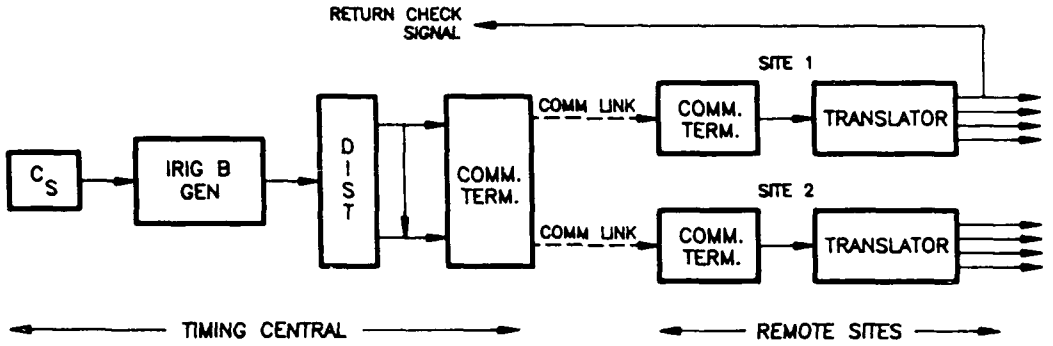

FIGURE 1B. NEW STYLE RANGE TIMING NETWORK

FIGURE 1 RANGE TIMING NETWORKS

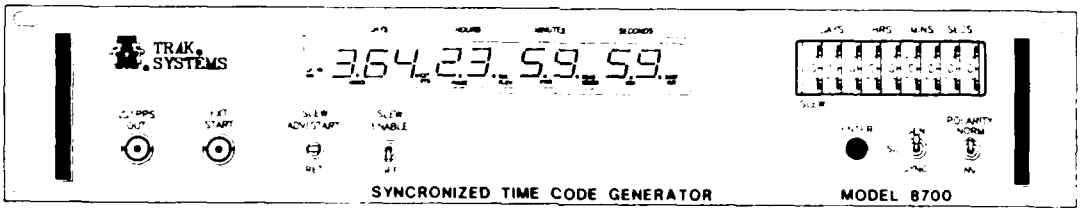

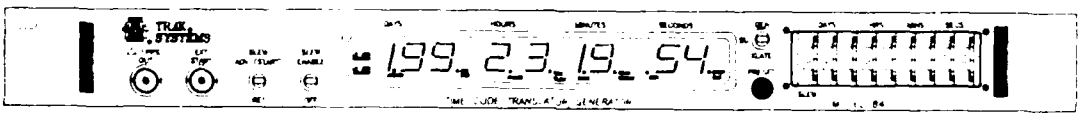

- IRIG B INPUT
- MULTI–CODE OUTPUTS
- INTERNAL OVENIZED QUARTZ OSCILLATOR
- 2nd ORDER PHASE – LOCKED LOOP
- MICROPROCESSOR BASED

FIGURE 2 TRAK MODELS 8700 AND 8400B

	GOALS	TRAK MODEL 8700	8400B
PEAK–TO–PEAK NOISE (OVER COMM. LINES)	1 μ SEC	500 nSEC	300 nSEC
OVERALL ACCURACY (OVER COMM. LINES)	1 μ SEC	* 1 μ SEC	*1 μ SEC
PEAK–TO–PEAK NOISE (OVER QUIET LINES)	———	200 nSEC	100 nSEC
ACQUISITION TIME	2 HRS	2 HRS	2 HRS

(*) NOT FULLY EVALUATED.

FIGURE 3 PERFORMANCE GOALS & RESULTS

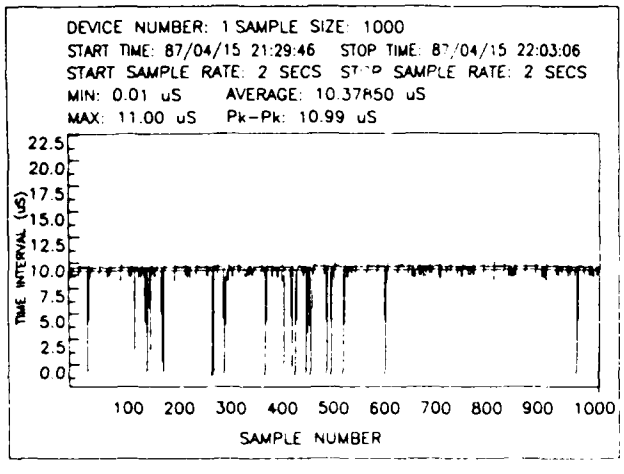

FIGURE 4A TYPICIAL INPUT NOISE

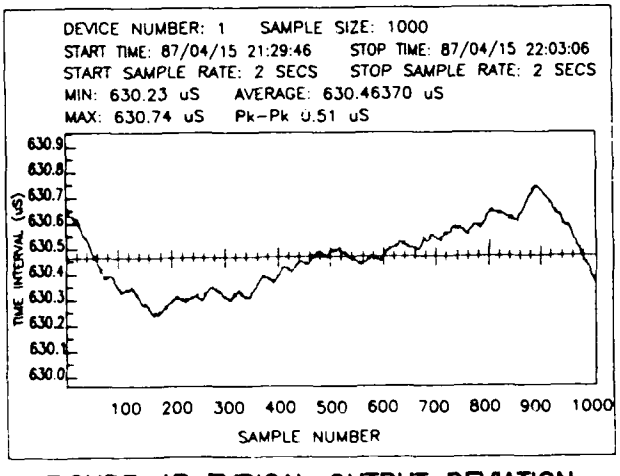

FIGURE 4B TYPICAL OUTPUT DEVIATION (WITH 10μS INPUT NOISE)

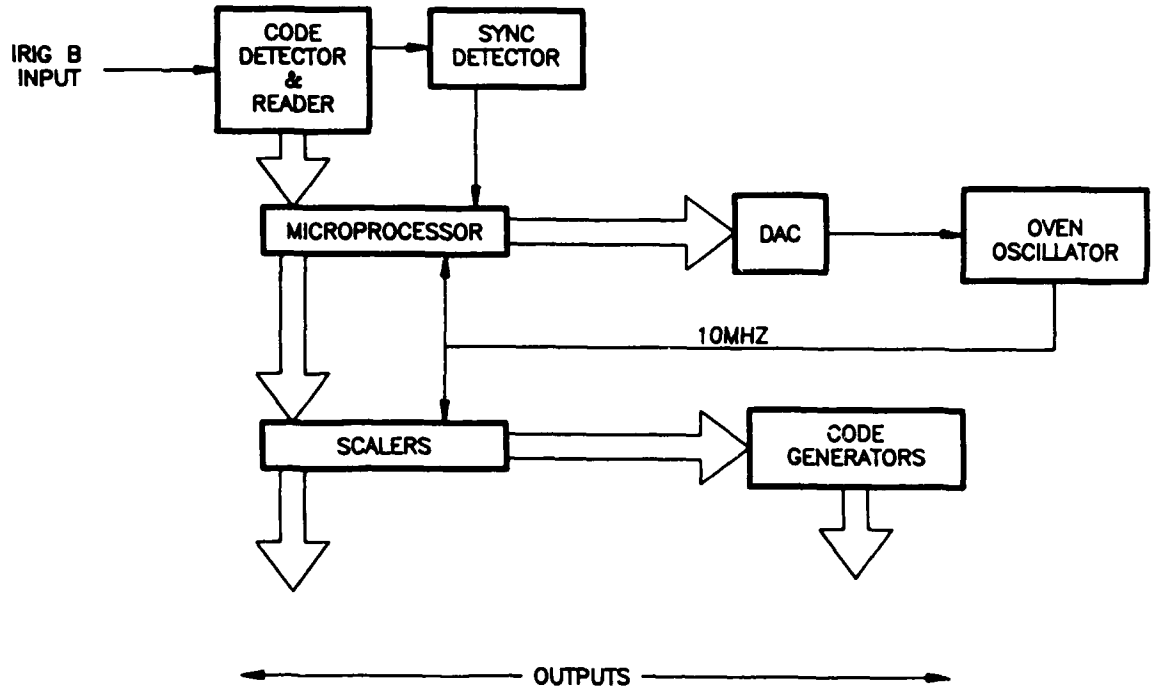

FIGURE 5 TRAK SYSTEMS MODEL 8400B
SIMPLIFIED BLOCK DIAGRAM

PROPORTIONAL PATH

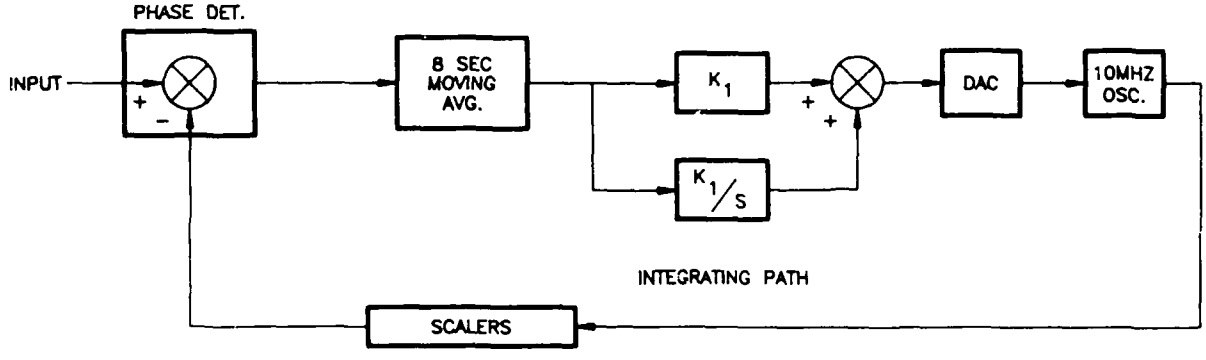

FIGURE 6 TRAK SYSTEMS MODEL 8700/8400B
FINAL CONTROL ALGORITHM

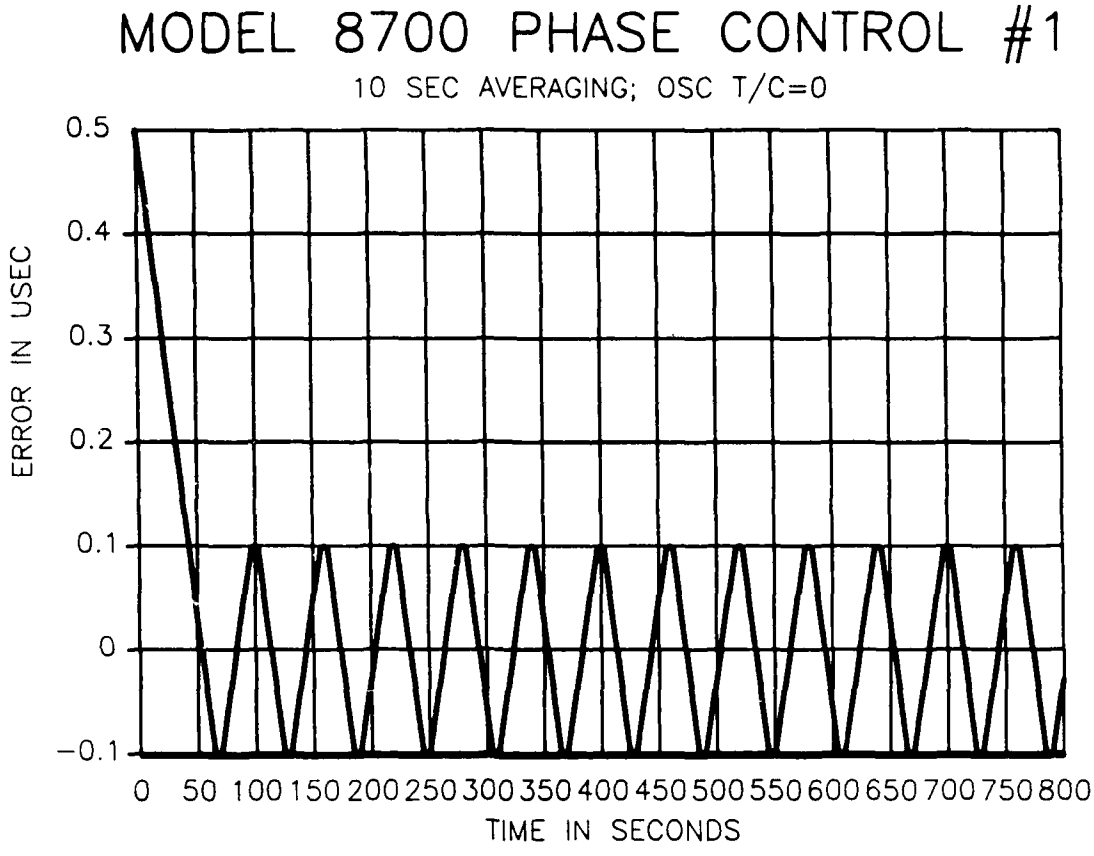

FIGURE 7 SIMULATION STUDIES TYPICAL PLOTS

FREQUENCY AND TIME SYNCHRONIZATION IN DIGITAL COMMUNICATIONS NETWORKS

M. Kihara and K. Hisadome
Nippon Telegraph and Telephone Corporation
1-2356, Take, Yokosuka-shi
Kanagawa 238-03, Japan

ABSTRACT

Frequency distribution performance will be improved with the installation of a new synchronization equipment (slave clock) in Nippon Telegraph and Telephone Corporation's (NTT's) network. In the slave clock system, the PLL has been optimally designed so that the total phase-time variation in the whole network is significantly less than 10 μs. This phase-time variation is recommended by International Telegraph and Telephone Consultative Committee (CCITT). The design method and PLL control algorithm enable both an optimum time constant of the PLL and a frequency departure of 10^{-12} in a holdover operation.

The functions of the frequency distribution system has the intrinsic capability of being expanded and applied to a time transfer system. Since the frequencies are synchronized, a phase-time of the standard frequency signal can be synchronized to a coordinate time scale by an initial time setting, e.g., using portable clocks. Time synchronization capability is determined by the relative phase-time variation of standard frequency signals and the time accuracy of the initial phase-time setting. Relative phase-time variation can be reduced to within 500 ns by using wander correction. The initial time accuracy is within 0.1 μs in conventional portable cesium beam standards. The time accuracy in NTT's digital networks is expected to 100 ns to 600 ns.

1. INTRODUCTION

Time and time intervals are important subjects in the digital communication network field. Digital multiplexing and time-division switching are based on precise time and time interval signals, controlled by so-called network synchronization. Network synchronization extends throughout the main nodes. Recently high-speed synchronous terminals also require reference clocks supplied by network synchronization[1].

Nippon Telegraph and Telephone Corporation (NTT) of its network will improve the frequency distribution performance with the installation of a new slave clock system. International Telegraph and Telephone Consultative Committee (CCITT) recommends requirements for reference clocks such as frequency departure with a national standard, slave clock performance and jitter and wander at node outputs[2]. This paper discusses the characteristics of the new slave clock system supposing the CCITT requirements are met.

Jitter and wander at node outputs are determined by the characteristics of the slave clock system. In master-slave synchronization, jitter and wander are accumulated

node by node. Jitter is caused by digital circuits and the digital signal configuration itself. It decreases if higher hierarchies are used for frequency distribution. However, wander depends on frequency distribution length, and cannot decrease except when transmission line media are changed.

To reduce wander, a positive wander correction is suggested. The correction can be achieved by assuming half of the measured round trip delay. Experimental results of delay variation in NTT's existing network are shown.

2. NETWORK SYNCHRONIZATION IN NTT

2.1 Basic configuration

NTT has adopted master-slave synchronization. The configuration of NTT's network synchronization is shown in Fig. 1. There are two master nodes in the first stage, and many slave nodes, each of which contains a slave clock system. The Tokyo node is the original master during normal operation[3]. The Osaka node is the backup. Two paths are usually selected for clock distribution: a primary and a secondary path. In the second stage, one path is from the Tokyo node, and the other is from the Osaka node. In the following stages, the clock distribution paths are selected from among different nodes if possible.

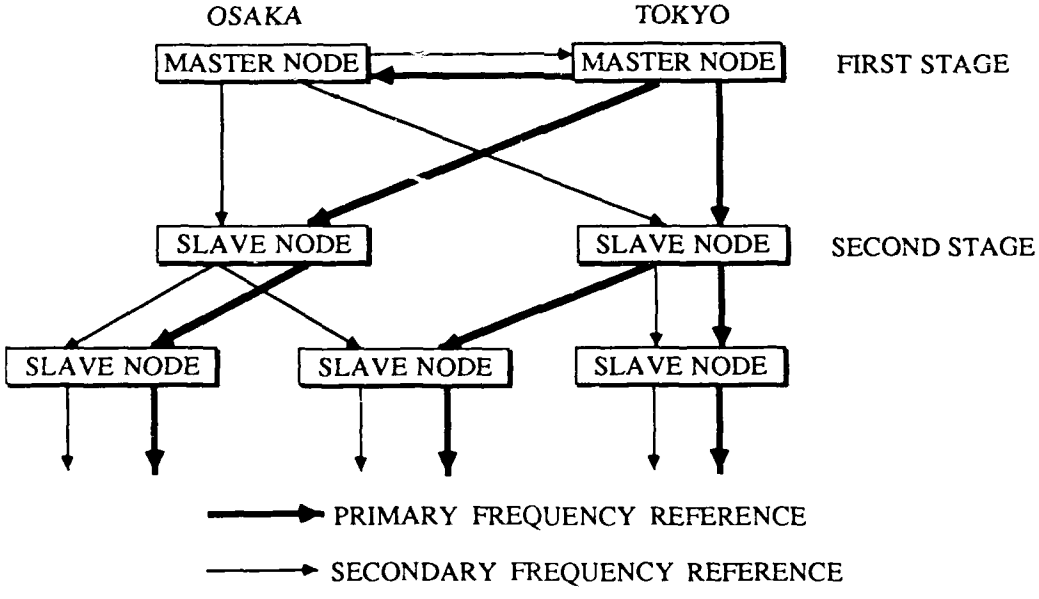

Fig. 1 NTT NETWORK SYNCHRONIZATION

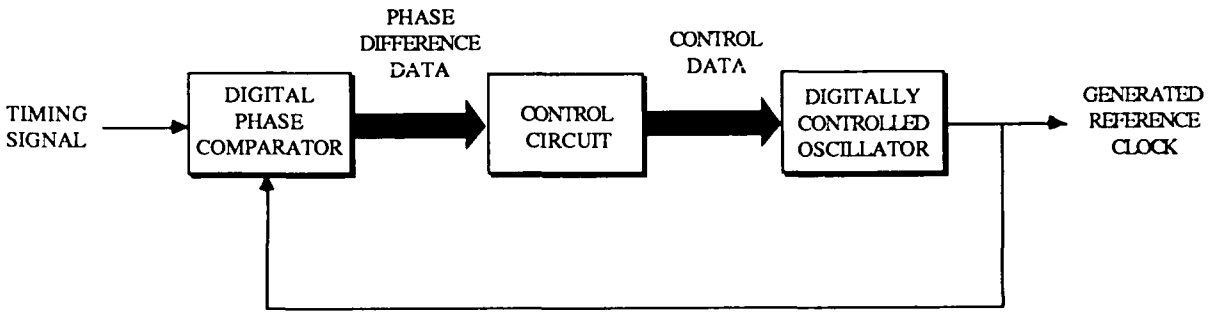

Fig. 2 BASIC CONFIGURATION OF SLAVE CLOCK SYSTEM

2.2 Design of the slave clock system

A block diagram of the slave clock system is shown in Fig. 2. The basic configuration of the slave clock system is a phase-locked loop (PLL). The timing signal from the higher level slave node or from the master node is input to a phase comparator. The PLL locks to this timing signal, and generates the new reference clock. In the new slave clock system, a Rubidium atomic oscillator is used, and it is digitally controlled. The frequency control resolution of the Rubidium atomic oscillator is better than 10^{-12}. Therefore, the output frequency deviation is kept on the order of 10^{-12}, even if the input timing signal fails.

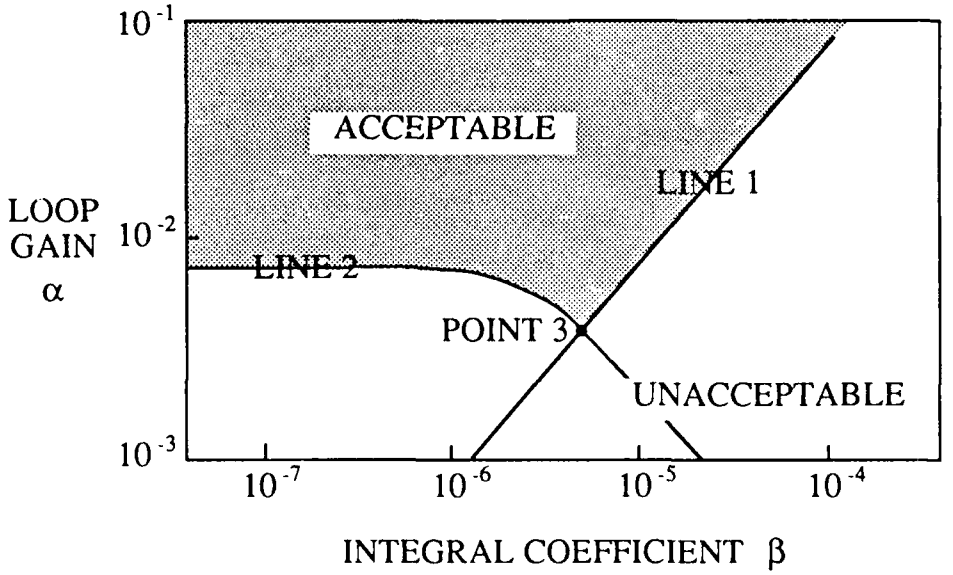

Fig. 3 ACCEPTABLE COMBINATION OF LOOP GAIN AND INTEGRAL COEFFICIENT

The time constant is an important parameter in PLLs, since it determines the budget of reduced and traced frequency components. If a loop filter is a perfect integral plus proportional filter, the PLL time constant is determined by loop gain and integral coefficient values. A PLL with a perfect integral plus proportional filter has the advantage of a constant steady state phase error. However, there are frequency areas that amplify noises. Therefore, to restrict the gain of the amplitude, the coefficients must have values as represented by the area to the left of line 1 shown in Fig. 3. In addition, the PLL should trace the input timing signal to reduce oscillator frequency deviations such as those caused by temperature dependence. Thus, the area above line 2 in Fig. 3 represents acceptable loop gain values. Since lower loop gain means better input noise reduction, point 3 in Fig. 3 is the optimum combination of values.

If the frequency control resolution of a variable frequency oscillator is upgraded to improve the frequency holdover characteristics, the loop gain becomes lower. Generally the loop gain is lower than the optimum point. To increase the loop gain, the resolution of the phase difference detection at the phase comparator has to be improved. However, the resolution of the digital phase difference detection is limited by processing speed in the digital circuits. Therefore, to vary the loop gain, it is suggested to change the frequency control resolution without degradation of the frequency holdover characteristics. The control algorithm of the variable frequency oscillator is shown in Fig. 4. In this algorithm, two resolutions of frequency control are used. One is selected to be N times as many as the minimum frequency control resolution. This allows increasing the time constant. The other is selected to be the minimum frequency control resolution for the frequency holdover so that the holdover frequency deviation is decreased. The control data for the holdover operation consists of the filtered normal operation data. In Fig. 4, N is given value of 4.

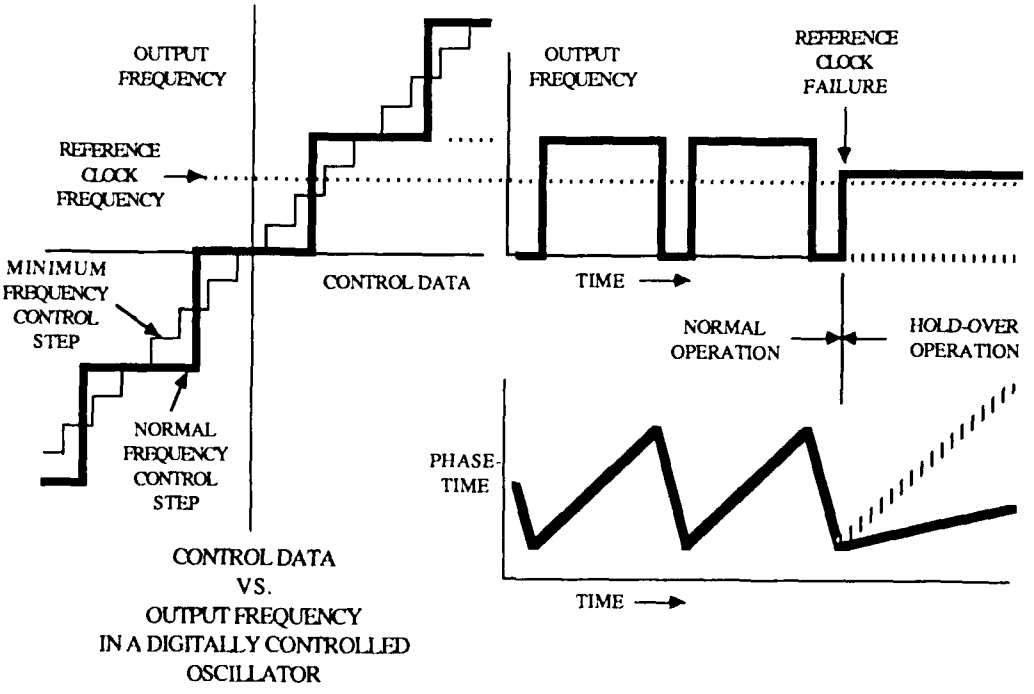

Fig. 4 PLL CONTROL ALGORITHM

2.3 Reference clock performance

The transfer function of a PLL is shown in Fig. 5, and the output gain for the variable frequency oscillator of a PLL in a slave node is shown in Fig. 6. The optimum values are selected as PLL loop parameters. The black points show the actual measurement results, and the line shows the theoretical values. The cutoff frequency is 4.17×10^{-4} Hz, which corresponds to a time constant of about 2,000 s.

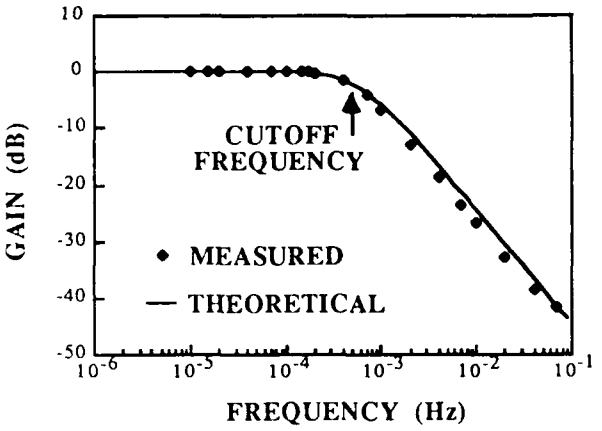

Fig. 5 TRANSFER FUNCTION OF PLL IN THE SLAVE NODE

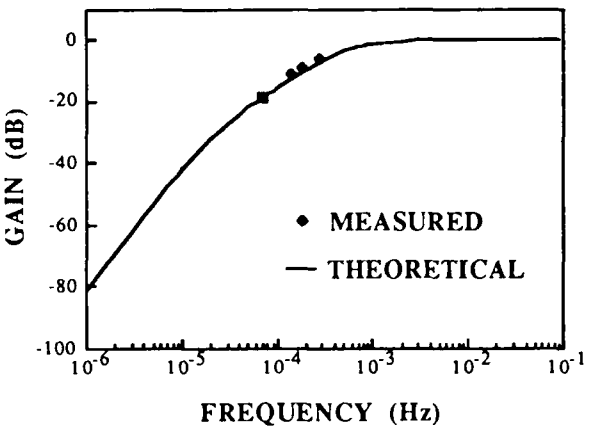

Fig. 6 OUTPUT GAIN FOR THE VARIABLE FREQUENCY OSCILLATOR OF PLL IN THE SLAVE NODE

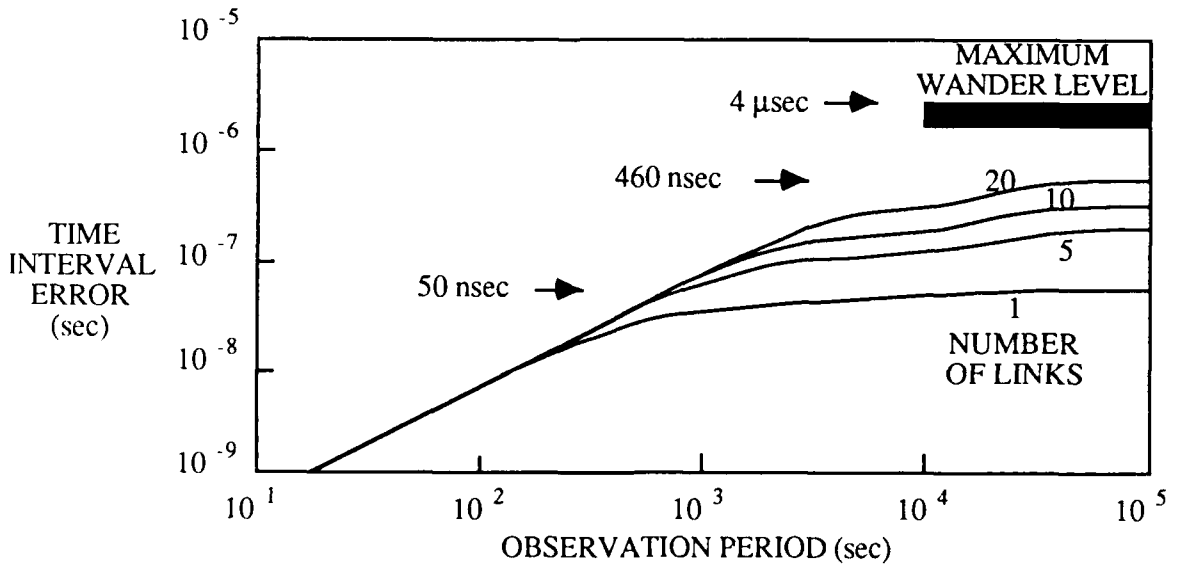

Fig. 7 TIME INTERVAL ERROR OF THE REFERENCE CLOCK

Assuming the PLL characteristics shown in Figs. 5 and 6, the phase-time variation of the slave node outputs is calculated as shown in Fig. 7. The X-axis here is the observation period, and the y-axis is the time interval error, which corresponds to phase-time variation. The time interval error per link of the slave node is within 50 ns. That means a frequency distribution capability of 5×10^{-13} over the observation period of 10^5 s. The maximum time interval error is 460 ns. The maximum number of links is assumed to be 20. These error values represent a reduction to one 20th compared with the error values in NTT's previous network synchronization scheme employing an arbitrary time constant.

Actually, phase-time variation over a long period, called wander, should be considered. The maximum wander is estimated to be 4 μs in NTT's network. This value satisfies the recommended characteristics in CCITT.

3. TIME TRANSFER IN DIGITAL COMMUNICATIONS NETWORKS

3.1 Basic method

The maximum phase-time variation of 4 μs indirectly means frequency distribution makes it possible to provide a relative time transfer accuracy of 4 μs. Next, a method is presented for positive time transfer. Time transfer from a reference time node to a slave time node with a digital path like the master-slave technique for the frequency distribution is shown at the top of Fig. 8. The path delay is necessary to correct the transferred reference time. A basic simple technique to determine the path delay is to assume half of measured round trip delay, as shown at the bottom of Fig. 8.

This method is based on the assumption that the delay of the outgoing path is identical with that of the incoming path. However, actual transmission paths are not constructed to guarantee this. Therefore, consider here the correction of the path delay variation instead of the path delay itself. In this case, the outgoing path delay variation can be assumed with measurement of round trip delay variation. If the delay variation of the outgoing path is identical with that of the incoming path, the outgoing path delay variation is half the delay variation of the round trip path. This is positive wander correction.

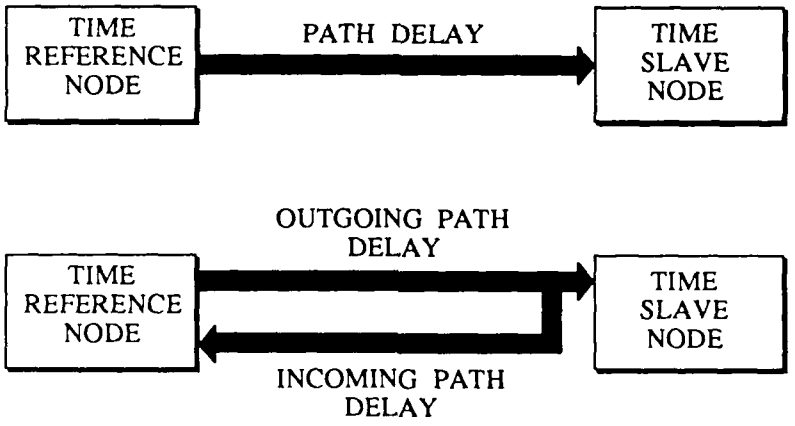

Fig. 8 BASIC TIME TRANSFER

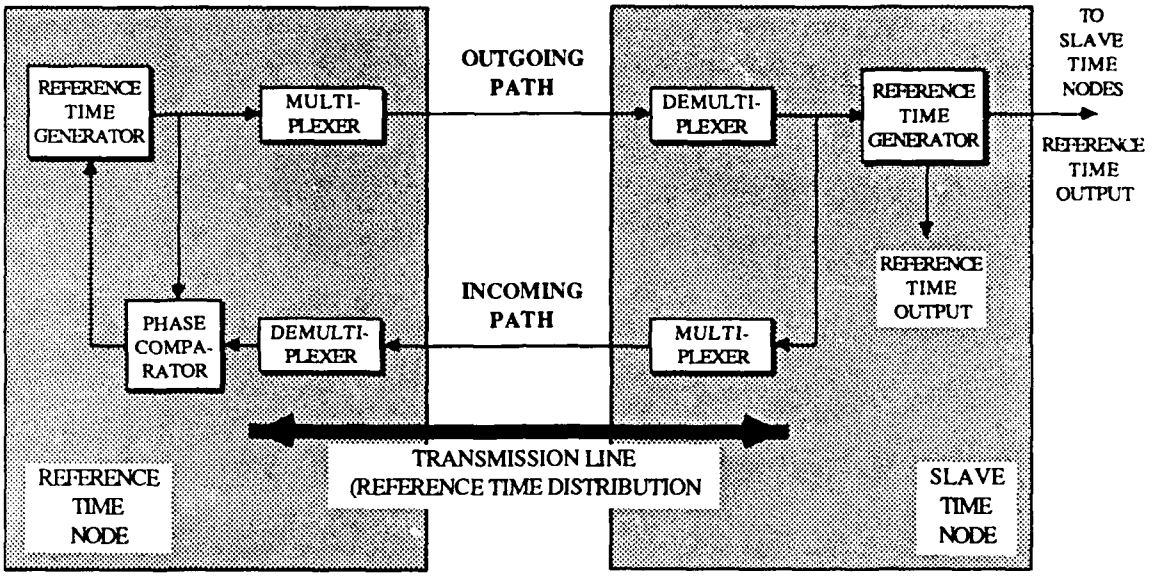

Fig. 9 ROUND TRIP PATH MEASUREMENT CONFIGURATION

The configuration for the actual round trip measurement is shown in Fig. 9. The reference time signal is transferred over the outgoing path from the left side, the time reference node, to the right side, the time slave node. The slave node returns a reference time signal over the incoming path. The delay variation of the round trip path is measured by the phase comparator.

The delay variation of the outgoing path can be estimated to be half the delay variation of the round trip path. This variation corresponds to the correction value for the transferred reference time in the slave time node.

3.2 Time transfer capability

To test the feasibility of the method mentioned above, phase-time variations of both the outgoing and incoming path are measured simultaneously. Figure 10 shows the delay variation of each path for 17 days in the existing NTT's network. Its total transmission length was 2,291 km. The Y-axis is phase-time, and its absolute value is arbitrary. The delay changes about 150 ns over 17 days. However, Fig. 10 shows that the delay variation of the outgoing path is essentially the same as that of the incoming path. This implies that delay variation tendencies are essentially the same in the same transmission line, even if delays are not the same.

It is effective to subtract the delay variation of the outgoing from that of the incoming path in order to confirm this correlation. The differential data is shown at the top of Fig. 11. The bottom of Fig. 11 is the filtered data. The most significant feature is that the average differential delay value is not divergent but constant. This means that the initial phase-time can be controlled and kept constant.

The square root of the two-sample variance of the differential delay variation is

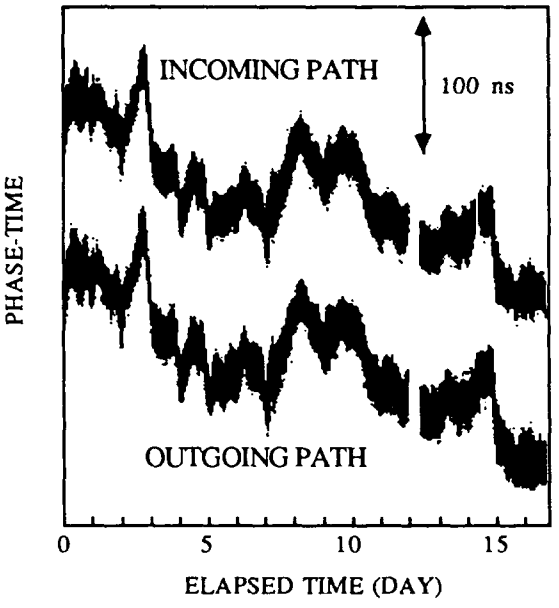

Fig. 10 DELAY VARIATION OF TRANSMISSION LINES

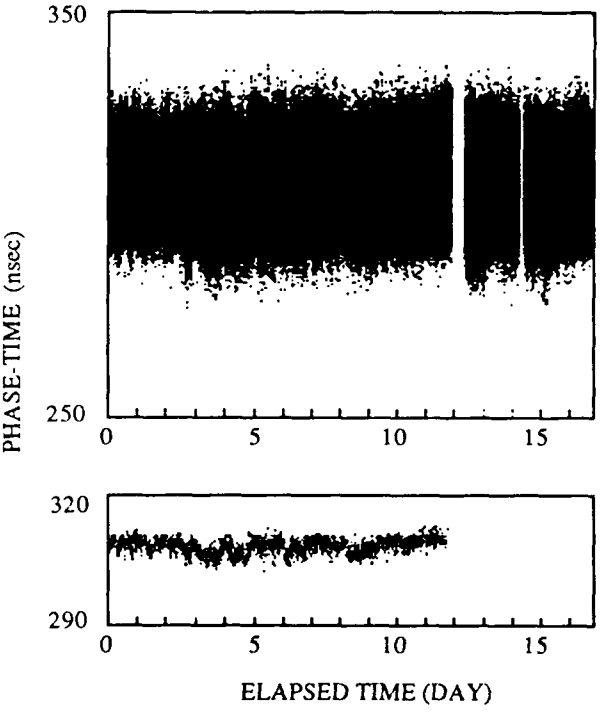

Fig. 11 DELAY VARIATION OF THE SUBTRACTION DATA

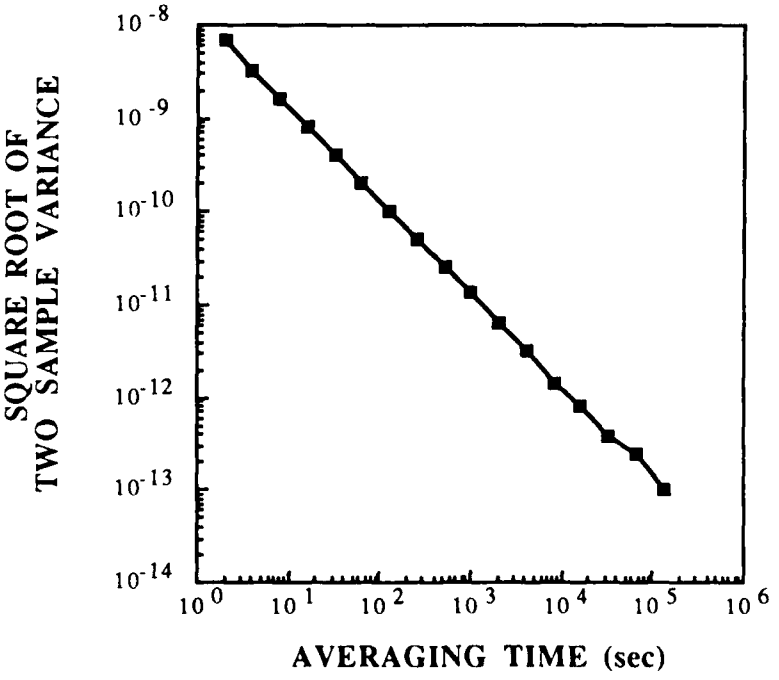

Fig. 12 STABILITY OF TRANSMISSION LINES

10^{-13} over the averaging time of 10^5 s, as shown in Fig. 12. This corresponds to about 10 ns in phase-time. The variation tends to be white phase noise up to the averaging time of 10^5 s.

4. CONCLUSION

The experimental results mean the time transfer capability of this wander correction method is 10 to 30 ns/link. Considering the frequency distribution characteristics and the multi-link of time slave nodes, the total relative time accuracy is within 500 ns.

If this time transfer method could be combined with an initial absolute time setting such as by using portable clocks, the absolute time scale tracing UTC might be provided. We have been developing a portable optically pumped cesium beam standard[4]. The portable clock method employing this oscillator is expected to have an accuracy on the order of 10 ns. The time accuracy in NTT's digital networks is expected to 100 ns to 600 ns.

ACKNOWLEDGEMENTS

We are grateful to Dr. Masaki Koyama and Mr. Katsuaki Kikuchi of NTT Transmission Systems Laboratories for their encouragement. We would like to thank Mr. Kenichiro Kuroishi of NTT Sapporo Network Center for his help with the experiments.

REFERENCES

[1] H. Ueda and I. Tokizawa,"A Aynchronous DS4 Multiplexer with Cross-connect Function and Its Impact on the Network", GLOBECOM'85, 1985

[2] CCITT Recommendations, Recs. G. 811, G. 812, G. 824 and G.825, AP IX-150

[3] M. Kihara and H. Jumonji,"Frequency Keeping Algorithm for Atomic Reference Frequency and Clock Supply", Elect. and Comm. in Japan, Vol. 66-B, No. 11, pp. 76-84, Nov. 1983

[4] M. Kihara and K. Hisadome, "Design of High Performance, Portable Optically Pumped Cesium Beam Standards", CPEM'88, pp.248-249, 1988

IONOSPHERIC CORRECTIONS FOR TIMING APPLICATIONS

John A. Klobuchar
Ionospheric Physics Division
Air Force Geophysics Laboratory
Hanscom AFB, MA 01731

ABSTRACT

The group retardation effect of the electrons in the earth's ionosphere can seriously limit the accuracy of time transfer by radio waves relayed via satellite. The dual frequency approach used in the GPS satellite system eliminates this potential problem, but other techniques, such as the use of models of the ionosphere, can only partially remove the ionospheric time delay error. Since the ionosphere is a dispersive medium the best approach to removing this error source is to directly measure the time delay at two, sufficiently widely spaced, frequencies as the dual frequency GPS system does automatically. If one does not have access to dual frequency GPS capability, various other techniques can be used with varying degrees of success in correcting for ionospheric time delay.

Work currently being done in the ionospheric research community should help increase the capability of the time transfer community to make corrections for ionospheric time delay effects on time transfer by satellite. 1) Research is continuing on improving theoretical models of ionospheric behavior, especially during disturbed conditions when the largest deviations from median model time delay values normally occur. 2) A network of stations making real time measurements of the time delay of the earth's ionosphere is in its preliminary phase and, when completed, will provide qualified DoD users with real time updates of the time delay corrections over large regions of the globe. 3) Work is in progress on development of what is expected to be inexpensive code-free receiving systems using the dual frequency signals from the GPS satellites to directly measure ionospheric time delay in multiple directions simultaneously to allow greatly improved corrections for ionospheric time delay. These code-free GPS receivers should provide an excellent correction for the effects of the ionosphere on time transfer by satellite.

Predictions of the magnitude of the current solar cycle are for a nearly record high cycle, with the maximum to be reached in late 1989, or early 1990, and staying high for several years thereafter. The implications for ionospheric time delay errors are for very high values for the next several years, with daytime ionospheric time delay values at 1.6 GHz from several tens of nanoseconds, to well over one hundred nanoseconds along the slant paths normally used with simultaneous satellite viewing for pairs of stations.

INTRODUCTION - TOTAL ELECTRON CONTENT

The accuracy of time transfer by means of radio frequency signals via satellites can be limited by the number of free electrons in the earth's ionosphere encountered along the path from the earth to the satellite. The magnitude of this effect is:

$$t = \frac{40.3}{3 \times 10^8 \times f^2} \int N \, dl$$

where f is the system operating frequency in Hertz, and N dl is simply the total number of electrons encountered along the path, or the Total Electron

Content, (TEC), along an equivalent column having a cross section of one square meter, from the earth to the satellite.

The greatest contribution to TEC comes from the F2 region of the ionosphere. A typical daytime, mid-latitude, high solar maximum electron density profile is illustrated in Figures 1A and 1B. The curve in Figure 1A is the log of N_e plotted versus height as normally shown by ionospheric workers. Since the TEC is represented by the area under the curve of a linear plot of N_e versus height, a more representative plot is illustrated in Figure 1B, where the abscissa is in linear units of electron density, rather than a logarithmic plot. Note that most of the contribution to TEC ocurs near the peak of the F2 region, which is fortunate, as ground-based ionosondes have been used since the 1930's to make continuous, routine measurements of the density at the peak of the F2 region. Ionosondes measure foF2, which is related to N_{max} by: $(foF2)^2 = 80.6 * N_{max}$ where foF2 is in MegaHertz, and M_{max} is in units of 10^6 el/cc.

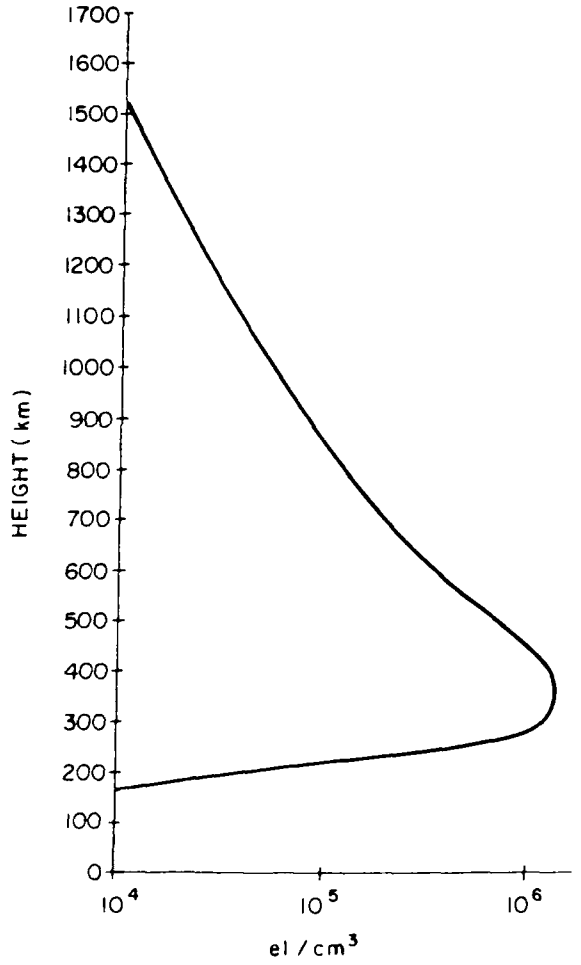

Figure 1A. Electron density (log scale) versus height.

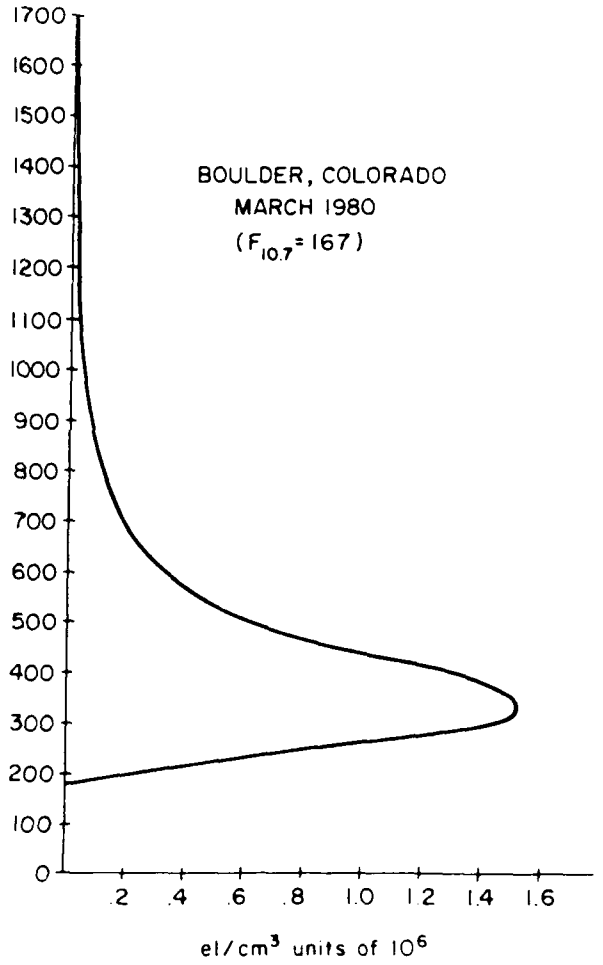

Figure 1B. Electron density (linear scale) versus height.

AVERAGE IONOSPHERIC MODELS

In the 1950's and 1960's, continuing to a more limited extent even today, upwards of 150 ionosondes were operated throughout the world to provide improved prediction capability for long distance high frequency propagation by means of ionospheric refraction. Various models of the critical frequency of foF2 were developed for this purpose, one of the more popular ones being commonly known as ITS-78 (Barghausen, et. al., 1969) after the report number which described the model. This model, among other things, characterized the 10 day average world-wide behavior of foF2 by Fourier temporal components and Legendre polynomial geographic coefficients ordered by mangetic, rather than geographic, latitude. The success of this experimental, data based empirical model, in representing the actual world-wide foF2 is due to the large amount of data available from ionosondes located in many regions of the world. Other characteristics of this models are discussed in Dandekar, 1982).

For the TEC parameter, data availability have been, and will likely continue to be, much more sparse. First, TEC measurements have been made generally by using measurements of Faraday polarization rotation using VHF signals of opportunity transmitted from geostationary satellite telemetry transmitters. A few lunar reflected Faraday rotation measurements in the late 1950's and early 1960's, and the TEC obtained from a few early, low orbit satellites did not contribute significantly to our knowledge of world-wide TEc behavior, at least not for modelling average ionospheric conditions. Only since the early to mid-1960's have TEC values been obtained on a more-or-less regular basis, but even today fewer than approximately one dozen stations regularly contribute TEC data, which can be used in TEC modelling purposes, to a world data center. The outlook for any world-wide model of TEC, made from direct measurements of TEC is poor, and will likely remain so for at least this current solar cycle maximum period of the next few years.

Fortunately, most of the contribution to TEC comes from near the F2 region density peak where models of foF2 are available. These foF2 models can be combined with some limited knowledge of topside ionospheric thickness obtained from topside ionospheric sounders and topside in-situ density measurements to produce a complete ionospheric height profile model. The most well known of these models is the one by Bent (Llewellyn and Bent, 1973), which uses ITS-78 coefficients for foF2 and topside exponential shapes from which the TEC is computed.

Other world-wide ionospheric electron density profile models, from which average TEC can be obtained, include the International Reference Ionospheric, (IRI), model, and the Penn State Mark III model (see Conkright, private communication). Several other models exist, but they are currently used only in by ionospheric researchers and are not generally available to users. All the models discussed here only attempt to represent the monthly average ionospheric profiles, though the Bent model is one which can be updated with real-time ionosonde and/or TEC measurements at up to several stations, to give a specification of the ionosphere over a nearby location.

Figure 2A illustrates the worldwide vertical time delay produced by the earth's ionosphere for solar maximum conditions in March 1980. Note that in the near-equatorial portion of the world there is a region where the mean vertical one-way ionospheric time delay is 50 nanoseconds. Major portions of the world have a vertical ionospheric time delay which exceeds 25 nanoseconds. In Figure 2B the worldwide vertical average time delay produced by the earth's ionosphere is plotted for solar minimum conditions. The highest vertical ionospheric time delay value is less than 25 nanoseconds, and only a small fraction of the world encounters a vertical time delay greater than 15 nanoseconds. The Bent model

was us. .o generate the contours of TEC shown in Figures 2A and 2B, and is a reasonably good representation of actual worldwide average ionospheric time delay error.

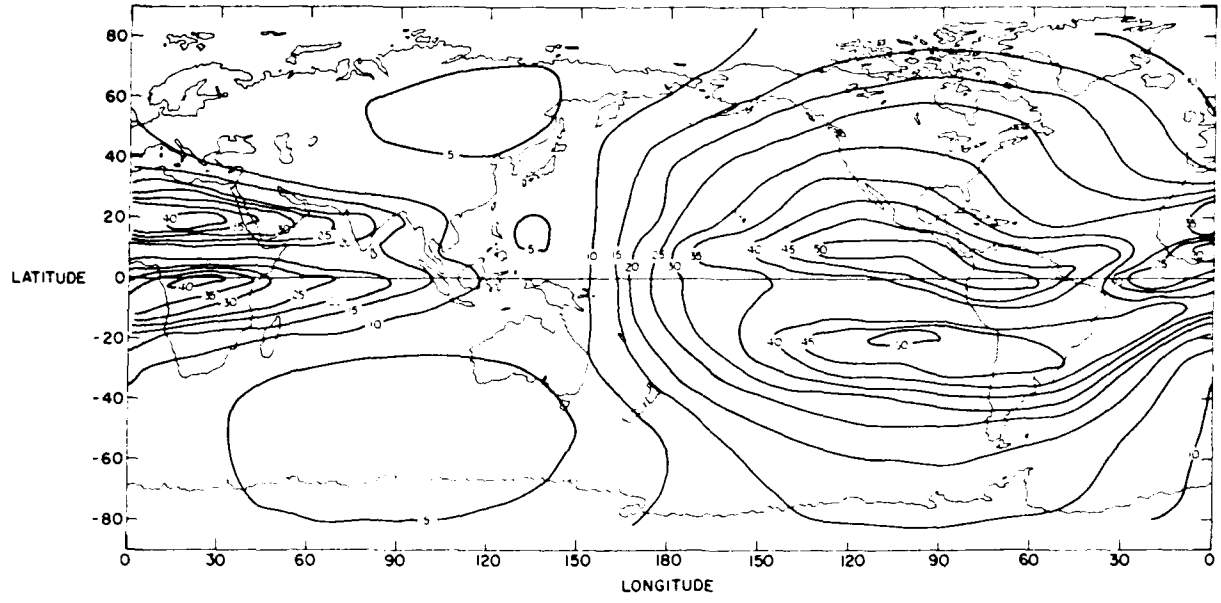

CONTOURS OF IONOSPHERIC TIME DELAY AT L1 (1575GHz) IN NANOSECONDS
MARCH 1980 ($F_{10.7}$ = 167)
2000 UT

Figure 2A. Contours of Ionospheric Time Delay at L1 (1.575 GHz) in Nanoseconds Solar Maximum ($F_{10.7cm}$ = 167) ; 2000 U. T.

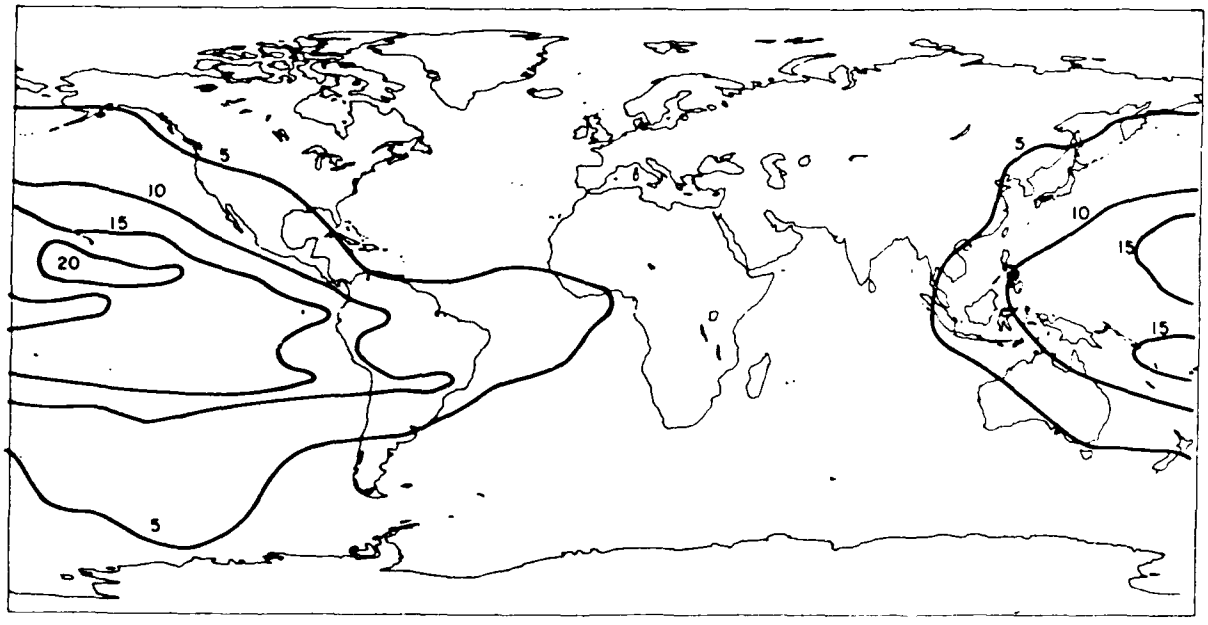

Figure 2B. Contours of Ionospheric Time Delay at L1 (1.575 GHz) in Nanoseconds Solar Minimum ($F_{10.7cm}$ = 70) ; 0000 U. T.

DAY-TO-DAY VARIABILITY OF IONOSPHERIC TEC

The day-to-day variability of ionospheric time delay for a mid-latitude station is illustrated in Figure 3 where a year's TEC data from Hamilton, MA is plotted versus local time in the form of 12 monthly overplots. Note that the annual highest values of daytime TEC do not occur during the summer months when the sun is at its highest elevation, but rather during the equinoxes. This is due to the effects of the heating of the neutral atmosphere with resulting greater loss rates from molecular species during the summer months. In Figure 3 one can also see the large day-to-day variability in the TEC values. The standard deviation of the actual TEC from its monthly mean behavior for most months is generally 20% to 25%, at least during the daytime hours when the absolute TEC values are greatest. Research is being carried out in the community of ionospheric physicists to attempt to understand and model, from first principles, the reasons for this large day to day variability. Geophysical effects which can modify the TEC from its monthly median behavior include: changing chemical composition at ionospheric heights, neutral wind variability, day to day changes in electric fields which drive ionization across the earth's magnetic field lines, and heat input into the high latitude ionosphere from magnetic storms which causes subsequent effects on TEC in the mid-latitudes.

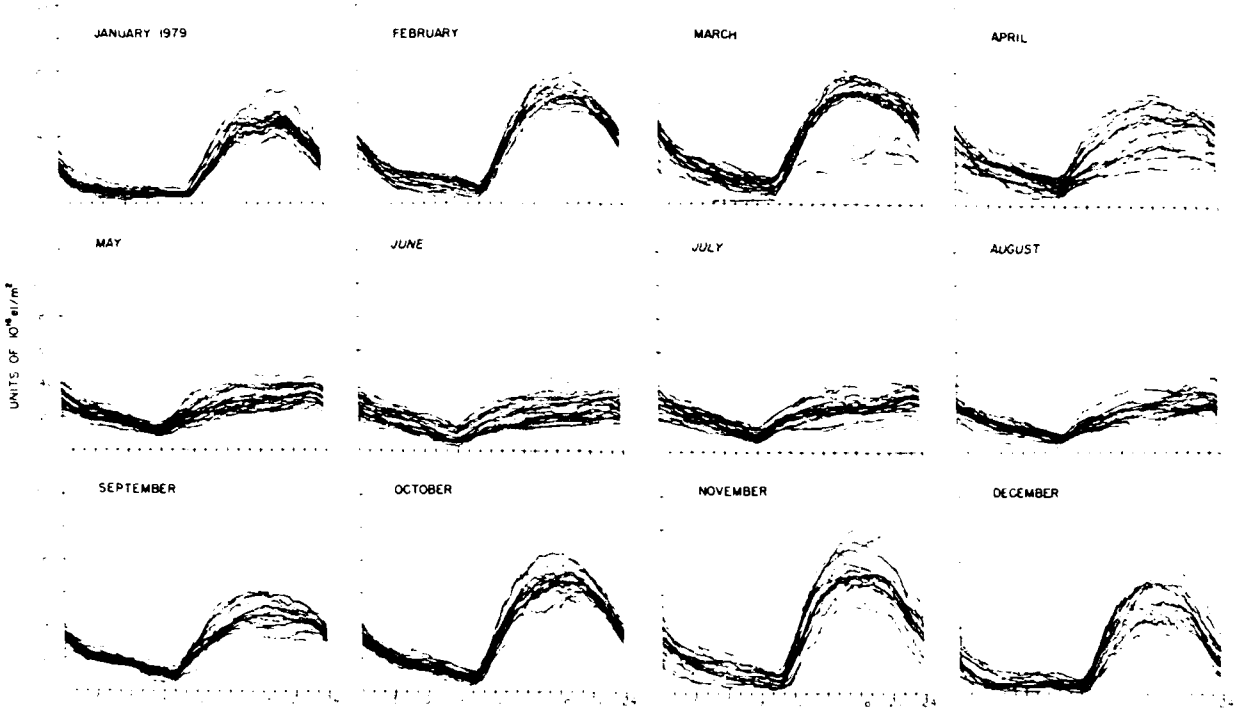

Figure 3. Monthly Overplots of Equivalent Vertical Total Electron Content for Hamilton, Massachusetts versus UT for 1979, (Near Solar Maximum).

SOLAR CYCLE ACTIVITY PREDICTIONS

The Ultra-Violet, (UV) flux from the sun is the major driver in long-term TEC behavior. However, short term changes in solar UV flux do not correlate well with day-to-day changes in TEC. Therefore, even if we had good direct measures of solar UV flux, they would not be very useful in solving the day-to-day TEC variability problem. However, long term changes in solar UV flux certainly would be helpful in predicting what magnitude of solar cycle effects to expect for the next solar cycle. Unfortunately, the state of the art of long

term solar predictions is not as precise as one would like. The present solar cycle, number 22, is the current example of uncertainty in long term solar activity predictions. Figure 4 depicts the sunspot activity over the last approximate 200 years. While there is a general 11 year periodic behavior, the magnitude of each cycle is different. The largest cycle ever recorded peaked in 1958 and the second and third largest cycle peaks were in 1981 and 1949, respectively. One prediction for the current cycle is for a maximum sunspot number of approximately 150, with a peak as early as February 1990. However, even now in late 1988, this prediction is uncertain, with the range of maximum sunspot numbers going from 115 to over 200, (Hirman, et. al., 1988). The system user who requires long term ionospheric time delay predictions should be aware that the science of long term solar UV flux predictions is far from exact, and he must be prepared to keep updated on current monthly, or at least several day averaged, measured values if he wants to make the best use of models which give monthly average TEC.

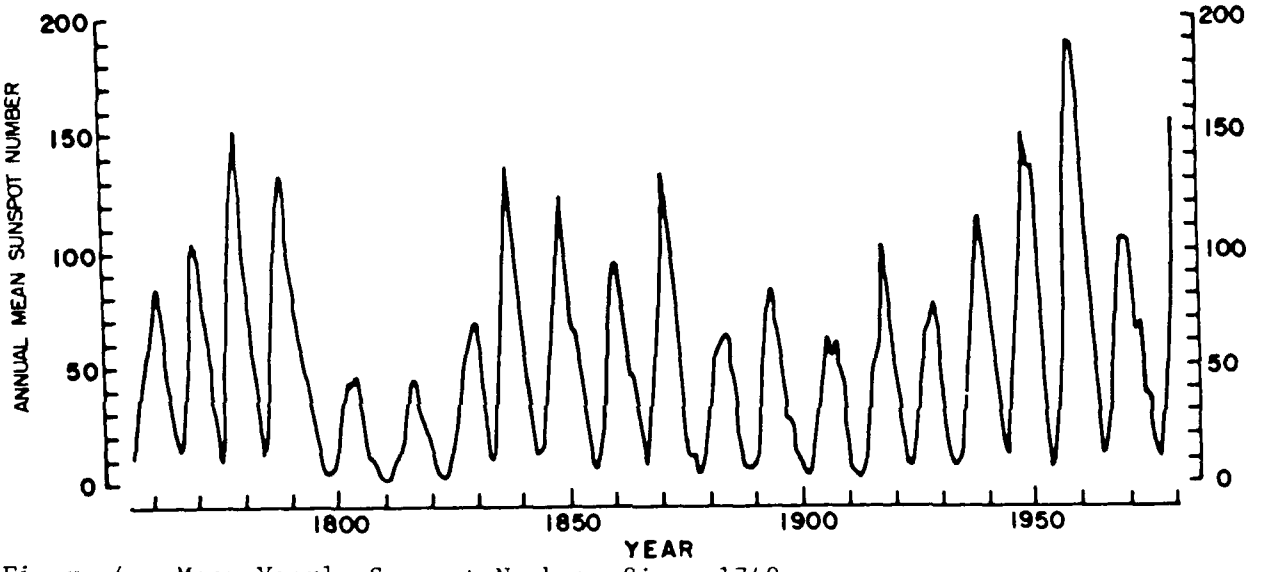

Figure 4. Mean Yearly Sunspot Numbers Since 1749.

MEAN MODELS VERSUS SPECIFICATION

It is one thing to make a model of monthly mean behavior of TEC, and several such models of the ionospheric F region exist which can be used for this purpose. It is quite another matter to be able to specify the actual TEC at the present time, or to predict it at a future time with an accuracy sufficient to satisfy time transfer needs. Depending upon the ionospheric correction accuracy required, one has several choices. These choices are:

1. Live with the ionospheric error; do nothing about it!
2. Correct for an approximate 50% rms ionospheric error by using the ionospheric algorithm designed for single frequency GPS system users.
3. Correct for approximately 75% of the rms ionospheric error by using a "state-of-the-art" ionospheric model, but with no attempt at updating with a real-time measurement.
4. Use a real-time ionospheric monitoring capability, but not necessarily measuring the time delay parameter directly, or making a measurement from the same direction, or from the same location as where the ionospheric correction is desired.

5. Incorporate a real-time ionospheric monitoring capability at an observation location to remove over between 90 to 95% of the ionospheric time delay error.

Let us take these five possibilities listed above in turn and discuss the implications of a user making any one of the above choices. Firstly, if a user completely ignored any possible ionospheric correction, he should at least become familiar with the price he is paying to neglect the effects of ionospheric time delay. That is, he should know when, and how much, the ionosphere is apt to be a major limitation to his time transfer accuracy. At least he should know that the ionosphere has a diurnal maximum in time delay, with that maximum occurring in the mid-afternoon period, the equinoctial values are larger than those during summer, and those within approximately plus and minus 15 to 20^{o} either side of the geomagnetic equator are usually the world's highest. He should also know that during years of high solar activity the ionospheric time delay values are from three to four times higher than during solar minimum years, and that during times of high geomagnetic activity the largest deviations from average ionospheric time delay behavior generally occur. Armed with those few facts about the ionosphere, the user in this first category will at least know when to expect large errors from the ionosphere in his attempts to transfer precise time via satellite.

Since it is relatively trivial to include the single frequency GPS user ionospheric time delay algorithm into a time transfer system, perhaps the majority of people will first use this option. The algorithm was described by Klobuchar, (1987), and tests of its accuracy have been described by Feess and Stephens, (1987). Its use is recommended for those who can be content with an approximate 50% rms ionospheric time delay correction. The user must be aware of the significance of rms deviations from the algorithm, and their potential limitations to overall accuracy.

Choice number three given above is best illustrated by Figure 5 in which ionospheric error correction is plotted versus a measure of model complexity. Note that there is no scale on the abscissa in Figure 5, but model complexity can be related to computer assets required to run the model.

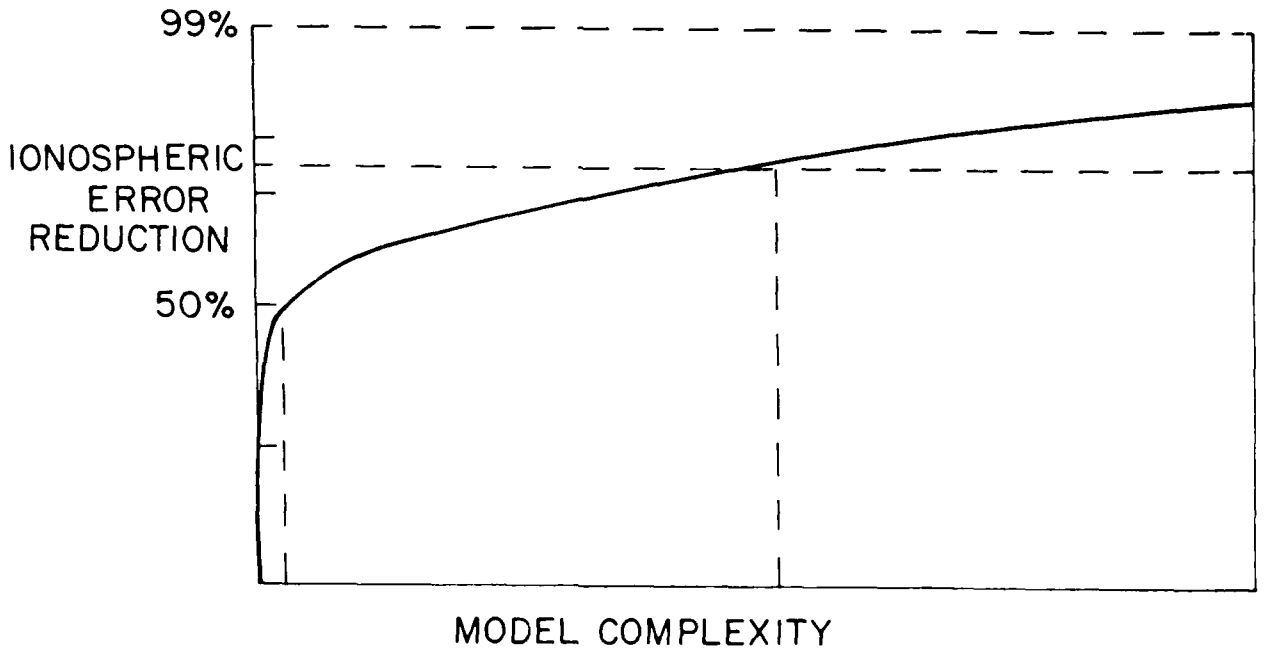

Figure 5. Ionospheric Error Reduction Versus Model Complexity.

For instance, the algorithm designed for a 50% rms ionospheric correction for single frequency GPS users is certainly not complex, yet it has been shown by Feess and Stephens, (1987), to give at least a 50% rms ionospheric error correction capability. State-of-the-art ionospheric models can be quite complex, and at present give only monthly mean ionospheric behavior without any near-real-time updating. Consequently, state-of-the-art ionospheric models can be expected to have as remaining errors any of the day-to-day deviations from monthly mean behavior, which are approximately 20 to 25%. By going from the simple ionospheric single frequency user algorithm, which gives an approximate 50% rms correction, to a state-of-the-art ionospheric time delay model, one adds a lot of model calculation complexity, yet only gains from 50% to perhaps 70-80% ionospheric error reduction. Some state-of-the-art ionospheric time delay correction models are available. These include the Bent Model, the International Reference Ionosphere, or IRI model, and the Penn State model. The first two can be obtained from the World Data Center-A, (Conkright, private communication), and the Penn State Model can be obtained from Nisbet, (private communication). The additional ionospheric time delay correction obtainable from any of these models, as compared with the model complexity, may make a user go to choices number 4 or 5 listed above.

If a user really needs to have the best currently available ionospheric time delay correction for his time transfer system then the thing to do is to make a dual frequency measurement of the actual ionospheric time delay along the actual satellite path of interest, such as the dual-frequency GPS system does automatically. Even with this technique one cannot expect to completely remove the effects of the ionosphere, but a correction exceeding approximately 95% of the ionospheric time delay can likely be expected. In order to make precise measurements of ionospheric time delay using two frequencies, their separation should be very wide, the transmitted carrier phase offsets must be known precisely, the receiving system must be carefully calibrated, careful attention must be paid to potential multi-path effects and the signal to noise of the signal must be high enough, or the integration time chosen long enough to make a precise measurement. It is doubtful that all these factors can be controlled accurately enough to make a 99% ionospheric error correction, but one in the mid 90% correction range is possible, if careful attention is given to these measurement details.

At least four groups are working on dual frequency, code-free receiving systems to make absolute measurements of ionospheric time delay using the GPS satellite signals. In a short time one of more such receiving systems, coupled with an ionospheric model to smooth over the necessary spatial distances between multi-satellite observations, may provide users with a correction for ionospheric time delay in the mid-90% range.

CONCLUSIONS

The total electron content of the earth's ionosphere can produce time delay errors in excess of 100 nanoseconds at the GPS L1 frequency. Models of the ionosphere vary in complexity, but even state-of-the-art models can correct, in general, for only 70 to 80% of the ionospheric time delay. The best correction for the effects of ionospheric time delay can only be made by an actual measurement along the same path as that along which the time transfer is being accomplished.

REFERENCES

Barghausen, A. L., J. W. Finner, L. L. Proctor, and L. D. Schultz, "Predicting Longterm Operational Parameters of High-Frequency Sky-wave Telecommunication Systems, ESSA Tech Report, ERL 110-ITS 78, 1969.

Conkright, R., private communication. For information on obtaining the International Reference Ionosphere, (IRI), or the Bent Model of the Ionosphere, contact Mr. R. Conkright, World Data Center-A, 325 Broadway, Boulder, Co. 80303.

Dandekar, B. S. "Ionospheric Modeling", AFGL-TR-82-0024, AD A115243, 1982.

Feess, W. A. and S. G. Stephens, " Evaluation of GPS Ionospheric Time-Delay Model", IEEE Trans. on Aerospace and Electronic Systems, Vol. AES-23, No. 3, pp 332-338, May 1987.

Hirman, J. W., G. R. Heckman, M. S. Greer, and J. B. Smith, "Solar and Geomagnetic Activity During Cycle 21 and Implications for Cycle 22", EOS, p. 962, October 18, 1988.

Klobuchar, J. A., "Ionospheric Time-Delay Algorithm for Single-Frequency GPS Users", IEEE Trans. on Aerospace and Electronic Systems, Vol. AES-23, No. 3, pp 325-331, May 1987.

Llewellyn, S. K., and R. B. Bent, "Documentation and Description of the Bent Ionospheric Model", AFCRL-TR-73-0657, AD 772733, 1973.

Nisbet, J., private communication, For information on obtaining the Penn State Ionospheric Model, contact: Professor, J. Nisbet at Communication and Space Sciences Laboratory, Penn State University, 316 Electrical Engineering East, University Park, PA 16802.

PAUL CASPER, ATMOSPHERIC RESEARCH SYSTEMS: Do you have any idea what the ionospheric delay is at ten times higher frequency? Up at Ku–Band?

MR. KLOBUCHAR: Yes, its one over f–squared, so it is one one–hundredth of these delays.

DR. WINKLER, USNO: I think that you can do another thing in order to reduce the effects and the errors, and that is just to observe during the night. The relative errors during the night are, of course, proportionally smaller. I have another question.

MR. KLOBUCHAR: Wait a minute. Do you have night at both places all the time. If you are trying to transfer time between here and India, under common view, it would be impossible to have night at both places.

DR. WINKLER: But we are not interested in common view. Most of the DoD does not use it for the simple reason that they cannot communicate. But I do have a question and that is: The phase noise which we have observed on dual frequency from six seconds to sixty seconds is much greater than on a single frequency. We have ascribed that, not to a spottiness or a phase jitter due to the ionosphere, but due to the measurement uncertainty. Is that correct?

MR. KLOBUCHAR: That is correct in nice, comfortable mid–latitudes. There are times when you can get in the auroral and polar cap regions some pretty fast phase jitter. Most certainly your observations have been under quiet mid–latitude conditions and on a second–by–second basis you would have very slow variations.

DR. LAPACHELLE, UNIVERSITY OF CALGARY: We already have the multi–channel receivers that can make dual–frequency phase measurements, by squaring the L2 without decoding. We also call them codeless receivers. Of course this type of receiver is quite different from the L1–L2 cross correlation. This type of receiver allows us to measure the rate of ionospheric variation over time. If we combine this technique with the L1–L2 cross–correlation technique that we saw yesterday, then we have a very powerful machine that does not require decoding of the code, and yet does everything we want as far as the ionosphere. I have the following question. Can you comment on the effect of phase scintillation on carrier phase lock? There are problems with that not only in the auroral zone, but also probably near the equator. This loss of phase lock has already been experienced and could possibly cause a lot of problems, at least for navigation. Could you comment on the extent of this, when the sunspot reaches a maximum?

MR. KLOBUCHAR: Yes, you are certainly correct that in the equatorial part of the world and maybe in the high latitudes there are times that you can get such severe phase scintillation that you can lose lock. The program office became aware of this in '79 or '80 we went to Ascension Island to make some measurements with a, at the time state–of–the–art receiver. Ascension Island is right down near the peak of the anomaly of very high peak electron density. Sure enough, the receiver was in and out of lock a lot of the time. We also made measurements in Kwajalein Island over in the Pacific and similar kinds of things happened. You could get amplitude fades in excess of 20–25 dB. We reported this to the JPO and they made some changes on their receivers to allow the receivers to "coast" through these amplitude fades and to continue at the same cycle rate that they had as they entered the fades. That helped the problem to some extent. In the high latitudes, we have had three receivers working up at Thule, Greenland for the last couple of years and we don't see as severe effects. We see some changes in group delay or absolute time change that are great. We haven't ever lost lock yet, I guess, but we are not at solar maximum. The times when this occurs in the equatorial region are well known. It is very patchy and only occurs from local sunset to around midnight, but only in patches. I don't

think that it will put anybody out of business unless they need to know it right then and there. Certainly JPO has stations all over this area. I asked them how they could tell where the satellites are when they are in this very strongly scintillating region and they said that they just have a little higher errors and average a little longer and discard data if it is too bad. They don't have a real time requirement. The time transfer community can do the same thing because their requirement is not real time either. The problem is different if you are a naval vessel that wants to launch a missile and needs positions right away. In the high latitudes, you don't have a simple diurnal variation like you do in the equatorial region where it starts up like clock work at sunset and goes on to midnight almost every night for six months of the year. The high latitudes are not as predictable, but the problem is not quite as severe there.

SKIP OSBORNE, ALLEN OSBORNE ASSOCIATES: Even though the spread between L1 and L2 isn't as great as you would like it, is there any advantage to using L3?

MR. KLOBUCHAR: No. It isn't on all the time and it isn't even as far apart as L1 and L2. They didn't do a bad job in selecting L1 and L2.

MR. OSBORNE: T sub g–is there anything that you recommend? It sounds like we are stuck.

MR. KLOBUCHAR:I think that we had better continue this off line since we are out of time.

AN ADAPTIVE ALGORITHM TO EVALUATE CLOCK PERFORMANCE IN REAL TIME*

Dr. James A. Barnes
Austron
Boulder, Co.

Abstract

Kalman filters and ARIMA models provide optimum control and evaluation techniques (in a minimum squared error sense) for clocks and precision oscillators. Typically, before the models can be used, an analysis of data provides estimates of the model parameters (e.g., the phi's and theta's for an ARIMA model). These model parameters are often evaluated in a batch mode on a computer after a large amount of data is obtained.

An alternative approach is to devise an adaptive algorithm which "learns" the important parameters while the device is being used and up–dates the parameters recursively. Clearly, one must give up some amount of precision if one deviates even slightly from the truly optimum techniques, but, as this study shows, the costs in performance are not large at all. If one chooses the best sampling intervals, the loss in precision can be negligible.

The physical models used in this paper are based on the assumption of a combination of white PM, white FM, random walk FM, and linear frequency drift. In ARIMA models, this is equivalent to an ARIMA(0,2,2) with a non–zero average second difference. Using simulation techniques, this paper compares real–time estimation techniques with the conventional batch mode. The criterion for judging performance is to compare the mean square errors of prediction between the batch mode and the recursive mode of parameter estimation operating on the same data sets.

INTRODUCTION

Before working directly on the ARIMA(0,2,2) models [1], it is of value to establish a few important relations. An ARIMA(1,0,0) model is often referred to as an exponential filter since its impulse response function is an exponential. That is:

$$\begin{aligned} x_n &= \phi X_{n-1} + a_n \\ &= \phi^n \qquad \text{for } n = 1,\ 2,\ \ldots \end{aligned} \tag{1}$$

Where the input to the filter, a_n, is taken to be $a_0 = 1$ and $a_n = 0$ for $n > 0$ (the unit impulse). This filter is the digital equivalent of a simple $R - C$ low–pass filter with $\phi = \exp(-t/RC)$ where

*Work supported in part by the Defense Communications Agency, DCA 100–88–c–0072

t is the time interval between steps in the counting index, n, and R and C are the resistance and capacitance values in the analog filter. In frequency domain, the filter transfer function is unity for low frequencies and drops off at -6dB/octave from the cut–off frequency, f_c , given by:

$$f_c = 1/(2\pi RC) \tag{2}$$

Given the cut–off frequency, f_c, and the sample time interval, t, the ARIMA coefficient, ϕ, can be calculated with the equation:

$$\phi = \exp(-2\pi f_c t_0) = \exp(-t_0/\tau) \tag{3}$$

Thus, for a given physical system, the ARIMA parameter is dependent on the data sampling rate.

The inverse function for the ARIMA(1,0,0) is just an ARIMA(0,0,1) which can be seen by solving Eq. 1 for a_n. Such a filter would be constant for the low frequency end changing to an increase of gain by +6dB/octave above the same cut–off frequency derived above.

The ARIMA models considered here are models for the phase of the clock comparisons (not their instantaneous frequencies). We can begin with a physical model of a clock with pure White FM. Since the ARIMA model is for phase, this first example would be given by an ARIMA(0,1,0) model, a random walk of phase. The power spectral density (of phase) for this noise is that of a constant decrease of -6dB/octave everywhere below the Nyquist frequency, $1/(2t_0)$.

We can add white noise modulation to this model by going to an ARIMA(0,1,1) model where the moving average parameter, θ, is computed from Eqs. 2 and 3, above, for $\tau = RC$. In actuality this is not an adequate model for many real clocks. One often encounters more low frequency divergent noises than the ARIMA(0,1,1) which require an additional integration: that is, one needs either an ARIMA(0,2,1) or an ARIMA(0,2,2). Physically, the ARIMA(0,2,1) model corresponds to a superposition of white FM and random walk FM. Again the transition between the two noise regimes is accomplished by using Eqs. 2 and 3, above.

If one now adds white PM one must go to the ARIMA(0,2,2) model (see Fig. 1), which has two break points corresponding to the transitions between random walk and white FM and between white FM and white PM. The equations above allow one to calculate the two parameters separately, say, θ_1' and θ_2', for theta–values of two cascaded, MA filters. These two filters can be combined in one MA(2) filter whose theta–parameters must be combined as factors to realize the correct MA filter. This combination is obtained as follows:

$$(1 - \theta_1' B)(1 - \theta_2' B) = (1 - \theta_1 B - \theta_2 B^2) \tag{4}$$

which yields $\theta_1 = (\theta_1' + \theta_2')$ and $\theta_2 = -(\theta_1'\theta_2')$ where B is the index lowering operator [1] and θ_1' and θ_2' are calculated using Eqs. 2 and 3. A linear frequency drift can also be important.

ADAPTIVE APPROACH TO TESTING ARIMA PARAMETERS

There are many methods of estimating parameters — for example, just a guess is one means. Of importance are issues such as bias, confidence intervals, efficiency, and likelihood. While it is easy to present various estimating procedures that "work" it is often difficult to evaluate how well they perform. This section develops theoretically the effects of errors in the ARIMA parameters.

Using simulation techniques, these errors are evaluated in "real–time" and compared to the conventional batch method, after the fact. The theoretical consequences of parameter errors are surprisingly mild. That is, many models are robust in regard to fairly poor estimates and they can give surprisingly good results. Still there are regions of operation where problems can arise. For example, taking data

very frequently does not improve one's knowledge of basically long-term performance. Knowledge of the long-term performance simply requires long-term data.

The adaptive (real-time) estimation is based on the fact that an ARIMA(0,0,1) has an autocorrelation function given by:

$$R(n) = \begin{cases} 1 & \text{for } n = 0 \\ -\theta/(1+\theta^2) & \text{for } n = 1 \\ 0 & \text{otherwise} \end{cases} \tag{5}$$

Figure 2 presents a block diagram of an adaptive algorithm which effectively servos the theta-estimate (denoted "ϕ") to the "true" theta-value and also provides a current estimate of the variance of the residuals and a drift estimate. Basically the algorithm computes contributions to the first autocorrelation coefficient which in turn adjusts the estimated theta-value, effectively driving the first autocorrelation coefficient of the residuals to zero. The first autocorrelation coefficient of the residuals (given by Eq. 8, below) is proportional to the difference — (see Ref. [1]) giving both direction and value for the servo. Figure 3 depicts a simulation of the servo performance. Although the servo "works" we need to compare its performance with a conventional batch approach for estimation.

THE ARIMA(0,2,1) MODEL

Figure 4 is a diagram of the forecast system for an ARIMA(0,2,1) noise model. In this case, theta is the "real" parameter which is unknown, but is estimated with the value of phi. If phi were to equal theta, then the system would provide an optimal forecast of X_n. Since there will always be some error in the estimate of theta, it is of value to explore the consequences of such an error. The following is a detailed description of the estimation process and the evaluation of the errors caused by an error in phi.

Following Fig. 4, the data, X_n, are the only observables from the clock comparisons and the model is white noise FM and random walk FM: That is, an ARIMA(0,2,1) model. I explicitly assume that the model is a good model, but theta is unknown. Theta can be estimated by the methods given in Ref. [1], or by recursive filters developed here.

The output data, X_n, are filtered with an "inverse" filter and the residuals, W_n, are obtained. In the Box and Jenkins method, phi would be adjusted to give minimum variance to W_n. This, however, is accomplished in a batch mode after the fact and not in real-time. Regardless of how theta is estimated, phi is used in the forecaster as shown in Fig. 4: Indeed, there is no other value to use. With W_n as input to the forecaster (the switch in Fig. 4 in the "up" position), the system is allowed to run for a time to let all transients die out. At this point the estimated output, $\hat{X}_n = X_n$ exactly since the inverse filter is the exact inverse of the forecast filter.

At some point in time, $t = n + 1$, W_n is no longer available as input to the forecast filter and its input is set to zero (switch in the "down" position). For the first forecast value $\hat{X}_n + 1$, the two previous values, X_n and X_{n-1} are available to use in the forecast as shown. The error of the forecast (after the fact), can be found by subtraction of the two equations:

$$\begin{array}{rcll} X_{n+1} & = & 2X_n - X_{n-1} + a_{n+1} - \theta a_n & \\ \tilde{X}_{n+1} & = & 2X_n - X_{n-1} - \theta W_n & \\ \hline \delta_1 & = & X_{n+1} - \hat{X}_{n+1} & = \quad a_{n+1} - \theta a_n - \theta W_n \end{array} \tag{6}$$

where δ_1 is the error in the first forecast.

Following Box and Jenkins [1], W_n can be expressed as an infinite series which incorporates the psi–weights and the uncorrelated innovations, a_n:

$$W_n = \sum_0^\infty \Psi_i a_{n-i} \tag{7}$$

The psi–weights can be expressed in terms of phi, theta, and the innovations, a_n, as shown below by requiring W_n to satisfy the equation (see Fig. 4):

$$W_n - \phi W_{n-1} = a_n - \theta a_{n-1} \tag{8}$$

for all n, the result is given by:

$$\Psi = \begin{cases} 1 & \text{for } i = 0 \\ (\phi - \theta)\phi^{i-1} & \text{for } i = 1,\ 2,\ 3,\ \cdots \end{cases} \tag{9}$$

We can now evaluate the expected square of the first forecast error as:

$$E[\delta^2] = \sigma^2[1 + \frac{(\phi - \theta)^2}{1 - \phi^2}] \tag{10}$$

For phi equal to theta we obtain the classical result that the variance of the first forecast error is just the variance of the innovations.

We can repeat this calculation for $t = n + 2$ by using the forecast value X_{n+1} in place of the (unknown) value, X_{n+1}. Similarly, for $t = n + 3$ and so forth. The result can be summarized in the following formula for the mean square time interval error for M lags in the future:

$$E|\delta_M^2| = M\sigma_a^2 \left\{1 + (1 - \theta)(M - 1)[1 + (1 - \theta)(2M - 1)/6] + M(\phi - \theta)^2/(1 - \phi^2)\right\} \tag{11}$$

This formula has been verified using simulation techniques.

There are two points to make in regard to this relation: (1) for phi equal to theta the result is identical to the classical results as it should be, and (2) as M gets larger, the variance grows as M–cubed but the term proportional to $(\phi - \theta)$ grows as M–squared. That is, for sufficiently large M, the errors of parameter estimation become unimportant. Figure 5 shows the regions of forecast errors (1) primarily due to conventional analyses and (2) those due primarily to an error in the estimate of theta, i.e., phi.

Figure 5 shows clearly that problems develop near theta=1 and near phi=1 with phi and theta not near each other in value. The problems near theta equal to 1 can be reduced by having longer term data. Having more frequent data doesn't help.

COMPARISONS BETWEEN ADAPTIVE AND CONVENTIONAL PARAMETER ESTIMATION

Given an ARIMA model corresponding to a physical model we can simulate a noise sample and treat the data as if it were real–time data and estimate the parameters recursively. The same data can be treated in batch mode and find those estimates which minimize the sum of the squares of the residuals. Table 1 summarizes the results of the estimation process. The program generated 100 noise samples each of 200 data points in duration. Each sample noise was processed through the adaptive estimation procedure developed here and the conventional Box and Jenkins [1] treatment. Of course, the "true" values of the parameters are also known since this is only a simulation.

TABLE 1 ARIMA(0,2,1) Theta = .9049 Sig-A = 1.1051			
Quantity		Conventional Method	Adaptive Method
Phi	(Actual=.9049)	.8983	.8577
	Std. dev. of mean	.0042	.0074
	Bias rel. Actual	-.0066	-.0471
	T-ratio	-1.58	-6.38
Sig-A	(actual=1.1051)	1.1161	1.1726
	Std. dev. of mean	.0119	.0146
	Bias rel. Actual	.0111	-.0674
	T-ratio	.93	-4.63

As expected, the conventional estimates are more accurate and more precise than the adaptive methods developed here. Still, with reference to Fig. 5, even fairly large errors in phi relative to theta are soon covered by the conventional errors. Table 1 shows that for theta = .9049, the adaptive method produces statistically significant biases (T–ratios of -4.63 and -6.38).

ARIMA(0,2,2) NOISE ANALYSIS

To estimate the theta–value the servo was based on the fact that an ARIMA(0,0,1) model has only the zeroth and first autocorrelation coefficients non–zero. An ARIMA(0,0,2) model has an additional non–zero coefficient at lag 2, which is strongly dependent on the second MA coefficient. The new servo has a separate loop which takes samples of the (lag n) (lag n-2) product and adjusts ϕ_2 to null the average similarly to the loop shown in Fig. 2, for ϕ_1.

Similarly to Fig. 3, Figure 6 depicts the transient response of the ARIMA(0,2,2) adaptive estimation. As noted above, the important performance is that of forecast errors not the intermediate values of θ_1 and θ_2 shown in Fig. 6. Still it does show how the parameters stabilize.

As noted above, the means of comparing algorithms is to compare the forecast errors for similar data situations. The Box and Jenkins method can be used to estimate the forecast errors using the "psi–weights", as in equations 8 and 9, above. The model for consideration now is as ARIMA(0,2,2). The theoretical forecast errors for the model can be computed similarly to Eq. 11:

$$E[\delta_M^2] = \sigma_\alpha^2\{1 + (M-1)[(1+\theta_2)^2 + M(1-\theta_1-\theta_2)[1+\theta_2+(1-\theta_1-\theta_2)(2M-1)/6]]\} \qquad (12)$$

For the complete model, a linear frequency drift term can be added. That is, we assume that one has an initial data set (chosen to be 100 time differences between a pair of clocks). The number of data points are the same for both the adaptive servo and the batch processing. The introduction of a non–zero frequency drift significantly affects both the adaptive servo and the conventional Box and Jenkins analysis. Equation 13, below, provides the additional, independent error to the forecast errors of Eq. 12 due to frequency drift:

$$D_M^2 = \sigma_a^2\{1 + (1-\theta_1)^2 + (\theta_1+\theta_2)^2 + \theta_2^2 + (M-2)(1-\theta_1-\theta_2)^2\}/M^2 \qquad (13)$$

This noise addition assumes that while θ_1 and θ_2 are known exactly, the drift term is estimated from the mean second difference time error and its variance. Appendix A contains a derivation of Eqs. 12 and 13.

It is important to realize that the actual errors in real applications are calculated on the basis of the ESTIMATED model parameters, not the "true" parameters which are unknown. This usage of the estimated parameters renders the computed errors a bit on the optimistic side because Eq. 12 does not include the errors in the estimated parameters. Figure 7a shows the theoretical contributions of the conventional Box and Jenkins analysis and the imperfect knowledge of the drift rate for various theta values. Figure 7 gives graphical views of Eqs. 12 and 13.

Figure 8a shows the theoretical forecast errors as calculated using Eqs. 12 and 13. For simulation purposes, the "true" parameter values are known. Simulation techniques allow one to verify Eqs. 12 and 13 by repeated calculation of the forecasts compared to the "true" values after the fact.

The bases for the data plotted in Fig. 8a, b, and c are:

1. ARIMA (0,2,2) model
2. Linear frequency drift
3. Data length of 100 points (Initial randomization of filter required)
4. Forecast 100 lags beyond the data length using estimated parameters
5. Repeat above for independent noise samples for at least 500 individual runs.

For Fig. 8a, the errors in the forecast for the simulated data are -.22 dB worse than the theoretical value. (This number is probably within the uncertainty limits of the experiment.) The solid line is the theoretical result of Eqs. 12 and 13. The small dots near the solid line are the results of simulation.

The next step was to estimate the theta parameters using a conventional Box and Jenkins approach. Figure 8b indicates the impact on the forecasts using imperfect parameters. The error is now about 1.01 dB worse than optimum after 100 lags. Theoretical errors (i.e., solid line) are identical in Figs. 8a, 8b, and 8c, as calculated using Eqs. 12 and 13.

The third step is to simulate the results of a "real-time" estimation procedure where the parameters are "learned" during a single pass through the 100 data points. That is, the adaptive approach is used for the forecasts. As shown on Fig. 8c, the error after 100 lags is now 1.14 dB relative to optimal or .13 dB relative to the Box and Jenkins approach. It is interesting to note that, at least for the given parameters, the adaptive forecaster is close to the Box and Jenkins forecaster in performance.

With the above approach, we can now evaluate the adaptive forecasting performance for various physical models by using different "true" values for the theta parameters, drift rate, and noise level. Further, we can estimate the relative performances of "perfect" parameters, Box and Jenkins estimations, and "real-time", adaptive method. In effect, we can evaluate the costs in accuracy of using the much simpler adaptive approach.

Reference

- G.E.P. Box and G.M. Jenkins, "Time Series Analysis", Holden-Day San Francisco, 1970.

APPENDIX A

PSI-WEIGHTS FOR AN ARIMA (0, 2, 1)

Given an ARIMA(0, 2, 1) Model:

$$X_n - 2 \cdot X_{n-1} + X_{n-2} - a_n + \theta \cdot a_{n-1} = 0 \qquad \text{A-1}$$

We define the Ψ-weights by the relation:

$$X_n = \sum_{i=0}^{\infty} \Psi_i \cdot a_{n-1} \qquad \text{for } n = 0 \text{ to } \infty \qquad \text{A-2}$$

In order to have both (A-1) and (A-2) valid for all n, we substitute (A-2) into (A-1) and group coefficients of the a_n together and require the resulting coefficient to vanish, That is, the net coefficient of a_n is just $\Psi_0 - 1$. The first few relations for the Ψ-weights are:

$$\begin{aligned} \Psi_0 &= 1 \\ \Psi_1 &= (2 - \theta) \\ \Psi_2 &= (3 - 2 \cdot \theta) \\ \Psi_3 &= (4 - 3 \cdot \theta) \\ &\vdots \\ \Psi_m &= (m + 1) - m \cdot \theta \end{aligned} \qquad \text{A-3}$$

The mean square forecast errors (See Box and Jenkins) are given by:

$$E\left\{\delta_M^2\right\} = \sigma^2 \sum_{m=0}^{M-1} \left\{(1-\theta)^2 \cdot m^2 + 2 \cdot (1-\theta) \cdot m + 1\right\} \qquad \text{A-4}$$

$$= M\sigma_a^2 \{1 + (1-\theta)(M-1)\,[1 + (1-\theta)(2M-1)/6]\} \qquad \text{A-5}$$

PSI–WEIGHTS FOR AN ARIMA (0, 2, 2)

Given an ARIMA (0, 2, 2):

$$X_n - 2X_{n-1} + X_{n-2} - a_n + \theta_1 a_{n-1} + \theta_2 a_{n-2} = 0$$

A-6

We define the Ψ–weights as is (A–2). The first few relations for the Ψ–weights are:

$$\begin{aligned}
\Psi_0 &= 1 \\
\Psi_1 &= 2 - \theta_1 \\
\Psi_2 &= 2(2 - \theta_1) - (1 + \theta_2) \\
\Psi_3 &= 3(2 - \theta_1) - 2(1 + \theta_2) \\
&\vdots \\
\Psi_m &= \begin{cases} m(1 - \theta_1 - \theta_2) + (1 + \theta_2) & \text{for } m > 0 \\ 1 & \text{for } m = 0 \end{cases}
\end{aligned}$$

The mean square forecast errors become:

$$E\{\delta_M^2\} = \sigma_a^2 \left\{1 + (M-1)\left[(1+\theta_2)^2 + M(1-\theta_1-\theta_2)\left[1+\theta_2+(1-\theta_1-\theta_2)(2M-1)/6\right]\right]\right\}$$

APPENDIX B

Mean and variance of an ARIMA (0, 2, 2)

$$Z_n = a_n - \theta_1 a_{n-1} - \theta_2 a_{n-2} + Av$$

B–1

The sum of the first M values of Z_n are:

$$\sum_{n=1}^{M} Z_n = a_M + (1-\theta_1)a_{M-1} + (1-\theta_1-\theta_2)a_{M-2} + \cdots - (\theta_1+\theta_2)a_0 - \theta_2 a_{-1} + M \cdot Av$$

B–2

Since the a_n are independent random numbers with zero mean, the mean value is obtained by dividing the sum, above, by M. The variance of the estimate is obtained by taking the expectation value of the square of (B–2). That is:

$$V^2 = \sigma^2 \left\{ 1 + (1-\theta_1)^2 + (\theta_1+\theta_2)^2 + (M-2)(1-\theta_1-\theta_2)^2 + \theta_2^2 \right\} / M^2$$

B–3

where V^2 is the variance of the estimated mean of Z_n.

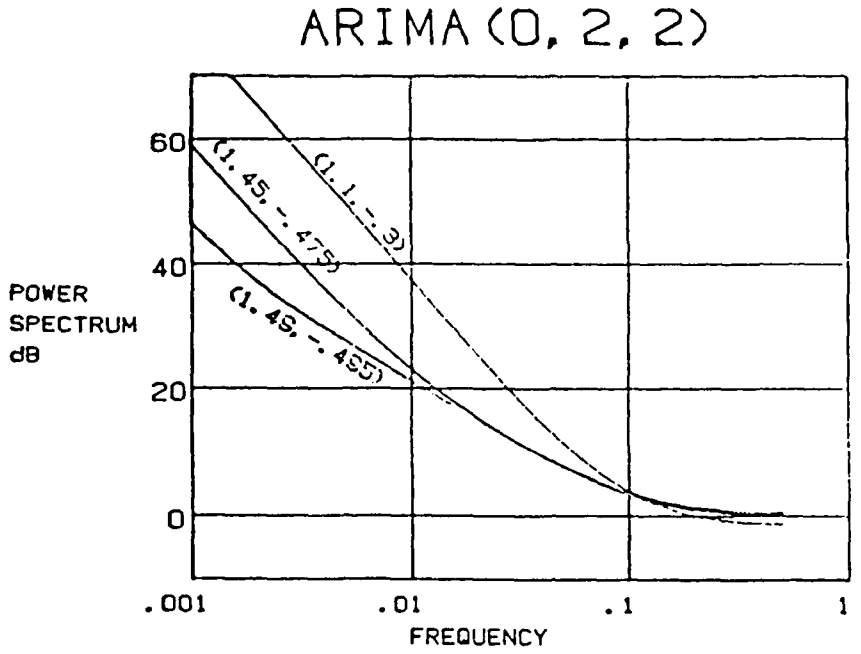

Fig. 1 Power Spectra for θ_1, θ_2.

FIG2, ARIMA(0,2,1) Parameter Estimation

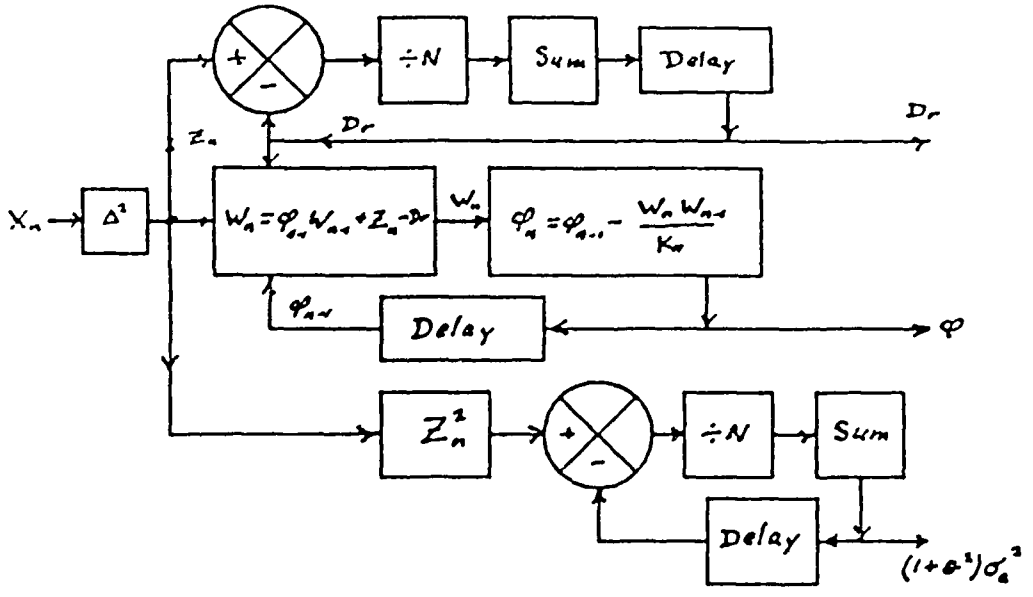

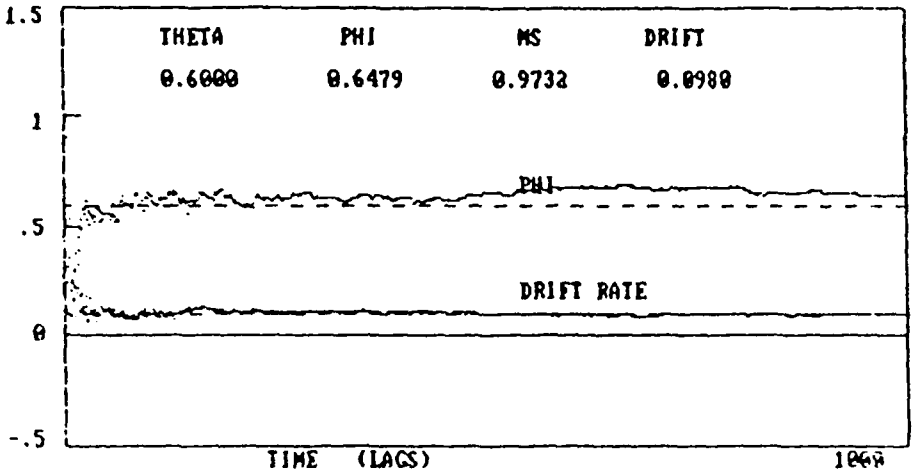

Fig. 3 Transient Response for an ARIMA(0,2,1)

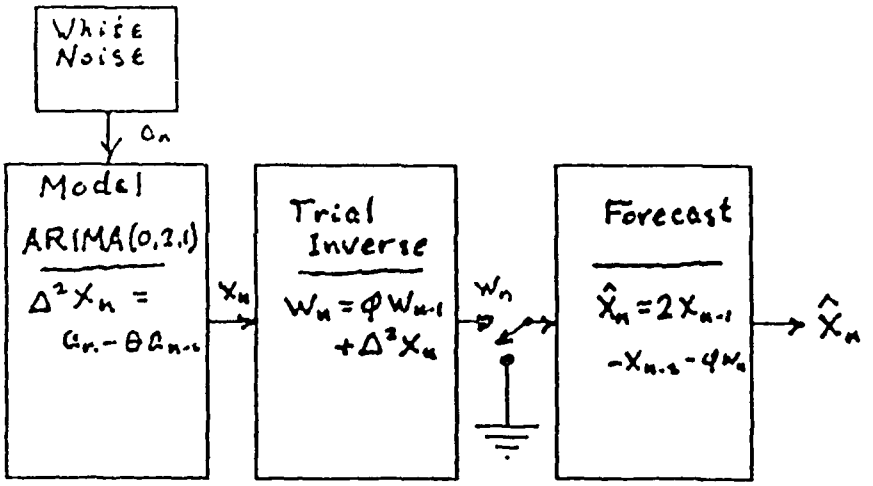

FIG. 4 ARIMA FORECAST SCHEME

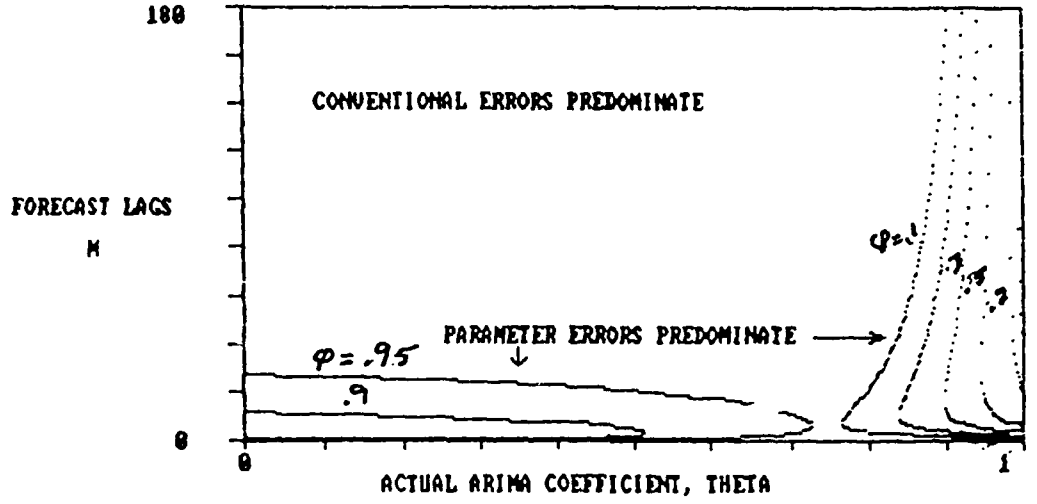

Fig. 5 Predominate Errors for ARIMA(0,2,2)

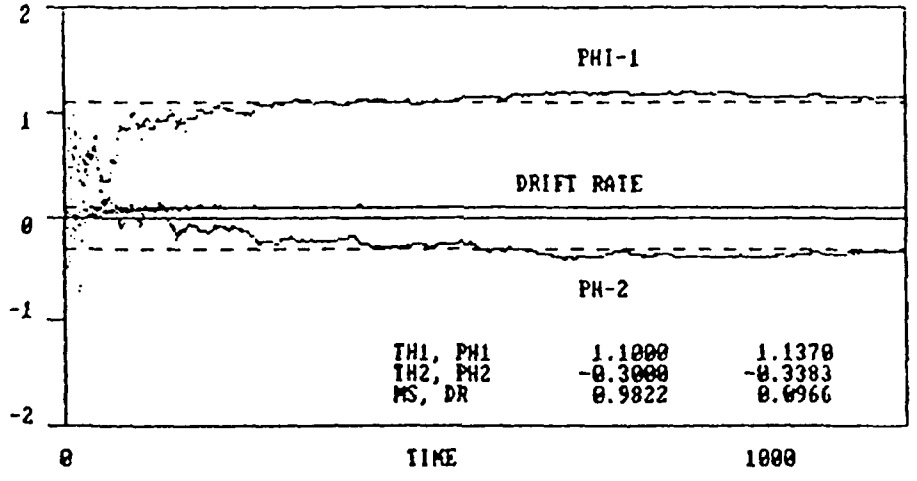

Fig. 6 Transient response for ARIMA(0,2,2)

FIG. 7 FORECAST TIME ERRORS FOR AN ARIMA (0, 2, 2)

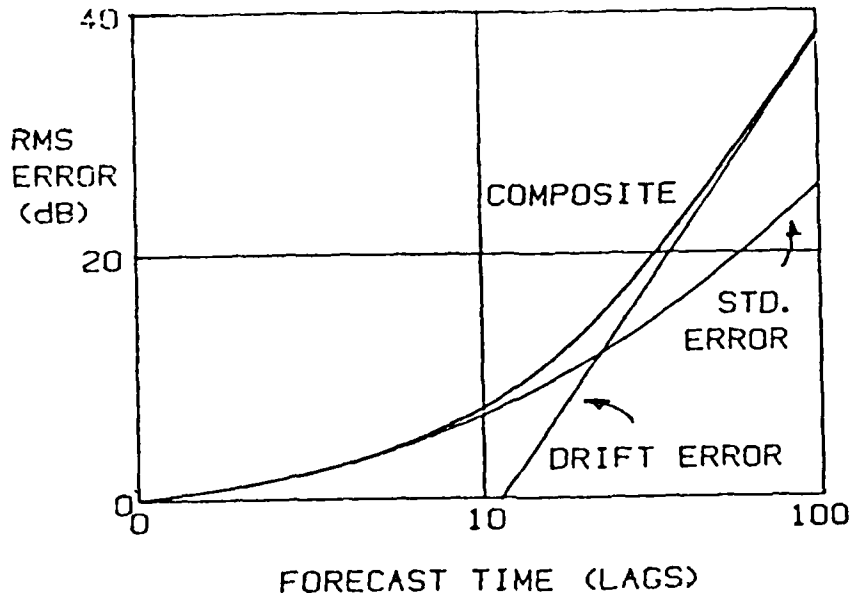

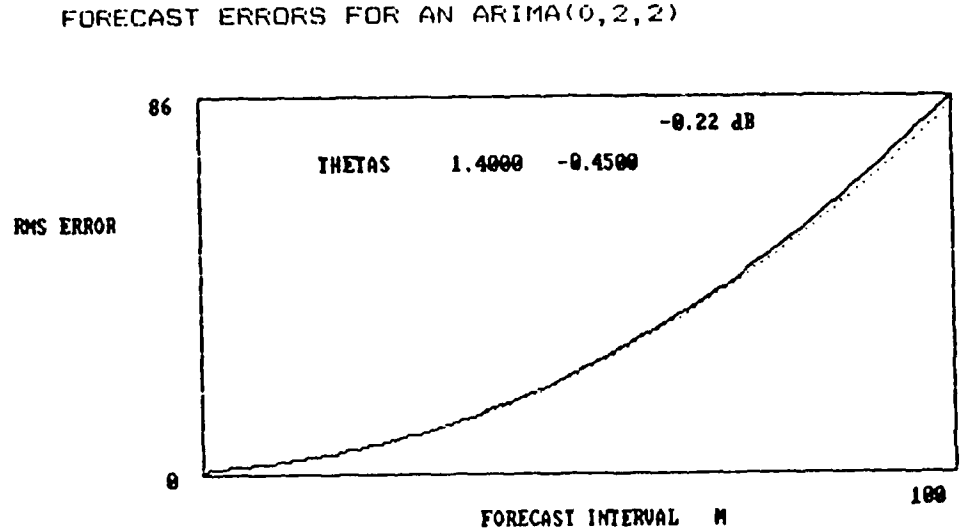

Fig. 8a Errors Using Exact Parameters

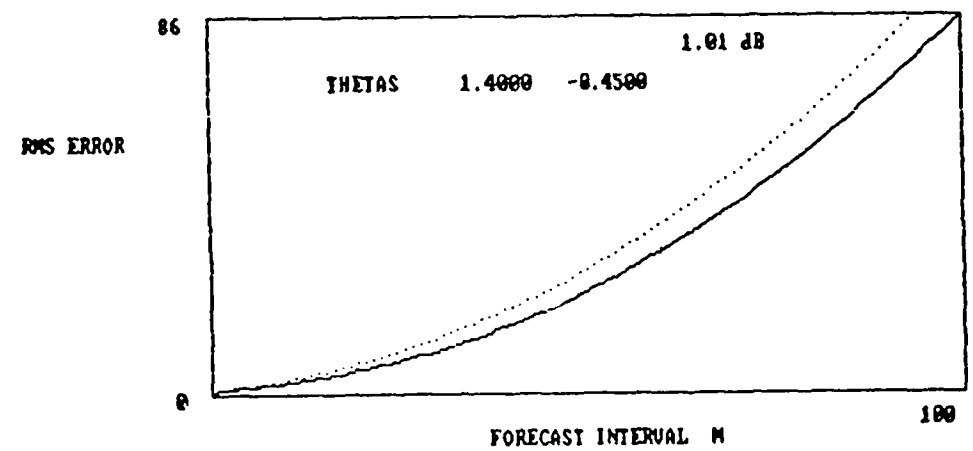

Fig. 8B Errors Using Box/Jenkins Estimation

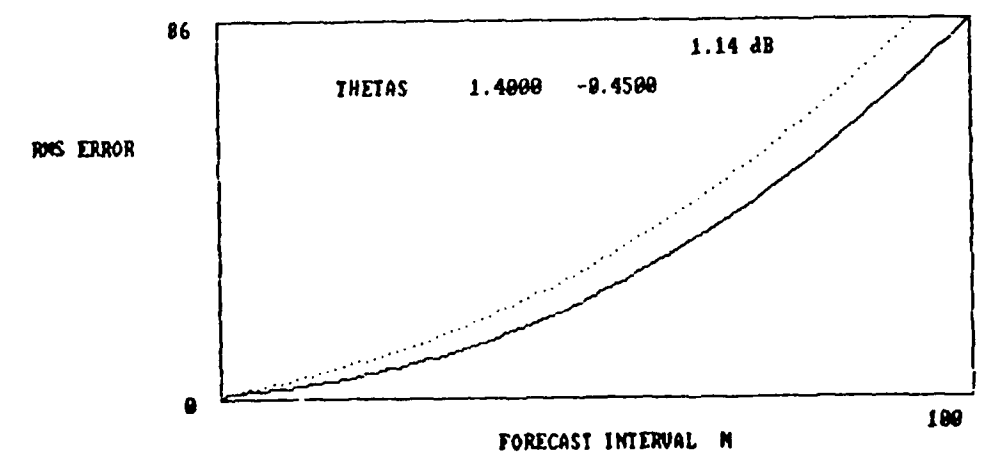

Fig 8C Errors Using Adaptive Estimation

QUESTIONS AND ANSWERS

DR. GERNOT WINKLER, USNO: Since you can do your parameter estimation on the run, you can, of course, allow a change in the characteristics of your frequency standards with time. Its an adaptive method.

DR. BARNES: That is true. It will adapt to the new value if the standard changes. I guess that I should point out on the last plot, I am assuming that I have 100 points of data and I am forecasting for the next 100 points. It is not a lot of data that I am working with. We are still seeing agreements to a fraction of a dB in this approach.

THE EFFECTS OF DATA PROCESSING AND ENVIRONMENTAL CONDITIONS ON THE ACCURACY OF THE USNO TIMESCALE

Lee A. Breakiron
U. S. Naval Observatory
Time Service Department
34th and Massachusetts Avenue, N. W.
Washington, DC 20392-5100

Abstract

Humidity has significant long-term effects on cesium clock rates that may be controlled environmentally, but not during data processing. Allan variances are minimized at a temperature depending on the clock and clock type. There is no dependence of Allan variance on manufacturing batch. A surprisingly large fraction of clock rate and variance changes may be attributed to human interference or the need for it. Little or no improvement is obtained by altering the unity-or-zero weighting scheme of the current USNO timescale algorithm. An algorithm based on robust ARIMA modelling yields a timescale that may differ markedly and is in most respects inferior to that generated by the current algorithm. The NIST algorithm is comparable in accuracy and stability to the current algorithm, except on the short term, where it is significantly less stable.

INTRODUCTION

USNO is in the process of reevaluating the accuracy and stability of its timescale algorithm relative to other algorithms and determining how best to minimize the effects of changes in environmental conditions on the cesium-beam atomic clocks that generate our timescale. The first phase of this study [1] found that temperature effects on the clock rates (relative frequencies) were negligible when the clock vault temperature was controlled to within ± 1 deg C. No short-term humidity effects were evident, but there appeared to be an annual variation in the clock rates dependent on absolute humidity, confirming results found at PTB [2] and IEN [3] and being in turn confirmed at NBS [4].

DATA

The data consisted of two years of hourly clock differences for each of 44 commercial cesium frequency standards located in six well-separated vaults at USNO, as well as temperature and relative humidity measurements for each vault. The absolute humidity was computed from the temperature, relative humidity, and Figure 15 in [5]. The clocks were restricted to those that were weighted, i.e. that contributed to the USNO timescale, in order to be certain that we were dealing with well-known and well-behaved clocks.

Frequency instability in the time domain is defined by the Allan, or two–sample, variance [6]. Allan variances were computed for each of the clocks at six different sampling times, τ: 1 hour, 5 hours, 1 day, 5 days, 25 days, and 50 days. The mean values of their square roots are given in Table 1, the associated errors having been calculated from the 30–day (for the first four τ's), 180-day (for τ = 25 days), or 360-day (for τ = 50 days) binned values. In some cases, the data were not extensive enough to compute all the values or their errors. Next, the value and time of minimum Allan variance were estimated by second–order interpolation to the lowest three values.

ENVIRONMENTAL EFFECTS

Linear regression of the rates against absolute humidity (both averaged over 10 days) for 5 clocks in the Building 1 vault yielded the coefficents in Table 2. The coefficients agree well with results obtained elsewhere [3,4,5], but are not well determined due to imprecise temperature control. Hence, correction for humidity effects during data processing is not feasible. Only one of our vaults is presently humidity controlled, but two new vaults now under construction will be.

In order to gauge the effects of ambient conditions on frequency stability, the vault temperatures, relative and absolute humidities, and their time gradients were investigated for correlations with the square root of the Allan variance for τ = 1 hour, 5 hours, 1 day, and 5 days. The only significant correlations were with temperature; the mean absolute values of the linear correlation coefficients ranged from 0.21±0.03 to 0.37±0.04, depending on τ, corresponding to confidence levels of from 86% to 99%. The coefficients varied from negative to positive, depending on the clock, suggesting that each clock has a peculiar temperature at which its variance is minimized. No dependence on age or manufacturing batch were noted.

The mean absolute values of the temperature coefficients are given in Table 3. J45–option (high–performance/high–stability beam tube) clocks had temperature coefficients that were significantly more positive than those of the 004–option (high–performance tube) clocks for most of the τ's, indicating that the former either are more temperature–sensitive, have a lower variance–minimizing temperature, or both.

MAINTENANCE ACTIVITY EFFECTS

In a search for possible effects of human activity (e.g. routine maintenance) on clock rates, maintenance logs were compared with the times of significant nontransient rate changes (arbitrarily defined as ¿ 2 ns/day). After elimination of rate changes caused by nonroutine events (e.g. gross movement or degaussing of clock; large temperature excursions; etc.), a background level for the frequency of these changes was established. Then, excess occurrences of rate changes were looked for around the times of maintenance checks. It was found that a typical clock underwent 2.0 unexplained (and presumably spontaneous) rate changes per year and 0.9 rate changes per year attributable to maintenance checks, even if no adjustments were made. If controls had to be adjusted, there was an 13% chance that a rate change would result. Of the adjustments that caused rate changes, 82% were of the second–harmonic control.

A similar investigation was made of the square root σ of the Allan variance for τ = 1 hour, 5 hours, 1 day, and 5 days. Defining a significant change as twice the standard error of σ or more, eliminating changes caused by nonroutine events, and averaging over all clocks and τ's, it was found that 55% more changes in σ occurred when an adjustment had to be made; virtually all of these adjustments were of the second–harmonic control.

Inasmuch as the data were binned in intervals of 5 days (for rates) or 30 days (for τ's), the time resolution was inadequate to determine what was cause and what was effect, i.e. whether it was the condition that necessitated the adjustment, or the adjustment itself, that altered the rate or σ.

We also looked for any dependence of Allan variance on clock serial number (hence, manufacturing batch) or, roughly, age. Figure 1 shows no such dependence, but one must keep in mind that any clock showing significant aging would produce degraded data that would have been rejected from our data set by the deweighting of the clock to zero.

CLOCK WEIGHTING

The USNO uses a linear timescale algorithm (the "old" one described by Percival [7]), which is generated hourly and reprocessed about twice a week, at which time clock weights and rates may be revised, based on an examination of least-squares solutions for the rates generally solved for every 5 days. The mean ("paper") timescale is generated from the average of each of the individual clock rates (after removal of a nominal rate relative to the rest of the ensemble), wherein clocks are either weighted unity or zero. Clocks are deweighted in the preliminary timescale if their rate change exceeds 3 parts in 10^{13}. During reprocessing, they are deweighted if a change in rate exceeds about 6 ns/day, its rms frequency error of unit weight exceeds about 5 ns, or if the rate appears to be drifting. Consequently, the algorithm is iterative and "unweighted" and the data are filtered.

In order to provide a physical realization of this time, called UTC (USNO), a cesium clock, Master Clock (MC) #1, is steered toward the mean timescale, as is one of our passive hydrogen masers, MC #2. GPS and all other USNO-derived timescales are traceable to MC #2. The mean timescale itself may be steered by steering the MC's (to which it and all clock time differences are referred), as is currently being done, toward TAI. The steered and unsteered mean timescales relative to TAI are shown in Figure 2 for the years 1986-87.

In order to investigate the effect of altering the weights, seven different mean timescales were computed using weights equal to the inverse Allan variances for the sampling times in Table 1, as well as the inverse minimum Allan variance. Attention was paid to significant changes in each clock's variance with time, since, as noted in the previous section, these did occasionally occur.

The short-term errors of the unweighted and weighted timescales were evaluated by comparing them to our MC #2 maser, which is more stable than cesium clocks at sampling times shorter than a few days. Table 4 lists the mean square roots of the Allan variance of the differences between the timescale and the maser for the six sampling times. Weighting with 5-day variances yields better results than not weighting at all, but to such a small extent that one questions whether it justifies even the relatively little extra labor involved.

The long-term systematic errors of the weighted timescales were studied by solving by least squares for the slope of their drifts relative to the unweighted timescale. According to Table 5, none of the weighted timescales drift significantly from the unweighted timescale.

The long-term nonuniformities of the unweighted and weighted time- scales were analyzed by averaging daily time differences over 10 days, referring the averages to TAI (available only every 10 days), removing the steering, fitting a parabola or a line (whichever fit best) to the 1986 and 1987 data by least squares, and looking at the standard error of the estimate (the scatter after removal of the parabolic or linear trend). Allan variances would have underestimated the errors due to the serial correlation of the residuals. Since the standard errors of the standard errors themselves are about ± 8 ns and ± 5 ns for 1986 and 1987 respectively, it is evident from Table 5 that weighting does not significantly decrease the long-term nonuniformities.

Therefore, little or nothing is to be gained by weighting our clocks any differently, at least with

our current algorithm. This is probably due to the homogeneity of the clock types in our ensemble. It also implies that the Allan variance is not the best measure of the contribution of a clock to the stability of a timescale. Previous discussions of this matter [8, 9] have assumed that the outputs of clocks are statistically independent. However, it has been shown [1] that USNO clocks are significantly intercorrelated and even that study would not have been able to detect correlations apparent only with reference to clocks of other types and in other locations. These correlations cause one to underestimate the errors when using an internal estimate like the Allan variance. Apparently, they do so to such an extent that the Allan variance overestimates a clock's contribution when the "optimum-weighting method' [9] is employed.

ROBUST ARIMA ALGORITHM

Percival [7] proposed an algorithm based on ARIMA forecasting. An- ARIMA (Autoregressive Integrated Moving Average) model is described by:

$$z_t - \sum_{j=1}^{p} \phi_j z_{t-j} = \theta_0 + a_t - \sum_{j=1}^{q} \theta_j a_{t-j} \tag{1}$$

where z_t is the d^{th} finite time difference; d is the number of times the elements of the time series have to be differenced to render the series stationary; $\phi_1, \ldots, \phi_p$ are autoregressive parameters; θ_0 is a correction for a systematic d^{th}-order drift; $\theta_1, \ldots, \theta_q$ are moving-average parameters; and $a_t, \ldots, a_{t-q}$ are uncorrelated random variables with zero mean and constant variance. Such a model allows one to make use of short-term trends in the data to predict a real-time timescale and, hence, quickly to sense any significant rate change and downweight such a clock until its rate is stable again.

Downweighting was accomplished by means of a robust filter, namely Hampel's psi function (Figure 3), as also proposed by Percival [10]. The weight of a clock was given by:

$$\frac{\sigma_t \psi(e_t/\sigma_t)}{e_t} \tag{2}$$

where σ_t is the square root of the Allan variance at a sampling time t (the time interval of rate and weight revision) and e_t is the difference between the observed and the ARIMA-predicted frequency.

Each clock's data were divided into segments of constant rate and variance and at least 50 t in length; an initial model was assumed for the clock; and the model was iteratively improved until the rms error of the fit to the data was minimized. The results of the modelling were as follows: (1) d = 2; (2) t = 1 day was the smallest time step for which the minimal number of parameters needed to be solved for; (3) p = 0; (4) θ_0 could not be determined because the coefficients of each model changed significantly too frequently, typically every few months at one or more of the times of rate change; (5) 96% of the time, q = 1, and the rest of the time, q = 2; and (6) θ_1 and θ_2 averaged 0.721±0.015 and 0.819±0.019 respectively.

A timescale was computed hourly with the robust ARIMA algorithm by enforcing equality with the unweighted USNO timescale for the first 10 days (during which the ARIMA prediction errors, required by the weighting procedure, initialized themselves) and then letting the ARIMA algorithm take over for the remainder of the year. The results for 1986 and 1987 are shown in Figure 4. Little difference was found between using weights based on the variance of the fit rather than the Allan variance.

Of the weighted clocks used by the USNO algorithm, those given full weight by the ARIMA algorithm averaged 93.4%, those given partial weight averaged 5.5%, and those given no weight averaged

1.1%. For a normal distribution of errors, the sum of the last two would be 4.6%. In practice, the ARIMA algorithm could have made partial use of some of the clocks given zero weight by the USNO algorithm.

Evaluating the short–term errors, again through comparison with our maser, we obtained the mean square roots of the Allan variance given in Table 6. The ARIMA timescale is significantly less stable than the USNO timescale for every sampling time except 1 day (probably because of the 1–day weighting). Also, its time of minimum variance occurs at a shorter sampling time.

The stability of the robust ARIMA timescale could probably be improved, at least over times longer than a day, by increasing t from 1 day to, say, 5 days (nearer the average time of minimum Allan variance for our clocks). As it stands, the ARIMA algorithm corrects the rate daily, which may be decreasing the ensemble's stability by following the cesium clocks too closely, i.e. tracking some of their noise. Unfortunately, increasing t decreases the number of data points by the same factor, which makes it more difficult to derive the ARIMA coefficients with sufficient accuracy. ARIMA modelling requires a minimum of about 50 data points, but our clocks went only an average of 126 days between significant rate changes (at which time the ARIMA coefficients usually changed significantly). The inaccuracy of the ARIMA parameters could also have contributed to the timescale's instability.

As is evident from Figure 4 and Table 7, the ARIMA algorithm on the long term can drift markedly relative to the USNO timescale in either direction, depending on the prevailing ARIMA parameters. The ARIMA timescale was significantly less stable than the USNO timescale during 1986, but was about as stable during 1987. Since there were fewer clocks and more rate changes in 1987 than in 1986, the only apparent reason for this difference in stability between years is a greater susceptibility of the ARIMA algorithm to nonuniformities in the data; that these nonuniformities were larger in 1986 than in 1987 is clear from the corresponding errors for the USNO algorithm.

Consequently, ARIMA modelling yields a timescale that is no better than, and is in most respects significantly inferior to, that generated by the USNO timescale, for reasons connected with the practical determination of the ARIMA parameters and their apparent sensitivity to noise and nonuniform data.

NIST ALGORITHM

Another important algorithm is that used by NIST (formerly NBS) to generate their AT1 timescale. The algorithm is an asymptotic form of a Kalman filter designed for a steady-state ensemble manifesting the types of noise typical of cesium clocks [11, 12]. Either linear or nonlinear, depending on the clock, it utilizes exponential filters in the rate correction and weight revision. As used here and at NIST, it utilizes daily measurments and weights based mainly on the clock stability at a sampling time of 1 day. We did not use the nonlinear option because any clocks with drifting rates had already been eliminated from our data.

Using initial weights based on 1-day Allan variances, a timescale was generated with the NIST algorithm. Evaluating the short-term errors as before, we obtained the results in Table 6. Both the USNO and the ARIMA timescales are more stable on the short term than the NIST time–scale. The reason for this is unclear. The ratio of the highest clock weight to the lowest clock weight averaged 21.1 ± 1.1 – this for clocks all given equal weight by the USNO algorithm and whose time–scale computed therefrom has been shown above not to be improved by weighting. Experiments with setting an upper bound on the weights and with increasing the time constant of the rate–correction filter failed to improve the NIST timescale's short–term stability.

As seen in Figure 5 and Table 7, on the long term the NIST time–scale agrees well with that of the USNO algorithm as far as both drift and nonuniformities are concerned, as may be expected because of their basic linearity.

Thus, use of the NIST algorithm would not improve the long-term accuracy or stability of the USNO timescale and would apparently degrade its short-term stability.

CONCLUSIONS

Humidity should, and increasingly will be, controlled in our clock vaults. A significant fraction of clock rate and variance changes might be eliminated by reducing the extent of human interaction or the need for it. No improvement in either accuracy, short-term stability, or long-term stability would be achieved by weighting the individual clocks differently from unity or zero with the current USNO algorithm or by employing either the NIST algorithm or one based on ARIMA modelling.

REFERENCES

{1} Breakiron, L. A., "The Effects of Ambient Conditions on Cesium Clock Rates," Proceedings of the 19th Annual Precise Time and Time Interval (PTTI) Applications and Planning Meeting, 1–3 December, 1987, Redondo Beach, CA, pp. 175–84.

{2} Dorenwendt, K., "Das verhalten kommerzieller Casium–Atomuhren und die Zeitskalen der PTB," Proceedings of the 31st International Congress of Chronometry, 1984, Besancon, France, vol. 1, pp. 37–40 = PTB Mitteilungen 94, pp. 35–43.

{3} Bava, E., Cordara, F., Pettiti, V., and Tavella, P., "Analysis of the Seasonal Effects on Cesium Clocks to Improve the Long–Term Stability of a Time Scale," Proceedings of the 19th Annual Precise Time and Time Interval (PTTI) Applications and Planning Meeting, 1–3 December, 1987, Redondo Beach, CA, pp. 185–202.

{4} Gray, J. E., Machlan, H. E., and Allan, D. W., "The Effects of Humidity on Commercial Cesium Beam Atomic Clocks," Proceedings of the 42nd Annual Frequency Control Symposium, 1–3 June, 1988, Baltimore, MD, pp. 514–18.

{5} Iijima, S., Fujiwara, K., Kobayashi, H., and Kato, T., "Effect of Environmental Conditions on the Rate of a Cesium Clock," 1978, Annals of the Tokyo Observatory, 2nd series, vol. 17, #1, pp. 50–67.

{6} Allan, D., Hellwig, H., Kartaschoff, P., Vanier, J., Vig, J., Winkler, G. M. R., and Yannoni, N. F., "Standard Terminology for Fundamental Frequency and Time Metrology," Proceedings of the 42nd Annual Frequency Control Symposium, 1–3 June, 1988, Baltimore, MD, pp. 419–25.

{7} Percival, D. B., "The U. S. Naval Observatory Clock Time Scales," 1978, IEEE Transactions on Instrumentation and Measurement, vol. IM–27, #4, pp. 376–85.

{8} Winkler, G. M. R., Hall, R. G., and Percival, D. B., "The U. S. Naval Observatory Clock Time Reference and the Performance of a Sample of Atomic Clocks," 1970, Metrologia, vol. 6, #4, pp. 126–34.

{9} Allan, D. W. and Gray, J. E., "Comments on the October 1970 Metrologia Paper 'The U. S. Naval Observatory Clock Time Reference and the Performance of a Sample of Atomic Clocks'," 1971, Metrologia, vol. 7, #2, pp. 79–82.

{10} Percival, D. B., "Use of Robust Statistical Techniques in Time Scale Formulation," presented at the 2nd Symposium on Atomic Time Scale Algorithms, 23–25 June 1982, Boulder, CO = report on USNO contract N70092–82–M–0579.

{11} Allan, D. W., Gray, J. E., and Machlan, H. E., "The National Bureau of Standards Atomic Time Scale: Generation, Stability, Accuracy, and Accessibility," chap. 9, Time and Frequency: Theory and Fundamentals (B. E. Blair, ed.), 1974, National Bureau of Standards Monograph #140.

{12} Varnum, F. B., Brown, D. R., Allan, D. W., and Peppler, T. K., "Comparison of Time Scales Generated with the NBS Enabling Algorithm," Proceedings of the 19th Annual Precise Time and Time Interval (PTTI) Applications and Planning Meeting, 1–3 December, 1987, Redondo Beach, CA, pp. 13–23.

Table 1. Mean square roots σ of the Allan variance for 44 USNO cesium clocks in units of parts in 10^{13} at 6 different sampling times τ, with standard errors in units of parts in 10^{16} given in parentheses. The clock type is given by a key at the bottom. The J45–option clocks do have significantly lower variances, as advertised. There is no dependence of variance on vault or location therein.

Clock Ser. No.	Sampling Times 1^h	5^h	1^d	5^d	25^d	50^d	Type	Vault in Bldg. No.
0116	2.791(48)	0.679(08)	0.284(22)	0.310(49)	0.39(186)	0.723	b	82
0133	3.039(65)	.021(17)	0.508(43)	0.367(49)	0.305(27)	0.571	d	16
0571	3.45(100)	1.171(46)	0.543(41)	0.360(48)	0.274		b	52
0571	3.662(66)	1.169(14)	0.491(13)	0.294(08)			b	82
0653	3.367(56)	1.250(22)	0.546(19)	0.402(29)	0.373(38)	0.465	b	1
0656	4.416	1.666	0.844	0.346			b	16
0752	6.205	2.528	1.365	0.807			b	3
0778	3.860(93)	1.435(48)	0.630(29)	0.400(25)	0.395(59)	0.753	a	16
0787	2.691(60)	0.826(40)	0.391(45)	0.47(101)	0.776		b	52
0837	3.020(69)	0.985(29)	0.446(19)	0.300(19)	0.312(92)	0.48(204)	b	16
0862	2.766(43)	0.879(13)	0.366(09)	0.269(20)	0.334(40)	0.619(93)	b	16
0873	7.178	2.835	1.264	1.157			b	52
0875	2.718(27)	0.807(12)	0.337(10)	0.292(20)	0.300(83)	0.49(151)	b	16
1025	2.562(46)	0.744(18)	0.313(33)	0.354(64)			b	1
1028	2.794(94)	0.850(08)	0.383(25)	0.285(56)			b	52
1094	2.803(40)	0.711(25)	0.279(10)	0.241(34)			b	78
1104	2.872(37)	0.802(20)	0.328(16)	0.268(50)	0.290		b	1
1117	.636(48)	1.806(30)	0.858(28)	0.441(20)	20.318(89)	0.51(308)	b	1
1300	3.680(38)	1.321(20)	0.615(21)	0.398(27)	0.32(140)	0.36(224)	b	1
1301	2.767(74)	0.815(08)	0.347(09)	0.256(44)	0.36(199)	0.675	b	16
1301	2.996(36)	0.932(08)	0.353(17)	0.229(02)			b	82
1305	3.672(61)	1.340(42)	0.599(20)	0.399(63)	0.413		b	52
1343	3.04(125)	0.859(17)	0.371(29)	0.318(36)	0.431		b	16
1423	3.954(28)	1.484(18)	0.660(12)	0.431(30)	0.33(121)	0.677	b	16
1449	2.494(71)	0.763(26)	0.252(19)	0.193(18)			b	1
1452	3.659(56)	1.364(24)	0.662(15)	0.530(56)	0.43(202)	0.615	b	1
1586	2.837(62)	0.848(26)	0.367(27)	0.322(38)	0.40(164)	0.403	b	16
1586	2.945(47)	0.877(51)	0.415(59)	0.288(37)			b	82

Type Key:
a: Hewlett–Packard model 5061A
b: Hewlett–Packard model 5061A option 004
c: Hewlett–Packard model 5061A option J45
d: Frequency and Time Systems model 4050 with high–performance tube

Table 1. Continued

Clock Ser. No.	Sampling Times 1^h	5^h	1^d	5^d	25^d	50^l	Type	Vault in Bldg. No.
1605	3.645(44)	1.336(11)	0.612(14)	0.387(20)	0.374(68)	0.63(225)	b	1
1809	2.992(24)	0.953(13)	0.430(22)	0.328(31)	0.346(57)	0.68(113)	b	16
1846	2.936(33)	0.957(15)	0.389(14)	0.266(17)	0.301(74)	0.51(274)	b	52
1986	3.99(110)	1.52(103)	0.79(126)	0.703			b	1
2098	2.817(50)	0.819(10)	0.349(12)	0.297(23)	0.345(94)	0.409	b	16
2098	2.862(41)	0.915(20)	0.415(59)	0.315(63)	0.323		b	82
2100	2.621(42)	0.724(09)	0.288(11)	0.274(31)	0.312(44)	0.41(150)	b	1
2157	2.691(34)	0.753(13)	0.323(17)	0.262(29)	0.191		b	1
2277	2.764(43)	0.693(11)	0.296(10)	0.310(23)	0.37(123)	0.643	b	1
2285	2.672	0.860	0.374	0.446			b	1
2314	2.64(294)	0.703(12)	0.253(01)	0.179(07)			b	1
2315	2.600(60)	0.691(10)	0.361(54)	0.369(50)	0.382		b	1
2481	2.809(32)	0.838(18)	0.340(13)	0.280(28)	0.418(71)	0.54(198)	c	16
2482	3.08(161)	0.86(102)	0.355(67)	0.273(72)	0.250(70)	0.226	c	52
2483	2.667(30)	0.751(13)	0.359(19)	0.320(39)	0.349(90)	0.53(180)	c	52
2484	2.453(48)	0.693(07)	0.271(07)	0.198(18)	0.408(90)	0.390	c	1
2485	2.71(103)	0.787(57)	0.53(125)	0.98(354)			c	52
2485	2.811(61)	0.743(17)	0.296(17)	0.285(32)	0.377(82)	0.488	c	78
2487	2.630(52)	0.765(13)	0.322(14)	0.268(27)	0.193(07)	0.108	c	3
2488	2.86(125)	0.824(53)	0.366(21)	0.405(60)	0.510		c	52
2493	2.555	0.716	0.327				c	1

Type Key:
a: Hewlett-Packard model 5061A
b: Hewlett-Packard model 5061A option 004
c: Hewlett-Packard model 5061A option J45
d: Frequency and Time Systems model 4050 with high-performance tube

Table 2. Mean coefficients relating the frequency and the absolute humidity for 5 cesium clocks in the USNO Building 1 vault.

Clock Serial No.	Absolute Humidity Coefficient
1117	$-0.95 \pm 0.72 \times 10^{-14} g\ m^{-3}$
1300	$-1.01 \pm 0.62 \times 10^{-14} g\ m^{-3}$
2100	$+1.64 \pm 0.60 \times 10^{-14} g\ m^{-3}$
2277	$-1.71 \pm 0.56 \times 10^{-14} g\ m^{-3}$
2484	$-0.51 \pm 0.43 \times 10^{-14} g\ m^{-3}$

Table 3. Mean absolute values for the coefficients relating the square root of the Allan variance and temperature in units of parts in 10^{15} per $°C$ for two types of Hewlett-Packard cesium clocks at USNO.

Clock Type	Sampling Time 1^h	5^h	1^d	5^d
HP option 004	7.2 ± 1.6	4.0 ± 0.9	3.5 ± 0.7	2.8 ± 0.5
HP option J45	11.3 ± 3.0	6.3 ± 1.7	4.1 ± 1.2	0.4 ± 1.3

Table 4. The mean square roots of the Allan variances of the maser relative to the USNO unweighted mean timescale and seven weighted mean timescales in units of parts in 10^{13} for 6 sampling times, with standard errors in units of parts in 10^{16}

Mean Computed Using:	Sampling Time 1^h	5^h	1^d	5^d	25^d	50^d
no weights	2.044 ± 27	0.489 ± 08	0.252 ± 27	0.180 ± 11	0.086 ± 22	0.063 ± 01
$1/\sigma^2(\tau = 1^h)$	2.080 ± 26	0.486 ± 09	0.248 ± 28	0.172 ± 11	0.097 ± 21	0.067 ± 03
$1/\sigma^2(\tau = 5^h)$	2.061 ± 25	0.474 ± 08	0.242 ± 27	0.172 ± 11	0.089 ± 23	0.061 ± 10
$1/\sigma^2(\tau = 1^d)$	2.066 ± 31	0.476 ± 08	0.242 ± 27	0.169 ± 10	0.091 ± 24	0.063 ± 01
$1/\sigma^2(\tau = 5^d)$	2.014 ± 27	$0.473 \pm 07^*$	0.243 ± 27	0.172 ± 10	0.090 ± 21	$0.056 \pm 04^*$
$1/\sigma^2(\tau = 25^d)$	2.056 ± 27	0.489 ± 08	0.253 ± 26	0.177 ± 10	0.086 ± 20	0.061 ± 06
$1/\sigma^2(\tau = 50^d)$	2.098 ± 25	0.518 ± 08	0.271 ± 24	0.192 ± 09	0.108 ± 15	0.116 ± 25
$1/\sigma^2(\tau = \tau_{min})$	2.059 ± 21	0.486 ± 08	0.252 ± 26	0.177 ± 10	0.089 ± 18	0.071 ± 09

* The only values significantly smaller than for the unweighted mean.

Table 5. The drifts and nonuniformities of the unweighted and weighted USNO timescales. The standard errors of the estimate are for a parabolic (1986) or linear (1987) fit.

Mean Computed Using:	Drift Relative to Unweighted Mean (ns/day)	Standard Error of Estimate of TAI-Unsteered USNO Mean (ns)	
		1986	1987
no weights			$+65.3 \pm 39.9$
$1/\sigma^2(\tau = 1^h)$	0.011 ± 0.006	± 68.6	± 37.9
$1/\sigma^2(\tau = 5^h)$	0.039 ± 0.007	± 69.0	± 38.8
$1/\sigma^2(\tau = 1^d)$	0.011 ± 0.011	± 70.2	± 36.5
$1/\sigma^2(\tau = 5^d)$	-0.041 ± 0.010	± 68.2	± 38.1
$1/\sigma^2(\tau = 25^d)$	0.018 ± 0.012	± 69.7	± 37.8
$1/\sigma^2(\tau = 50^d)$	0.004 ± 0.021	± 72.5	± 38.1
$1/\sigma^2(\tau = \tau_{min})$	0.051 ± 0.009	± 67.6	± 41.1

Table 6. The mean square roots of the Allan variances of the maser relative to the timescale generated by three algorithms (using USNO cesium data) in units of parts in 10^{13} for 6 sampling times, with standard errors in units of parts in 10^{16}

Algorithm	Sampling Time 1^h	5^h	1^d	5^d	25^d	50^d
Unweighted USNO	2.044 ± 27	0.489 ± 08	0.252 ± 27	0.180 ± 11	0.086 ± 22	0.063 ± 01
Robust ARIMA	2.260 ± 23	0.570 ± 11	0.265 ± 29	0.215 ± 15	0.257 ± 64	0.417 ± 63
NIST			0.469 ± 39	0.348 ± 34	0.095 ± 16	0.075 ± 21

Table 7. The drifts and nonuniformities of timescales generated by three algorithms using USNO data for the years 1986 and 1987

Algorithm	Drift Relative to Unweighted USNO Mean (ns/day)		Standard Error of Estimate of TAI–Unsteered Mean (ns)	
	1986	1987	1986	1987
Unweighted USNO			±65.3*	±39.9
Robust ARIMA	-3.40 ± 0.18	3.95 ± 0.07	158.7*	44.7*
NIST	0.0113 ± 0.0096		70.3	40.6

*Quadratic fits; the other fits are linear.

FIG. 1. SQUARE ROOT OF ALLAN VARIANCE VS. SERIAL NUMBER (TAU OF MIN. VARIANCE)

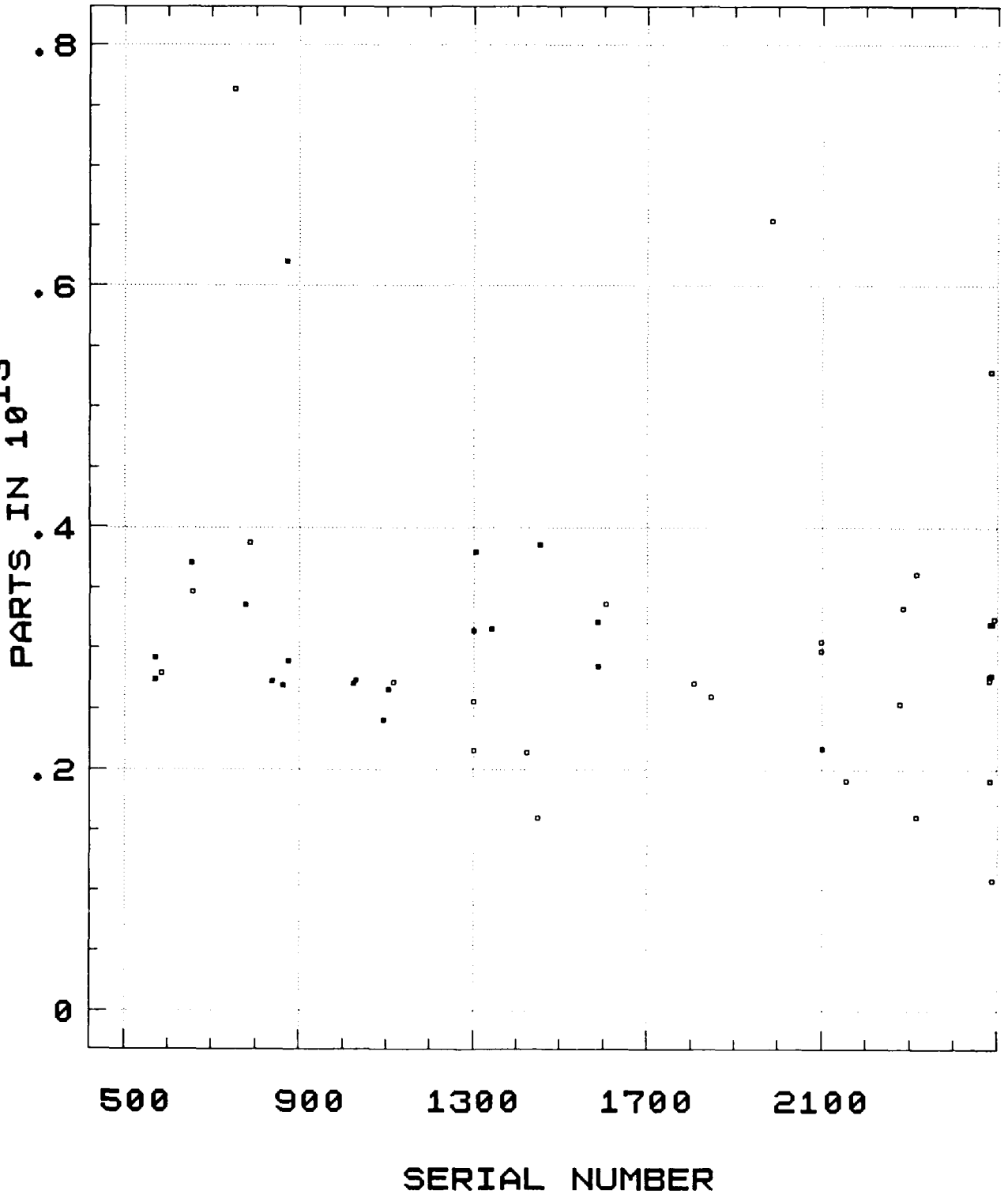

FIG. 2. TAI - USNO MEAN

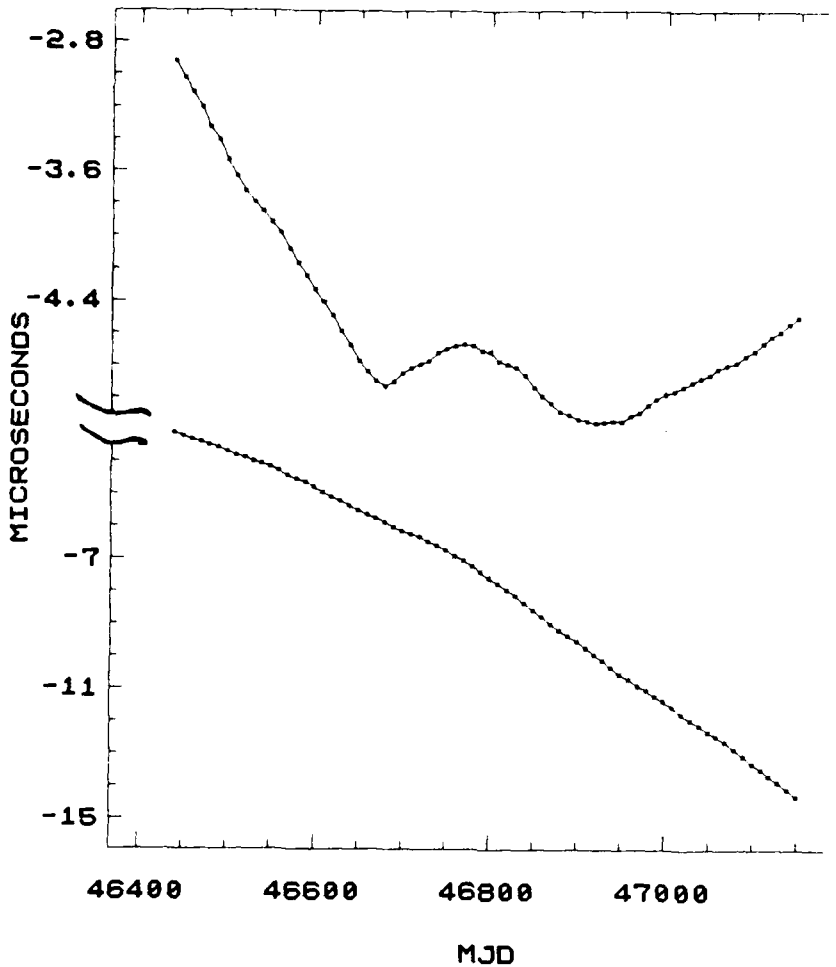

FIG. 3. HAMPEL'S PSI FUNCTION

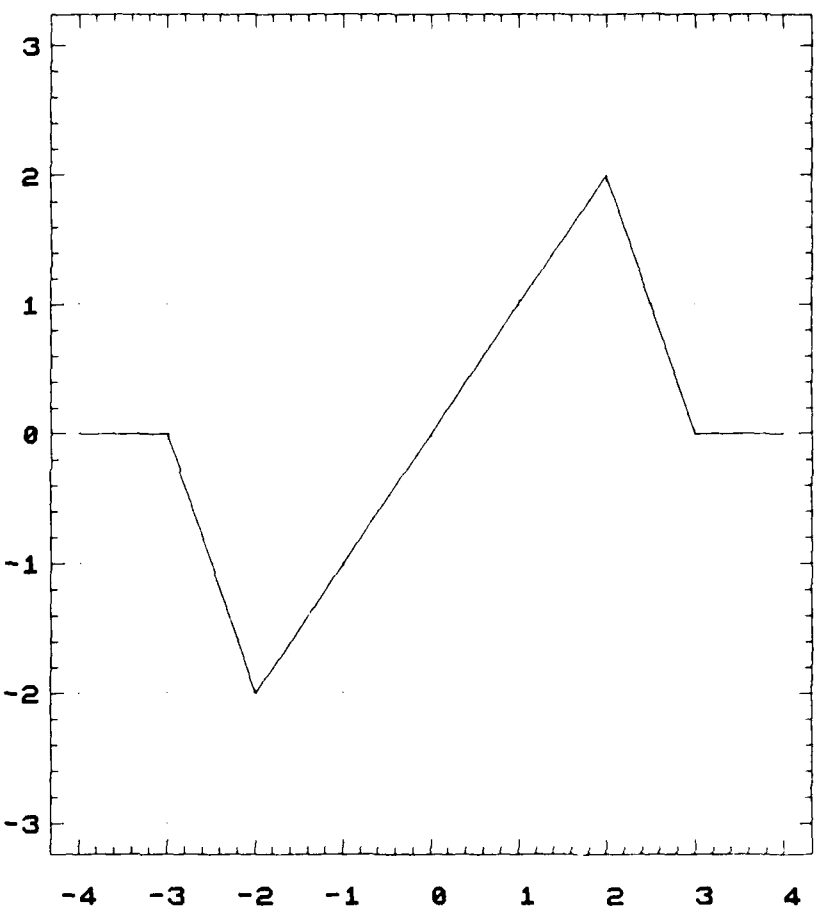

FIG. 4. USNO MEAN - ROBUST ARIMA

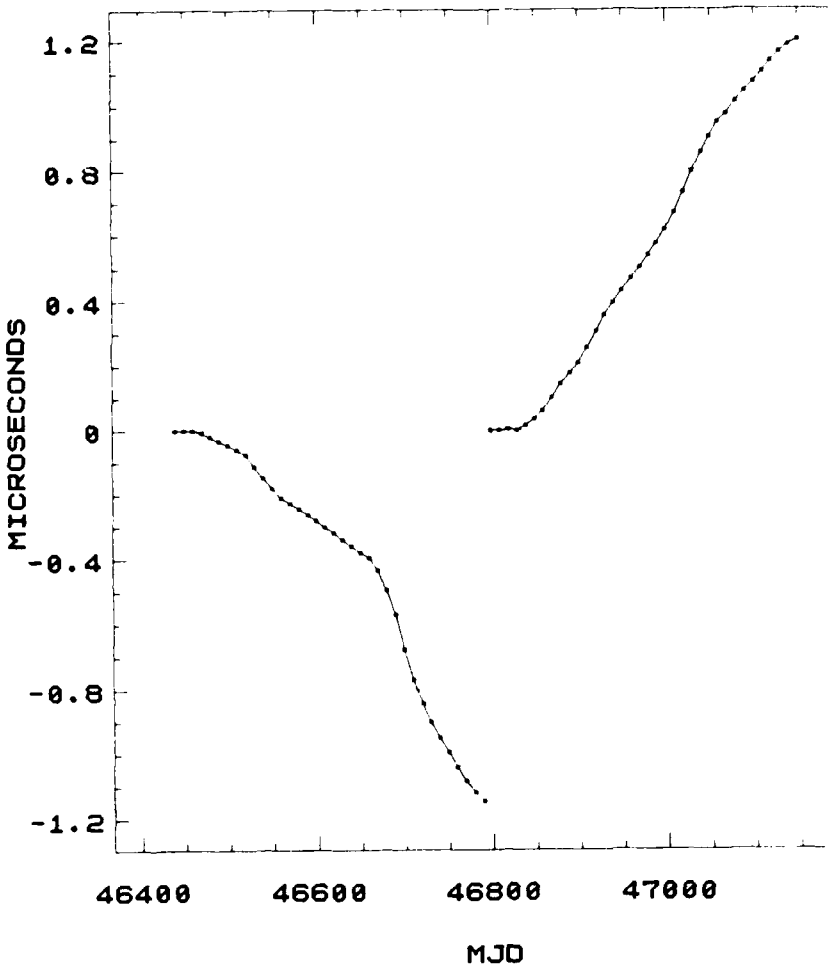

FIG. 5. USNO MEAN - NIST MEAN

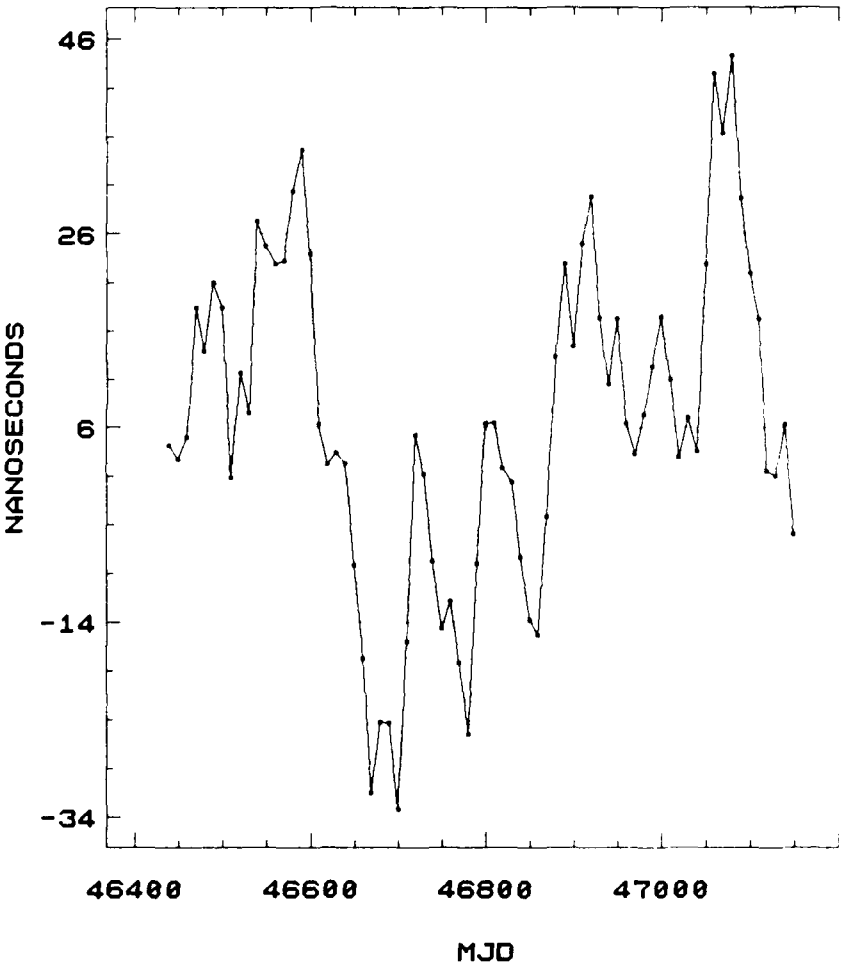

THIRD INTERNATIONAL TIME SCALE ALGORITHM SYMPOSIUM*

David Allan
National Institute of Standards and Technology

12–13 September 1988–Turin, Italy

Program Committee

General Chairman:	Bernard Guinot Bureau International des Poids et Mesures, Paris, France
Program Chairman:	David W. Allan National Institute of Standards & Technology (Formerly The National Bureau of Standards) Boulder, Colorado, USA
Local Coordinator:	Pier Giorgio Galliano Istituto Elettrotecnico Nazionale, Turin, Italy

Copies of the proceedings can be obtained from:
NATIONAL INSTITUTE OF STANDARDS AND TECHNOLOGY
TIME AND FREQUENCY DIVISION
325 Broadway
Boulder, CO 80303-3328
(Published October, 1988)

*The following are excerpts from the proceedings

TABLE OF CONTENTS

(extracted from the proceedings)
page numbers refer to the proceedings

Opening Address

Dr. Bernard Guinot

Bureau International Des Poids Et Mesures
Section du temps Pavillon de Breteuil
F92312 Sevres Cedex
FRANCE

One of the roles of the talk to open a session is to demonstrate that what we will do is quite important. Of course you already know the importance of the subject since you are here. Nevertheless a confirmation that we are performing essential duties is always satisfactory, and it helps in warming up the engine.

There has been contrasting opinions concerning the algorithms for time scales.

For instance, some years ago, our colleague from NRC, Costain, was somewhat skeptical. He told me "have a good clock and don't care for algorithms." It might be a good solution, but it is not a natural one. The natural evolution, both for physical and psychological reasons, is that when you have a good clock, you manage to get a second one, then a third one, and you are all faced with the algorithms. On the opposite, Barnes told me that if he can gain 10% by statistics, it saves the cost of one clock over 10 to achieve the same performances, which is by no means negligible.

At the beginning of the era of atomic time, the algorithms for time scales were essentially machines which avoided phase and frequency jumps when clocks failed or when new clocks were entered in the system. Nowadays, to maintain the stability in spite of modifications of the clock ensemble, which includes change in the weighting, remains an essential role of the algorithms. But we have recognized that the result is strongly dependent on the quality of the prediction of the clock frequency.

We have also recognized that there is no unique ideal time scale algorithm. We have to specify first what the criteria of the time scale that have to be fulfilled: frequency accuracy, stability for some given sample time. As I believe that this is an important point, I would like to illustrate by two examples how the criteria may differ.

There are many systems where remote clocks must be maintained in synchronization within stated tolerances. Examples: navigation systems such as GPS, master clocks of time services,... The most convenient method consists in maintaining the synchronism with a master clock of the system. It is evident that the master clock must be more stable than any other clock of the system. More precisely the stability of the master clock must be optimized for a sample time which is of the order of the re-synchronization by absolute means, which are anyway needed. An additional requirement is the reliability of the master clock. This is clearly a domain where we have to rely on an ensemble of clocks and a well adapted algorithm.

I will spend a little more time on the second example which illustrates the need of the very long term stability, which is often loosely referred to as "uniformity", in celestial dynamics.

In this type of research, we observe space coordinates (angles, distances) as a function of time read on a realized time scale. The goal is to fit later a theory. Limitations are the errors of the dimensional measurement and the departure of the realized time scale from ideal. The important point is that the errors of dimensional measurement progressively decrease as a result of improvement of the observational techniques. At the same time the time error increases indefinitely because atomic time is the result of integration of imperfect frequencies. Therefore it will primarily happen that the atomic time error will exceed what should correspond to the dimensional error.

In current solar system dynamics this crowning point appears sufficiently remote, even without progress of the atomic clocks, may be in centuries, so that we feel reasonably comfortable.

But Backer (1982) discovered the first millisecond pulsar and we realized that our crowning point had suddenly jumped to a year, maybe less, after the start of precise pulsar timing. We have to be aware of the importance of this discovery for the time metrology.

Of course, the progress in long term stability needed by pulsar studies is not within the reach of better algorithms: we need better clocks. Nevertheless we cannot change the clock data: but we can use them in an optimum way and the gain is not marginal. This gives life to a new activity: the reprocessing of past data with appropriate algorithms, for which it might be possible to use multi-weight approaches which could use all the clocks in their domain of excellence.

Concerning the algorithms themselves, I would like to paraphrase a famous sentence of Sully, unfortunately I cannot translate it into English "La fourage et pastourage sont les deux mamelles de la France". I will say that prediction and weighting are the two main features of the time scale algorithms. But it appears that with new methods, such as the Kalman filtering, prediction and weights do not appear explicitly anymore. They should nevertheless exist and I believe that it is important to understand what they really are in order to avoid misusing these powerful tools.

I am also convinced that the classical algorithms still require further studies and may offer improved possibilities.

I would also like to mention that the establishment of time scales is not the only domain where stability and accuracy algorithms are realized. Similar problems occur with series of measurements in astronomy and geophysics: for instance, the evaluation of the motion of the terrestrial pole from many observatories. Maybe it was not so crucial than with time, but it may become more important. Our community of time scale algorithms designers is small; it might be useful in the future to share our experience with other researchers in nearby domains.

I personally look forward with the greatest interest the discussions of these two days.

I would like to express to our program chairman David Allan, our thanks for having so timely initiated the 3rd Symp. on time scale algorithms. The IENGF has kindly accepted to host our symposium. I wish to express to them our gratitude to Prof. G.F. Micheletti, Special Commissioner of the Institute for putting such a pleasant meeting place at our disposal and for his welcome address and to Dr. Galliano, local coordinator, and his staff, for the charge of the local organization.

J.S. Boulanger, NRC

Status and Plans for the NRC Primary Cesium and for Synchronizing UTC(NRC)

Notes: Plan to use Hydrogen, Commercial Cs and Primary Cs. over the next year and test algorithm. Overlap for approximately 1 year. UTC(NRC) will continue from Cs V until algorithm version has been well demonstrated to be better. Cs VIB will be an experimental clock. Cs VIC provided input to GPS receiver after July failure of Cs V for two months (2030 UTC, 31 Aug. 1988 Cs V began again to provide the reference).

L.A. Breakiron, USNO

Progress Report on the Time Scale Evaluation Project at USNO

The Time Service Department of the U.S. Naval Observatory has begun a project of research aimed at reevaluating the time–scale algorithm currently in use for the processing of cesium clock data. In particular, our linear algorithm is being compared to higher-order and ARIMA–type algorithms. Also, our unweighted, filtered scheme is being compared to more sophisticated filtering and weighting schemes involving the Allan variance. Increased attention is being paid to environmental factors. A report summarizing the results to data will be presented.

Notes: 40 Cs clocks in six (one with humidity control) vaults. Found annual absolute humidity dependence of either sign. Found temperature coefficient. J45 series tended to be positive relative to option 004. Looked at non equal weighting approach. Used weights at 6 g values and constructed 6 scales plus the regular UT(USNO) algorithm (0,1 weights). H–maser, used in short term and TAI for long term reference: g = 1 hr., 5 hr., 1 d, 5 d, 25 d, 50 d. g = 5 d gave some marginal improvement. Fit a parabola to part of the data and a straight line to the rest. 37% of Δy changes occurred at maintenance periods. 55% of the time something was changed the variance changed. Tested Percival ARIMA algorithm with Robust statistics, and Hampel's Psi function. Two more vaults being built with humidity control.

F. Cordara, V. Pettiti, P. Tavella, IEN

Status Report and Future Trends of the IEN Time Scale

The time scale UTC(IEN) of the Istituto Elettrotecnico Nazionale (IEN) of Torino, Italy, has been realized since 1976 by means of an industrial cesium clock whose rate has been corrected with a phase microstepper to maintain UTC(IEN) in close agreement with UTC.

In recent years, the analysis of the influence of the environmental parameters on the frequency of the atomic clocks maintained at IEN allowed to improve the long term stability of the time scale adopting a compensation of the seasonal rate of changes of some clocks.

Further steps towards a more uniform and reliable time scale generation will be possible adopting suitable algorithms for a small clock ensemble. Some preliminary results obtained using a different weighting criteria and future trends for the IEN time scale realization are analyzed.

Notes: GPS comparison started mid 1985. Last year micro–stepper control was added. Ser. 893 004 Cs with 12 years of life. TA2 is NBS algorithm, target is 20 days. TA1 is simple average. TA1 is better in long-term, TA2 in short term. τ_{min} = approximately 2 weeks, at $\approx 3 \times 10^{-14}$. Temperature control at 0.5° C; plan to control humidity to 5%. Environmental perturbations predominate in long–term. That TA1 is better in long–term than TA2 was not statistically significant.

H. De Boer, PTB

Development of Time Scales at PTB

Notes: Don't need sophisticated algorithms. Cs3 now in test. (69 m/s = $\bar{v}$; $\Delta\nu$ = 44 Hz, $\sigma_y(1s)$ = 6×10^{-12} and 3×10^{-12} for Cs1 and Cs2 respectively. Frequency accuracy primarily due to cavity ϕ-shift of 30×15^{-15} and 15×10^{-15} respectively. $\sigma_y(90\ d) \simeq 6 \times 15^{-15}$ from 10 values. Beam reversal every few weeks causes modulation. Hence after 90 d $\sigma_y(\tau)$ may go as $\tau^{-1/2}$. Measurement period, $\tau_0 = 1/2$ hour. Micro-stepper set once/week. Future plans: Prefer to use the best of primary standards and decrease the steering time. Accuracy of Cs's 3 and 4 expected to be about the same as Cs2, i.e., 1.5×10^{-14}.

M. Granveaud, LPTF

Are the Independent Atomic Time Scales Worth of Interest?

International atomic time references are available to the time/frequency community and to the potential users. They are computed by the BIPM time section according to three forms: coordinated as UTC, free as EAL — available upon request — and worldwide scientific reference as TAI. End 1987, 13 laboratories compute their own independent atomic time scales which are published in the BIH/BIPM circular. Some of them are based on the same stability concept as EAL; others are of the TAI type.

From the user's point of view, it is worth wondering if these local independent time scales have specific qualities with respect to the international references.

It is intended to point out this problem.

Notes: Cir. T. 39 UTC(k) + 11 TA(lab) + 4 TA(country). TAI less stable than TA(PTB), long-term (80 d to 320 d). APL H-maser same stability as TAI. TAI time-link noise $\sigma_y(\tau = 10d) \simeq 1.9 \times 10^{-14}$. TA(labs) tend to be better than TAI $\tau \lesssim 20d$. TAI better than most TA(labs) at 20 $d \lesssim \tau \lesssim 440$ d. TA(PTB) better than TAI $\tau > 440$ d.

A. Shenhar, W. Litman, INPL; A. Lepek, A. Citrinovitch, Time and Frequency Limited; D.W. Allan, T.K. Peppler, NIST

Israel's New Synchronized Time Scale, UTC(INPL)

Notes: "UTC(INPL): a near real time software clock". 15 day filter on $\overline{(\Delta^2 x^2)}$ with $\tau_0 = 24$ hours—to alias away diurnal variation. Perform interpolated weighting for any point between. Paper scale performed much better than single clock which has been UTC(INPL).

C. Thomas, BIPM

Long-Term Stability of the International Atomic Time

TAI is a weighted average time scale based on the readings of an ensemble of about 180 atomic clocks. Improving its very long term stability needs to have the optimal mode of prediction for the rate of the operating clocks, especially when changes of weights occur. Various studies tend to prove that relatively long samples (two months) and the choice of what is called "linear prediction" are the best suitable for that purpose. In particular, trying to modelize the seasonal variation of TAI or tempting to include a longer past for the clocks seem to be unavailing.

Notes: Predicted frequency equal to a linear combination of five past two- month frequency samples → $a_{-5} = 0.1$, a_{-4} small, $a_{-2} < 0$, $a_{-1} = 0.3$ concluded to continue using one-step linear prediction. Weight limit changed to 1000 from 200 for TAI. Compute $\sigma(5, 2mo)$ and infer $\sigma(6, 2mo)$ assuming RWFM then test if $\Delta y > 3\sigma(6,2)mo$ to turn the weight to zero). 14% (24 clocks) are at 1000, which implies 6 $\sigma_{TAI}((6, 2mo) = 4 \times 10^{-15}$.

M. Weiss, D.W. Allan, and T.K. Peppler, NIST

A Study of the NBS Time Scale Algorithm

Since 1968 the NBS time scale algorithm has been generating a clock which is theoretically better than any of the individual clocks in its ensemble. In the last few years, thanks to the Global Positioning System, we have been able to measure the time difference between the NBS time scale algorithm and the other time standards around the world. We are able to study long term stability of the order of years, and short term stability of the order of days. We now have estimated fractional frequency stabilities for averaging time out to a year of 1×10^{-14}. This paper studies the behavior of the algorithm from a theoretical point of view, characterizing its performance.

Notes: Defining frequency steps is difficult but very important. 3σ reject yields a factor of 2 improvement in $\sigma_y(\tau = 1/2\ yr)$ which implies you could get by with 1/4 the number of clocks from a statistical point of view. Redundancy and reliability are separate issues from stability. 2σ reject yields factor of 4 improvement, which would imply 1/16 the number of clocks.

D.W. Allan, M.A. Weiss, and T.K. Peppler, NIST

In Search of the Best Clock

Because of the increased need for better clock performance than is currently available, this paper addresses some fundamental questions regarding clock metrology. Heretofore, most work has focussed on improving the clocks to meet the increased need. Though this is fundamental, we will show that significant gains are also available through the algorithms (computational methods for optimally combining the information) which process the readings of the clocks and through international comparisons now available via satellite. Proper algorithms for processing seem to be more important than the proportionate attention generally given them. In fact, to date, the only way we have been able to investigate some of the outstanding time predictability in long)term of the millisecond pulsar, PSR 1937+21, is by using such optimization algorithms.

D.W. Allan, NIST

In Search of the Best Clock, An Update

Because of the increased need for better clock performance than is currently available, this paper addresses some fundamental questions regarding clock metrology. Heretofore, most work has focussed on improving the clocks to meet the increased need. Though this is fundamental, we will show that significant gains are also available through the algorithms (computational methods for optimally combining the information) which process the readings of the clocks and through international comparisons now available via satellite. Proper algorithms for processing seem to be more important than the proportionate attention generally given them. In fact, to date, the only way we have been able to investigate some of the outstanding time predictability in long)term of the millisecond pulsar, PSR 1937+21, is by using such optimization algorithms.

J.A. Barnes, Austron, Inc.

An Adaptive Algorithm to Evaluate Clock Performance in Real Time

ARIMA Models and Kalman filters allow one to evaluate noises in clocks and oscillators and to forecast clock performance into the future with known confidence intervals. The coefficients used in an ARIMA model (as in Kalman filters) are normally estimated before the clock has been put into service. The parameter estimation procedures often minimize a variance function of many variables which can require significant "number crunching" capabilities. This batch mode of operations can give poor results, especially if the parameters are not absolutely constant in time (i.e., an imperfect physical model). It is possible to quantify the model parameters recursively, in real time, even while the system is running. Of course, the issue is the cost measured in terms of reduced system performance. The evaluation of system performance was accomplished using simulation techniques. The models considered were white noise PM, white FM, random)walk FM, and linear frequency drift (aging) in some realistic combination in a conventional application of ARIMA analysis (i.e., batch mode). The same data sets were used to evaluate the real time (recursive) analysis techniques. Only a single pass through the data was allowed as a simulation of the real time analysis. The parameter estimators were based on the fact that the ARIMA model corresponding to the noise types noted above is the ARIMA(0,2,2,) model. In typical ARIMA analyses, the raw data are processed by trial inverse filters to find those coefficients which minimize the variance of the residuals. In the real)time analysis the correlation coefficients for lags 1 and 2 of the inverse filtered data go to zero when the estimated MA coefficients (inverse filter) approach the "real" coefficients respectively. At each time point estimates of the first two auto correlation coefficients are taken as input to two first order servos which independently control each of the two estimated MA parameters. As the system runs, the MA parameter estimates improve)) they are not constant. The comparison of the batch and real)time modes was based on forecast applications, NOT the variances in the MA parameters themselves since the MA parameters are only one source of uncertainty. In the very long term, the errors due to inaccuracies of the MA parameters become insignificant relative to the normal forecast errors (assuming the models are good). Parameter errors are only transient problems for the real)time analysis.

Wei Guo, Song Jin)An, Shaanxi Astronomical Observatory

Characteristic Analysis of Clock Noise: A Dynamic Model

Power spectral density and autocorrelation function are two indispensable aspects to describe a stochastic signal, in frequency domain and time domain respectively. Of course, the fluctuations of clock time can be treated as a kind of stochastic signal. However, there is an inevitable difficulty in the widely used model—power law model—about this signal, it is merely in frequency domain and does not result in time domain; Atomic time scale algorithm designing depends mainly on the characteristics of the time fluctuations, so the usage of the power law model is limited quite in such field. In fact, some models relating to the time scale algorithm, such as polynomial model and ARIMA model, do not take the advantage of the power law model. All of these are concerned with the defect of the power law model itself: because of the nonstationarity of the noise, Wiener–Khintchine relations are untenable and $R_x(\tau)$ diverges. To counter this question, a dynamic model is introduced in this paper. From this dynamic model, a set of autocorrelation functions is obtained. With the aid of such results, it can be seen that the quantities of stability characterization in time domain (e.g., Allan variance) depend on the stationarity of the statistic. On other hand, a Kalman filter is derived with such model. This filter can be used as a optimal estimator for the clock states (phase and frequency) as well as a predictor of frequency and time. As a comparison, time

predictions of the difference between two commercial cesium clocks are carried out with Kalman model, ARIMA model and quadratics model respectively. It is indicated that Kalman model is superior to the others, especially in prediction multi)step ahead. Also, the relation between the noise covariance matrix and the power law parameters is presented in this paper.

Wei Guo, Song Jin)An, Shaanxi Astronomical Observatory

The Measurement Error of Quadratic Polynomial Parameter in Atomic Clock

Clock Quadratic polynomial is a simplified model in time scale algorithm. The least square method has been used to estimate the quadratics parameters (i.e., a,b and c) all along. When LS is used, it is assumed actually that the noise in the model is white and the conventional error formulae for white noise are used to estimate the accuracy of the measurement. However, facts show that the parameters measured by LS are quite instable and the errors are far beyond the range given by the conventional formulae. A detailed analysis about this question is presented in this paper according to the dynamic model. A new set of error formulae are derived. By these new formulae, it is indicated that the measurement error of parameter a and b increased with sample number N under the nonstationary noise, and even though the error of parameter c can be decreased by increasing N, the error is much greater than the one obtained under the white noise. Such conclusions are verified by computer simulations.

In recent years Kalman filter method has appeared in the field of frequency and time. This result shows clearly that it is reasonable to describe a clock with dynamical variable (i.e., phase, frequency and drift). In fact, clock itself is a dynamic system. It is why a dynamic model is introduced. In this paper, a Kalman filter is derived according to the dynamic model. This filter can be used as a optimal estimator for the clock states (phase and frequency) as well as a predictor of frequency and time. As a comparison, time predictions of the difference between two commercial cesium clocks are carried out with Kalman model, ARIMA model and quadratics model respectively. It is indicated that Kalman model is superior to the others, especially in multiple steps prediction.

Notes: Kalman gives better prediction error than ARIMA? (Appears to have used a non opt. model for ARIMA, used a (1,2,1) model).

B. Guinot, BIPM

Time Scales Established in Retrospect

Notes: TTBIPM (post analysis) Vondrak method used in astronomy '69, modified by Guinot. Yields weighting according to the Fourier components of the clock. PRB Cs 1 ends up being predominant in the long)term. Annual term is assumed to be in EAL or TAI and not in Cs1 and is subtracted to generate TTBIPMXX.

A. Gifford, NRL; F. Varnum, Falcon AFS

The NRL Hydrogen Maser Ensemble and a GPS Time Steer Experiment

The Naval Research Laboratory (NRL) has developed and is installing a Clock Ensemble in the Master Control Station (MCS) of the Global Position System (GPS) at the Consolidated Space Operational Command (CSOC), FALCON AFS, Colorado Springs, CO. This system is described, current performance data are presented, and several methods of integrating the NRL ensemble with GPS are outlined. One method which uses the current steering mechanism of GPS is described in detail. The current method of estimating GPS clock states and steering those states to UTC(USNO) is reviewed.

J. Levine, D.W. Allan, NIST

The Steering of a Real-Time Clock to UTC(NBS) to UTC

We describe the procedures that we use to define UTC(NBS) and to steer it towards UTC(BIPM) using an averaging process with a time constant of about 1 year. In addition, we describe the hardware and software that is used to steer a physical clock so that its output realizes UTC(NBS) in real time. The method uses a micro)stepper whose frequency offset is updated 5 times per hour by the time scale computer. The corrections applied to the micro)stepper yield a physical tick whose average offset from UTC(NBS) is less than 0.5 nanoseconds. The algorithm can cope with various fault conditions and can also provide remote notification of a fault.

M.A. Weiss, NIST

The Design of Kalman Smoothers for Global Positioning System Data

Measurements of clocks aboard Global Positioning System (GPS) satellites as well as GPS system time are made many times per day at time standards laboratories around the world according to a tracking schedule issued by the Bureau International des Poids et Mesures (International Bureau of Weights and Measures). We use common view differences of these data as input to a Kalman smoother. Biases in measurements repeated one per sidereal day produce apparent diurnal effects in the data. A composite time and frequency Kalman estimator is used here. This allows frequency updates of clocks at time intervals less than one day while aliasing diurnal variations, and updating time once per day.

Notes: $F + T$ Kalman smoothed. Diurnal variations in global GPS data. Use frequency estimate once per sidereal day for each SV and daily average of all SV times for $F + T$ Kalman updates. Eliminate diurnal variation and allows an estimate of SV + GPS clock stability for $1/2$ *day and* $1/4$ *day* τ *values.*

P.A. Clements, JPL; B.P. Gibbs, J.S. Vandergraft, Computational Engineering Inc.

Stable Kalman Filters for Processing Clock Measurement Data

Kalman filters have been used, for some time, to process clock measurement data. Due to instabilities in the standard Kalman filter algorithms, the results can be unreliable requiring manual intervention of the data, the models, or the filter to obtain reasonable estimates. During the past several years stable forms of the Kalman filter have been developed, implemented, and used in many diverse applications. These algorithms, while algebraically equivalent to the standard Kalman filter, exhibit excellent numerical properties. Two of these stable algorithms, the UD filter and the Square Root Information Filter (SRIF) have been implemented to replace the standard Kalman filter used to process data from the Jet Propulsion Laboratory's Deep Space Network's (DSN) Hydrogen Maser clocks. The clocks are located at the DSN tracking complexes located in California, Australia and Spain. The data are time offsets between the clocks in the DSN, the timescale at the National Bureau of Standards and two geographically intermediate clocks. The measurements are made using the GPS navigation satellites in mutual view between clocks. The filter programs allow the user to easily modify the clock models, the GPS satellite dependent biases, and the random noise levels in order to compare different modeling assumptions.

The results of this study, to be presented in this paper, show the usefulness of such software in developing accurate models. Moreover, the results demonstrate that the new filter algorithms are indeed stable, efficient, and flexible. They provide reliable tools for obtaining better estimates of

time, frequency and drift than do current methods. The talk will include a brief overview of these stable filters.

Notes: To avoid instabilities that can occur in Kalman filters, tested UD filter and SRIF modification of Kalman filter approach. UD seems to avoid instabilities and agrees well with 10 day averages. New approach will make system automatic in estimating T/F of masers in Spain, CA, and Australia (DSN tracking sites). With respect to UTC(NBS) to a few nanoseconds and a few parts in 10^{14}. *SRIF is more reliable, but with increased compute time. Since that is not a problem, may use SRIF.*

B. Guinot, BIPM

Importance and Limitation of the Algorithms for Time Scales

The frequency prediction in usual algorithms is based on frequency samples not referred to an ideal time scale, but to the scale to which the clocks contribute. This is a severe limitation. In particular, if there are no changes of the clock ensemble, no changes of the weights and if the same predictive filter is applied to all clocks, the prediction is absolutely useless. We have tried to overcome this difficulty. However, if one wishes to optimize the stability over a sampling time tau, that requires that the time scale be issued after a delay tau.

M. Mnackri, LPTF; C. Thomas, BIPM

A Comparative Study of Two Procedures for Generating

Ensemble Time: Kalman Filters and Weighted Averages

Different algorithms are being used in construction of local atomic time scales. They are based upon different statistical models; It is often difficult to make "a posteriori" comparison between algorithms results; so, it could be worth of interest to compare time scale algorithms through "a priori" assumptions and computational parameters. Availability of sets of data and time sampling of clock readings are of prime importance in a time scale algorithm.

Notes: A study of Kalman filter approach was performed and it was shown that ALGOS is a special form. The Kalman gives a weighting according to two stochastic parameters. (White FM $\tau^{1/2}$, *and random walk FM* $\tau^{1/2}$ *for* $\sigma_y(\tau)$. *ALGOS weights the clocks according to random walk FM because* τ *= 60 days.*

D. Percival, APL for USNO

Comparison of Two U.S.N.O. Time Scale Algorithms

Notes: Poisson distr of Δy *steps gives reasonable* $\sigma_y(\tau)$ *diagrams.*

Current algorithm

Key points: a) manual procedure, b) smoothing algorithm, c) equal weights for all clocks.

Robust Alg $\Delta^2 x = \epsilon_t(i) - \theta(i)\epsilon_{t-1}(i)$

ARIMA (0,2,1)

Estimate $\mu_+ \equiv x_t(0)$ *Weight is constant out to* 2σ, *then linear decay to* ϕ *to* σ.

Need 186 days to characterize, next 186 to test. Took 80 hrs. to run 20 repetitions.

Real data non normal (heavier task)–more energy in the tails.

$\tau_{min} \sim 2$ *weeks*

1 dB improvement

Conclusion: robust simpler, clock modeling question

S.R. Stein, Ball Aerospace (funded by NRL)

Kalman Ensembling Algorithm: Aiding Sources Approach

Notes: NBS(AT1) is steady state Kalman but is "performing better because of difference in weighting functions".

Advantages of modified Kalman approach:

a) Estimates states of measurables

b) Weights explicitly account for correlations between each clock and ensemble

c) Covariance matrix is bounded

d) Used robust statistical rejection

Tested with simulation and real data for CSOC clocks

Simulated white FM clock and R.W. FM clock

Output $\sigma_y(\tau)$ *reflected white FM level well and long-term within* $\sim$ *3 dB of best clock.*

QUESTIONS AND ANSWERS

DAVID ALLAN, NIST: Let me say that we have produced copies of the proceeding for those people that want them. The attendees received them, but we have produced extras. Order forms are available.

JIM SEMLER, INTERSTATE ELECTRONICS: First of all, a general comment regarding Kalman filters. Before I got into time and frequency I worked very closely with some engineers regarding navigation filters. The one thing that we found more than anything else is that you have to have an extremely accurate model. The quality of the model is really the limiting force on how well you can use the Kalman approach to solve your problems. Now I have a quick question regarding the Israeli time ensemble. How are they doing their time steering, were they using a microstepper?

MR. ALLAN: What was shown on the plot was simply a computer software output. Eventually they plan to have a microstepper, but at the moment it is just a software value. All I can say to your comment about the Kalman filter and the model is "amen." That is an extremely important point.

SAM WARD, BENDIX/JPL: The steering that you do is fine, but we would like to know the magnitude of the steering and the period over which it would be done so that we don't over-model it.

MR. ALLAN: That is reported every month and sent to you.

MR. WARD: The other problem that we have to deal with is sometimes, for some projects, we need to find syntonization data in near real time. With the means that we have been using for the simulated or pseudo-simultaneous view, we have been relying on your data base, the GE data base and some of the others. Whenever those data bases go down or there is a communications problem, then we are left high and dry. We would like to have suggestions as to how to get even with just the spacecraft versus our stations data. That is one way for us to get it quicker.

MR. ALLAN: You raise a very good question. A couple of thoughts that I would have is that assuming that the GPS satellites mature and assuming that we are going to have some access to the satellites in the future, we will see the GPS clock improve and hence it will become an independent flywheel reference. That will be very useful to the community. I think that will happen with time. The other thing is that the SV clocks themselves can be used independently of the GPS time. They have very respectable stabilities. We could talk to you about how to use them on an independent basis and that might also provide a flywheel for you as an independent reference should you lose contact with the ground tie.

RESULTS OF A NEW TEST OF RELATIVITY*

Timothy P. Krisher, Lute Maleki, Lori E. Primas,
Ronald T. Logan, George F. Lutes, and John D. Anderson
Jet Propulsion Laboratory
California Institute of Technology
Pasadena, California

Clifford M. Will
McDonnell Center for the Space Sciences
Department of Physics, Washington University
St. Louis, Missouri

Abstract

A modernized version of the classical Michelson–Morley experiment has recently been performed. The purpose of the experiment was to test the constancy of the velocity of light over a long baseline with light propagated one–way instead of back–and–forth. This was performed with instrumentation of the National Aeronautics and Space Administration Deep Space Network (DSN). In particular, measurements were made of the phases of two hydrogen maser frequency standards separated by 29 kilometers by propagating a laser signal over a highly stable fiberoptics cable. Presented are the results obtained for measurements performed continuously during a full rotation of the Earth.

I. INTRODUCTION

Recent developments in the time and frequency technology used by the National Aeronautics and Space Administration Deep Space Network (DSN) have made it possible to compare precisely the phase and frequency of atomic standards separated by several kilometers. In particular, a highly stable fiberoptics network has been installed at the Goldstone Deep Space Communications Complex. A principle advantage of this system lies in the fact that a fiberoptics cable can provide a much more stable propagation path than conventional coaxial cable, microwave link, or waveguides. Because of this attribute, along with high bandwidth, a primary function of the network is to support connected element interferometry for spacecraft navigation and astrometry [1]. Nevertheless, it became clear that the system could also be applied to a possible test of relativity. The test concerns the isotropy of the velocity of light.

Most experiments to test the isotropy of the velocity of light have involved propagation in a closed path over limited spacetime separations, the classical example being the Michelson–Morley experiment ([2],[3],[4]). Because the signal is propagated back–and–forth, two–way experiments are possibly limited, for example, in the sense that it is the isotropy of the average velocity that is tested. There have been attempts recently to test precisely the isotropy of the one–way velocity of light;

*Supported by the President's Fund of the California Institute of Technology and by the National Aeronautics and Space Administration [NAS 7-918].

i.e., the velocity of light propagated in a single direction instead of back–and–forth ([5],[6]). However, these experiments did not test the isotropy by propagating a signal one–way between two synchronized clocks. The technology now available at Goldstone has made it possible to perform a precise test of the isotropy of the one–way velocity of light by this approach over larger spacetime separations than has been previously accessible.

The general concept of the experiment was discussed at the previous PTTI meeting [7]. Basically, a fiberoptics cable spanning a distance of 29 kilometers can be used to compare a hydrogen maser at Deep Space Station (DSS) 13 with another hydrogen maser at DSS 14 (see Figure [1]). The cable is buried five feet underground, which helps to maintain a constant and uniform temperature along its entire length, thus minimizing unwanted temperature–dependent cable delays. The relative phases of the 100 MHz output frequency of the separated masers can be measured directly and recorded as a function of time. It can be seen from Figure 1 that the cable provides a propagation path that is mainly along the North–South direction. Nevertheless, the cable spans a distance of about 10 kilometers in the East–West direction. It is this projection of the path in the East–West direction which is most relevant to the experiment, because the orientation of this direction changes with respect to the stars as the Earth rotates in space.

The possible effect of an anistropy in the speed of light on the phase measurements can be modeled at a simple level by considering

$$c = c_0 + \delta(\tau) \tag{1}$$

where c_0 is the average value of the speed of light, or perhaps the value that is determined from laboratory measurements (i.e., $c_0 = 299,792,458$ m/sec) [8], while $\delta c(\tau)$ represents a generalized perturbation which could vary with time (τ) as the Earth rotates in space. To lowest order, this leads to a phase variation of magnitude

$$|\delta\phi(\tau)| = f(\frac{L}{c_0})\frac{|\delta c(\tau)|}{c_0} \tag{2}$$

where $f = 100$ MHz and L is the baseline pertaining to the possible anisotropy and the geometry of the experiment. Taking $l = 10$ kilometers yields in units of degrees

$$|\delta\phi(\tau)| = 1.2 \times 10^6 \frac{|\delta c(\tau)|}{c_0}. \tag{3}$$

According to special relativity, $\delta\phi(\tau)$ should be zero for all τ. Our goal is to test as precisely as possible the validity of this prediction under the particular conditions of the experiment. A more detailed discussion of the theory underlying a possible anisotropy in the one–way velocity of light is beyond the scope of this report.

For the past year, preparations have been underway to perform continuous phase measurements over several rotations of the Earth. A few tests were performed during this time to evaluate the performance of the system and to determine what improvements needed to be made. Just two weeks before this PTTI meeeting, we were able to successfully run the experiment continuously for nearly five days. In the remainder of this report, we will discuss how the experiment was performed and consider the results of a preliminary analysis of the data that was obtained. The instrumentation and the procedures used in the experiment are described in Section II. Presented in Section III are the results of the preliminary data analysis. Concluding remarks are made in Section IV.

II. INSTRUMENTATION AND PROCEDURE

Illustrated in Figure 2 is the instrumentation that was used to perform the phase measurements. Identical instrumentation was used at each site. The 100 MHz output frequency of the masers was split into two signals. One signal was fed directly into one channel of a Hewlett–Packard 8753A Network Analyzer. The other signal was fed into a fiberoptics laser transmitter, which used the signal to modulate the optical carrier along the fiber. This modulation was detected at the far end of the fiber with a fiberoptics receiver, the output of which was fed into the second channel of the network analyzer at that end. The network analyzers measured the relative signal phase between the two channels. Although the fiberoptics cable contains several single–mode optical fibers, a single fiber only was used in the experiment. Because the 100 MHz modulations from each maser were propagated one–way simultaneously in both directions along the same fiber, isolators were required to separate the received and transmitted signals.

In performing the experiment, the relative signal phases between the two masers was measured once every ten seconds continuously for nearly five days and was recorded as a function of time. The observations began on November 12, 1988 at 20:00:00 (UTC) and ended on November 17, 1988 at 17:30:14 (UTC). An IBM personal computer was used at each site to control the network analyzer and to automate the collection of the data. Simultaneous phase measurements were performed at each site in order to provide the capability to difference the data, which would remove common–mode errors, such as due to maser frequency fluctuations or residual temperature–dependent delays along the optical fiber.

III. PRELIMINARY DATA ANALYSIS

In order to reduce the large volume of data that was generated and to filter unwanted high frequency signatures, the data has been sampled at 1000 second intervals. Plotted in Figure 3 is the resulting phase record obtained at DSS 13 only. (A similar plot results from the data obtained at DSS 14 only.) The linear drift in the phase is due to the slight offset in frequency between the two masers. A record of this frequency offset can be obtained by differencing successive phase measurements and dividing by the associated time interval, the results of which have been plotted in Figure 4. It can be seen that the frequency offset is about 57×10^{-6} Hz. Most noticable is a sinusoidal modulation in the frequency offset whose cause we are trying to determine but which appears to be associated with the instrumentation. Also apparent in Figure 4 is an anomalous excursion in the offset starting after about 88 hours.

If we consider only the first three days of data, then we can at least model the bias and drift in the maser offset according to

$$\Delta f = A_0 + A_1 t \tag{4}$$

where A_0 represents the bias and A_1 represents the drift rate. A least–squares fit to this first three days of the frequency record yields $A_0 = 56.566 \times 10^{-6}$ Hz and $A_1 = 1.55 \times 10^{-11}$ Hz/sec. Because phase is related to frequency according to $d\phi = f dt$, the effect on the phase measurements is given by

$$\Delta\phi = A_0 t + \frac{1}{2} A_1 t^2 \tag{5}$$

After the phase measurements are calibrated according to equation (5), the linear drift is removed and finer structure in the phase record becomes apparent, which can be seen in Figure 5. Most apparent is the unexplained sinusoidal variation seen in Figure 4. It should be noted, however, that the phase variations over 24 hours are as small as 10 degrees.

If both the calibrated phase records from DSS 13 and DSS 14 are differenced to remove common-mode errors, then there results the plot in Figure 6. A sinusoidal variation is seen to persist. Nevertheless, it can be seen that the phase variations over 24 hours are again as small as 10 degrees.

IV. CONCLUSION

A preliminary analysis of the data has revealed some systematic effects which appear to be instrumental in origin and therefore need to be corrected. Our future plans are to account for these effects so that we may see what phase fluctuations remain and to perform a more detailed data analysis. For now, the data suggests that the remaining phase variations are probably limited to less than 10 degrees over 24 hour periods. From equation (3), a limit of $\delta\phi < 10$ degrees would imply a limit of $(\frac{\delta c}{c}) < 10^{-5}$. It should be possible to improve upon this limit by at least an order of magnitude.

ACKNOWLEDGEMENTS

We are especially indebted to Dr. N. A. Renzetti, without whose continued support and encouragement this research would not be possible. Our thanks also go to Dr. R. L. Sydnor for helpful comments. The research described in this report was carried out by the Jet Propulsion Laboratory, California Institute of Technology, under a contract with the National Aeronautics and Space Administration and was funded through the Caltech President's Fund.

REFERENCES

1. C. D. Edwards, in Proceedings of the AIAA/AAS Astrodynamics Conference, August 15–17, 1988, Paper 88–4287–CP, pp. 545–548.

2. R. S. Shankland, S. W. McCuskey, F. C. Leone, and G. Kuerti, Rev. Mod. Phys 27, 167 (1955), Table 1.

3. A. Brillet and J. L. Hall, Phys. Rev. Lett. 42, 549 (1979).

4. J. L. Hall, in Atomic Physics, Vol. 7, edited by Daniel Kleppner and Francis M. Pipkin (Plenum Press, New York, 1981), pp. 267–296.

5. E. Riis, L.–U. A. Andersen, N. Bjerre, O. Poulsen, S. A. Lee, and J. L. Hall, Phys. Rev. Lett. 60, 81 (1988).

6. D. R. Gagnon, D. G. Torr, P. T. Kolen, and T. Chang, Phys. Rev. A 38, 1767 (1988).

7. T. P. Krisher, L. Maleki, J. D. Anderson, and C. M. Will, in Proceedings of the Nineteenth Annual Precise Time and Time Interval (PTTI) Applications and Planning Meeting, December 1–3, 1987, pp. 367–373.

8. R. P. Hudson, Metrologia 19, 163 (1984).

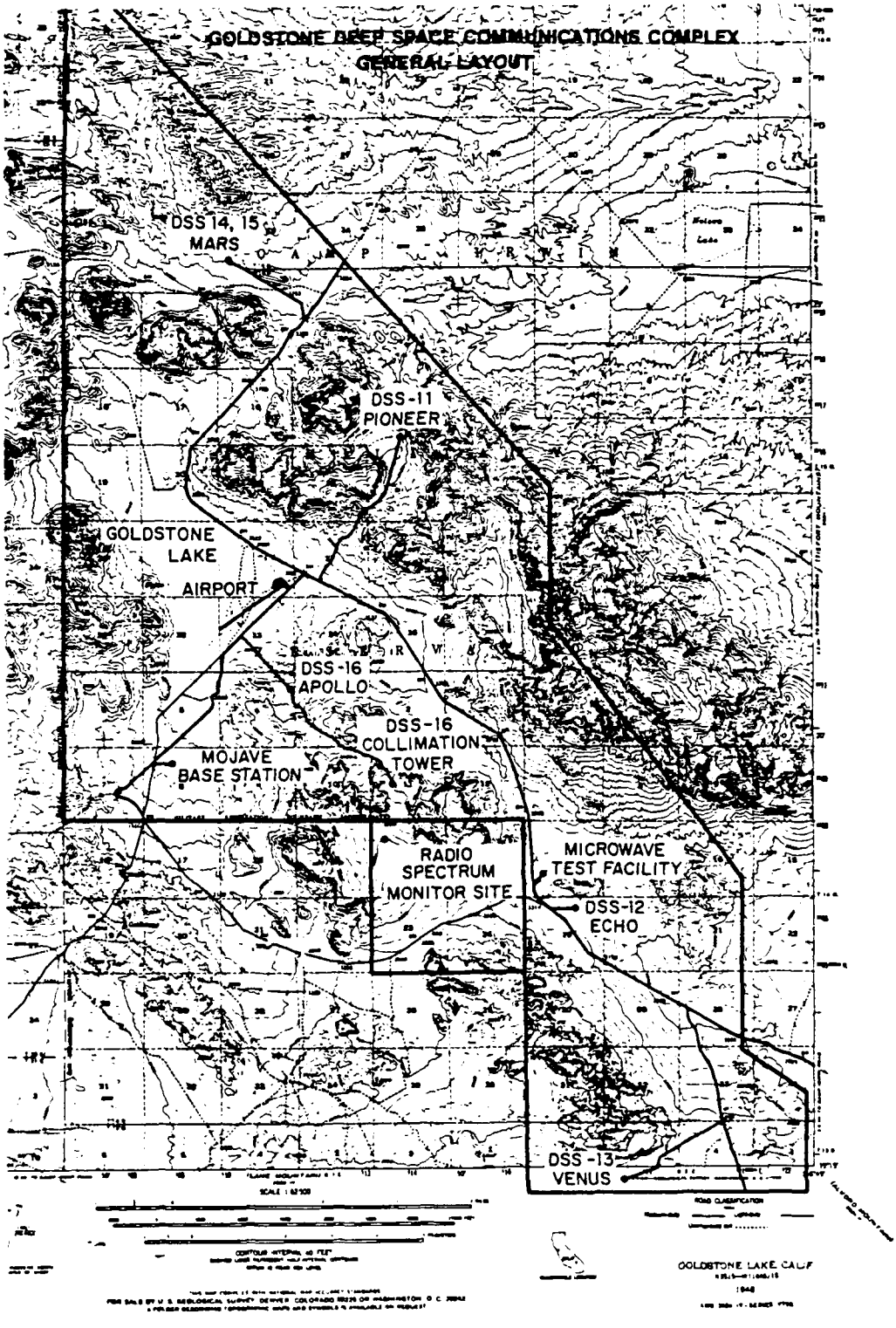

Figure 1. Goldstone Deep Space Communications Complex

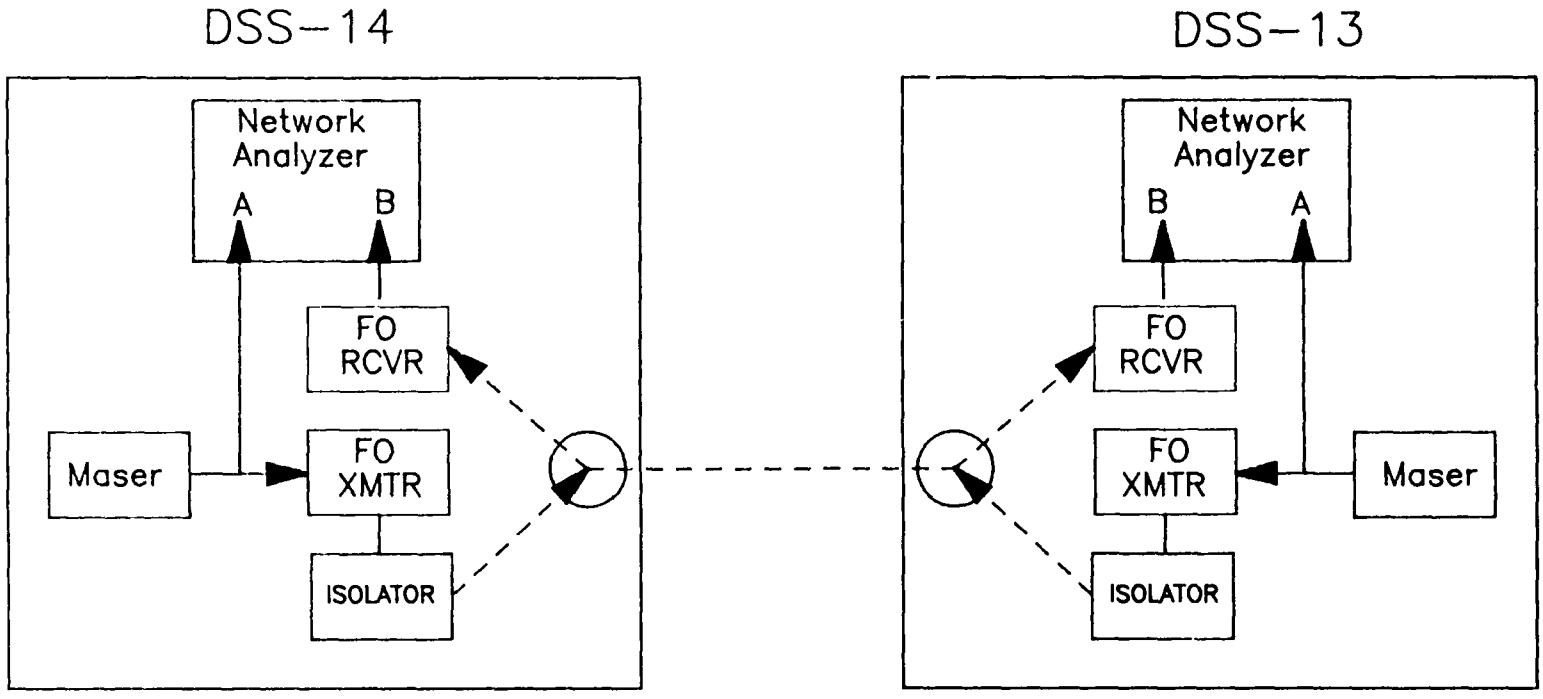

Figure 2. Instrumentation used to perform maser phase comparison.

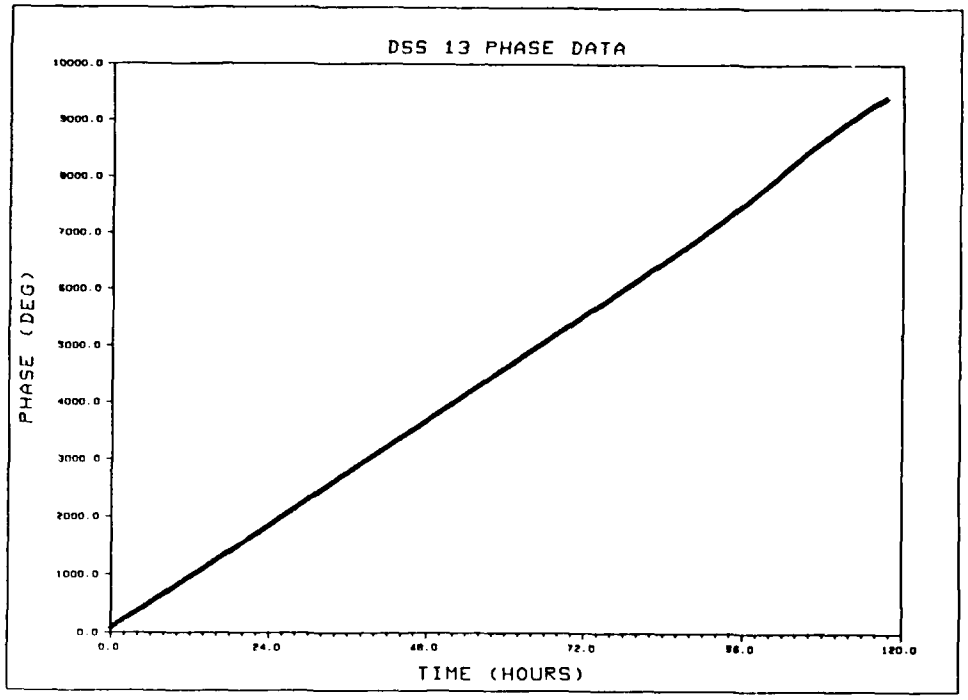

Figure 3.

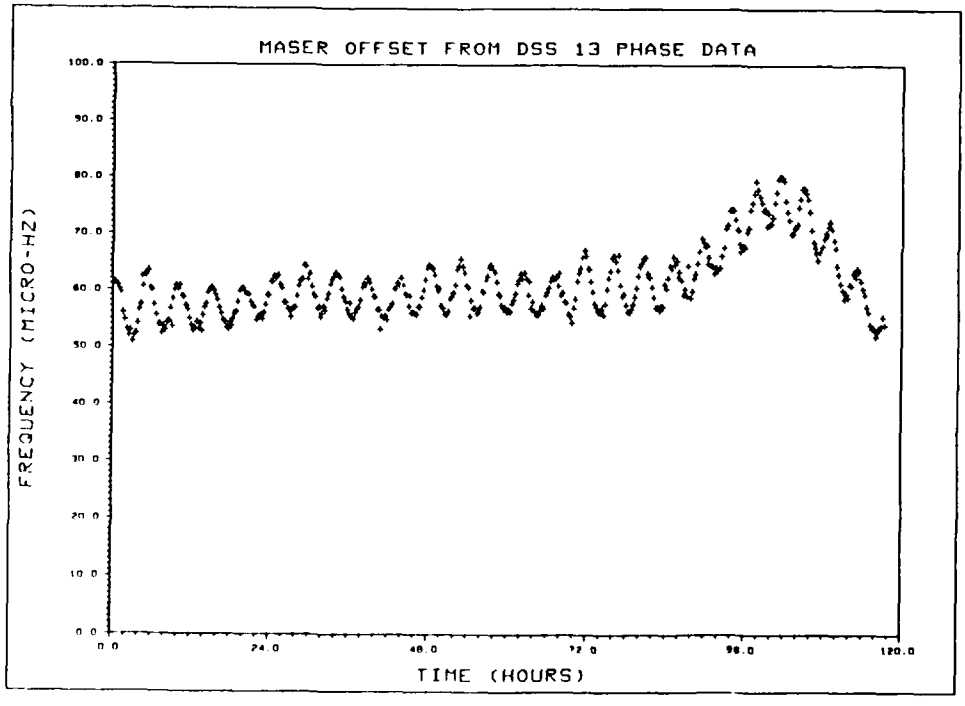

Figure 4.

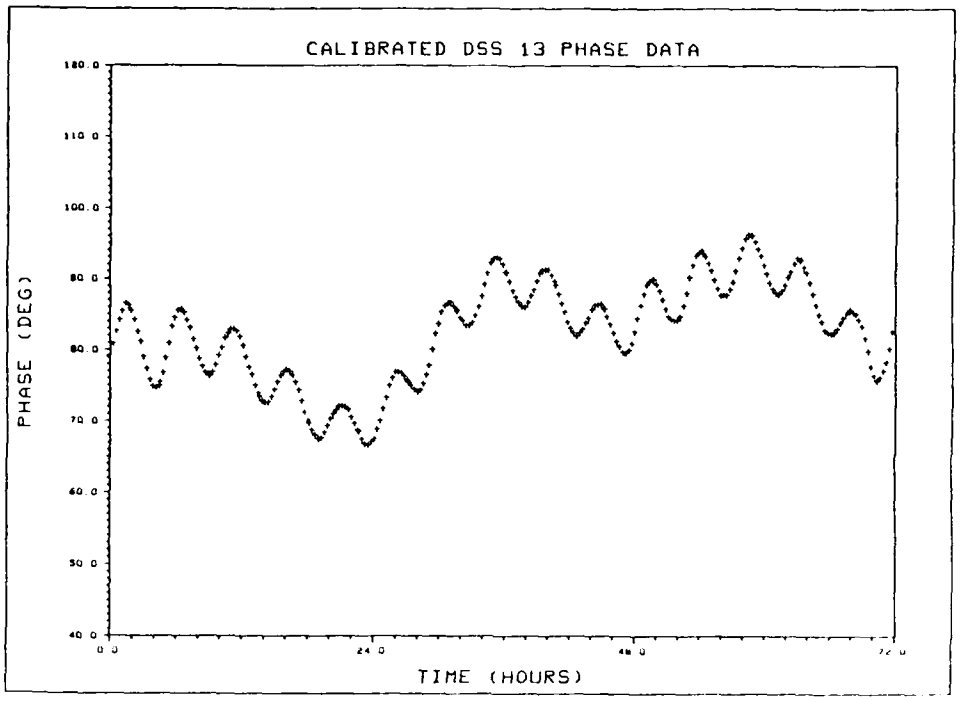

Figure 5.

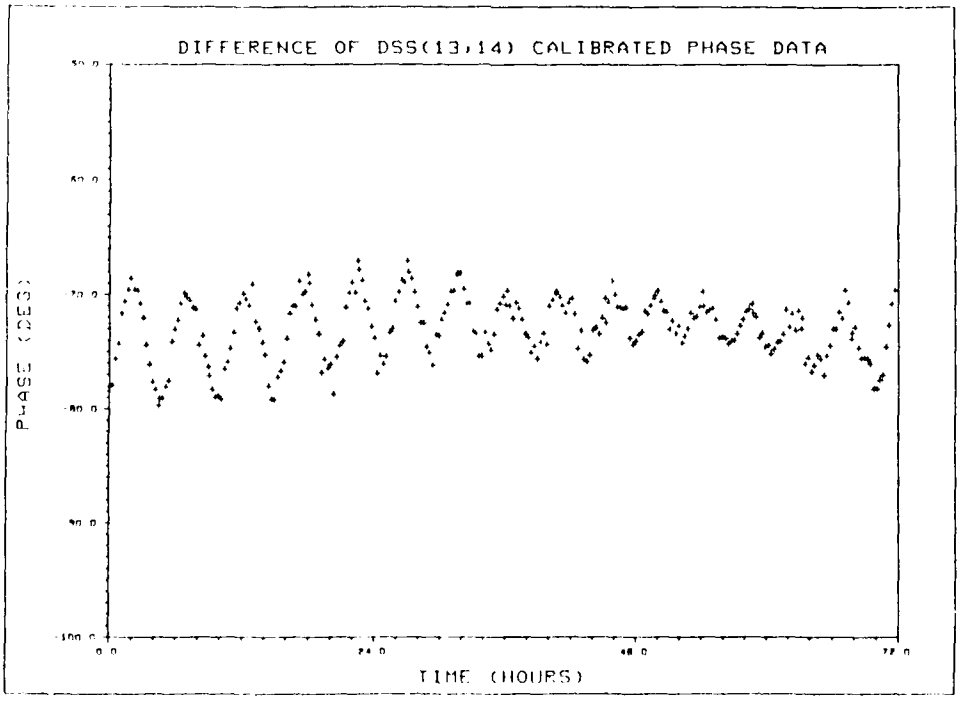

Figure 6.

QUESTIONS AND ANSWERS

DR. GERNOT WINKLER, USNO: Which masers did you use in the two stations?

MR. KRISHER: We used an SAO maser at station 14 and the station 13 maser was built at JPL.

DR. WINKLER: Do they have automatic cavity lock?

MR. KRISHER: No, they free–run.

DR. WINKLER: If I figure correctly, that is almost one part in ten to the fourteenth change, isn't it?

MR. KRISHER: That is correct.

DAVID ALLAN, NIST: One of the things that you are going to have to do is evaluate the differential diurnal variation in the masers, because that is the component that you are looking for. The other question is what is the best previous value of the one–way anisotropy in the speed of light? You have 8 times ten to the minus six, what is the previous value?

MR. KRISHER: Laboratory experiments give a limit of one part in ten to the ninth. However, one point that I would like to make about our experiment is that it is very simple, probably the simplest way to make this experiment. Laboratory experiments try to infer a limit from some sort of atomic frequency measurements or comparing frequency offsets in wave–guides or something of this nature. Here we are trying to measure directly the advance in phase of a signal propagated over the base–line.

DIFFERENTIAL COMPARISON OF THE ONE-WAY SPEED OF LIGHT IN THE EAST-WEST AND WEST-EAST DIRECTIONS ON THE ROTATING EARTH

C.O. Alley, R.A. Nelson, Y.H. Shih,
B.W. Agnew, R.E. Bartolo, J.T. Broomfield, J.A. Fogleman, J.C. Hunt,
M.G. Li, M.A. Perry, J.D. Rayner, C.A. Steggerda, B.C. Wang
Department of Physics and Astronomy
University of Maryland
College Park, Maryland 20742

M.J. Chandler
Bendix Field Engineering Corporation
One Bendix Road
Columbia, Maryland 20745

L.J. Rueger, J.L. Wilcox
Johns Hopkins University/Applied Physics Laboratory
Laurel, Maryland 20707

ABSTRACT

A status report is presented for a time transfer experiment which compares the times of flight in the east-west and west-east directions of short pulses of light sent *from* a laser coupled to the 48-inch telescope at the NASA Goddard Optical Research Facility to the U.S. Naval Observatory and reflected back over the same path. The times t_1 and t_3 when each light pulse leaves GORF and returns are measured with an event timer referenced to a hydrogen maser. The time t_2 when the pulse is reflected at USNO is measured with a portable event timer and maser combination carried in a heated and air-conditioned truck. Each maser is maintained in a temperature-controlled environment. The portable maser enclosure is supported by pneumatic shock and vibration suppression mounts. The quantity

$$\Delta T \equiv t_2 - \frac{1}{2}(t_1 + t_3) = \frac{1}{2}[(t_2 - t_1) - (t_3 - t_2)]$$

is determined. The apparatus is calibrated by performing corresponding measurements with the portable detector at GORF in the same equipment configuration used at USNO while also monitoring the phase difference between the masers.

The central question to be answered by the experiment is whether the Einstein prescription for the synchronization of clocks with light pulses occurs automatically ($\Delta T = 0$) or must be imposed by convention in the context of a theory ($\Delta T \neq 0$). The necessary precision of ≤ 50 ps has not yet been achieved for the complete measurement although it has been accomplished for clock trips and laser pulse detection on separate occasions.

INTRODUCTION

A fully successful theory of space, time, and gravity must be founded upon actual experience with the behavior of clocks and the propagation of light pulses in gravitational fields and in accelerated frames of reference. The remarkable stability of current atomic clocks and the precision of short pulse laser ranging and time transfer systems now allow new types of experiments to be undertaken. These will allow the necessary experience to be gained. Indeed, the originally astonishing predictions of special and general relativity about the behavior of clocks in relative motion and experiencing different gravitational potentials have become part of engineering practice, as the PTTI community knows well.[1] With these refined techniques the foundations of curved spacetime theories of gravity can be probed and crucial tests of alternative theories performed. Our comprehension and understanding of the theories will surely benefit from actually doing such experiments.

The central role of clocks in the description of gravity as curved spacetime -- Einstein's grand concept -- is most appropriately expressed, in the words of John Leighton Synge,[2] as "Riemannian Spacetime *Chronometry*," rather than *geometry*. The spacetime interval with metric $g_{\mu\nu}$ is given by

$$ds^2 = g_{\mu\nu}\, dx^\mu\, dx^\nu = g_{00}\,(dx^0)^2 + 2\, g_{0j}\, dx^0\, dt + g_{ij}\, dx^i\, dx^j \qquad (1)$$

where a repeated Greek index is summed 0 to 3, a repeated Latin index is summed 1 to 3, and $x^0 \equiv c\ t$. For a clock $ds^2 = c^2\, d\tau^2$, where $d\tau$ is the increment of "proper time" read by the clock between neighboring events which occur at the position of the clock. In contrast, dt is the increment of "coordinate time" between the same two neighboring events inferred by an observer who could be in relative motion, or in a different location, with respect to the clock. Another convention is that the "coordinate speed" of light is to be given by setting $ds^2 = 0$.

In a 1982 PTTI paper[3] describing time transfer experiments between the NASA Goddard Optical Research Facility and the U.S. Naval Observatory using short pulses of laser light, it was noted that on the rotating earth the metric usually ascribed to general relativity[4-6] seems to predict an asymmetry in the one-way speed of light between the east-west and west-east directions, the fractional difference being $\pm\ v/c$, where v is the surface speed of the earth due to its rotation. For the latitude of Washington, DC, $v \approx 361$ m/s and $v/c \approx 1.2 \times 10^{-6}$, leading to a difference in propagation times of 165 ps. It was suggested that this difference might be detected in future experiments.

The importance and significance of actually performing such experiments were recognized as a result of many clarifying discussions with Professor Hüseyin Yilmaz about his new theory of space, time, and gravitation.[7] This is a fully developed curved spacetime alternative theory to that of Einstein. (The differences between the new theory and general relativity are briefly sketched at the end of this paper.) In the new theory of Yilmaz, if the Einstein prescription for synchronization with light pulses is automatic, then the theory predicts that the local speed of light is isotropic, even in an accelerated frame of reference such as the surface of the rotating earth. If the speed of light is not isotropic, it can be made so by an imposed Einstein

synchronization (for example, by physically resetting the distant clock), in which case, however, the constancy of the velocity of light is more like a convention than a law. In other words, this experiment may resolve the old unresolved controversy (Poincaré *vs.* Einstein) as to whether the constancy of the speed of light is a convention or a law.

Several features of the experiment should be emphasized. We believe that it is the first comparison of the one way speeds of light in different directions along a path in which the time of arrival of the light pulse is actually registered on a clock which has been slowly transported from one end to the other of the path. Also, in contrast to the optical experiments of the Michelson-Morley type[8], the Mössbauer gamma ray absorption experiments on a rotating disk,[9] and recent comparisons of two separated atomic clocks using a continuous wave laser signal modulated at 100 MHz and propagated over a fiber optics cable,[10] we work with short pulses involving the group velocity and actual measurements of time rather than with waves involving the phase velocity and measurements of phase difference or frequency. Note also that we do not physically adjust the transported clock in any way.

DESIGN OF EXPERIMENT

Test of the Einstein prescription.

According to the Einstein prescription in special relativity for the synchronization of two clocks using light pulses, if a pulse is sent out at time t_1, reflected from a distant point at time t_2, and received back at time t_3, then t_2 is to be identified with the midpoint in time between t_1 and t_3,

$$t_2 = \frac{1}{2}(t_1 + t_3) . \qquad (2)$$

It is usually assumed that this relation is appropriate for all inertial observers. Define the time difference

$$\Delta T \equiv t_2 - \frac{1}{2}(t_1 + t_3) = \frac{1}{2}[(t_2 - t_1) - (t_3 - t_2)]. \qquad (3)$$

The Einstein prescription implies that for all inertial observers $\Delta T = 0$. It follows that the times of light propagation between the two clocks are equal. The object of the experiment is to determine whether the Einstein prescription is also valid for accelerated observers on the rotating earth by measuring the difference in times of light propagation in the east-west and west-east directions from the readings of a stationary clock and a clock transported from the stationary clock to a distant place.

Another way of viewing the experiment is as the comparison of two different methods for the synchronization of two remote clocks: by the transmission and reception of light signals and by the slow transport of an atomic clock. Does the Einstein prescription from special relativity, which assumes the speed of light is c both ways, occur automatically for local measurements on the rotating earth ($\Delta T = 0$) or must it be imposed by convention in the context of a theory ($\Delta T \neq 0$)?

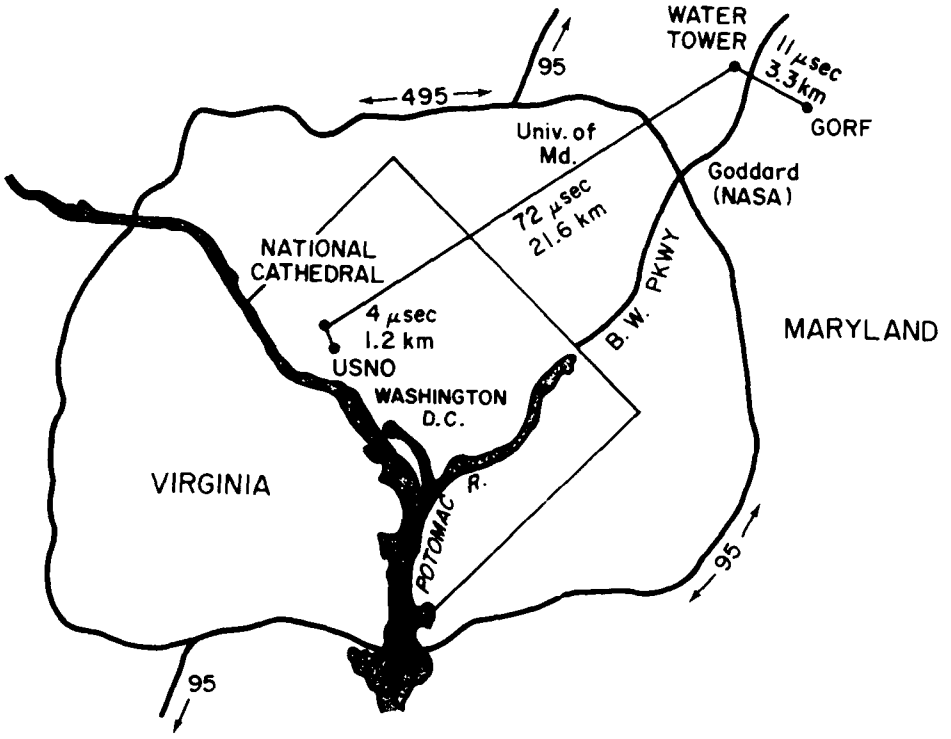

Fig. 1. Optical path across Washington.

Optical path.

In our experiment we send short pulses of green light from a laser coupled to the 48-inch telescope at the NASA Goddard Optical Research Facility in Greenbelt, MD (longitude 76° 49.'7, latitude 39° 01.'3, elevation 42 m) to a portable detector set up on the grounds of the U.S. Naval Observatory in Washington, DC (longitude 77° 04.'0, latitude 38° 55.'3, elevation 78 m). Although there is no direct line of sight, the optical path is made possible by a 30-cm flat mirror on a water tower near GORF and a 25-cm flat mirror on top of the Washington National Cathedral near USNO.[3] The cathedral can be seen on the horizon from the water tower. There are three corner cubes mounted on a support ring surrounding the detector. The corner cubes are of the type used in the American Laser Ranging Retro-Reflectors left on the moon by the Apollo 11, Apollo 14, and Apollo 15 astronauts.[11,12] Usually only one of these is left uncovered and reflects the light pulses back over the same path. The light travel time is 87.1 μs over a distance of 26.1 km, as illustrated in Fig. 1. The east-west component is 20.6 km.

Measurements are made of the time t_1 when a laser pulse leaves the telescope and the time t_3 when it returns using an event timer whose frequency standard is a hydrogen maser kept in the telescope building at GORF. The time t_2 when it is reflected at USNO is measured with a second, portable event timer and hydrogen maser combination carried in a field laboratory truck owned

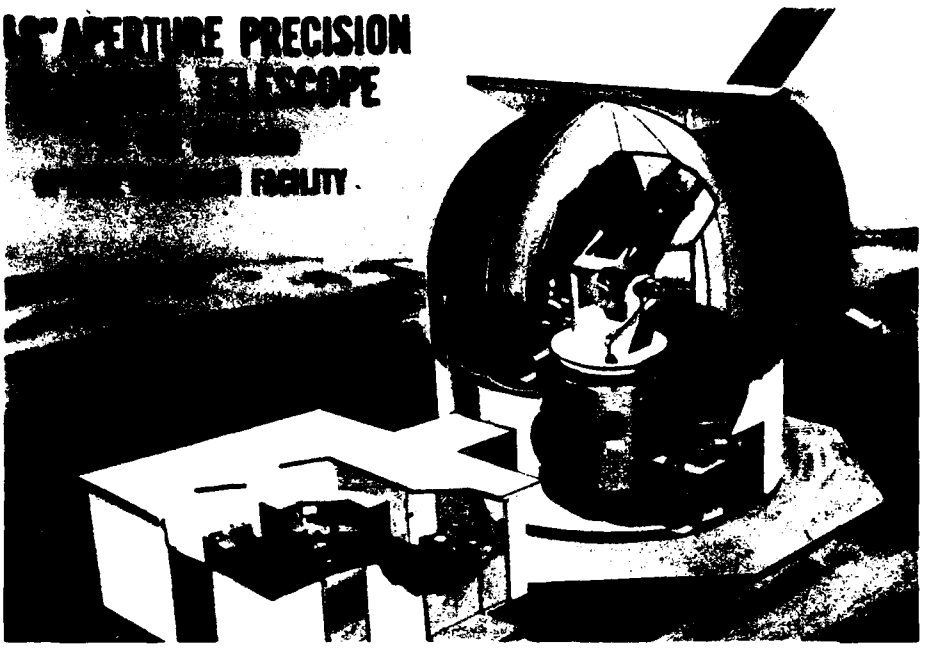

Fig. 2. The 48-inch telescope at the NASA Goddard Optical Research Facility.

by the Applied Physics Laboratory. Both masers and their environments are maintained at controlled temperatures. The portable maser is protected from shock and vibration by pneumatic support mounts. The t_1 and t_3 detectors are located on the laser table below the telescope. The t_2 detector is set up on a tripod next to the truck. A diagram illustrating the geometry of the telescope and laser is shown in Fig. 2.

Mirror alignment.

The mirrors used for the across-Washington optical link were installed in 198[illegible] for use in earlier laser time transfer tests and are illustrated in Ref. [3] For this experiment a third mirror was installed on a tower about 100 meters from the GORF telescope for routine tests and local calibration. It is shown in Figures 3 and 4.

The water tower and cathedral mirrors must be aligned very precisely. A small Edmund Scientific company telescope modified with a retroreflector that partially obscures the aperture is used to sight in the forward and backward directions simultaneously.[3] When the water tower mirror is properly aligned, the image of the cathedral appears inverted and superposed on top of the image of the Goddard 48-inch telescope. Similarly, the cathedral mirror is aligned to superpose the image of the location of the USNO t_2 detector on top of the image of the water tower. During a night when measurements are taken, people must be dispatched to the water tower and cathedral in order to make minor mirror adjustments caused by initial alignment errors, changing

Fig. 3. Local calibration mirror on top of tower near telescope.

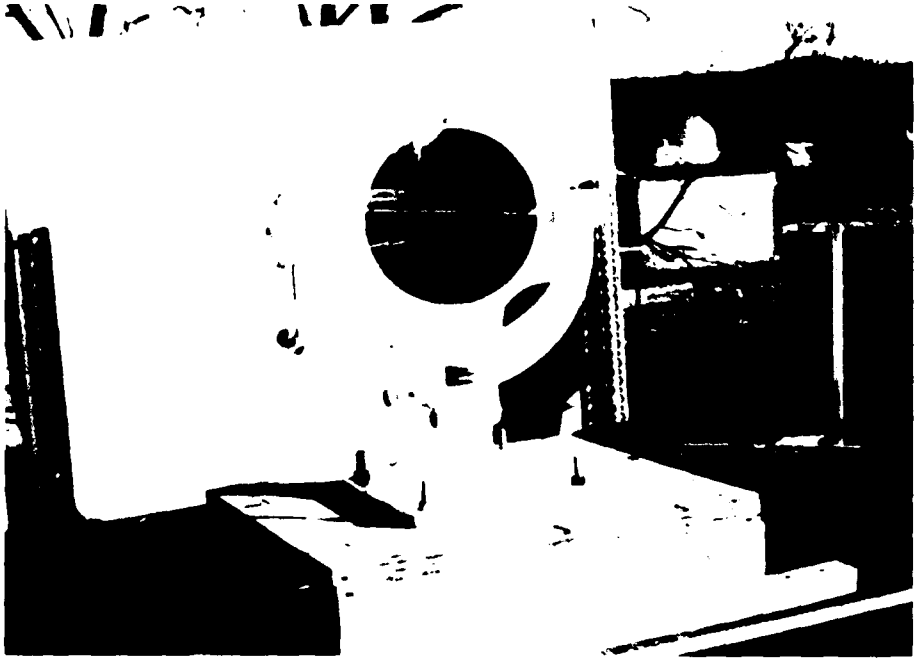

Fig. 4. Closeup view of local mirror.

atmospheric conditions, and movement of the water tower. The activities at the various locations are coordinated by means of a telephone conference call. On a clear night the laser signal arriving at USNO is bright enough to project its image on a screen and cast shadows of the detector package against the side of the truck. Our experience has been that bright signals can be seen easily when the visibility is 15 to 20 miles according to reports for National, Dulles, and BWI airports. During much of the summer it was not possible to establish the optical link because the visibility was only about 5 miles due to haze.

Effect of the atmosphere.

The Einstein prescription is essentially unaffected by the atmosphere. Assume that the atmosphere introduces a delay Δt_1 for the emitted pulse and a delay Δt_3 for the received pulse. The Einstein prescription becomes

$$t_2 = \frac{1}{2}\left[(t_1 - \Delta t_1) + (t_3 + \Delta t_3)\right]$$

$$= \frac{1}{2}(t_1 + t_3) + \frac{1}{2}(\Delta t_3 - \Delta t_1) . \qquad (4)$$

The atmospheric delays in the second term are each about 26 ns but they nearly cancel since the paths are nearly the same. (Of course, atmospheric delays do affect measurements of range, where they are additive.) Since we are measuring differences in the times of propagation, each set of pulse times is independent. It is known that fluctuations in the atmosphere occur over intervals on the order of 1 ms or more, whereas the round trip time for a single pulse is about 174 μs.

Clock registration times.

The times t_1, t_2, and t_3 are ideal times that do not account for detector rise times, cable delays, event timer processing times, and other systematic errors. We must also account for the changing relative phase between the masers. In the experiment our actual measurements are the "registration times" t_1^*, t_2^*, and t_3^* recorded by the electronic timing equipment and atomic clocks instead of the ideal times. The ideal time of each event is related to the registration time by

$$t = t^* - \Delta t_{DEL} - \Delta t_{PHASE} \qquad (5)$$

where Δt_{DEL} is the total delay time comprising the rise times, cable delays, and processing times, Δt_{PHASE} is the clock phase difference including clock drifts, synchronization errors, and relativistic effects due to clock transport. Substituting the relation given by Eq. (5) for times represented

in Eq. (3) we obtain

$$\Delta T = \Delta T^{*} - [\Delta t_{DEL2} - \frac{1}{2}(\Delta t_{DEL1} + \Delta t_{DEL3})] - \Delta t_{PHASE2} \qquad (6)$$

where we assume the reference clock for relative phase comparisons is the stationary clock and

$$\Delta T^{*} \equiv t_2^{*} - \frac{1}{2}(t_1^{*} + t_3^{*}) . \qquad (7)$$

The quantity ΔT^{*} is the quantity we measure in the experiment.

A critical feature in the design of the experiment is that the entire timekeeping apparatus for the t_2 measurement is a portable, self-contained system. This permits us to perform local calibration measurements at GORF in exactly the same configuration of equipment as the measurements made at USNO. The instrumental delay times are unknowable. However, assuming that environmental factors do not cause significant shifts, they remain constant and can be eliminated by the local calibration measurements. The phase difference is determined independently during the optical calibration.

Measurement procedure and analysis.

In each experiment exercise we first perform a series of optical calibration measurements of t_1, t_2, and t_3 at GORF using the local mirror while the phase difference between the masers is monitored. Next the t_2 event timer, maser, and detector are transported to USNO and the measurements are repeated using the across-Washington optical link. While at USNO the phase of the portable maser is compared against the USNO maser master reference. Finally, the equipment is brought back to GORF and the local calibration measurements are repeated. The procedure is summarized in a schematic diagram in Fig. 5. Figure 6 shows the truck and detector at GORF and Fig. 7 shows the position in front of Building 1 at USNO.

The optical measurements of t_1, t_2, and t_3 are merged on a computer for all laser pulses for which a complete set is obtained. The matching program produces distributions for the differences $t_{31}^{*} \equiv t_3^{*} - t_1^{*}$ and $t_{21}^{*} \equiv t_2^{*} - t_1^{*}$. Then we calculate

$$\Delta T^{*} = t_{21}^{*} - \frac{1}{2} t_{31}^{*} . \qquad (8)$$

We can rearrange Eq. (6) in the form

$$\Delta T^{*} = \Delta T + [\Delta t_{DEL2} - \frac{1}{2}(\Delta t_{DEL1} + \Delta t_{DEL3})] + \Delta t_{PHASE2} . \qquad (9)$$

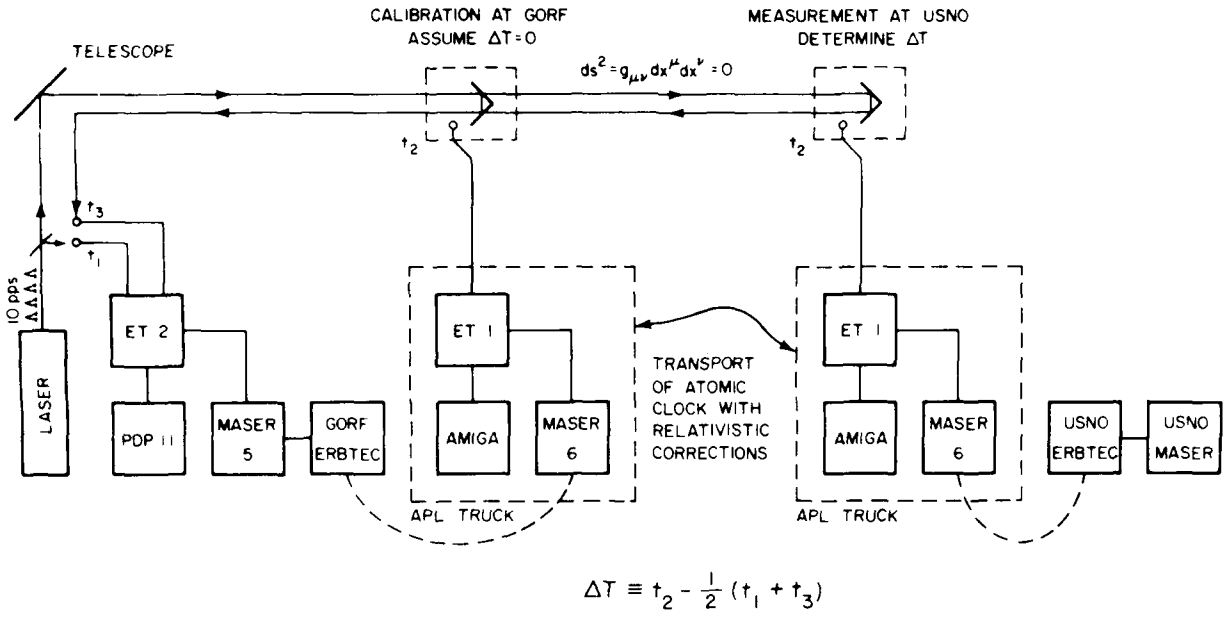

Fig. 5. Schematic diagram of experiment.

For the local measurements at GORF we assume $\Delta T^* = 0$. The second term is constant for all measurements. The variation in ΔT^* measured optically should thus track the variation in Δt_{PHASE2} measured by the maser phase comparison.

Relativistic corrections must be applied to the t_2^* measurements due to the velocity and change in elevation of the truck. During a trip the velocity of the truck is measured continuously on a strip chart recorder and annotations of location are made at various points along the route. The maximum truck speed is 65 km/h (40 mph). The elevation of USNO is 36 m higher than GORF. Each trip requires about one hour to drive from GORF to USNO, two or three hours of dwell time, and one hour to return. The relativistic corrections for the entire trip are on the order of - 10 ps for velocity and + 14 ps per hour of dwell time for elevation. There may also be a relativistic correction due to the earth's rotation. Part of this investigation entails clarification of the nature of this correction.

If the Einstein prescription is valid on the rotating earth, optical measurements of ΔT^* made at USNO should agree with values obtained by interpolation of the calibration measurements after appropriate relativistic corrections are applied to t_2^* to account for the transportation of the atomic clock. Since the configuration of equipment remains the same, a discrepancy between the measured and interpolated values of ΔT^* would imply a nonzero value for the quantity ΔT of Eq. (2). For an asymmetry in the coordinate speed of light, as discussed in the INTRODUCTION, the difference in propagation coordinate times is $2\ v\ d/c^2 \approx 165$ ps where d is the east-west distance between the ends of the light path at GORF and USNO and v is the surface velocity, according to a possible interpretation of general relativity. This is developed explicitly in Eq. (19) below.

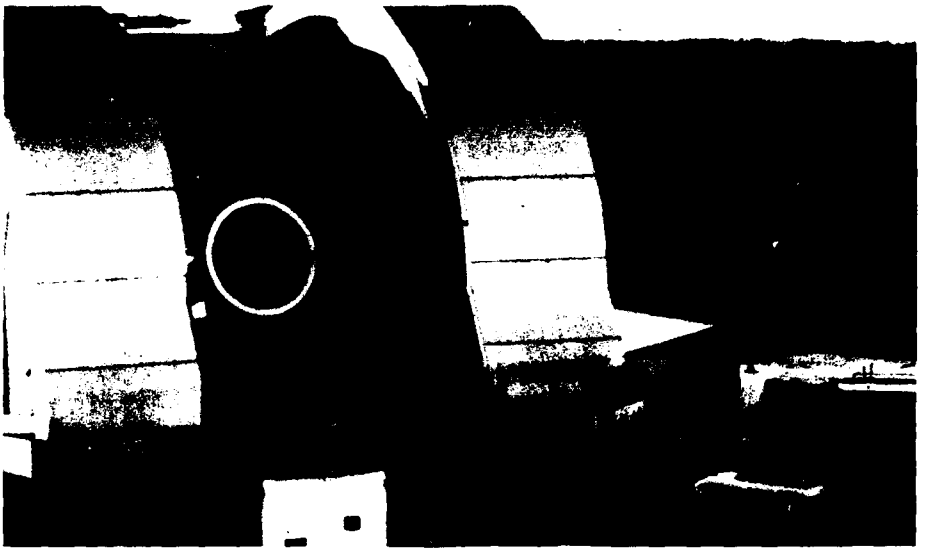

Fig. 6. Truck and detector at GORF with water tower visible on the horizon as seen from the calibration mirror tower.

Fig. 7. Truck parked at USNO during a maser comparison test.

DESCRIPTION OF EQUIPMENT

Laser and detectors.

The light pulses are generated by a Q-switched, mode-locked, neodymium YAG laser with two amplifiers. The fundamental infrared wavelength 1064 nm is converted to be green at 532 nm by frequency doubling. The pulse width is 70 ± 10 ps. The output energy in the green is 15 ± 2 mJ per pulse and the repetition rate is 10 Hz. The t_1 detector is a PIN diode sensitive to infrared wavelengths with 50 ps rise time. The diode is placed after the oscillator but before the amplifiers and frequency doubler. The t_3 detector is a Hamamatsu R2809U microchannel plate photomultiplier tube with a rise time of 150 ps and a transit time spread of 55 ps. The output of the microchannel plate tube is attenuated by 7 dB and then amplified by two Mini Circuits ZFL-2000 2-GHz amplifiers for a net gain of 36 dB. The t_1 and t_3 signals are fed into two channels of a Tennelec 455 constant fraction discriminator modified to discriminate on the fast rise times and are recorded by two channels of the event timer, respectively. The measurements are stored on a PDP-11/73 computer. The t_2 detector is an RCA C30902E avalanche photodiode operating in the avalanche mode with a rise time of less than 500 ps. The diode is cooled to - 65 °C with dry ice and produces an output of 150 mV by itself. The signal is fed directly into a Tennelec 453 constant fraction discriminator and measured by one channel of the portable event timer carried in the APL truck. The data are stored on an Amiga personal computer.

Masers.

The masers that we are using in this experiment are Sigma Tau masers 5 and 6 on loan to us from the National Radio Astronomy Observatory near Socorro, NM. Maser 5 is used as the stationary maser at GORF and maser 6 is used as the portable maser in the APL truck. These masers are part of a group of ten, model VLBA-112, being constructed for NRAO by Harry Peters and his associates[13] at the Sigma Tau Standards Corporation and are shown in Fig. 8. We have measured their relative phase to have a root Allan variance of about 2×10^{-15} at 3 hours. The performance of these two masers is consistent with characteristics reported by T.K. Tucker in his evaluation of masers 2 and 3.[14] Masers 5 and 6, however, have the additional feature of a servo loop that compensates for changes in the z-component of the magnetic field of the environment.

In earlier measurements during the summer of 1988 we used Peters maser *ST*1 provided by the Applied Physics Laboratory through the courtesy of JPL and an APL-designed NR-series maser on loan from the NASA Crustal Dynamics Project and the Bendix Field Engineering Corporation. The JPL Peters maser was also used last year in the APL truck for time transfer experiments between the USNO and APL to test the feasibility of making precision time comparisons using a carefully packaged hydrogen maser as a portable clock.[15]

The relative phase of the 5-MHz outputs of masers 5 and 6 is measured at GORF using an Erbtec Engineering Co. double mixing system and an HP 9826 computer lent to us by the Naval Research Laboratory and the U.S. Naval Observatory. Maser 6 is compared with the USNO maser standard during an optical measurement with another Erbtec system when at USNO.

Fig. 8. Masers 5 and 6 at Sigma Tau Standards Corporation.

Event timers.

The two event timers used in this experiment are dual frequency, dual channel event timers designed and constructed in the Quantum Electronics Group of the University of Maryland Department of Physics.[16] Each event timer can measure the epoch of events to a precision of 20 ps on two different channels. With its Z-80 microprocessor system, the event timer serves as a time of day clock and as a range gate system operated under external computer control. The event timer contains a Z-80 microprocessor system with 60 K of ROM and 2 K of RAM memory and may operate with other computers via an RS-232 serial port or IEEE 488 parallel bus (GPIB).

The event timer uses dual frequency verniers developed by Hewlett Packard for their HP5370 time interval meter. Figure 9 illustrates the principle of operation. One of the dual frequencies, *F*1, is produced by a 200-MHz tunable crystal oscillator which is synchronized to a 5- or 10-MHz output of a hydrogen maser. The *F*1 oscillator runs continuously to drive a 26 bit synchronous counter which is the time generator. The time generator has exactly 50 000 000 states so it repeats every quarter second. The second of the dual frequencies, *F*2, is produced by a restartable delay line oscillator which is adjusted by other circuits to operate at 199.221 7899 MHz (abbreviated 199* MHz) and is derived from *F*1 by the equation *F*1 - *F*2 = *F*2/256. Thus for every 256 cycles of *F*2 there are exactly 257 cycles of *F*1.

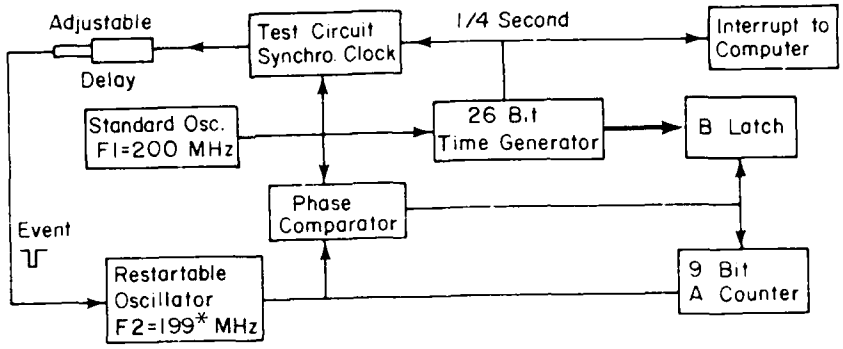

Concept Block Diagram

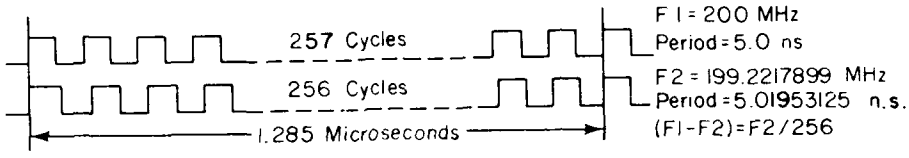

F1 and F2 Relationship

Epoch = Time at Coincidence-A*(5.01953125) ns
Epoch = B*5.0-A*5.01953125 ns
Epoch = (B-A)*5.0-A*0.01953125 ns

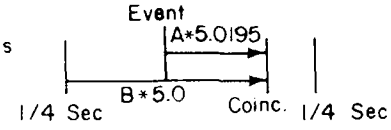

Epoch Calculation

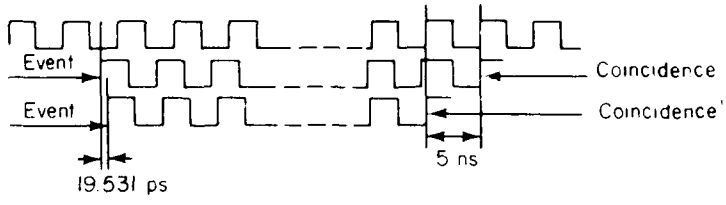

If Event is Delayed by 19.531 ps, New Coincidence Point Occurrs 5 ns Sooner

Epoch' = $\left[(B-1)-(A-1)\right]*5.0-(A-1)(0.019531)$ ns

Epoch' = $(B-A)*5.0-A(0.019531)+0.019531$ ns

Epoch' = Epoch + 19.531 ps

Effect of Moving Event by 19.531 p.s.

Fig. 9. Dual frequency event timer concepts.

The event to be timed stops, then restarts the $F2$ oscillation, which is counted by a 9-bit A counter from the point of restart. Constantly monitoring the two frequencies is a D type flip flop phase comparator which looks for a special point of closest coincidence of the rising edges of the two voltage waveforms. When this coincidence point is found the A counter is stopped and a B latch system freezes and then stores the state of the synchronous counter time generator. From the contents of the A and B registers the epoch of the event can be computed to within a quarter second interval.

Vernier action occurs because the period of $F1$ and $F2$ differ by 19.53125 ps. Theoretically, any coincidence point can be used to compute the epoch. For the Nth coincidence point,

$$\begin{aligned} \textit{event epoch} &= (B + 257\,N) \times 5 \text{ ns} - (A + 256\,N) \times [(257/256) \times 5 \text{ ns}] \\ &= (B - A) \times 5 \text{ ns} - A \times (5/256) \text{ ns} \\ &= (B - A) \times 5 \text{ ns} - A \times 19.53125 \text{ ps} . \end{aligned} \tag{10}$$

The resolution of the event timer for a single event is thus approximately 20 ps.

Portable maser vehicle.

The APL truck is equipped with heating and air conditioning and has a gasoline-powered generator capable of supplying 10 kW of power for mobile operation. Between trips the truck is parked next to the telescope building and is connected to the building electrical power. The power to the portable maser and event timer is supplied via uninterruptible power supplies which provide continuous power during switchover from house to generator power and remove all vehicle electrical transients, spikes, and frequency variations.

The portable maser is housed within a highly insulated enclosure which is supported by pneumatic shock and vibration isolation mounts. Air is drawn in through a duct and is maintained at a controlled temperature. The enclosure is loaded onto a set of rails using a forklift and rolled into the truck, as shown in Fig. 10. When the enclosure is in place the supports are pressurized and the rails are removed. Once loaded, the maser is kept in the truck at all times. The arrangement of the maser within the insulated enclosure is shown in Fig. 11.

The truck speed is measured with a Stewart-Warner "sender" unit attached to the speedometer cable that produces a square wave signal whose frequency is proportional to the vehicle speed. This frequency is converted to a dc voltage and is measured by a strip chart recorder. This system has replaced a mechanically driven generator attached to the drive shaft used in earlier measurements.

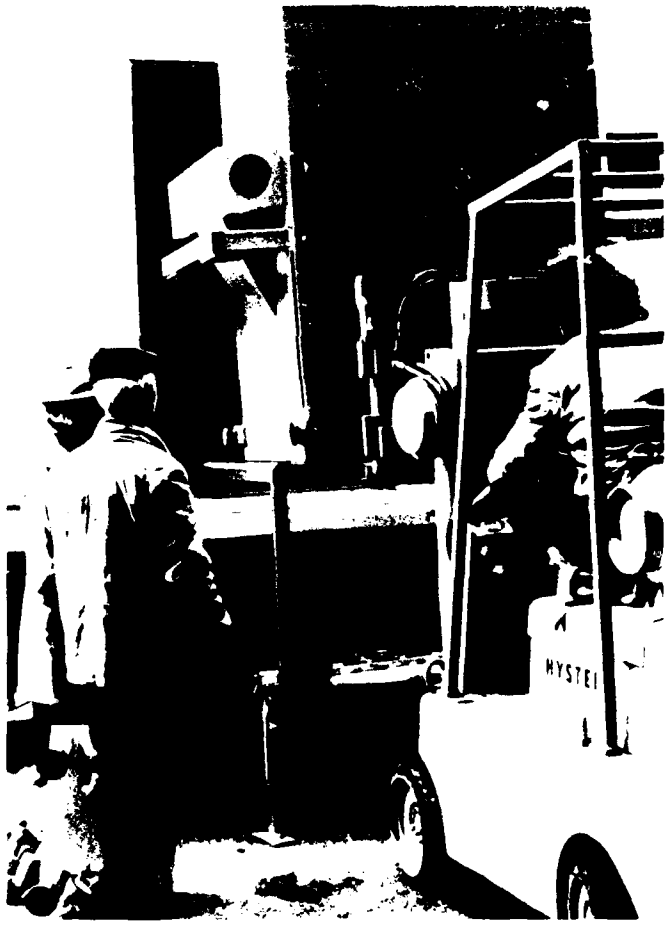

Fig. 10. Maser enclosure being loaded into APL truck.

Temperature control.

The temperature of the air entering each maser enclosure is maintained by a resistive heater controlled by a proportional, integral, derivative (PID) microprocessor that measures the temperature with a 100-ohm RTD sensor and provides a 4 - 20 mA control current to a zero-crossing power regulator. The temperatures are monitored by arrays of thermistors whose resistances are measured by an HP 3421A Data Acquisition/Control Unit run with an HP 71 calculator. Similarly, the truck interior and maser room of the telescope building are also temperature controlled. During periods of limited access, the truck and room temperatures are maintained at 23 °C within a few tenths of a degree and the maser enclosures are maintained at 24 °C within about one tenth of a degree. Four controllers and power regulators are thus in operation to regulate the temperatures of the two masers and their environments. We have found that the Shimaden SR-22 controller performs very well for this purpose. These controllers have an auto-tune feature that automatically performs a temperature cycle and selects the appropriate parameters for the system.

Fig. 11. Maser 6 inside temperature-controlled enclosure.

We have taken care to select coaxial cables with low temperature sensitivity and to minimize their lengths so as to eliminate the effect of environmental temperature fluctuations on the measurements. We have replaced our original RG223 cables, with a sensitivity on the order of 200 ppm/ °C, with expansion-compensated cables having copper conductor and foam dielectric, Cablewave Systems FLC 12-50J, which have a temperature coefficient of about 10 ppm/ °C. Also, we have minimized the lengths of the cables. During the summer we performed the t_2 measurements from the dome on top of the Time Services Building at USNO where the original optical link was established. This location required running cables over the roof to the truck below. In order to account for possible fluctuations in delay caused by changes in temperature, we made measurements on two channels with cables of different length and determined their difference. In order to eliminate, rather than correct for, the problem we have redirected the cathedral mirror to a point in front of USNO Building 1 where the cathedral bell tower can be seen from ground level. We are now able to set up the t_2 detector next to the parked truck with cables short enough to ignore the temperature change.

Remote comparison of masers.

Besides the Erbtec double mixing systems used to compare maser 6 with maser 5 at GORF and maser 6 with the USNO master maser, we have set up a double mixing system to compare maser 5 directly with the USNO maser by means

of a TV signal link. The technique is similar to that originally used by Claude Audouin and his colleagues in Paris[17] The carrier signal of station WTTG, Channel 5, in Washington uses a cesium clock as a reference. This standard was set up several years ago by USNO engineers in cooperation with WTTG in order to use the technique to compare masers between USNO and the Naval Research Laboratory. The 77.240 MHz carrier is mixed with a 77.242 250 MHz signal synthesized at the USNO with their maser. The resulting 2.250 kHz beat note is sent to GORF over a dedicated telephone line. At GORF another 77.242 250 MHz signal is synthesized from the 5 MHz of maser 5. The phase between the GORF-derived 2.250 kHz signal is measured with respect to the USNO-derived 2.250 kHz signal using a linear phase-comparator. The resolution is equivalent to between 50 and 100 ps between masers. The output voltage is recorded on a strip chart and stored by the HP 3421A Data Acquisition/Control Unit for future study. By combining the frequency offset of maser 6 with respect to the USNO maser during an across-Washington optical measurement with the frequency offset of maser 5 with respect to the USNO maser obtained via the TV link, we can draw an inference about the relative phases of masers 5 and 6 even while they are separated. These data are used to estimate the effects of transportation on the frequency of maser 6 and to interpolate the phase data acquired with the Erbtec system during calibration measurements at GORF.

PRELIMINARY RESULTS

We have been able to obtain clock closures for a round trip of under 50 ps after allowing for the measured rate difference between masers 5 and 6 before and after the trip and applying relativity corrections for speed and elevation difference. The optical measurements during calibration follow the clock phase difference determined by the independent phase comparison. The precision of timing of the 70 ps pulses of laser light has been observed to be as low as 30 ps (standard deviation of the mean).

We need to achieve these performances for both clocks and optical detection simultaneously for a number of clock trips so that we can measure ΔT to within less than 50 ps in order to test for a possible asymmetry in the speed of light with respect to the rotating earth. Many improvements are being made as this investigation continues.

DISCUSSION OF THEORY

Only the briefest impressions will be given here.

As mentioned in the INTRODUCTION, for a clock the metric coefficients $g_{\mu\nu}$ of Eq. (1) are intended to relate the increment $d\tau$ of the clock's own time -- usually called its proper time -- between two neighboring events on the clock's path and the spacetime coordinate increments dx^{μ} (equal, for example, to $c\,dt$, dx, dy, and dz) between the same two events as inferred by some observer according to his space and time coordinate system. In general, the metric coefficients are functions of the four spacetime coordinates x^{μ}. There are ten independent components because of the symmetry $g_{\mu\nu} = g_{\nu\mu}$. In this discussion we adopt a sign convention with signature (+ - - -).

It should be the task of the field equations of a curved spacetime theory of gravitation to provide solutions for the appropriate $g_{\mu\nu}$ which describe a given physical situation. Einstein has written,

> My equation is like a house with two wings. The left hand side is made of fine marble but the right hand side is of perishable wood.

His field equation is

$$R_{\mu\nu} - \frac{1}{2} g_{\mu\nu} R = \frac{8 \pi G}{c^4} T_{\mu\nu} \tag{11}$$

where $R_{\mu\nu}$ is the Ricci tensor constructed from a nonlinear combination of the $g_{\mu\nu}$ and their first and second derivatives, R is the scalar curvature, $T_{\mu\nu}$ is the stress energy tensor for matter, and G is the Newtonian gravitational constant. Equation (11) represents ten equations (for μ, ν = 0,1,2,3 with symmetry) to be solved for the $g_{\mu\nu}$ in terms of the x^{μ}.

In the new theory of Yilmaz[7] the left hand side of the field equation is kept the same but the right hand side is changed to include the stress-energy tensor $t_{\mu\nu}$ of the gravitational field,

$$R_{\mu\nu} - \frac{1}{2} g_{\mu\nu} R = \frac{8 \pi G}{c^4} (T_{\mu\nu} + t_{\mu\nu}) . \tag{12}$$

The field equations apparently become more complicated but their solution becomes easier. The general solution is of the form of an exponential,

$$g_{\mu\nu} = \{\eta \exp[2(\phi - 2 \hat{\phi})]\}_{\mu\nu} \tag{13}$$

where $\hat{\phi} \equiv \phi_{\mu}{}^{\nu}$, a generalized gravitational field satisfying a wave equation with matter sources, and $\phi = \phi_{\mu}{}^{\mu}$. In the low velocity limit for the motion of the sources, when the retardation effects of field propagation can be ignored, the $g_{\mu\nu}$ become exponential functions of the familiar Newtonian potential ϕ. The symbol η represents the Minkowski metric coefficients.

The new theory successfully treats all of the classical tests of general relativity at the first order of accuracy but differs from general relativity in its second order predictions. The new theory handles many important problems extremely effectively, in part because of the simple exponential dependence of the metric coefficients on the Newtonian N-body potential in the limit discussed above. These include the problem of N interacting masses (our solar system, for example) and the calculation of gravitational radiation. For these reasons the theory of Yilmaz has been called "Deputy General Relativity" by Professor John Wheeler.[18]

There seem to be kinematic differences in the metrics for rotating systems given by the two theories. For a disk rotating with angular velocity ω the metric of general relativity usually given,[4-6] combined with a term "added by hand" representing the gravitational potential, is

$$\begin{aligned} g_{00} &= 1 - (\vec{\omega} \times \vec{r})^2/c^2 + 2\,\phi/c^2 \\ g_{0j} &= -\frac{1}{c}\,(\vec{\omega} \times \vec{r})_j \\ g_{ij} &= -\delta_{ij} \end{aligned} \tag{14}$$

so that for a coordinate system whose z-axis coincides with the axis of rotation,

$$ds^2 = (1 - \omega^2\, r^2/c^2 + 2\,\phi/c^2)\, c^2\, dt^2 - 2\,\omega\, r^2\, d\theta\, dt - r^2\, d\theta^2 - dr^2 \tag{15}$$

where r and θ are the polar coordinates with respect to the center of the disk. These metric components without the addition of the gravitational potential arise from the metric of flat spacetime with the transformation $r \rightarrow r$, $\theta \rightarrow \theta - \omega\, t$, $t \rightarrow t$, thereby preserving the flat spacetime. It can be shown, however, that this combined form of the metric follows from an iterative solution of the Einstein field equations for a rotating frame of reference.[19]

If Eq. (15) is applied to light propagation on the rotating earth by setting $ds^2 = 0$, one obtains a quadratic equation for dt. Assuming $dr = 0$ and neglecting ϕ/c^2, the solution is

$$dt = \frac{r\, d\theta}{-\omega\, r \pm c} \,. \tag{16}$$

For the outgoing (east to west) pulse $d\theta$ is negative and $d\theta = -|d\theta|$. To obtain a positive time we choose the minus sign and obtain

$$\Delta t_{EW} = \frac{r\,|\Delta\theta|}{c + \omega\, r} = \frac{d}{c + v} \tag{17}$$

where d is the east-west distance and v is the speed of the earth's surface. For the reflected (west to east) pulse $d\theta$ is positive so we choose the positive sign and obtain

$$\Delta t_{WE} = \frac{r\,|\Delta\theta|}{c - \omega\, r} = \frac{d}{c - v} \,. \tag{18}$$

From this point of view, the coordinate time difference is

$$\Delta t_{EW} - \Delta t_{WE} = -\frac{2\,\omega\, r^2 |\Delta\theta|}{c^2 - \omega^2\, r^2} \approx -\frac{2\,v\,d}{c^2} \,. \tag{19}$$

The apparent coordinate speed of light is $c + v$ going west and $c - v$ going east. It is not clear whether we should actually observe this difference, however, since the metric of Eq. (15) seems to assume that the observer is located at the center of rotation.

The solution for the metric on a rotating disk in the limit discussed above of the Yilmaz theory is

$$ds^2 = [1 - \omega^2 (r^2 - r_0^2)/c^2 + 2 (\phi - \phi_0)/c^2] c^2 dt^2$$

$$- 2 \omega |\vec{r} - \vec{r}_0|^2 d\theta dt - r^2 d\theta^2 - dr^2 . \qquad (20)$$

In this expression $\vec{r}_0$ denotes the position of the observer on the disk with respect to the center and ϕ_0 is the gravitational potential at the observer. For a local measurement $\vec{r} \approx \vec{r}_0$ and $\phi \approx \phi_0$ and the solution for the light propagation equation $ds^2 = 0$ is

$$r \frac{d\theta}{dt} = \pm c \qquad (21)$$

This metric has a nonzero spacetime curvature, even without the gravitational potential term $\phi - \phi_0$. This can be traced to the very strong principle of equivalence among inertial mass, passive gravitational mass, and active gravitational mass in the new theory.[17]

Another approach to the study of the appropriate metric for a rotating system is based on a generalization of the Lorentz transformation for an accelerated, rotating frame of reference. This approach has been pursued by the second author and yields the following metric for an observer at any point on the rotating disk:

$$g_{00} = (1 + \vec{W}\cdot\vec{\rho}/c^2)^2 - (\vec{\omega} \times \vec{\rho})^2/c^2 + 2 \phi/c^2$$

$$g_{0j} = - \frac{1}{c} (\vec{\omega} \times \vec{\rho})_j \qquad (22)$$

$$g_{ij} = - \delta_{ij}$$

where $\vec{\rho}$ is measured from the origin of coordinates on the earth's surface and $\vec{W}$ is the acceleration of the origin due to its circular motion. With this metric the relativistic effects on light propagation and the atomic clock transport due to the earth's rotation are negligible because of the small value of $\vec{\rho}$. However, the atomic clock must still be corrected for speed and elevation effects.

The purely inertial part of this metric is exact and is obtained by applying to the flat spacetime Minkowski metric a coordinate transformation that represents a generalization of the Lorentz transformation for an accelerated, rotating observer.[20] In general, $\vec{W}$ may represent any linear acceleration of the origin as measured in the observer's own rest frame. It may be shown that the combined metric with inertial terms and gravitational term above, together with higher order gravitational and mixed gravitational-inertial terms neglected here, may be derived from an iterative solution of Einstein's field equation using the method of Ref. [19].

We realize that our discussion of the theory is inadequate, given the importance of the subject. We hope that our experimental measurements will help to clarify the conceptual foundations by giving further operational significance to the distinction between coordinate and proper times. We intend to discuss the completed measurements more thoroughly in this context in a later publication.

ACKNOWLEDGMENTS

We wish to express our great appreciation to Professor Hüseyin Yilmaz for the generous investment of his time in patiently explaining his theory and the fundamental questions addressed by this experiment through many personal discussions, letters, and lectures.

We are highly indebted to the many organizations and individuals whose generous support in diverse ways is making this experiment possible:

U.S. Naval Observatory *Financial support* *(Contract* N00014-87-K-0811*)* *Technical assistance* *Loan of equipment*	Gernot Winkler, Gart Westerhout, Paul Wheeler
U.S. Air Force, Global Positioning System Program *Financial support* *(supplement to USNO Contract)*	Warner Miller, Henry Fliegel
Naval Research Laboratory *Technical assistance* *Loan of equipment*	Ron Beard, Joe White, Al Gifford
Applied Physics Laboratory *Technical assistance* *Loan of APL truck* *Loan of ST1 maser*	Al Bates, Lee Stillman, Steve Deines, Mary Chiu
Jet Propulsion Laboratory *Loan of ST1 maser*	Lute Maleki
Bendix Field Engineering Corporation *Technical support* *Loan of NR10 maser*	Peter Dachel, Bob Price, Larry Johnson

National Radio Astronomy Observatory *Loan of Sigma Tau masers 5 and 6*	Peter Napier, Larry Beno, Sam Honeywell
Sigma Tau Standards Corporation *Technical advice*	Harry Peters
Hamamatsu Photonics *Loan of MCP-PMT*	Teruo Hiruma, David Fatlowitz, Y. Shinoda
NASA Goddard Space Flight Center *Use of 48-inch telescope* *Laboratory space* *Loan of NR10 maser*	Robert Coates, John Degnan, Tom Zagwodski, Jim Abshire, Arnie Abbott, Jan McGarry
Department of Physics and Astronomy University of Maryland *Technical Support*	Frank Desrosier, Karl Harzer, Frank San Sebastian, Ed Gorsky, Ernie Grossenbacher, Jack Touart, John Mullendore, Ben Scesa, Rob Giraldi, Camille Vogts

REFERENCES

[1] An introduction to Einstein's curved spacetime theory of gravity for the PTTI community was given by the first author in "Introduction to Some Fundamental Concepts of General Relativity and to Their Required Use in Some Modern Timekeeping Systems," *Proc. 13th Annual Precise Time and Time Interval (PTTI) Applications and Planning Meeting*, December 1981, pp. 687 - 724.

See also C.O. Alley, "Proper Time Experiments in Gravitational Fields With Atomic Clocks, Aircraft, and Laser Light Pulses," in *Quantum Optics, Experimental Gravitation, and Measurement Theory*, edited by P. Meystre and M.O. Scully (Plenum, New York, 1983).

[2] J.L. Synge, *Relativity: The General Theory* (North-Holland, Amsterdam, 1964), p. 103.

[3] C.O. Alley, J.D. Rayner, C.A. Steggerda, J.V. Mullendore, L. Small, and S. Wagner, "Time Transfer Between the Goddard Optical Research Facility and the U.S. Naval Observatory Using 100 Picosecond Laser Pulses," *Proc. 14th Annual Precise Time and Time Interval (PTTI) Applications and Planning Meeting*, December 1982, pp. 243-267.

[4] L.D. Landau and E.M. Lifshitz, *The Classical Theory of Fields*, 4th rev. English ed. (Pergamon, New York, 1975), p. 254.

[5] C. Møller, *The Theory of Relativity*, 2nd ed. (Oxford, New York, 1972), p. 253.

[6] V. Fock, *The Theory of Space, Time and Gravitation*, 2nd rev. ed. (Pergamon, New York, 1964), 119.

[7] A few selected references to the Yilmaz theory are given below. The Maryland lecture notes contain reprints of many other papers.

H. Yilmaz, "New Theory of Gravitation" [Notes for ten lectures presented at the University of Maryland, Fall semester, 1987];

H. Yilmaz, "Relativity and Quantum Mechanics," *International Journal of Theoretical Physics* **21**, 871 (1982) [paper given at the celebration of the 80th birthday of F.A.M. Dirac];

H. Yilmaz, "Recent Developments in Gravity Theory," in *Problems of High Energy Physics and Field Theory*, edited by S.N. Sokolov (Nauka, Moscow, 1988) [lectures at the Protvino Workshop, USSR, July, 1987];

H. Yilmaz, "Physical Foundations of the New Theory of Gravitation," *Annals of Physics* **101**, 413 (1976).

[8] The most accurate is that of A. Brillet and J. Hall, *Phys. Rev. Lett.* **42**, 549 (1979), giving a difference in the inferred one-way speeds of light at right angles as $\Delta c < 15$ m/s.

[9] K.C. Turner and H.A. Hill, *Phys. Rev. B* **134**, 252 (1964). See also C.W. Misner, K.S. Thorne, and J.A. Wheeler, *Gravitation* (W.H. Freeman, New York, 1973), p. 1064.

The most accurate are those of G.R. Isaak, *Phys. Bull.* **21**, 255 (1970), giving a variation $\Delta c < 5$ cm/s. See also J.D. Jackson, *Classical Electrodynamics*, 2nd ed. (Wiley, New York, 1975), p. 511.

[10] T.P. Krisher, L. Maleki, L.E. Primas, G.F. Lutes, J.D. Anderson, and C.M. Will, "Results of a New Test of Relativity," this proceedings, Paper 25.

[11] C.O. Alley, "Laser Ranging to Retro-Reflectors on the Moon as a Test of Theories of Gravity," in *Quantum Optics, Experimental Gravitation, and Measurement Theory*, edited by P. Meystre and M.O. Scully (Plenum, New York, 1983).

[12] S.R. Bowman, "The Design, Construction, and Testing of a High Precision Lunar Laser Ranging Station", Ph.D thesis, University of Maryland, 1986.

[13] H.E. Peters, H.B. Owings, and P. Koppang, "Atomic Hydrogen Masers With Self Auto-Tune System and Magnetic Field Cancellation Servo," this proceedings, Paper 32.

[14] T.K. Tucker, "Operating and Environmental Characteristics of Sigma Tau Hydrogen Masers Used in the Very Long Baseline Array (VLBA)," this proceedings, Paper 33.

[15] L.J. Rueger, M.C. Chiu, S.D. Deines, R.A. Nelson, J.T. Broomfield, and C.O. Alley, "Portable Hydrogen Maser Clock Time Transfer at the Subnanosecond Level," *Proc. 19th Annual Precise Time and Time Interval (PTTI) Application and Planning Meeting*, December, 1987, pp. 345-364; *Errata*, pp.365 to 365-5.

[16] C.A. Steggerda, "The Development of a Dual Frequency Event Timer,"

in *Sixth Annual International Workshop on Laser Ranging and Instrumentation*, edited by J. Gaignebet and F. Baumont, September, 1986;

C.A. Steggerda, "A Dual Frequency Precision Event Timer for Satellite and Lunar Ranging," Technical Report 88-169, University of Maryland Department of Physics and Astronomy, February 1988.

[17] A. Gabry, G. Faucheron, B. Dubouis, and P. Petit, "Distant Comparison of Stable Frequency Standards by Means of the Transmission of a Beat Note Between the Carrier of a TV Broadcast Signal and a Frequency Synthesized from the Frequency Standards," *Proc. 31st Annual Symposium on Frequency Control*, June 1977, p. 499.

[18] J.A. Wheeler, private communication to the first author.
Definition of "deputy" from *Webster's 7th New Collegiate Dictionary*:
1. A person appointed as a substitute with power to act;
2. A second-in-command or assistant who usually takes charge when his commander is absent.

[19] R.A. Nelson, "Post-Newtonian Approximation for a Rotating Frame of Reference," *Gen. Rel. Grav.* **17**, 637 (1985).

[20] R.A. Nelson, "Generalized Lorentz Transformation for an Accelerated, Rotating Frame of Reference," *J. Math. Phys.* **28**, 2379 (1987).

DR. GERNOT WINKLER, USNO: Actually, I have a comment. I would like to emphasize your remark that there is a dispute about the interpretation of the Sagnac Effect on the basis of General Relativity. It is not uniformly understood. I think that the least that one can expect from an experiment like this is that is to settle that kind of a dispute.

DR. ALLEY: I am not sure that these disputes will get settled, but I think that it may help to clarify the situation.

Velocity Distribution Measurement of an Optically Pumped Cesium Frequency Standard at the NRLM

Y. Nakadan, S. Ohshima, T. Ikegami, and Y. Koga

National Research Laboratory of Metrology,
1-1-4, Umezono, Tsukuba, Ibaraki 305, Japan

ABSTRACT

The velocity distributions of the optically pumped Cs frequency standard are measured using the rf pulse excitation method. The results are shifted toward higher beam velocity than the Maxwellian distribution and suggest a dependence on vacuum pressure. The velocity distribution is not sensitive to the laser power for pumping and detection, if the power is more than a few mW. The second-order Doppler shift was estimated as $\Delta f = -3.1 \pm 0.1$ mHz.

1. INTRODUCTION

The National Research Laboratory of Metrology is developing an optically pumped cesium frequency standard[1] that is expected to improve remarkably the accuracy of the standard. For the accuracy evaluation of a primary laboratory type standard, it is very important to know the velocity distribution of the atomic beam. The second-order Doppler shift is estimated by measuring the velocity distribution using the pulse excitation method[2].

When we denote the length between the two microwave cavities L and the interval of pulse period T, only the atoms with velocity $v=L/T$ contribute to the Ramsey resonance signal. We applied a long pulse method which is suitable for laboratory type long tubes. The long pulse means $t > l/v$, where l is the length of the single cavity section, and t is the microwave pulse duration. If the phase difference between the two microwave cavities is zero, the Ramsey resonance signal is given by

$$P \propto \sin^2 2b\tau \cdot \cos^2(\lambda T/2), \qquad (1)$$

where $\tau = l/v$, $\lambda = 2\pi(\nu - \nu_0)$ and b is proportional to the square root of the microwave power. When we maintain $2b\tau = \pi/2$ by con-

trolling the microwave power, the amplitude of the Ramsey resonance signal S can be written as

$$S \propto (t/T) \cdot \Delta v \cdot \rho(v), \quad (2)$$

where $\rho(v)$ is the velocity distribution function and Δv is the velocity window given by $\Delta v \approx (l/L + t/T) \cdot v$.
If we also keep t/T= const., we can easily obtain

$$\rho(v) \propto S \cdot T. \quad (3)$$

This paper presents the results of the velocity distribution measurements and the estimation of the second-order Doppler shift of the optically pumped standard.

2. MEASURING SYSTEM

Figure 1 shows a block diagram of the automated velocity distribution measurement system. The pumping laser is stabilized to the F=4− F′=4 component in the D_2 line while the detection laser is stabilized to the F=4− F′=5 component. Both laser lights are σ polarized. The cross sections of the laser beams are about 2 mm × 4 mm. Our apparatus has L of 0.96 m and l of 0.01 m. The C-field strength is 7.9 A/m and the effective cross section of the Cs atomic beam is 3.2 mm × 3.2 mm. The beam is reversible for the correction of cavity phase difference. The ovens were normally operated at 110 ℃. The room temperature was maintained at 23± 1 ℃.

In Fig. 1, the microwave power from the gunn diode oscillator is chopped into a pulse width t and a period T using a pulse generator and a PIN-diode modulator, and it is provided to the Ramsey cavity. We set at t/T=1/10. Although the velocity window is not so narrow, its influence on the estimation of the second-order Doppler shift is less than 1% [3].

The microwave power level is also adjusted using step attenuators. The signal from the tube's detector is amplified and measured with a digital voltmeter. This output is fed to a personal computer, thus the frequencies of the peak and valley of Ramsey resonance are automatically searched by the computer and the peak-to-valley amplitude is calculated.

3. EXPERIMENTAL RESULTS

Figure 2 shows the typical velocity distributions in both beam directions obtained by the experiments. The frequency stand-

ards in the NRLM are placed in an east(E)- west(W) direction for effective magnetic shielding from the earth. We then indicate the atomic beam directions as E→W or W→E.
The second-order Doppler shift was calculated using

$$\Delta f = -\frac{f_o}{2c^2} \cdot \frac{\int_0^\infty \rho(v)\sin^2(2bl/v)dv}{\int_0^\infty 1/v^2\,\rho(v)\sin^2(2bl/v)dv}, \quad (4)$$

where f_o is the resonance frequency.
At the optimum microwave power, b was found to be 20.8 krad/s experimentally. Then the second-order Doppler shift from the velocity distribution was calculated as

$$\Delta f = -3.1 \pm 0.1 \text{ mHz}. \quad (5)$$

The difference of the second-order Doppler shifts in both beam directions was within 0.1 mHz.

As we used cycling transition for detection, the velocity distribution function should be expressed by the Maxwellian distribution as $\propto v^2 \exp(-mv^2/2k\Theta)$, where m is the mass of a Cs atom, k is the Boltzmann constant and Θ is oven temperature in K. The solid line in Fig. 2 shows the predicted distribution at the oven temperature of 110 ℃. We can see the results are shifted from the Maxwellian distribution. We supposed that it might come from the scattering of lower velocity atoms by the residual gas molecules in the vacuum chamber. We therefore took some measurements at the different vacuum pressures. Figure 3 is the velocity distribution measured for the vacuum pressures of 1×10^{-5} Pa and 6×10^{-5} Pa. The results show that the shifting depends on the degree of vacuum. At the higher vacuum pressure, the second-order Doppler shift at the optimum microwave power was estimated as $\Delta f = -3.4 \pm 0.1$ mHz. As the vacuum pressure does not change so much during the continuous operation, this influence is negligible.

Figure 4 shows the velocity distributions in two different oven temperatures; one is with a nominal temperature (110 ℃) and the other is with a low temperature (83 ℃). We can recognize that the difference between the experimental result and theoretical prediction becomes smaller at the temperature of 83 ℃.

We measured the velocity distributions in different laser power conditions, because it is considered that the laser power would play a very important roll in the forming of the velocity distributions in the optically pumped atomic beam. Figure 5 shows

the dependence of the laser power for pumping and detection. When the pumping power is decreased to 40% (4 mW), there is no change in the velocity distribution and signal intensity. When the detection laser power is decreased to 40% (1.4 mW), the signal intensity decreases to 30%. However the velocity distribution does not depend on detection laser power. These are very important results for the measurement of the velocity-dependent frequency shifts.

As optically pumped Cs frequency standard have generally broad velocity distributions, we expected to encounter the second sub-harmonic signal. However the effect on the velocity distribution was smaller than we expected. We have not observed the effect of it yet.

4. CONCLUSIONS

We drew the following conclusions:

(1) Velocity distributions are shifted toward higher velocity than the Maxwellian distribution, the shifts depend on the vacuum pressure and become smaller at lower oven temperature.

(2) The velocity distribution is not sensitive to the laser power for pumping and detection, if the power is more than a few mW.

(3) The second-order Doppler shift at the optimum microwave power was estimated to be $\Delta f = -3.1 \pm 0.1$ mHz.

ACKNOWLEDGMENT

The authors thank Mr. T. Honda for his assistance in the computer programming for the automated measurement system.

REFERENCES

[1] S. Ohshima, Y. Nakadan, and Y. Koga: IEEE Trans. Instrum. Meas., vol. IM-37, 409 (1988).

[2] H. Hellwig, S. Jarvis, Jr., D. Halford and H.E. Bell: Metrologia 9, 107 (1973).

[3] S. Ohshima, Y. Nakadan, and Y. Koga: Japanese J. Appl. Phys., vol. 25, No. 9, 1453 (1986).

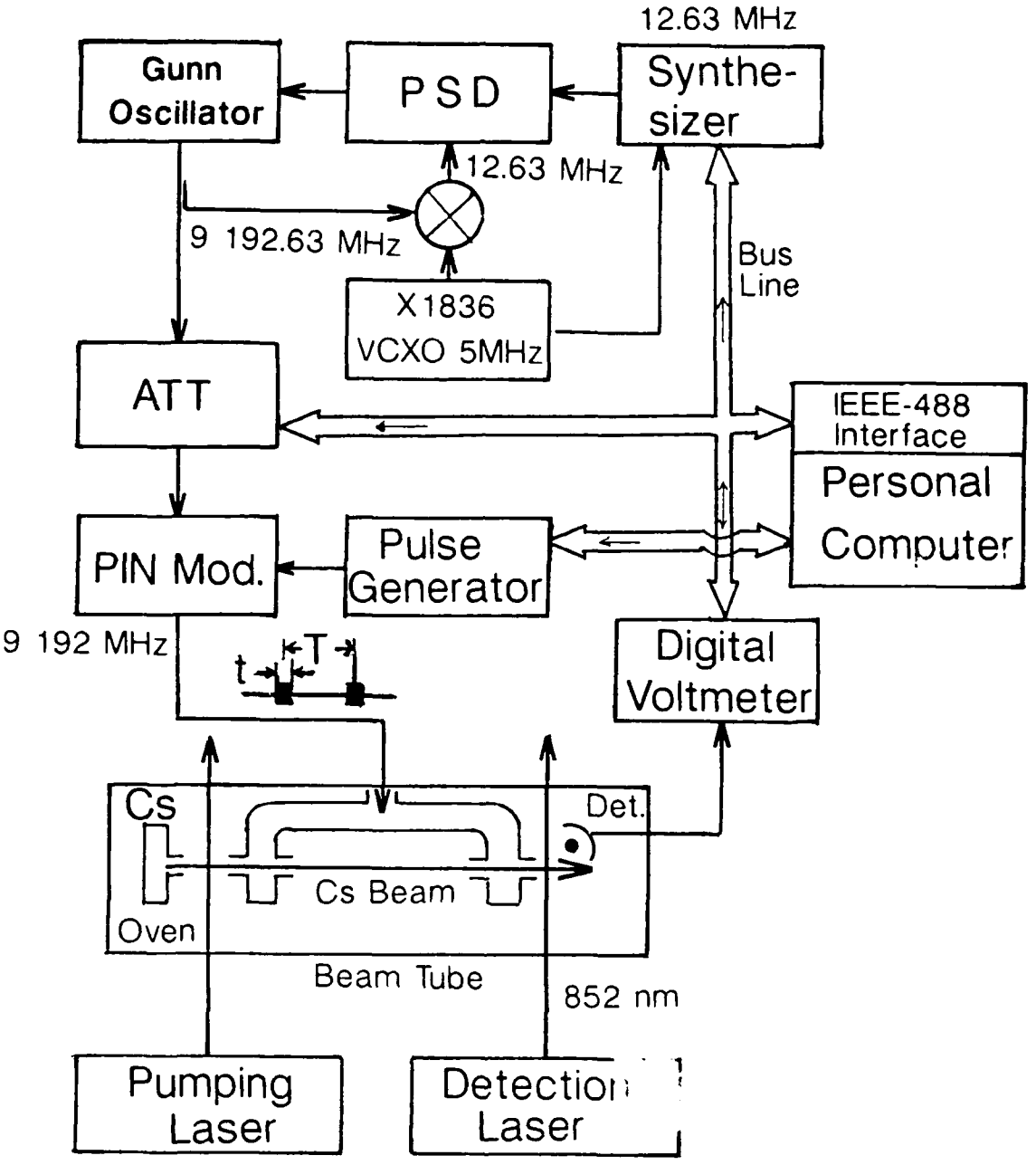

Fig. 1 Block diagram of the automated velocity distribution measurement system.
PSD: Phase Sensitive Detector, ATT: Attenuator,
VCXO: Voltage Controlled Crystal Oscillator.

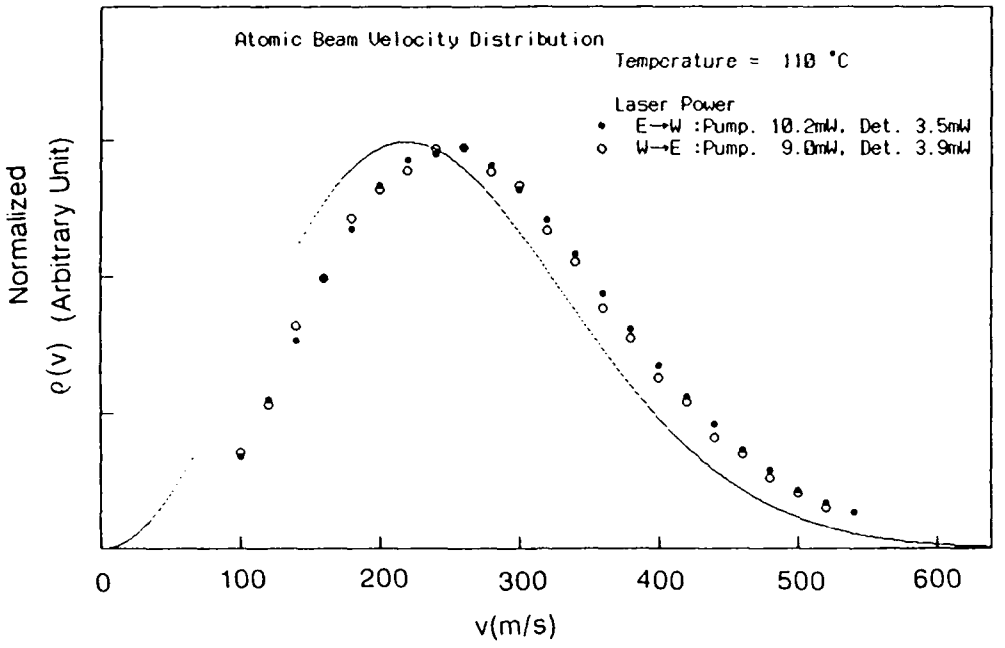

Fig. 2 Typical velocity distributions of the optically pumped Cs standard at the NRLM. The solid curve is the calculated Maxwellian distribution.

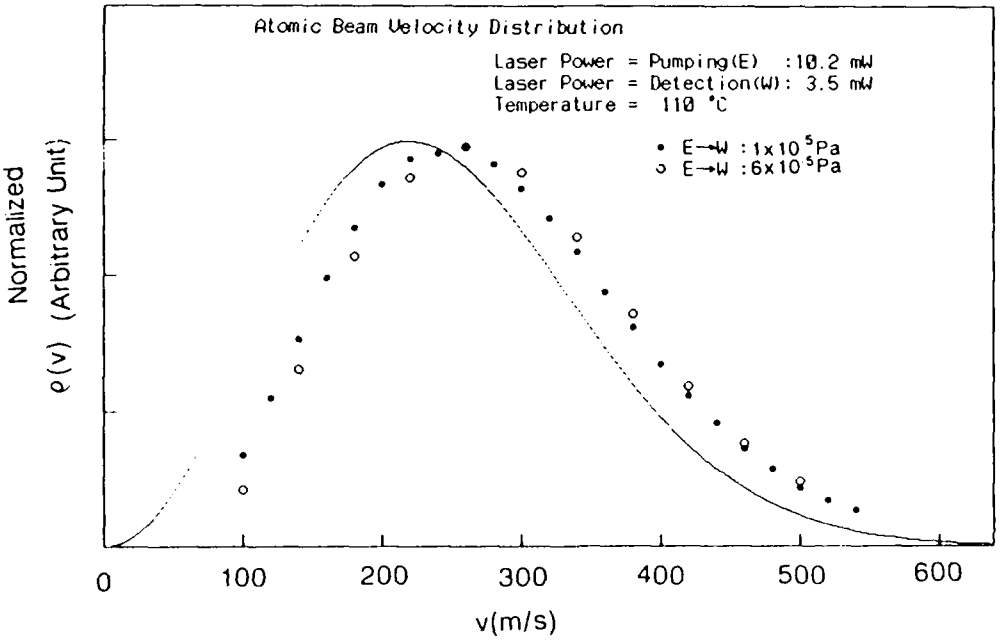

Fig. 3 Velocity distributions at the vacuum pressure 1×10^{-5} Pa and 6×10^{-5} Pa.

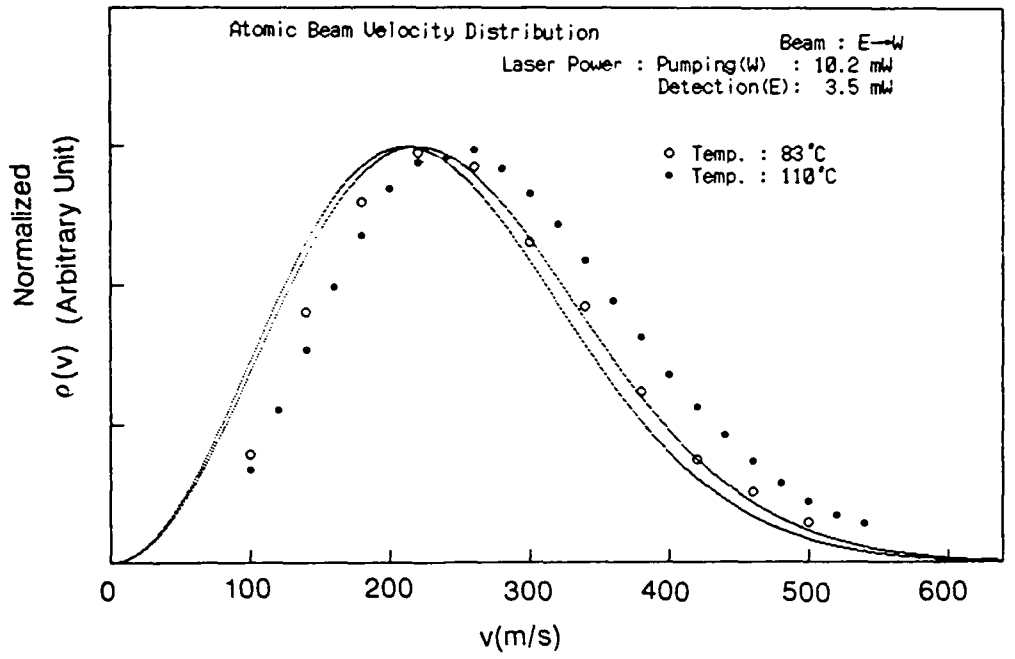

Fig. 4 Velocity distributions at the oven temperatures of 110 ℃ and 83 ℃.

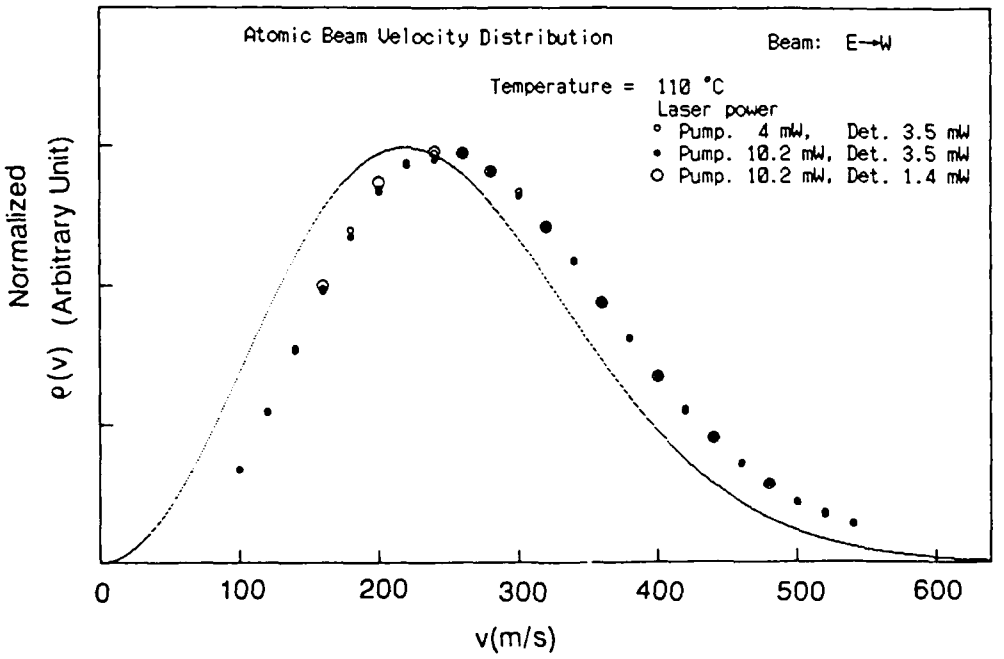

Fig. 5 Velocity distributions for the different laser power for pumping and detection.

TECHNIQUE FOR MEASURING THE ACCELERATION SENSITIVITY OF QUARTZ RESONATORS

Milton H. Watts
Errol P. EerNisse
Roger W. Ward
Robert B. Wiggins

Quartztronics, Inc.
1020 Atherton Drive
Building C
Salt Lake City, UT 84123

SUMMARY

We present a simple method for measuring the acceleration sensitivity of quartz resonators. This method utilizes readily available electronic components and the voltage-frequency effect in doubly-rotated cuts, or a simple VCO for singly-rotated cuts, to determine both phase and magnitude information. The method is based on monitoring vibration-induced FM sidebands of an oscillator with a spectrum analyzer while applying acceleration compensation. An op amp circuit with reversible polarity is used to supply a compensation signal which is proportional to an accelerometer output. Since the goal is to observe a reduction or increase in FM sideband magnitude, the phase and magnitude requirements of the compensation circuit are less than that required for high level compensation.

Examples will be given of the method. Typical reductions or enhancements of 6 to 20db can be seen easily and are sufficient to establish the absolute phase (sign) of each gamma vector component. Data is presented to show that acceleration sensitivities of 1E-10/g can be measured with confidence.

INTRODUCTION

The acceleration sensitivity of quartz resonators arises from the stresses caused by the mass of the resonator blank reacting against the resonator mounting structure during acceleration. A common method of representing the acceleration sensitivity is by the gamma vector, made up of the frequency shifts observed for unit acceleration in three orthogonal axes[1]. Typical numbers for the components of the gamma vector range from low E-9/g to mid-E-10/g. The acceleration-induced frequency response of a resonator is then the dot product of the gamma vector and the applied acceleration. In research and development, a measurement technique for the gamma vector is required for a wide range of frequencies, resonator configurations, and overtone operation. Often measurements must be done on unsealed devices: the Q will typically be lower, and the resistance higher, than under ideal, sealed conditions. Many situations require knowing both the magnitude and the direction of the gamma vector. These include anticipation of using various compensation techniques such as opposed-pair compensation, accelerometer feedback compensation, and spring/mass compensating systems[1]. Also, when applying theories regarding the acceleration performance of a device, a full description of the gamma vector is needed.

Measurement techniques commonly used have a number of disadvantages which make them less than ideal in R & D environments. A method commonly used is observing, with a spectrum analyzer, the FM sidebands generated by sinusoidal acceleration of the crystal under test[2]. With this method, one is able to obtain the magnitude, but not the phase, of the gamma vector. Another common method is FM demodulation[3]. This technique requires virtually noise free demodulation circuitry to detect sensitivities as low as 1E-10/g. The voltage controlled oscillators used in such circuitry usually have a small frequency range over which they are useful. Retooling for crystals of varying frequencies can become time consuming and expensive. Another method which is used is the 2-g tip-over test. Because of the small frequency shifts involved, an extremely stable temperature environment and a high resolution counter is necessary to obtain useful results for crystals with low sensitivities. However, the 2-g tip-over test does provide the sign (phase) of the gamma vector. The reader is referred to Filler's tutorial on acceleration effects on crystals[1] for more details.

Errors can occur in the measurement of small gamma components in the low E-10/g to high E-11/g range. The errors are related to cable reactance modulation due to vibration of power cables and signal cables passing to and from the shaker table. The problem was observed in varying degrees for all the different methods tried in this work.

Presented here is a versatile method of determining both the magnitude and direction of the gamma vector for crystals with a broad range of frequencies. The equipment used is readily available laboratory equipment. Cable modulation effects are addressed.

THEORETICAL BASIS

When a crystal is under vibration, its resonant frequency is shifted due to stresses induced by the interaction of the resonator blank and its mounting structure. The frequency shift df_a is proportional to the acceleration. The frequency/voltage effect of an SC cut crystal (or other doubly rotated crystals) also results in a shift of the resonant frequency (df_v)[4]. If the applied voltage and the acceleration are correlated such that df_v and df_a are equal in magnitude but opposite in sign, an apparent decrease in the g-sensitivity of the device can be observed. This effect has been used previously by Rosatti and Filler as a compensation technique[5].

In the case of singly-rotated quartz cuts, such as the AT-cut, that do not have a voltage-frequency effect, a voltage controlled phase shift network may be used to modulate the frequency of oscillation.

As discussed recently[6], the phase relationship between the acceleration and the applied compensation signal must be accurately controlled near 180° to achieve compensation. Figure 9 shows a theoretical plot of how much sideband suppression can be accomplished for phases approaching 180° as the ratio df_v/df_a is varied. In order to observe a significant decrease in g-sensitivity, the amplitude and phase of the compensating signal must match the amplitude and phase of the acceleration effect of the device quite closely. Assuming precise amplitude control, the phase of the compensating signal must match the phase of the acceleration effect to within +/-5 degrees to achieve 20db sideband reduction. We have found that 10-20 db is adequate to identify the phase of df_v that reduces the acceleration-induced df_a sideband.

Logically, if the quartz crystal is turned upside down, the gamma vector component should be equal in magnitude and opposite in sign for the two orientations. This has never occured in any experiment we have tried when dealing with gamma responses below 2E-10/g. We attribute this to the fact that the cables passing to and from the shaker, no matter what test configuration is used, are modulated by the vibration. The cable vibration sinusoidily detunes the oscillator, to varying degrees, depending upon the test configuration and the Q of the crystal or circuit under test. This creates an effect that adds vectorially to the gamma vector being studied, and is therefore a source of error. (In the configuration to be described this effect is repeatable, and on the order of 1E-10/g at 50 MHz. The effect is much less significant at lower frequencies. When testing the same crystal either in the setup described herein or when shaking the complete oscillator circuit, some cable effects are observed.)

The present experimental equipment and procedures are based on holding cable effects constant and measuring the crystal both right side up and upside down. Since the cable effects add primarily in-phase or out-of-phase with the acceleration effect of the crystal, the algebraic average of the two readings is approximately equal to the crystal effect, with the cable effect cancelling. In other words, if df_c is the cable effect, and assuming it is additive to the df_a in the +x direction, it will be subtractive from the df_a measured in the -x direction. The measured df is, thus

$$df(+x) = df_c + df_a \qquad [1]$$

$$df(-x) = df_c - df_a \qquad [2]$$

and the desired df_a is given by

$$df_a = [df(+x) - df(-x)]/2. \qquad [3]$$

EQUIPMENT USED

A block diagram of the test system is shown in Figure 1. The test equipment used includes a LING Electronics Inc. model 203B shaker table driven by a variable frequency audio oscillator and an audio amplifier. Attached to the shaker is a fixture for mounting the crystal in any of 6 directions (+/- X,Y,Z).

Figure 2 shows the crystal fixture. Rigid wiring is used inside the cube to minimize motion during vibration. The cube can be turned over to test all six axes. The cables running to the shaker are carefully fixed so that their effects remain constant, allowing cancellation using Equation 3 above.

A Saunders & Associates 100HF CI meter was chosen as the oscillator circuit in order to drive crystals with a broad range of frequencies and impedances. It is connected to the crystal through a pair of coaxial cables clamped at both ends. Figure 2 shows a block diagram of the oscillator, cable, and filter used with SC-cuts. Figure 3 shows the phase shift network used for AT-cuts. The phase shift network can also be used with SC-cuts, but is not preferred because of its susceptibility to power supply noise. The output of the oscillator is observed on an HP3585A spectrum analyzer. High frequency crystals (greater than

40 MHz) require a mixer with a relatively low noise reference oscillator (HP3325A Frequency Synthesizer) to shift the signal to a frequency within the operating range of the spectrum analyzer.

The compensation signal is obtained from an accelerometer mounted on the fixture that holds the crystal. (The shaker table driving signal may also be used for compensation as long as the phase requirements previously mentioned are satisfied.) The signal is fed through a variable gain op-amp circuit with switch selectable polarity and an option to apply a dc voltage. This op-amp circuit is shown in Figure 5. The output of this circuit is fed back to the crystal via the filter network of Figure 3 or the phase-shift network of Figure 4.

MEASUREMENT PROCEDURE

The crystal under test is clamped in the cube, which provides for easy, repeatable alignment of the crystal in any of 6 directions. The polarity of the frequency shift effect of a crystal is determined by observing a slight shift in frequency when a dc voltage is applied to either the crystal (doubly rotated case) or the phase shift network. The device is then shaken at approximately $3g_{rms}$ and the sideband amplitudes are measured using the spectrum analyzer.

The phase of the gamma vector in the axis of vibration is measured by slowly increasing the level of compensation from zero while observing the sideband amplitude. Referring to Figure 9, if the compensation signal is of the correct phase to cancel the crystal's acceleration effect, the sideband amplitude will first decrease, and then increase. The opposite phase will show only an increase in sideband amplitude as shown in Figure 9 for 0° phase. Switching the phase of the compensation without changing its amplitude will result in a fairly large difference in the amplitude of the sideband peaks. By correlating this information with the polarity of the accelerometer output relative to the crystal acceleration, the magnitude and direction of the gamma vector component can be uniquely determined.

The polarity of the voltage frequency effect reverses when a doubly rotated crystal is turned upside down in our fixture because the pin polarity of the crystal is reversed, while the polarity of the compensating circuit stays the same. It is important to keep track of this! By referencing everything to the dc shift test, one can keep the signs straight. If the cable capacitance effect is predominant, the compensation amplifier circuit requires a polarity reversal when the doubly rotated crystal is inverted. In contrast, when the crystal acceleration effect predominates, no polarity reversal is needed because both the acceleration effect and voltage effect in the crystal change sign. In contrast, for crystals where the phase shift network is used, no polarity reversal is needed when the cable capacitance effect predominates but polarity reversal is needed when the crystal effect predominates as the crystal is reversed.

Measurements are made for opposing directions. The true answer (if cable effects are constant and in phase with the crystal acceleration effect) is found by using Equation 3.

RESULTS

Several shaker frequencies were used to verify that no structural resonances occur in either the experimental fixturing or the crystal package. No structural resonances are observed from 30 Hz to 200 Hz in our fixturing.

When measuring small gamma vector components, one can see some variation with shaker frequency that we attribute to standing wave acoustic resonance in the cables. Figure 6 shows results for a crystal with a low Q (in air), where the cable modulation effects are larger than the acceleration effect in the crystal. Note that one would measure an erroneously high gamma value if only one orientation of the crystal was measured (either the open circles or filled circles of Figure 6). Also, one would erroneously conclude that there was a structural resonance. In fact, the true answer (x's in Figure 6) is approximately $-6E\text{-}11/g_{rms}$ ($-4E\text{-}11/g$), as seen by using Equation 3 with the two measurements at each shaker frequency.

Figure 7 shows a histogram of the gamma vector components measured for a group of 10 MHz, 3rd overtone, SC-cut, two-point mount crystals. Included in Figure 7 are theoretical results obtained using finite element modeling to calculate the stress in the quartz and the theoretical development of Tiersten[7] to calculate the frequency shift. The theoretical methods will be published later, but the comparison between the experimental average and the theory is excellent.

As a demonstration of the present experimental techniques, the magnitude of the full gamma vector is shown in Figure 8 before and after proprietary treatment of four of the resonators of Figure 7. Note that all four devices measure tightly around $2.7E\text{-}10/g_{rms}$ or ($1.9E\text{-}10/g$). This means that the technique described herein can consistently measure components on the order of $1E\text{-}10/g$.

CONCLUSIONS

The method described for measuring the gamma-vector of quartz crystal resonators is quite practical in a research and development environment, and may be applicable to production facilities as well. The method is able to detect both the magnitude and phase of g-sensitivities less than $1E\text{-}10/g$ in crystals having a variety of frequencies and designs. The measurement procedure is rapid and uses equipment readily available in most laboratories.

ACKNOWLEDGEMENTS

The authors wish to thank Mr. Kevin Kelly for making the measurements described herein.

REFERENCES

[1] R.L. Filler, "Th Acceleration Sensitivity of Quartz Crystal Oscillators: A Review," Proceedings 41st Annual Symposium on Frequency Control, pp. 398-408, 1987.

[2] A. Warner, B. Goldfrank, M. Meirs, and M. Rosenfeld, "Low 'g' Sensitivity Crystal Units and Their Testing," Proceedings 33rd Annual Symposium on Frequency Control, pp. 306-310, 1979.

[3] K.K. Tuladhor, et. al., "High Frequency Quartz Crystal Oscillators for Avionic Systems," Proceedings International Conference Frequency Control and Synthesis, University of Surrey, pp. 67-73, April 8-10, 1987.

[4] J. Kusters, "The Effect of Static Electric Fields on the Elastic Constants of Alpha Quartz," Proceedings 24th Annual Frequency Control Symposium, pp. 46-54, 1970.

[5] V.J. Rosatti and R.L. Filler, "Reduction of the Effects of Vibration on SC-Cut Quartz Crystal Oscillators," Proceedings 35th Annual Symposium on Frequency Control, pp. 117-121, 1981.

[6] V.J. Rosatti, "Supression of Vibration-Induced Phase Noise In Crystal Oscillators: An Update," Proceedings 41st Annual Symposium on Frequency Control, pp. 409-412, 1987.

[7] H.F. Tiersten, "Electroelastic Interactions and the Piezoelectric Equations," Journal Acoustics Society of America, 70, p. 1567, 1981.

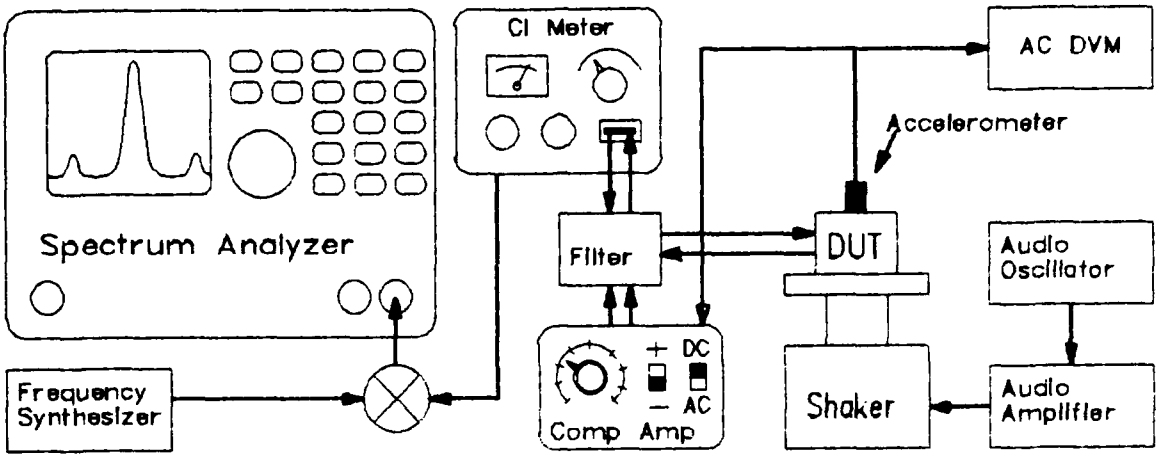

FIGURE 1. Block diagram of the test system used to determine the acceleration sensitivity of doubly-rotated quartz resonators. The spectrum analyzer is used to measure the magnitude of the sensitivity vector. Determining the polarity of compensation required for sideband suppression yields the absolute sign of the acceleration sensitivity vector.

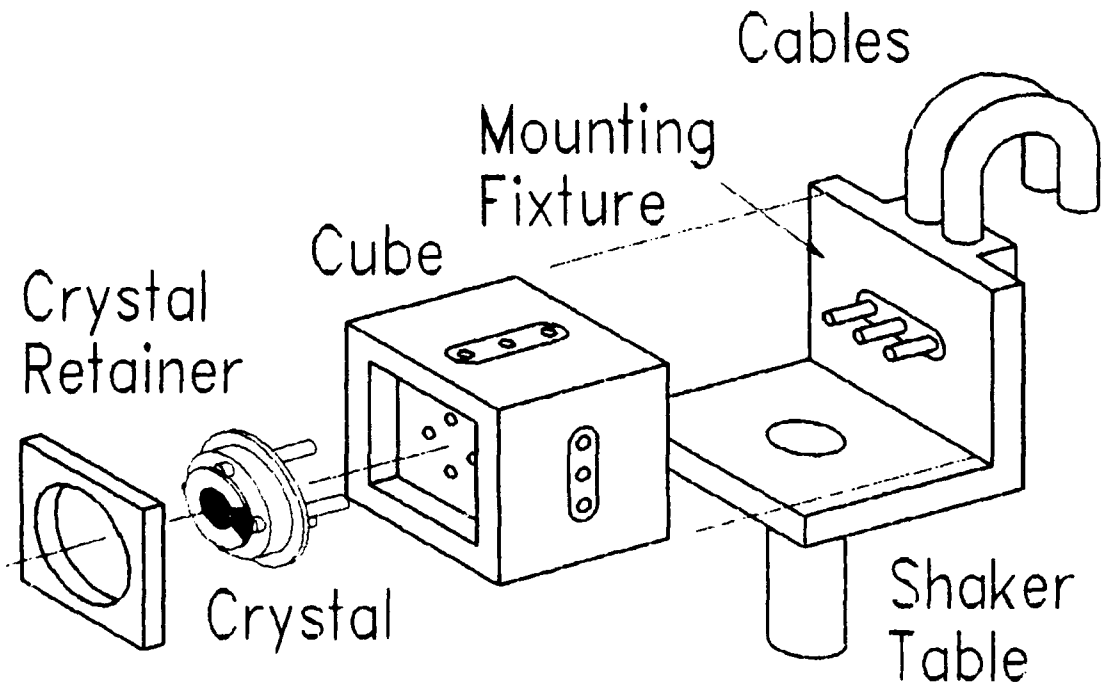

FIGURE 2. Fixture for measuring the acceleration sensitivity of quartz resonators. The crystal is secured in the cube, which can be rotated into +/- X,Y, and Z orientations. The cube is secured to the mounting fixture by a clamp (not shown). Cable effects are repeatable and do not change with cube orientation.

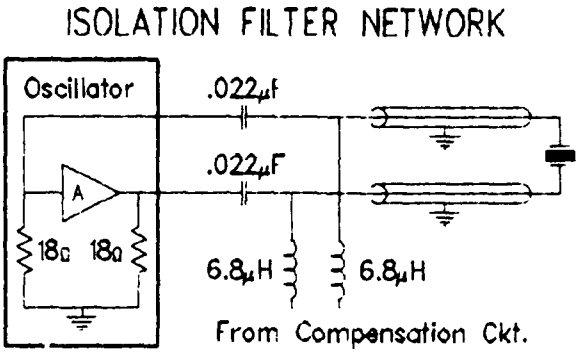

FIGURE 3. Typical filter network used with SC-cuts to isolate the oscillator from the compensation circuitry. Actual component values will vary depending on the crystal frequency and oscillator circuit used.

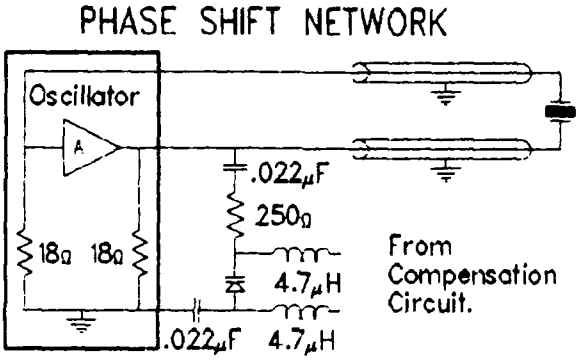

FIGURE 4. Typical phase shift network used for measuring AT-cut crystals. The varactor (SK332) reacts with the output resistance of the oscillator to modulate the phase of the circuit. The series resistor is used to reduce the sensitivity.

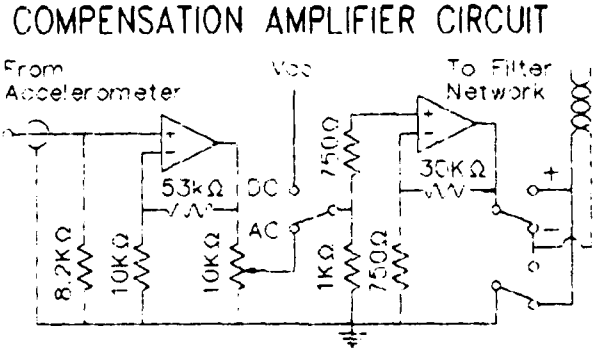

FIGURE 5. Simplified schematic of the compensation amplifier showing the buffer and gain stages, amplitude control, and switching schemes for phase reversal and D.C. voltage effect polarity checking.

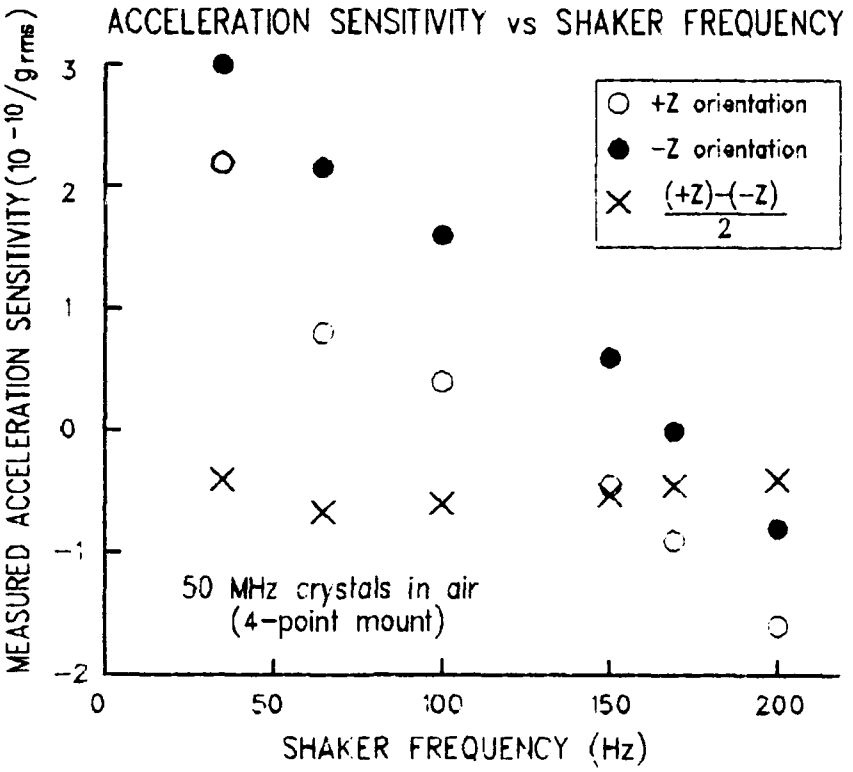

FIGURE 6. Measured acceleration sensitivity versus shaker table frequency for a 50 MHz, 4-point mount, SC-cut crystal. The effects of the cables are subtracted by measuring both + and - orientations for each axis. Note that once these cable effects are eliminated the measured acceleration sensitivity is independent of frequency.

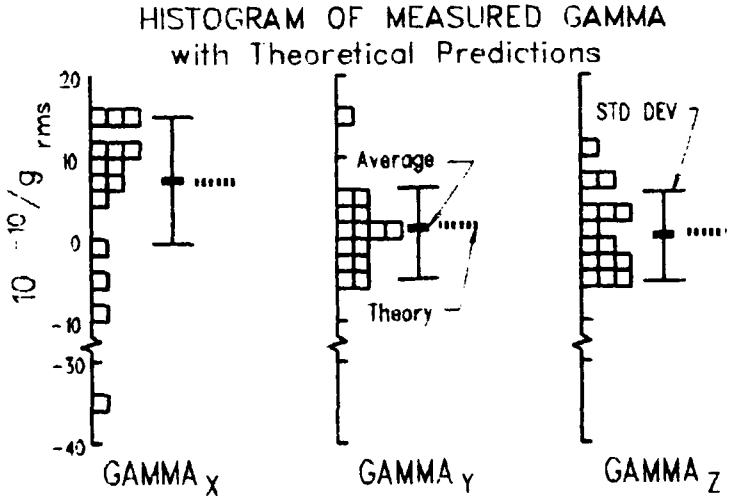

FIGURE 7. Histogram of gamma measured on each axis of 15 resonators (10 MHz, 3rd, SC-cut, 2-point mount.) Average and standard deviation of measured values are compared to analytically predicted values.

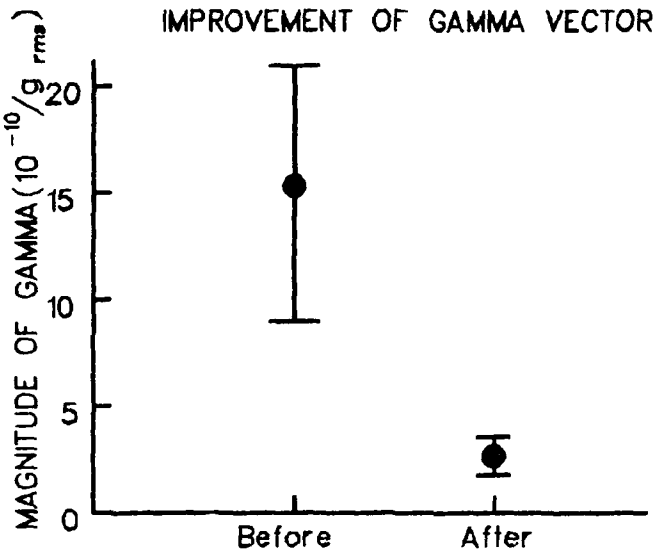

FIGURE 8. Improvement of gamma vector by proprietary processing. Mean and standard deviation of gamma vector magnitude of 4 units (10 MHz, 3rd, SC-cut, 2-point mount) before and after processing.

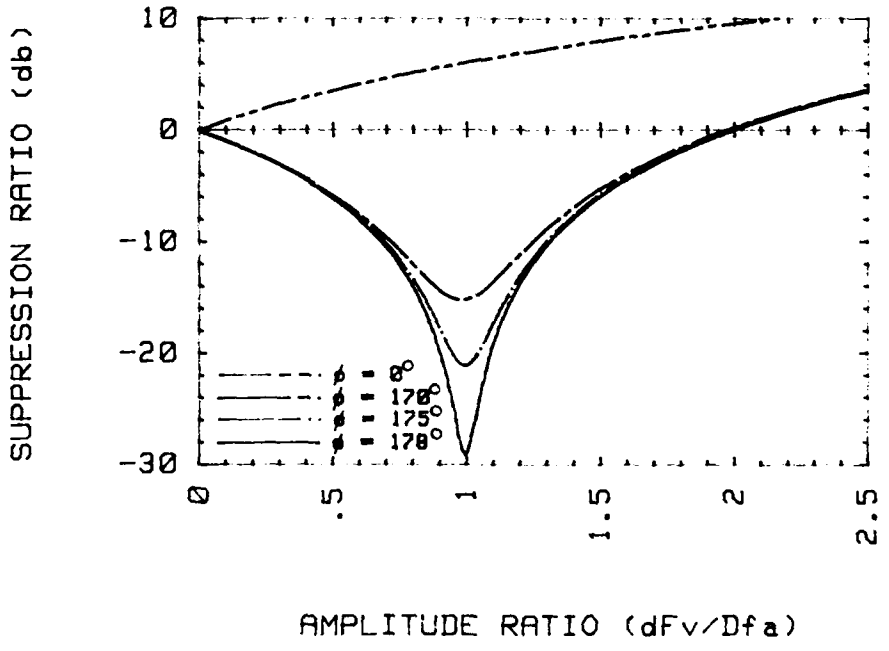

FIGURE 9. Maximum expected sideband suppression as a function of the amplitude ratio df_v/df_a of two sinusoidal modulating functions at various phase angles. Sideband suppression occurs when the phase of the acceleration effect and the voltage effect approach 180°. If the phase is close to zero, the two effects add, and no sideband suppression occurs.

NEW ION TRAP FOR FREQUENCY STANDARD APPLICATIONS*

J. D. Prestage, G. J. Dick, and L. Maleki
California Institute of Technology
Jet Propulsion Laboratory
4800 Oak Grove Drive
Pasadena, California 91109

Abstract

We have designed and built a novel linear ion trap which permits storage of a large number of ions with reduced susceptibility to the second order Doppler effect caused by the RF confining fields. This new trap should store about 20 times the number of ions as a conventional RF trap with no corresponding increase in second order Doppler shift from the confining field. Other comparisons to standard RF ion traps will be made.

Introduction

We have designed and constructed a hybrid RF/DC linear ion trap for use as a frequency standard. This new trap has about 20 times the storage volume as a conventional RF trap with hyperbolic electrodes with no corresponding increase in second order Doppler shift from the micro-motion induced by the RF trapping fields. Alternatively, if loaded with $2 \cdot 10^6$ ions, the Doppler shift from the trapping fields is reduced by a factor of 10 below comparably loaded hyperbolic traps.

Second Order Doppler Shift for Ions in an RF Trap

Figure 1 shows a conventional RF ion trap along with the applied voltages. The trapping forces are generated by the driven motion of the ions (at frequency Ω) in the inhomogeneous electric field created by the trap electrodes[1]. Ions are trapped around the node point of the oscillating electric field at the center of the trap for certain trap voltages, ionic masses, etc. The motion in each of three directions for a single ion in an RF trap is characterized by two frequencies , the fast driving frequency Ω and a slower secular frequency ω. An exact solution to the equations of motion shows that frequencies $k \cdot \Omega \pm \omega$, k = 2, 3, ... are also present. However, in the limit $\omega/\Omega \ll 1$ the ω and $\Omega \pm \omega$ frequencies dominate and the kinetic energy of a particle, averaged over one cycle of Ω, separates into the kinetic energy of the secular motion and the kinetic energy of the driven motion. The average kinetic energy is transferred from the secular to the driven motion and back while the sum remains constant just as a harmonic oscillator transfers energy from kinetic to potential and back. The second order Doppler shift for a small and/or hot ion cloud, where interactions between ions are negligible is:

*This work represents the results of one phase of research carried out at the Jet Propulsion Laboratory, California Institute of Technology, under contract sponsored by the National Aeronautics and Space Administration.

$$\frac{\Delta f}{f} = -\frac{1}{2}\frac{< v^2 >}{c^2} = \frac{< \text{total K.E.} >}{mc^2}$$
$$= \frac{< \text{secular K.E.} + \text{driven K.E.} >}{mc^2}$$
$$= 2\frac{< \text{secular K.E.} >}{mc^2}$$
$$= \frac{3k_BT}{mc^2}.$$

where <> indicates a time average over one cycle of Ω. We have also averaged over one cycle of ω to equate the secular and driven K.E. This is the same as a simple harmonic oscillator where the average K.E. is equal to the average potential.

We now consider the case where many ions are contained in a trap and interactions between ions dominate. In this cold cloud model[2] of the trapped ions displacements of individual ions from the trap center is primarily due to electrostatic repulsion between the ions and random thermal motion associated with temperature can be assumed to be small compared to driven motion due to the trap fields. Such clouds will have a constant ion density out to the edge of the plasma where the density falls off in a distance characterized by the Debye length[3]:

$$\lambda_D = \sqrt{\frac{k_BT\epsilon_o}{n_oq^2}}. \tag{1}$$

This cold cloud model should be useful provided the ion cloud size is large compared to the Debye length. For room temperature Hg ions held in a trap with 50 kHz secular frequency the Debye length is about 1/5 mm.

The trap shown in Figure 1 is described by a pseudo-potential energy[4]:

$$\phi = \frac{1}{2}\left(m{\omega_\rho}^2\rho^2 + m{\omega_z}^2z^2\right), \tag{2}$$

where:

$${\omega_\rho}^2 = \frac{2q^2{V_o}^2}{m^2\Omega^2\epsilon^4} + \frac{2qU_o}{m\epsilon^2}, \tag{3}$$

and:

$${\omega_z}^2 = \frac{8q^2{V_o}^2}{m^2\Omega^2\epsilon^4} - \frac{4qU_o}{m\epsilon^2}, \tag{4}$$

and ϵ describes the trap size.

We assume that the DC and RF voltages are adjusted to make the trapping forces spherical so that the ion cloud is a sphere containing N ions out to radius R_{sph}.

This pseudo-potential depicts trap forces as arising from a uniform "background" charge density computed from Poisson's equation with the above pseudo-potential:

$$n_o = \frac{3\epsilon_o m\omega^2}{q^2}. \tag{5}$$

Trapped positive ions neutralize the negative background of charge, matching its density out to a radius where the supply of ions is used up.

The oscillating electric field which generates the trapping force grows linearly with distance from the trap center. The corresponding amplitude of any ion's driven oscillation is proportional to the strength of the driving field, i.e., also increasing linearly with the distance from the trap center. The average square velocity of the driven motion for an ion at position (ρ,z) is:

$$< v^2 >= \frac{1}{2}\omega^2 \left(\rho^2 + 4z^2\right). \tag{6}$$

For a given trapping strength, reflected in force constant ω^2, the density is fixed by eq (5) while the radius of the spherical cloud is determined once the ion number N has been specified. The second order Doppler shift due to the micro-motion is the spatial average of -(1/2)($<v^2>/c^2$) over the spherical ion cloud. Using eq (6) for the spatial variation of the micromotion:

$$\left(\frac{\Delta f}{f}\right)_{sph} = -\frac{1}{2}\frac{\overline{< v^2 >}}{c^2} \tag{7}$$

$$= -\frac{3}{10}\frac{\omega^2 {R_{sph}}^2}{c^2} \tag{8}$$

$$= -\frac{3}{10}\frac{1}{c^2}\left(\frac{N\omega q^2}{4\pi\epsilon_o m}\right)^{2/3}. \tag{9}$$

For typical operating conditions[2], $N = 2 \cdot 10^6$ and $\omega = (2\pi) \cdot 50\text{kHz}$, $\Delta f/f = 2 \cdot 10^{-12}$. This corresponds to a second order Doppler shift that is about 10 times higher than the shift for free ^{199}Hg ions at room temperature, $\Delta f/f = 3k_BT/2mc^2 = 2 \cdot 10^{-13}$.

For increased signal to noise in the measured atomic resonance used in frequency standard applications, it is desirable to have as many trapped ions as possible. However, as we have just seen larger ion clouds have larger second order Doppler shifts.This frequency offset must be stabilized a high degree in order to prevent degradation of long term performance.

To reduce this susceptibility to 2nd order Doppler shift we have designed and constructed a hybrid RF/DC ion trap which replaces the single field node of the hyperbolic trap with a line of nodes. The RF electrode structure producing this line of nodes of the RF field is shown in Figure 2. The ions are trapped in the radial direction by the same RF trapping forces used in a conventional RF trap and we assume a secular motion in that direction of frequency ω. To prevent ions from escaping along the axis of the trap DC biased "endcap" needle electrodes are mounted on each end. Unlike conventional RF or Paul traps this linear trap will hold positive or negative ions but not both simultaneously.

Near the central axis of the trap we assume a quadrupolar RF electric field:

$$\phi = \frac{V_o\left(x^2 - y^2\right)\cos(\Omega t)}{2R^2}, \tag{10}$$

which gives the corresponding pseudopotential energy:

$$\Phi = \frac{q^2 {V_o}^2}{4R^4 m\Omega^2}\left(x^2 + y^2\right) \tag{11}$$

$$\equiv m\frac{\omega^2}{2}\rho^2. \tag{12}$$

Poisson's equation leads to a limiting charge density,

$$n_o = \frac{2\epsilon_o m\omega^2}{q^2}, \tag{13}$$

for ions held in this linear trap, where:

$$\omega^2 = \frac{q^2 {V_o}^2}{2m^2\Omega^2 R^4}. \tag{14}$$

The motion induced by the RF trapping field is purely transverse and is given by:

$$< v^2 >= \omega^2 \rho^2. \tag{15}$$

As before we average this quantity over the ion cloud to find the second order Doppler shift:

$$\left(\frac{\Delta f}{f}\right)_{lin} = -\frac{1}{2}\frac{\overline{< v^2 >}}{c^2} = -\frac{\omega^2 {R_c}^2}{4c^2}. \tag{16}$$

We have assumed for simplicity a cylindrical ion cloud of radius R_c and length L. Equation (16) can be written in terms of total ion number, N, and trap length, L,

$$\left(\frac{\Delta f}{f}\right)_{lin} = \left(\frac{q^2}{8\pi\epsilon_o mc^2}\right)\frac{N}{L}. \tag{17}$$

We can compare the second order Doppler shift for the two traps assuming both hold the same number of ions and that ions bound in both traps have the same secular frequency, ω. The cloud radii in the two traps then satisfy $(1/2){R_c}^2 L = {R_{sph}}^3$ giving:

$$\left(\frac{\Delta f}{f}\right)_{lin} = \frac{5}{3}\frac{R_{sph}}{L}\left(\frac{\Delta f}{f}\right)_{sph}. \tag{18}$$

As more ions are added to the linear trap their average second order Doppler shift will increase. It will equal that of the spherical ion cloud in the hyperbolic trap when:

$$N_{lin} = \frac{3}{5}\frac{L}{R_{sph}} N_{sph}. \tag{19}$$

It should be repeated that these expressions are valid in the cold cloud limit, where the radius of each of the clouds is large compared to the Debye length given in eq(1).

A linear trap can thus store $(3/5)(L/R_{sph})$ times the ion number as a conventional RF trap with no increase in average second order Doppler shift. For the trap we have built , L = 75 mm. Taking R_{sph} = 2.5 mm for $2 \cdot 10^6$ $^{199}Hg^+$ ions[2] we see that our linear trap should hold about 18 times the number of ions as that of Reference 2.

Construction of a Linear Ion Trap

We have built a linear trap consisting of 4 molybdenum rods equally spaced on an approximately 1 cm radius. OFHC copper pins with dc bias are located at each end to confine ions in the axial direction and are about 75 mm apart.

The input optical system which performs state selection and also determines which hyperfine state the ions are in has been modified from the previous system[4]. The present system illuminates about 1/3 of the 75 mm long cylindrical ion cloud. An ion's room temperature thermal motion along the axis of the trap will give an average round trip time of 1.4 msec, a value which is much smaller than any optical pumping,interrogation or microwave resonance time. Thus, all the ions will be illuminated, but with a lower average intensity.

In order to operate within the Lambe-Dicke regime the 40.5 Ghz microwave resonance radiation will be propagated perpendicular to the line of ions. The ions should then all feel phase variations of this radiation which is less than π so that the 1st order Doppler absorption in sidebands induced by an ions motion will not degrade the 40.5 Ghz fundamental.

The optical axis of the fluorescence collection system is perpendicular to the axis of the input optical system as in the previous system. There is one difference, however. In the hyperbolic trap the collection has in its field of view the ion cloud and the semitransparent mesh of both endcap trap electrodes. This mesh can scatter stray light into the collection system which will degrade the signal to noise ratio in the clock resonance. This linear trap has no trap electrodes, mesh or otherwise, in its field of view and, consequently, should have less detected stray light.

In summary, we have designed an constructed an ion trap which confines ions with a combination of RF and DC electric fields. This trap has 15 to 20 times the ion storage volume as conventional RF traps with no increase in second order Doppler shift from the trapping fields.

Acknowledgements

We wish to thank Dave Seidel for assisting in the design of the linear trap described here.

References

[1] Dehmelt, H. G., "Radio Frequency Spectroscopy of Stored Ions," *Adv. At. Mol. Phys.* **3**, (1967), p. 53- 154.

[2] Cutler, L. S., Giffard, R. P., and McGuire, M. D., "Thermalization of ^{199}Hg Ion Macromotion by a Light Background Gas in an RF Quadrupole Trap," *Appl. Phys. B* **36**, (1985), p.137-142.

[3] Prasad, S. A., O'Neil, T. M., "Finite Length Thermal Equilibria of a Pure Electron Plasma Column," *Phys. Fluids* **22** (2), (1979), p. 278-281.

[4] Prestage, J. D., Dick, G. J., Maleki, L., "The JPL Trapped Ion Frequency Standard Development," *Proc. 19th Ann. PTTI App. Plan. Meeting*, (1987), p. 285-297.

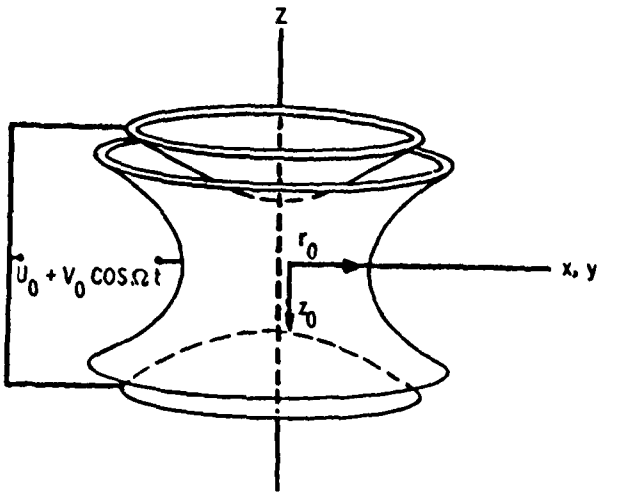

Figure 1. A conventional hyperbolic RF ion trap. A node of the RF and DC fields is produced at the origin of the coordinate system shown.

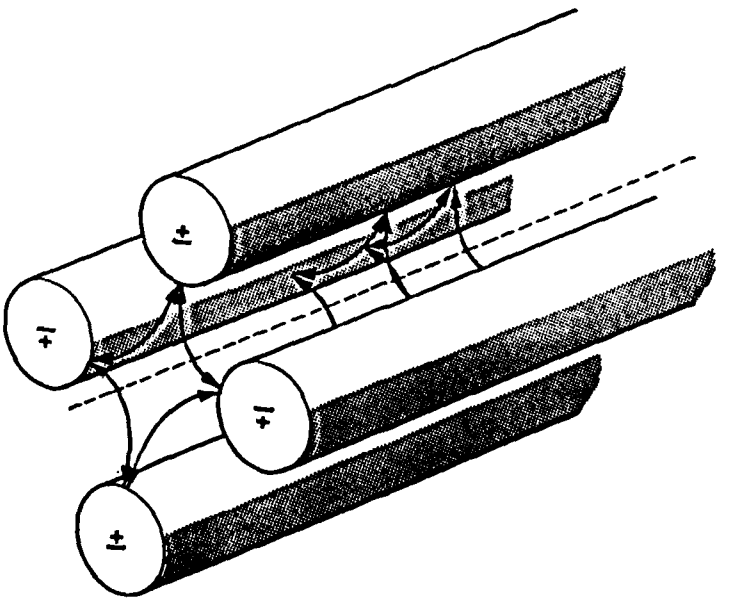

Figure 2. The RF electrodes for a linear ion trap. Not shown are the DC endcap needle electrodes used to prevent the ions from escaping along the longitudinal axis. Ions will be trapped around the line of nodes of the RF field with reduced susceptibility to second order Doppler frequency shift.

QUESTIONS AND ANSWERS

DAVID ALLAN, NIST: Can you remind us, from fundamental physical principles, what you hope to get in stability and accuracy once you have achieved your goals?

DR. PRESTAGE: This will probably start out at one second below ten to the minus twelve. One of the nice things about this concept is that we can scale this up to have many more ions. We are down many orders of magnitude compared to a hydrogen maser in terms of number of atoms or ions. One of the approaches to improve the mercury device is to get better signal–to–noise. It is sort of feeble now, ten to the sixth ions is not a lot. If we can get a factor of a hundred over that it will show up in the short term performance. We then would also have very good accuracy, the best of cesium, say, and the best of hydrogen masers. That is the goal.

DR. ED MATTISON, SAO: What does the cylindrical geometry do to your detection and optics scheme? Does it make it considerably more complicated?

DR. PRESTAGE: We haven't done measurements yet, but it actually makes it simpler. There are fewer scatterers in the field of view than there are in the present trap.

DR. MATTISON: Do you have to change your mirror and detector geometry to capture the fluorescence from that cylindrical arrangement?

DR. PRESTAGE: Not really.

TIME and TEMPERATURE STABILITY of SILVER-COATED CERAMICS for HYDROGEN MASER RESONANT CAVITIES

Edward M. Mattison and Robert F.C. Vessot
Smithsonian Astrophysical Observatory
Cambridge, Massachusetts 02178

ABSTRACT

We have investigated the dimensional stability, as a function of time and temperature, of silver-coated glass-ceramics typical of those used in hydrogen maser resonant cavities. The measurements show that (a) the stress in the silver coating decreases with time at a rate proportional to the initial coating stress, and (b) the variation in stress with temperature is proportional to the initial stress, and decreases with time. Observations indicate that the coating stress can be relieved by precooling the materials.

INTRODUCTION

Like many precision oscillators, the hydrogen maser is subject to long-term ($>10^5$ seconds) frequency drifts, generally assumed to be caused by systematic effects. Masers built by the Smithsonian Astrophysical Observatory (SAO) have been observed to drift toward higher frequencies beginning when they are built, the rate of drift decreasing over periods of months to years. This behavior is believed to be due to a monotonic increase in the resonance frequency of the maser's microwave cavity, which produces a proportional variation in the maser's output frequency through the cavity pulling effect[1]. The cavity frequency drifts are most likely caused by decrease in the cavity's size. (Cavity frequency variations can also be caused by other effects, such as changes in the impedance or reflectivity of external circuits coupled to the cavity.) The resonant cavity consists of a cylindrical tube approximately 24 cm long and 28 cm in diameter, capped by two circular endplates. It is made of a low-expansion glass-ceramic material (Cervit C-101) coated on its inside with silver to form the conductive surface.

A substantial contribution toward the change in cavity size has been identified as shrinkage of the joints between the cavity's cylinder and endplates. Similar shrinkage has been observed in polished, optically contacted joints by Jacobs[2], who found that the length decreased roughly exponentially with a characteristic time on the order of months. Changing the cavity construction from ground to polished joint surfaces has reduced initial frequency drifts substantially. Nevertheless, drift rates on the order of a part in 10^{15} per day remain over periods of years, when joint shrinkage is expected to have become negligible.

Another possible source of cavity frequency drift is change in cavity shape due to relaxation of the mechanical stress in the silver coating. We knew that the coating is under tensile stress at room temperature, bending the endplates concave toward the inside of the cavity. The tensile stress results from the technique by which the silver is applied. The silver coating material is sprayed onto the cavity surface and dried, after which the cavity is

fired at 700°C and returned to room temperature over several hours. Oxides in the coating material bond the silver to the substrate at high temperature. As the temperature decreases the silver contracts, resulting in the concave endplate shape. Any decrease in the coating stress would tend to flatten the endplates, shortening the cavity and raising its frequency.

To test this hypothesis we investigated the dimensional stability of silver-coated samples of low-expansion ceramics over a period of six years. Early measurements[3] yielded information on the initial thermal expansivity of the coated samples and on the surface stress produced by grinding the ceramic materials. Here we report on the results of the long-term observations.

EXPERIMENTAL TECHNIQUE

Samples of Cervit C-101 (Owens-Illinois Corp.), Zerodur (Schott Glass Corp.) and ULE (Corning Glass Works) were ground to rectangular shapes, 4x.75x.25 inches (10.2x1.9x0.6 cm). Both broad faces of each sample were polished flat, with enough material removed to eliminate the surface stress caused by grinding. One face was then reground to produce the surface texture found in maser cavities. This face was etched with hydrofluoric acid to remove the grinding stress, as is done with maser cavities, and then coated with silver (Engelhard type 421), using the spraying and heat treatment procedure described above for maser cavities.

The stress in the finished silver coatings was determined from interferometric measurements of the bending of the rectangular samples. Optical interference patterns between the samples and a reference optical flat were created using a He-Ne laser interferometer[4]. The fringe patterns were photographed, manually digitized, and analyzed by a computer program[5] that fits a series of Zernike polynomials to the pattern. A three-parameter fit was used, producing coefficients C_1, C_2 and C_3. C_1 and C_2 are proportional to the tilt of the sample, in two dimensions, relative to the reference flat, while C_3 is proportional to the sample's curvature, often referred to as "focus" in optics. As discussed below, the curvature is proportional to the surface stress in the coating.

To determine the time variation of the coating stress, the effect of temperature must be removed. The curvature was measured at several temperatures during each experiment period. The 1981-82 measurements were made at 23°C and 33°C, with the temperature measured by a mercury thermometer (resolution <0.5°C). The 1988 measurements were carried out at several temperatures between 23°C and 51°C, with the temperature measured by a platinum resistance thermometer (precision <0.1°C) and verified with a thermistor . Between the measurement periods the samples were held at normal room temperature (roughly 23°C) .

RELATIONSHIP BETWEEN SAMPLE BENDING AND COATING STRESS

It can be shown[6] that a thin rectangular beam coated on one side with a stressed film will bend into a parabolic shape. The deflection y a distance x from the center of the beam, with x measured along the beam's long axis, is given by

$$y = \left[\sigma \frac{3(1-\nu)}{E_s} \frac{t_f}{t_s^2}\right] x^2 \tag{1}$$

Here t_s is the beam thickness, ν is the Poisson's ratio of the substrate material, E_s is the substrate's Young's modulus, and t_f and σ are the thickness and internal stress of the film, respectively. The criterion for a "thin" beam is that its length-to-thickness ratio L/t_s should be large compared to unity. For our samples, $L/t_s = 16$, and this criterion is reasonably well satisfied. As shown in the Appendix, a linear relationship exists between the measured Zernike coefficient C_3 and the coating stress:

$$\sigma = \frac{2C_3}{t_f} \frac{E_s}{3(1-\nu)} \left(\frac{t_s}{r_o}\right)^2 \tag{2}$$

For our samples $t_s = 0.635$ cm and $r_o = 5.088$ cm, giving $(t_s/r_o)^2 = 1.51 \times 10^{-2}$. The Young's moduli and Poisson's ratios for the substrate materials[7] used in these measurements are given in Table 1.

Table 1
Mechanical Parameters for Low-expansion Sample Materials

Material	E_s (10^{10}N/m^2)	ν
Zerodur	9.1	0.24
Cervit C101	9.2	0.25
ULE	6.8	0.17

RESULTS

SAMPLE CURVATURE

Fig. 1 shows the curvature, as expressed by the Zernike coefficient C_3, as a function of temperature for sample plate number 9 (Cervit, 0.0042 inch thick coating). The data show that (a) the rate of change of curvature with temperature is lower in 1988 than in 1982, and (b) the plate is less concave (C_3 is less negative) in 1988 than in 1982. The same behavior was observed in the other coated plates. To determine the time dependence of the stress we linearly extrapolated the values of C_3 for each plate, measured at different temperatures, to a single temperature, using the measured values of dC_3/dT for the 1982 and 1988 time periods. Fig. 2. shows the values of C_3 for plate 9, extrapolated to 34°C, as a function of time. The slope $dC_3(34)/dt$ is positive, confirming the observation from Fig.1 that the plate became less concave with time. The same behavior is found for the other coated plates.

For comparison we measured the curvature of an uncoated Cervit sample (plate number 6). Unlike the others, this plate was not acid etched after its polished face was ground. No significant variation of C_3 with temperature or time was observed, as is expected for the uniform, low-expansion materials used in this study.

COATING STRESS

The behavior of the coating stress for the six coated samples is shown in Table 2.

1	2	3	4	5	6	7	8	9	10	11
Plate	Material	Coating Thickness	Stress σ_0@73°F (10^7Nm^{-2})		$d\sigma/dT$ (10^5Nm^{-2}C^{-1})		$(1/\sigma_0)(d\sigma/dT)$ (10^{-2}C^{-1})		$d\sigma/dt$ (10^5Nm^{-2}yr^{-1})	$(1/\sigma_0)(d\sigma/dt)$ (10^{-2}yr^{-1})
		(.001 inch)	1982	1988	1982	1988	1982	1988		
4	Zerodur	6.25±0.6	2.17	1.36	-9.47	-6.03	-4.36	-4.43	-6.7	-3.10
7	Cervit	4.88±0.5	3.76	2.57	-10.60	-6.95	-2.81	-2.70	-13.9	-3.70
9	Cervit	4.20±1.1	3.07	2.23	-9.11	-7.27	-2.97	-3.26	-10.3	-3.40
11	Cervit	1.00±0.4	4.12	2.48	-13.40	-8.06	-3.24	-3.26	-12.7	-3.10
24	ULE	4.37±1.0	2.73	1.87	-12.10	-6.50	-4.41	-3.47	-3.9	-1.40
30	ULE	1.05±0.2	4.14	1.30	-13.60	-7.00	-3.29	-5.38	-16.5	-4.00
						Avg:	-3.5	-3.8		-3.1
						Std Dev:	0.7	1.0		

Table 2. Variation of coating stress in coated samples

Calculating the stress from the measured curvature requires a knowledge of the film thickness. This was determined by etching small portions of silver from the four corners of each sample and measuring the film thickness with a dial indicator at each. The uncertainties given in column 3 of Table 2 are the 95% confidence limits of the measurements, calculated with Student's t statistic.

The coating stress for each sample was less in 1988 than in 1982, as shown in columns 5 and 6. Columns 6 and 7 show that the rate of change of stress with temperature was less for each sample in 1988 than in 1982. The thermal expansion coefficient is proportional to initial stress, as indicated by the uniformity of the normalized coefficients $(1/\sigma_0)(d\sigma/dT)$ in columns 8 and 9. The average values for 1988 and 1982, approximately -3.7 percent per degree Celsius, do not differ significantly. Because this coefficient is independent of σ, its value is not affected by uncertainty in the coating thickness.

The rate of change of the coating stress is negative for all samples, as shown in column 10. The normalized rate of stress change $(1/\sigma_0)(d\sigma/dt)$ is quite uniform across the samples, with the exception of an anomalously low value for plate 24; the average rate of change of stress is -3.1 percent per year. To determine whether errors in temperature measurement between the 1982 and 1988 experimental periods could account for the observed stress relaxation, we estimate the temperature change that would be required to give the stress change measured over the approximately 6.5 year span of the experiment. Table 3 shows the total stress change $\Delta\sigma$ for each plate and the temperature change ΔT_{error} that would produce that change if the entire change were caused by thermal expansion at the 1982 rate (the most conservative value). The values of ΔT_{error} range between 2.1 °C

and 8.5 °C, all much larger than the 0.5 °C maximum error in the temperature measurement. Therefore we conclude that the observed stress relaxation was greater than could be accounted for by temperature measurement errors.

Table 3
Temperature Error Budget and Zero-Stress Temperatures

Plate	$\Delta\sigma$(6.5 yrs) (10^5N/m^2)	ΔT_{error} (°C)	T(σ=0) (°C)
4	-43.6	4.6	45.5
7	-90.4	8.5	59.8
9	-67.0	7.4	53.5
11	-82.6	6.2	53.6
24	-25.4	2.1	51.6
30	-107.3	7.9	41.4

The initial coating stresses measured in 1982, extrapolated to 23°C, are between 2×10^7 and 4×10^7 N/m^2. If the expected stress at room temperature is calculated from the measured values of $d\sigma/dT$, roughly -10^6Nm^{-2}C^{-1}, and one assumes a temperature change from 700°C to 23°C, one calculates a room temperature stress on the order of 7×10^8 Nm^{-2}C^{-1}. The apparent discrepancy between calculated and observed stress is explained by the fact that annealed silver has a yield stress σ_y of $(1-5) \times 10^7$ N/m^2[8]. The average of reported values[8] of σ_y is 3.5×10^7 N/m^2, in good agreement with the observed initial 23°C stress values.

EFFECT OF STRESS RELAXATION ON MASER FREQUENCY

To estimate the possible effect of coating stress relaxation on a maser's output frequency, we carried out a finite-element calculation of the change in cavity shape caused by a change in coating stress. If the endplates and cylinder are assumed to be unconstrained, then a change in coating stress of 1×10^6 N/m^2 (typical of the yearly relaxation rates observed in these experiments) in a coating thickness of 0.003 inches, typical for maser cavities, causes the rim of the endplate to move approximately 1.5×10^{-5} cm longitudinally, while the cylinder moves roughly 1.8×10^{-6} cm radially. The major effect is due to the endplate, whose distortion increases the effective (electromagnetic) cavity length L on the order of 1.5×10^{-5} cm (including both endplates, and assuming that the effective change in electromagnetic length corresponds to about half the rim motion of each endplate). For a cavity resonance frequency f_c and maser output frequency f_o, a typical maser has $df_c/dL = 9 \times 10^5$ Hz/cm and a pulling factor $df_o/df_c = 1/30000$; thus the estimated rate of change of maser frequency due to coating stress relaxation for an unconstrained cavity is on the order of $(1/f_o)(df_o/dt) \sim 3 \times 10^{-12}$/yr $\sim 9 \times 10^{-15}$/day, which is roughly an order of magnitude larger than the observed drifts.

Two phenomena tend to reduce the effect of coating stress relaxation on the maser frequency. First, in the maser the polished endplate surfaces are pressed against the cylinder ends by Belleville springs, with a total force of about 450 pounds. This constrains

the cylinder and endplates to move together radially, since the mating surfaces do not slide, and reduces the tendency of the endplate rim lift from the cylinder (curl). If the cylinder and endplates were solidly attached to each other, the endplate distortion due to coating stress change would be reduced by about a factor of 10 from the unconstrained values, and would be opposite in sign to the cylinder distortion, thus reducing the maser frequency shift by at least an order of magnitude. In reality, the cylinder and endplates are prevented from sliding against each other, but the clamping force is not enough to eliminate edge curl entirely. Therefore the estimated frequency shift is expected to be reduced from the unconstrained value calculated above by a factor of perhaps 3 to 10.

The second mitigating consideration is the fact that in operating SAO masers the cavity is maintained at a temperature of 50°C. Since raising the coating temperature above room temperature reduces the tensile stress, as is seen in Fig. 1, a higher ambient temperature also reduces the rate of stress relaxation. Table ? shows the temperature at which the coating stress for each sample is expected to be zero, based upon the average 1988 stress at 23°C and the measured temperature coefficient for each sample. The values of $T(\sigma = 0)$ lie between 41°C and 60°C. Thus we can expect that maintaining the cavity at 50°C would reduce stress-induced maser frequency shifts considerably below the values estimated from the measurements made for a 23°C holding temperature. The combined effects of endplate constraint and 50°C holding temperature might reduce the frequency drift rate by one to two orders of magnitude, to between 1×10^{-15}/day and 1×10^{-16}/day, a range on the order of, to somewhat lower than, observed drift rates.

RELIEVING COATING STRESS

It appears possible to reduce the coating stress substantially for any particular holding temperature by appropriately precooling the sample or cavity. If the sample is cooled from an initially tensile state until the silver yields, and is then reheated to its original temperature, the final stress will be reduced. This effect can be seen in Fig. 3, which shows the bending of plate 9 as a function of time during the 1988 measurement period. When the plate was heated from 34°C (93°F) to 51°C (124°F) and returned to 34°C, its final shape was more concave than it was initially, C_3(34°C) changing from -1.37λ to -1.80λ. Similar behavior was observed for the other coated plates. Cooling is expected to produce the opposite stress change. Such behavior was observed when a sample was cooled to 77°K and rewarmed to room temperature.

These observations suggest a technique for determining whether stress relaxation plays a significant role in the frequency drift of operating masers, as well as a method for minimizing such an effect. A maser cavity could be precooled to a temperature, roughly 0°C or lower, such that rewarming to 50°C would place the coating in compressive stress. A long-term drift of the oscillating maser toward lower frequencies would indicate the influence of stress relaxation. Such relaxation could then be reduced, or even reversed, by heating the maser, using its internal temperature-control heaters, by approximately 30°C, and returning it to its usual temperature.

CONCLUSIONS

The measurements described here show that (a) the internal stress in silver coatings bonded to low-expansion substrates relaxes at a rate of approximately 3 percent per year, and (b) the stress varies with temperature at a rate of approximately 3.6 percent per degree Celcius, with the thermal expansion coefficient decreasing with time as the internal stress decreases. Estimates of relaxation-induced frequency shifts, based on finite-element stress calculations, indicate that stress relaxation is capable of producing frequency drifts of the order of magnitude of those observed in masers, but that in any particular situation the stress effect may be less than observed drifts. It is possible to reduce the coating stress for any final temperature by appropriate precooling or preheating of the maser cavity. Such a technique should make it possible to measure the magnitude and sign of stress-induced frequency drifts, and to minimize any such effects.

ACKNOWLEDGEMENTS

The work reported here was supported by the Jet Propulsion Laboratory. We are grateful to Richard Sumner and Laurie King (University of Arizona Optical Sciences Center) for their close collaboration in the measurement phase; Lester Cohen (SAO) for structural analyses; Ronald Walsworth, Jr. (Harvard University) and Gernot Winkler (U.S. Naval Observatory) for useful discussions; and Donald Graveline (SAO) for constructing the temperature control chamber.

APPENDIX

The computer curve-fitting program expresses the three-dimensional deflection of a sample in terms of Zernike polynomials as follows:

$$y(r,\phi) = C_1(\frac{r}{r_o})\cos\phi + C_2(\frac{r}{r_o})\sin\phi + C_3\left[2(\frac{r}{r_o})^2 - 1\right] \qquad \text{(A.1)}$$

Here r is measured from the center of the rectangular sample, r_o is the distance from the center to the corner of the rectangle, and ϕ is the azimuthal position measured from the long axis of the rectangle. For variations parallel to the long axis, $\phi = 0$ and $x = r\cos\phi = r$, giving

$$y(r,0) = y(x) = C_1(\frac{x}{r_o}) + C_3\left[2(\frac{x}{r_o})^2 - 1\right] \qquad \text{(A.2)}$$

The curvature $K(x)$ of the function $y(x)$ is given by[9]

$$K(x) = \frac{d^2y/dx^2}{\left[1+(dy/dx)^2\right]^{3/2}} = \frac{4C_3}{r_o^2\left[1+(\frac{C_1}{r_o}+\frac{4C_3x}{r_o})^2\right]^{3/2}} \qquad \text{(A.3)}$$

and the curvature at the center of the sample, $K_o \equiv K(x=0)$, is

$$K_o = \frac{4C_3}{r_o^2\left[1+(C_1/r_o)^2\right]^{3/2}} \qquad \text{(A.4)}$$

For eqs. A.3 and A.4 to have meaning, all quantities must be measured in the same units. The coefficients $C_1 - C_3$ are on the order of several wavelengths λ of 6328Å light, and

r_o = 5.17 cm=8.2×10$^4\lambda$, so $(C_1/r_o)^2 \sim 10^{-10} \ll 1$ and can be neglected in Eq. A.4. Therefore the central curvature of the sample is proportional to C_3:

$$K_o = \frac{4C_3}{r_o^2} \tag{A.5}$$

In a similar manner, the curvature of the parabola described by Eq. 1 is

$$K = 2\sigma \frac{3(1-\nu)}{E_s} \frac{t_f}{t_s^2} \tag{A.6}$$

Comparison of Eqs. A.5 and A.6 yields the result given in Eq. 2.

REFERENCES

1. D. Kleppner, H.M. Goldenberg, and N.F. Ramsey, "Theory of the hydrogen maser." *Phys. Rev.* **126**, 603 (1962)

2. S.F. Jacobs, "Dimensional stability measurements of low thermal expansivity materials using an iodine stabilized laser." *Proc. 2nd Frequency Standards and Metrology Symposium*, p. 269 (1976).

3. E.M. Mattison, R.F.C. Vessot, and S.F. Jacobs, "Properties of low-expansion materials for hydrogen maser cavities." *Proc. 39th Annual Frequency Control Symposium*, pp. 75-79 (1985).

4. Zygo Corporation, Middlefield, Conn., Model 1.

5. Wyco Corp, Tucson, Arizona, Wyco Interferometer Software Package (WISP).

6. D.S. Campbell, "Mechanical properties of thin films." In Handbook of thin film technology, L.I. Maissel and R. Glang, eds.,pp. 12-3–12-50 (McGraw Hill, 1970).

7. ULE titanium silicate, code 7971, brochure LEM-ULE-2/72, Corning Glass Works, Corning, New York (1972)
   Zerodur transparent glass ceramics, Schott Optical Glass Inc., Duryea, Pa (undated).
   Cer-Vit material for reflective optics, brochure RO-3 3-69, Owens-Illinois, Inc., Toledo, Ohio (1969).

8. J.L. Everhart, W.E. Lindlief, J. Kanegis, P.G. Weissler, and F. Siegel, Mechanical Properties of Metals and Alloys, National Bureau of Standards circular C447, U.S. Government Printing Office (1943).

9. A.E. Taylor, Advanced Calculus, p. 40. (Ginn, 1955).

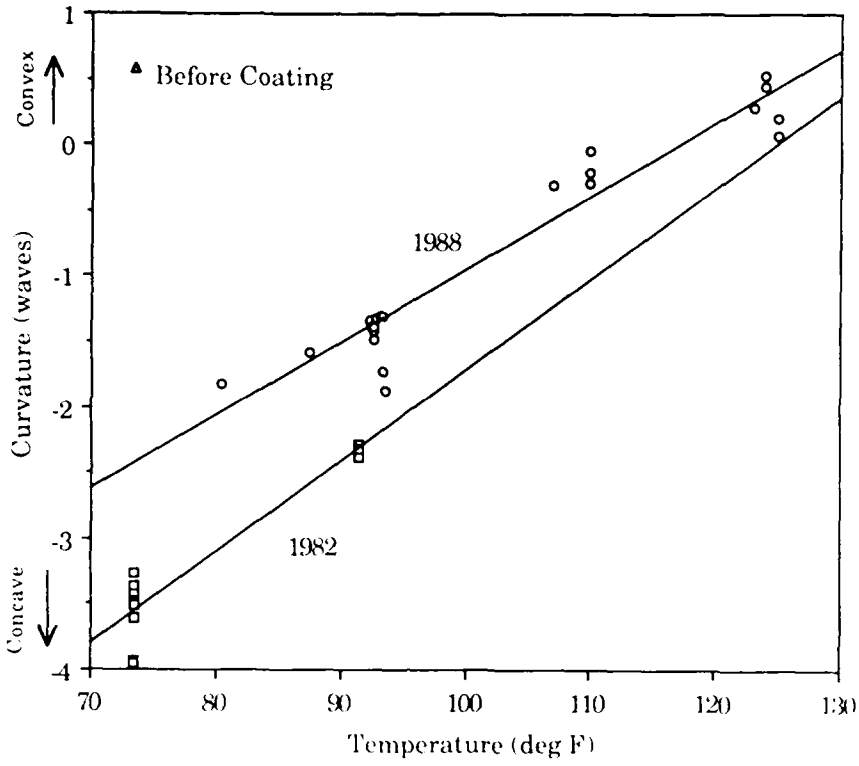

Figure 1. Plate 9 curvature as a function of temperature.

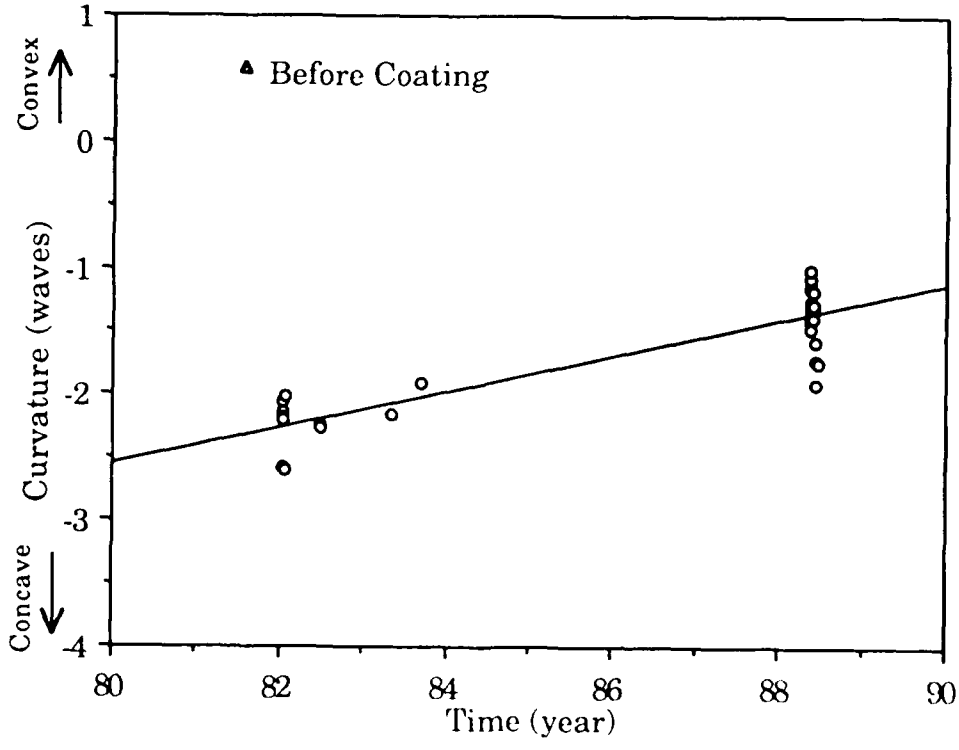

Figure 2. Plate 9 curvature, extrapolated to 34°C, as a function of time.

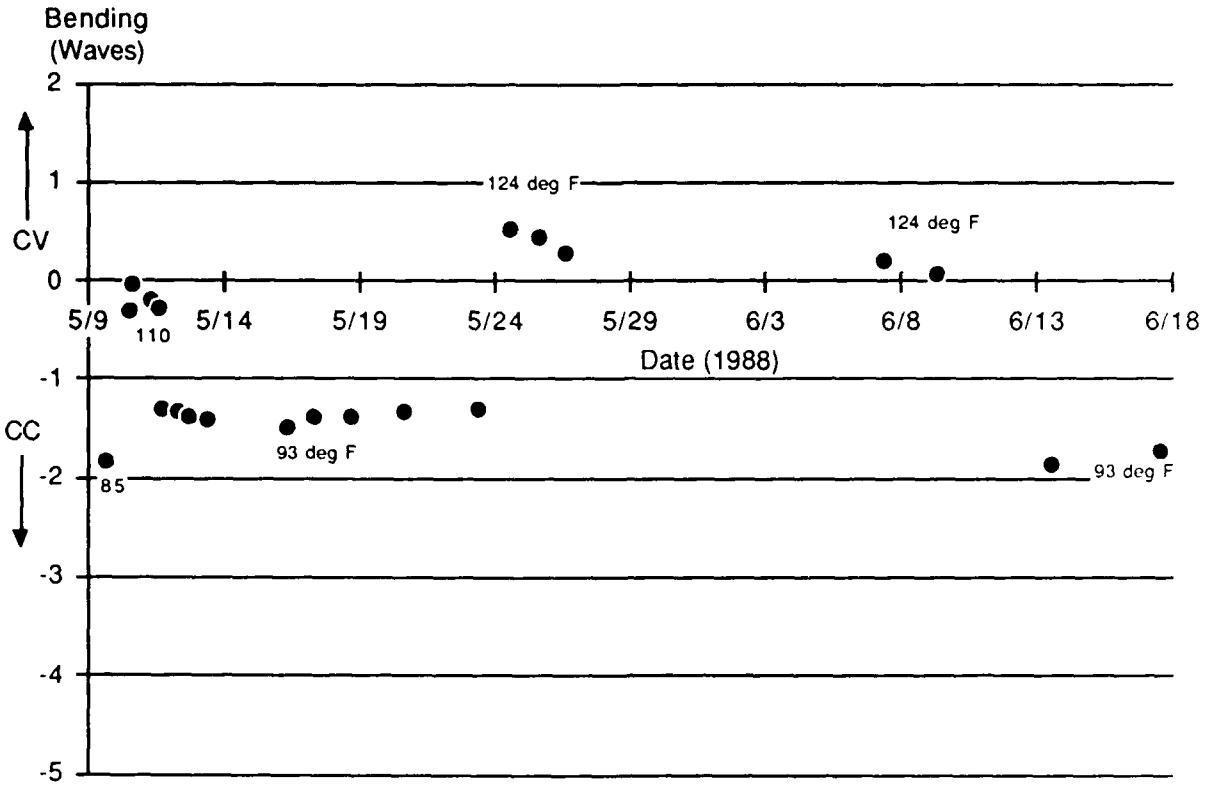

Figure 3. Plate 9 curvature as a function of time, 1988.

QUESTIONS AND ANSWERS

KEN UGLOW, UGLOW ELECTRONICS: What would be the hazards of coating both sides of the ceramic? Would there be problems with resonance between the two surfaces in the ceramic?

DR. MATTISON: There are no hazards. In fact, it might give further RF shielding. It might be beneficial.

DR. JOHN DICK, JPL: Do you have a mechanical or mechanistic explanation for the change of temperature coefficient with time?

DR. MATTISON: The temperature coefficient should be proportional to the effective Young's modulus of the coating. As time progresses, because the coating is basically particulate, the effective Young's modulus decreases.

OPERATING AND ENVIRONMENTAL CHARACTERISTICS OF SIGMA TAU HYDROGEN MASERS USED IN THE VERY LONG BASELINE ARRAY(VLBA)*

T. K. Tucker
Jet Propulsion Laboratory
California Institute of Technology
4800 Oak Grove Drive
Pasadena, California 91109

Abstract

This paper presents the results obtained from performance evaluation of a pair of Sigma Tau Standards Corporation, Model VLBA-112, active hydrogen maser frequency standards. These masers were manufactured for the National Radio Astronomy Observatory (NRAO), for use on the Very Long Baseline Array (VLBA) project, and were furnished to the Jet Propulsion Laboratory (JPL) for the purpose of these tests.

Tests on the two masers were performed in the JPL Frequency Standards Laboratory (FSL), and included the characterization of output frequency stability versus environmental factors such as temperature, humidity, magnetic field and barometric pressure. The performance tests also included the determination of phase noise and Allan Variance using both FSL and Sigma Tau masers as references. All tests were conducted under controlled laboratory conditions, with only the desired environmental and operational parameters varied to determine sensitivity to external environment.

INTRODUCTION

Purpose:

The tests described herein were performed by the Jet Propulsion Laboratory (JPL) at the request of the National Radio Astronomy Observatory (NRAO). JPL was chosen for this evaluation because of its unique testing capability and facilities, and in order to provide an independent evaluation of Sigma Tau hydrogen maser performance.

All tests were conducted at JPL in the Frequency Standards Research Laboratory Test Facility in Pasadena, California, between March and September 1988.

*This work represents the results of one phase of research carried out at the Jet Propulsion Laboratory, California Institute of Technolgy, under contract with the National Aeronautics and Space Administration.

Sigma Tau Hydrogen Masers:

The Model VLBA–112 is a compact and ruggedized active hydrogen maser manufactured by the Sigma Tau Corporation for NRAO for use on the Very Large Baseline Array (VLBA) Project. The essential physical and electrical characteristics, as given by the manufacturer, are outlined in Table 1 below:

Table 1.
Physical and Electrical Characteristics:

Size:	Height	107cm (42 inches)
	Width	46cm (18 inches)
	Depth	76cm (30 inches)
Weight:	238kg (525 lbs)	
Input Power:	AC 115V ±10% rms, 50–60 Hz, 140 Watts	
	DC 24 to 28 V, 4 Amp. (typ.)	
	Built–in Standby Battery Supply	
Outputs:	100 MHz (2 ea.), 1 ±0.3V rms	
	10 MHz (1 ea.), ≈0.5V rms	
	5 MHz (2 ea.), 1 ±0.3V rms	

Prior to performance and environmental testing, the critical operating parameters of each of the two masers, identified as Serial Numbers 2 and 3, were determined and recorded as follows in Table 2.

Table 2.
Operating Characteristics:

Parameter	S/N 2	S/N 3
Output Power:	–100 dBm	–100 dBm
Line Q:	1.82×10^9	1.64×10^9
Cavity Loaded Q:	33,000	37,800
Coupling Factor:	0.35	0.30
Rx Noise Figure:	< 1 dB	< 1 dB
Zeeman Frequency:	827.7 Hz	808.9 Hz

Note: All tests were performed in the AUTOTUNE mode.

Test Facilities:

The JPL Frequency Standards Laboratory is responsible for the research, development and implementation of a wide variety of state–of–the–art frequency generation and distribution equipment used within the Deep Space Network (DSN). In order to achieve the demanding performance and reliability requirements, a substantial amount of assembly and subassembly testing is required. Toward this end, an extensive testing capability has been developed which includes special equipment, facilties, procedures and personnel skilled in the testing and characterization of precision oscillators and other signal sources.

The stability and environmental tests which are routinely performed, in this facility, are as follows:

1. Allan Variance
2. Spectral Density of Phase
3. Temperature Sensitivity
4. Humidity Sensitivity
5. Barometric Pressure Sensitivity
6. Magnetic Field Sensitivity

The instrumentation and test area has approximately 2,700 square feet of floor space, and houses the necessary instrumentation and test equipment. Additionally, two active hydrogen maser frequency references are conveniently located in this area. All critical equipment as well as the units under test are powered by an uninterruptable power source. The entire test area, as well as the environmental control system is backed up by an automatically switched motor generator. Temperature control is maintained to within ±0.05 degrees Centigrade through the use of a doubly redundant air conditioning system. Magnetic field variations are minimized by the use of non–magnetic construction materials throughout the facility. As an additional precaution, one of the reference hydrogen masers is housed in a magnetically shielded enclosure.

Environmental testing capability is provided by three Tenny Corporation environmental test chambers. Each chamber includes 64 square feet of floor space and is approximately 10 feet high, providing adequate space for equipment under test as well as required cables and peripherals.

The environmental testing capabilities are as shown in Table 3 below:

Table 3.
Environmental Test Capability

Parameter	Range
Temperature	15 to 35 deg. C ±0.05 deg.
Pressure	±24 inches of water ±0.5 inches.
Relative Humidity	11 to 90% RH ±5%
Magnetic Field	±0.5 Gauss

Measurement System

Figure 1 is a block diagram of the measurement system used to determine frequency stability and the Allan variance (deviation) between the Sigma Tau masers and the laboratory reference masers. Figure 2 is a block diagram of the measurement system used to determine the spectral density of phase of the two Sigma Tau masers at the 5, 10 and 100 MHz outputs.

TEST RESULTS

Sequence of Tests:

The tests and test limits are as follows in Table 4:

Table 4.
Test Sequence and Limits

Parameter	Range
Allan Variance	
Spectral Density of Phase	
Temperature	17 to 27 Deg. C
Humidity	20 to 80% RH
Barometric Pressure	±24 inches of water
Magnetic Field	±0.5 Gauss
Power Supply Variations	24 to 28 VDC

Allan Variance and Spectral Density of Phase Tests:

Figures 3, 4 and 5 are plots of the Allan Variance between the two Sigma Tau masers, and also between each of the Sigma Tau masers and one of the laboratory reference masers which serve to verify near equal performance of the two Sigma Tau masers. Included in Figure 2 is the measurement system noise floor. Figures 6, 7 and 8 are plots of the spectral density of phase between the two Sigma Tau masers at the 5, 10 and 100 MHz outputs. The spurious signals seen in each of the plots is predominantly the result of the autotuner modulation signal with some additional contribution from power supply noise.

Environmental Tests:

The purpose of these tests was to characterize each maser in terms of frequency shift for a given change in environmental condition. In each test, the output frequency was carefully monitored while one of the environmental conditions was varied as specified in Table 4. The results of each of these environmental tests is itemized below:

1. Output Frequency vs Temperature Tests — The masers were individually placed in the test chamber and the chamber temperature was cycled between 17 and 27 °C, the resultant variation in output frequency was plotted. The frequency sensitivity as a function ambient temperature is shown in Figure 9.

2. Output Frequency vs Relative Humidity Tests — With the chamber temperature held constant, the chamber relative humidity was cycled between 20 and 80% , with a 48 hour stabilization period at each limit. The observed variations in output frequency vs the relative humidity were well below 1×10^{-14}.

3. Barometric Pressure Tests — No output frequency variations were observed as the masers were individually subjected to barometric pressures of 24 inches of water above and below ambient pressure with a two hour dwell at each extreme.

4. Magnetic Field Sensitivity Tests — In order to determine the maser magnetic field sensitivity, a large (90 inch) Helmholtz coil was placed around the maser. The coil was positioned to provide a vertical magnetic field and was centered around the maser physics unit. Since the magnetic shielding effectiveness is dependent upon the magnitude of the magnetic field, the sensitivity was measured at three different field values. The magnetic field sensitivity of each maser is shown in Table 5 below:

Table 5.
Magnetic Field Sensitivity

Field	S/N 2	S/N 3
Small Field (± 0.1 G)	-1.42×10^{-13}/ Gauss	-4.74×10^{-13}/ Gauss
Medium Field (± 0.25 G)	-1.05×10^{-13}/ Gauss	-3.98×10^{-13}/ Gauss
Large Field (± 0.5 G)	-8.04×10^{-14}/ Gauss	-3.17×10^{-13}/ Gauss

5. Output Frequency vs Power Supply Variations — With the internal battery supply disconnected, the input DC voltage was varied between 24 to 28 VDC. No output frequency shift was observed as a result of these supply variations.

SUMMARY

A summary of the environmental sensitivities of the two Sigma Tau masers is presented in Table 6 below:

Table 6.
Environmental Sensitivity Summary

Condition	S/N 2	S/N 3
Temperature (17 to 27 °C)	1.37×10^{-14}/°C	4.2×10^{-14}/°C
Humidity (20 to 80% RH)	$< 1 \times 10^{-14}$	$< 1 \times 10^{-14}$
Barometric Pressure (±24 in. Water)	$< 1 \times 10^{-14}$	$< 1 \times 10^{-14}$
Magnetic Field (± 0.1 Gauss)	-1.42×10^{-13}/Gauss	-4.74×10^{-13}/Gauss
Power Supply Variations (24 to 28 VDC)	$< 1 \times 10^{-14}$	$< 1 \times 10^{-14}$

Throughout the test series the Sigma Tau performed reliably, and were well behaved. Of particular interest is the fact that both masers were transported from Soccoro, NM to Pasadena, CA, a distance of some 800 miles, in the back of a carryall van. Only a minimum of protection from shock and

vibration was provided during transit, and upon arrival both masers were within normal operating parameters.

ACKNOWLEDGEMENTS

The author wishes to acknowledge the generous contributions of several individuals to this effort. In particular, that of Albert Kirk and Bill Deiner of JPL for their assistance in the performance of the many tests. Additionally, the generous technical assistance of Harry Peters of the Sigma Tau Corp. during the initial setup and preparation for testing is gratefully acknowledged.

REFERENCES

[1] Peters, H., Owings, B., Oakley, T., and Beno L., "Hydrogen Masers for Radio Astronomy," *Proc. 41st Ann. Freq. Control Symposium,* (1987), p. 75 - 81.

[2] Peters, H., "Design and Performance of New Hydrogen Masers Using Cavity Frequency Switching Servos," *Proc. 38th Ann. Freq. Control Symposium,* (1984), p. 420 - 427.

[3] "Operation and Instruction Manual, Atomic Hydrogen Maser Frequency Standard, Model VLBA-112," Sigma Tau Standards Corporation, (1985).

[4] Sydnor, R., "Phase Noise Test Procedures," Jet Propulsion Laboratory Internal Document, (Nov. 1988).

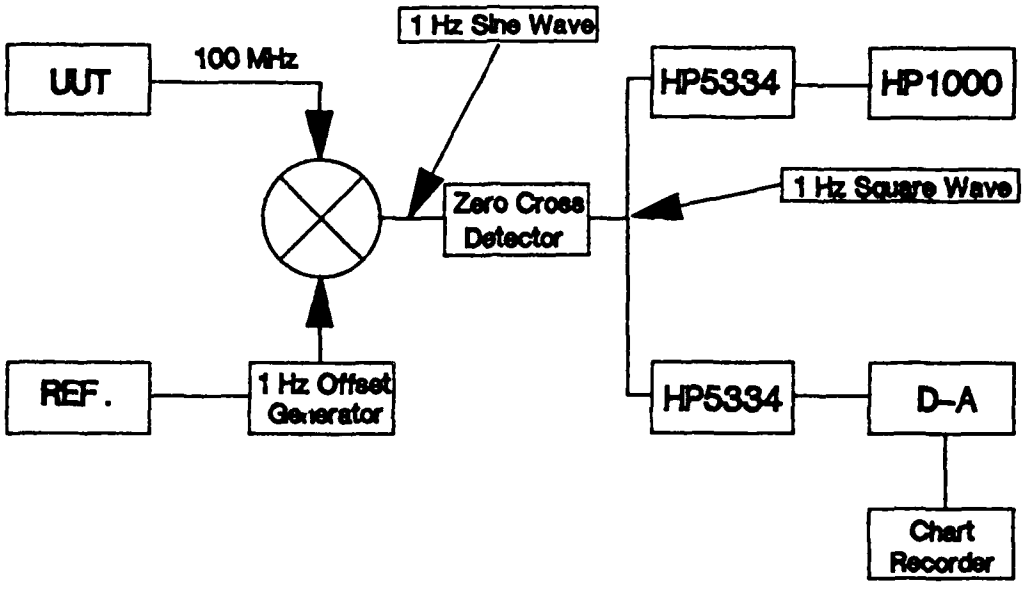

Figure 1. Measurement System for
Frequency Shift & Allan Variance

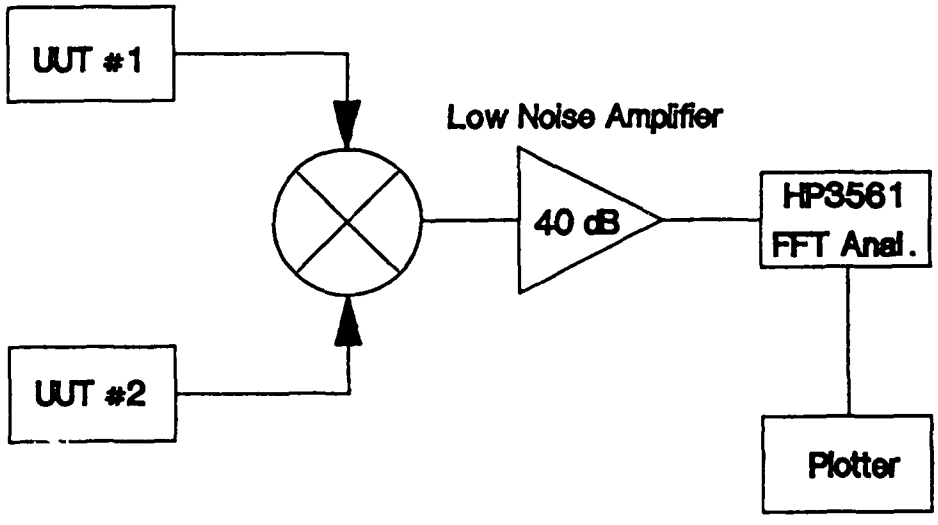

Figure 2. Phase Noise Measurement System

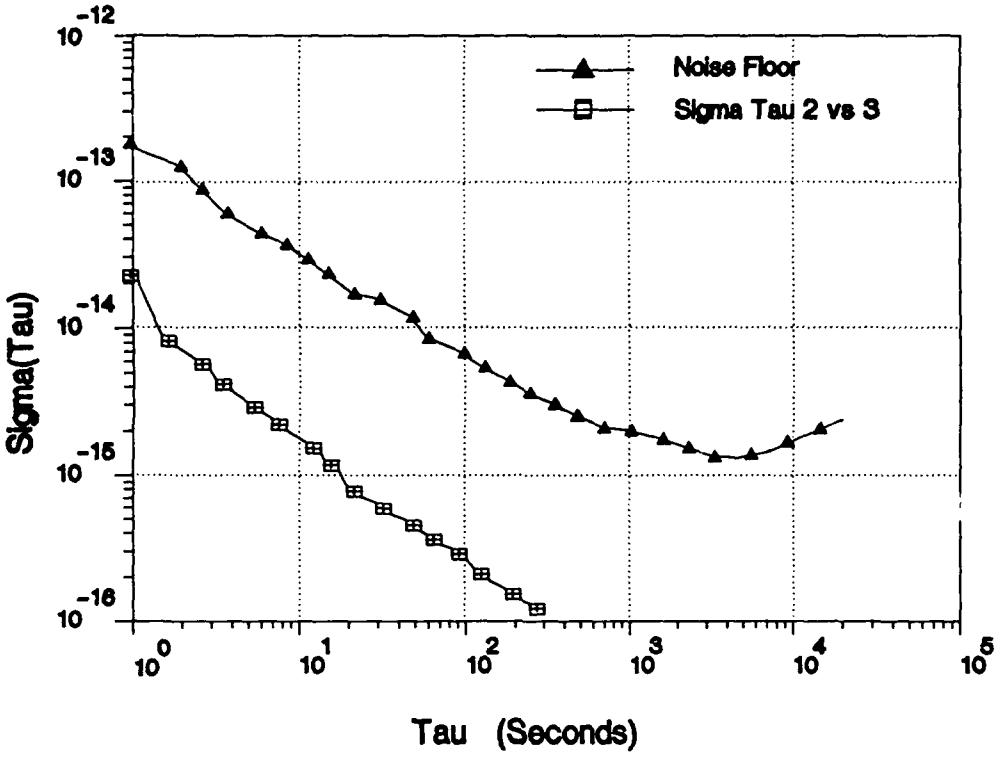

Figure 3. Allan Variance - Sigma Tau 2 vs 3

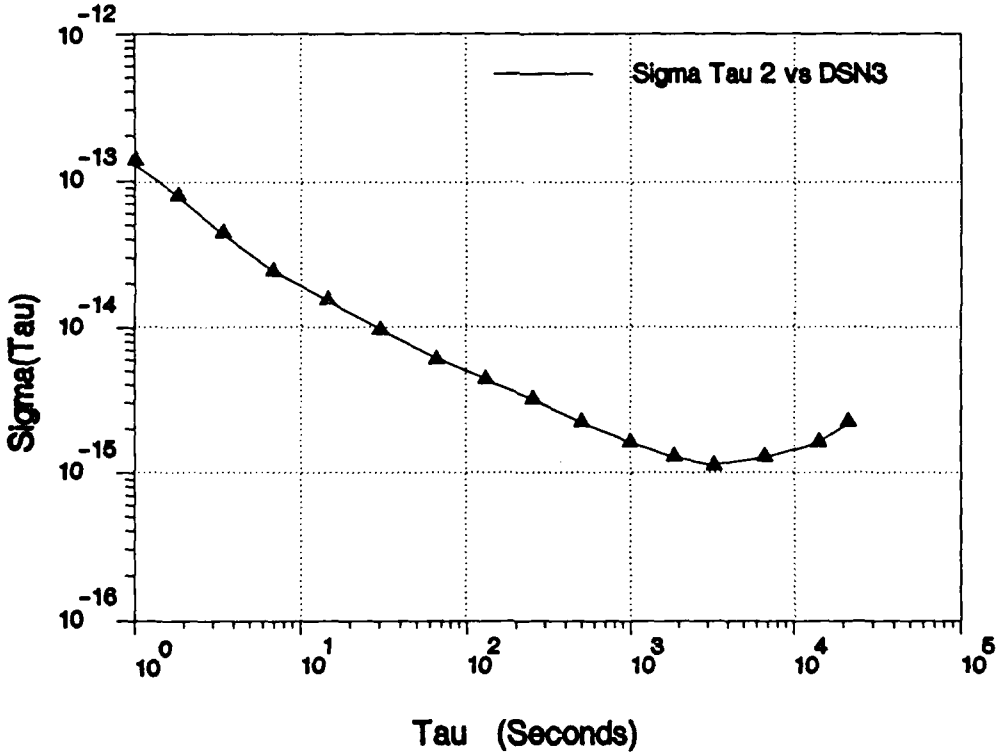

Figure 4. Allan Variance - Sigma Tau 2 vs Ref.

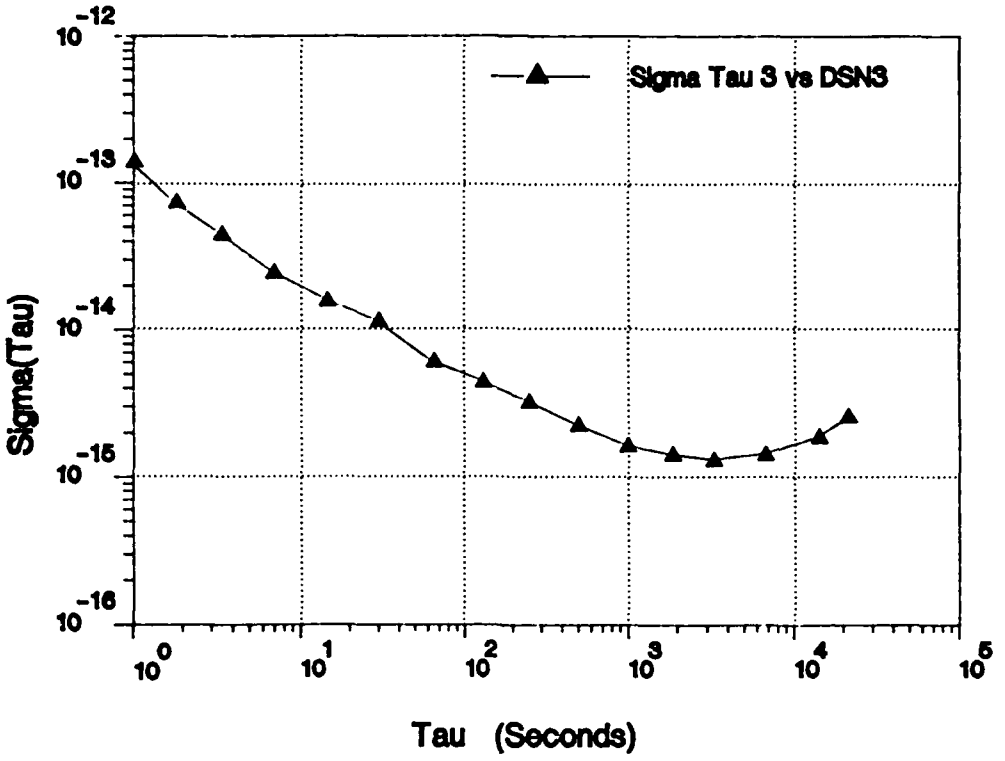

Figure 5. Allan Variance – Sigma Tau 3 vs Ref.

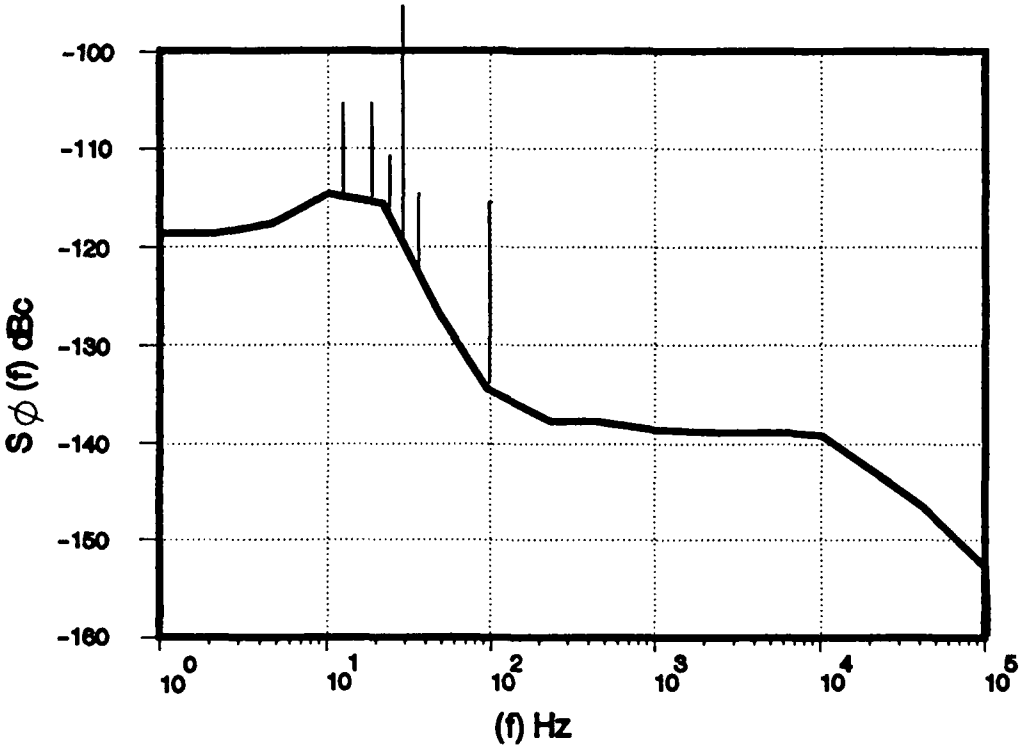

Figure 6. Phase Noise at 5 MHz Outputs

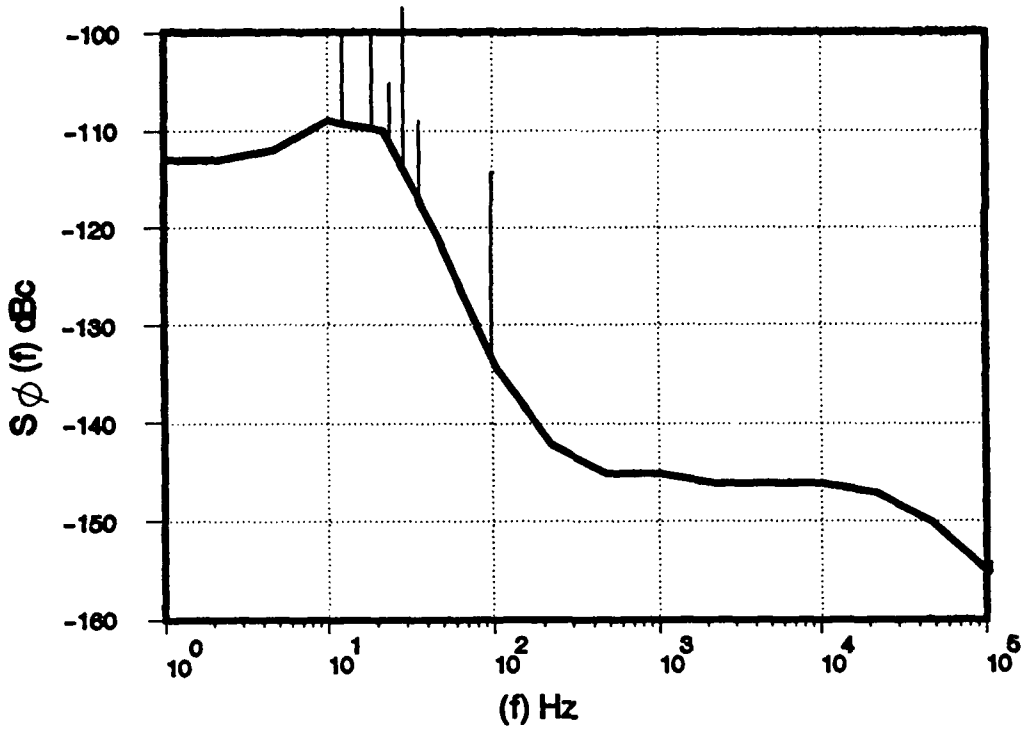

Figure 7. Phase Noise at 10 MHz Outputs

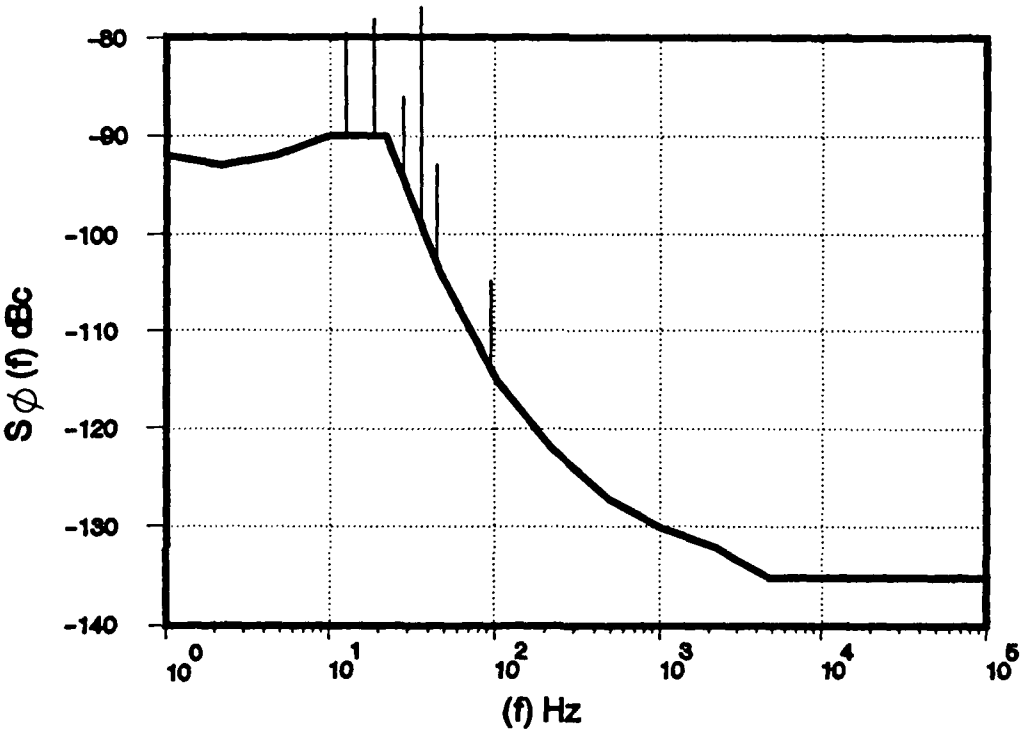

Figure 8. Phase Noise at 100 MHz Outputs

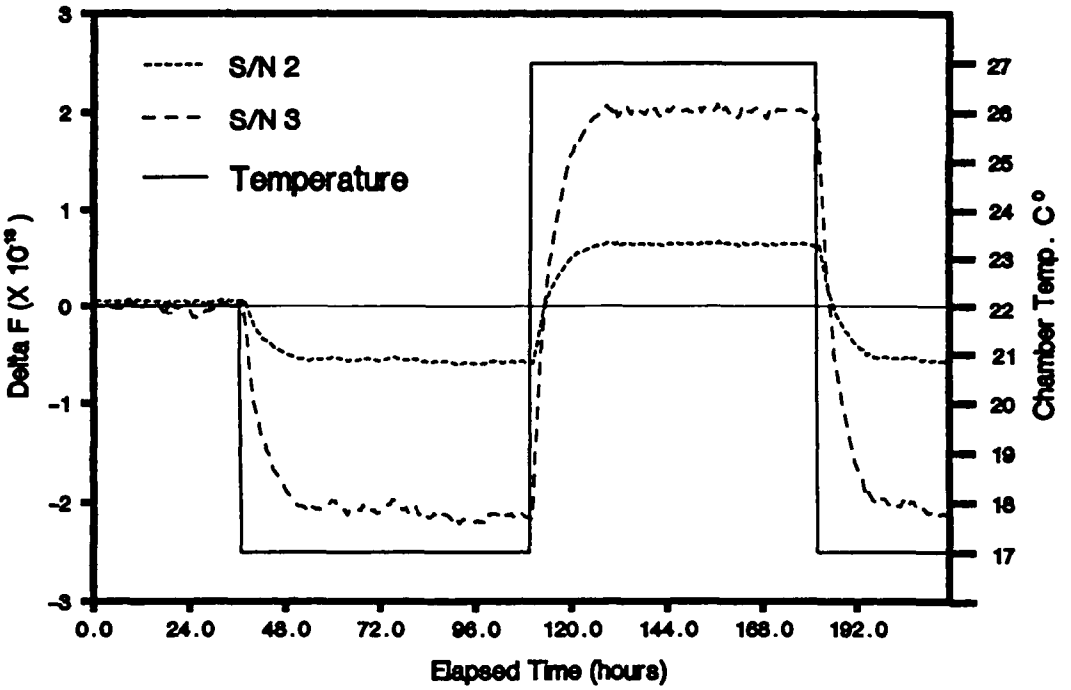

Figure 9. Output Frequency vs Temperature

QUESTIONS AND ANSWERS

HARRY PETERS, SIGMA TAU CORPORATION: I just thought that I would mention that the magnetic tests for ±0.1 gauss and ±1.0 gauss–it is sort of characteristic of magnetic shields that the hysteresis affect inherent in shielding is such that, for lower values of the ambient field change, you would expect larger shielding factors. However, the practical importance goes down because, if you look at the actual shift of parts in ten to the fourteenth, the shift is nearly the same as for the high field shift. We did have trouble with the early masers with the shields, but I hope that we are overcoming that.

MR. TUCKER: Yes, we were forewarned by you that one maser did have a little worse shielding than the other one.

ATOMIC HYDROGEN MASERS WITH SELF AUTO-TUNE SYSTEM AND MAGNETIC FIELD CANCELLATION SERVO

H. E. Peters, H. B. Owings and P. A. Koppang
Sigma Tau Standards Corporation
Tuscaloosa, AL 35403

Abstract

Atomic hydrogen masers of the classic active oscillator type which produce the characteristic high stability required by standards laboratories, radio astronomers and other critical scientific applications are described. Features of these masers include automatic cavity stabilization, active magnetic field cancellation servo, relatively small size and weight and other characteristics which adapt them well to use in remote field station operation and long term time and frequency related applications requiring the highest performance.

INTRODUCTION

Sigma Tau Standards Corporation atomic hydrogen masers have evolved from the original atomic and molecular beam research done at Harvard University in the late 1950's and the first operational hydrogen maser standards developed for field use at Varian Associates QED Division in the early 1960's. Further extensive research and development by the National Aeronautics and Space Administration and research at Sigma Tau Standards Corporation funded by NASA, NRL, the USAF and APL (Johns Hopkins University) has resulted in a maser design which is presently being placed in service by the National Radio Astronomy Observatory for the Very Long Baseline Array system of 10 VLBI radio telescopes.

The scientific principles of a classic hydrogen maser are quite straightforward, although in practice very careful attention to the developed state of the art is required to attain a successful device design. In essence, a source of hydrogen atoms is produced by an RF discharge within a glass source bulb; the atoms are collimated by a tubular exit orifice and pass in a beam through a magnetic state selector wherein atoms in the upper hyperfine quantum levels are focussed into a Teflon lined quartz storage bulb located upstream within a microwave cavity which is tuned to the hydrogen transition frequency. When the density of atoms, magnetic field homogeneity and other design parameters are correct, continuous maser action occurs spontaneously and an RF signal is produced, nominally 1,420.405 MHz, which is translated to standard output frequencies by a low noise receiver-synthesizer system.

I General Design and Performance

The general Sigma Tau Standards Corporation (STSC) hydrogen maser design is described in more detail in references 1, 2 and 3. It is noteworthy that the unique automatic cavity tuning system described in the above references has proven to be very effective in practice and has contributed to

the excellent long term stability and reproducibility exhibited by these masers without significantly degrading the short term stability.

A significant new development in the STSC masers is an automatic magnetic field cancellation servo system which effectively eliminates the perturbing systematic effects on maser stability produced by external magnetic field variations. This servo system, as well as a magnetic field test system, a newly constructed frequency stability measuring system, and experimental results of tests on the STSC hydrogen masers form the remainder of this paper.

II Magnetic Field Control System

Figure 1 illustrates the dependence of the oscillation frequency of the hydrogen maser on the magnetic field present in the cavity interaction region. As shown in the figure, the frequency variation is quadratically dependent on the field and so approaches zero as the field approaches zero. In practice it is not practical to operate too close to zero field since field inhomogeneities will eventually become important and produce departures from the ideal frequency dependence or create other functional problems.

At a typical internal field used in the STSC masers of 500 microgauss, the fractional frequency variation dependence on the internal field is $(f - f_o)/f_o = 9.6 \times 10^{-16}$ per microgauss variation. So, to maintain the magnetic sensitivity to 1×10^{-14} or less for a one gauss external field change, a shielding factor of $1 \times 10^{+5}$ is required. The STSC hydrogen masers use a very effective four level set of magnetic shields surrounding the cavity region, however unless great care is used in properly annealing the magnetic shield material during fabrication, the above shielding factor is difficult to attain.

To improve upon the static shielding factor an active field stabilization servo system has been developed and is presently used in the STSC hydrogen masers. Figure 2 is a diagram showing the general geometric arrangement of the two outer magnetic shields. It is generally found, as demonstrated later, that the sensitivity of the maser to the horizontal component of the external field is negligible. This is due to the short horizontal magnetic paths and favorable transverse shield spacings. Thus, it is only necessary to stabilize the vertical field component, and to accomplish this a magnetic sensor has been placed in the space between the outer shield and the next shield cylinder top as illustrated in the figure.

The sensor element is a Hall effect probe which is placed near the center of the temperature controlled plate on which some of the maser receiver and control modules are mounted. To increase the probes sensitivity and to raise the probe output voltage well above the noise level, a field enhancement arrangement has been devised using two high permeability plates, one above and one below the probe, with a concentrated field path created by small magnetic posts that direct a concentrated sample of the field through the probe. The two plates are perpendicular to the Z-Axis field direction, so the probe responds mainly to Z-Axis field variations.

Figure 3 is a diagram illustrating the overall magnetic servo system. Coil windings are placed at the ends of the cylindrical shield located below the magnetic sensor assembly and a precision integrated circuit preamplifier is located near the Hall probe. A buffer amplifier to drive the field coils and a current regulator for the Hall probe bias current are located in a small module on the maser frame. The voltage variations developed by the sensor are thus amplified and produce a compensating current in the coil windings which effectively nullifies the Z-Axis field variations between the shields due to external perturbations.

III Magnetic Field Sensitivity Tests

Tests of magnetic field sensitivity have been performed on several hydrogen masers equipped with the new servo system. The results reported herein are typical. A set of Helmholtz coils one meter in diameter was calibrated in air to produce a known field as a function of coil current. The coils were then placed around the maser to be tested, oriented to produce an external perturbing field in one of the three orthogonal axes.

Two methods were used to evaluate the frequency variations associated with field changes; in one case the test maser frequency was compared with the frequency of another hydrogen maser located remotely from the test station; in the second method the Zeeman frequency was measured and the magnetic frequency shift and shielding factor were calculated. Since the measured magnetic shifts with the magnetic servo on were too small, less than 1×10^{-14} per gauss, to measure by the first method using measuring intervals of the order of 1000 seconds, the Zeeman frequency method was used to obtain the results given in Chart 1.

MAGNETIC TEST PERFORMED ON NRAO MASER SN V-7				
Internal field set at 640 microgauss External perturbation 1 gauss				
ORIENTATION AXIS	SERVO ON/OFF	FREQUENCY VARIATION/GAUSS	SHIELDING FACTOR	IMPROVEMENT IN SENSITIVITY
Z-Axis (Vertical)	ON	5.2×10^{-16}	4,700,000	} 30/1
	OFF	1.6×10^{-14}	160,000	
X-Axis (F To B)	ON	4.7×10^{-16}	$> 10^{+6}$	None
	OFF	3.4×10^{-16}		
Y-Axis (L To R)	ON	2.5×10^{-16}	$> 10^{6}$	None
	OFF	1.6×10^{-16}		

CHART 1. Magnetic Field Sensitivity Test Results

In a stationary installation, typical ambient magnetic field variations are usually less than 10 or 20 milligauss. In mobile situations (traveling clocks), or in installations with nearby large moving magnetic structures, such as elevators, cars or radio telescope dishes, the ambient field variations are unlikely to exceed plus or minus 1 gauss. Therefore the results of tests on the STSC hydrogen masers indicate that magnetic perturbations are not likely to be the dominant source of systematic instabilities.

IV Frequency Stability Measuring System

A computer based system for measuring phase, frequency and frequency stability has been assembled and programed at STSC for evaluating the performance of the hydrogen masers. A block diagram of the system is shown in Figure 4. The system may be used with any standard input frequency such as 5 MHz, 10 MHz, 100 MHz or higher frequencies which can be offset relative to a standard reference maser output by 1 Hz. In the example given here, the 100 MHz output of one maser is offset relative to the other by 1 Hz using one of the maser synthesizers; the signals are then sent to a double balanced mixer with a one Hz

filter, amplifier and Schmitt trigger circuit which produces a 1 Hz beat pulse. A second 1 Hz reference pulse is generated by division from the 10 MHz output of one of the masers. The two pulses are input to the A and B ports of a counter which continuously measures the periods $(T_a - T_b)$, which are sent to an AT compatible computer using the GPIB control bus. The computer calculates and stores the relevant parameters and generates curves and data to be printed out.

V Frequency Stability Data

Figure 5 shows a plot of data which is continuously accumulated and displayed on the computer screen as the measurement progresses. The curve showing phase, with the scale on left, gives the phase relative to the one Hz difference frequency $(T_a - T_b)$ in units of seconds. The relative fractional frequency is calculated from the slope of the phase curve; this is given by the scale on the right with $\pm 5 \times 10^{-13}$ full scale. The total measurement interval for this curve is 60,000 seconds. The fractional frequency data (Allan Variance) for decade multiples of 1, 2 and 5 seconds is displayed above the phase and frequency curves.

When the measurement is finished, the computer may be commanded to display and to print the stability plot as shown in Figure 6, which is the Sigma Tau plot of the data shown in Figure 5. It should be emphasized that this data has no drift removed.

Acknowledgments

The authors gratefully acknowledge the support of the National Radio Astronomy Observatory under Contract VLBA–112 as well as the Associated Universities Inc., and the National Science Foundation.

References

1. H. Peters, B. Owings and T. Oakley, "Hydrogen Masers For Radio Astronomy," 41st Symposium on Frequency Control, May 1987.

2. H. E. Peters, "Design and Performance of New Hydrogen Masers Using Cavity Frequency Switching Servos," 38th Symposium on Frequency Control, June 1984.

3. H. E. Peters and P. J. Washburn, "Atomic Hydrogen Maser Active Oscillator Cavity and Bulb Design Optimization," 16th Annual PTTI Applications and Planning Meeting, November 1984.

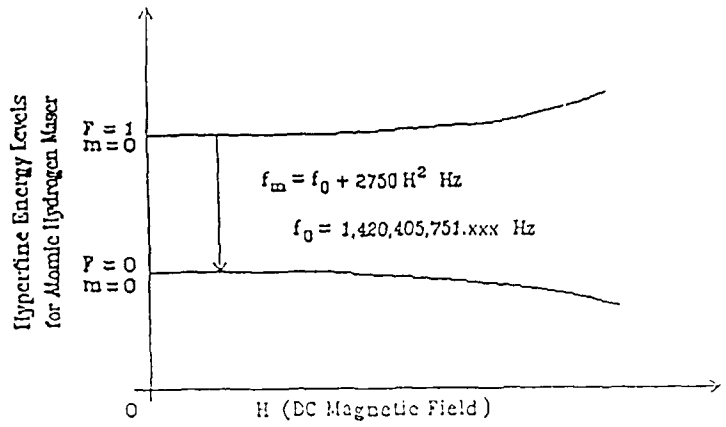

Figure 1. Frequency Dependence on Magnetic Field

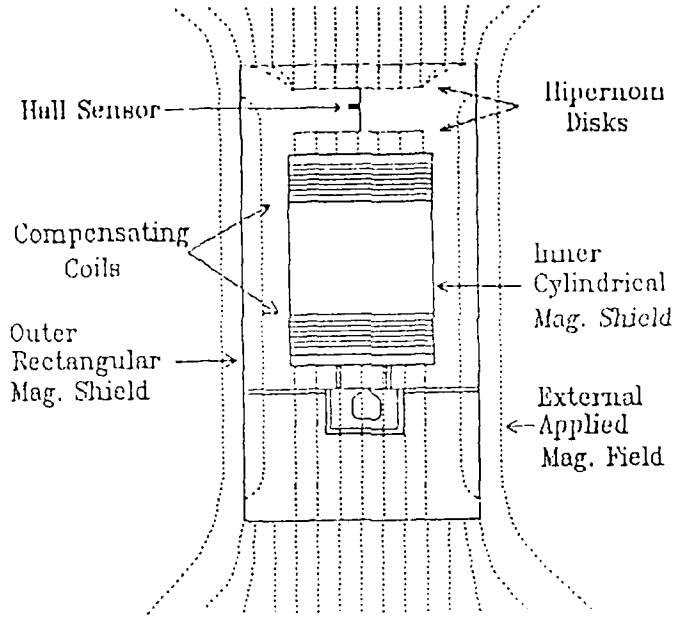

Figure 2. Magnetic Shield and Sensor Configuration

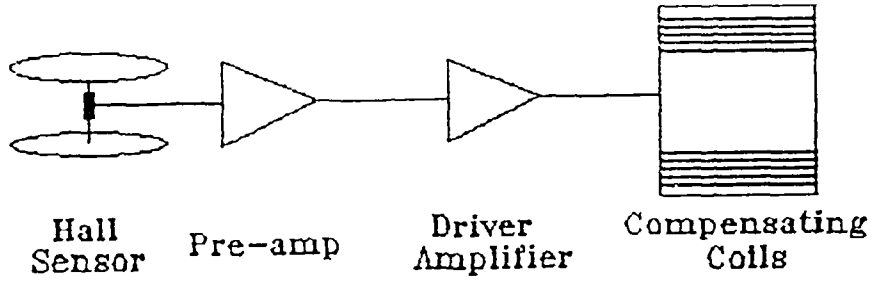

Figure 3. Diagram of Magnetic Servo System

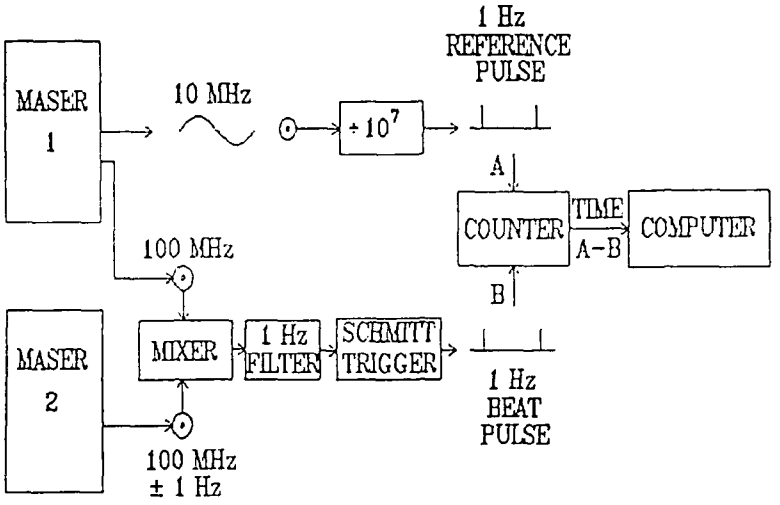

Figure 4. Frequency Stability Measuring System

Figure 5. Frequency and Phase Data

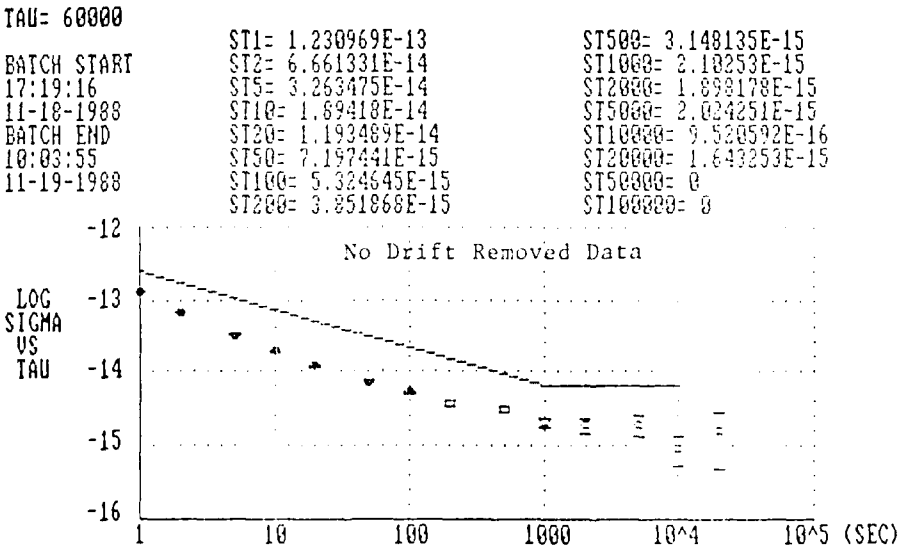

Figure 6. Frequency Stability, 100 Mhz Outputs

DAVID ALLAN, NIST: What was the measurement floor of the measurement system with the ten to the seventh divider?

MR. KOPPANG: We did some measurements on that. It was down in the minus eighteens, I believe. We did a run from one to a thousand seconds and it was from ten to the minus seventeen to ten to the minus eighteen.

MR. ALLAN: So that is well below the maser noise. The other question is that with the masers you should have in principle white phase noise in the short term. I don't know whether you thought about using the modified two sample approach or not, but that would show that up nicely if that were the case.

MR. KOPPANG: Thank you, we will look into that.

DR. HARRY WANG, HUGHES AIRCRAFT: Can you comment on the magnitude of your correction field? Do you see any hysteresis effect of that correction field on the magnetic shielding?

MR. KOPPANG: Well, the outer shield has a shielding factor of approximately 300 to 500. The magnetic concentrator magnifies the magnetic field approximately 100. We could calculate the internal fields, but we haven't done that. We haven't checked on any hysteresis effects on the magnetic shields.

HARRY PETERS, SIGMA TAU CORPORATION: The shielding factors were derived using fields of plus and minus one gauss. As far as the hysteresis as seen by measurement of the frequency, it was below ten to the minus fourteenth. Inevitably you get hysteresis in the shields, but the servo itself has no noticeable hysteresis because the field is concentrated adequately to get out of the hysteresis range.

DR. WANG: Off mike, not decipherable...

MR. PETERS: We have this installed in four masers at the moment and the stability is very good as long as we run the concentrator high enough to get out of the instabilities in the Hall probe. We certainly don't have any long term data on the stability of the transverse effect.

OPERATIONAL PARAMETERS FOR THE SUPERCONDUCTING CAVITY MASER*

R. T. Wang† G. J. Dick, and D. M. Strayer
Jet Propulsion Laboratory
Pasadena, California 91109

Abstract

Tests of the superconducting cavity maser (SCM) ultra-stable frequency source have been made for the first time using a hydrogen maser for a frequency reference. In addition to characterizing the frequency stability, the sensitivity of the output frequency to several crucial parameters was determined for various operating conditions. Based on this determination, the refrigeration and thermal control systems of the SCM were modified. Subsequent tests showed substantially improved performance, especially at the longest averaging times.

In frequency stability tests, characterization of the short term performance of the SCM was not possible due to hydrogen maser fluctuations, but for the longest measuring time the low SCM instabilities could be characterized. This was expected, since cryogenic cavity oscillators show unsurpassed performance for short measuring times. In initial tests, our measurements showed a frequency stability of about $2 \cdot 10^{-14}$ for times between 30 and 3000 seconds. The long term stability (3000 s) is approximately 5 times better than we were previously able to measure.

In order to better understand the limits to SCM stability we performed a detailed study of the dependence of the operating microwave frequency ($\approx$ 2.69GHz) on: operational temperature, pump frequency, pump power, coupling strength and the bias field applied to the ruby maser. Of these, sensitivity to changes in temperature and pump power are crucial because of the great difficulty in stabilizing these two parameters. We discovered operational parameters for which both of these sensitivity coefficients approach zero, and have identified a sixth parameter, the temperature gradient across the oscillator, the effects of which severely compromised the effectiveness of our thermal regulation system.

After the first tests the low temperature cryogenic system was rebuilt with two changes. Conversion to a continuous-flow cooling system appropriate to the new 1.57K operating temperature allows long term operation without the refill cycles required by the previous 1.0K closed cryostat. Secondly, cooling and thermal regulation were arranged in such a way that neither the heater power required for temperature regulation, nor thermal leakage due to mechanical supports, flow through the body of the oscillator itself. This prevents unavoidable fluctuations in heat flow from generating corresponding frequency fluctuations due to thermal gradients across the oscillator. Frequency stability measurements on the rebuilt oscillator showed improved results, giving fractional frequency stability in the mid-10^{-15} range for times between 100 and 1000 seconds.

*This work represents the results of one phase of research carried out at the Jet Propulsion Laboratory, California Institute of Technology, under contract sponsored by the National Aeronautics and Space Administration.

†During the time the work was done this author held a National Research Council-NASA/JPL Research Associatship.

Introduction

The superconducting cavity maser (SCM)[1,2,3] is an all-cryogenic oscillator which, like other cryogenic cavity oscillators, gives stability at short measuring times which is superior to that achievable by any other means. It differs from other superconducting cavity stabilized oscillator (SCSO) designs[4] in its use of a very rigid ($Q \approx 10^9$) sapphire-filled stabilizing cavity, and in its all-cryogenic design; excitation being provided by an ultra-low noise cryogenic ruby maser.

Performance of the SCM at short times is superior to all conventional or atomic sources, even surpassing that of the active hydrogen maser. With similar Q's, the advantage of the SCM is its larger output power; $\approx 10^{-9}$Watt vs $\approx 10^{-12}$Watt for the hydrogen maser. Long term performance is limited by variations in the various operating parameters, such as temperature, drive power, output VSWR etc., depending on the sensitivity of the SCM to these various parameters.

Figure 1 shows a block diagram of the oscillator. The three-cavity design has been previously discussed[2]. Oscillation at the signal frequency (2.69GHz) results from application of pump power (13.15GHz) to the ruby, which creates an inversion of the energy level populations in the ruby crystal. The frequencies of the three modes of the coupled cavity system are spaced relatively close to each other (5% spacing) in order to couple effectively, but are spaced far enough from each other to allow mode selection. Only one of the modes is suitable for ultra-stable operation. Tuning the regenerative frequency of the ruby (2% bandwidth) to that of this high-Q stabilized mode is accomplished by adjusting the current through the superconducting solenoid. The purpose of the coupling resonator is to provide physical separation of the lead-coated sapphire resonator from the magnetic field of the solenoid.

Cooling of the oscillator itself is provided by the liquid helium pot attached to the bottom cavity, and thermal regulation is achieved by varying the power dissipation in the heater as shown. Both the heat leak into the system from the waveguide at the top, and the cooling power of the helium pot are subject to variation, and it is seen that, even if the changes in these heat flows are exactly cancelled by the effect of the heater, varying temperature gradients in the oscillator will still result.

Figure 2 shows the stability of this oscillator when measured with a hydrogen maser as reference. Also shown are the measured stability of the H-maser and calculated short term stability for the SCM due to additive and in-oscillator noise for the present configuration. The major features shown in Figure 2 are:

1 The need for a better reference at short times in order to properly characterize the SCM.

2 The presence of in-oscillator noise due to back-coupling from the room-temperature amplifier.

3 The presence of substantial long-term variations in the SCM.

The first of these considerations can be dealt with only by the provision of a second cryogenic oscillator, something outside the scope of this paper. The second can be solved by the addition of a cryogenic isolator to prevent room-temperature radiation from coupling from the output port back into the oscillator itself. This issue is addressed by a redesign of the oscillator to allow primary coupling of the signal from an additional port in the high-Q resonator.

The long-term variations, on the other hand could arise from any of the various parameters on which the frequency of the SCM depends. This paper primarily considers the sensitivity to and variation of the operational parameters for the SCM.

Operational Parameters

The significant operational parameters (parameters subject to variation during operation) of the SCM are presented in the table below. Each of these parameters is described in terms of its significance as a tuning parameter, and as a likely source of variability in the output frequency. Several of the parameters are discussed in more detail in the text that follows.

Parameter	Tuning Functionality	Significant Variability
Temperature	Operating range from below 0.8K to above 2.0K for normal SCM operation. Variation changes sign of sensitivity of operational frequency to Temperature. Proper choice allows operation with near zero temperature coefficient.	Substantial instability. Medium and long term variability of 10^{-4} to 10^{-5}K. Sensitivity coefficient 0 to $\pm 10^{-9}$/K.
Thermal Gradient	No functional significance.	Marked problems due to variation in regulating heater power. Best expressed in terms of sensitivity to heat flow. Value is $\approx 10^{-9}$/Watt. Value of heater power is typically 10^{-3} to 10^{-2} watts. Variability of heater power is 10% to 50%.
Magnetic Bias	Variable by 2% about optimum value of $\approx$ 500 gauss. No important effect on frequency sensitivity coefficients.	No problems observed. Sensitivity is $\approx 10^{-9}$/gauss. Use of a persistent-mode superconducting magnet at this relatively low field allows very high stability.
Pump Power	Oscillation requires 10^{-4} Watts or more to be coupled to low temperature region. Depending on pump VSWR matching, may have 5 to 20db of range available for oscillation using 10mW Klystron source. Significant influence on sensitivity to pump power and frequency.	Substantial instability. Variability of amplitude of typical microwave sources is 10^{-2} to 10^{-4} db. Essentially impossible to regulate power actually applied to ruby due to variations in thermal profile of feed waveguide. Sensitivity is 0 to 10^{-11}/db.
Pump Frequency	$\approx$20MHz variation allowed about optimum frequency of 13.15 GHz. Important influence on sensitivity of operational frequency to pump power.	No problems in principle due to ability to "bootstrap" pump stability from SCM stability. No significant problems in practice with quartz crystal-stabilized klystron source.
Signal Coupling	Influences fractional output power and signal VSWR sensitivity. Also (incidentally) an important tool for adjustment of pump VSWR.	Possible source of drift due to varying temperature profile with helium level. Magnitude *not* known.
Signal VSWR	No significant function	Substantial burden placed on stability of room temperature signal connections. Maximum variability is $\approx 10^{-10}$. The fix for this is addition of a low-temperature isolator.

Technical

In this section the dependence of frequency on temperature, and on pump power and frequency are discussed in more detail. Additionally, the discovery of sensitivity of the output frequency to thermal gradient across the 3–cavity system has given rise to a new thermal regulation system. A block diagram of this system (Fig. 1b) and improved frequency stability results (Fig 5) are presented.

Temperature Dependence

Figure 3 shows a plot of the temperature dependence of the output frequency for the SCM over the temperature range between 1 and 2 Kelvins. From a functional point of view, the presence of a frequency maximum at about 1.57 Kelvin is an extremely desirable feature since it allows operation of the oscillator in a region of nominally zero temperature coefficient. The quadratic coefficient in δf/f at the maximum is $3.3 \cdot 10^{-9}$/Kelvin^2. This means that a temperature accuracy of one milliKelvin together with a stability of 30 microKelvins would allow a frequency stability of $\frac{\delta f}{f} = 2 \cdot 10^{-16}$.

An additional advantage of this mode of operation is the ease of refrigeration at a temperature of 1.57K in comparison to our initial design temperature of 0.9K. New options for refrigeration are also available. For example, operation at 1.57K allows the use of a continuous–flow helium cryostat rather than the batch-mode system required at the lower temperature.

The negative temperature coefficient exhibited by the data in Figure 3 at the higher temperatures is easy to understand, and had been anticipated in the design of the SCM. It is due to a combination of thermal expansion and superconducting penetration depth effects, both of which show a negative slope. However, both of these effects were expected to "freeze out" at the lowest temperatures–hence our (previous) 0.9 Kelvin operating temperature. The contribution with positive slope at the lower temperatures has been observed previously but its nature and cause had not been identified, nor had its consequence, the maximum with temperature, been discovered.

Measurements of the effect on the operating frequency of a temperature gradient across the oscillator now point to the ruby resonator as a likely candidate for the positive slope. The sign of the thermal gradient effect is consistent with this identification. In addition, the magnitude agrees with the measured slopes of low– and high–temperature parts combined with a rough estimate of the thermal conductivity of the coupling resonator. A positive temperature coefficient would result from the demagnetization field due to the changing alignment of chromium spins in the ruby. While the ruby resonator seems a likely candidate, the effect has not been positively identified.

Pump Power and Frequency

Figure 4 shows a plot based on measurements of the SCM output frequency dependence on pump power and frequency. Pump amplitude is shown in terms of the attenuation inserted in the pump waveguide. Due to vagaries of the plotting routine, attenuation was divided by a factor of 1000 before plotting. The discrete nature of the data is discernable in (e.g.) the ripples at the bottom of the valley in the center of the figure.

Since the pump power is very much more difficult to stabilize than its frequency, the major feature of the plot shown is the valley down the middle where the sensitivity to pump power is greatly reduced. In this region the slope is typically $\leq 2 \cdot 10^{-13}$/db, a value 100 times smaller than on the outside slopes. A second feature is the saturation at higher power, where the frequency changes less rapidly. These features are somewhat variable, with an extremum at low power also sometimes observed. Associated with pump frequencies showing the rapid variation of frequency with amplitude is also a pronounced limiting effect, where the oscillation amplitude shows a somewhat soft "clipping" effect. Because of the variability between subsequent reworks of the oscillator assembly, it seems likely that this interaction is

not fundamental to either the ruby maser or to the high-Q resonator but may be due to an interaction between pump and oscillation frequencies at a demountable joint in the coupling resonator.

Modification and Test

The right hand side of Figure 1 shows a block diagram showing the modified refrigeration and thermal regulation system. Where the old helium tank was located below the oscillator and attached at its lower extremity, the continuous flow cooler is now mounted above the oscillator in order to intercept the varying heat flow from above. Compensation for these variations is now accomplished by means of a heater placed above the refrigerator, so that no thermal gradients are generated below the heater itself. Variations in cooling power in the refrigerator are also compensated by this heater with no resultant gradients below the refrigerator. Except for incidental electrical leads associated with the thermometry, the only thermal contact to the oscillator takes place at one point, the top, and so thermal gradients should be effectively eliminated.

Stability results obtained with the modified oscillator are shown in Figure 6. Again, little information can be discerned regarding the short term stability, except that it is better than that of the best available reference, the hydrogen maser. Long term stability, however has been significantly improved by the modifications, with results in the mid-10^{-15} range obtained for times longer than 30 seconds.

Conclusions

A detailed study of the operating parameters of the superconducting cavity maser has disclosed regions of operation for the various parameters which are substantially more advantageous than previously found. On the basis of this study the cryogenics of the oscillator were modified to optimize operation at a new operating temperature and to eliminate thermal gradients. Stability results for the modified SCM show substantially improved long-term stability compared to previous results. Results for shorter measuring times continue to be better than can be measured using the best reference presently available.

With the addition of the continuous flow refrigerator, it may now be possible to incorporate a closed-cycle refrigerator and so eliminate all need of disposable cryogens. Commercial coolers are available that could provide the needed 20 milliwatt helium flow presently used. Such a cooler would reduce the overall size by eliminating the need for a the large helium reservoir. Possible performance degradation due to mechanical motion in the cooler would need to be examined experimentally.

Acknowledgements

Special thanks to Bill Diener for his assistance in ultrastable measurements, Roland Taylor for easy access to the capabilities of the Test Facility, Chuck Greenhall for software enhancements meeting our special requirements and Tom Tucker, for assistance and support with hydrogen maser measurements.

References

[1] S. Thakoor, D. M. Strayer, G. J. Dick and J. E. Mercereau, "A Lead-on-Sapphire Superconducting Cavity of Superior Quality," *J. Appl. Phys.*, **59**, 854 (1986).

[2] G. J. Dick and D. M. Strayer, "Development of the Superconducting Cavity Maser as a Stable Frequency Source," in *Proceedings of the 38th Annual Frequency Control Symposium*, 414 (1984).

[3] D. M. Strayer and G. J. Dick, "The Superconducting Cavity Maser Oscillator – Toward Higher Stability," in *Proceedings of the 18th Annual Precise Time and Time interval (PTTI) Planning and Applications Meeting,* 601 (1986).

[4] S. R. Stein and J. P. Turneaure, in *Proceedings of the 27th Annual Frequency Control Symposium,* 414 (1975).

[5] V. I. Panov and P. R. Stankov, "Stabilization of Oscillators with High-Q Leucosapphire Dielectric Resonators," *Radiotechnika i Electronika,* **31**, 213 (1986).

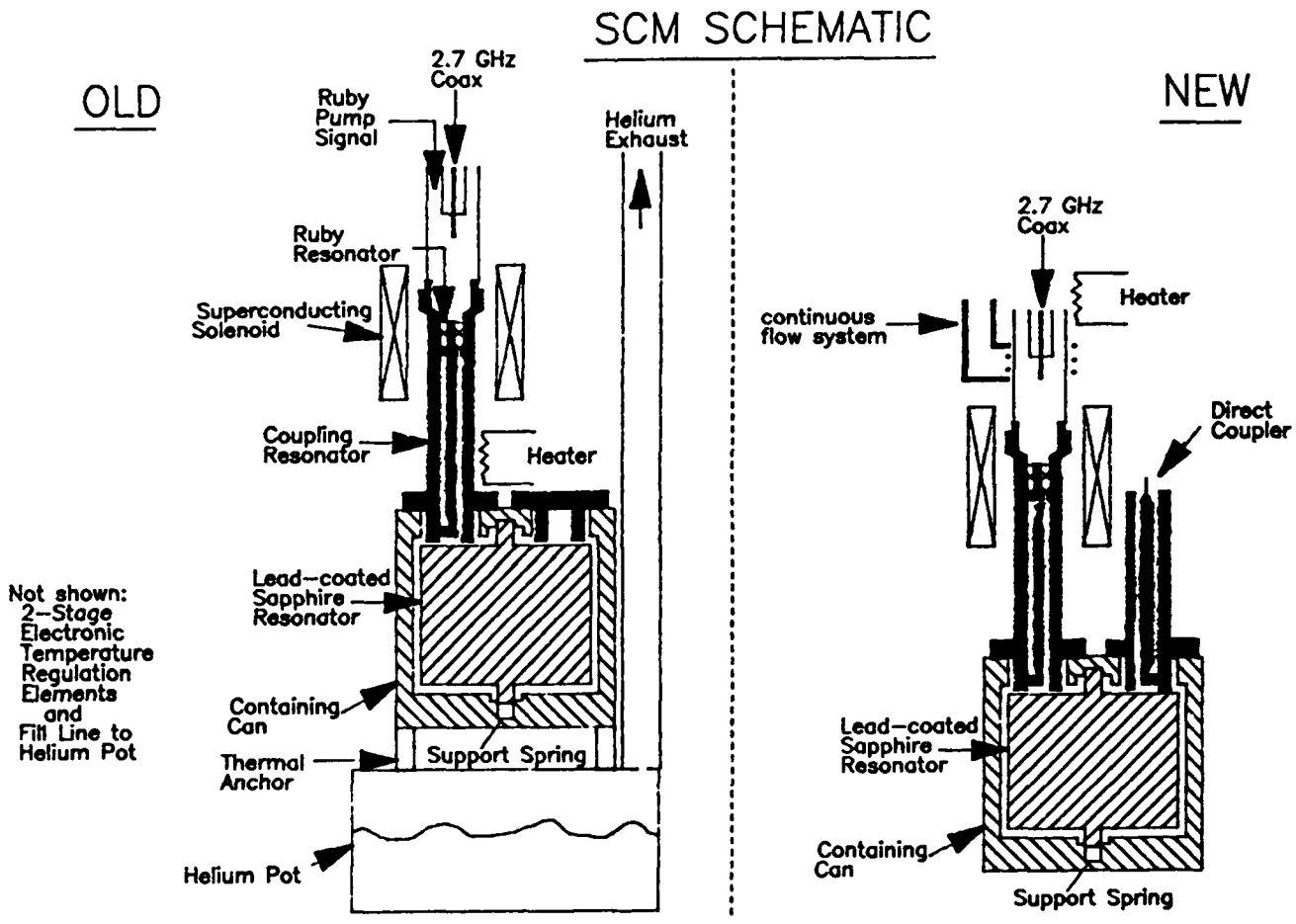

Figure 1. Schematic diagram of SCM oscillator. Original configuration is shown at left and the modified oscillator at right. Modifications prevent regulating heat flow from flowing through oscillator itself. Direct coupler was not implemented for any data presented in this paper.

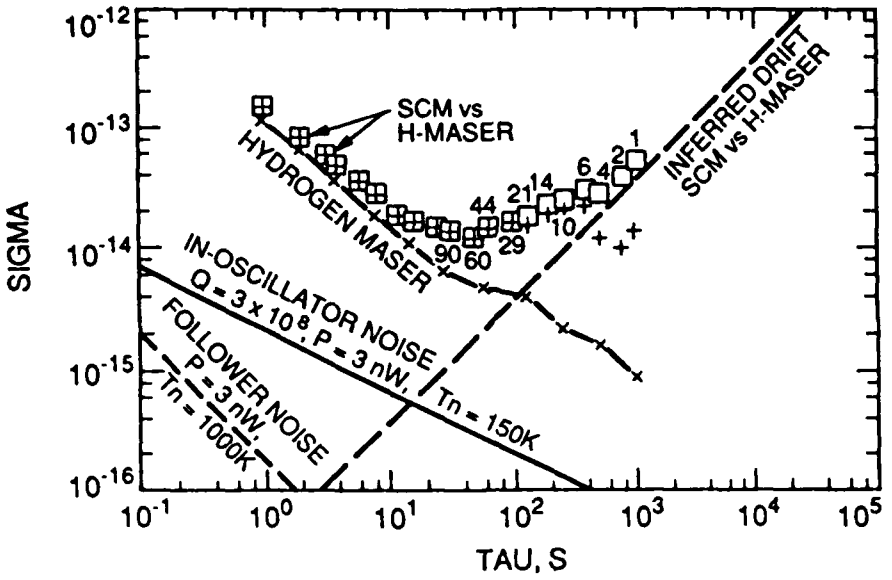

Figure 2. Allan Variance of stability of Superconducting Cavity Maser in first tests with Hydrogen Maser reference oscillator. Points marked + show data with drift removed; data (squares) are accompanied by number of samples. Also shown are measured Hydrogen Maser stability and the calculated effect of in–oscillator and added noise based on measured operating conditions and an assumed in–oscillator noise temperature of 150 Kelvin.

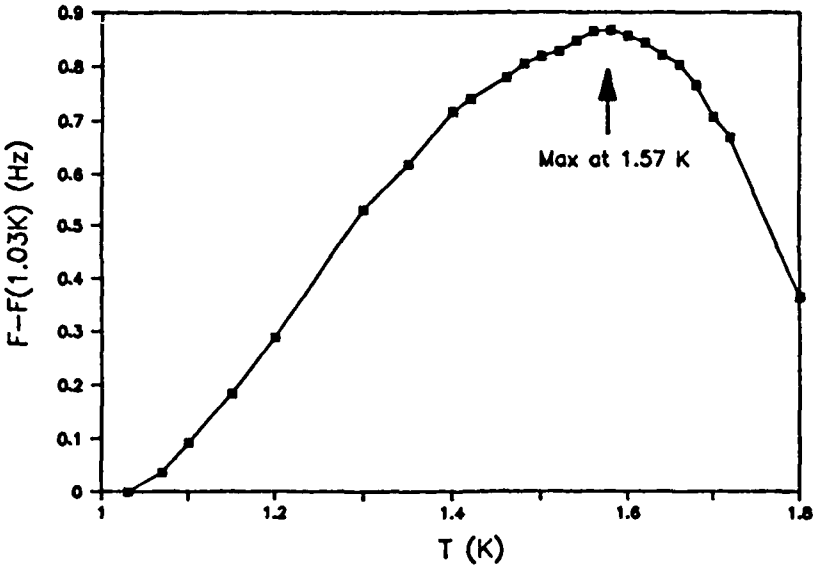

Figure 3. Measured frequency vs Temperature plot for range 1 – 1.8 Kelvin. 0.9 Hz frequency variation is referred to ≈ 2.69 GHz reference.

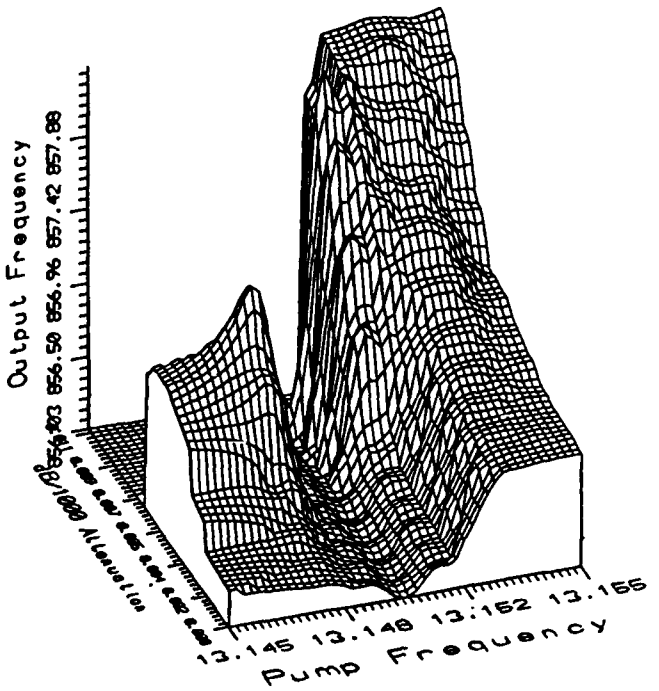

Figure 4. Three–dimensional plot showing dependence of output frequency on Pump frequency and power. Output frequency is referred to ≈ 2.69 GHz reference. Pump power is indicated by attenuation value. Due to vagaries of plotting routine, 0–11 db attenuation range is plotted as db/1000. Pump Frequency is measured in GHz.

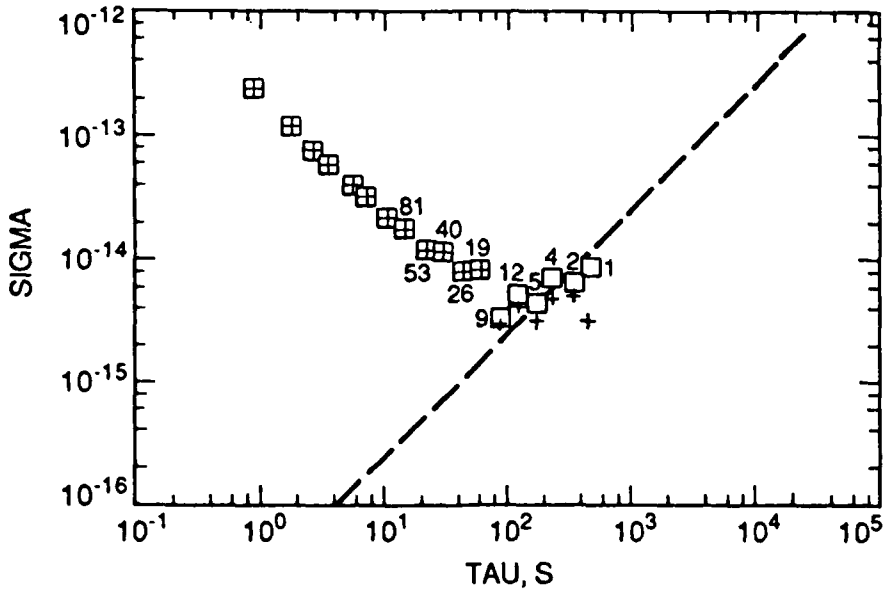

Figure 5. Plot of Allan Variance of SCM stability after modifications, H–Maser reference.

AN AUTOMATIC MEASUREMENT SYSTEM FOR RF PULSE STABILITY PARAMETERS

Liu Xiaofan and Mao Ruida
Beijing Institute of Radio Metrology & Measurements
P.O.Box 3930. Beijing, P.R.China

ABSTRACT

This paper describes a new automatic system for measurement of transmitter stability parameters, esp. the frequency stability of RF pules series, which can limit the performance of variours coherent pulse radars.The practicability to characterize the stability of RF pulse series with interpulse variance in time domain and near–carrier phase noise in frequency domain is studied in the paper. The operation principle, system construction and calibration methods of quadrature dual channel frequency and phase discrimination system for the measurement of interpulse variance are discussed here. This system is effectively used in the measurement of stability of radar transmitters.

INTRODUCTION

The phase parameter is used to transfer information in most modern radar systems. Thus there are more and more requirements on high frequency stability and low phase noise. It becomes more important how to characterize and measure the stability of radar transmitters. Most of radar transmitters,however, do not use continuous wave (CW) but pulse–modulated wave,whose stability determines the general performance of radar systems. There is still no unanimous method in characterization of the carrier frequency stability on pulsed wave. And the measurement technique is much more difficult for pulsed wave than for CW. Therefor, some radar parameters, for example, improvement factor or visibility, are usually used to evaluate the stability of radar system, which is measured by self–check method.

The study on the frequency stability of pulse modulated wave started in 1960's. The microwave phase bridge was used to measure the additive phase noise of pulsed power amplifiers in microwave frequencies with high sensitivity[1] and is still used to measure the additive noise in amplifier transmitters. While the microwave frequency discrimination bridge is frequently used in measurement of oscillator transmitters, with microwave cavity[2][3] or delayer[4][5] as frequency discriminators. After 1970's, computers are used for data processing in these systems[6]. A special equipment, which can measure transmitter stability parameters, such as frequency, phase, timing,pulsewidth and amplitude fluctuations, was developed by Milan afterward[7]. Beijing Institute of Radio Metrology and Measurements also works in this field.[8][9]

The measurement system raised in this paper still uses microwave phase bridge to measure interpulse phase fluctuation in amplifiers. The frequency stability of oscillation transmitters can be measured by IF quadrature dual channel technics. One of them is quadrature dual channel phase discrimination system, which can measure frequency / phase fluctuation automatically with fast sampler and digital convolution unit. A quick agile frequency synthesizer is developed to overcome the influence of frequency shift and realize the automatical frequency tracking. At the same time, another new way, named quadrature dual channel frequency discrimination bridge , has been developed in our laboratory. It is proved that the method combines the advantages of microwave frequency discrimination bridge and I.Q. branch technic in measuring the stability of RF pulses. Besides, other interpulse fluctuations of the parameters, such as amplitude, timing, and pulsewidth, can also be measured in this system.

In this paper the interpulse variance is raised to characterize the frequency stability of RF. pulses in time domain. The video signals are acquisited at high speed through A / D converter and DMA unit and fed into the computer for data processing. The measurement results of interpulse variance are given by the statistic treatment, and FFT is used to analyze the spectrum, which can be evaluated as the near carrier phase noise.

CHARACTERIZATION FOR FREQUENCY STABILITY OF RF PULSE SERIES

A variety of radars has a basic requirement on the frequency stability of their transmitters. The performance of Moving Target Indicator (MTI) radar can be defined by Improvement Factor(I), which is written:

$$I = \frac{\bar{S}_0}{S_i} CA$$

where CA = Clutter attenuation
S_i = Input signal
$\bar{S}_0$ = Output sigual averaged over all target velocities

Any instability in radar transmitter can limit the Improvement Factor of MTI System. Because the radar signal will be cancelled between adjacent pulses to indicate the moving target signal submerged in clutter,the interpulse fluctuation of various parameters are vitally important. The relations between improvement factor limitations and interpulse fluctuations are listed as follows:

$$I_A = 20lg\frac{A}{\Delta A}; \qquad I_\varphi = 20lg\frac{\pi}{2\Delta\varphi}; \qquad I_f = 20lg\frac{1}{4\tau\Delta f}$$

$$I_t = 20lg\frac{\tau}{\sqrt{2}\,\Delta t} \qquad I_\tau = 20lg\frac{\tau}{\Delta\tau}$$

where A and τ are the amplitude and pulsewidth of RF pulses, and $\Delta A, \Delta\varphi, \Delta f, \Delta t$ and $\Delta\tau$ are respectively amplitude, phase, frequency, timing and pulsewidth fluctuations of RF pulses. The results are similar to that deduced seperately by Skolnik[10] and Milan.

The interpulse instability in oscillators is reflected by frequency fluctuation mainly, while in amplifiers, that is reflected by phase fluctuation. The total improvement factor limitation is the combination, which can be written:

$$I_T = \frac{1}{\frac{1}{I_1} + \frac{1}{I_2} + \cdots + \frac{1}{I_N}}$$

The visibility of Pulse Doppler Radar is determined by near–carrier phase noise of the transmitting signal. In order that the echo, which includes Doppler frequency shift f_d, will not be submerged by phase noise, the phase noise must be

$$S_\varphi(f_d) \leqslant V(f_d) - 10dB$$

It can be seen that it is possible to have a integrate characterization for the frequency stability of RF pulse series in radar transmitters.

The proper method is: using interpulse variance as the characterization for the frequency stability of RF pulse series in time domain, and near–carrier phase noise as that in frequency domain.

The interpulse variance is determined with the average square value of avereged frequencies in two adjacent pulses, as

$$\sigma^2 = \langle(\bar{F}_1 - \bar{F}_2)^2\rangle$$

This expression is coincident with the first difference variance or cancellation of MTI radar. While, the near–carrier phase noise means the phase noise power spectrum density whose difference frequencies to the carrier are no larger than one half of the repeat frequency(i.e.$f_m \leqslant \frac{f_r}{2}$) in sampling function frequency spectrum of RF pulse series.

When sampling the output video signal at the rate of the pulse repeat frequency, the obtained data is a separate time series:

$$\Delta f(t_i) = \Delta f(t)|_{t=iT+T_0} \qquad i = 1,2,\cdots N$$

where N is sampling number, T is pulse repeat period, $T_0$is synchronization delay.

After FFT transformation, this series is transformed into a frequency or phase series in frequency domain:

$$\Delta f(f_{mi}) = \Delta f(f_m)|_{f_m = i\frac{1}{2NT}} \qquad i = 1,2,\cdots$$

$$\varphi(f_{mi}) = \left.\frac{\Delta f(f_m)}{f_m}\right|_{f_m = i\frac{1}{2NT}}$$

The expression of interpulse frequency variance is

$$\sigma_f^2 = \frac{1}{N-1}\sum_{i=1}^{N-1}[\Delta f(t_{i+1}) - \Delta f(t_i)]^2$$

The power spectrum density of near-carrier phase noise is

$$S_\varphi(f_{mi}) = 20lg\frac{\varphi(f_{mi})}{\sqrt{\Delta B}}\frac{\tau}{T} \qquad (dB/Hz)$$

In the formula, $\Delta B = \frac{1}{2NT}$ is the sampling interval in frequency domain.

Above all, this characterization method has three advantages:

(1) It can characterize directly the performance of radars.

(2) It is similar to the method for continous wave[11] so that some measurement technique for CW can still be applicable.[12]

(3) It is convenient to make data processing by computer.

SYSTEM CONSTRUCTION AND OPERATION PRINCIPLE

Fig. 1 is the general block diagram of the measurement system. The subsystems to measure frequency, phase and amplitude are seperated. These subsystems are connected to the same A / D sampler and data processing unit with an IBM-PC computer. The timing and pulsewidth are measured by a counter with analogue interpolation and transfered to computer through digital interface.

1. Quadrature Dual Channel Phase Discrimination

Quadrature dual-channel phase discrimination is a method to measure interpulse frequency stability, as shown in Fig.2. The radio pulsed signal from transmitter is transformed twice to the fixed frequencies(300MHz,30MHz) in order to broad the frequency range. I.Q. quadrature video outputs are obtained by quadrature dual-channel discrimination of the 30MHz pulsed signal.

The first local oscillator is a broad width and low noise frequency synthesizer. The second LO is a fast agile frequency synthesizer developed in our lab [13]. The frequency change is controlled digitally in step of 1MHz, 100kHz, and 10kHz. The change time is within 10μs. Thus the automatic frequency control (AFC) is realized.

The quadrature video signals are converted with 12-bit fast A / D to two finite series $e_t(l)$ and $e_t'(l)$ in two adjacent pulses. The convolution of these two signal is expressed as:

$$Y(K) = e_t(l) * e_t'(l) = \sum_{l=0}^{K} e_t(l)e_t'(K-l)$$

Suppose the pulse is rectangular wave and sampled at the rate of Δt, Y(K) is an ideal triangle whose baseline is 2N-1 and the peak value appears at K = N-1. After nomalization:

$$D_I = 2\sum_{l=1}^{\frac{1}{2}N-1} \cos l\omega\Delta t$$

$$D_Q = -2\sum_{l=1}^{\frac{1}{2}N-1} \sin l\Delta\omega\Delta t$$

Then we can get frequency discrimination curves of D_I, D_Q. The following can be done accordiog to these curves.

(1) interpulse frequency fluctuation measurement from $D_Q$feature.

(2) automatic frequency control to compensate the radio frequency shift.

(3) measurement of interpulse amplitude and phase fluctuations.

(4)fast spectrum estimation of signal.

2. Quadrature Dual Channel Frequency discrimination

Fig.3 is the basic block diagram of the quadrature dual-channel frequency discrimination system [14]. At first the radio frequency is mixed down to an intermediate frequency, which still remains all the original phase and amplitude information of the transmitters. Then the measurement is made by the IF quadrature dual channel frequency discrimination bridge with a delayer as the frequency discriminator. It can be deduced that the output signals are:

$$A_s(t) = rect(\frac{t}{\tau}).A\sin(\Phi(t) - \Phi(t-\tau_0))$$

$$A_c(t) = rect(\frac{t}{\tau}).A\cos(\Phi(t) - \Phi(t-\tau_0))$$

where: $rect(\frac{t}{\tau}) = \begin{cases} 1 & NT < t < NT + \tau \\ 0 & other\ time \end{cases}$ $\quad N = 0,1,2,\cdots\cdots$

A: the signal amplitude.

$\Phi(t)$: random phase fluctuation of transmitter signal.

τ_0 :the delay time of IF dlayer

T and τ: repeat period and pulsewidth of the RF pulse.

The average frequency fluctuation in the interval between $t-\tau_0$and t is:

$$\Delta f = \frac{1}{2\pi\tau_0}\int_{t-\tau_0}^{t}\Phi'(t)dt = \frac{1}{2\pi\tau_0}[\Phi(t) - \Phi(t-\tau_0)]$$

Combining the Taylor progressions of $Sin\Delta\Phi$, and $tg\Delta\Phi$,we can express $\Delta\Phi$ and Δf with $A_s(t)$ and $A_c(t)$ as follows:

$$\Delta\Phi = \frac{2}{3}[\frac{A_s(t)}{A} + \frac{1}{2}\frac{A_s(t)}{A_c(t)}]$$

$$\Delta f = \frac{A_s(t)}{3\pi\tau_0}[\frac{1}{A} + \frac{1}{2A_c(t)}]$$

In this case, the nonlinear errors are less than 0.8% in the range $\Delta\Phi \leqq 1.8$ rad. Using the mathmatical method for data processing, very big frequency fluctuations can be measured. However, only when $\Delta\Phi$ is much smaller than 1 rad, can $\sin\Delta\Phi$ be approximately expressed by $\Delta\Phi$. The transfer function of the system is shown in Fig.4

In short, the quadrature dual-channel frequency discrimination method has the following characteristics.

(1) The system can be operated in a large frequency range and measure the stability of RF pulses with a high sensitivity.

(2) The zero-beat discrimination can be easily realized without the coherent oscillator and the influence of amplitude fluctuation and frequency shift of RF pulses on the measurement can be removed by the system.

(3) With the self-convolution of the system's output signals, we can obtain a function of intrapulse phase fluctuation with the items t, as well as t^2 and t^3, which are useful for the pulse compressibility radars.

3. Microwave Phase Bridge

The microwave phase bridge is used to measure the additive phase noise of the transmitters with amplifier chains. In our system, the reference signal of the phase bridge is a RF pulse series synchronized with the measured amplifiers. Thus the noise of phase discriminator can be reduced. Low-pass filter is used to filter out the pulse side-band in video signal. Therefore, the sensitivity has been increased in the measurement of phase noise by spectrum analyzer.

The sensitivity in Fourier frequency $f_m = 1kHz$ is better than $-120dB/Hz$. The block diagram is shown in Fig.5.

4.Amplitude Measurement

Quadrature dual–channel systems can be used to measure interpulse amplitude fluctuation. The sensitivity is not high, because of the limitation on dynamic range of the video amplifier and A / D converter. The differential amplifier is used to amplify the fluctuation at the pluse tops, the $\Delta A / A$ measurement resolution is up to 0.1% as shown in Fig.6.

5.Time Interval Measurement

The time interval measurement on interpulse timing and pulsewidth is accomplished by a counting unit with analogue interpolation. The resolution in single measurement is 0.1ns with precision of 1ns. The block diagram is shown in Fig.7.

SYSTEM CALIBRATION AND MEASUREMENT RESULTS

1.System Calibration Methods

The measurement system is calibrated with two methods so as to measure the phase and frequency stabilities accurately.

(1)Frequency Modulation Method

The principle of the frequency modulation method is shown in Fig.8. The modulation frequency of the oscillator is doubled and reshaped to drive a PIN pulse modulator. Then we can obtain a RF series whose frequency offset is changed alternately. The system is calibrated with this known frequency offset. And the calibration accuracy is just the same as the oscillator itself.

(2)Phase Modulation Method

Fig.9 is the principle diagram of phase modulator set up with varactor diode used in the microwave phase bridge. The phase modulation linearity is better than ± 1dB.

2.Measurement Results

Measurements with the system were made on various radar transmitters. We have worked in the experiments on the stability measurements as follow:

(1) The system has been calibrated with the phase or frequency modulation methods.

(2) The types of MTI radar transmitters with magnetron oscillators, whose operation wavelenth were 30cm, 10cm and 5cm, pulsewidth is 0.5–10μs and repeat frequency is 500Hz–10KHz , were measured with the quadrature dual–channel discrimination system. The system measurement resolution for interpulse frequency stability is 100Hz with accuracy 1kHz. The improvement factor of MTI radar can be measured up to 60 dB.

(3) The phase noise of the transmitters with travelling–wave tube (TWT)amplifers and the coherent responders at 10cm and 5cm were measured by phase bridge, the sensitivity of which is better than −120dB / Hz.

CONCLUSIONS

As stated above , we have come to the conclusions as follows:

1. The frequency stability of RF pulse series can be charaterized with the interpulse variance in time domain, and with the near–carrier phase noise in frequency domain.

2. Quadrature dual–channel frequency and phase discimination methods are effective for the measurement of interpulse frequency stability.

3. We have made successful measurements with the system designed with the above techniques.

REFERENCES

[1] K.H. Sann, "The Measurement of Near–Carrier Noise in Microwave Amplifiers" IEEE Trans. on MTT, Vol. MTT–16, Sept. 1968 pp 761–766

[2] J.R.Ashcley, et al, "The measurement of Oscillator Noise at Microwave frequencies" IEEE Trans. on MTT, Vol. MTT–16, No.9 Sept. 1968. pp753–760

[3] J. G. Ondria, "A Microwave System for Measurement of AM and FM Noise Spectra" IEEE Trans. on MTT, Vol. MTT–16 No.9 sept. 1968 pp 753–760

[4] A. Lance et al, " Phase Noise Measurement in the Frequency Domain" 1977 IEEE–S Interna-

tional Microwave Symposium Digest

[5] " Optimum Length Transmission Line Discriminator with Low Noise Detector" United States Patent No. 4, 002, 970 Jan . 11, 1977

[6] J.R. Asheley et al, "The measurement of Noise in Microwave transmitters" IEEE Trans. on MTT, Vol. MTT-25 No. 4 April 1977 . p294

[7] John M.Milan " Test set for the measurement of Transmitter Stability Parameters" Proc. 29th Annual Frequency Control Symposium, 1975. pp270-284

[8] Liu Xiaofan, " The Measurement of Near-Carrier Noise on RF Pulse Serise" Journal of Astronautic Metrology and measurement No.3, 1984. pp41-49

[9] Tang Shensheng, " The Development of a Radar Digital Stability Test Set " Journal of Astronautic Metrology and Measurement, No.3 1988 pp16-24

[10] M.J. Skonic, " Radar Handbook " Chapter 17, 1970

[11] J. Rutman, " Characterization of phase and Frequency Instabilities in Precision Frequency Sources: Fifteen Years of Progress " PIEEE 1978, Vol. 66 No.9 Sept. 1978 pp1048-1075

[12] C.H.Grauling and D.J.Healey, " Intrumentation for Measurement of Short-term Frequency Stability of Microwave Sources " Proc. IEEE. Vol. 54. No.2 Feb . 1966, pp249-257

[13] Zhou Liren, " A 330 MHz Low Noise Frequency-Agile Synthesizer" Journal of Astronautic Metrology and Measurement, No.1, 1988 pp17-25

[14] Liu Zhongying, "A New Method for Measuring the Stability of RF Pulse Series " Journal of Astronautic Metrology and Measurement, No.3.1988 pp29-35

[15] A.L. Gardner and R.S. Hawke, " High Speed Microwave Phase Shifers Varactor Diodes" The Review of Scientific Instruments , No.1, Jan. 1966, pp19-22

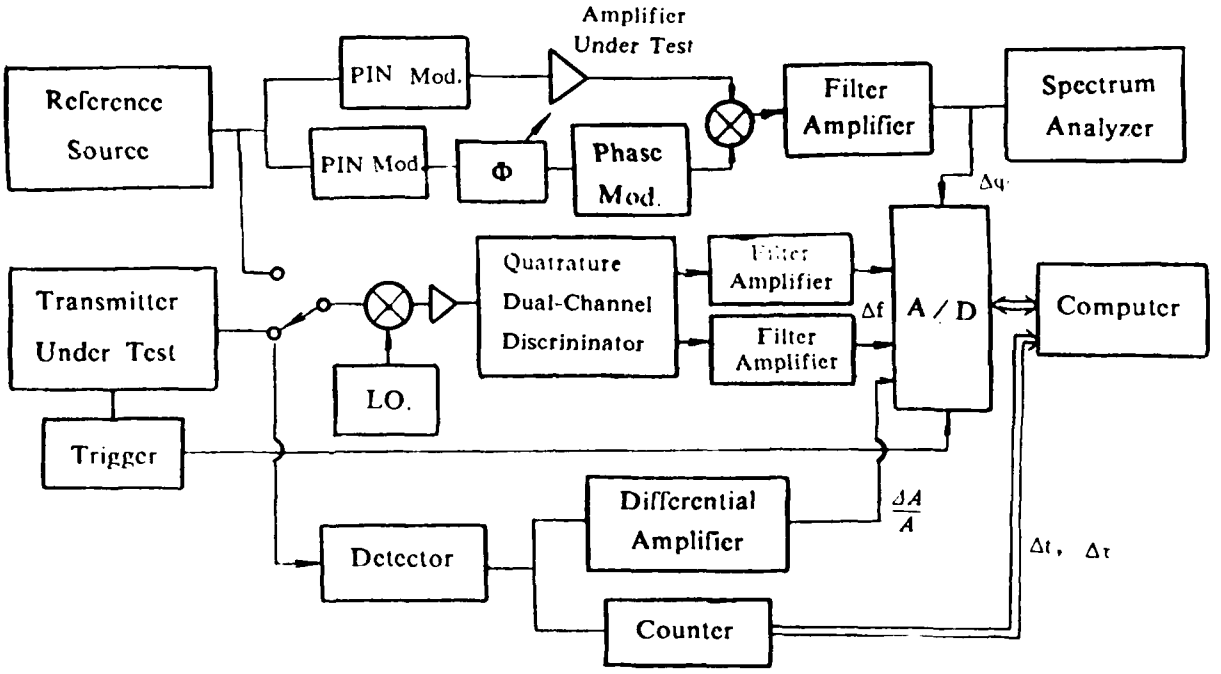

Figure 1. General Measurement System Block Diagram

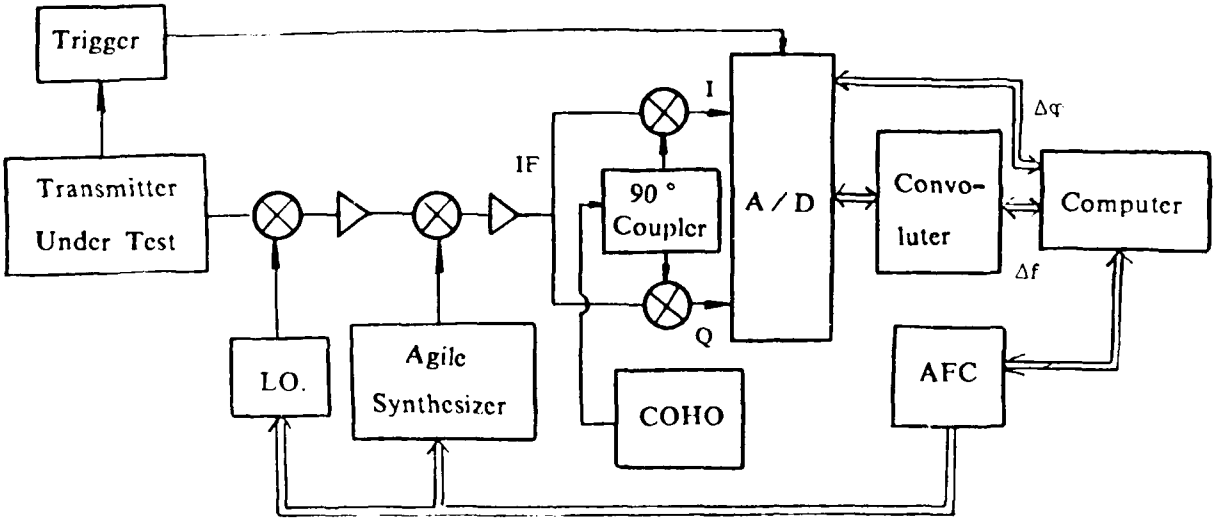

Figure 2. Quatrature Dual Channel Phase Discrinination System Block Diagram

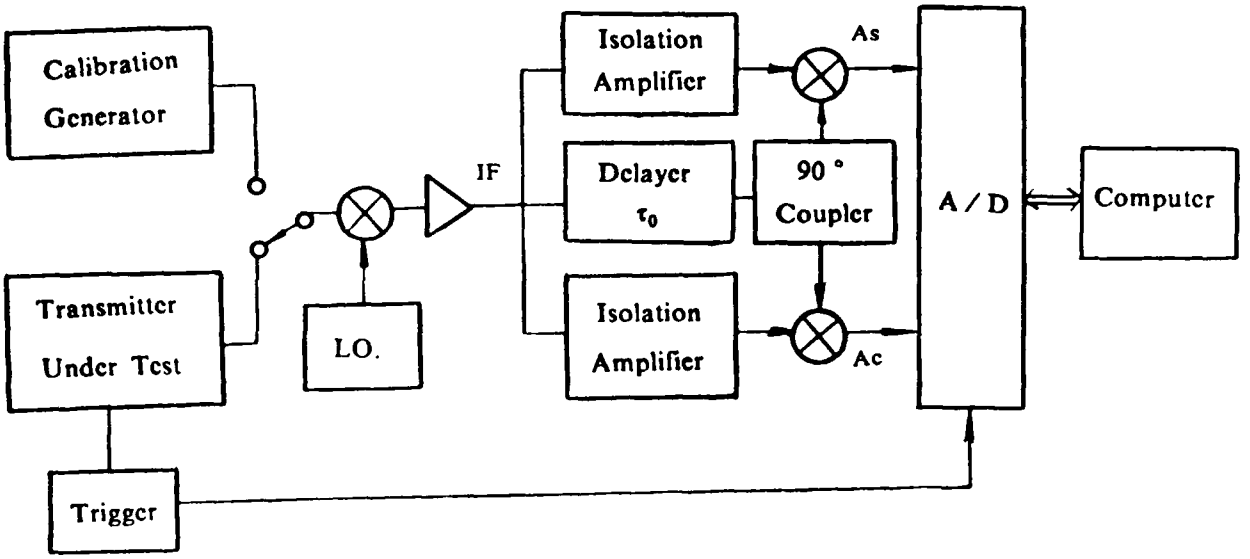

Figure 3. Quatrature Dual Channel Frequency Discrimination System Block Diagram

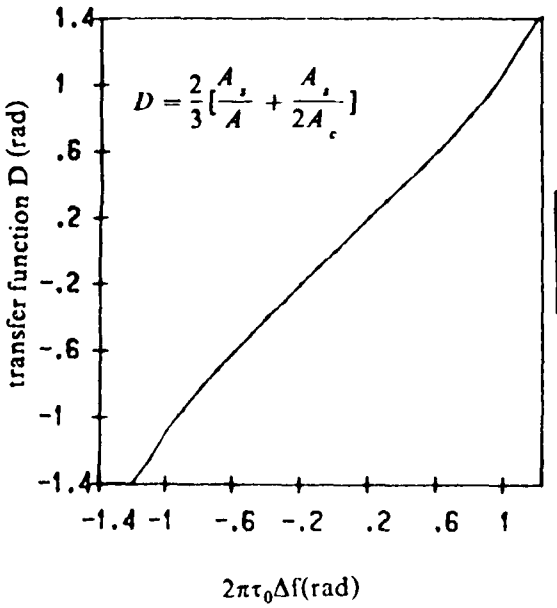

Figure 4. Transfer Function of Frequency Discriminator

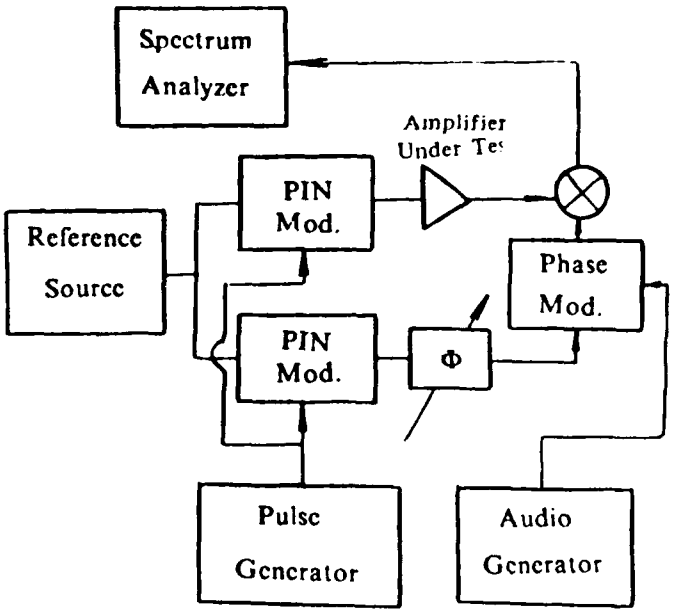

Figure 5. Microwave Phase Bridge Block Diagram

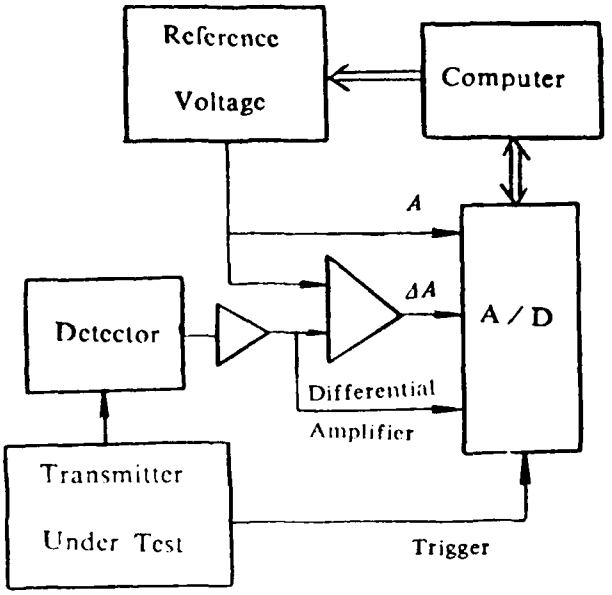

Figure 6. Amplitude Fluctuation Measurement Block Diagram

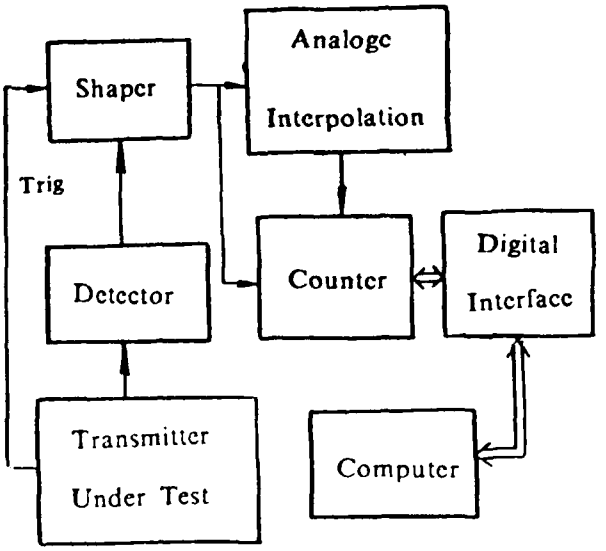

Figure 7. Time Interval Measurement Block Diagram

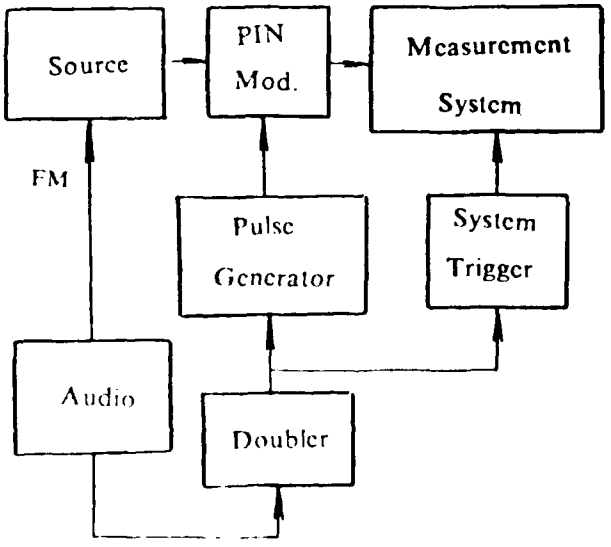

Figure 8. FM Calibration Block Diagram

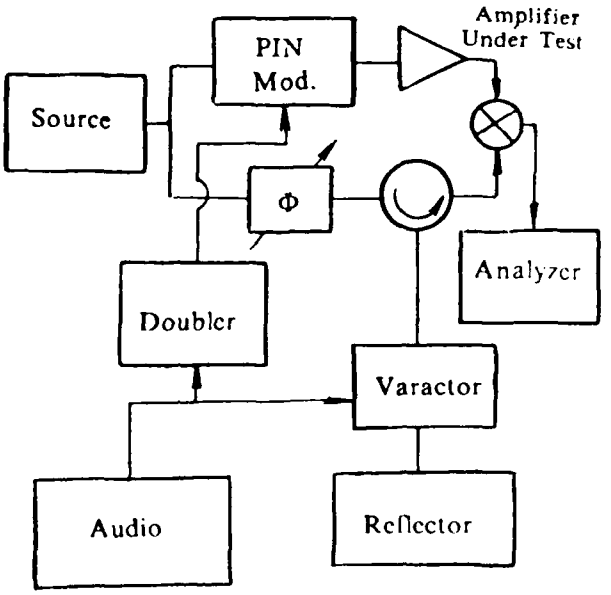

Figure 9. PM Calibration Block Diagram

1988 PTTI CONFERENCE
ATTENDEES LIST

Jay E. Albrecht
PMTC
Code 3421.3
Point Mugu, CA 93042
805-989-8180

David W. Allan
National Institute of Standards and Technology
Time and Frequency Division
325 Broadway
Boulder, CO 80303
303-497-5637

Carroll O. Alley
University of Maryland
Department of Physics and Astronomy
College Park, MD 20742
301-454-3405

James A. Barnes
Austron, Inc.
3772 Lakebriar Drive
Boulder, CO 80301

Thomas R. Bartholomew
TASC
1190 Winterson Road
Linthicum, MD 21090
301-850-0070

Shelby D. Bass
Bass Associates, Inc.
P.O. Box 20788
Sarasota, FL 23431
813-922-9538

Andrew P. Baugh
Pan Am World Services
P.O. Box 1413
APO San Francisco, CA 96555
805-238-7994

Eugene E. Baumert
Planning Research Corporation
2862 South Circle Drive
Colorado Springs, CO 80906
719-540-0700

Francoise S. Baumont
OCA/CERGA
Avenue Nicolas Copernic
Grasse, France 06130
33. 93 365849

Ronald L. Beard
Naval Research Laboratory
4555 Overlook Avenue Southwest
Washington, D.C. 20375-5000
202-767-2595

Roger E. Beehler
National Institute of Standards and Technology
325 Broadway
Boulder, CO 80303
303-497-3281

Jeffrey S. Bergdahl
SPAWAR
9533 Poplar Leaf Court
Fairfax, VA 22031
703-352-3515

Edward J. Besecky
Defense Mapping Agency
6500 Brookes Lane
Washington, D.C. 20315-0030
202-227-3175

Stephen M. Bloor
7929 Barnhill Circle
Severn, MD 21144
301-551-2799

Lt. Sheldon B. Blue
U.S. Coast Guard Electronics
Engineering Center
P.O. Box 60
Wildwood, NJ 08260-0060
609-727-8955

Edwin A. Bondurant
MCI
12369 Sunrise Valley Drive
Reston, VA 22101
703-648-8220

Patrick T. Boyle
Computer Sciences Corporation
Edwards Air Force Base
P.O. Box 325
Pinion Hills, CA 92372
619-868-3779

Lee A. Breakiron
U.S. Naval Observatory
Time Service Department
34th and Massachusetts Avenue, N.W.
Washington, D.C. 20395-5100
202-653-1888

Archie W. Brown
Bendix Field Engineering Corporation
One Bendix Road
Columbia, MD 21045
301-964-7570

Eric A. Brown
IBM
9231 Corporate Boulevard
Rockville, MD 20850
301-640-3127

Edward E. Burkhardt
Burkhardt Monitoring Service
P.O. Box 1411
Glen Allen, VA 23060
804-266-9065

Edgar W. Butterline
AT&T Network Operations Group
Routes 202 and 206 North
Bedminster, NJ 07921
201-234-4545

Paul W. Casper
Atmospheric Research Systems, Inc.
2350 Commerce Park Drive N.E., Suite 3
Palm Bay, FL 32905
407-725-8001

David N. Chalmers
U.S. Naval Observatory
Time Service Department
34th and Massachusetts Avenue, N.W.
Washington, D.C. 20392-5100
202-653-1412

Laura G. Charron
U.S. Naval Observatory
Time Service Department
34th and Massachusetts Avenue, N.W.
Washingon, D.C. 20392-5100
202-653-1529

Randolph T. Clarke
U.S. Naval Observatory
Time Service Department
34th and Massachusetts Avenue, N.W.
Washington, D.C. 20392-5100
202-653-1562

Walter E. Cote
Rome Air Development Center
1605 Gardner Street
Utica, NY 13501
315-730-3891

John C. Cuthbertson
Ball Corporation, Efratom Division
29 Beaumont Lane
Lake Grove, NY 11755
516-467-5616

Gerrit DeJong
Van Swinden Laboratory
P.O. Box 654
Delft, Netherlands 2600AR
(0)-15-620372

Patricia A. Delaere
Jet Propulsion Laboratory 298/100
4800 Oak Grove Drive
Pasadena, CA 91109
818-354-7055

Andrea DeMarchi
Universita' di Ancona
DIP. Elettronica
Via Brecce Bianche
Ancona, Italy 60131

Edoardo Detoma
SEPA SpA (FIAT)
Corso Giulio Cesare, 294
Torino, Italy 10154
(11) 205-3371, X-480

George J. Dick
Jet Propulsion Laboratory 298/100
4800 Oak Grove Drive
Pasadena, CA 91109
818-354-6393

Christina E. Dise
U.S. Naval Observatory
Time Service Department
34th and Massachusetts Avenue, N.W.
Washington, D.C. 20392-5100
202-653-1525

Christopher S. Duffy
CSR
Building 989
Patrick Air Force Base, FL 32925
407-494-2014

Chauncey P. Dunn
Computer Sciences Raytheon (CSR)
P.O. Box 4127, CSR 4500
Patrick Air Force Base, FL 32925
407-853-9057

Michael J. Ellett
Hughes Aircraft Corporation
1625 Redondo Avenue, Apt. 108
Long Beach, CA 90804
213-513-4210

Robert F. Ellis
Austron, Inc.
P.O. Box 14766
Austin, TX 78761-4766
512-251-2313

Barry Elson
Joint Tactical Command, Control and
Communications Agency
11440 Isaac Newton Square North, Suite 210
Reston, VA 22090-5006
703-487-8067

John W. Evans
Defense Communications Agency
1860 Wiehle Avenue
Reston, VA 22090
703-437-2598

Shiela C. Faulkner
U.S. Naval Observatory
Time Service Department
34th and Massachusetts Avenue, N.W.
Washington, D.C. 20392-5100
202-653-1460

Henry F. Fliegel
The Aerospace Corporation
2350 El Segundo Boulevard
El Segundo, CA 90245
213-336-1710

Robert P. Frueholz
The Aerospace Corporation
P.O. Box 92957
Los Angeles, CA 90009
213-336-6975

Jean C. Gaignebet
OCA/CERGA
Avenue Nicolas Copernic
Grasse, France 06130
33. 93365849

Michael Garvey
Frequency and Time Systems, Inc.
34 Tozer Road
Beverly, MA 01915
508-927-8220

Gary L. Geil
Datum, Inc.
1363 South State College Boulevard
Anaheim, CA 92806-5790
714-533-6333

Al Gifford
Naval Research Laboratory
Code 8321
4555 Overlook Avenue Southwest
Washington, D.C. 20375-5000
202-767-2595

William B. Golding
Naval Research Laboratory
Code 8320
4555 Overlook Avenue Southwest
Washington, D.C. 20375-5000
202-767-2595

Raymond L. Granata
National Aeronautics and Space
Administration - Goddard
Code 534.3
Greenbelt, MD 20783
301-286-7037

Larry V. Grant
U.S. Department of Transportation
RSPA
4317 Starr Jordan Drive
Annandale, VA 22003
202-366-4354

Albert E. Guevara
USAF 2 Satellite Control Squadron
2745 Frazier Lane
Colorado Springs, CO 80922
719-550-6377

Captain J. B. Hagen
U.S. Naval Observatory
34th and Massachusetts Avenue, N.W.
Washington, D.C. 20392-5100
202-653-1538

Robert Hamell
Jet Propulsion Laboratory 298 100
4800 Oak Grove Drive
Pasadena, CA 91109
818-354-4944

William P. Hanrahan
Bendix Field Engineering Corporation
One Bendix Road
Columbia, MD 21045
301-964-7749

Wayne Hanson
National Institute for Standards and
Technology
325 Broadway
Boulder, CO 80307
303-497-5233

Walter R. Harding
NAVELEX
P.O. Box 55
Portsmouth, VA 23705-0055
804-396-7992

Ilan Havered
Datum, Inc.
1363 South State College Boulevard
Anaheim, CA 92806-5790
714-533-6333

Helmut W. Hellwig
National Institute of Standards and Technology
Administration Building, Room A921
Gaithersburg, MD 20899
301-975-3690

Bruce R. Hermann
Naval Surface Warfare Center
Dahlgren, VA 22448
703-663-7155

Robert J. Hesselberth
Spectracom Corporation
101 Despatch Drive
East Rochester, NY 14445
716-381-4827

Jeffrey S. Ingold
Bendix Field Engineering Corporation
One Bendix Road
Columbia, MD 21045
301-964-7188

Nicolette M. Jardine
U.S. Naval Observatory
Time Service Department
34th and Massachusetts Avenue, N.W.
Washington, D.C. 20392-5100
202-653-1662

Charles J. Jensik
Piezo Crystal Company
100 K Street
Carlisle, PA 17013
717-249-2151

Jim Jespersen
National Institute of Standards and Technology
325 Broadway
Boulder, CO 80303
303-497-3849

Andrew C. Johnson
U.S. Naval Observatory
34th and Massachusetts Avenue, N.W.
Washington, D.C. 20390-5100
202-653-1022

Edward C. Jones
Naval Research Laboratory
Overlook Drive Southeast
Washington, D.C. 20375
213-643-0608

Sarunas K. Karuza
The Aerospace Corporation
2350 East El Segundo Boulevard
El Segundo, CA 90245-4691
336-6837

Richard E. Keating
U.S. Naval Observatory
Time Service Department
34th and Massachusetts Avenue, N.W.
Washington, D.C. 20392-5100
202-653-1022

Debra A. Kerns
Bonneville Power Administration
P.O. Box 3621 - EEDC
Portland, OR 97208-3621
503-230-3769

Masami Kihara
NTT Transmission Systems Labs
1-2356 Take
Yokosuka-shi Kanagawa, Japan 238-03
81 468 59 3164

William J. Klepczynski
U.S. Naval Observatory
Time Service Department
34th and Massachusetts Avenue, N.W.
Washington, D.C. 20392-5100
202-653-1521

John A. Klobuchar
Air Force Geophysics Laboratory
Ionospheric Physics Division/LIS
Hanscom Air Force Base, MA 01731
617-377-3988

David J. E. Knight
National Physical Laboratory
Queens Road
Teddington, MIDDX TW11 0LW, UK
01-943-6796

Stephen H. Knowles
NAVSPASUR
Dahlgren, VA 22448
703-663-8191

Douglas E. Koch
Naval Space Surveillance Center
Dahlgren, VA 22448
703-663-8561

Paul A. Koppang
Sigma Tau Standards Corporation
P.O. Box 1877
Tuscaloosa, AL 35403
205-553-0038

Timothy P. Krisher
Jet Propulsion Laboratory
4800 Oak Grove Drive
Pasadena, CA 91109
818-354-7577

Paul F. Kuhnle
Jet Propulsion Laboratory 298-100
4800 Oak Grove Drive
Pasadena, CA 91109
818-354-2715

Richard Kunski
Bendix Field Engineering Corporation
One Bendix Road
Columbia, MD 21045
301-964-7190

Paul J. Kushmeider
Bendix Field Engineering Corporation
MS VLBI
One Bendix Road
Columbia, MD 21045
301-964-7672

Gerard Lachapelle
The University of Calgary Surveying
Engineering
2500 University Drive, N.W.
Calgary Alta, Canada T2N 1N4
403-220-7104

Marie M. Largay
Naval Research Laboratory
Code 8323
4555 Overlook Avenue, Southeast
Washington, D.C. 20375
202-767-2595

Leonard R. Lathrem
Bendix Field Engineering Corporation
One Bendix Road
Columbia, MD 21045
301-964-7187

Felix F. L. Lazarus
Hewlett-Packard AG
150, Route du Nant d'Avril
CH - 1217 MEYRIN 2 Switzerland
022-83.81.40

Weodzimierz Lewandowski
BIPM
Pavillon de Breteuil
92370 Sevres, France
1-45-34-00-51

Gil Lieberman
Israel Military Industries
Ramat Hasharon 47 100 Israel
P.O.B. 1044
03 489222

Ronald T. Logan, Jr.
Jet Propulsion Laboratory 298/100
4800 Oak Grove Drive
Pasadena, CA 91109
818-354-2471

Pete R. Lopez
Trak Systems
4726 Eisenhower Boulevard
Tampa, FL 33615
813-884-1411

Edward M. Lukas
U.S. Naval Observatory - NOTSAS
11820 Southwest 166 Street
Miami, FL 33177
305-255-4915

George F. Lutes
Jet Propulsion Laboratory 298/100
4800 Oak Grove Drive
Pasadena, CA 91109
818-354-6210

Lute Maleki
Jet Propulsion Laboratory 298/100
4800 Oak Grove Drive
Pasadena, CA 91109
818-354-3688

Zoran M. Markovic
Federal Bureau of Measures and
Precious Metals
14 Miue Alasa
Belgrade, Yugoslavia 11000

Edward M. Mattison
Smithsonian Astrophysical Observatory
60 Garden Street, MS-59
Cambridge, MA 02138
617-495-7265

Scott E. McCarty
Navy Space Systems Activity
9037 Hargis Street
Los Angeles, CA 90034-1926
213-643-0590

W. E. McCarty
IBM
9201 Corporate Boulevard
Rockville, MD 20850
301-640-3120

Thomas B. McCaskill
Naval Research Laboratory
Code 8323
4555 Overlook Avenue Southwest
Washington, D.C. 20375
202-767-2595

Ralph E. McCollum
Naval Telecommunications Command
4401 Massachusetts Avenue, N.W.
Washington, D.C. 20394
202-282-0288

John W. McDonough
LeCroy Corporation
7000 Infantry Ridge Road
Manassas, VA 22110
703-368-1033

Henry J. McManus
USCG - Omega Navigation System Center
7323 Telegraph Road
Alexandria, VA 22310
703-866-3870

Robert W. McMurrough
Hughes Aircraft Company
3100 Lomith Building
Torrance, CA 90509
213-517-6145

Jack McNabb
Trak Systems
4726 Eisenhower Boulevard
Tampa, FL 34232
813-884-1411

Brett D. Merritt
TASC
12132 Stirrup Road
Reston, VA 22091
703-834-5000

Alan L. Milton
Computer Sciences Raytheon
P.O. Box 4127 CSR 4500
Patrick Air Force Base, FL 32925
407-853-9057

Mihran Miranian
U.S. Naval Observatory
Time Service Department
34th Street and Massachusetts Avenue, N.W.
Washington, D.C. 20392-5100
202-653-1522

Donald H. Mitchell
Austron, Inc.
P.O. Box 14766
Austin, TX 78761-4766
512-251-2313

Shawn P. Monaghan
CSE
P.O. Box 9703, Terminal
Ottawa, Ontario, Canada KIG 3Z4
613-991-7474

Louis F. Mueller
Hewlett-Packard
5301 Stevens Creek Boulevard
Santa Clara, CA 95052
408-553-2347

Frank Mullen
FTS
34 Tozer Road
Beverly, MA 01867
508-927-8220

William J. Murphy
Computer Sciences Corporation
P.O. Box 446
Edwards Air Force Base, CA
805-277-2004

James A. Murray
Sachs/Freeman Associates
6215 Houston Court
Alexandria, VA 22310
202-404-7056

Yasuhiro N. Nakadan
National Research Laboratory of Metrology
1-1-4, Umezono, Tsukuba
Ibaraki, 305, Japan
81-298-54-4035

Robert H. Neff
U.S. Air Force
AFE/TSS, Bolling Air Force Base
Washington, D.C. 20332
202-767-3968

Robert A. Nelson
Department of Physics and Astronomy
University of Maryland
College Park, MD 20742
301-454-3407

Clyde C. Norris
Computer Sciences Corporation
P.O. Box 217
Clearfield, UT 84015
801-777-4845

Allen W. Osborne
Allen Osborne Associates
756 Lakefield Road, Building J
Westlake Village, CA 91361
805-495-8420

Allan Oster
USAF Space Division
WPC Box 92960 Code: CWNUI
Los Angeles, CA 90009
213-643-1206

Terry N. Osterdock
Stanford Telecommunications, Inc.
2421 Mission College Boulevard
Santa Clara, CA 95054
408-982-5903

Howard Bryan Owings
Sigma Tau Standards Corporation
1711 Holt Road
Tuscaloosa, AL 35403
205-553-0038

Angel L. Padilla
U.S. Army
AMXTM-SS, Building 5435
Redstone Arsenal, AL 35898
876-9505- X-205

Bradford W. Parkinson
Stanford University
817 Santa Rita
Los Altos, CA 94022
415-725-4100

Ralph E. Partridge
Los Alamos National Laboratory
P.O. Box 1663, Mail Stop P947
Los Alamos, NM 87545
505-665-1617

Peter Z. Paulovich
Navelex Systems Engineering Center
P.O. Box 55
Portsmouth, VA 23705
804-396-0287

James C. Perry
National Aeronautics and Space
Administration/GSFC
Greenbelt Road
Greenbelt, MD 20715
301-286-3471

Harry E. Peters
Sigma Tau Standards Corporation
P.O. Box 1877
Tuscaloosa, AL 35403
205-553-0038

Edward L. Petroka
Kinemetrics/Truetime
3243 Santa Rosa Avenue
Santa Rosa, CA 95407
707-528-1230

Michael F. Peyton
MCI
8003 Westpark Drive
McLean, VA 22102
703-749-7381

James S. Phelps
General Electric
2010 Miracle Lane
Falls Church, VA 22043
703-866-3222

Edward D. Powers
Naval Research Laboratory
4555 Overlook Avenue, Southwest
Washington, D.C. 20375
202-404-7066

Physikalsich-Technische Bundesanstalt
Library
Bundesallee 100, P.O. Box 3345
D-3300 Braunschweig
Federal Republic of Germany

John Prestage
Jet Propulsion Laboratory 298/100
4800 Oak Grove Drive
Pasadena, CA 91109
818-354-3515

Robert E. Price
Bendix Field Engineering Corporation
One Bendix Road
Columbia, MD 21045
301-964-7437

Lori E. Primas
Jet Propulsion Laboratory 298/100
4800 Oak Grove Drive
Pasadena, CA 91109
818-354-1873

Joe W. Rahail
U.S. Navy, SSP 24235
CP 3, Room 917
Washington, D.C. 20376
202-697-5314

Eric S. Richter
Hughes Aircraft Company
Space and Communications Group
P.O. Box 92919 SC/S4/X325
Los Angeles, CA 90009
213-648-0580

William J. Riley
EG&G Frequency Products Division, Inc.
35 Congress Street
Salem, MA 01970
508-745-3200

Mao Ruida
Yong Ding Road #50
Beijing, Peoples Republic of China

Jonathan Santos
Bendix Field Engineering Corporation
One Bendix Road
Columbia, MD 21045
301-964-9648

Bruce R. Schupler
Bendix Field Engineering Corporation
One Bendix Road
Columbia, MD 21045
301-964-7901

Malvin C. Schwalje
EG&G Frequency Products Division, Inc.
35 Congress Street
Salem, MA 01970
508-745-3200 X-506

Anthony R. Seabrook
Royal Greenwich Observatory
Herstmoncelix Castle
Hailsham, East Sussex, UK
BN27 1RP
323-833171

James R. Semler
Interstate Electronics Corporation
707 East Vermont Avenue
Anaheim, CA 92803
714-758-2754

Richard T. Sharpe
Magnavox Advanced Products and Systems Company
2829 Maricopa Street
Torrance, CA 90503
213-618-1200

R. Shelley-Jones, Librarian
CSIRO Division of Applied Physics
P.O. Box 218
Lindfield, N.S.W.
Australia, 2070

Norman J. Shenton
Bendix
989 Fall Circle Way
Gambrills, MD 21054
301-964-7072

Thomas J. Skiera
Telecom Solutions
733 Lions Trail
Stone Mountain, GA 30087
404-381-5769

Oliver N. Skoglund
Pan Am World Services
2003 Byrd Spring Road
Huntsville, AL 35802
205-883-9690

James A. Slater
Defense Mapping Agency Systems Center/SGS
8301 Greensboro Drive
McLean, VA 22101
202-227-2476

Gary H. Smith
Odetics, Kode Division
1515 South Manchester Avenue
Anaheim, CA 92802
714-758-0400

Michael J. Soha
DEC, MS LKG 1-2/A19
550 King Street
Littleton, MA 01460
508-486-5678

Yanamandra V. Somayajulu
S.M. Systems and Research Corporation
8401 Corporate Drive, Suite 510
Landover, MD 20785
301-459-3322

Sarah B. Stebbins
Naval Research Laboratory
4555 Overlook Avenue
Washington, D.C. 20375
202-767-2595

Samuel R. Stein
Ball Aerospace
P.O. Box 1235
Broomfield, CO 80020
303-460-2017

Charles S. Stone
Brightline Corporation/FEI
Box 1299
Cedar Park, TX 78613
512-258-3701

David A. Stowers
Jet Propulsion Laboratory 298/100
4800 Oak Grove Drive
Pasadena, CA 91109
818-354-7055

John T. Strain
Frequency Electronics, Inc.
1688 East Jude Drive #304
Rockville, MD 20850
301-251-8990

Alvin Strauss
Frequency Electronics, Inc.
1626 Wantagh Avenue
Wantagh, NY 11793

Everett R. Swift
Naval Surface Warfare Center
Space and Ocean Geodesy Branch (K12)
Dahlgren, VA 22448
703-663-7200

Richard L. Sydnor
Jet Propulsion Laboratory 298/100
4800 Oak Grove Drive
Pasadena, CA 91109
818-354-2763

Ali Syed
Brightline Corporation/Frequency Electric
2407 South Bell Boulevard
Cedar Park, TX 78753
512-258-3701

Jimmie B. Thigpen
Naval Space Surveillance System
Building 183
Dahlgren, VA 22448
703-663-8561

Dr. Claudine Thomas
Bureau International des Poids et Mesures
Pavillon de Breteuil
92372 Sevres Cedex, France
45-34-00-51

Thomas K. Tucker
Jet Propulsion Laboratory 298/100
4800 Oak Grove Drive
Pasadena, CA 91109
818-354-2164

Kenneth M. Uglow
P.O. Box 2260
Sarasota, FL 34230
813-955-5856

Elizabeth M. Valiulis
U.S. Naval Observatory
34th and Massachusetts Avenue, N.W.
Washington, D.C. 20392-5100
202-653-1525

John L. Van Groos
Kinemetrics/Truetime
3243 Santa Rosa Avenue
Santa Rosa, CA 95405
707-528-1230

Jacques Vanier
National Research Council
Montreal Road
Ottawa, ON KIA Ot>
613-993-9326

Francine M. Vannicola
U.S. Naval Observatory
Time Service Department
34th and Massachusetts Avenue, N.W.
Washington, D.C. 20392-5100
202-653-1525

Vinicio Vannicola
U.S. Coast Guard
7323 Telegraph Road
Alexandria, VA 2?310
703-866-3840

Lester Veenstra
INTELSAT
Communications Development and Support
3400 International Drive, N.W.
Washington, D.C. 20008-3098
202-944-7090

John R. Vig
Department of the Army
U.S. Army Electronics Technology
and Devices Laboratory, SLCET-EQ
Fort Monmouth, NJ 07703-5000
201-544-4275

Frank J. Voit
The Aerospace Corporation
P.O. Box 92957 M1-110
Los Angeles, CA 90009
213-336-6764

William C. Walker
Computer Sciences Raytheon
Building 989, Mail Unit 2230
Patrick Air Force Base, FL 32925
407-494-7176

Harry T. M. Wang
Hughes Research Labs
3011 Malibu Canyon Road
Malibu, CA 90265
213-317-5431

Rabi T. Wang
Jet Propulsion Laboratory 298/100
4800 Oak Grove Drive
Pasadena, CA 91109
818-393-6944

Roger W. Ward, V.P.
Quartztronics, Inc.
1020 Atherton Drive, Building C
Salt Lake City, UT 84123
801-266-6994

Samuel C. Ward
Bendix Field Engineering Corporation
129 North Hill Street (Mail Sta 507-215)
Pasadena, CA 91106
818-584-4457

Clark S. Wardrip
Bendix Field Engineering Corporation
726 Foxenwood Drive
Santa Maria, CA 93455
805-865-3214

Hugh E. Warren
Allied Signal/NRL
4555 Overlook Avenue, Code 8323
Washington, D.C. 20375
202-404-7068

John C. Webber
Interferometrics, Inc.
8150 Leesburg Pike
Vienna, VA 22180
703-790-8500

Marc A. Weiss
National Institute of Standards
and Technology
325 Broadway, 576
Boulder, CO 80303
303-497-3261

Gart Westerhout
U.S. Naval Observatory
Time Service Department
34th and Massachusetts Avenue, N.W.
Washington, D.C. 20392-5100
202-653-1513

Paul J. Wheeler
U.S. Naval Observatory
Time Service Department
34th and Massachusetts Avenue, N.W.
Washington, D.C. 20392-5100

Joe D. White
U.S. Naval Research Laboratory
Code 8321
4555 Overlook Avenue
Washington, D.C. 20375
202-404-7060

Mark S. Whitty
MCI Telecommunications Corporation
8283 Greensboro Drive
McLean, VA 22102
703-442-5277

Robert E. Wilson
Western Area Power Administration
U.S. DOE
1250A South Plaza Way
Flagstaff, AZ 86001
602-527-7501

Warren L. Wilson
Lockheed Missiles and Space Company
707 Spindrift Drive
San Jose, CA 95139-1346
408-743-1213

Mark A. Williams
U.S. Government
CIA
Washington, D.C. 20505
703-874-0502

Louis A. Williams, Jr.
Standard Frequency Measuring Service
2092 Arrowood Place
Cincinnati, OH 45231
513-851-4964

Dr. William H. Wooden
DMASC/SGS
8301 Greensboro Drive, Suite 800
McLean, VA 22102-3692
703-285-5977

Warren K. Wordsworth
Austron, Inc.
1930 Isaac Newton Square, Suite 111
Reston, VA 22090
703-471-7963

James L. Wright
CSR
CSR 2230, Building 989
Patrick Air Force Base, FL 32925
407-494-2014

Liu Xiaofan
Yong Ding Road #50
Beijing, Peoples Republic of China

Nicholas F. Yannoni
Rome Air Development Center
Hanscom Air Force Base
Bedford, MA 01731
617-377-2206

Eric Youngblood
Hewlett Packard
5301 Stevens Creek Boulevard
Santa Clara, CA 95052
408-246-4300

Edward Yrisarri
Ball Corporation, Efratom Division
3 Parker
Irvine, CA 92718
714-770-5000

Robert R. Zeigler
Piezo Crystal Company
100 K Street
Carlisle, PA 17013
717-249-2151

Elizabeth A. Zubritsky
Bendix Field Engineering Corporation
One Bendix Road, Mail Stop: RMG
Columbia, MD 21045
301-964-7342